WAKE BURSTING: A COMPUTATIONAL AND EXPERIMENTAL INVESTIGATION FOR APPLICATION TO HIGH-LIFT MULTIELEMENT AIRFOIL DESIGN

BY

BRENT WILLIAM POMEROY

DISSERTATION

Submitted in partial fulfillment of the requirements
for the degree of Doctor of Philosophy in Aerospace Engineering
in the Graduate College of the
University of Illinois at Urbana-Champaign, 2016

Urbana, Illinois

Doctoral Committee:

Professor Michael S. Selig, Director of Research and Chair
Professor Gregory S. Elliott
Assistant Professor Leonardo P. Chamorro
Dr. John C. Vassberg

Abstract

High-lift aerodynamic flowfields are complex, and the potentially-adverse wake development associated with these high-lift systems is not fully understood. Thus, an exhaustive investigation including both experimental and computational efforts is needed to gain an increased understanding of the flowfield. Previous work indicates the strong off-the-surface adverse pressure gradients created by flaps may cause the main-element wake to "separate" in an aerodynamic phenomena known as wake bursting. Previous experimental research efforts to study wake bursting over a multielement airfoil are lacking a detailed study of the burst wakes in a wide range of spatial coordinates. In addition, no thorough comparison between the experimentally-captured data and computational simulations of a high-lift multielement airfoil has been performed.

A variety of different experimental and computational tools can be used to study the burst-wake flowfield. These experimental techniques include the standard aerodynamic-performance and flow-visualization techniques in addition to complex wake survey methods. These wake surveys can be executed with one of a variety of probes to capture unsteady or steady data such as pressures or velocities. Because all desired flowfield parameters cannot be captured by one probe, results from different probes must be carefully analyzed and compared to other data such that a full understanding of the flowfield can be gained. Computational methods to study the burst-wake flowfield must adequately solve both the inviscid and viscous regions of the flowfield. Computations can be performed with low-order coupled viscous/inviscid program in addition to more-robust Navier-Stokes solvers, such as Reynolds-averaged Navier Stokes (RANS) programs. It is necessary to carefully compare the experimental and computational results such that the flowfield can be understood in greater detail. These comparisons will also yield insight into the effects of experimental testing environments and the weaknesses of computational solvers.

Results for a three-element airfoil, consisting of a main element and a double-slotted flap, were determined using various experimental methods. Experimental results included aerodynamic polars, flow visualization, and wake surveys with both split-film and 7-hole probes. The split-film probe yielded two-dimensional unsteady velocity measurements while the 7-hole probe was use to capture time-averaged velocity vector, static pressure, and total pressure. The burst-wake region consisted of increased turbulence intensities and extremely-high turbulence production when compared to the flow outside of the wake. An increase in wake thickness with increasing downstream distance was

captured from each probe, and the relationship between the wake thickness and freestream conditions was established. Low Reynolds numbers and increased angle of attack yielded the thickest wakes of all tested freestream conditions. In addition, flaps with extremely small gap sizes also yielded increased wake bursting than the large-gap airfoils. In general, minimal differences in the burst-wake flowfield were observed for small- or large-overhang simulations, and the results are found in the experiment. Three novel criterion are proposed such that burst-wake flowfields can be readily compared to other flowfields. These thresholds are applied to determine the existence of wake bursting, the spatial point at which the wake bursts, and the severity of the wake bursting.

Two-dimensional computational results were captured for low-order and higher-order methods including both a panel code and a RANS program. In general, the RANS solver indicated larger and thicker wakes than the wakes predicted by the panel code or captured in the wake surveys. This result of larger and thicker wakes was found to be independent of the selected turbulence model. Further investigation suggested a large vortex resulted from the junction between the airfoil and the wind tunnel wall at both ends of the airfoil. These vortices introduced non-constant spanwise lift distributions for the multielement airfoil. When the effect of the vortices was considered, computational results matched the experimental data better than without the vortices, but differences still remained. These differences are attributed to difficulties in turbulence model development for computational simulations as well as limitations of the experimental probes (mainly resulting from finite probe size).

Numerous different airfoils were designed such that the presence of the burst wakes was mitigated when compared to a baseline airfoil at a given value of lift for specific freestream conditions. These three airfoils were designed using different geometry constraints and different freestream conditions. Wake bursting was reduced by moving the transition point far downstream and applying a very weak pressure gradient on the forward portion of the suction surface. Increased aft loading, increased thickness in the upstream part of the airfoil, and careful control of the boundary layer yielded increased aerodynamic performance, including reduced drag and increased lift-to-drag ratio, due in large part to decreased wake bursting.

To Leslie, my partner in Chrime

Acknowledgments

Research presented in this document would not have occurred if it were not for the love and support of many different individuals.

First, I am deeply appreciative of the technical guidance that my adviser, Prof. Michael Selig, has given to me over the last six years. My understanding of aerodynamics has greatly improved under his mentorship, and I gratefully acknowledge all of the information you have helped me learn. Whether teaching me something directly or loosely advising future directions for my research, you always wanted me to succeed in everything at Illinois.

I never would have completed this dissertation without the deep love and unwavering support of those closest to my heart. To my parents, Lin and Walt, you inspired me to never walk away from challenges but rather to embrace them with the most energy I could muster. From a very young age, you taught me that learning is important, and that the knowledge and wisdom gained through education is invaluable. To my brother Brian, my fellow aerospace Ph.D., it has been an awesome opportunity to loosely follow in your footsteps. In all my work, you encouraged me to ask, and attempt to answer, life's most challenging questions. Whether talking shop around the dinner table or talking about life, I've grown an enormous amount because of you.

The technical guidance and critical examination of my work by my committee and other professionals is deeply valued. Through meticulous inspection of this project and probing questions demanding defense and justification, the quality of my research project was greatly improved. Dr. John Vassberg provided significant guidance regarding the comparison of computational and experimental methods through numerous conversations. Experimental methods and results were improved through useful suggestions from Professors Greg Elliott and Leo Chamorro.

This project would not have been half the project it is without the technical support and guidance of my fellow AE graduate students. To Phil Ansell and Jeff Diebold, I am grateful that you both supported me in a joint project that ultimately laid the cornerstone for this research. In particular, I value Phil's deep knowledge of unsteady aerodynamics (i.e. "squiggly line plots") which was freely given to me when I was first exposed to the field. You also provided me with invaluable friendship and deep conversations (and nachos), which I still value today. Jeff – you provided an enormous amount of experimental guidance in our joint project and in the lab in general. I fondly remember our pumpkin chucker efforts and concerts at the school of music in addition to the long hours that we spent in lab together.

The help of my labmates, both past and present, is duly acknowledged including: Daniel Uhlig for guidance and mentorship, Rob Deters for 7-hole probe help, Adam Ragheb for airfoil design discussions, and Gavin Ananda for experimental and design methods. A variety of undergraduate mentees are noted including: Leigh Honzatko for 7-hole probe uncertainty quantification, Aaron Perry for implementing the foundation of the parametric sweeps and advanced wake metrics, and David Caruthers and Sarosh Hussain for assisting in the construction of the new 7-hole probe wooden sidewall and experimental setup. The early-morning radio DJ for one of the local stations provided hundreds of hours of company in the wee hours of the morning, and I thank you for that. The hardware design for the flap positioning system was assisted by Greg Williamson, a former labmate.

Numerous professional individuals supported this research, as well. In particular, the many conversations with Bob Liebeck, Eric Dickey, and Neal Harrison proved to be especially valuable and formative. Computational aerodynamicists Dick Campbell, Mohagna Pandya, and Craig Hunter provided additional enhancements and technical guidance for the USM3D code relating to my research. Finally, wind tunnel model support and repair was graciously provided by Sean Cassidy.

I am forever indebted to Leslie for your love, agape, and never-ending patience for me, my research, and all things grad school. From reading and editing my dissertation to lending a compassionate heart, you have always been there for me. Our shared joy in eternal life brings me great happiness, and I'm blessed to be sharing life with you on this journey - this adventure.

God, you have provided for me and blessed me in ways that I could never imagine. I pray that all things I do are under, and for, You and Your kingdom.

Table of Contents

List of Figures

List of Tables

Nomenclature

Symbols

English

A	=	area
a	=	curvature scaling coefficient
b	=	span
b	=	curvature exponent
C	=	a constant
C_a	=	center-hole calibration coefficient for 7-hole probe
C_b	=	center-hole calibration coefficient for 7-hole probe
C_d	=	drag coefficient
C_f	=	skin-friction coefficient
C_l	=	lift coefficient
C_m	=	pitching moment coefficient
C_p	=	static pressure coefficient
C_p	=	heat capacity at constant pressure
$C_{p,t}$	=	total pressure coefficient
C_c	=	center-hole calibration coefficient for 7-hole probe
$C_{s_{1...7}}$	=	static pressure calibration coefficient for 7-hole probe
$C_{t_{1...7}}$	=	total pressure calibration coefficient for 7-hole probe
$C_{\theta_{1...7}}$	=	cone angle calibration coefficient for 7-hole probe
$C_{\phi_{1...7}}$	=	roll angle calibration coefficient for 7-hole probe
c	=	vector defining direction of chord line
$\mathbf{c}$	=	column vector containing chord lengths of all elements

D = drag

d = probe diameter

E = split-film probe excitation voltage

E = expected value function

F = force

f = dummy function

f = frequency

G = unstructured grid source term

G_{xx} = Fourier transform

gap = gap size between two airfoil elements

H = boundary-layer shape factor

h = height of wind tunnel

h_t = stagnation enthalpy

h_w = wake thickness

I = integrated area of power spectral density

i = unit-vector in x axis direction

i = dummy index number

i = $\sqrt{-1}$

j = unit-vector in y axis direction

j = dummy index number

K_s = trailing-edge thickness parameter

K = velocity-dependent function for split-film probe calibration

k = unit-vector in z axis direction

k = thermal conductivity

k = dummy constant

k_{smooth} = relative smoothness parameter

L = lift

L = power spectral density

M = moment

M = number of values in the computationally-mapped η direction

$\dot{m}$ = mass flux

N = number of values in the computationally-mapped ξ direction

N = a number of items

n = normal vector

n = airfoil element number

n = relating to parameter n out of N values

$\mathbf{n}$ = column vector containing chord-normal vectors

$overhang$ = overhang distance between two airfoil elements

P_0 = reference power level

P_1 = measured signal power

Pr = Prandtl number

p = pressure

p = solution order of accuracy

$\overline{p}$ = average pressure of numerous holes

p_s = static pressure

p_t = total pressure

Q = grid index in computational coordinate system

q = dynamic pressure

R = gas constant

RR = range ratio

Re = Reynolds number

Rec = pressure-recovery parameter

R_w = electrical resistance of split film wire

r = dependent fidelity variable to be regularized

r = unstructured grid growth rate

r = radial distance

r = growth rate

S = planform area

S = scalar multiplier for regularization

S = unstructured grid source stretching parameter

S_w = area of wake

s = node spacing

s = unstructured grid source size

s = magnitude of wake brusting

T = temperature

t = time

t = airfoil thickness

U_t = total velocity

U_t' = unsteady fluctuation of total velocity

u = streamwise velocity component

u' = unsteady fluctuation of streamwise velocity component

V = voltage

V = velocity vector

V = dummy function

v = transverse (chord-normal) velocity component

u' = unsteady fluctuation of transverse velocity component

WTP = wake-thickness parameter

W = weighting coefficients for interpolant

w = spanwise velocity component

X = signal in frequency domain

x = imaginary representation of signal in temporal domain

x = Earth-fixed Cartesian coordinate parallel to chord line

y = Earth-fixed Cartesian coordinate normal to chord line

y^+ = nondimensional wall distance

Z = flow angularity function used in split-film probe calibration

z = Earth-fixed Cartesian coordinate in spanwise direction

Greek

α = angle of attack

α^* = angle of attack for which the velocity distribution is constant

β = sideslip angle

Γ = bound circulation

γ = spanwise circulation

γ = heat capacity ratio

Δ = a difference between two quantities

Δ = cell size

Δ = cell height in viscous layers

δ = absolute flap deflection angle

δ = average cell volume

δ = wake thickness

δ^* = displacement thickness

ε = convergence tolerance

ε = wind-tunnel correction for blockage

ζ = velocity in the ξ direction

η = computational-grid-fixed coordinate

η = nondimensional span location

θ = momentum thickness

θ = 7-hole probe cone angle

κ = solid blockage correction constant

κ = surface curvature

κ = turbulence kinetic energy

λ = local flow angle

μ = dynamic viscosity

ν = kinematic viscosity

ξ = streamwise vorticity

ξ = computational-grid-fixed coordinate

π = constant equal to 3.14159...

ρ = air density

σ = curvature correction parameter

τ = distance between isolines of $C_{p,t}$

τ_{le} = leading-edge radius

Υ = uncertainty value

ϕ = 7-hole probe roll angle

ϕ = conformally-mapped airfoil arc limit

χ = velocity in the η direction

χ = velocity-gradient correction value

ψ = source intensity factor

ω = rotational speed

Other

$\mathcal{V}$	=	model volume
$\wp$	=	turbulence kinetic energy production
∂	=	partial differential operator
∇	=	multi-dimensional gradient operator
ℓ	=	length of a linear source
SA	=	one-equation Spalart-Allmaras turbulence model
SST	=	two-equation shear stress transport turbulence model
k-ω	=	two-equation turbulence model based upon turbulent kinetic energy and specific dissipation
k-ε	=	two-equation turbulence model based upon turbulent kinetic energy and turbulent dissipation

Subscripts

A	=	axial
abs	=	absolute
amb	=	ambient
b	=	boundary condition
cal	=	of or relating to data collected during a calibration
cor	=	corrected value
d	=	a downstream location
e	=	edge
$film$	=	relating to the split-film probe
l	=	pertaining to the lower portion of the wake
le	=	leading edge
M	=	moment
ME	=	main element
max	=	a maximum value
$meas$	=	value as measured in wind tunnel
min	=	a minimum value
N	=	normal
n	=	parameter relating to element n
$offset$	=	relating the cruciform center to model center

ref = reference condition at beginning of wind tunnel run

rel = relative

run = data acquired during a wind tunnel run

s = static

sb = solid blockage

ss = settling section

sys = corresponding to the airfoil system

t = total

$true$ = actual value of parameter without experimental effects

ts = test section

u = pertaining to the upper portion of the wake

u = an upstream location

unc = uncorrected value

w = pertaining to the wake

wb = wake blockage

∞ = freestream conditions

0 = initial condition

1, 2, ... i = pertaining to data point i

Superscripts

$(\tilde{})$ = dimensionless value of variable

$(\bar{})$ = temporal mean value of variable

$(')$ = force or moment per unit span

$(')$ = unsteady fluctuation

$(\hat{})$ = unit vector

(1, 2, ...) = transformation index (contained in parentheses)

Abbreviations

CMM = coordinate measuring machine

CNC = computer numerical control

DOF	=	degrees of freedom
FPS	=	flap positioning system
GTC	=	Grid Tool Cocoa
NASA	=	National Aeronautics and Space Administration
PSD	=	power spectral density
RANS	=	Reynolds-averaged Navier Stokes
RMS	=	root mean square
RPM	=	revolutions per minute
TetrUSS	=	Tetrahedral Unstructured Software System
TKE	=	turbulence kinetic energy
UIUC	=	University of Illinois at Urbana–Champaign

Chapter 1

Introduction

1.1 High-Lift Aerodynamics

High-lift systems are integral to the performance in a variety of vehicles, most notably for aircraft and high-performance race cars. These systems, which include multiple different airfoils (or multielement airfoils), generate increased lift when compared to a standard single-element airfoil, and have been studied for nearly 100 years. While the topic has been of interest since early aircraft development, high-lift aerodynamics are still being studied. A variety of aerodynamic elements can be used in a high lift system such as a main element, slats and flaps. Slat performance is not of particular interest in the current study, and thus the discussion will be limited to trailing-edge flaps.

Trailing-edge flaps were pioneered by both the Royal Aircraft Factory and the Fairey Aviation corporation. The first design and tests of flaps and high-lift systems were performed by the Royal Aircraft Factory in 1913, but a practical method to operate these flaps was not implemented until 1917 in the Fairey Aviation Parnall-built Hamble Baby float plane shown in Fig. 1.1 [1, 2]. The Fairey Hamble Baby, a modification of the Sopwith Baby, contained pilot-controlled variable-placement flaps to improve lift in both takeoff and landing conditions. Originally designed as flaperons, the trailing-edge simple flaps, referred to as the Fairey Patent Camber Gear, were able to increase lift over the wing and thus improve both takeoff and landing performance. As the bodies of water in which the takeoff

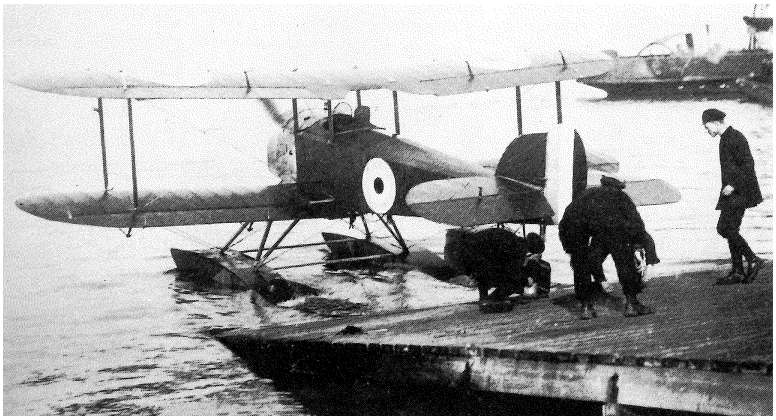

Figure 1.1: Fairey Hamble Baby aircraft with trailing-edge flaps (taken from Ref. 1).

or landing occurred generated significant drag over the floatplane pontoons, the takeoff length for the weak-engined World War I aircraft was quite long. In addition, the increased lift on the Hamble Baby aircraft, which was a result of the trailing-edge flaps, allowed the plane to be landed in both large and small lakes, and this was especially important as the versatile aircraft was generally used for coastal-protection missions [1].

Numerous types of leading- or trailing-edge surfaces can be incorporated into wing design, and these flaps are selected based upon design constrains and desired performance. A photograph of a commercial transport aircraft during a landing maneuver with all high-lift devices deployed is shown in Fig. 1.2. The leading-edge flaps and trailing-edge slats are labeled. Leading edge high-lift devices, known as slats, are extended in front of the wing and generally used to increase performance at high angles of attack and increase the stall angle of attack. Trailing-edge flaps are implemented to increase the camber of the multielement airfoil system; the most-commonly-used flaps include the plain flap, single- or double-slotted flap, and Fowler flap. Other less-common flaps include the split flap, Junkers flap, and Gurney flap. Information presented in this dissertation primarily concerns a double-slotted Junkers flap.

High-lift systems are critically important to achieve the desired takeoff and landing metrics for aircraft. A typical high-lift system may consist of a leading-edge slat and one or more trailing-edge flaps. Takeoff conditions require the aircraft to decrease the takeoff velocity to attain a given runway distance and to climb out of the aircraft with minimal distance. However, when the landing conditions are considered, it is desired to decrease the stall speed by increasing $C_{L,max}$ to minimize both the acoustic footprint and landing field length. Because of these desired characteristics, aircraft L/D in the takeoff configuration is considered as well as the value of C_L for a high-lift system. On the other hand, landing configurations typically emphasize high values of C_L with minimal consideration to L/D. The aerodynamic

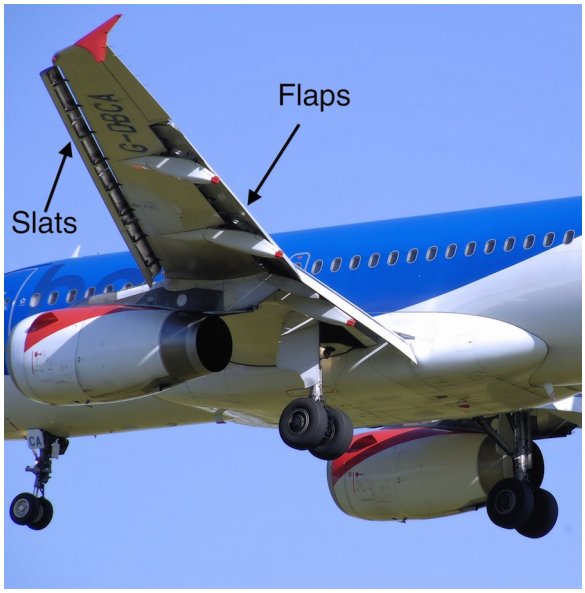

Figure 1.2: Commercial aircraft during landing with high-lift devices deployed.

performance of a high-lift system can dramatically affect the performance parameters of the entire aircraft, and these effects are highlighted in trade studies performed in the preliminary design environment. Mack and McMasters [3] performed some trade studies for a generic 150-passenger with a range of 2,700 nm in 1992. They concluded that a 5% increase in takeoff L/D results in an 11% increase in range for a given payload while a 5% increase in $C_{L,max}$ during landing results in a 20% increase in payload fraction for a given approach speed. Typically, the increased lift of a high-lift system is of greatest interest, but the effect of drag cannot be neglected. In landing conditions, it may be desirable to somewhat increase the drag of the aircraft to increase the glide slope of the aircraft, but minimal drag is desired upon takeoff. These two design considerations must be appropriately considered in the design process.

As previously mentioned, high-lift systems are central to improving the performance of high-speed race cars. A set of multielement airfoils, or rather wings, generate increased downward-pointing lift (or down force) at both the forward and aft part of the car. As a certain quantity of friction is needed for the car to not spin out in a corner, increased downforce increases traction and improves cornering speed. In general, the rear wing, which is closely regulated, is used to maximize the down force for the car while the forward wing is used to trim the aerodynamic performance. In addition to the complex high-lift flowfield, the aerodynamics of race car wings is further complicated by low-aspect-ration wings and low-Reynolds-number effects. Freestream Reynolds numbers between 0.5×10^6 and 3×10^6 may be encountered for a variety of different race cars, and the control of laminar-separation bubbles to yield increased performance is critically important in this Reynolds-number regime.

The classic paper by Smith [4] in 1975 presents a detailed discussion of multielement airfoil aerodynamics. When considering a main element with one or more flaps, five different aerodynamic effects yield increased lift over the airfoil. The slat effect, one of the five topics, is not of interest in this dissertation and thus will not be discussed. The four flap effects include the circulation effect, dumping effect, off-the-surface pressure recovery, and fresh-boundary-layer effect. In general, these four topics are so closely intertwined that one cannot definitively quantify the effect of one of the four topics, but rather the combined effect of all four topics must be simultaneously considered. Each of these four topics focused upon flaps are discussed in the following paragraphs as discussed in Smith [4].

Lift is increased through what is known as the circulation effect. Consider a single-element airfoil with a lumped vortex located immediately behind and below the airfoil trailing edge, as sketched in Fig. 1.3. The point vortex represents the circulation caused by a single slotted flap. Due to the point-vortex circulation, the flow near the trailing edge of the element occurs at a slightly increased angle of attack, α. Consequently, the circulation around the airfoil must increase to satisfy the Kutta condition in which the stagnation point is located at the airfoil trailing edge. The airfoil/vortex combination together satisfy the Kutta condition, but the pressure distribution over the main element without the presence of the vortex does not itself satisfy the Kutta condition. As noted in Smith [4], a point vortex located anywhere near the trailing edge of an airfoil will affect the lift of the airfoil. Thus, the position of the flap is

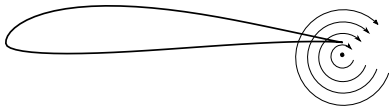

Figure 1.3: Multielement airfoil including a single element and a point vortex representing a slotted flap.

critical to generate the most lift. While a point vortex alters the lift for the multielement airfoil, the circulation effect can be more widely stated in which any device which affects the chord-normal velocity will in turn change the lift over the airfoil.

The second effect discussed by Smith [4] is the dumping effect, which is closely related to the aforementioned circulation effect. A point doublet/vortex pair representing a slotted flap will introduce increased streamwise flow velocity in which the flow from the main-element is "dumped" into a region with increased velocity relative to the freestream condition. As the flow over the airfoil is dumped into a faster velocity field, the pressure at the airfoil trailing edge is less than if the air were dumped into a flowfield without the point vortex. Consequently, the decreased trailing-edge pressure decreases the pressure that must be recovered over the airfoil when compared with a single-element airfoil in isolation. The decreased pressure recovery is significantly more favorable to boundary layers over the airfoil and may reduce/eliminate flow separation.

Thirdly, it is noted that the pressure can be recovered by not only the main element, but also in the wake region shed from the airfoil. This so-called off-the-surface pressure recovery may be more efficient than if all the pressure recovered over the main element airfoil surface [4]. As boundary layers are more prone to separation than wakes, it is possible that the pressure gradient applied to a boundary layer may cause it to separate while the flow in the wake is well behaved [5]. However, a sufficiently-large adverse pressure gradient in the wake may cause the wake to separate from itself in a phenomena known as wake bursting. The contents of this dissertation include an investigation into burst wakes.

Finally, multielement airfoils yield improved aerodynamic performance relative to a single-element airfoil as a new boundary layer begins with each element [4]. The fresh, thin, boundary layers over a flap element are thinner and may be laminar if the airfoil is properly designed. In addition, thinner boundary layers are less prone to separation for a given adverse pressure gradient than thicker boundary layers. Consequently, a stronger adverse pressure gradient can be applied to a flap element than the pressure gradient over a single-element airfoil.

Many research projects have studied the aerodynamic performance of multielement airfoil systems through either experimental wind tunnel tests or computational simulations. Experimental studies of multielement airfoils were first performed in the 1940s and were studied as part of the classic two-dimensional tests by Abbott and von Doenhoff [6] and additional tests performed by Jacobs, et al. [7]. Since these tests, many studies have attempted to determine the "best" flap and slat location for a multielement airfoil flowfield. With increased CFD capabilities and optimization

methods, some researchers have optimized both the shape of the multielement airfoils as well as the location of the slats and flaps relative to the main element [8–18]. While these simulations may provide a result indicating the optimal geometry for the multielement airfoil, limitations in the capability of Reynolds-averaged Navier Stokes (RANS) simulations must be considered.

Numerous flight-test campaigns have been executed to evaluate high-lift systems during flight, and some of these studies have been compared to experimental and/or computational data [12, 13, 19–25]. Some of the most comprehensive efforts were part of the DLR HIVNA program in which an Airbus A320-232 D-ATRA was flown with a variety of high-lift device settings, and the flight regimes of interest included both takeoff and landing configurations. Tests were performed in steady-level flight as well as in an aerodynamic stall. Numerous instruments were installed on the aircraft to study the flow including cameras and image pattern markers, hot films, pressure taps, and surface flow visualization. As a result of this project, it was learned that wing and flap deformation can significantly affect the high-lift aerodynamic flowfield, and that these surface deflections should be considered in the wing rigging process. Data collected in this project were used to improve computational programs.

Considerable efforts have been made to develop methods which accurately predict high-lift multielement airfoil flowfields, and many of these results have been discussed in great detail during the two AIAA CFD High-Lift Prediction Workshops [26–29]. Some of the key conclusions of these concentrated efforts indicate that simulations tended to under-predict lift, drag, and the magnitude of pitching moment when compared with experimental data. In general, industry-standard one- and two-equation turbulence models yielded nearly-identical results. Results indicate it may be necessary to accurately model experimental hardware (support brackets and pressure tube bundles) in the simulation when attempting to capture performance near stall. Overall, velocity profiles in the wakes agreed well between most structured and unstructured codes when there was sufficient grid refinement in the wake region.

Despite advances in computational models and solvers, high-lift flowfields are still difficult to capture computationally. In general, most turbulence models for RANS solvers have been developed to accurately capture boundary layers around an aerodynamic body, and thus these solvers are not necessarily capable of accurately predicting wakes. Because of these limitations, RANS methods can have limited accuracy in the prediction of massively-separated flows. Because of these challenges, evidence suggests the existence of non-unique flowfield solutions for a given geometry, operating conditions, and computational grid in which as many as eight different machine-zero flowfields have been predicted [30, 31]. This behavior is attributed to differences in the initial guess for the computational domain and to the iteration path history. Typically, the freestream solution is taken as the initial guess for the calculation, but this is not always the case. Alternatively, a previously-computed solution at a different α could be used as an initial guess such that hysteresis effects can be captured. Additional non-unique solutions have been found with different treatment of the boundary conditions in the early iterations for the solver or through a wide variety of initial guesses for the

flowfield. Overall, the existence of non-unique flowfields can be caused by differences in the path history through the iterations or to the initial guess supplied to the solver.

Results from various studies indicate that aerodynamics of high-lift systems are sensitive to the location and size of the gap between elements. In general, a smaller gap accelerates the flow more rapidly while a large gap does not accelerate the flow as much. However, confluent boundary layers and complex wake interactions can adversely affect the performance of the system if the gap is too small [32]. A smaller gap increases the magnitude of the suction peak of the flap and may reduce drag compared to a larger gap configuration [16, 33]. Reduction in gap size can also reduce or eliminate separation over the flap, but small gaps may be more sensitive to earlier stall than larger gap configurations [32, 33]. Experimental and computational results indicate the best gap size is typically between 1.3% and 2.0% system chord for a wide Reynolds number range ($1 \times 10^6 \leq Re \leq 9 \times 10^6$) [15, 33–36].

Performance as a result of the overhang distance of the flaps has not been studied in the literature in as much detail as the effect of the gap. While a few studies are presented in the open literature, such as the 1975 work by Smith [4], a significant amount of research has been performed in industry. However, this knowledge is proprietary, and thus the public is not privy to these findings. As far as the author knows, the location of the flap was first discussed in 1975, but limited discussion regarding overhang distances was presented [4]. According to Lin, et al. [34], the best overhang value is approximately -0.25%, which indicates the leading edge of the flap is behind the trailing edge of the previous element. A positive overhang corresponds to an element which is tucked under the previous element, and a negative overhang indicates the leading edge of an element is aft of the trailing edge of the previous element. If the overhang is too far behind the trailing edge, the flow will not be accelerated around the leading edge of the flap, and the flap will not create as much lift as compared with a case with a smaller overhang [34]. Additional tests by Coiro, et al. [15] indicate the best overhang is between 2% and 3% for $Re \approx 4 \times 10^6$, which is different than the best value of -0.25% suggested by Lin. It is worth noting that Coiro, et al. did not study cases with a negative overhang. It has also been observed that an overhang that is too far forward will accelerate the flow over the lower surface of the previous element and cause a decrease in lift of the previous element [15]. Thus, as previously mentioned, the "best" flap location is different for various multielement airfoils as this location is a function of the airfoil geometry. This conclusion is further supported by the contradictory results between Lin [34] and Coiro [15].

1.2 Wake Behavior in Adverse Pressure Gradients

Multielement airfoils generate strong adverse pressure gradients that can adversely affect wakes generated by each element. Wake interactions off the surface of multielement airfoils can be highly complex and difficult to predict. The pressure field off the surface of the airfoil system is driven by the shape and location of each element as well

as the wake behavior of each element. Research indicates that these strong adverse pressure gradients can affect the shape of the wakes in an undesired manner. If adverse pressure gradients are strong enough, the wakes may merge and interact or even burst. Burst wakes are characterized by a rapid thickening and deceleration of the flowfield and have been shown to dominate flowfields and reduce $C_{L,max}$ in some instances. A thicker wake effectively decambers the multielement airfoil system resulting in a reduction of C_L at a given α compared to a non-burst wake. These large wakes also suppress, or flatten, the C_p curve over the flaps such that the flaps produce markedly less lift than if the wake was not burst. Thus, the performance of the multielement airfoil system can be greatly influenced by the presence of burst wakes.

Despite limited knowledge of burst wakes, this flowfield has been of interest for many years. Wake bursting was first observed and discussed through flight tests in 1958 on both a full-scale Cessna O-1/L-19 Bird Dog and a Super Cub L-21 [25]. The study, which analyzed the effect of boundary-layer flow control, high-lift airfoil design, and effect of planform shape were analyzed with respect to aerodynamic performance in takeoff configurations. The single-slotted airfoil on the Cessna aircraft was of particular interest in the project. Despite entering an aerodynamic stall, surface mini tufts showed that the flow over the wing surface was fully attached. Further observations indicated that a large low-velocity wake region was present immediately above and behind the multielement airfoil. The researchers observed this region of flow reversal in the wake of the flap and correctly attributed the loss of lift to the separated wakes. Ultimately, the researchers asserted that a better-designed slot between the main element and the flap would reduce the effect of the separated wake, deemed "wake bursting," and improve aerodynamic performance. The first investigation into airfoil design and wake bursting indicated that wake bursting could be mitigated if the boundary layers from all elements did not merge and become confluent. Later studies confirmed the burst-wake hypothesis and observed that the burst wake of a flap can cause an aircraft to stall, despite the flow being attached to the surface of the main element and all flaps [37]. The region of flow reversal was observed to grow in thickness with increasing angle of attack and flap deflection angle, and the burst wake limited the maximum obtainable lift for the high-lift system.

Research concludes that burst wakes (characterized by rapid wake thickening, decreased centerline velocity, and possibly flow reversal) are due to the streamwise pressure gradient [4, 38–48]. Investigations have studied wake bursting in either a "real" or "simulated" environment, and key results from each of these methods are discussed herein. Wake bursting can be caused by the pressure gradient imposed by one or more flaps in a multielement airfoil flowfield, as documented by a few experimental investigations [38, 39, 49–52]. The focus of some of these research projects with multielement airfoils was to determine the turbulence intensity values to aid turbulence model development [38, 39, 50, 51]. To date, only one project has focused on the various effects that can strengthen or weaken wake bursting over a multielement airfoil flowfield [39]. This investigation in the NASA Langley LTPT (low-turbulence pressure tunnel) concluded that larger angles of attack yield thicker wakes with larger velocity deficits along the wake centerline.

Additionally, wake bursting was observed to increase with smaller gap sizes. Larger gaps were found to exhibit less wake spreading and less wake merging when compared to the small-gap configuration. Finally, lower Reynolds numbers were found to increase the size of the main element wake and shift the entire wake structure further from the flap surface.

Simulated wake bursting has been invoked on wakes by imposing a streamwise pressure gradient from any device other than an airfoil (or airfoils) in cascade with the main element. Numerous researchers have generated constant or variable pressure gradients with the use of moveable wind tunnel walls or mirrored airfoils [40–48]. All of these studies created a wake from a flat plate and then burst the wake from the flat plate with strong pressure gradients. Similar to the multielement airfoil flowfield wake bursting, a number of these studies captured turbulence intensities to aid in turbulence model development.

Chapter 2

Goals and Objectives

The overall goal of this research is to use computational and experimental tools to understand wake bursting of multielement airfoils and to determine the aerodynamic performance and the corresponding fluid mechanics in the multielement airfoil flowfield. Experimental studies of wake bursting over a multielement airfoil were previously lacking, as previously discussed, and this research serves as a way to characterize the behavior of burst wakes over multielement airfoils with numerous different experimental methods. Detailed comparisons will be made between these experimental data and different computational simulations. In some cases, it has been shown that computational methods poorly predict some high-lift aerodynamic flowfields, and thus detailed comparisons will be made between the computational simulations and the experimentally captured data. It is of particular interest to establish and quantify the deficiencies of these computational codes such that the models can be further improved. Information gathered during these investigations will be synthesized to supply a set of design considerations which will then be implemented to design a family of multielement airfoils with decreased wake bursting. The specific goals of this research include:

1. Increase the understanding of turbulence in multielement airfoil burst wakes using high-frequency unsteady measurements to determine the role of turbulence in burst wakes with flow curvature

2. Develop a methodology to quantitatively define different regions of the burst wake and to determine differences in turbulent fluctuations between these locations to characterize similarities and differences within the flowfield

3. Determine the wake behavior at downstream locations for numerous different multielement airfoil configurations to understand the developing and merging wakes that can lead to wake bursting

4. Evaluate the effects of different airfoil configurations (including changes in gap size, overhang distance, and deflection angle), Reynolds number, and angle of attack on the viscous-dominated wake in an effort to develop an understanding regarding how to decrease the effect of wake bursting

5. Design a series of multielement airfoils which reduce or eliminate the presence of wake bursting, thus significantly improving aerodynamic performance of the airfoils, as predicted by computational methods

None of these goals have been addressed in any literature, and thus these goals will add to the knowledge of high-lift aerodynamic flowfields. Throughout this document, each of these goals will be directly addressed in which each goal is accompanied by an extensive and exhaustive discussion.

Chapter 3

Experimental and Computational Methodology

This chapter describes the experimental and computational methods and tools that were used during the course of this research project. First, a description of the geometry and coordinate systems is presented to define the multielement airfoil nomenclature. Then, a discussion of the experimental facilities is presented, including both the historic "baseline" setup as well as an overview of the new equipment that was designed and fabricated; the models tested are also presented. The computational and design codes are then discussed in the latter portion of this chapter. Efforts were made to provide as many details regarding the operation and use of these tools to provide a strong starting point for future researchers who may utilize these tools.

3.1 Coordinate Systems

A wide range of multielement airfoils were designed, analyzed, and tested over the course of this dissertation. A representative multielement airfoil consisting of one main element and two flaps is presented in Fig. 3.1. As shown in the figure, the angle of the main element chord line was set to be 0 deg, and the system chord line was prescribed to be unity. Two different coordinate systems were used to define the location of each element in the airfoil system including an absolute coordinate system and a relative coordinate system. Throughout this section, coordinates are

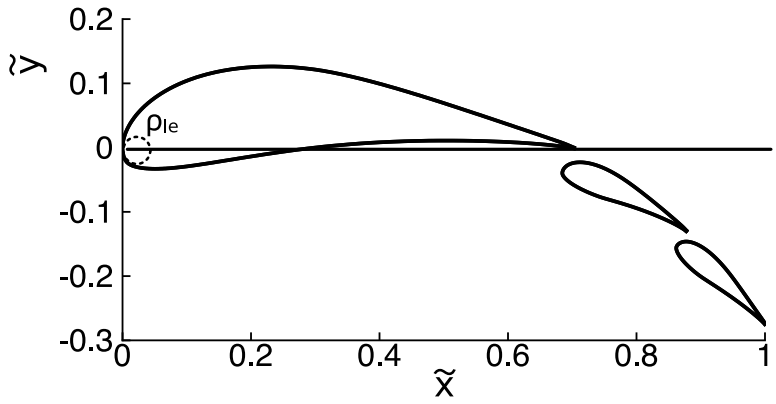

Figure 3.1: Representative three-element airfoil.

presented using a notation such as x_i^j which denotes the j^{th} x value of element i. If all indices are represented, then the notation is simply x_i to represent all x values in element i. It is noted that j is a numeric value, but it is sometimes represented with LE or TE which correspond to the numeric index at the leading and trailing edge, respectively.

3.1.1 Absolute Coordinate System

A coordinate system was used to define the location of each element in terms of a leading-edge coordinate $(x,y)_i^{LE}$ and an absolute deflection angle $\delta_{abs,i}$, as shown in Fig. 3.2. The deflection angle of each flap element was defined relative to the main-element chord line, and a positive deflection angle corresponds to a downward (clockwise) flap deflection. The leading edge of the main element was located at $(0,0)$, and the leading edges of each element were located at the prescribed spatial positions. As discussed later in this document, the system chord length for the multielement airfoil was defined to be unity for all airfoils. Thus, for airfoils in which the flaps are rigged in a location other than that of the baseline airfoil, $x_{te_1} \neq 0.70$, the value of x_{te_1} for the baseline airfoil.

3.1.2 Relative Coordinate System

A second coordinate system, deemed a relative coordinate system, was used to define the location of each element by parameters that govern the flow (including gap size, overhang distance, and relative deflection angle) as seen in Fig. 3.3. The gap size between elements (gap_i) was defined as the distance from the trailing edge of element i to the closest point on element $i+1$. Secondly, the overhang distance $(overhang_i)$ between element i and $i+1$ was defined as the distance from the leading edge of element $i+1$ to the trailing edge of element i projected along the chord line of element i, as shown in the lower portion of Fig. 3.3. Finally, the relative deflection angle $(\delta_{rel,i})$ is the angle between the chord line of element i and the chord line of element $i+1$ in which a positive deflection angle corresponded to a downward flap deflection.

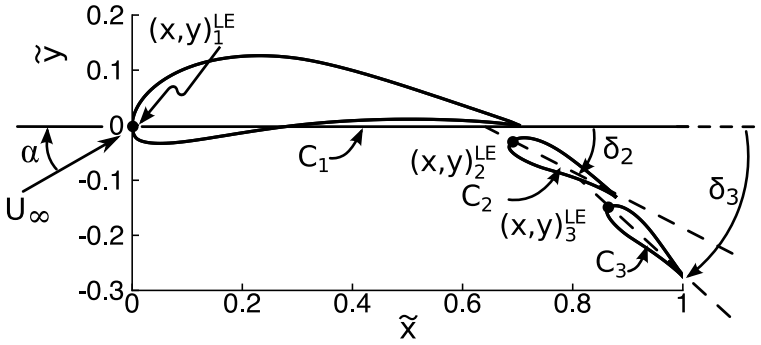

Figure 3.2: Definition of absolute coordinate system.

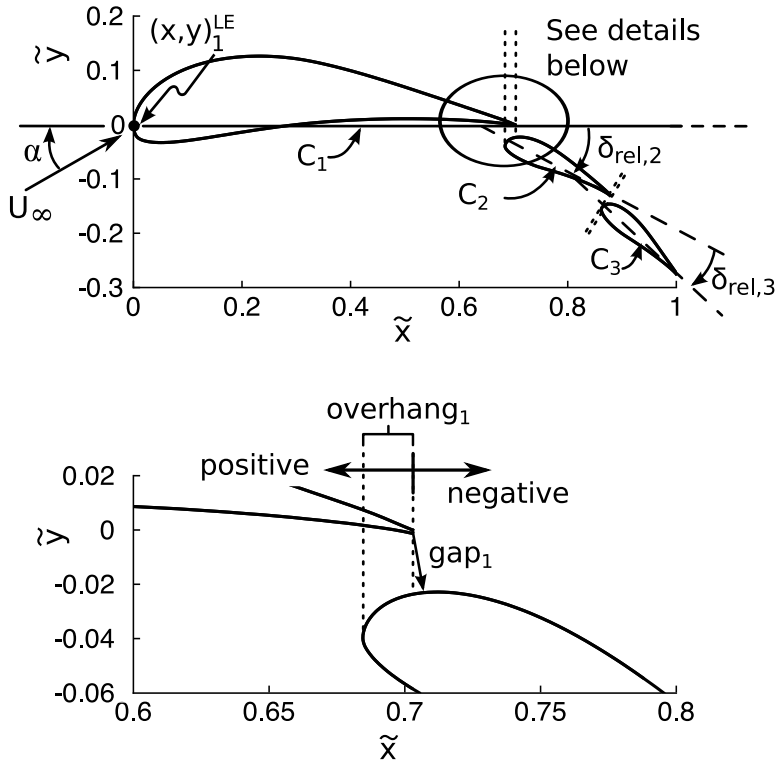

Figure 3.3: Definition of relative coordinate system.

3.1.3 Geometry Generation

A computer program was written to generate a multielement airfoil system based upon desired relative coordinate values. Inputs to the program included the desired relative chord lengths, gap sizes, overhang distances, relative deflection angles, and the element to which the relative coordinates are defined. While the coordinate transformations for c, δ_r, *overhang*, and *gap* are linear and can be implemented with algebraic and trigonometric closed-form solutions, an iterative scheme was employed to satisfy the system chord length of unity. First, the main element was scaled and located such that the leading edge and trailing edge of the airfoil were colocated on the x axis. Elements two through n, where n is the number of elements, were then scaled and moved to satisfy the desired input values by use of four different transformations.

As all four transformations (chord length, rotation angle, overhang distance, and gap size) are linear transformations, these steps can be performed in series without invalidating previous geometric manipulations. In this discussion, the notation $x_i^{(a)j}$ is used to denote the x values of element i after application of the a^{th} transformation concerning airfoil coordinate index j. As previously mentioned, j is a numeric value, but it can also be represented with LE or TE which correspond to the index at the leading or trailing edge, respectively. The superscript a is bounded inclusively between 0 and 4, and the superscript corresponds to the following transformations that have been applied to the airfoil:

(0) unit-chord airfoil; provided as input

(1) elemental chord lengths scaled

(2) rotated to δ_{rel} (rotation only)

(3) overhang transformation complete (translation only; affects absolute chord length and nondimensional overhang distance)

(4) gap size specified; final geometry (translation only; affects absolute chord length and nondimensional gap size)

Please note: while these transformations are linear, they both affect and depend upon the absolute chord length of the multielement airfoil. Hence, this cyclic dependence is solved iteratively.

Consider the movements associated with element i which is defined relative to element f. In many cases, $f = i-1$, but this is not always the case. For this reason, the equations are presented to some arbitrary element f instead of element $i-1$. The unit-chord airfoil, represented by $(x,y)_i^{(0)}$, was first scaled to the desired predicted chord length of element i by

$$\begin{bmatrix} x_i^{(1)} \\ y_i^{(1)} \end{bmatrix} = c_i \begin{bmatrix} x_i^{(0)} \\ y_i^{(0)} \end{bmatrix} \tag{3.1}$$

where c_i is a scalar number specifying the desired chord length. It is important to note that the chord length of the airfoil system after this first transformation is not necessarily the desired chord length of the multielement airfoil. The final chord lengths were determined through an iterative process such that the system chord length was unity. This iterative process will be discussed in further detail later in this section. Nevertheless, the chord vector for element i was defined by

$$\mathbf{c_i} = \begin{bmatrix} x_i^{(1)TE} - x_i^{(1)LE} \\ y_i^{(1)TE} - y_i^{(1)LE} \end{bmatrix} \tag{3.2}$$

from which the unit-vector chord was calculated by the vector norm $\|\mathbf{c_i}\|$ such that

$$\hat{\mathbf{c}}_\mathbf{i} = \frac{\mathbf{c_i}}{\|\mathbf{c_i}\|}. \tag{3.3}$$

The vectors normal to each chord line were

$$\mathbf{n_i} = \begin{bmatrix} y_i^{(1)LE} - y_i^{(1)TE} \\ x_i^{(1)TE} - x_i^{(1)LE} \end{bmatrix} \tag{3.4}$$

which were subsequently normalized by

$$\hat{\mathbf{n}}_\mathbf{i} = \frac{\mathbf{n_i}}{\|\mathbf{n_i}\|}. \tag{3.5}$$

Knowing that $\delta_{abs,f}$, the absolute deflection angle of element f, was

$$\delta_{abs,f} = -\arctan\left(\frac{y_f^{TE} - y_f^{LE}}{x_f^{TE} - x_f^{LE}}\right), \tag{3.6}$$

the deflection angle $\delta_{abs,i}$ was readily calculated by

$$\delta_{abs,i} = \delta_{abs,f} + \delta_{rel,i}. \tag{3.7}$$

A left-handed rotation was subsequently applied to $(x,y)_i$ to yield

$$\begin{bmatrix} x_i^{(2)} \\ y_i^{(2)} \end{bmatrix} = \begin{bmatrix} \cos\delta_{abs,i} & \sin\delta_{abs,i} \\ -\sin\delta_{abs,i} & \cos\delta_{abs,i} \end{bmatrix} \begin{bmatrix} x_i^{(1)} \\ y_i^{(1)} \end{bmatrix}. \tag{3.8}$$

The third transformation was an x-y spatial transformation to yield the proper overhang distance. As defined in Fig. 3.3, the overhang distance is defined as the distance (in percent chord) that element i is "tucked under" element f projected along the chord line of element f. As shown in Fig. 3.4, the furthest point of element i "forward" along the chord line of element f is not necessarily $(x,y)_i^{LE}$. In the figure, a gray line is presented which passes through the leading and trailing edge coordinates of the airfoil system, but the point that is tucked furthest forward is plotted as a blue triangle. The point was determined as the index at which

$$\min\left(\begin{bmatrix} x_i^{(2)} - x_f^{TE} \\ y_i^{(2)} - y_f^{TE} \end{bmatrix} \cdot \hat{c}_f\right) \tag{3.9}$$

occurred; let this index be denoted by j. Thus, the overhang transformation was applied through

$$\begin{bmatrix} x_i^{(3)} \\ y_i^{(3)} \end{bmatrix} = \begin{bmatrix} x_i^{(2)} \\ y_i^{(2)} \end{bmatrix} - \begin{bmatrix} x_i^{(2)j} \\ y_i^{(2)j} \end{bmatrix} + \begin{bmatrix} x_f^{(2)TE} \\ y_f^{(2)TE} \end{bmatrix} + overhang_i \begin{bmatrix} -\cos\delta_{abs,f} \\ \sin\delta_{abs,f} \end{bmatrix}. \tag{3.10}$$

The final transformation, to yield the appropriate gap size, was an iterative process. As the element was moved to different gap locations, the $(x,y)_i^k$ at which the gap is minimized changes. This point k is plotted as a small red circle in Fig. 3.4 and the gap size is denoted as a solid red line. Thus, as the index changed with differing gap sizes, a closed-form solution does not exist and an iterative process was employed. Even though iterations were utilized,

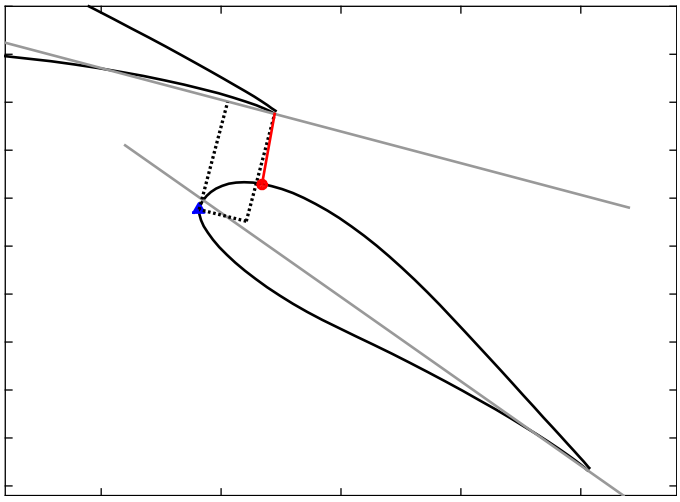

Figure 3.4: Summary of geometric transformations to generate geometry from relative coordinates.

linear non-destructive transformations were implemented within the iterative loop such that previous transformations were not invalidated. It was assumed that the user specified a sufficiently-good guess for the chord lengths such that the system chord length was fairly close to unity. Thus, the position of element i was adjusted to be

$$\begin{bmatrix} x_i^{(4)} \\ y_i^{(4)} \end{bmatrix} = \begin{bmatrix} x_i^{(3)} \\ y_i^{(3)} \end{bmatrix} + gap_i \cdot \hat{\mathbf{n}}_\mathbf{f}. \tag{3.11}$$

After all four of these transformations were applied, the system chord length, as defined in Fig. 3.1, was calculated. The length of the elemental chords ($\mathbf{c}$) was then adjusted using a Newton-Rhapson scheme until the system chord length was unity (to within a given ε). The system typically converged in less than five iterations. Upon convergence, the multielement geometry was complete, and the coordinates were saved. This global scaling included scaling of the main element and both flaps.

3.2 Experimental Facilities and Methods

Experiments conducted for this study were performed in the Aerodynamics Research Laboratory at the University of Illinois at Urbana–Champaign, and all experiments were completed prior to the new construction for the 2015 lab addition. An overview of the lab, prior to the addition, is presented in Fig. 3.5. The laboratory is divided into a control room, a large high-bay room, a model shop, and the plasma center. Data acquisition was monitored from the control room through use of the DAQ computer, and some measurement equipment was mounted on the tunnel control rack. As shown in the figure, two subsonic wind tunnels are housed in the high-bay room, and the 3×4 ft tunnel was used

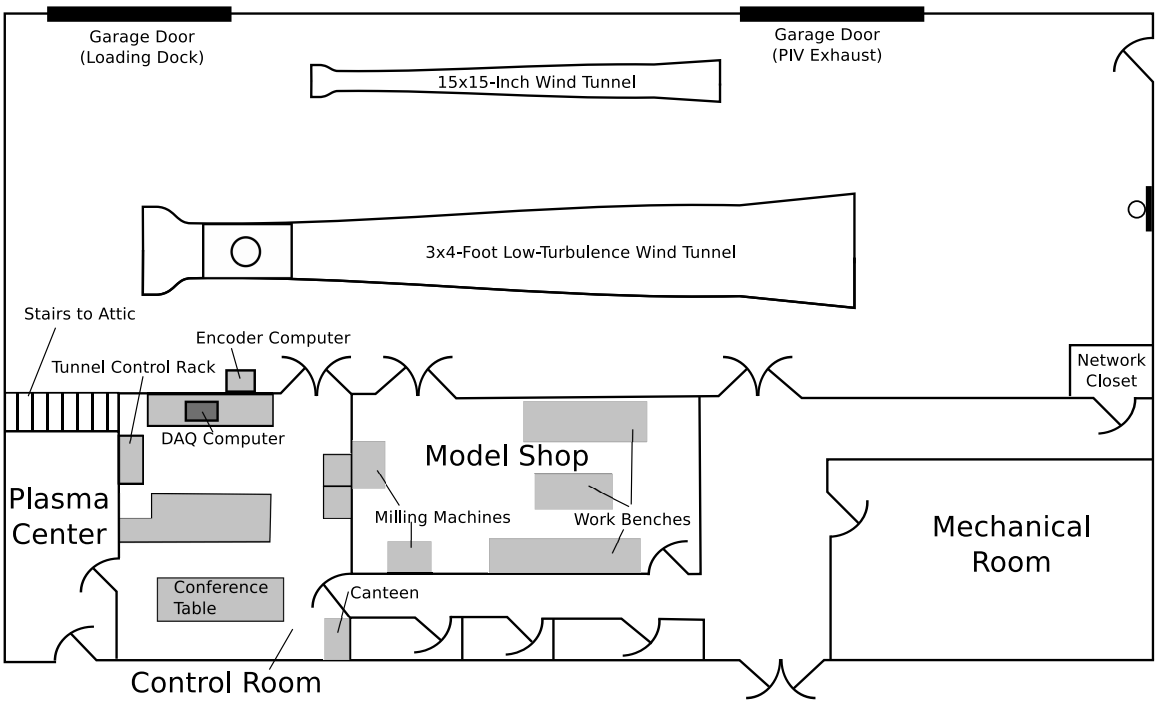

Figure 3.5: University of Illinois Aerodynamics Research Laboratory prior to addition completion (wind tunnel drawings not accurate to scale).

during this project. Simple parts were machined using the mills and tools available for student use in the model shop, and higher-quality parts were manufactured after the acquisition of a new digital-read-out end-mill machine.

3.2.1 Wind Tunnel Overview

Aerodynamic tests were performed in the University of Illinois low-speed low-turbulence wind tunnel as sketched in Fig. 3.6. The tunnel is an open-return-type wind tunnel, and the rectangular cross section is 2.8 ft (0.85 m) by 4.0 ft (1.22 m) and 8.0 ft (2.44 m) long. The downstream location of the test section is 0.5 in (1.3 cm) wider than the upstream end to account for boundary layer growth along the walls. To ensure good flow quality, the air passes through a 4-in (10.2 cm) thick honeycomb mesh, four stainless steel anti-turbulence screens, and a 7.5:1 inlet contraction. The flow conditioning reduced the empty test section turbulence intensity to less than 0.1% at all operating speeds, which range from 20 mph to 165 mph [53]. The airfoil is located at 728 ft above sea level for standard atmosphere and pressure. Flow angularity in the test section has been measured an dis less than 1 deg at all operating conditions [54].

3.2.2 Airfoil Models

A three-element wind tunnel model was used for all experimental tests presented in this thesis. The MFFS(ns)-026 airfoil is similar to the MFFS-026 airfoil originally designed by Ragheb [55] with the difference being that the strut

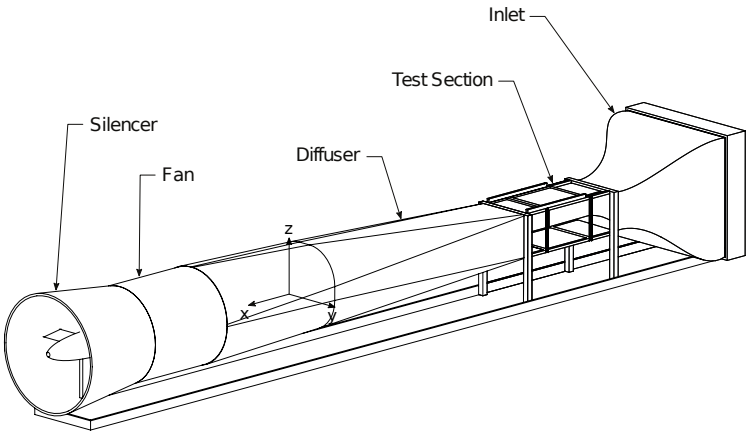

Figure 3.6: University of Illinois low-speed low-turbulence open-return wind tunnel.

Figure 3.7: Front view of MFFS(ns)-026 airfoil mounted for testing.

element was not used. The additional (ns) notation signifies that no strut element was used in this research project. It is noted that the MFFS(ns)-026 airfoil represents the shape and relative size of the three airfoil elements, but the rigging location of the flaps is not specified. Design of the airfoil model was performed in PTC Pro/Engineer Wildfire 4.0, a commercially-available parametric three-dimensional CAD package. Parts were machined using Wagner Machine, Inc. in Champaign, IL, and the model was fabricated by Sean Cassidy, LLC, also located in Champaign, IL. The final model, mounted vertically in the wind tunnel, is presented in Fig. 3.7. The model was originally designed for application to a wind turbine, and supporting CAD drawings for the airfoil model can be found in Appendix E of Ref. 56.

As shown in Fig. 3.8, three different airfoil elements defined the model. Each element was manufactured independently, and the elements were attached to each other through the use of three spanwise tongue-and-groove attachment brackets. These clamps were located on the lower surface of the airfoil, and were necessary to ensure the structural integrity of the airfoil and the devices used to rig the location of the flaps (discussed in Sec. 3.2.3).

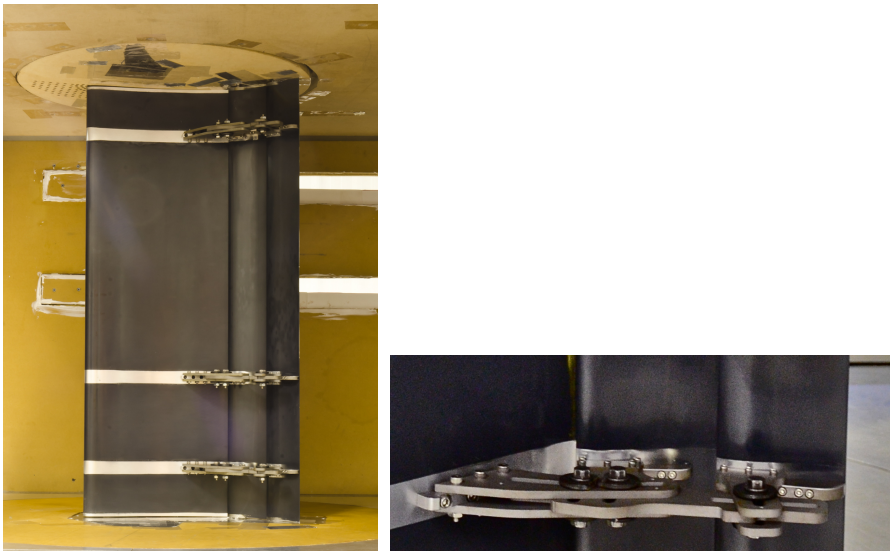

(a) (b)

Figure 3.8: Flap attachment tongue-and-groove clamps for model including a) view of lower surface of airfoil and b) detailed photograph of clamps.

Construction of the main element consisted of a foam core, three spanwise aluminum support ribs, and two steel end caps. Three aluminum ribs were spread out in the spanwise direction which provided a surface to which the mounting brackets were attached. Two ¼-in end caps were manufactured from stainless steel and were attached on each end of the model. External dimensions of the end caps and interior ribs were CNC milled to a tolerance of 0.001 in. Foam cores were placed between the metal ribs to create the basic shape of the airfoil. The cores were undercut by 1/16-in relative to the true airfoil profile; a commercial vendor used a CNC hot wire to cut the profile of the cores, and these cores were subsequently provided to the model maker. An epoxy-resin/Bondo filler was applied to the outer surface of the foam cores to create the true outline of the airfoil, and the model maker used a sand rail and the machined ribs as a guide to ensure the spanwise accuracy of the airfoil shape. Successively finer and finer sand paper and ultimately polish was used to create the near mirror finish of the wind tunnel model. The main element was supported by a main spar, which connected to the center of the wind tunnel balance cruciform plate, and a secondary spar to add structural integrity. Spar integration in the model was challenging due to the small size of the main element. Measurements of the two spars were 0.75 in by 1.5 in and 1.5 in by 3 in for the main and secondary spar respectively. The secondary spar was larger and was mounted at a 20-deg angle relative to the main spar to allow the spars to fit in the model. The main spar and the secondary spar were attached to the metric adaption plate with custom made mounting brackets, and Fig. 3.9 depicts the cruciform mounting plate as well as the custom-made mounting brackets.

The flaps were not manufactured using the same method as the main element. Instead of foam cores and spanwise support ribs, the flaps were made of 33 vertically stacked 1-in wide (spanwise) aluminum ribs. The flap cores were

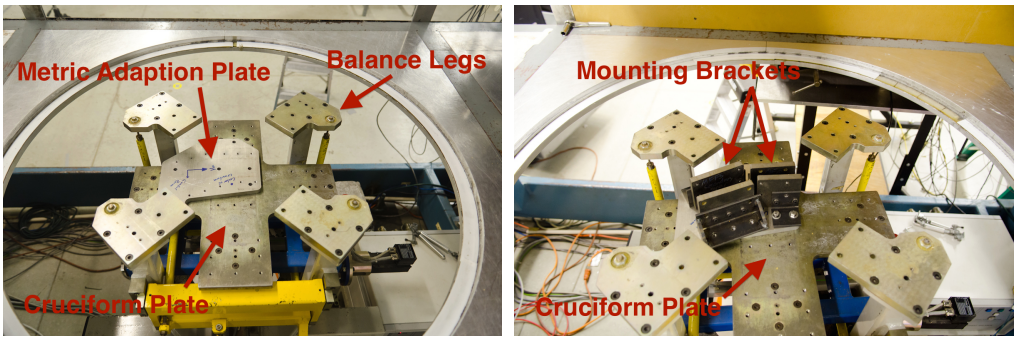

(a) (b)

Figure 3.9: Hardware connections between wind tunnel balance and main element including a) cruciform and metric adaption plate and b) spar brackets.

undercut by 0.030 in for the front portion of the airfoil, and an epoxy-resin/Bondo filler was used to build up the profiles to the desired shape. A CNC mill was used to manufacture the trailing edges to a tolerance of 0.005 in, and the epoxy/Bondo filler was not applied to this portion of the airfoil. Two precision aluminum rods were used to hold the location of the stacked ribs in place in which one 0.5-in diameter circular steel spar was designed to support the loads on the flap, and a second rod was installed for alignment purposes. The large 0.5-in spar was attached to the flap positioning system, as described in Sec. 3.2.3.

After construction was completed, the coordinates of the models were measured with a three-axis coordinate-measuring machine (CMM). Figure 3.10 presents the airfoil coordinates both as designed and as built. Some slight differences between the designed and manufactured airfoils are noticed, and the coordinates for the as-designed airfoils are presented in Pomeroy's M.S. thesis [56]. The dimensional chord length of the main element was 11.5 in, flap 1 measured 3.5 in, and the chord of flap 2 was 3.0 in. As the flap chord lengths were significantly smaller than the main element, small manufacturing errors in the flaps resulted in larger nondimensional errors than the main element.

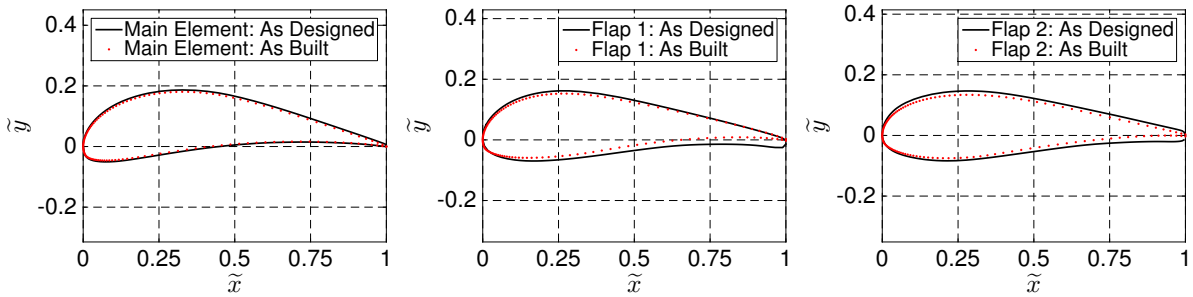

(a) (b) (c)

Figure 3.10: Coplotted coordinates of airfoils as designed and as manufactured with a) main element, b) flap 1, and c) flap 2.

3.2.3 Flap Positioning System

A flap positioning system (FPS) was designed to accurately rig flaps in three degrees of freedom. Each flap was able to independently traverse in the x_{tunnel} and y_{tunnel} directions as well as rotate in δ. Multielement aerodynamics are highly sensitive to the location of the flaps and a small difference in the gap size or overhang distance can have large effects on the performance of the system. Consequently, slight spanwise deflections in the model can result in drastically different aerodynamic performance than for the undeformed model. To minimize deflections and reduce spanwise variation of flap location, traverses were attached to the model on the top and bottom of the tunnel. Two traverses, one per flap, were installed on the top of the wind tunnel and two traverses, one per flap, were installed on the bottom of the wind tunnel. A wooden box was constructed to enclose the traverses on the top of the wind tunnel; a removable lid allowed the traverses supporting the top of the flaps to be adjusted to various positions. The wind tunnel and traverse locations are shown below in Fig. 3.11. As discussed in Sec. 3.2.2, multiple clamps attached the flaps to the main element.

Traverses

As previously mentioned, four traverses were fabricated for use in the FPS. These traverses, shown in Fig. 3.12, consist of two pairs of top and bottom traverses. External dimensions of each traverse measured approximately 3.5 in wide, 3.5 in long, and 2.0 in tall. Size was minimized so the traverses could fit onto the existing wind tunnel balance, and each traverse consisted of multiple machined components, gears, and encoders. A label was applied to the outside of all traverses corresponding to a number between one and four.

Figure 3.11: Location of four traverses in wind tunnel.

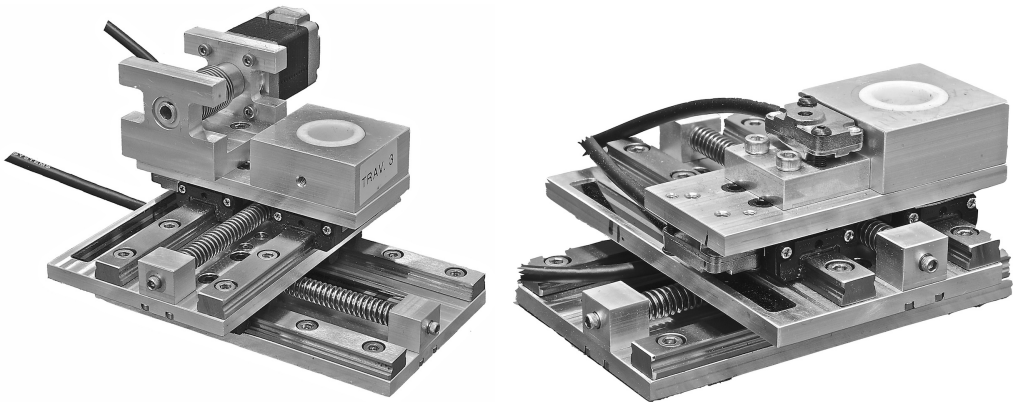

(a) (b)

Figure 3.12: Detailed photographs of FPS traverses including a) top traverse and b) bottom traverse.

The custom-designed traverses were designed in Pro/E Wildfire, and parts were manufactured through use of a computer-controlled CNC mill or a computer-controlled water jet by Wagner Machine Company in Champaign, IL. As seen in Fig. 3.12, each traverse consisted of two primary layers which were supported by a combination of metal blocks, worm screws, and linear rails. Each of these layers allowed the traverse to freely move in the x_{tunnel} and y_{tunnel} directions while the additional blocks and gear on top of the traverse controlled deflection angle of each flap. Supporting two-dimensional drawings for significant components are included in Appendix E of Ref. 56.

Linear and Rotary Motion

Linear movement of the system was accomplished through a combination of custom-made components and commercially-available products. The position of the traverse in the two linear directions was set by hand through use of a 0.050-in hex key which was inserted into a small 2-56 hex screw at the end of the traverse, as shown in Fig. 3.13(a). Holes were drilled and tapped in the ends of a ¼-20 Acme-threaded precision rod, and hex screws were secured on both ends of the threaded rod with Loctite. In this manner, rotation of the hex screw also rotated the threaded rod. A small aluminum cube with a clearance hole, named the worm mount, was attached to a stationary plate; this cube supported the hex screw/threaded-rod system and also allowed it to freely rotate as is visible in Fig. 3.13(a). A small rectangular worm collar, with a ¼-20 internal threading, was attached to the bottom of the plate which was traversed. In this manner, the worm mounts were metric to a stationary plate and the worm collar was metric to the plate which was being moved. Thus, as the hex key was rotated, it rotated the threaded rod which was mounted in the threaded worm collar and moved the plate in a linear direction. A pair of small SRS9M block and rail systems, containing a number of small ball bearings, manufactured by THK were used to guide the linear motion. The position of the linear traverses was monitored simultaneously on both the top and bottom of the wind tunnel through the use of Micro-E Mercury

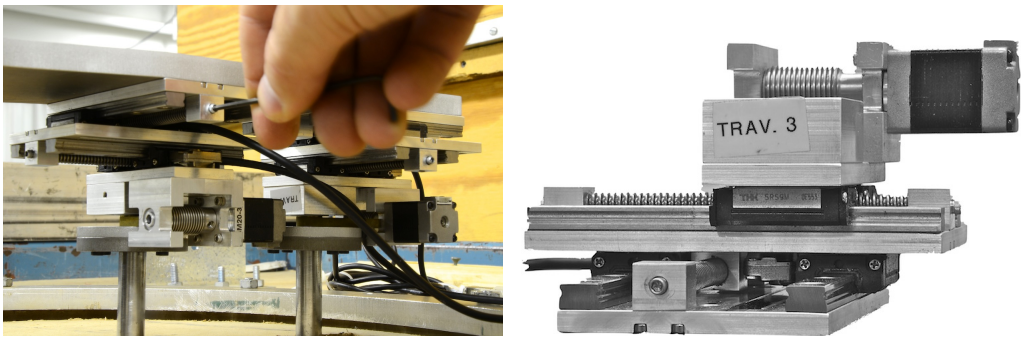

(a) (b)

Figure 3.13: Additional photographs of traverse a) author adjusting linear position and b) side view.

1500-S optical encoders, which are discussed later in this section. It is noted that the linear motion systems on the top and bottom traverses were identical. A slightly offset side view of the entire traverse is presented in Fig. 3.13(b) wherein the worm mounts, threaded rods, and optical encoders are clearly visible from this perspective.

Rotary position was controlled independently for each flap, and the position was set using computer software which interfaced with a stepper motor. A suite of software programs was developed in the National Instruments LabView programming language, and serial commands were sent via RS232-DB9 communication protocol to a power junction box. The power and signals were combined in this junction box, and then both power and signal were sent via RS232-DB15 to a 2A-TTL bipolar controller manufactured by Excitron Corporation. A SM20-30 micro stepper motor, also manufactured by Excitron Corporation, was used to set the angle of each flap. These motors were mounted to a U-shaped mounting bracket on the traverses on top of the wind tunnel; stepper motors were not installed on the lower traverses. The drive shaft of the motor was connected to the inside of a worm drive collar, a long and thin aluminum annular cylinder that spanned the width of the motor-mount, to which a S1D96Z-P064SS worm gear manufactured by SDP/SI was attached. Two teflon bushing were installed between the motor shaft extension and the motor mount to reduce friction of the system. In an effort to reduce experimental uncertainty of the flap angles, the worm gear fit tightly into the motor mount block, and less than 0.050 in separated the inside of the motor mount and the worm. This worm gear drove a 40 deg sector of the SDP/SI S1C86Z-P064B180S rotational gear. Figure 3.14 presents a horizontal cross-section slice of the entire rotary angle-drive system. Similar to the linear traverses, position was monitored through use of a Micro-E Mercury 1500-S optical encoder.

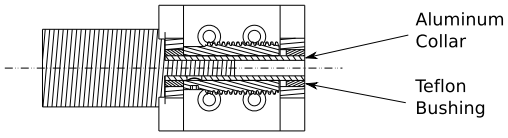

Figure 3.14: Cross-section of motor mount and rotary motor.

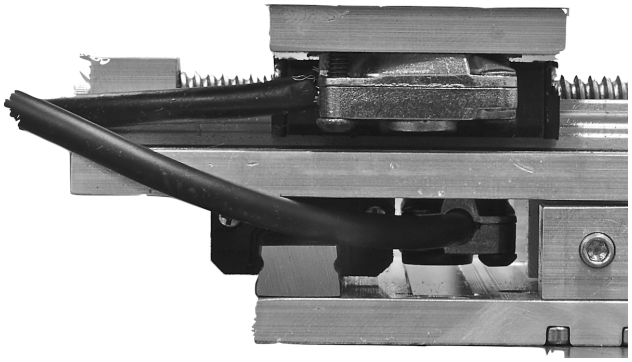

Figure 3.15: Side view of FPS traverse exhibiting two linear optical encoders.

Optical Encoders

The location of each degree of freedom in each traverse of the FPS was determined through the use of multiple incremental digital optical encoders. A total of five encoders measured the location of each flap; three encoders were attached to the traverse on the bottom of the tunnel and two encoders were attached to the traverse on the top of the tunnel. The linear position in both the x_{tunnel} and y_{tunnel} direction was measured on both the top and the bottom of the tunnel, and the rotation angle was measured on the bottom of the tunnel. A total of ten Mercury 1500-S optical encoders, five for each flap, manufactured by GSI Group (MicroE Systems) were used in all four traverses. Small encoders were used to satisfy the height constraint between the wind tunnel balance and wind tunnel floor, which was approximately 3 in. Two linear encoders can be seen in Fig. 3.15 with a black signal cable exiting each encoder head. An L80A glass optical tape, also visible in the figure, was mounted below each optical encoder. An electronic optical sensor inside the encoder tracked the glass tape which was demarcated with a line every 0.5 μm. The position of the encoder was tracked by incrementally adding or subtracting a count from the previous total number of counts each time the electronic sensor passed a demarcated line.

Glass Tapes

Eight of the L80A linear glass optical tapes, with a resolution of 0.5 μm (1.97×10^{-5} in) and an accuracy of ± 3 μm (1.18×10^{-4} in), were used for the x_{tunnel} and y_{tunnel} directions. The angular alignment tolerance for the optical encoders was ± 2 deg (0.0349 radians) and the tolerance of vertical displacement difference between the glass tape and the optical eye was ± 0.15 mm (5.91×10^{-3} in). Each encoder required a maximum of 40 mA at +5 V or 0 V, and the encoders are transistor-transistor logic (TTL) capable. To ensure the optical sensor was able to read the glass tape, a small slot was recessed into the aluminum plates which were stationary, and tight tolerances on these slots ensured that the tape would be located in the correct position such that the optical eye would be able to read the optical tape.

The glass optical tapes were secured to each aluminum plate with a small portion of epoxy applied to the slot into which the tapes were fit prior to insertion of the tape into the slot. Care was taken to ensure the traverse tapes were level inside the slot; if the tape was not level, the proper vertical offset between the tape and the encoder eye would not be achieved.

An R5725-HC hub and rotary grating fixture, also manufactured by GSI Group (MicroE systems), with a resolution of 39.6 arc-seconds (0.011 deg corresponding to 32,768 counts per revolution) and an accuracy of ± 3.9 arc-seconds (0.0011 deg) was used to measure the rotary angles. To ensure proper vertical displacement between the rotary optical encoder and the rotary tape, a small encoder spacer was manufactured to raise the encoder up to the proper level to read the underside of the optical tape. This optical tape was attached to a system which rested in the pillow block. Great care was taken to ensure the encoders were level as they were attached to the traverses. The standoff distance between the encoder eye and the rotary optical tape was required to be 2.4 mm (0.0945 in) ± 0.015 mm (5.91×10^{-3} in) for the encoder to work properly. If the distance between the tape and the encoder was too large, the encoder would not tick with each grated line on the tape; alternatively, if the encoder was too close, the electronic sensor would not be able to focus upon the tape and no signal will be returned.

Alignment and Maintenance

Proper alignment of the linear and rotary optical tapes was verified with the use of an analog Mercury SS-AT 1500S-120 alignment tool manufactured by GSI Group (MicroE Systems), as shown below in Fig. 3.16. It is noted that analog sin+ and cos+ signals were used only by the alignment tool as all other signals to determine position were digital. During alignment, the male pigtail from the encoder was plugged into the female pigtail extending from the alignment tool. The alignment tool checked for signal strength and signal quality which are both functions of vertical displacement, encoder yaw angle, and tape angle alignment. Signal quality was indicated by green, yellow, and red LED lights which corresponded to strong, weak, and unreadable signals respectively.

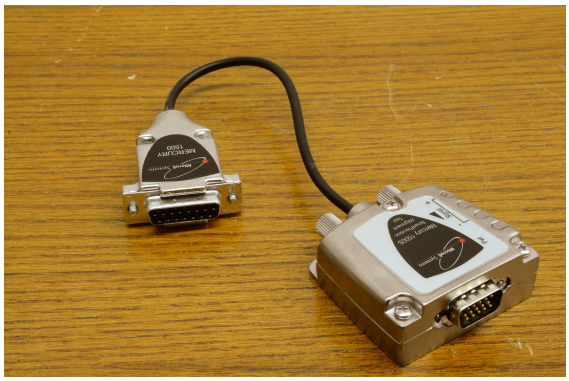

Figure 3.16: Analog SS-AT 1500S-120 tool used to verify alignment of optical tapes and encoders.

Optical tapes used in the FPS were sensitive to contamination by foreign debris and surface smudges. Debris such as dust and dirt inevitably settled on the surface of the linear optical encoders on the lower traverses despite efforts to contain the traverses and keep them clean. Difficulties were encountered when the surface was contaminated with foreign debris or with a smudge such as a fingerprint. When the surface was dirty, the incremental distances read by the head would jump by as much as 0.3 in over a very short distance and this fault would be reflected in the LabView program used to monitor the position of the encoders; the magnitude the distance would jump was not repeatable. In some instances, the interference would only occur while the traverse was moved in one direction. A lint-free glasses cleaning cloth and acetone were used to clean the surface of the optical tapes, and care was taken to be careful with the fragile tapes. The markings on the optical tapes were chromoly steel (CRMO) and were not scratched by the cloth. Accurate and repeatable positions were returned by the optical encoders with clean optical tapes.

Signal and Home Position

The relative digital encoders were A-quad-B in differential, and this signal format is presented in Fig. 3.17. Four digital pulses were sent for each tick on the encoder tape; one tick for A+ up, one tick for A+ down, one tick for B+ up, and one tick for B+ down. If A+ lead B+, as shown in Fig. 3.17(a), the value of Index+ was positive. Alternatively, if B+ lead A+, seen in Fig. 3.17(b), the value of Index+ was negative.

A zero-gate location on each optical tape, both rotary and linear, indicated the home position of each optical encoder. A Boolean value was sent from the encoder as the head passed over the zero-gate indicator. Cables were manufactured to allow use of the zero-gate Boolean, however functionality of this gate was not used in this research

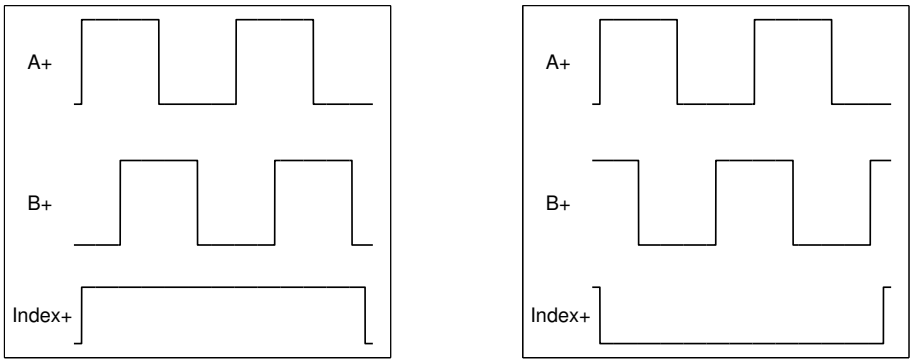

(a) (b)

Figure 3.17: A-quad-B differential signal a) A+ leading B+ resulting in positive Index+ value and b) B+ leading A+ resulting in negative Index+ value.

project because the location of the zero-gate on each tape was irrelevant. The position of each encoder was measured relative to the baseline airfoil position.

Traverse Installation

The FPS was designed for robust use for the current application as well as for easy adaptability for future projects. While some supporting hardware may need to be manufactured, the overall system should be able to be used by future researchers. An adaption plate was manufactured to attach the FPS plates to the balance cruciform plate, as shown below in Fig. 3.18. Future models may require a different metric adaption plate than the one pictured if the spar clamps are located in different positions. In addition to the hardware pictured in Fig. 3.18, the traverses must also be installed on the top of the tunnel. The details of the installation on the top of the wind tunnel are presented later in this section. It is observed, however, that the hardware attachments on both the bottom and top of the wind tunnel would most likely need to be manufactured for application to future models. A more detailed discussion of requirements for future models is presented later in this subsection.

Electronic digital signals originated at the optical encoders and were transferred via RS422-DB15 to a series of breakout cables which were read by a digital counter card in the computer, and a wiring diagram of the entire system is presented in Fig. 3.19(a). As seen in the diagram, two National Instruments PCI-6602 digital counter DAQ cards were used to interface with the 10 optical encoders as five RS422-DB15 cables plugged into each DAQ card. Figure 3.19(b) presents the pinout for the digital-counter DAQ cards. The pinouts for the DAQ cards were the same between the two cards, and a 68-pin connector was used to interface with the cards. Each encoder required three pins including a source, a gate, and a direction (up/down). These three values are outlined in red, blue, orange, green, and purple for each of the five encoders. Two custom-manufactured adaption breakout cables, as pictured in Fig. 3.20(a), were used to convert the signal from 68-pin to five different RS422-DB15 pigtails, one for each encoder. Breakout cables were manufactured by GSI Group/Micro-E to interface with the PCI-6602 DAQ cards. Each pigtail from the breakout

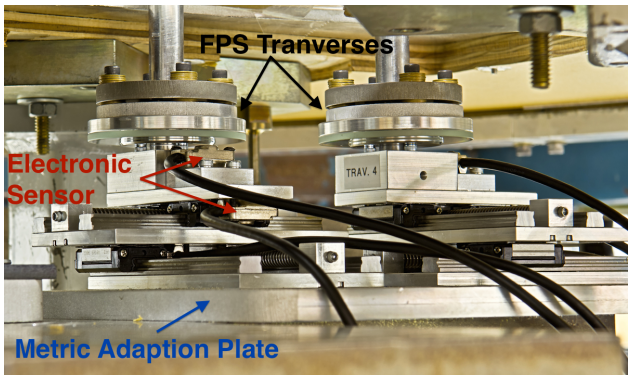

Figure 3.18: View of lower FPS traverses, metric adaption plate, and cruciform plate.

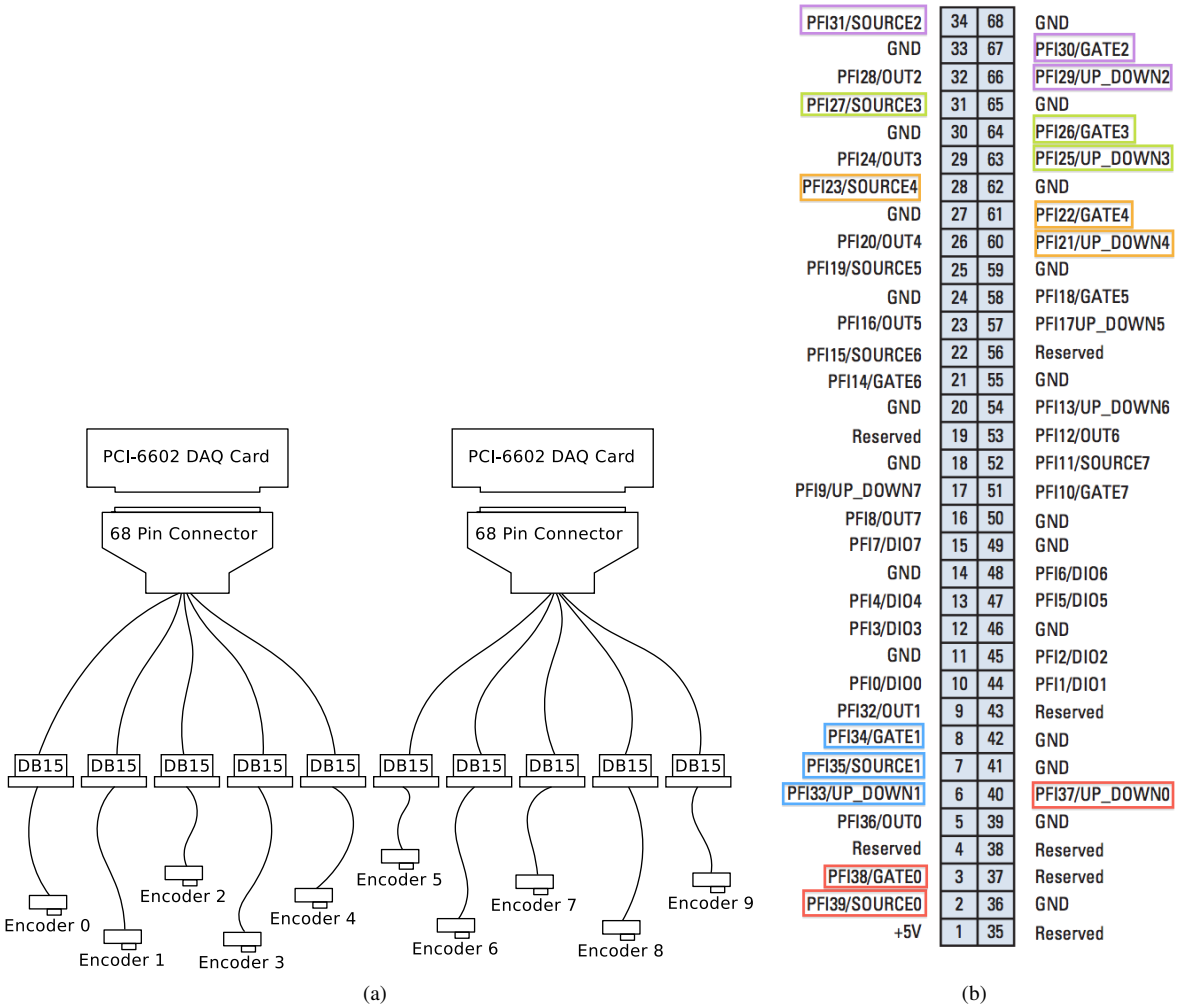

Figure 3.19: Communication from two DAQ cards to encoders as highlighted by a) wiring diagram and b) DAQ card pinout.

cables was connected to a 25-ft long shielded RS422-DB15 cable. Each cable, ten in total, was securely fastened to a 2-m long pigtail which extended from each encoder head. The pinout for the optical encoder is shown in Fig. 3.20(b). Airfoil deformations due to aerodynamic loads were not monitored in the current project.

In addition to the traverses and hardware on the bottom of the tunnel, a corresponding system existed on the top of the wind tunnel. This portion of the system was contained within an air-tight pressure box that was manufactured for this specific project, as seen in Fig. 3.21. Two large gray steel bars spanned the width of the wind tunnel, and a secondary force balance could attached to these bars if desired. This one-dimensional force balance was unconstrained in drag and pitching moment, but was constrained by a load cell in the lift direction. The system was not used in this research project, but more details can be found in Ref. 56; the reader is simply alerted to the presence and need for the

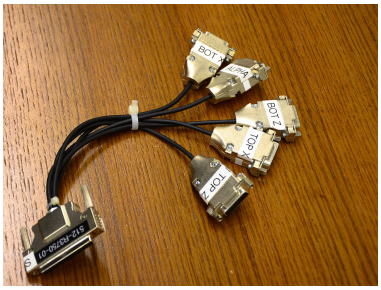

(a)

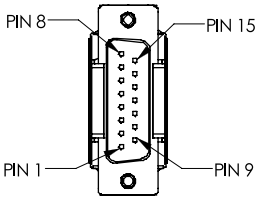

Pin	Function
1	Reserved
2	Reserved
3	Reserved
4	A- quadrature
5	A+ quadrature
6	Reserved
7	Sine+ (analog)
8	Cosine+ (analog)
9	B- quadrature
10	B+ quadrature
11	Reserved
12	+5 V DC
13	Ground
14	Index+
15	Index-

(b)

Figure 3.20: Details of cables to connect DAQ cards to encoders showing a) custom-made breakout cables and b) 15-pin encoder pinout.

Figure 3.21: Air-tight containment box and contents located on top of wind tunnel; FPS and secondary force balance are both visible.

large gray bars. Water-proof silicone caulk was used to seal the junction between the pressure box and the wind tunnel ceiling as well as the junctions between the secondary force balance and the edges of the box. A removable wooden top was manufactured, and this top could be easily removed to gain access to the FPS on top of the wind tunnel. A series of latches and weather-proof rubber tape were used to seal the junction between the top of the box and the main portion of the box. A bright light was placed inside of the box and turned on to inspect for any leaks or gaps in the system, and these holes were subsequently sealed with caulk or tape.

As depicted above in Fig. 3.12 on page 22, the traverses on the top and the bottom of the wind tunnel were different. A stepper motor was attached to the upper traverse to set the rotation angle of each flap while a rotary encoder on the lower traverse determined the precise position of the flap. A view of the upper FPS and a detailed view of the traverse, when connected to an airfoil model, are both presented in Fig. 3.22. Numerous pieces of hardware were required to attach the FPS to the wind tunnel model, as seen in the figure. Two traverses were attached to a large attachment plate, and this attachment plate was subsequently attached to the main spar of the main element. A specific series of steps

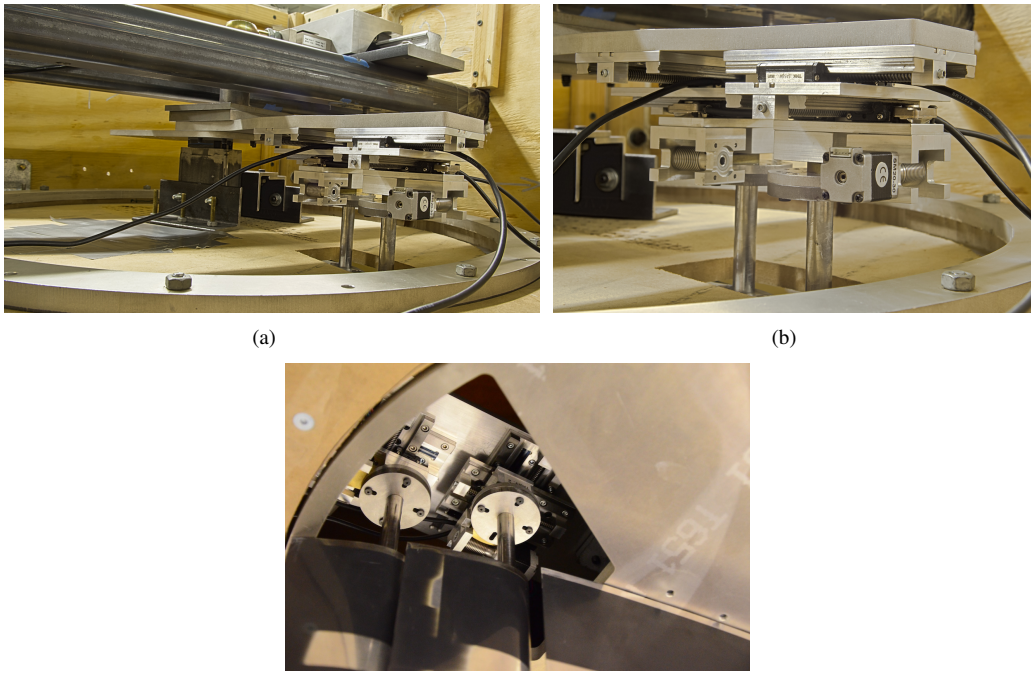

(a) (b)

(c)

Figure 3.22: FPS on top of wind tunnel with lid removed including a) system setup, b) FPS detail, and c) attachment between flaps and FPS traverses.

were executed to install the traverses. The first priority was to locate the x and y positions of each traverse such that the spars of the two flaps were able to be mounted to the traverses. After this point, the x-y position of the top set of traverses were adjusted to be the same as the lower set of traverses. This position was set with a physical jig as the relative optical encoders had not yet been referenced to a home position. When the traverses for the top and bottom of the wind tunnel rigged the flaps in the desired location, the traverse attachment plate was then connected to the top of the main-element spar.

Requirements for Future Models

Future models are able to utilize the FPS. The total span of the flap was a critical distance as a flap that is too large will not fit in the wind tunnel while a flap that is too small would yield aerodynamic tip effects that would cause the flow not to be two-dimensional. Similarly, the distance between the top traverse and the end of the model is critically important. Supporting hardware on the top of the wind tunnel determined the location of the traverses above the ceiling of the wind tunnel. Traverses on the bottom of the tunnel were mounted to an adaption plate which was attached to the cruciform plate.

Each flap assembly consisted of two airfoil attachment plates, a flap lower spar, a flap upper spar, and the flap itself; the airfoil attachment plates on the top and bottom of the flap were identical. Height of the airfoil upper spar

was determined by the distance between the supporting hardware on top of the tunnel and the ceiling of the wind tunnel. Similarly, the lower-spar length was determined based upon the distance from the metric adaption plate to the wind tunnel floor as found in supporting CAD for the FPS. Unfortunately, CAD of the tunnel supplied to the researcher was incorrect; the actual distance from the balance cruciform to the bottom floor of the wind tunnel was 0.345 in larger than the provided CAD of the force balance and wind tunnel floor. An adaption spacer plate was manufactured and washers were stacked between the two spacer plates to lengthen the lower spar. For further details on the CAD development of the FPS, the reader is referred to Ref. 56.

3.2.4 Freestream Conditions

All tests performed in this research, with the exception of flow-visualization runs, were executed at a constant Reynolds number, as controlled by a computer program. Reynolds number for the airfoil tests was calculated using the standard equation

$$Re_{system} = \frac{\rho_{amb} U_\infty c_{sys}}{\mu_{amb}} \tag{3.12}$$

in which ρ_{amb} and μ_{amb} are the ambient air density and ambient dynamic viscosity, as determined in the high-bay room, respectively. Freestream conditions were taken at a far upstream location deemed to be the inlet to the test section, and the velocity at this station is represented by U_∞. Finally, the system chord length, as defined in Figs. 3.2–3.3, is defined by c_{sys}. The ambient density of the high-bay room was calculated using the ideal gas law

$$p_{amb} = \rho_{amb} R T_{amb} \tag{3.13}$$

which can be rearranged to be

$$\rho_{amb} = \frac{p_{amb}}{R T_{amb}} \tag{3.14}$$

where p_{amb} and T_{amb} are the ambient atmospheric pressure and temperature in the high-bay room, respectively, and R is the ideal gas constant for air. As conditions in the ambient air were not at extremely-high temperatures or extremely-low pressures, the ideal gas law could be appropriately applied to the governing equation of state. As the ambient viscosity cannot be directly measured, Sutherland's law yielded an estimate for μ_{amb} [57]

$$\mu_{amb} = \mu_1 \frac{T_1 + C_1}{T_{amb} + C_1} \left(\frac{T_{amb}}{T_1} \right)^{3/2} \tag{3.15}$$

in which μ_1, T_1, and C_1 are known constants of 3.58404×10^{-7} slug/ft-sec, 491.6 deg R, and 199.8 deg R, respectively. As the only unknown in Eq. 3.15 is T_{amb}, the value of μ_{amb} was readily calculated. Ambient pressure was directly measured by using a Setra 270 absolute-pressure transducer which was located in the control room. For most of

the data presented in this research, an analog type-K battery-powered Omega thermocouple was used to measure the ambient temperature. However, the thermocouple, which was tempermental throughout the tests, was finally replaced with an AC-powered USB-TC01 type-J grounded thermocouple from National Instruments. While it may be obvious, the ambient temperature conditions between the control room and the high-bay room were assumed to be equal. A similar assumption was made in which p_{atm} was assumed to be equal in both the control room and high-bay room. It is noted, however, that the ambient total pressure was not the same as the total pressure in the wind tunnel since the anti-turbulence screens removed total head from the flow and the fan added total head to the flow.

Tunnel air speeds were computer-controlled in which a five-bladed metal fan was driven by a 125-HP AC motor-controlled with an ABB ACS 800 Low-Voltage AC Drive. As previously mentioned, tests were performed at a constant Reynolds number by way of a computer program that controlled the AC drive, which in turn dictated the rotational speed of the fan, to yield the desired Reynolds number to within 0.5%. Air speed in the test section was calculated by determining the differential pressure Δp between the settling section (p_{ss}) and the test section (p_{ts}). Throughout this discussion, the subscripts *ts* and *ss* correspond to the test section and settling section, respectively, while the subscript ∞ refers to the freestream condition (taken at the upstream edge of the test section). A set of four static pressure taps were located on each wall of the settling section (immediately downstream of the anti-turbulence screens). These four taps were all connected to a single pressure tube, thus yielding an average p_{ss} over the four walls by

$$p_{ss} = \frac{1}{4}\sum_{i=1}^{4} p_i. \tag{3.16}$$

Individual pressures of p_i were not recorded in the current research as these four tubes were attached to a four-tube junction which was then in turn attached to one pressure port. The p_{ss} pressure tube was attached to one of the ports on a DTC Initium module, which will be discussed in greater detail later, and the pressure relative to p_{atm} was measured. Similarly, four wall-mounted ports were located at the upstream portion of the test section and these four taps were all connected to one pressure tube. In this manner, p_{ts} was found to be

$$p_{ts} = \frac{1}{4}\sum_{i=1}^{4} p_i. \tag{3.17}$$

where p_i refers to the pressure at each of the four taps in the test section. After directly measuring $p_{ss} - p_{atm}$ and $p_{ts} - p_{atm}$, the value of Δp from the test section to the settling section was found by

$$\Delta p = p_{ss} - p_{ts} = (p_{ss} - p_{amb}) - (p_{ts} - p_{amb}). \tag{3.18}$$

Measurements of Δp were acquired using a DTC Initium differential pressure module system and also a Setra 239 differential pressure transducer. Steady and inviscid flow between the settling section and test section were assumed, and thus calculations using the inviscid conservation of mass (Eq. 3.19) and Bernoulli's equation (Eq. 3.20) yield the test section velocity (Eq. 3.21).

$$A_{ss}U_{ss} = A_{ts}U_{ts} \tag{3.19}$$

$$\frac{1}{2}\rho U_{ts}^2 + p_{ts} = \frac{1}{2}\rho U_{ss}^2 + p_{ss} \tag{3.20}$$

$$U_{ts} = \sqrt{\frac{2(p_{ss} - p_{ts})}{\rho_{amb}\left[1 - \left(\frac{A_{ts}}{A_{ss}}\right)^2\right]}}. \tag{3.21}$$

It is noted in Eq. 3.21 that A_{ts}/A_{ss} is the reciprocal of the contraction area ratio, and the density of the air was calculated by Eq. 3.14. Freestream dynamic pressure is defined as

$$q_\infty = \frac{1}{2}\rho_\infty U_\infty^2, \tag{3.22}$$

and application of incompressible conservation of mass, Eq. 3.19, and Bernoulli's equation, Eq. 3.20, yielded

$$q_\infty = \frac{1}{2}\rho_\infty U_{ts}^2 = \frac{p_{ss} - p_{ts}}{1 - \left(\frac{A_{ts}}{A_{ss}}\right)^2} \tag{3.23}$$

which completes the discussion of the freestream conditions.

3.2.5 Data Acquisition System

All data in this project were acquired using the National Instruments LabView programming language, which was used to interface with the DAQ cards and equipment mentioned herein. Two different computers were used for data acquisition; one computer was used to collect all aerodynamic data associated with the wind tunnel while a second computer was used to interface with the FPS. Tunnel-related data were collected on a Dell Precision T3400 computer with 4 GB of RAM and a 2.83 GHz Intel quad-core processor running a 32-bit version of Windows XP operating system on a small 150 GB hard drive. DAQ software included a front-end graphical user interface (GUI) with which the researcher could interact with the software as well as support "under-the-hood" code. Analog commands were sent using RS-232 communication to the following systems: force and moment balance, absolute-pressure transducer, nitrogen solenoid valve, the original Omega thermocouple (prior to device failure), an IDC drive device which controlled the original Lintech traverse (prior to device failure), and the variable-frequency drive for the wind tunnel fan. Digital signals through USB were used to communicate with the new National Instruments thermocouple and the new

Table 3.1: Encoder Locations on FPS

Encoder Number	DAQ Card	Location
0	1	Bottom x_1
1	1	Bottom y_1
2	1	Top x_1
3	1	Top y_1
4	1	δ_1
0	2	Bottom x_2
1	2	Bottom y_2
2	2	Top x_2
3	2	Top y_2
4	2	δ_2

Zaber two-axis traverse system. Pressure measurements collected with the DTC/Initium system were acquired through TCP/IP Ethernet protocol. Analog signals from the three-component balance were digitized with a National Instruments PCI-6052E 15-bit analog-to-digital data acquisition board. Unsteady data collected with the split-film probe were simultaneously sampled with a National Instruments SCXI scanning system in which a sample-and-hold algorithm was utilized to simultaneously collect the unsteady data of the two split films. Analog signals from the split-film probe were passed through a set of signal conditioners prior to being passed to a PCI-MIO-16XE-10 analog-to-digital board.

Additional software was developed to interface with the ten optical encoders in the FPS to simultaneously determine the location of each flap. The digital FPS signals were transferred to a computer located in the high bay using RS-422 digital signal protocol. The location of each encoder was continuously monitored in dimensional coordinates (inches and degrees), and these values were displayed in large color-coded text on a large computer screen which was attached to the computer that monitored the encoder positions. The sample rate for all encoders in the PCI-6602 cards was set at 1 MHz, and therefore each encoder could simultaneously move at 1 m/s without the a DAQ card missing any lines read by the encoder eye. Connection from the pigtails to each encoder was performed as presented in Table 3.1. In essence, each flap was monitored by one DAQ card and one set of breakout cables. As many cables were stretched across the floor of the high-bay lab for an extended period of time, an industrial carpet was placed over the cables to ensure a safe, trip-free working environment for all individuals in the Aerodynamics Research Lab.

3.2.6 Three-DOF Force and Moment Balance

An external three-component force and moment balance was used to determine lift, drag, and pitching moment of the airfoil system. As previously mentioned, a set of L-shaped mounting brackets were used to attach the wind tunnel models directly to the balance. The balance, constructed by Aerotech ATE Limited in Heathfield, U.K., was securely

mounted to the floor of the high-bay room with a series of large steel bolts. A turntable was attached to the balance legs, and the angle of this turntable was the same as the airfoil angle of attack.

Balance Operations and Parameters

The airfoil system was attached to the force balance with mounting brackets, and measurements were taken using three load cells that measured forces in both the normal and axial directions as well as a pitching moment about center of the plate. Additional information regarding alignment of the balance and the balance coordinate system can be found in Noe [58]. Loads can be acquired in three different load ranges, including low, medium, and high, as shown below in Table 3.2. Proper setting of the balance was necessary to maximize accuracy without overloading the balance; the high-range setting was used for all experiments presented in this dissertation. Each load cell had a full-scale voltage range of $\pm$20 mV, and these signals were low-pass filtered at 1 Hz and amplified to a full-scale voltage of $\pm$5 V by use of a signal conditioner. Angle of attack, α, of the model was controlled with a mechanical turntable which was controllable to $\pm$0.1 deg. Position was measured with a rotary optical encoder with a resolution of 0.001 deg. Balance load measurements were taken at a sample rate of 100 Hz for a period of 5 sec and were subsequently averaged.

External balance tares were measured at 1.0 deg increments for the angle-of-attack range tested in which voltage tares were acquired for each of the three components. Measurements taken during a run subtracted the previously-measured tare voltage at the corresponding angle of attack. Voltage out of the signal conditioner (V_{0i}) was multiplied by a range ratio (RR_i) which yielded a scaled voltage (V_i) by

$$V_i = V_{0i} \cdot RR_i. \tag{3.24}$$

Values of the range ratio were determined from the load setting and are shown in Table 3.3. The resulting scaled

Table 3.2: Three-Component Balance Load Ranges

	High Range	Medium Range	Low Range
Normal Force	$\pm$450 lb	$\pm$225 lb	$\pm$90 lb
Axial Force	$\pm$90 lb	$\pm$55 lb	$\pm$18 lb
Pitching Moment	$\pm$45 ft-lb	$\pm$30 ft-lb	$\pm$15 ft-lb

Table 3.3: Three-Component Balance Range Ratios

	High Range	Medium Range	Low Range
Normal, RR_N	1	0.4944	0.2046
Axial, RR_A	1	0.6278	0.2173
Moment, RR_M	1	0.6755	0.3413

voltages were evaluated in a second-order calibration matrix of the force balance shown in Eq. 3.25.

$$\begin{Bmatrix} F_N \\ F_A \\ M \end{Bmatrix} = \begin{bmatrix} 37.7 & 0.01359 & -0.2095 & 0.01094 & 0 & -0.000865 \\ -0.1607 & 8.3125 & -0.01638 & 0.007084 & 0 & 0.007660 \\ -0.01299 & -0.005521 & 1.247 & -0.002122 & 0 & 0.0001497 \end{bmatrix} \begin{Bmatrix} V_N \\ V_A \\ V_M \\ V_N^2 \\ V_A^2 \\ V_M^2 \end{Bmatrix} \tag{3.25}$$

This calibration matrix was determined by the balance manufacturer, and the calibration matrix was then supplied to the university facility.

Force and Moment Calculations

Evaluation of the calibration matrix in Eq. 3.25 yielded the normal force (F_N), axial force (F_A), and pitching moment about the center of the cruciform (M). These were subsequently reduced into lift (L), drag (D), and pitching moment about the quarter-chord of the system $(M_{c_{sys}/4})$. The variables x_{offset} and y_{offset} correspond to the distance the quarter-chord of the system is translated from the center of the cruciform.

$$L = F_N \cos\alpha - F_A \sin\alpha \tag{3.26a}$$

$$D = F_N \sin\alpha + F_A \cos\alpha \tag{3.26b}$$

$$M_{c_{sys}/4} = M + x_{offset} F_N + y_{offset} F_A \tag{3.26c}$$

The non-dimensional coefficient of lift (C_l), coefficient of drag (C_d), and quarter-chord pitching moment coefficient $(C_{m,c_{sys}/4})$ were calculated by dividing the dimensional forces and moments by the freestream dynamic pressure (q_∞) and the model planform area (S). The model planform area was calculated by multiplying the system chord, as shown in Fig. 3.1, by the span of the model in which

$$S = c_{sys} b_{model}. \tag{3.27}$$

In addition to freestream dynamic pressure and model planform area, the pitching moment was also divided by the model chord (c). Drag data were measured and collected for the wind-tunnel balance but results will not be presented in this dissertation as wake profiles were used to calculate the drag of the model. Values of drag from the balance included the drag of the large flap-support clamps which yielded higher drag than the wake-survey system, which is discussed later in this section. Two-dimensional airfoil section coefficients were obtained from the standard equations given by

$$C_l = \frac{L}{q_\infty S} \tag{3.28}$$

$$C_d = \frac{D}{q_\infty S} \tag{3.29}$$

$$C_m = \frac{M_{c_{sys}/4}}{q_\infty S c} \tag{3.30}$$

where q_∞ was determined as discussed in Eq. 3.23.

3.2.7 Wind Tunnel Corrections

Aerodynamic performance data of airfoils in a finite-volume wind tunnel is different than performance data of the airfoil in freestream as wind tunnel walls interfere with the flow around the airfoil. Therefore, corrections must be made to account for the effect of the finite test section and presence of the wind tunnel walls. Corrections used in this research were based on those discussed by Barlow, Rae, and Pope [59].

Solid Blockage

Wind-tunnel walls restrain the flow through the test section and the wind-tunnel model reduces the area through which the flow can pass compared to freestream conditions. Simple application of Bernoulli's equation indicates that a decrease in cross-sectional area causes results in an incresae in local velocity through a phenomenon known as solid blockage (ε_{sb}). The magnitude of the solid blockage is a function of model thickness, the thickness distribution, model size, and angle of attack. Camber of the model does not affect solid blockage. While multiple methods have been developed to account for solid blockage, the two-dimensional corrections developed by Thom were used in this research [60, 61]. The solid blockage was calculated by

$$\varepsilon_{sb} = \frac{\kappa_1 \mathcal{V}}{A^{3/2}} \tag{3.31}$$

in which $\mathcal{V}$ represents the volume of the airfoil model and κ_1 is 0.52 for a model spanning the tunnel height as noted in Barlow, Rae, and Pope [59]. The cross-sectional area of the test section is denoted by A. Solid blockage affects the value of C_l, C_d, and C_m as discussed later in this section.

Wake Blockage

Drag on the airfoil system creates a wake with a mean velocity lower than that of the freestream conditions. Application of the conservation of mass law suggests that the velocity outside the wake in a finite cross-section must be greater than the freestream condition to maintain flow continuity, and Bernoulli's relationship suggests that the higher velocity flow outside the wake has a lower pressure than the freestream condition. This increased velocity in the field imposes a pressure gradient on the airfoil model which results in a velocity increase at the model. The value of wake blockage is a function of ratio of the wind tunnel model chord length to the test section height, denoted as c/h. Maskell [62] developed a correction based upon a mirror and estimated the wake blockage by using the equation

$$\varepsilon_{wb} = \frac{c/h}{2} C_{d,\text{unc}}. \tag{3.32}$$

The effect of both blockage parameters can be expressed as a total velocity increment(ε) where

$$\varepsilon = \varepsilon_{sb} + \varepsilon_{wb}. \tag{3.33}$$

This correction will be applied to C_l, C_d, and C_m at the end of this section.

Streamline Curvature

The wind tunnel floor and ceiling restrict the flow from developing the natural curvature of the streamlines and straightens the flow near the walls. Consequently, the airfoil appears to have more camber than the actual geometry. The increase in camber is approximately 1% for typical airfoil models. As a result of the artificial increase in camber, the determined values of C_l, C_m, and α are too large. Vortex theory discussed by Barlow, Rae, and Pope [59] suggests that data can be corrected with the streamline curvature correction calculated by

$$\sigma = \frac{\pi^2}{48}\left(\frac{c}{h}\right)^2, \tag{3.34}$$

and this correction is applied later in this section.

Correction Formulae

Two-dimensional corrections were applied to the measured wind-tunnel data including corrections for solid blockage, wake blockage, and streamline curvature as discussed in Barlow, Rae, and Pope [59]. The *unc* subscript in this section corresponds to an uncorrected value while the *cor* subscript represents a corrected value. Corrections for α are dependent upon the streamline curvature such that

$$\alpha_{cor} = \alpha_{unc} + \frac{57.3\sigma}{2\pi}(C_{l,unc} + 4C_{m,unc}). \tag{3.35}$$

Lift must be corrected for streamline curvature and blockage effects, where

$$C_{l,cor} = C_{l,unc}(1 - \sigma - 2\varepsilon), \tag{3.36}$$

and the quarter-chord pitching moment is corrected for streamline curvature and blockage so that

$$C_{m,cor} = C_{m_{\frac{1}{4}},unc}(1 - 2\varepsilon) + \frac{1}{4}C_{l,cor}. \tag{3.37}$$

Finally, drag is corrected by incorporating the effects of solid blockage and wake blockage where

$$C_{d,cor} = C_{d,unc}(1 - 3\varepsilon_{sb} - 2\varepsilon_{wb}). \tag{3.38}$$

Unless otherwise stated, all data presented in this dissertation were corrected appropriately. No corrections were applied for a decrease of spanload near the wind tunnel walls.

3.2.8 Wake Integration System and Governing Equations

A one-dimensional wake-survey system was used to determine drag from momentum-deficit theory in which a wake rake that contained 59 total-pressure probes was installed at a location downstream of the airfoil. The rake, as seen in Fig. 3.23(a), was mounted to a two-axis Lintech traverse or a two-axis Zaber traverse installed on top of the wind tunnel. The total-pressure probes were manufactured from straight, thin-walled, stainless steel tubing in which the probes were aligned with the freestream flow, and the openings pointed upstream. Each of the probes had an outer diameter of 0.040 in (1.0 mm) and were spaced across the 9.75-in wide wake rake. Probes in the center of the rake were installed at 0.135 in (3.43 mm) spacing, while the probes at the edges of the wake rake were spaced at 0.270 in (6.86 mm) increments. Wake surveys were acquired approximately 23 in downstream of the airfoil trailing edge. A two-axis traverse was used to move the wake rake to various positions. As the Lintech traverse was ultimately replaced

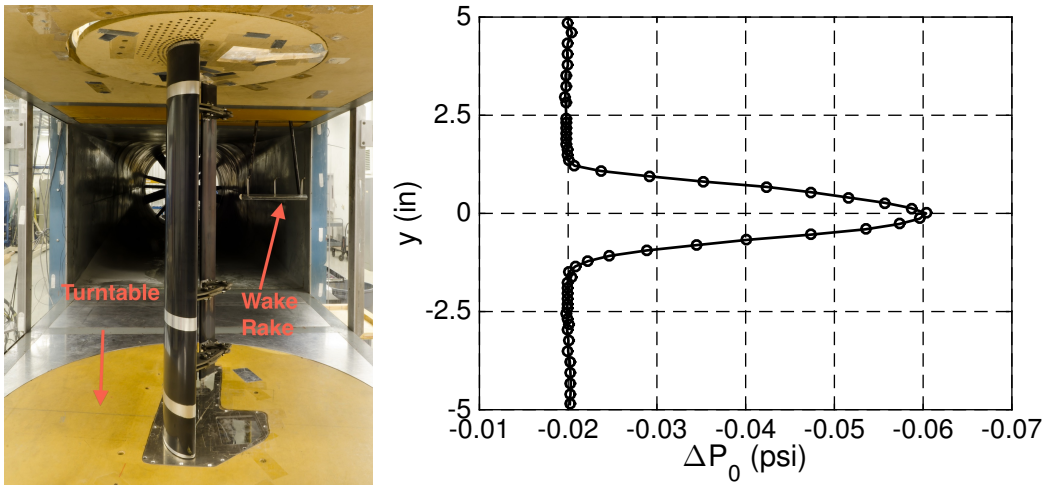

(a) (b)

Figure 3.23: Experimental configuration for one-dimensional wake surveys showing a) front view of MFFS(ns)-026 airfoil with wake rake and b) representative wake profile captured by wake rake.

during the course of this research project, some aerodynamic polars were collected using the older Lintech traverse while others were collected using the newer Zaber traverse. For both traverses, the two axes were independently controlled, and an optical encoder created a closed-loop control law to move the traverse. A large plenum box, which had been previously constructed by graduate students, was installed around the Lintech traverse system in an attempt to prevent air leakage into the test section. Wake profiles were taken for the full width of the tunnel in an effort to capture any secondary wake bursting that may occur off the surface of the airfoil system, and a representative profile with pressures relative to p_{atm} is plotted in Fig. 3.23(b). Methods to reduce the wake profile and further details of the traverses are both discussed later in this section.

One-Dimensional Wake Integration Theory

One-dimensional momentum-deficit theory, as discussed by Jones [63] and Schlichting [64], was used to determine the drag of the airfoil by integrating the momentum deficit across the wake. In essence, momentum-deficit theory integrates a wake profile to calculate a total momentum loss. A control-volume analysis representation is shown in Fig. 3.24. A plane, noted by the subscript 1, perpendicular to U_∞ was assumed to exist far downstream at a location such that the airfoil wake has spread over such a large area that the static pressure p_1 in this wake plane is equal to the freestream pressure (p_∞). After this assumption was made, the sectional drag can be calculated by integrating the difference in velocities between the freestream and the velocity in the plane as shown by

$$D' = \int \rho U_1 (U_\infty - U_1)\, dy_1. \tag{3.39}$$

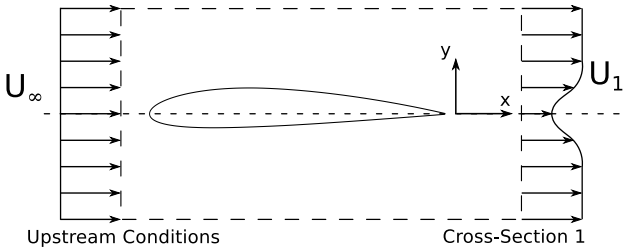

Figure 3.24: Control volume for the one-dimensional momentum deficit method.

While physically correct, Eq. 3.39 is impractical to determine drag as u_1 represents a theoretical wake-velocity deficit at a location in plane 1 that does not actually exist. Consequently, a second plane is assumed to exist parallel to plane 1 but closer to the airfoil model; this plane is denoted as plane w, and it is the plane in which experimental data were collected. It is assumed that a streamtube passes through plane w and plane 1, and thus incompressible conservation of mass is applied such that

$$U_1 dy_1 = U_w dy_w. \tag{3.40}$$

Substitution of Eq. 3.40 into Eq. 3.39 yields the sectional drag at plane w as

$$D' = \int \rho U_w (U_\infty - U_1)\, dy. \tag{3.41}$$

It can be shown that total pressure in the freestream, plane 1, and the wake plane could be calculated by Bernoulli's equation, which is true in a lossless, incompressible flow, and are shown to be

$$p_\infty + \frac{1}{2}\rho U_\infty^2 = p_{t,\infty} \tag{3.42a}$$

$$p_1 + \frac{1}{2}\rho U_1^2 = p_{t,1} \tag{3.42b}$$

$$p_w + \frac{1}{2}\rho U_w^2 = p_{t,w}. \tag{3.42c}$$

It is assumed that no changes in total pressure exist between plane 1 and the wake plane where $p_{t,1} = p_{t,w}$ as the airfoil is located upstream of plane w. Equations 3.42(a-c) can be solved in terms of the velocities U_∞, U_1, and U_w and substituted into Eq. 3.41 such that the drag per unit span was calculated as

$$D' = 2\int \sqrt{(p_{t,w} - p_w)}\left(\sqrt{(p_{t,\infty} - p_\infty)} - \sqrt{(p_{t,w} - p_\infty)}\right) dy. \tag{3.43}$$

It is surmised and assumed that all pressure losses in the wake are attributed to the wake-velocity deficit, and thus it is assumed that $p_w = p_\infty$. The assumption that $p_w = p_\infty$ and combination of Eq. 3.42 yield

$$q_w = q_\infty - \left(p_{t,\infty} - p_{t,w}\right). \tag{3.44}$$

It is noted that Eq. 3.41 can be expressed in terms of dynamic pressure by substituting Eq. 3.44 into Eq. 3.43 to yield [65]

$$D' = 2\int \sqrt{q_\infty - (p_{t,\infty} - p_{t,w})}\left(\sqrt{q_\infty} - \sqrt{q_\infty - \left(p_{t,\infty} - p_{t,w}\right)}\right) dy. \tag{3.45}$$

The drag equation expressed in Eq. 3.45 is preferred over the form expressed in Eq. 3.41 as the pressure difference $(p_{t,\infty} - p_{t,w})$ can be measured in the wake survey. While Eq. 3.41 is usable, an additional probe would need to be installed to determine freestream total pressure. Consequently, Eq. 3.45 was used to determine the drag on the airfoil.

As pressure modules used to capture wake information were referenced to the ambient pressure, the Δp value returned from the pressure modules was $(p_{t,w} - p_{atm})$ in the wake of the airfoil. At the edges of the wake, it is assumed that the total pressure of the local flow is equal to the freestream total pressure. Consequently, measurements by the wake rake outside of the wake of the airfoil yielded a value of $(p_{t,\infty} - p_w)$ which can be calculated by

$$p_{t,\infty} - p_{t,w} = \left(p_{t,\infty} - p_{atm}\right) - \left(p_{t,w} - p_{atm}\right). \tag{3.46}$$

The determined value of $(p_{t,\infty} - p_{t,w}$ and the freestream dynamic pressure q_∞ were both substituted into Eq. 3.45 to yield the sectional drag of the airfoil. A numerical trapezoidal integration scheme was used to evaluate Eq. 3.45. The incremental drag value between node i and $i+1$ was calculated by

$$\Delta D'_i = \left[\sqrt{q_\infty - \left(P_{0,\infty} - P_{0,w_i}\right)}\left(\sqrt{q_\infty} - \sqrt{q_\infty - \left(P_{0,\infty} - P_{0,w_i}\right)}\right) + \sqrt{q_\infty - \left(P_{0,\infty} - P_{0,w_{i+1}}\right)}\left(\sqrt{q_\infty} - \sqrt{q_\infty - \left(P_{0,\infty} - P_{0,w_{i+1}}\right)}\right)\right]\left(y_i - y_{i+1}\right). \tag{3.47}$$

The total drag per unit span was determined by summing all the incremental sectional drag values for the number of points collected N such that

$$D' = \sum_{i=1}^{N_{nodes}} \Delta D'_i. \tag{3.48}$$

It is noted that the number of data points N is greater than the number of probes in the wake rake as data were taken at three positions across the tunnel since the wake rake did not span the width of the tunnel. Finally, the coefficient of drag was calculated using the standard equation

$$C_d = \frac{D'}{q_\infty c} \tag{3.49}$$

to which the corrections discussed in Sec. 3.2.7 were applied. Derivation of the simplified Jones equation required several assumptions, namely:

1. negligible Reynolds stresses

2. constant total pressure along streamlines

3. static pressure in the wake is constant and equal to static pressure at the edge of the wake

In general, these three assumptions are not correct, but the derived drag equation presented in Eq. 3.45 has been shown to yield accurate results. It is worth noting that the wakes studied in this research were highly turbulent. Nevertheless, previous results indicate the simple Jones equation, without accounting for turbulent fluctuations, is accurate at turbulence intensity levels observed in this research [66].

Two-Dimensional Wake Integration Theory

Numerous two-dimensional wake surveys in the *y*-*z* plane (in which *z* is in the spanwise direction) were also executed during this research project using a standard 7-hole probe. A truncated view of the wind tunnel and the associated coordinate system is shown in Fig. 3.25. Wake-survey methods have been developed to yield wake-integral expressions to determine the lift distribution on a three-dimensional model, such as a wing. While methods have been developed to calculate both lift and drag, only the theory regarding the calculation of lift is presented herein, as only lift values were determined with the wake-survey methods in this project. As presented in the literature, a wake-integral expression for lift can be developed, and the derivation and theory of these methods is discussed in this document based upon previous research findings [67–71]. Assuming data were collected at a plane as defined by S_w (as discussed above), it is known that the force on an aerodynamic body is expressed as

$$\mathbf{F} = -\iint_{S_w} \left[(p - p_\infty)\mathbf{n} + \rho \mathbf{V}\left(\mathbf{n}\cdot\mathbf{V}\right)\right] dydz \tag{3.50}$$

in which the variables **F**, **n**, and **V** represent the three-dimensional force, unit-normal, and velocity-perturbation vectors, respectively. This equation can be expanded such that

$$\mathbf{F} = -\iint_{S_w} \left\{(p - p_\infty)\,\mathbf{n} + \rho\left[\left(U_\infty + u\right)\hat{i}\right) + v\hat{j} + w\hat{k}\right]\left[\left(U_\infty + u\right)n_x + vn_y + wn_z\right]\right\} dydz \tag{3.51}$$

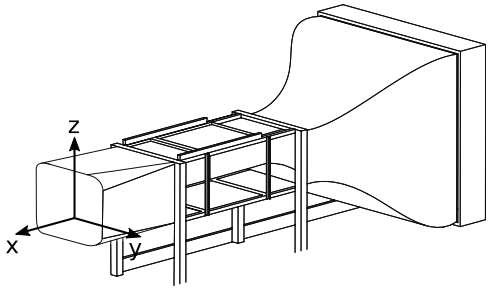

Figure 3.25: Truncated view of wind tunnel and wind tunnel coordinate system.

and by declaring the lift force to act in the y direction, taken in the chord-normal direction, it is shown that

$$L = -\iint_{S_w} \left\{ (p - p_\infty) n_y + \rho \left[v \left(U_\infty + u \right) n_x + vwn_z + v^2 n_y \right] \right\} dydz. \tag{3.52}$$

Terms that are a product of two perturbations will be very small, and thus can be removed from the equation. Upon introduction of

$$p = p_\infty + \Delta p \tag{3.53}$$

and removal of the perturbation product terms, the governing equation is thus

$$L = -\iint_{S_2} \left[(\Delta p) n_y + (\rho U_\infty v) n_x \right] dydz. \tag{3.54}$$

The pressure perturbation term Δp can be expressed as

$$\Delta p = -\rho u U_\infty \tag{3.55}$$

which leads to

$$L = \rho U_\infty \iint_{S_w} \left(u n_y - v n_x \right) dydz. \tag{3.56}$$

This equation can also be written as

$$L = \rho U_\infty \iint_{S_2} \left[\left(\hat{k} \times u \right) \cdot \mathbf{n} \right] dydz \tag{3.57}$$

which can be rearranged using a series of vector identities to be [68, 72]

$$L = \rho U_\infty \iint_{S_w} z \xi dydz \tag{3.58}$$

where ξ is the streamwise vorticity defined by

$$\xi = \frac{\partial v}{\partial z} - \frac{\partial w}{\partial y}. \tag{3.59}$$

It is beneficial to present the governing equations in terms of vorticity since the streamwise vorticity is zero outside of the wake and thus the integral need not be evaluated from $-\infty$ to $+\infty$ but merely over a given sample region W. Consequently, the governing equation is expressed over a finite sample size to be

$$L = \rho U_\infty \iint_{W} z \xi dydz. \tag{3.60}$$

Methods employing classical wing theory and the assumption of a planar wake yields the vorticity in the vortex sheet to be [73]

$$\gamma(z) = -\int_W \xi(y,z)dz \tag{3.61}$$

in which γ is the bound-vortex strength per unit length at a given point and is related to the circulation of the vortex sheet Γ by

$$\Gamma(z) = -\int_{-z}^{z} \gamma(z)dz. \tag{3.62}$$

Finally, the sectional-lift distribution is calculated using the Kutta-Joukowsi theorem to yield

$$C_l(z) = \frac{2}{U_\infty c(z)}\Gamma(z) \tag{3.63}$$

where $c(z)$ is the chord distribution over the aerodynamic body.

3.2.9 Two-Dimensional Wake-Survey System

In addition to the previously-discussed one-dimensional wake surveys, a series of two-dimensional wake surveys were performed in this research to capture the off-body aerodynamic flowfield. Wake surveys were performed in two different geometric configurations including a survey in the *x*-*y* plane, which was at a constant span station, and a survey in the *y*-*z* plane, which was a survey at a constant downstream location. Figure 3.26 presents a truncated view of the wind tunnel and the two sample planes in which data were collected. In the figure, the *x*-*y* sample plane is shown in gray, and the *y*-*z* sample plane is blue. In this research, the *x* axis is aligned with the freestream flow, the *y* axis is in the chord-normal direction, and the *z* axis is in the spanwise direction, as shown in the figure. Full two-dimensional wake surveys were captured in the *x*-*y* plane in an attempt to understand the off-body aerodynamics. As previously discussed, one-dimensional wake surveys were performed in the *y*-*z* plane to yield a more accurate value of drag. Additionally, two-dimensional surveys were performed in the *y*-*z* plane to characterize the effects of the wind-tunnel testing environment. As discussed in Sec. 3.2.8, one-dimensional wake surveys were performed with an array of total-pressure probes. While these data are useful, additional probes were used in the two-dimensional surveys to yield more information. Unsteady velocity data were collected using a split-film probe, and time-averaged velocity, static pressure, and total pressure were collected with a 7-hole probe. The details of the operation of these probes is presented in Chap. 4. Only the traverse equipment and execution of the two-dimensional surveys are discussed in this section.

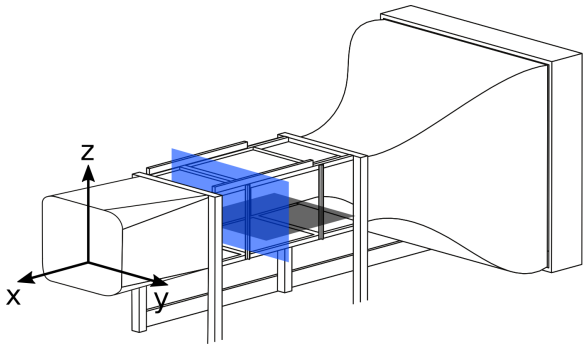

Figure 3.26: Truncated view of wind tunnel showing *x*-*y* sample plane (gray) and *y*-*z* sample plane (blue).

Lintech Traverse Equipment

Wake surveys were performed with two sets of equipment, namely a Lintech two-axis traverse and a Zaber two-axis traverse. The Lintech traverse system has been used at the University of Illinois for over 15 years, and the equipment began to show signs of age and wear over the course of this research and was ultimately replaced by a new two-axis Zaber part way through the research due to continuing failures of the Lintech system. Performance of the Lintech traverse was reliable enough to perform surveys in the *x*-*y* plane, which were collected in wind tunnel entries during the years 2011–2014. The two axes were independently controlled by an IDC S6962 Stepper Motor Drive control box, and this control box was able to be controlled by a user through either a keypad on the front of the control panel or through software commands. Except for rare cases, the Lintech traverse was always moved with automated software using RS232 communication protocol. The custom-made traverse was manufactured by Lintech Motion; as it was custom-made equipment, there was no model number, but the serial number of the traverse was 973501.

Even though the Lintech traverse included two absolute optical encoders to yield position of the traverse at all times, these coordinates were relative to a point $(0,0)$ in a coordinate system fixed to the Lintech traverse. When power was first supplied to the Lintech traverse, the position of the traverse was defined to be $(0,0)$, or the home position. This point was defined to be the home position for all operations of the traverse until the traverse lost power or was power cycled. Consequently, efforts were taken to ensure power was always supplied to the Lintech traverse and that this home position was not lost. If the reference position was lost, the coordinate transformations between the Lintech traverse and the wind tunnel coordinate systems had to be re-determined. A discussion of these transformations and methods are presented later in this section following the discussion of traverse hardware.

Movement commands to the Lintech traverse were sent as a distance to move relative to the current position. Consequently, when it was desired to move the Lintech traverse to an exact location and not just a specified distance, the position of each axis was determined using the optical encoder, and then the relative distance to move was calculated. This linear distance was converted to a finite number of steps for the stepper motor, and this command was finally

passed to the control box. The position of the Lintech traverse during the move was monitored by the control box, and this position was returned to the LabView software once per second. At the completion of the move, the status of the Lintech traverse was returned to the software; the move was either successful or an error was encountered in which the error was displayed on the front panel of the control box. Errors were encountered with increasing frequency and severity over the course of the various wind tunnel entries. Some errors include a "Following Error" meaning that the encoder was either unable to determine the position of the Lintech traverse, or the position reported by the encoder was sufficiently different than the expected location of the traverse. This error typically occurred if there was a cable that became unplugged or if the encoder encountered a dirty spot on the demarcated glass tape. The most severe error was an "Amplifier Fault Error" which was only encountered on Axis 1. Information on the control panel read: "Axis One has an amplifier fault. The drive may have an overtemperature, motor short circuit condition, or an inverted FAULT polarity on a 961/2 indexer." When this error occurred, the only way to circumvent this system failure was to manually remove power to the Lintech traverse and then turn the Lintech traverse back on. When this error occurred, the home position, which had been meticulously determined, was lost. This failure also meant that the partial data set that had been collected was unusable. Conversations with employees at Lintech Motion yielded no further information about the fault or error. As a result of the increasing frequency of this error, the Lintech traverse was decommissioned, and it was replaced with a new two-axis Zaber traverse.

Zaber Traverse Equipment

A new two-axis traverse system was configured and installed to replace the failing Lintech traverse. Two separate linear stages were selected, and these two stages together created a two-axis traverse. Two high-load closed-loop linear stages with a built-in stepper motor, encoder, and controller were acquired from Zaber Technologies, Inc. in Vancouver, British Columbia, Canada. The vertical stage was selected to be part number A-LST1000A-E01-KT07, and the horizontal stage was custom-made and declared to be part number A-LST1250B-E01-ENG1561-KT07. The positions "horizontal" and "vertical" refer to the location of each stage in the standard configuration in which the traverse is mounted on top of the wind tunnel with a wake rake hanging from the traverse. The custom-made horizontal stage is similar to the off-the-shelf A-LST-1000B-E01 with the exception that the custom-made traverse has a travel range of 1250 mm (49.21 in) as opposed to 1000 mm (39.37 in). The longer stage was selected to ensure complete coverage of the wind-tunnel test section was possible. Both linear stages were purchased from the same line of products and thus numerous similarities exist between the systems. A summary of similarities and differences between the two stages is presented in Table 3.4 while exhaustive lists of performance metrics are shown in Table 3.5 in both metric and English units. The metric data in Table 3.5 and associate significant figures are provided exactly the same as data published by the manufacturer; the English values in the table are converted from the metric data, and the proper

number of significant digits is retained during the conversion. A period indicates that trailing zeros for a number in the table are significant.

As seen in the two tables, the peak thrust and maximum speeds for the two linear stages are different. A slower, stronger stage was selected for the vertical traverse while a medium-strength, medium-speed traverse was selected for the horizontal stage. A stronger stage was required for the vertical stage to ensure that enough thrust was able to be produced to move the heaviest wake rakes currently or historically in use in the University of Illinois wind tunnel facility; this traverse was found to be 45 lb. During operation, the user prescribes a desired linear velocity for the Zaber stages, and the precision lead screw is rotated by the motor at a certain rotational speed to yield the desired linear velocity. The maximum thrust applied by the stage was a function of the selected speed in which slower speeds yielded higher thrust and faster speeds resulted in decreased thrust. Figure 3.27 shows the relationship between linear speed and thrust produced for each of the two stages. As seen in the figure, a slower speed yields a higher thrust while a faster speed produces a smaller quantity of thrust. During this research, the speeds of the vertical and

Table 3.4: Configuration Summary for Zaber Traverse

Controller	Built in
Encoder Type	Rotary quadrature encoder
Communication Interface	RS-232
Communication Protocol	Zaber ASCII and Zaber Binary
Maximum Centered Load	1000 N (224.3 lb)
Maximum Cantilever Load	3000 N-cm (4248 oz-in)
Guide Type	roller bearing
Vertical Runout	$< 13\mu$m ($<$ 0.000512 in)
Horizontal Runout	$< 13\mu$m ($<$ 0.000512 in)
Pitch	0.10 deg
Roll	0.08 deg
Yaw	0.05 deg
Maximum Current Draw	1200 mA
Power Supply	12-48 VDC
Power Plug	Molex Mini-Fit Jr. 3-pin
Motor Steps per Revolution	200
Motor Type	2-phase stepper
Inductance	1.6 mH
Data Cable Connection	Minidin 6 M/F
Mechanical Drive System	Precision lead screw
Limit or Home Sensing	Magnetic home sensor
Manual Control	Indexed knob with push switch
Axes of Motion	1
LED Indicators	Yes, 1
Mounting Interface	M6 and M3 threaded holes
Operating Temperature Range	0–50 deg C (32–122 deg F)
ROHS Compliant	Yes
CE Compliant	Yes

Table 3.5: Zaber Traverse Performance Metrics

	Vertical Stage	Horizontal Stage
Model	A-LST1000A-E01-KT07	A-LST1250B-E01-ENG1561-KT07
Microstep Size	0.124023438 μm (0.00000488281251 in)	0.49609375 μm (0.000019531250 in)
Linear Motion per Motor Revolution	1.5875 mm (0.062500 in)	6.35 mm (0.250 in)
Travel Range	1000. mm (39.37 in)	1250. mm (49.21 in)
Accuracy (Unidirectional)	250. μm (0.00984 in)	250. μm (0.00984 in)
Repeatability	$< 2\mu$m ($<$ 0.00005 in)	$< 2\mu$m ($<$ 0.00008 in)
Backlash	$< 5\mu$m ($<$ 0.0002 in)	$< 10\mu$m ($<$ 0.0004 in)
Maximum Speed	22 mm/sec (0.87 in/sec)	100. mm/sec (3.94 in/sec)
Minimum Speed	0.0012 mm/sec (0.000047 in/sec)	0.00465 mm/sec (0.000183 in/sec)
Speed Resolution	0.0012 mm/sec (0.000047 in/sec)	0.00465 mm/sec (0.000183 in/sec)
Peak Thrust	700. N (157 lb)	260. N (58.5 lb)
Maximum Continuous Thrust	560. N (126 lb)	260. N (58.5 lb)
Mass	6.90 kg (0.473 slug)	6.90 kg (0.473 slug)

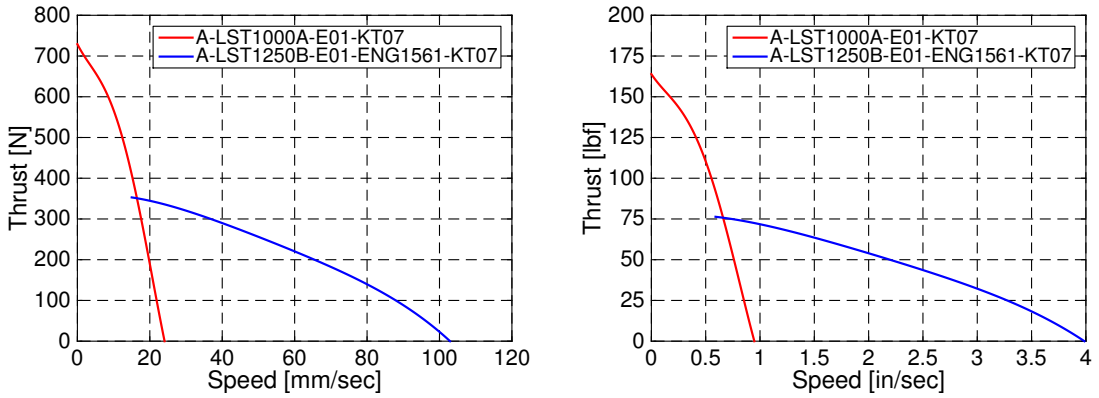

(a) (b)

Figure 3.27: Relationship between translational speed and maximum supplied thrust for two Zaber stages in a) metric and b) English units (data taken from Ref. 74).

horizontal stages were set to be 0.787 in/sec (20.0 mm/sec) and 1.83 in/sec (46.5 mm/sec) with a linear acceleration of 6.11 in/sec^2 (155.2 mm/sec^2) and 24.43 in/sec^2 (620.7 mm/sec^2), respectively. According to Fig. 3.27, the estimated thrust for the vertical and horizontal stage were estimated to be 45 lb (200 N) and 60 lb (270 N). These thrust values were sufficiently high to move the wake rake and traverse arm for all wake-survey configurations.

Similar to the Lintech traverse, it was possible to communicate with the Zaber traverses using both a manual input mode and software. The only modes of operation in manual mode are to turn a small knob clockwise or counterclockwise to change the speed of the stage. This knob can be depressed which stops all movement of the stage immediately. Only the speed of the stage can be set manually; no other communication with the Zaber is possible when in manual mode. New software was written in Labview to communicate with the Zaber controllers using the

Zaber binary protocol [75]. Both controllers contained firmware version 6.17, which was the most-current version of the firmware when the devices were acquired in August 2014. Finally, the closed-loop mode was prescribed to be mode 3 in which the device sends a `SLIP` command if and when slipping is detected. If this is the case, the `CURRENT POSITION` value is updated to the actual location at which a slip was detected.

Hardware and Setup for *y*-*z* Survey

Some measurements were taken in the *y*-*z* plane for the purposes of capturing a drag polar and for performing a wake survey with the 7-hole probe. This configuration is the standard setup for the traverse in the wind tunnel, but some modifications and enhancements were made to the stock setup. As the new Zaber traverse system was acquired for application to this research project, a variety of steps were taken to fully integrate the new Zaber traverse with the wind tunnel. A significant amount of software was added and changed in the data acquisition LabView code such that the computer could interface with the Zaber traverse. In addition to the software additions, a new pressure box was manufactured to house the Zaber traverse on top of the wind tunnel. This pressure box, pictured in Fig. 3.28(a), was manufactured out of a combination of 5/8-in plywood supported by 2 in$\times$2 in pine wood. Support members made of steel and wood were placed longitudinally across the box to ensure structural integrity during full-speed operation of the wind tunnel. Access to the box is possible through three different doors including one large plywood door on top of the box, a medium-sized acrylic plastic door on the downstream side of the box, and a small plywood door on the side of the box pointing in the southern direction. The small access door on the side and the door on the top provide access to the manual control knobs discussed earlier in this section. The support and mounting brackets for the wake rake and traverse arms are visible through the downstream plastic see-through door. Two mounting points were constructed and installed on the top of the box to allow the box to be hoisted with a small crane and straps. After construction of the new setup, data were collected using the wake rake to acquire a drag polar, as shown in Fig. 3.7 and with a 7-hole probe as pictured in Fig. 3.7.

Hardware and Setup for *x*-*y* Survey

Measurements in the *x*-*y* plane were taken by moving the traverse, which is usually located on top of the wind tunnel, to the sidewall of the wind tunnel. In this configuration, the traverse was able to be moved in the streamwise and chord-normal directions (x and y, respectively). These wake surveys were all collected with the Lintech traverse. It was during these long runs that the Lintech traverse began to perform unreliably, which ultimately led to the new Zaber traverse purchase. Surveys in this plane were collected using both a split-film probe and a 7-hole probe, and slightly different experimental setups were used for the two tests, as shown in Figs. 3.29–3.30. As seen in Fig. 3.29, the sidewall-attachment system consisted of an alternate wooden sidewall, a steel mounting table, numerous cinder

(a) (b)

Figure 3.28: Hardware for *y*-*z* wake survey including a) newly-constructed plenum box and b) 7-hole probe rig.

blocks to elevate the traverse to the proper height, two aluminum I-beam supports, a large block and rail, a black steel mounting block, a two-armed traverse that extended into the test section, and assorted hardware used to seal the test section. The large steel table was sufficiently heavy to stay in place, and the cinder blocks were clamped to the table using large carpenter's clamps and C-clamps. A detailed photograph of the block-and-rail system is presented in Fig. 3.30(a). A 1-inch thick aluminum plate was attached to the aluminum block, and the Lintech traverse traverse is shown to be attached to this plate in the figure. Figure 3.30(b) depicts the end of the horizontal support as it was installed inside the wind tunnel; a thin aluminum probe mount was attached to the end of the arm, and the probe was subsequently attached to this mount. As seen in the picture, a symmetric fairing was manufactured around the horizontal support to reduce the presence of unsteady vortex shedding.

Split-Film Probe Setup

The basic design for the sidewall used for the split-film probe experiment was developed by Whalen [76], but numerous modifications to the design were implemented for the split-film probe setup used in this research, as seen in Fig. 3.29(a). A large black steel support was mounted to the top of the Lintech traverse, and a two-arm horizontal support was mounted to this block. Two rubber sleeves made from high-strength-rubber pond liner acquired from a local garden center were wrapped around the traverse arms to minimized leakage. Rubber cement was used to seal the edges of the sleeves, and a worm-drive tube clamp secured the rubber sleeve to the steel arm near the mounting block, as seen in Fig. 3.31. An elegant slide system secured the rubber sleeves to the wind-tunnel wall and also sealed the test section. A system consisting of aluminum filler plates and balsa wood, measuring a total of 38.75 in long and 5 in wide, was manufactured to seal the test section. The components of this assembly consisted of an outer clam shell, an

(a)

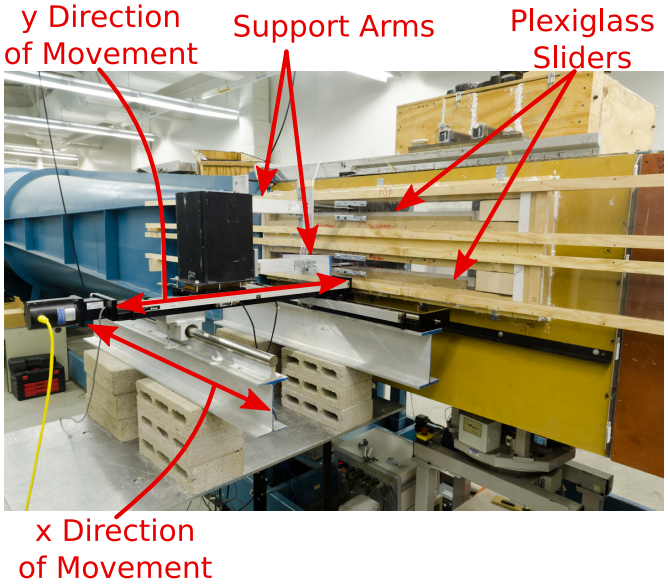

(b)

Figure 3.29: Wide view of sidewall-mounted traverse setup for a) split-film probe test and b) 7-hole probe test.

outer plate, two inner plates, four aluminum bars, and a balsa/teflon slider; both an assembled view and an exploded view of the assembly are presented in Fig. 3.31. The balsa/teflon slider was able to slide 11.5 inches in the upstream and downstream directions yielding a traversable range of 23.0 in. When assembled, this system could be installed into the existing sidewall in a variety of streamwise locations.

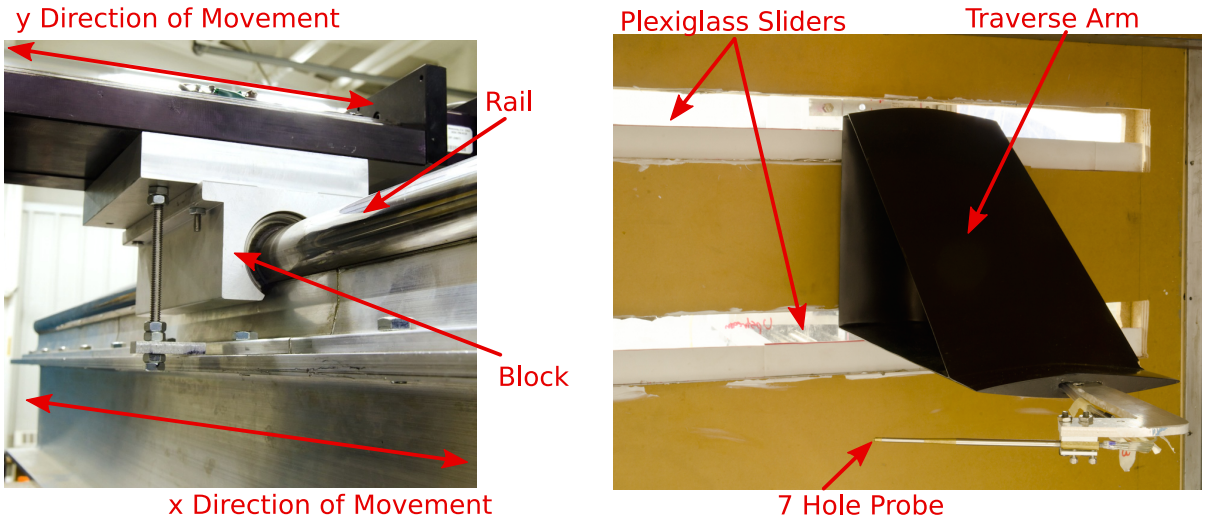

(a) (b)

Figure 3.30: Detailed view of a) block and rail traverse mechanism and b) traverse arm with 7-hole probe mounted in the wind tunnel.

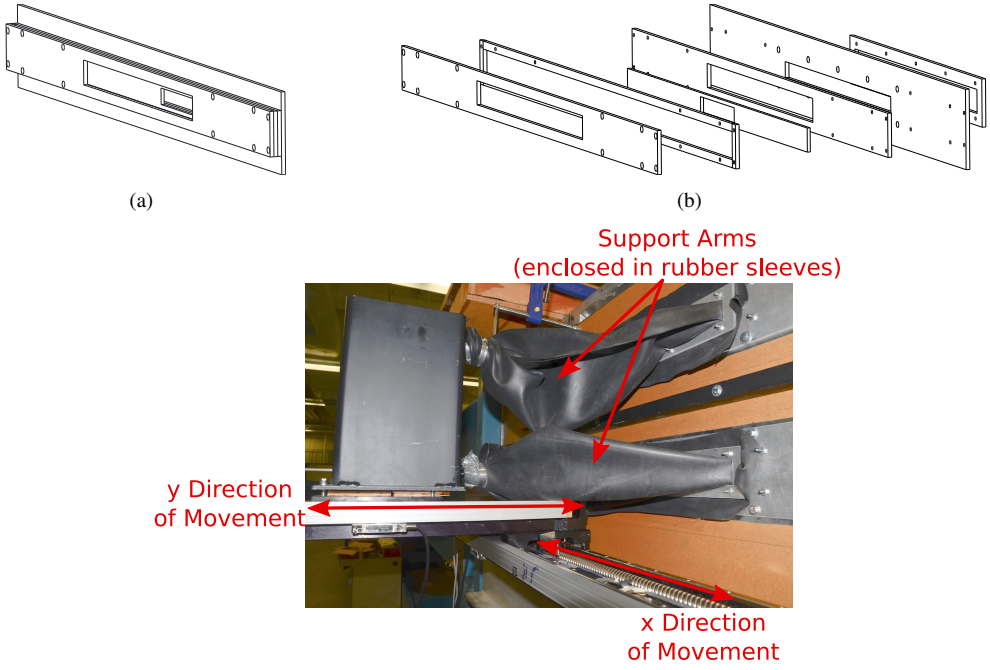

(a) (b) (c)

Figure 3.31: Sidewall sealing system used in split-film probe test a) assembly view, b) exploded view, and c) connection between mount and horizontal support.

7-Hole Probe Setup

Further modifications to the sidewall used during the split-film probe test were made such that the traverse could extend significantly further downstream than the original design permitted, as shown in Fig. 3.29(b). The horizontal

slots through which the arm traveled were extended an additional 6 inches in both the upstream and downstream directions. In addition, the internal sliding assembly used in the split-film probe experiment was replaced with a large external sliding assembly consisting of four 6 ft pieces of plastic acrylic ("plexiglass"), wooden supporting tracks, and a narrow wooden box; this system is shown in Fig. 3.32(a,b). In total, the pressure box measured 62 in long, 19 in high, and 3 in wide, and was attached to the sidewall with aluminum L-brackets. Two sets of wooden tracks, supporting the top and bottom of the plexiglass sliders, were nailed to the sidewall and supported by wooden jigs where the tracks extended beyond the sidewall. These long, thin wooden rails can be easily seen in Fig. 3.32(a,b). The distance between the two U-shaped tracks was slightly larger than the width of the plexiglass sliders such that the

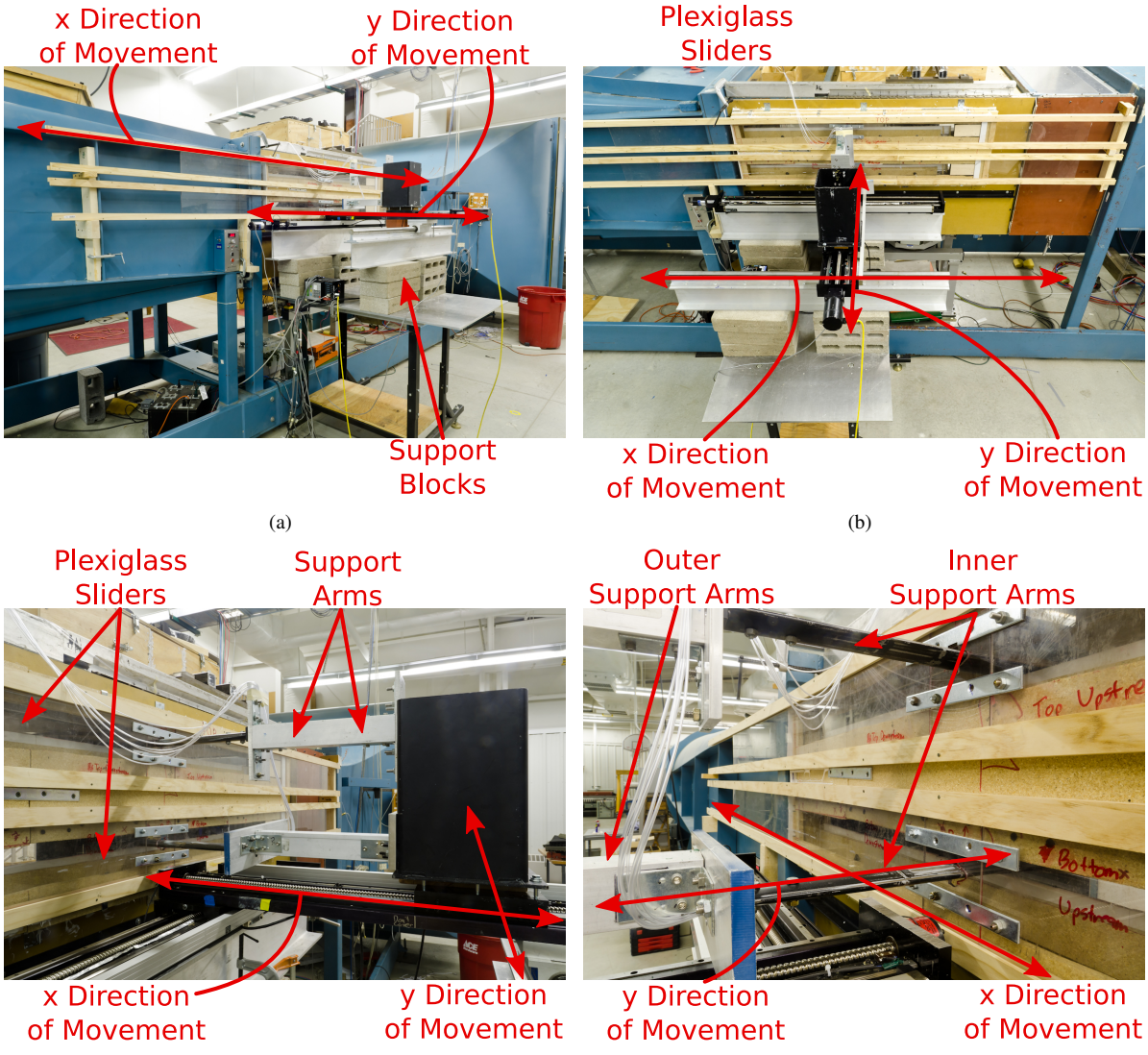

Figure 3.32: Detail of 7-hole probe sidewall attachment showing a) wide, isometric view of setup, b) top view clearly showing wooden guides, c) horizontal arm attachment, and d) acrylic slides and arm interface.

sliders would not experience significant friction or binding while being moved by the traverse. As the pressure in the test section was less than the atmospheric conditions, the plexiglass was sucked toward the test section and formed a tight seal against the wooden tracks. Due to the large size of the slot in the side of the wind tunnel, foam plates were installed to reduce unsteady aerodynamic effects. Rubber sleeves were not used to seal the horizontal arm in this setup, as the attachment image in Fig. 3.32(c) clearly depicts, because the sleeves were replaced with the acrylic sliding panels. Two aluminum extensions were manufactured to permit the traverse arm to extend further into the test section. As seen in Fig. 3.32(d), the steel horizontal arms passed through the acrylic sliders and into the wind tunnel.

3.2.10 Pressure Measurement System

All pressure measurements were collected using a Pressure System DTC Initium differential-pressure system with a combination of ± 10 in water column (0.36 psi, 2.5 kPa) and 1 psi (6.90 kPa) miniature electronically-scanned pressure (ESP) modules that contained 32 pressure ports on each module. Data were collected at 650 Hz per channel while sampling all 32 channels in sequence (not simultaneously). Digital measurements are corrected for temperature variations at each port, and thus the Initium system does not need to be frequently calibrated, but merely zeroed between runs. A large button on the front of the Initium control box, illuminated with a red or green LED light, was pressed to power cycle the Initium box thus effectively zeroing the Initium box. Differential pressure measurements were made between each of the 32 ports and one reference port.

In addition to the 32 ports, four additional ports labeled C1, C2, RREF, and CREF were on each module. The CREF (calibration reference) port was not used in the current study as calibrations were not re-determined; calibrations of each module were used as supplied by the vendor. The C1 and C2 lines were connected ("plumbed") to the Initium system to re-zero the modules at the beginning of each run. The RREF (run reference) port, the value to which Δp values were determined for all 32 ports, was connected to either p_{atm} or p_{ts} depending on the specific application. The Initium control box was connected to the main data acquisition computer through a 10/100 Base-T Ethernet cable through which TCP/IP protocol was used to communicate, and each ESP module was connected to the Initium box with a PSCB cable. A tank of compressed nitrogen, controlled with a solenoid valve by the data acquisition software, was connected to the Initium to zero the ESP modules. A supply line with 100 psi of compressed nitrogen was connected from the tank to the rear of the Initium box. The tubes labeled C1 and C2 were attached to the respective ports on all ESP modules. When desired, pressurized air was applied through the C1 line to shift a manifold within each module by a small linear distance, and each port was subsequently tared with the manifold in the shifted location. Upon completion of the zeroing, 100 psi of compressed nitrogen was applied to the C2 line which shifted the manifold back to the original position to be used for data acquisition.

The connections of these lines for each of the tests will now be briefly discussed. Modules were located in one of two locations including: on the floor next to the Initium control box, or on the ceiling of the wind tunnel immediately downstream of the large pressure box.

Drag Polar Tube Connections

Wind-tunnel tests that captured drag polars required the use of three different ESP modules. A 1 psi module was installed next to the Initium control box, and the PTS line was plugged into the RREF port. Nothing was plugged into CREF or CAL for any of the tests. A line labeled "PSS" was plugged into a port, usually port 32, on the module to capture $PSS - PTS$, which was used to determine q_∞. While the specific port used to measure q_∞ was irrelevant, the numeric value for this port was specified in the TapInfo.dat file. Two 10-in water column modules were installed on the ceiling of the wind tunnel. Tygon tubes connected to the 59 probes in the wake rake were connected to ports in the two modules, and the location of each of these tubes was specified in the `RakeInfo.dat` file. Finally, a PATM line was plugged into RREF.

7-Hole Probe Tube Connections

The plumbing for a 7-hole probe test was significantly simpler than that of a wind tunnel polar. In this case, one 10-in water column module was installed on the floor next to the Initium control box, and tubes for holes 1–7 were plugged into the ports labeled 1–7. The PTS line was plugged into RREF while nothing was plugged into either CREF nor CAL. The freestream dynamic pressure was determined by plugging the PSS line into the desired port on the Initium, and this port number was defined in the TapInfo.dat file.

Measure q_∞ Only

For cases in which only the freestream dynamic pressure was needed, such as during the split-film probe tests, one 10-in water column module was installed next to the Initium control box. The PSS line was plugged into a numbered port, and the selection of this port was specified in the TapInfo.dat file. A tube labeled PTS was connected to the RREF port, and, as was the case for the previous tests, no tubes were connected to the ports labeled CREF or CAL.

3.2.11 Wind Tunnel Adaptations

A new wind-tunnel floor and ceiling were both manufactured to be used with the multielement airfoil model. Figure 3.33 depicts the vertically-mounted airfoil model, the horizontal strut to which measurement probes were attached, and both the new floor and ceiling. The floor was adapted for the current project from an existing solid-wood floor that was used in a previous research project while the ceiling was manufactured from newly-acquired MDF wood.

Figure 3.33: Wind tunnel model including new floor and ceiling with horizontal brace for wake-survey measurements.

Standard wood-shop tools were used to create holes through which the struts for each element passed through to attach to the wind-tunnel force balance. A new ceiling was manufactured to interface with the FPS pressure box and to interface with the upper wooden model plug. This circular plug rotated with α and provided a solid wall for the top of the wind tunnel.

3.2.12 Flow Visualization Techniques

Fluorescent surface oil flow visualization techniques were applied to the multielement airfoil models. Flow visualization was performed by first applying a very thin layer of 10W-30 motor oil to the surface of the airfoil model. An airbrush was then used to apply a fluorescent leak detector dye and mineral oil mixture to the surface of the model. A single strip of yellow electrical tape was applied to the surface of the main element which was marked with chordwise x/c coordinates at 5% increments. The tape allowed the location of key flow features to be easily determined. Holes and gaps in the floor and ceiling of the wind tunnel were sealed with clear packing tape to ensure that no flow visualization oil leaked onto the traverses which may have damaged the optical tapes. The encoder tapes were sensitive to any type of foreign contaminant, as discussed in Sec. 3.2.3.

A coat of 10W-30 motor oil was applied to the surface of the airfoil model with a lint-free shop cloth. A lint-free cloth was used to ensure no particulates were deposited on the surface of the model which would trip the air from laminar to turbulent flow at a location upstream of the clean-model transition point. The oil was applied to reduce the surface sheer stress of the mineral oil so the oil could easily flow downstream over the model. Excess motor oil was wiped away with a dry lint-free cloth. Four drops of Tracer TP34000601 UV florescent leak-detector dye were

added to a bottle that contained approximately 250 mL of standard mineral oil. Nitrogen gas regulated to about 30 psi was used to apply the mixture to the surface of the model with an airbrush while the tunnel was operating at 30 RPM (approximately 6.1 ft/sec or 1.85 m/sec). The tunnel was turned on so the fumes of the airbrush would be convected down the tunnel so as not to adversely affect the health of researchers. An airbrush was used to ensure the spray particles were small enough to not be dominated by the downward force of gravity and slide down the model. The entire surface of the model was sprayed with the fluorescent mineral oil mixture so the surface resembled the surface of an orange peel. Four black lights were used to fluoresce the dye on the model to ensure complete and even coverage of the model.

After application of the mineral oil mixture, the desired angle of attack of the model was set. The tunnel was then ramped up to the desired RPM for 3–5 min. After the proper time elapsed, the tunnel was stopped. Black lights were again turned on and placed in the test section to minimize the glare reflecting from the surface of the model. Photographs were taken with a Nikon D7000 DSLR camera with a $f/2.8$ 17-55 mm DX Nikkor lens. Images were captured in standard raw NEF format and later postprocessed using Adobe Photoshop Lightroom to enhance contrast of the surface oil flow. Photographs were taken at a large $f/$ number for an exposure time of 3 sec at an ISO of approximately 200 to reduce image noise as well as increase clarity and sharpness in the photo. Focus was adjusted manually and proper image focus was ensured by using the LCD screen on the back of the camera. This was done by digitally zooming in on the yellow electrical tape and subsequently adjusting the focus until the written label was sharp and clear. The surface of the airfoil model was cleaned with standard glass cleaner after each run. The flow visualization process was repeated for each desired angle of attack.

Representative surface flow visualization on the upper surface of the system is shown in Fig. 3.34 in which the flow is from the left to the right. Movement of the oil on the surface is caused by the shear stress on the surface of the airfoil. Oil near the stagnation point of the airfoil system was in a region of high shear, so little oil remained in that region as the high-shear boundary layer moved much of the oil downstream. Regions of low shear are observed where the oil has not moved a significant amount. The oil accumulation line indicates that the base friction (resulting from the contact between the oil and the surface) balances C_f (between the oil and the air). A laminar separation bubble is present for all three airfoil elements, and it is easily seen over the main element as labeled in the photo. An oil accumulation line is present at the trailing edge of each airfoil element indicating the presence of a laminar separation bubble but no separation from the surface is observed.

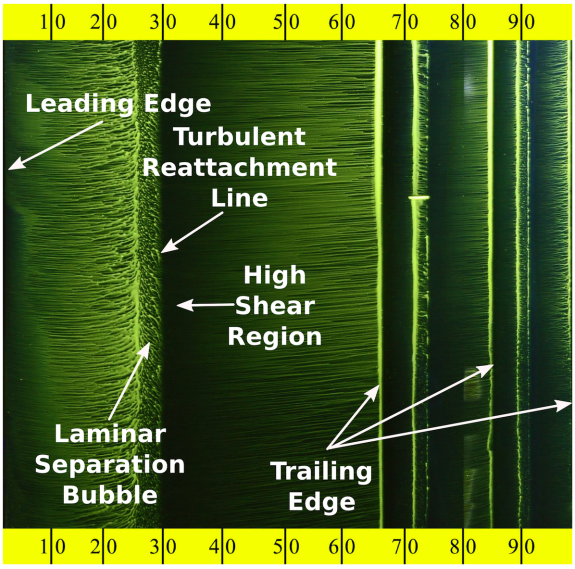

Figure 3.34: Representative flow visualization results with key features labeled.

3.3 MSES

The computational tool MSES was used to provide a low-order computational prediction of the aerodynamics and flowfield for a given airfoil. Throughout the course of this project, MSES v. 3.05, released in July 2007, was utilized [77]. MSES is a coupled inviscid/viscid suite of codes that can be used to predict the flow around multielement airfoils and is partially based upon the single-element ISES code, which in turn is partially based upon the single-element XFOIL code as documented in a wide number of papers [78–86]. A two-equation lagged-dissipation integral boundary layer formulation is coupled to an outer streamline-based Euler solution by the displacement thickness, and multi-dimensional Newton iteration is performed to simultaneously solve the viscous and inviscid regions. The steady-state Euler equations are discretized on an intrinsic curvilinear streamline-fixed finite-volume grid, in which the grid and the flowfield are simultaneously solved. Axisymmetric wakes and confluent boundary layers are modeled through a multi-deck integral boundary-layer formulation, and the location and size of wakes shed from multielement airfoils has been found to be reasonably accurate [87–89]. Transition from laminar to turbulent flow can be specified or predicted. Predictions are based upon the Orr-Sommerfeld equation in which the onset of Tolmein-Schlichting waves provides a manner to predict boundary-layer transition. Coupled inviscid/viscous solvers such as MSES are computationally cheaper in which results are returned in seconds than a Navier-Stokes solver wherein computations are performed over multiple hours. However, this decrease in cost is associated with a decrease in fidelity. Thus, the potential flow/boundary layer coupled solvers are typically deemed a low-order computational method. MSES was

only used in select cases in this research project when rapid solutions were needed, such as when designing an airfoil. The details of theory and operation of the MSES suite of programs will now be discussed in greater detail.

3.3.1 Grid Generation (MSET)

Surface preparation and grid generation were performed using the MSET program, which is included with the standard distribution of MSES. Airfoil coordinates are imported as discrete points, and then the points are fit with a spline curve. Node spacing on the spline curve, which defines the surface discretization, is determined from

$$\Delta s \sim \frac{1}{1+a|\kappa|^b} \tag{3.64}$$

in which Δs is the node spacing by arc length, k is the local surface curvature, a is the curvature coefficient, and b is the curvature exponent. The value of a is indirectly declared by the user through the specification of Δs at the stagnation point of the airfoil, and b is able to be directly declared by the user. A large value of b, such as $b = 2$, provides tight grid spacing in high-curvature regions while a smaller exponent, as in $b = 0.05$, yields a more-uniformly-spaced surface grid.

An intrinsic grid is used to discretize the governing equations in which one coordinate axis is aligned with a streamline and the other coordinate is orthogonal to the streamline. Through this representation, the continuity and energy equations are simplified into one condition of constant mass flux and one condition of constant stagnation enthalpy along each stream tube in which two cells, denoted as 1 and 2, are related by

$$\dot{m} = \rho_1 U_{t,1} A_1 = \rho_2 U_{t,2} A_2 \tag{3.65}$$

and

$$h_t = \frac{\gamma}{\gamma-1}\left(\frac{p_1}{\rho_1}\right) + \frac{1}{2}U_{t,1}^2 = \frac{\gamma}{\gamma-1}\left(\frac{p_2}{\rho_2}\right) + \frac{1}{2}U_{t,2}^2 \tag{3.66}$$

in which h_t is the stagnation enthalpy and γ is the ratio of specific heats. In this manner, the number of unknown flowfield parameters at each grid node is reduced from four unknowns to two unknowns. However, the intrinsic grid methods introduce two unknowns with regard to the x and y values of each node.

3.3.2 Flow Solver (MSES)

As previously mentioned, a viscous inner solution is coupled with an inviscid Euler outer solution. The steady-state conservative Euler equations govern this outer region in which the conservation of mass is expressed by

$$\oint \rho \mathbf{V} \cdot \mathbf{n} ds = 0 \tag{3.67}$$

where $\mathbf{V}$ and $\mathbf{n}$ are the velocity and face-normal vectors, respectively. The conservation of momentum is governed by

$$\oint \left[\rho \left(\mathbf{V} \cdot \mathbf{n}\right) \mathbf{V} + p\mathbf{n}\right] ds = 0 \tag{3.68}$$

and the conservation of energy is

$$\oint \rho \mathbf{V} \cdot \mathbf{n} h_t ds = 0. \tag{3.69}$$

While the Euler equations do not model viscous effects, it is assumed that viscous effects are confined to the boundary layer and wake region of the flowfield, and that the Euler equations can be applied to the external flowfield.

Calculations in the viscous-dominated regions of the flowfield, namely the boundary layers and wakes, are performed with the boundary-layer equations. In the coupled method utilized in MSES, it is known that the only effect of the boundary layer is to displace the inviscid flow away from an aerodynamic body or wake centerline which thus defines a new displacement body. The two-dimensional Prandtl boundary-layer equations are used to govern this region of the flowfield, and the continuity of mass, momentum, and energy are expressed in computational coordinates (ξ, η) with corresponding velocity components (ζ, χ) as

$$\frac{\partial \rho}{\partial t} + \frac{\partial (\rho \zeta)}{\partial \xi} + \frac{\partial (\rho \chi)}{\partial \eta} = 0 \tag{3.70a}$$

$$\rho \left(\frac{\partial \zeta}{\partial t} + \zeta \frac{\partial \zeta}{\partial \xi} + \chi \frac{\partial \zeta}{\partial \eta} \right) = -\frac{\partial p_e}{\partial \xi} + \frac{\partial}{\partial \eta} \left(\mu \frac{\partial \zeta}{\partial \eta} \right) \tag{3.70b}$$

$$\rho \zeta \frac{\partial h}{\partial \xi} + \rho \chi \frac{\partial h}{\partial \eta} = \zeta \frac{\partial p_e}{\partial \xi} + \frac{\partial}{\partial \eta} \left(\frac{\mu}{Pr} \frac{\partial h}{\partial \eta} \right) + \mu \left(\frac{\partial \zeta}{\partial \eta} \right)^2 \tag{3.70c}$$

wherein the subscript e refers to a value at the edge of the boundary layer and in which the Prandtl number Pr is defined by the standard equation

$$Pr = \frac{C_p \mu}{k} \tag{3.71}$$

where c_p is the specific heat capacity and k is the thermal conductivity. The assumption of a perfect gas and steady flow yield simplifications to Eq. 3.70 to be

$$\frac{\partial(\rho\zeta)}{\partial\xi}+\frac{\partial(\rho\chi)}{\partial\eta}=0 \tag{3.72a}$$

$$\rho\zeta\frac{\partial\zeta}{\partial\xi}+\rho\chi\frac{\partial\zeta}{\partial\eta}=-\frac{\partial p_e}{\partial\xi}+\frac{\partial}{\partial\eta}\left(\mu\frac{\partial\zeta}{\partial\eta}\right) \tag{3.72b}$$

$$\rho\zeta\frac{\partial h}{\partial\xi}+\rho\chi\frac{\partial h}{\partial\eta}=\zeta\frac{\partial p_e}{\partial\xi}+\frac{\partial}{\partial\eta}\left(\frac{\mu}{Pr}\frac{\partial h}{\partial\eta}\right)+\mu\left(\frac{\partial\zeta}{\partial\eta}\right)^2. \tag{3.72c}$$

It is noted that the velocity χ in the continuity equation [Eq. 3.72(a)] can be eliminated as there is no streamline-normal mass flux with the intrinsic grid formulation. Eqs. 3.72(b,c) are then integrated from the surface to infinity and, upon assuming freestream adiabatic conditions, the final governing equations are

$$\frac{d\theta}{d\xi}+\left(H+2-M_e^2\right)\frac{\theta}{\zeta_e}\frac{d\zeta_e}{d\xi}=\frac{C_f}{2} \tag{3.73a}$$

$$\theta\frac{dH^*}{d\xi}+\left[2H^{**}+H^*(1-H)\right]\frac{\theta}{\zeta_e}\frac{d\zeta_e}{d\xi}=2C_d-H^*\frac{C_f}{2}. \tag{3.73b}$$

Equation 3.73 is valid for laminar and turbulent boundary layers as well as for wakes. The final solution to the system of equations is closed with a series of empirical relationships for H^*, C_f, and C_d, which are different for laminar or turbulent boundary layers [79, 89, 90].

3.3.3 Postprocessing (MPLOT)

Upon convergence of a grid/flowfield solution, the user is able to postprocess the solution using MPLOT. MPLOT, built into the MSES package, is a terminal/X11-based program in which the flowfield can be visualized and various quantities can be displayed to the user. A solution, including grid and solution data, was also able to be exported through MPLOT. Force and moment values as well as the transition points are also able to be extracted and displayed to the user.

3.4 Tetrahedral Unstructured Software System (TetrUSS)

The Tetrahedral Unstructured Software System (TetrUSS) is an unstructured Reynolds-averaged Navier Stokes (RANS) computational fluid dynamics (CFD) package originally developed in the 1990s and supported by team of engineers at NASA Langley [91, 92]. TetrUSS is a loosely-coupled package in which Euler or Navier-Stokes solutions are computed using a tetrahedral grid with finite-volume equation formulation. The suite of programs consists of three major independent programs which are used to prepare the geometry, generate a grid, and predict the flow. These

three programs consist of GridTool Cocoa, VGrid/PostGrid, and USM3D, which will all be briefly discussed in this section. In addition, an assortment of postprocessing and parallelization utilities are also provided with the TetrUSS package. A variety of different turbulence models have been implemented for the viscous solutions.

3.4.1 Geometry Preparation (GridTool Cocoa)

GridTool Cocoa (GTC) was used to prepare the geometry of interest for use in the volumetric grid generator and flow solver [93]. GTC, the OS-X ported version of GridTool, utilizes a series of non-uniform rational B spline (NURBS) surfaces, represented by patches, to define the geometry. An assortment of tools are available to define, modify, or repair surfaces which are inputted in Initial Graphics Exchange Specifications (IGES) as either spline-defined surfaces or as discrete points. A quasi-two-dimensional representation of the airfoils, which is the standard manner to computationally simulate a two-dimensional flowfield, was implemented in which reflection planes were defined to bound the airfoil surfaces, and an isometric view of this airfoil representation is shown in Fig. 3.35(a). The reflection planes and outer computational domain are not plotted in the figure.

As previously mentioned, a series of patches are defined by the user to declare the geometry in NURBS surfaces. NURBS surfaces are preferred over discrete-point surfaces as the surface mesh can thus be represented by equations and curves instead of straight lines. Each patch was defined by a series of outer boundary curves in which the surface-normal vector pointed away from the geometry; the direction of the normal vector declares the direction in which the volumetric grid will grow. Each airfoil element was defined by two patches, one each for the suction and pressure sides of the airfoil, per recommendations from the software developers at NASA Langley. These patches are presented in Fig. 3.35(b) in which each patch is presented as a different color. All airfoils simulated in this research project contained sharp, infinitely-thin trailing edges.

In addition to defining the geometry, patches were used to specify boundary conditions on each surface. While numerous different boundary conditions are available in TetrUSS, only three different boundary conditions were required over the course of this research; these three conditions included boundary condition 1 as a reflection plane, boundary condition 2 as a full-extrapolation plane, boundary condition 3 as subsonic outer boundaries, and boundary

(a) (b)

Figure 3.35: Multielement airfoil in GridTool Cocoa showing a) quasi-2D geometry and b) patches defining surfaces.

condition 4 as a viscous surface. A boundary condition flag was selected from a drop-down menu in the patch dialog box in GTC to define each of the boundary conditions.

Boundary condition 1, a reflection plane, was used on the edges of the airfoil to create a quasi-two-dimensional simulation. The reflection plane is a no-flux boundary condition in which inviscid, tangent flow is declared on the surface. All three velocity components u, v, and w are extrapolated to the boundary surface via a Taylor series expansion from neighboring cells. This resultant three-component velocity vector is not tangent to the surface. Consequently, the surface-normal component of the extrapolated velocity vector is subtracted, which thus enforces tangent flow. Nodal-averaged quantities are handled differently with boundary condition 1 to ensure no corner leakage is observed at sharp corners intersecting the symmetry plane [94].

A select number of computational simulations in this research project utilized boundary condition 2, a full-extrapolation plane. This flag was only used for the domain outlet for wind-tunnel test-section simulations to yield computational convergence, which was not achieved with an inflow/outflow boundary condition. Values of density, the velocity tensor, and static pressure are extrapolated to this surface from the interior domain using a Taylor series expansion. Thus, the flowfield is not directly affected by the presence of this boundary condition, and it purely serves as the edge of the computational domain instead of enforcing the freestream conditions [94].

Outer flowfield conditions not defined by a reflection plane or full-extrapolation plane were assigned boundary condition flag 3, a characteristic inflow/outflow boundary condition. This was the selected farfield boundary condition as the surface-normal component of velocity was subsonic at all farfield locations. Both the fixed and extrapolated Riemann invariants, which correspond to the incoming and outgoing characteristic waves, yield the local surface-normal velocity component and the local speed of sound. Density is computed using the standard entropy relationship, and the ideal gas law defines the equation of state [94].

Surfaces on the airfoil were declared to be no-slip, viscous surfaces through use of boundary condition flag 4. The no-slip condition is applied at the wall in which $u = v = w = 0$. The viscous sublayer cells were modeled with the turbulence model as selected by the user with the no-slip cell serving as a boundary condition. Wall functions were not used in this research project [94].

The outer computational control volume was prescribed to be a rectangular prism located $10c$ upstream of the leading edge, $10c$ downstream of the trailing edge, and $10c$ above and below the $y = 0$ line. A study investigating the dependence of the solution on airfoil span is presented in Sec. 5.5. An x-y plot of the airfoil contained within the computational domain is presented in Fig. 3.36 in which the airfoil is plotted as a black line and the outer domain is a thick, blue line. This outer box consisted of six faces; two of the faces were reflection planes while the other four were prescribed as inflow/outflow surfaces.

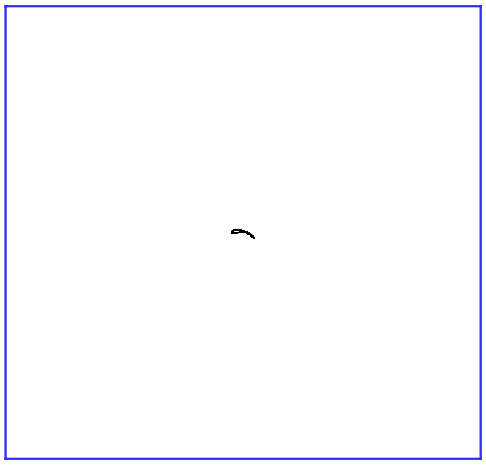

Figure 3.36: Multielement airfoil (black) inside outer computational domain (blue).

Preparations and selections for grid spacing are declared in GridTool prior to grid generation using VGrid. A viscous-spacing utility panel, Turbulent BL Spacing Calculator, is distributed with GridTool which allows the user to specify a target analysis Reynolds number and maximum desired surface y^+ value for the viscous grid. VGrid was used to generate volumetric grids using the advancing front and advancing layers methods for grid generation in the inviscid and viscous regions, respectively. An assortment of numeric inputs were specified by the user in the viscous-spacing utility to control viscous grid spacing; the details of this grid generation is discussed later in this section.

Volumetric grid density in the inviscid grid region was controlled through the use of numerous features known as sources. While a variety of source types are available in GTC, discussion in this document is limited to nodal and linear sources as those are the only types of sources used in the research. Grid size was specified in GTC through the use of sources of differing size and strength. By declaring smaller sources in regions where smaller grid cells were desired and larger sources where less refinement was needed, the size of the cells could be tailored to the desired grid distribution [93, 95–98]. Figure 3.37 presents three different sources including a nodal source with no stretching, a nodal source with stretching, and a linear source. A nodal source is an element that operates at one spatial location in which the influence of the source radiates symmetrically in all three directions. In an effort to decrease the size of the computational grid, a nodal source can be stretched in a given direction, as shown in Fig. 3.37(b). In this figure, the grid has higher density along the s axis than the grid density in the S direction. Finally, Fig. 3.37(c) presents a linear source that is defined by two nodal sources joined by a line. The size of the two end points is defined by a size parameter s and a stretching parameter S. While no stretching is shown for the two nodal sources, stretched nodal sources can be utilized at the end points. All parameters regarding the source distribution were declared by the user

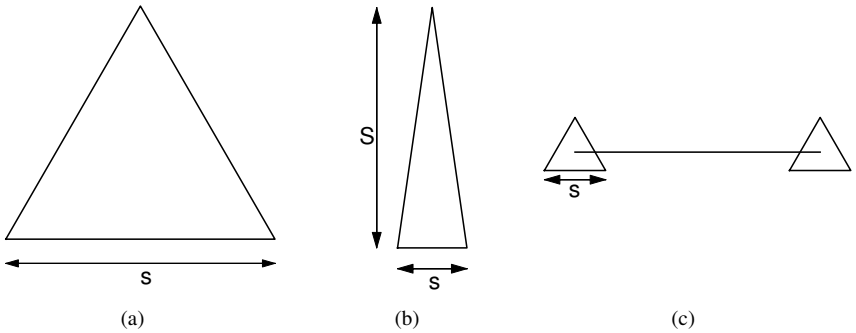

Figure 3.37: Size specifications of a) nodal source with no stretching, b) nodal source with stretching, and c) linear source with no stretching (adapted from Ref. 94).

in GTC. The user was also able to control the direction in which the strength of each source propagated into the field using the a_n and b_n parameters.

3.4.2 Grid Generation (VGrid)

VGrid is a three-dimensional unstructured grid generator that uses the advancing-front and advancing-layers techniques [97–99]. Based on the location, size, and strength of sources defined in GTC, VGrid was used to first create a surface grid from triangular elements on the geometry and on the edges of the control volume. After the user was satisfied with the surface mesh, volumetric grid generation was performed in the boundary-layer region based on the declared growth rates and value of y^+ in GTC. Grid generation typically took approximately 5 minutes for a fine 4.0 million cell mesh. Unstructured tetrahedral grids were generated using VGrid 4.1 and PostGrid 4.1. As previously mentioned, the advancing-layers method was used to create a tightly-spaced viscous grid growing from a triangular surface mesh out into the domain. As opposed to the traditional implementation of the advancing-front method in which volumetric cells are generated in a completely unstructured manner, the GTC/VGrid formulation generated layers of thin tetrahedral cells one layer at a time, and these cells were then split in half to yield tetrahedra. Each layer was progressively larger than the previous layer, and cell size (Δ) was defined by [100]

$$\Delta_n = \Delta_0 \left[1 + r_1(1 + r_2)^{n-1}\right]^{n-1} \tag{3.74}$$

wherein the initial cell height is Δ_0, r_1 is the geometric rate of expansion, r_2 is the secondary growth rate, and n is the number of points in the viscous grid.

Upon generation of the viscous grid, the outer grid was generated by the advancing-front method. Spatial discretization is governed by the Poisson equation is solved with a Dirichlet boundary condition, which is the heat equation [95]. This representation yields contours referred to as "pseudo-isotherms" in which the grid cell size varies

smoothly from regions of high potential, or small source size, to low potential, or large source size. It is also noted that this discretization is somewhat similar to the elliptic grid-generation methodologies with the exception that a single elliptic equation is solved in a predefined *x*-*y*-*z* computational domain in VGrid. As previously mentioned, the concentration of grid cells in a given region can be specified by the user by declaring the size and strength of sources. Grids in VGrid are developed by solving the Poisson equation

$$\nabla^2 S = G \tag{3.75}$$

subject to

$$S = S_b \tag{3.76}$$

wherein ∇ is the multi-dimensional gradient operator, S is the grid-spacing parameter, G is a source term yielding the spacing in the field, and S_b is the desired spacing at the boundary of the domain. Equation 3.75 can be discretized with a five-point stencil yielding the predicted grid spacing at a Cartesian point in space to be

$$G_{i,j} = \sum_{n=1}^{N} \psi_n \left(S_{i,j} J_n - I_n \right) \tag{3.77}$$

in which the grid node index is denoted by (i, j), N is the number of sources in the field, and ψ_n is the intensity factor of source n. The functions I_n and J_n are defined by

$$I_n = \begin{cases} S_n / r_n^2 & \text{nodal source} \\ \frac{1}{|\ell_n|} \int_{\ell_n} \frac{f(\ell)}{r(\ell)^2} d\ell & \text{linear source} \end{cases} \tag{3.78}$$

and

$$J_n = \begin{cases} 1 / r_n^2 & \text{nodal source} \\ \frac{1}{|\ell_n|} \int_{\ell_n} \frac{1}{r(\ell)^2} d\ell & \text{linear source} \end{cases} \tag{3.79}$$

in which S_n is the user-defined spacing at the n^{th} nodal source at a distance r from the Cartesian point of interest while $f(\ell)$ is a linear variation in spacing along line source n with length $|\ell_n|$. An iterative scheme is then employed in VGrid to numerically solve Eq. 3.77 with successive over relaxation. A crude first-order estimate for the grid size at a point in space is generated by interpolating source sizes with

$$S_{i,j} = \frac{\sum_{n=1}^{N} \psi_n I_n}{\sum_{n=1}^{N} \psi_n J_n}. \tag{3.80}$$

Grid cell sizes are then solved iteratively until a smooth distribution of cell sizes is achieved from source locations to the grid cell sizes on the boundary, S_b. After the iterations were complete, PostGrid was used to close the grid for regions in which iterative convergence was not achieved. For a more thorough discussion of the grid-generation and grid-spacing schemes employed in VGrid, the reader is referred to Pirzadeh [95].

3.4.3 RANS Solver (USM3D)

The flow solver, USM3D, is a finite-volume cell-centered tetrahedral-based upwind parallelized RANS solver [91, 101, 102]. Simulations can be performed to solve the Euler equations or the fully-viscous Navier-Stokes equations, and are obtained with an implicit point Gauss-Seidel and explicit Runge-Kutta with upwinding scheme. A wide variety of turbulence models, including both one- and two-equation models, can be used. Parallelized computations in USM3D can be performed on a desired number of nodes, as specified by the user. All computations were performed on a mid-2010 Apple iMac with a quad-core 2.8 Ghz i5 core processor with 16 GB of DDR3 RAM. A set of scripts were developed to postprocess solutions upon completion of the simulation to simplify and streamline the analysis process. Computation times varied depending on the turbulence model, but most simulations took between 12 and 18 hr on four processors.

3.5 MFOIL/PROFOIL

Airfoils were designed using MFOIL/PROFOIL, an inviscid multipoint inverse airfoil-design code [103–109]. While the direct-design method, in which the designer specifies the shape of the airfoil and the aerodynamic performance is determined from the shape, can be used, the more-desirable inverse design approach was implemented in this research. Contrary to the direct-design routines depicted in Fig. 3.38(a), inverse-design techniques yield an airfoil shape based upon various aerodynamic performance values and/or geometric constraints. In this way, the aerodynamic performance of an airfoil is easily controlled, and the airfoil shape that yields the desired performance is the output. One such inverse design method is to specify portions of the C_p distribution and subsequently determine the appropriate airfoil shape, as shown in Fig. 3.38(b).

The MFOIL/PROFOIL suite of codes can be used to prescribe a desired velocity distribution over an airfoil, from which the airfoil geometry is then determined through conformal mapping and multidimensional Newton iterations. In this method, the airfoil shape with n points is generated from a circle with n different segments. MFOIL, a MATLAB-based graphical user interface, serves as a front-end to the PROFOIL airfoil-design code which is based upon conformal mapping techniques. Prior to enhancements by the author, the aerodynamic flowfield was resolved

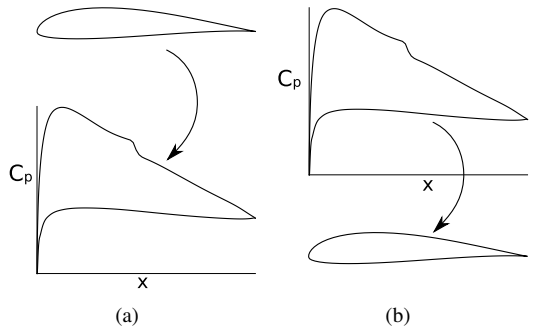

Figure 3.38: Conceptual representation of a) direct-design and b) inverse-design methods.

using the inviscid MCARF code from NASA Langley [110, 111]. As discussed in Sec. 7.2, improvements were made to the MFOIL code to incorporate viscous analysis with the MSES program.

The inverse-design routine PROFOIL, originally developed by Selig and then further expanded by others, was used to design multielement airfoils in this project [103–105, 112–117]. This software allows the user to specify different design angle of attack values relative to a zero-lift line for various locations on the airfoil. As the airfoil is discretized into a number of segments, the user is able to have a great deal of control of the desired airfoil performance, especially by controlling the velocity distribution over a given airfoil segment. It is possible to specify three types of velocity distributions over an airfoil segment including:

- constant velocity along a segment
- linearly-varying velocity distribution along a segment, and
- splined velocity distribution over a segment with control of the intermediate points and end conditions.

All airfoils designed during the course of this project were specified with constant velocity distributions along a given segment. It is possible to specify the design angle of attack for a segment, α^*, either directly or by determining it through a Newton iteration process in which additional constraints are satisfied. It is observed that the sectional lift coefficient is approximately equal to $0.11 \times \alpha$ in which α is in degrees, thus the designer can also use α^* to prescribe a desired lift coefficient for a segment instead of a design angle of attack. The arc limits for the segment at which α^* are specified are bounded by two values of ϕ which correspond to the arc limits for the conformal-mapped circle which can be divided into any number segments. In this project, the selected ϕ limits were selected to be 0 and 60 deg.

As the multipoint design formulation allows certain segments of the airfoil for a particular design angle of attack, careful adjustments of the drag polar can be made while leaving other portions of the polar largely unchanged. The importance of the multidimensional Newton iterations cannot be understated. For example, it is possible to simultaneously adjust the values of α^* of the upper-surface coordinates to achieve a desired maximum t/c while varying the α^*

values on the lower surface to yield a specified value of maximum camber. Further enhancements in PROFOIL permit finite as well as cusped trailing-edge geometries. It is also possible to directly specify boundary-layer parameters over a given segment. This inverse-design routine is coupled with a multidimensional Newton-Rhapson iteration scheme to satisfy additional performance metrics such as pitching moment coefficient, maximum airfoil thickness, maximum camber, minimum wing box volume, and a variety of other metrics.

Multielement airfoil design in MFOIL/PROFOIL is performed by designing each element in isolation and then assembling the system together for aerodynamic analysis. A Newton iteration scheme is then employed to adjust the various conformal mapping parameters to yield the desired aerodynamic and geometric properties of the multielement airfoil system. One advantage of this process is that the multielement airfoil design process retains all functionality and control of the isolated airfoil design. Consequently, aerodynamic and geometric constraints are prescribed in a manner very similar to that which is employed when designing a single-element airfoil. This method is computationally inexpensive as it is not necessary to compute the sensitivities for the Jacobian matrix in the Newton iteration scheme through the flow solver, but rather an approximate Jacobian matrix can be computed by evaluating most of the sensitivities through the conformal mapping method with the elements in isolation.

Chapter 4

Experimental Probe Usage and Data Reduction Techniques

Two different probes were used to experimentally interrogate the flowfield using wake survey techniques. These two probes, namely a split-film probe and a 7-hole probe, yielded different types of data regarding the flowfield. Point measurements in the flowfield were made by mounting each probe on the end of an arm that was controlled by a two-axis traverse, as discussed in Sec. 3.2.9. The theory, calibration, usage, and data reduction methods of the split-film probe and 7-hole probe will be presented in this section.

4.1 Split-Film Probe

Hot-wire anemometry is routinely used to measure turbulent fluctuations in low-to-moderate turbulence intensity flowfields with a high degree of accuracy. While a variety of techniques can be implemented to study turbulent flows, optical techniques, such as planar image velocimetry or laser doppler velocimetry, require expensive equipment to acquire and reduce data sets. In addition, these optical techniques can be time-intensive to set up in a new flowfield or experiment. Therefore, to minimize cost and to effectively leverage methods already in place in the Aerodynamics Research Lab, hot-wire anemometry was the experimental technique selected to study the turbulent nature of burst wakes.

4.1.1 Theory

The physics of hot-wire anemometry is governed by convective heat transfer from a heated metallic element to the surrounding flowfield. Hot-wire probes are in one of two methods of operation including constant-current or constant-temperature mode, but the discussion in this section will be limited to a constant-temperature anemometer as that was the selected mode of operation for this research project. A hot wire consists of a very small wire or piece of metal that is controlled to remain at a constant temperature. As air passes over a constant-temperature hot wire, the rate of heat transfer from the hot wire to the flow changes as a function of the air speed. Development of the equations governing the relationship between the voltage and thermal response of a finite-length heated cylinder in a crossflow is beyond the scope of this dissertation, but an excellent formulation is presented by Bruun [118]. Ultimately, it is shown that

the voltage of a probe can be shown to be

$$E = \sqrt{R_w(A + BU_t^n)(T_{film} - T_{amb})} \tag{4.1}$$

where R_w is the electrical resistance of the probe, A and B are calibration coefficients, T_{film} is the temperature of the probe, and T_{amb} is the temperature of the ambient air. Throughout the course of this dissertation, U_t represents the magnitude of total velocity, or

$$U_t = \sqrt{u^2 + v^2 + w^2} \tag{4.2}$$

which, if two-dimensional flow is assumed as is the case with the split-film measurements, is simplified to be

$$U_t = \sqrt{u^2 + v^2}. \tag{4.3}$$

Thus, in the simplest form, the heat transfer from the wire to the surrounding air is assumed to be proportional to the heat temperature differences between the probe and the air by

$$E \propto \sqrt{T_{film} - T_{amb}}. \tag{4.4}$$

Consequently, to maintain a constant temperature of the wire, the excitation voltage to the wire is altered as the probe is exposed to differing magnitudes of velocity. In other words, if the instantaneous velocity is slightly higher than the previous moment in time, the rate of heat transfer is increased, and thus the excitation voltage must also be increased to maintain a constant temperature of the wire. In this manner, the rate of heat transfer at a given velocity is instantaneously balanced by the heat generated by an excitation voltage across the hot wire. Calibrations, which are discussed later in this section, can then be applied to determine the relationship between the excitation voltage and the velocity of the flow [118–121]. In some instances, hot films, which consist of a non-conducting quartz core around which a thin film of metal is wrapped, are more desirable than hot wires as the additional quartz core makes a hot film significantly stronger, and thus less prone to physical damage, than a hot wire. Data are collected through the use of a thermally-conducting probe and an anemometer which is used to control the instantaneous excitation voltage of the probe to maintain a constant temperature of the probe.

It is possible to extend the theory of a one-component hot film to a two-component element known as a split-film probe. The device, originally developed by TSI, was first discussed in 1970 [122]. A split-film probe consists of a non-conducting cylindrical quartz core around which two different thin films of metal, measuring approximately 0.1 μm thick, are wrapped. These two films are separated longitudinally by a very small split, as shown in Fig. 4.1(a). Two-dimensional flow is assumed, and the probe therefore responds to $(\overline{u} + u', v)$ in the plane aligned with the split.

Due to the compact nature of the split-film probe, less spatial averaging occurs with a split-film probe when compared to a X wire. A non-uniform heat-transfer distribution accompanies the split-film probe which acts as a heated cylinder in an advancing flow, and a graphical depiction of the heat transfer distribution is presented in Fig. 4.1(b) [118]. As seen in the figure, the heat distribution is maximized upstream of the stagnation point in the flow and is minimized at locations in which the local flow is moving most quickly. It is assumed that the heat distribution remains fixed for a given velocity vector, including both magnitude and direction of the vector, and can be related to instantaneous changes in the freestream speed U_t and flow angularity λ. As increase in freestream speed will yield an increase in heat transfer, the excitation voltage of the two films must be increased by an anemometer to maintain a constant temperature of each film. Additionally, as the flow approaches the probe at an angle in which $\lambda \neq 0$, the heat transfer rate of the two films is observed to be different. Subsequently, the anemometer adjusts the excitation voltage of each film independently to maintain a constant temperature of each film. In this manner, the magnitude of the two probe voltages relative to a baseline voltage and the difference in the excitation voltages between the two films can be used to determine a time-dependent U_t and λ in which U_t is the magnitude of the total velocity and λ is the local flow angle in the *x*-*y* plane.

Split-film methods cannot be used to fully resolve the direction of the velocity vector, and the resulting velocity vector is ambiguous. This is because the split film will return the same result for a vector aligned at λ and $180-\lambda$. Thus, for any given measurement of E_1 and E_2, there exist two possible velocity vectors, of equal magnitude, that could produce those measurements. This is due to the fact that the films cannot resolve the direction of the flow passing the film as the heat transfer is not dependent upon the direction of flow. During the course of this research project, it was assumed that reverse flow (the condition corresponding to $180-\lambda$) was not present. Data are presented in Sec. 5.3 to defend this assumption.

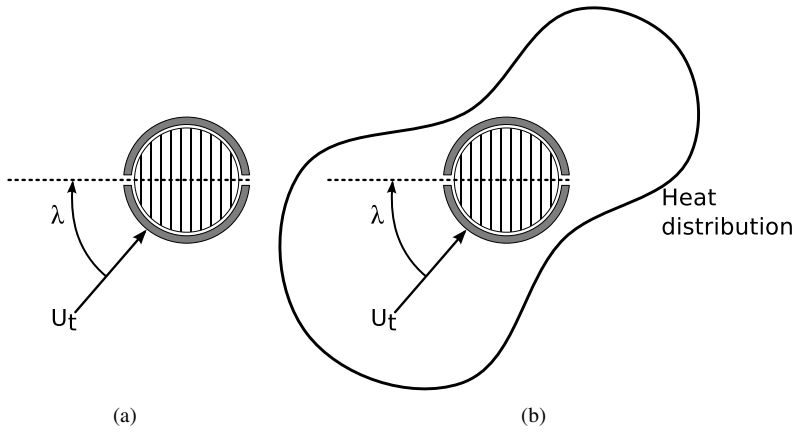

Figure 4.1: Schematics of split-film probe including a) cross-section of films and quartz core and b) heat distribution [subfigure b) modeled after Ref. 118].

In this research, a two-component TSI 1288 split-film probe was controlled by a TSI IFA 100 constant-temperature anemometer. The split of the probe is oriented as plotted in Fig. 4.1(a) in which the split of the sensor is parallel to the probe support. Cross flow is defined to be at a pitch angle λ of 0 deg when the flow is parallel to the split. End flow, which cannot be resolved by the probe, is parallel to the axis of symmetry for the probe. As the TSI 1288 split-film probe is no longer manufactured, it is difficult if not impossible to find any sufficient documentation for the probe, including from the manufacturer. To the best knowledge of the author, the wire diameter of the split-film was 0.0060 in (0.15 mm), and the width was 0.035 in (0.90 mm). The two anemometer channels (one for each film) were sampled simultaneously using a National Instruments SCXI scanning system. Measurements were acquired at a sample rate of 3 kHz for 10 sec, and data were filtered at the Nyquist cutoff frequency of 1.5 kHz using a low-pass Bessel filter. Overheat ratios of 1.523 and 1.526 were used for film 1 and 2, respectively, which resulted in a film temperature of 250°C.

4.1.2 Calibration

Calibration of the split-film probe was performed as a function of freestream velocity and local flow angle λ, and new calibration data sets were acquired prior to each wake survey. These data sets were collected in the same wind tunnel used to perform the wake-surveys, and a picture of the calibration rig is shown in Fig. 4.2. A small rotation plate was installed in the ceiling of the wind tunnel to which a support arm was attached, and the split film was subsequently mounted to this support arm. The rig was located in the far upstream portion of the wind tunnel to avoid streamline curvature effects caused by the airfoil model.

During calibration or wake-survey runs, the ambient temperature of the high-bay lab is not constant, and thus the heat transfer rate between the film and the surrounding air also changes (see Eq. 4.4). It is important to note that the heat transfer from the films to the air in Eq. 4.4 is a linear function of $T_{film} - T_{amb}$. Therefore, according to King's Law, which states the heat transfer rate is dependent upon the mass flow rate of the fluid, a correction can be implemented to account for temperature drift of the ambient air by

$$E_{cor} = E\sqrt{\frac{T_{film} - T_{ref}}{T_{film} - T_{amb}}} \tag{4.5}$$

where E_{cor} is the corrected probe voltage as a function of three temperatures, namely ambient temperature at the start of the run (T_{ref}), ambient temperature during the calibration (T_{amb}), and temperature of each film (T_{film}) [118]. A calibration routine was performed at $\lambda = 0$ deg over a range of freestream flow speeds to yield a polynomial for which $U_t = f(E_{cor})$. Unless otherwise stated, all excitation voltages discussed in this document are corrected according to Eq. 4.5. As documented by Bruun [118] as well as Siddal and Davies [119], the probe voltages of the two films E_1

Figure 4.2: Calibration rig for split-film probe.

and E_2 can be related to U_t by

$$K(U_t) = \left(\frac{E_1 + E_2}{2} \right)^2 \tag{4.6}$$

where the function $K(U_t)$ was selected to be a fifth-order polynomial fit of the data. The resulting calibration curves for each film, including excitation voltages and the $K(U_t)$ polynomial fit, are shown in Fig. 4.3.

A second calibration to determine flowfield angularity was performed at one velocity for a range of λ measured relative to the plane of the split between the films. As discussed by Bruun [118] and Seung-Ho [123], a calibration curve that is independent of velocity, denoted as $Z(\lambda)$, can be determined. The calibration curve $Z(\lambda)$ is a function of the probe voltages at two reference angles $E(\lambda_{ref,1})$ and $E(\lambda_{ref,2})$ and the probe voltages during the calibration run $E(\lambda)$; reference runs were taken at λ_{ref} values of -60 and 0 deg. A calibration was performed for a range of λ values, and the corresponding $Z(\lambda)$ value for each value of λ was calculated via

$$Z(\lambda) = \frac{E_1(\lambda) - E_1(\lambda_{ref,1})}{E_1(\lambda_{ref,2}) - E_1(\lambda_{ref,1})} + \frac{E_2(\lambda_{ref,1}) - E_2(\lambda)}{E_2(\lambda_{ref,1}) - E_2(\lambda_{ref,2})}. \tag{4.7}$$

A fifth-order polynomial fit was applied to the aforementioned calibration data to determine $Z(\lambda)$ across a range of λ. The excitation voltages for the two films as a function of λ are presented in Fig. 4.4(a), and, as previously discussed,

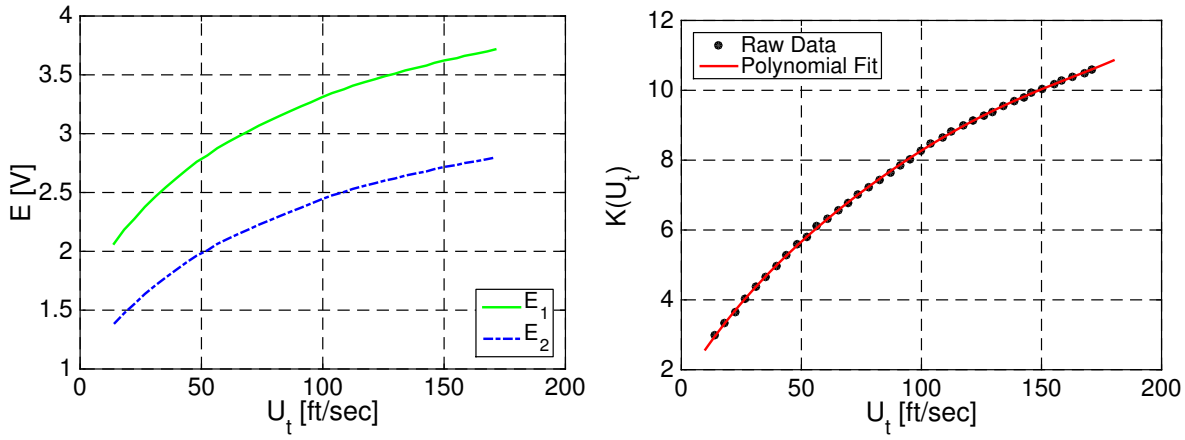

(a) (b)

Figure 4.3: Velocity-dependent calibrations for split-film probe including a) raw excitation voltages and b) $K(U_t)$ polynomial fit to raw data.

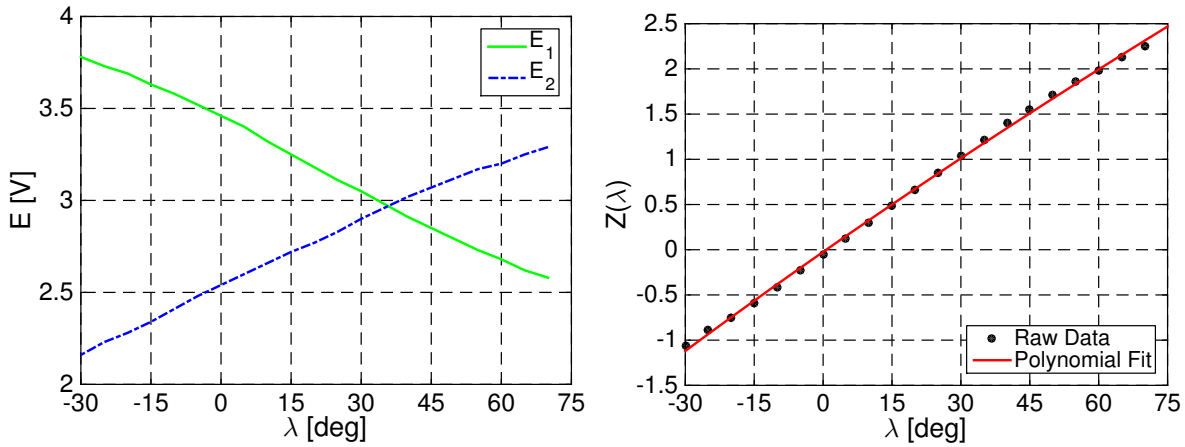

(a) (b)

Figure 4.4: Direction-dependent calibrations for split-film probe including a) raw excitation voltages and b) $Z(\lambda)$ polynomial fit to raw data.

it is the differences in heat transfer rates that cause the two films to need to be operated at different excitation voltages to maintain a constant temperature. Figure 4.4(b) presents the polynomial fit that was applied to the raw data, as calculated by Eq. 4.7.

4.1.3 Data Reduction

Data collected during a wake survey yielded time-dependent E_1 and E_2 at many different spatial locations, and values of K and Z were calculated using these excitation voltages according to Eqs. 4.6–4.7. Upon determination of these

values, a one-dimensional table lookup routine was employed in MATLAB to yield $U_t(t)$ and $\lambda(t)$ for the calculated values of K and Z.

It is not guaranteed that the ambient air temperature during a wake survey run is the same ambient air temperature as the calibration run. As the heat transfer is dependent upon the mass flow rate, a difference in ambient temperature will yield a different heat transfer rate, even if the freestream velocity is equal [124]. A correction is developed from conservation of mass during the calibration and during the experiment, viz

$$\rho_{run} U_{t,run} = \rho_{cal} U_{t,cal} \tag{4.8}$$

which can be rearranged to yield a corrected value of $U_{t,run}$ by

$$U_{t,run,cor} = \frac{\rho_{cal}}{\rho_{run}} U_{t,run,unc}. \tag{4.9}$$

Finally, the time-dependent streamwise and transverse components of velocity can be decomposed from U_t and λ by

$$u = U_t \sin\lambda \tag{4.10a}$$

$$v = \sqrt{U_t^2 - u^2}. \tag{4.10b}$$

As previously discussed, the split-film probe cannot resolve the sign of v, and thus v was assumed to be positive for all measurements.

4.1.4 Uncertainty

Uncertainty for the split-film probe was determined for the split-film probe. As uncertainty exists in both the calibration curve and the run data, it can be difficult to determine the uncertainty for the measurements and the implementation of the calibration. An experimental test was performed with the probe mounted in the calibration rig at a range of velocities for a $\lambda = 0$ deg. Utilizing methods discussed earlier in this section, values of K were calculated at each freestream velocity, and a fifth-order polynomial was then passed through these data; these values are plotted in Fig. 4.5(a). A second set of data was collected to which the calibration data were compared, and the raw values of K from this second run were compared to the previously-determined calibration curve. The root-mean square of these relative errors was found to be 0.97 ft/sec. Similar methods were employed to calculate the uncertainty in the determination of λ, as plotted in Fig. 4.5(b), and the total uncertainty of λ was found to be 1.01 deg.

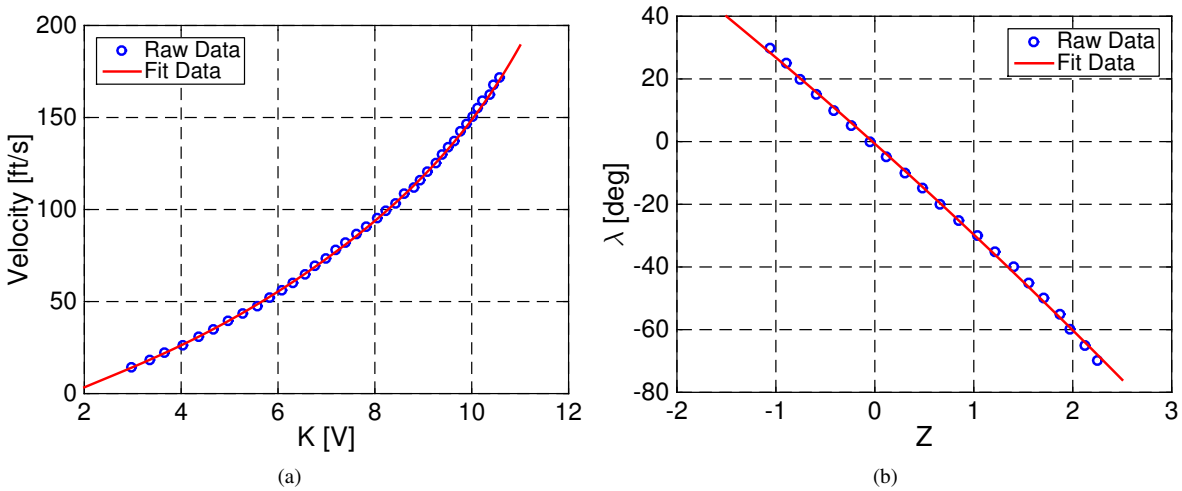

(a) (b)

Figure 4.5: Comparison of raw data and polynomial fits used to determine uncertainties for a) velocity and b) flow angularity.

4.2 Seven-Hole Probe

As previously mentioned, it is difficult to experimentally measure all velocity components and pressures in a flowfield simultaneously. While a split-film probe can capture unsteady velocity in two dimensions, it cannot be used to determine static, dynamic, or total pressure. In order to capture these parameters, it was necessary to use a multi-hole probe, such as a 7-hole probe. A 7-hole probe is able to capture time-averaged velocity components in three axes as well as determine the static, dynamic, and total pressure of a single point in the flowfield. After performing a calibration, methods can be implemented to determine air speed, flow direction, static pressure, and total pressure [125–130].

4.2.1 Theory

While simpler multi-hole probes can be used to determine the flow velocity and angle, use of a 7-hole probe yields accurate flow measurements up to a flow angle of 80 deg, which is significantly higher than that of a 5-hole probe. A 7-hole probe consists of a conical tip with a hole at the tip of the cone that is surrounded by six additional holes, each separated by 60 deg, as shown in Fig. 4.6(a). The probe used in this project measured 0.125 in (3.18 mm) in diameter and had a 30 deg conical tip, as shown in Fig. 4.6(b). By utilizing a technique known as sectoring, it is possible to measure very high flow angles with a 7-hole probe. Consider the high-angle flowfield surrounding the probe in Fig. 4.6(c,d) in which separated flow is observed. Pressure measurements from holes 1, 2, and 6 will be inaccurate, and thus unusable, as the flow is separated from the probe at the location of these holes. Despite the separated flow over holes 1, 2 and 6, attached flow is observed for holes 3, 4, 5, and 7. If sectoring methods are applied, the flowfield

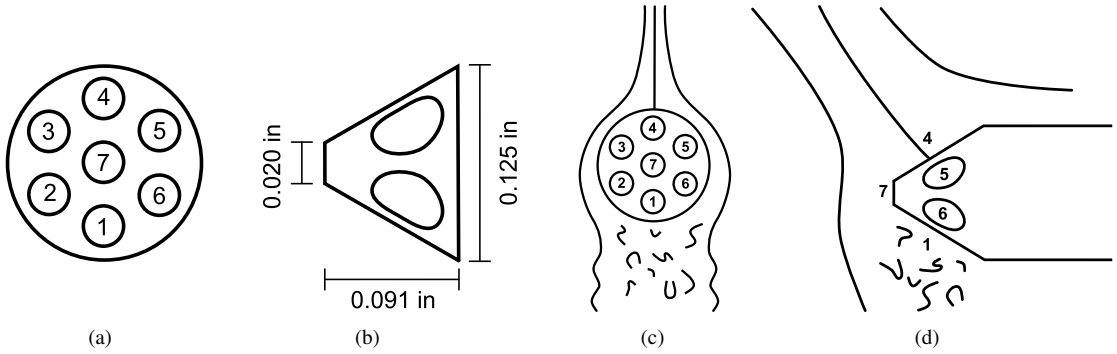

Figure 4.6: Schematics of the 7-hole probe used including a) hole pattern, b) probe tip dimensions, c) separated flow (front view), and d) separated flow (side view).

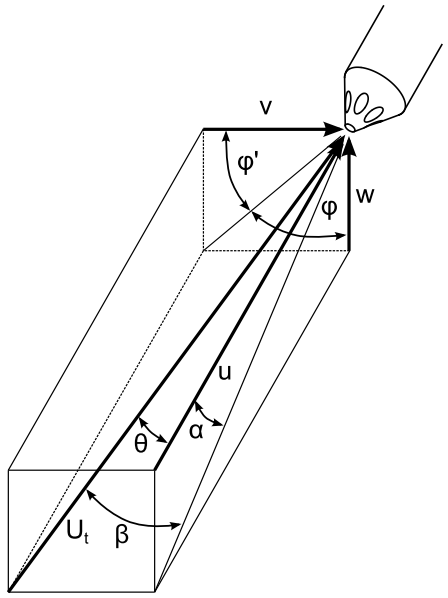

Figure 4.7: Coordinate system used to define flow for 7-hole probe.

can be determined from a minimum of four holes. The hole with the highest pressure and the three surrounding holes are used to determine the flow angle and flow speed. If the highest pressure is measured in hole 7, the center hole and all six surrounding holes are used to determine the relevant values. A spherical coordinate system (r, θ, ϕ) was used to define the flow at the tip of the 7-hole probe, as shown in Fig. 4.7. Calibrations were performed in the spherical coordinate system (U_t, θ, ϕ) and results were subsequently transformed into the standard wind axes (U_t, α, β) coordinate system, as depicted in the figure.

Calibration Coefficients in Absolute Pressure

A series of calibration coefficients were used to determine the flow angle, total pressure, and static pressure at the tip of the 7-hole probe by using the sectoring technique. After a measurement was recorded, the hole with the highest pressure determined which sector, and thus which set of calibration equations, would be used. Each sector consisted of four calibration coefficients in which each coefficient is dependent only upon cone angle (θ), roll angle (ϕ), total pressure (p_t), and static pressure (p_s). If hole 7, the center hole, has the highest pressure, a set of coefficients, as derived by Gallington [125], can be defined to be

$$C_a = \frac{p_1 - p_4}{p_7 - \overline{p}} \tag{4.11}$$

$$C_b = \frac{p_6 - p_3}{p_7 - \overline{p}} \tag{4.12}$$

$$C_c = \frac{p_5 - p_2}{p_7 - \overline{p}} \tag{4.13}$$

where

$$\overline{p} = \frac{1}{6}\sum_{i=1}^{6} p_i. \tag{4.14}$$

The set of coefficients C_a, C_b, and C_c can be used to define a final set of four final calibration coefficients. This final set of coefficients includes coefficients that are only sensitive to either cone angle (θ), roll angle (ϕ), total pressure (p_t), or static pressure (p_s), and are given by

$$C_{\theta_7} = \frac{1}{3}(2C_a + C_b - C_c) \qquad C_{\phi_7} = \frac{1}{\sqrt{3}}(C_b + C_c) \qquad C_{t_7} = \frac{p_7 - p_t}{p_7 - \overline{p}} \qquad C_{s_7} = \frac{\overline{p} - p_s}{p_7 - \overline{p}}. \tag{4.15}$$

Some cases exist for which hole 7 is not the hole with the highest pressure, but rather the highest pressure is measured by one of the outer holes. In these cases, the hole with the highest pressure and the three surrounding holes are used to determine the calibration coefficients, which can be expressed for sectors 1–6 as

$$C_{\theta_1} = \frac{p_1 - p_7}{p_1 - \frac{p_6+p_2}{2}} \qquad C_{\phi_1} = \frac{p_6 - p_2}{p_1 - \frac{p_6+p_2}{2}} \qquad C_{t_1} = \frac{p_1 - p_t}{p_1 - \frac{p_6+p_2}{2}} \qquad C_{s_1} = \frac{\frac{p_6+p_2}{2} - p_s}{p_1 - \frac{p_6+p_2}{2}} \tag{4.16}$$

$$C_{\theta_2} = \frac{p_2 - p_7}{p_2 - \frac{p_1+p_3}{2}} \qquad C_{\phi_2} = \frac{p_1 - p_3}{p_2 - \frac{p_1+p_3}{2}} \qquad C_{t_2} = \frac{p_2 - p_t}{p_2 - \frac{p_1+p_3}{2}} \qquad C_{s_2} = \frac{\frac{p_1+p_3}{2} - p_s}{p_2 - \frac{p_1+p_3}{2}} \tag{4.17}$$

$$C_{\theta_3} = \frac{p_3 - p_7}{p_3 - \frac{p_2+p_4}{2}} \qquad C_{\phi_3} = \frac{p_2 - p_4}{p_3 - \frac{p_2+p_4}{2}} \qquad C_{t_3} = \frac{p_3 - p_t}{p_3 - \frac{p_2+p_4}{2}} \qquad C_{s_3} = \frac{\frac{p_2+p_4}{2} - p_s}{p_3 - \frac{p_2+p_4}{2}} \tag{4.18}$$

$$C_{\theta_4} = \frac{p_4 - p_7}{p_4 - \frac{p_3+p_5}{2}} \qquad C_{\phi_4} = \frac{p_3 - p_5}{p_4 - \frac{p_3+p_5}{2}} \qquad C_{t_4} = \frac{p_4 - p_t}{p_4 - \frac{p_3+p_5}{2}} \qquad C_{s_4} = \frac{\frac{p_3+p_5}{2} - p_s}{p_4 - \frac{p_3+p_5}{2}} \tag{4.19}$$

$$C_{\theta_5} = \frac{p_5 - p_7}{p_5 - \frac{p_4+p_6}{2}} \qquad C_{\phi_5} = \frac{p_4 - p_6}{p_5 - \frac{p_4+p_6}{2}} \qquad C_{t_5} = \frac{p_5 - p_t}{p_5 - \frac{p_4+p_6}{2}} \qquad C_{s_5} = \frac{\frac{p_4+p_6}{2} - p_s}{p_5 - \frac{p_4+p_6}{2}} \tag{4.20}$$

$$C_{\theta_6} = \frac{p_6 - p_7}{p_6 - \frac{p_5+p_1}{2}} \qquad C_{\phi_6} = \frac{p_5 - p_1}{p_6 - \frac{p_5+p_1}{2}} \qquad C_{t_6} = \frac{p_6 - p_t}{p_6 - \frac{p_5+p_1}{2}} \qquad C_{s_6} = \frac{\frac{p_5+p_1}{2} - p_s}{p_6 - \frac{p_5+p_1}{2}}. \tag{4.21}$$

It is noted for sake of clarity that pressures in Eqs. 4.15-4.21 are absolute pressure.

Calibration Coefficients in Gauge Pressure (Calibration and Look-Up Tables)

Data measurements in the wind tunnel were taken as relative pressure measurements in which the pressure of each port was measured relative to the pressure in the test section, p_{ts}. Some slight modifications to the equations previously presented must be made for the case in which the gauge pressures, relative to p_{ts}, were captured. Development of the equations for the center hole as well as the outer holes in both the calibration runs and during wake-survey mode are presented in this section.

Consider hole 7, the center hole, as presented in Eqs. 4.11–4.15. The three calibration coefficients C_a, C_b, and C_c are shown in gauge pressure to be

$$C_a = \frac{(p_1 - p_{ts}) - (p_4 - p_{ts})}{(p_7 - p_{ts}) - \overline{p}} \tag{4.22}$$

$$C_b = \frac{(p_6 - p_{ts}) - (p_3 - p_{ts})}{(p_7 - p_{ts}) - \overline{p}} \tag{4.23}$$

$$C_c = \frac{(p_5 - p_{ts}) - (p_2 - p_{ts})}{(p_7 - p_{ts}) - \overline{p}} \tag{4.24}$$

where $\overline{p}$ is now expressed as

$$\overline{p} = \frac{1}{6}\sum_{i=1}^{6}(p_i - p_{ts}). \tag{4.25}$$

The angle-dependent coefficients are still the same in which

$$C_{\theta_7} = \frac{1}{3}(2C_a + C_b - C_c) \tag{4.26a}$$

$$C_{\phi_7} = \frac{1}{\sqrt{3}}(C_b + C_c). \tag{4.26b}$$

More significant changes must be made to C_{t_7} and C_{s_7} when data were taken in gauge pressure. It is shown that C_{t_7} can be expressed as

$$C_{t_7} = \frac{p_7 - p_t}{p_7 - \overline{p}} = \frac{(p_7 - p_{ts}) - (p_t - p_{ts})}{(p_7 - p_{ts}) - \overline{p}}. \tag{4.27}$$

If the calibration coefficients are being determined during a calibration run, the test section is empty and thus it can be assumed that

$$p_{s_{\text{local}}} = p_{ts} \tag{4.28a}$$

$$p_{t_{\text{local}}} = p_{t_{ts}} \tag{4.28b}$$

$$p_t - p_{ts} = q_{ts} = q_{local} \tag{4.28c}$$

as no losses are experienced in the test section and no static pressure gradient is present. Therefore, during a calibration run and only during a calibration run, Eq. 4.27 can be expressed as

$$C_{t_7,\text{ in cal}} = \frac{(p_7 - p_{ts}) - q_{ts}}{(p_7 - p_{ts}) - \overline{p}}. \tag{4.29}$$

If data are being collected during a wake survey, Eq. 4.28 is not correct. Consequently, if a lookup table is being employed, Eq. 4.27 must be rearranged and shown to be

$$C_{t_7,\text{in survey}} = \left[(p_7 - p_{ts}) - \overline{p}\right] = (p_7 - p_{ts}) - (p_{t_{\text{local}}} - p_{ts}) \tag{4.30}$$

which can be further manipulated to yield

$$(p_{t_{\text{local}}} - p_{ts})_{\text{in survey}} = (p_7 - p_{ts}) - C_{t_7,\text{in survey}}\left[(p_7 - p_{ts}) - \overline{p}\right]. \tag{4.31}$$

Similar modifications to C_{s_7} must be made, and it is shown that

$$C_{s_7} = \frac{\overline{p} - p_s}{p_7 - \overline{p}} = \frac{\overline{p} - (p_s - p_{ts})}{(p_7 - p_{ts}) - \overline{p}}. \tag{4.32}$$

If the calibration coefficient response surface is being constructed during a calibration run, it can be assumed that

$$p_s = p_{ts} \tag{4.33}$$

and thus

$$p_s - p_{ts} = 0 \tag{4.34}$$

which can be used to express Eq. 4.32 in a calibration run to be

$$C_{s_7,\text{in cal}} = \frac{\overline{p} - p_{ts}}{(p_7 - p_{ts}) - \overline{p}}. \tag{4.35}$$

If data are being taken in a wake survey and a lookup table is being employed, Eq. 4.32 can be rearranged to be

$$C_{s_7,\text{ in survey}}\left[(p_7 - p_{ts}) - \overline{p}\right] = \overline{p} - (p_{s,\text{ local}} - p_{ts}) \tag{4.36}$$

which can be used to determine the local static gauge pressure during a survey as

$$(p_{s_{\text{local}}} - p_{ts})_{\text{in survey}} = \overline{p} - C_{s_7,\text{ in survey}}\left[(p_7 - p_{ts}) - \overline{p}\right]. \tag{4.37}$$

The derivation of gauge pressures for hole 7 is now complete.

When collecting pressures in gauge pressure relative to p_{ts}, Eqs. 4.16–4.21 must be adapted accordingly. To simplify the expression of the equations, an index mapping, as presented in Table 4.1, is used in this derivation. Say the hole with the highest pressure is hole 2; in this case, $n = 2$, $y = 3$, and $z = 1$. Using this mapping, the angle-dependent calibration coefficients can be expressed in terms of n, y, and z as

$$C_{\theta_n} = \frac{p_n - p_7}{p_n - \frac{p_y + p_z}{2}} \tag{4.38a}$$

$$C_{\phi_n} = \frac{p_z - p_y}{p_n - \frac{p_y + p_z}{2}}. \tag{4.38b}$$

These equations can be expressed in gauge pressure and are shown to be

$$C_{\theta_n} = \frac{(p_n - p_{ts}) - (p_7 - p_{ts})}{(p_n - p_{ts}) - \frac{(p_y - p_{ts}) + (p_z - p_{ts})}{2}} \tag{4.39a}$$

$$C_{\phi_n} = \frac{(p_z - p_{ts}) - (p_y - p_{ts})}{(p_n - p_{ts}) - \frac{(p_y - p_{ts}) + (p_z - p_{ts})}{2}}. \tag{4.39b}$$

Table 4.1: 7-Hole Probe Index Mapping

	Hole 1	Hole 2	Hole 3	Hole 4	Hole 5	Hole 6
n	1	2	3	4	5	6
y	2	3	4	5	6	1
z	6	1	2	3	4	5

Similar modifications to C_{t_n} and C_{s_n} can be implemented. First consider C_{t_n}, which in index notation is

$$C_{t_n} = \frac{p_n - p_t}{p_n - \frac{p_y + p_z}{2}}, \tag{4.40}$$

that can then be expressed in gauge pressure relative to p_{ts} as

$$C_{t_n} = \frac{(p_n - p_{ts}) - (p_t - p_{ts})}{(p_n - p_{ts}) - \frac{(p_y - p_{ts}) + (p_z - p_{ts})}{2}}. \tag{4.41}$$

Using similar logic as before when considering hole 7, if the coefficients are being determined during a calibration run, it is known that

$$p_t - p_{ts} = q_{ts} = q_{\text{local}} \tag{4.42}$$

and can be substituted into Eq. 4.41 to be

$$C_{t_n,\,\text{in cal}} = \frac{(p_n - p_{ts}) - q_{ts}}{(p_n - p_{ts}) - \frac{(p_y - p_{ts}) + (p_z - p_{ts})}{2}}. \tag{4.43}$$

During a wake survey, it cannot be assumed that there are not total head losses or nor that there is not a static pressure gradient. Thus, Eq. 4.41 can be rearranged to be

$$(p_n - p_{ts}) - (p_t - p_{ts}) = C_{t_n,\,\text{in survey}} \left[(p_n - p_{ts}) - \frac{(p_y - p_{ts}) + (p_z - p_{ts})}{2} \right] \tag{4.44}$$

which can be further manipulated to yield the local total head gauge pressure in a wake survey while utilizing a table lookup routine to be

$$(p_t - p_{ts})_{\text{in survey}} = (p_n - p_{ts}) - C_{t_n,\,\text{in survey}} \left[(p_n - p_{ts}) - \frac{(p_y - p_{ts}) + (p_z - p_{ts})}{2} \right]. \tag{4.45}$$

The static pressure calibration coefficient in holes 1–6 can be expressed in gauge pressure as

$$C_{s_n} = \frac{\frac{p_y + p_z}{2} - p_s}{p_n - \frac{p_y + p_z}{2}} = \frac{\frac{(p_y - p_{ts}) + (p_z - p_{ts})}{2} - (p_s - p_{ts})}{(p_n - p_{ts}) - \frac{(p_y - p_{ts}) + (p_z - p_{ts})}{2}}. \tag{4.46}$$

During a calibration run, it is assumed that $p_s = p_{ts}$ and thus the static pressure calibration coefficient during a calibration run is seen to be

$$C_{s_n,\,\text{in cal}} = \frac{\frac{(p_y - p_{ts}) + (p_z - p_{ts})}{2}}{(p_n - p_{ts}) - \frac{(p_y - p_{ts}) + (p_z - p_{ts})}{2}}. \tag{4.47}$$

If a wake survey is being run and data are being determined from a lookup table, Eq. 4.46 can be algebraically manipulated to be

$$\frac{(p_y - p_{ts}) + (p_z - p_{ts})}{2} - (p_s - p_{ts}) = C_{s_n,\text{ in survey}} \left[(p_n - p_{ts}) - \frac{(p_y - p_{ts}) + (p_z - p_{ts})}{2} \right] \tag{4.48}$$

and further rearranged to yield

$$(p_s - p_{ts})_{\text{in survey}} = \frac{(p_y - p_{ts}) + p_z - p_{ts})}{2} - C_{s_n,\text{ in survey}} \left[(p_n - p_{ts}) - \frac{(p_y - p_{ts}) + (p_z - p_{ts})}{2} \right] \tag{4.49}$$

which is is the lookup-table formulation for the static pressure calibration coefficient during a wake survey.

4.2.2 Calibration

It is necessary to perform calibration routines on the 7-hole probe to determine the coefficients discussed in Eqs. 4.15–4.21. Calibration coefficients were determined from a series of tests that were performed at a known roll angle, cone angle, static pressure, and dynamic pressure. After the coefficients were determined, a series of lookup tables were employed to determine p_s, p_t, θ, and ϕ as a function of the four calibration coefficients. Calibration methods were performed using hardware developed by previous projects at UIUC [71, 130]. A wide view and a close-up view of the probe installed in the calibration rig is presented in Fig. 4.8. One side of the 7-hole probe is painted silver; the roll angle (ϕ) is defined to be 0 when this face of the probe is facing the ceiling. The calibration rig was attached to the turntable which automatically varied the cone angle (θ), and a gear was turned manually which set the roll angle for the probe. When mounted in the calibration rig, the tip of the probe was 9.625 in (24.25 cm) above the floor of the tunnel. The system was designed such that the tip of the probe remained in the same position in the wind tunnel as θ was varied.

Calibrations were performed at a range of velocities, cone angles, and roll angles. Six different velocities between 25 and 200 ft/sec (25, 50, 100, 150, 175, and 200 ft/sec) were tested to determine any Reynolds-number-dependent behavior of the probe, and calibrations were performed from a roll angle of 0 to 175 deg at 6 deg increments. The turntable angle was varied from -55 to 55 deg at an increment of 2 or 5 deg; small increments were performed at cone angles less than 10 deg while coarser spacing was specified at cone angles above 10 deg. It is worth noting that a calibration performed at a roll angle of ϕ and a turntable angle of γ is identical to a case at which $\phi = \phi + 180$ deg and a turntable angle of $-\gamma$. This knowledge was utilized to minimize the number of different calibration runs in the wind tunnel. While 7-hole probes can be used at flow angles up to 80 deg, the turntable in the wind tunnel could not be rotated beyond ± 55 deg. As polar coordinates were used to define the probe coordinate system (see Fig. 4.7), the cone angle of the probe is always positive by definition. A case in which the probe was located at a negative turntable angle

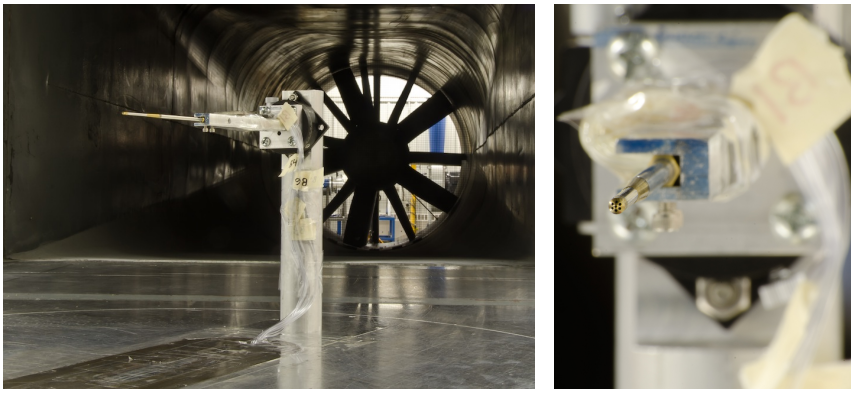

(a) (b)

Figure 4.8: Calibration rig for the 7-hole probe including a) wide view and b) detailed view.

α and roll angle ϕ is geometrically equivalent to the condition in which the probe is located at $+\alpha$ and $\phi + 180$ deg. Because of this symmetry, calibration runs were only required to be performed in which $0 \leq \phi \leq 180$ deg as data were collected at both positive and negative turntable angles.

Results from a calibration run in which $\phi = 90$ deg and freestream velocity was 200 ft/sec are plotted in Fig. 4.9. Nearly-symmetric behavior of the probes is observed about $\theta = 0$ deg, and slight differences are due to inconsistencies in the manufacturing of the probe or due to a slight misalignment of the probe in the wind tunnel. Results presented in Fig. 4.9 are representative of all calibration runs. A small "kink" in the data is observed at $\theta \approx 40$ deg for hole 4, and this small deviation is attributed to slight manufacturing defects. The behavior of hole 4 in this region does not affect any data as hole 1 yields the highest pressure, and thus hole 1, hole 2, hole 6, and hole 7 will be used in the previously-discussed methods. The sector boundaries were not affected by different freestream velocity values. As previously discussed, calibrations for a 7-hole probe were determined based upon the probe with the highest pressure. The resulting sector map, in which the probe that measured the highest pressure is depicted, is shown in Fig. 4.10(a) for a freestream speed of 200 ft/sec. Boundaries defining the edges of each sector are presented in Fig. 4.10(b).

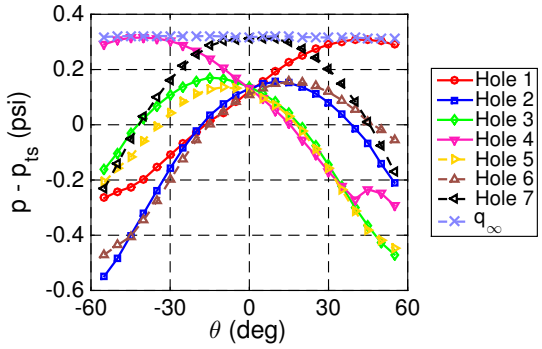

Figure 4.9: Representative 7-hole probe calibration results at freestream velocity of 200 ft/sec and $\phi = 90$ deg.

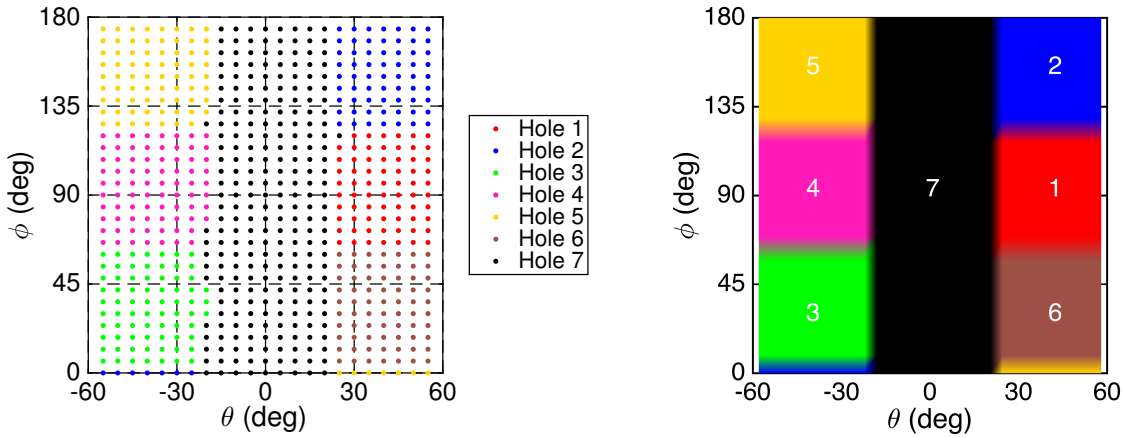

(a) (b)

Figure 4.10: Sector map at 200 ft/sec for 7-hole probe in θ-ϕ coordinates including a) individual points and b) defining boundaries for map.

As shown in Fig. 4.7, the velocity components, as a function of polar angles, are defined by

$$u = U_t \cos\theta \tag{4.50a}$$

$$v = U_t \sin\theta \sin\phi \tag{4.50b}$$

$$w = U_t \sin\theta \cos\phi \tag{4.50c}$$

where U_t is the defined as magnitude of total velocity such that

$$U_t = \sqrt{u^2 + v^2 + w^2}. \tag{4.51}$$

While calibrations were performed in θ-ϕ coordinates, aerodynamicists typically work in α-β coordinate system in which α is the angle of attack and β is the sideslip angle, which can both be calculated by

$$\alpha = \arcsin\left(\frac{\sin\theta\cos\phi}{\cos\beta}\right) \tag{4.52a}$$

$$\beta = \arcsin\left(\sin\theta\sin\phi\right). \tag{4.52b}$$

The three components of velocity can also be determined in the α-β coordinate system, viz

$$u = U_t \cos\alpha \cos\beta \tag{4.53a}$$

$$v = U_t \sin\alpha \tag{4.53b}$$

$$w = U_t \cos\alpha \sin\beta. \tag{4.53c}$$

All calibration points, which were collected in the θ-ϕ coordinate system, were converted to the α-β coordinate system. The resulting sector map in α-β coordinates is shown in Fig. 4.11. As all sectors have been defined, the calibration coefficients (C_ϕ, C_θ, C_s, and C_t) were calculated for each of the seven sectors. Four response surfaces were determined at each velocity in which

$$\alpha = f_1(C_\theta, C_\phi) \tag{4.54a}$$

$$\beta = f_2(C_\theta, C_\phi) \tag{4.54b}$$

$$C_s = f_3(C_\theta, C_\phi) \tag{4.54c}$$

$$C_t = f_4(C_\theta, C_\phi). \tag{4.54d}$$

The contour maps for sector 1 at 200 ft/sec are shown in Figs. 4.12-4.15, and are representative of all four velocities; few variations in α and β were observed between the different velocities, but some minor differences in C_s and C_t were observed.

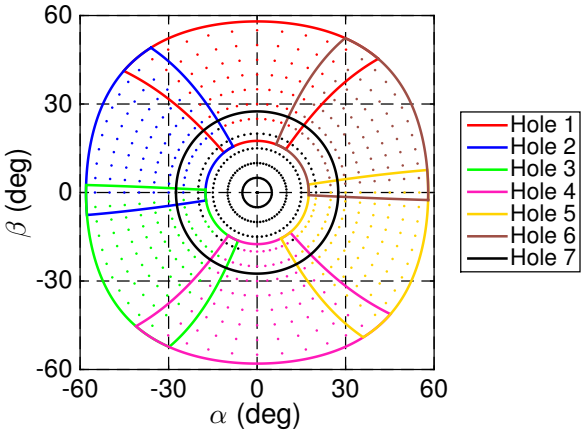

Figure 4.11: Sector map for 7-hole probe in α-β coordinates highlighted by sector boundaries.

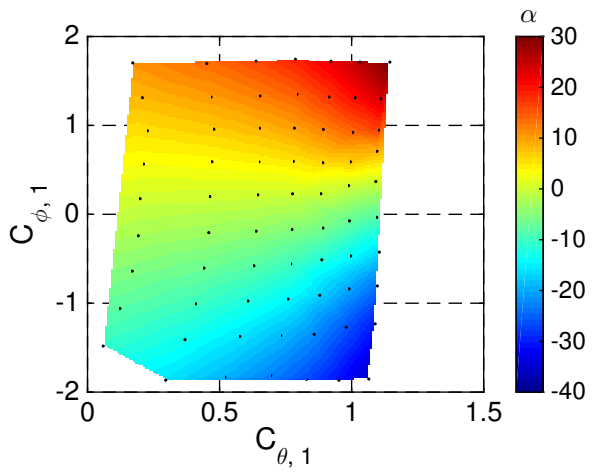

Figure 4.12: Sector 1 α (in deg) calibration map.

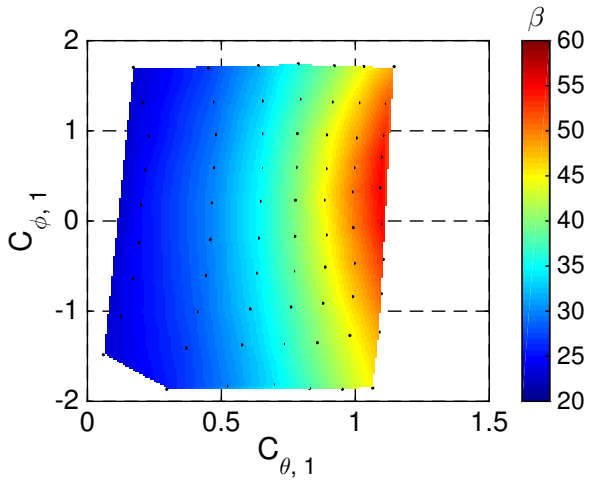

Figure 4.13: Sector 1 β (in deg) calibration map.

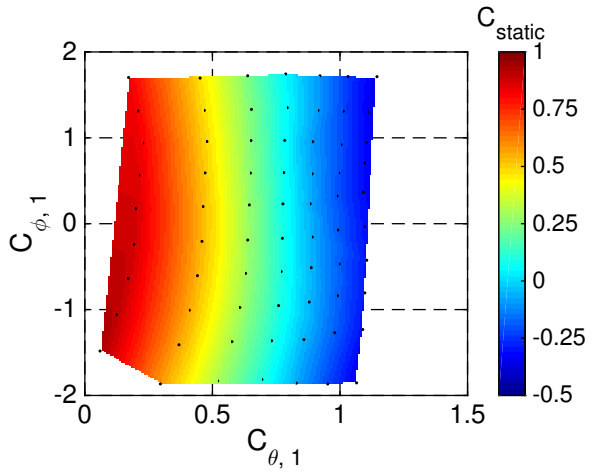

Figure 4.14: Sector 1 C_s calibration map.

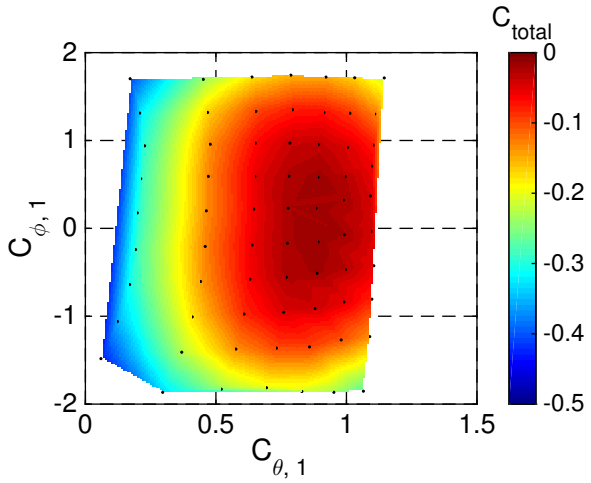

Figure 4.15: Sector 1 C_t calibration map.

4.2.3 Data Reduction

After calibration was complete, it was possible to use the previously-discussed look-up tables to determine an unknown flowfield using pressure measurements from the 7-hole probe. As all seven pressures were recorded, the hole with the highest pressure is used to define the sector in which the calibrations should be applied. The cone and roll angle calibration coefficients (C_θ and C_ϕ) could be calculated, as defined in Eqs. 4.15–4.21, and the four lookup tables,

defined in Eq. 4.54, could be accessed in which

$$\alpha = \alpha_{interp}\left(C_{\theta_n}, C_{\phi_n}\right) \tag{4.55a}$$

$$\beta = \beta_{interp}\left(C_{\theta_n}, C_{\phi_n}\right) \tag{4.55b}$$

$$C_t = C_{t,interp}\left(C_{\theta_n}, C_{\phi_n}\right) \tag{4.55c}$$

$$C_s = C_{s,interp}\left(C_{\theta_n}, C_{\phi_n}\right). \tag{4.55d}$$

In incompressible flow, the dynamic pressure is defined by the difference in total and static pressure in which

$$q = p_t - p_s \tag{4.56}$$

and thus the total velocity at the probe U_t can be found by

$$U_t = \sqrt{\frac{2q}{\rho}}. \tag{4.57}$$

The calibration methodology discussed in this section was applied at all speeds for which calibrations were performed. If the velocity determined from the calibration was less than 10 ft/sec different than the velocity in a calibration run, values from this close calibration were taken as the true values. If larger differences between the calculated velocity and calibration velocity existed, the true values were taken as the average between the two closest calibration velocities. The three components of velocity were then subsequently determined from the determined flow angles and speed, as shown in Eq. 4.53.

Verification of the calibration was performed by comparing data at a known α, β, and U_t to the values of α, β, and U_t determined from the calibration. A total of 624 data points were tested against the calibration; none of these points were used to generate the calibration. Tests were performed at a range of freestream velocities that were not equal to the calibration velocities, and various values of α and β were also selected. The results affirmed that the calibration was properly implemented. The mean error in α was less than 0.60 deg with a standard deviation in error of 0.53 deg, the average difference in β was determined to be 1.02 deg with a standard deviation in error of 0.69 deg, and the average difference in freestream velocity was 0.64 ft/sec with a standard deviation of 0.78 ft/sec.

4.2.4 Uncertainty

Uncertainty values for the 7-hole probe were determined by using the jitter method, which can be appropriately applied to 7-hole probes [129]. Uncertainty methods implemented in this research assume that a result R can be determined

by several independent variables x in which

$$R = R(x_0, x_1, x_2, \ldots, x_n). \tag{4.58}$$

Standard bias uncertainty calculations were determined through [131]

$$\Upsilon_{7HP} = \sqrt{\sum \left(\frac{\partial R}{\partial x_i} U_{x_i}^2 \right)} \tag{4.59}$$

where Υ is the uncertainty value and the variables x_i corresponded to the following independent variables: pressure of holes 1–7, freestream velocity, and freestream temperature. Values of each of these parameters were adjusted by a small value, known to be the uncertainty of the measurement (U_{x_i}), and the effects on α, β, and U_t were numerically computed. The uncertainty of the pressure measurements was ± 0.00036 psi. Ultimately, the uncertainties for α and β were determined to be 0.53 deg and 1.20 deg, respectively. The differences in the uncertainty values of α and β is due to the fact that probes 1 and 4 are the sole holes on the top and bottom of the 7-hole probe (in the β direction) while there are two holes on each side corresponding to an angle of α; for further details, the reader is referred to Fig. 4.6. Finally, the uncertainty in U_t was found to be 0.76 ft/sec. Average error is similar to that of previous studies [130].

4.3 Interpolation Techniques

While experimental data were collected in the flowfield, it was necessary to interpolate the coarse experimental data onto a finer mesh for plotting and postprocessing purposes. Experimental data were collected on a sample grid in the x_{tunnel}–y_{tunnel} coordinate system in which x_{tunnel} is aligned with the freestream velocity vector and y_{tunnel} is orthogonal to x_{tunnel}. A series of coordinate transformations were applied to transform (x_{tunnel}, y_{tunnel}) into (x, y) as defined in Sec. 3.1 in which the leading edge and trailing edge of the main element are located on the x axis, and the chord length of the system is unity. Point measurements, using both the split-film and 7-hole probe, were collected in (x, y), as shown in Fig. 4.16(a), and subsequently interpolated onto a finer grid in (x, y), plotted in Fig. 4.16(b). The interpolated grid covered the entire sample space in (x, y) with 450 points in x and 350 points in y. The value plotted in the figure is $\widetilde{U}_t$ which is calculated as

$$\widetilde{U}_t = \frac{U_t}{U_\infty}. \tag{4.60}$$

A more exhaustive discussion of the aerodynamic results is presented in Chapters 5 and 6.

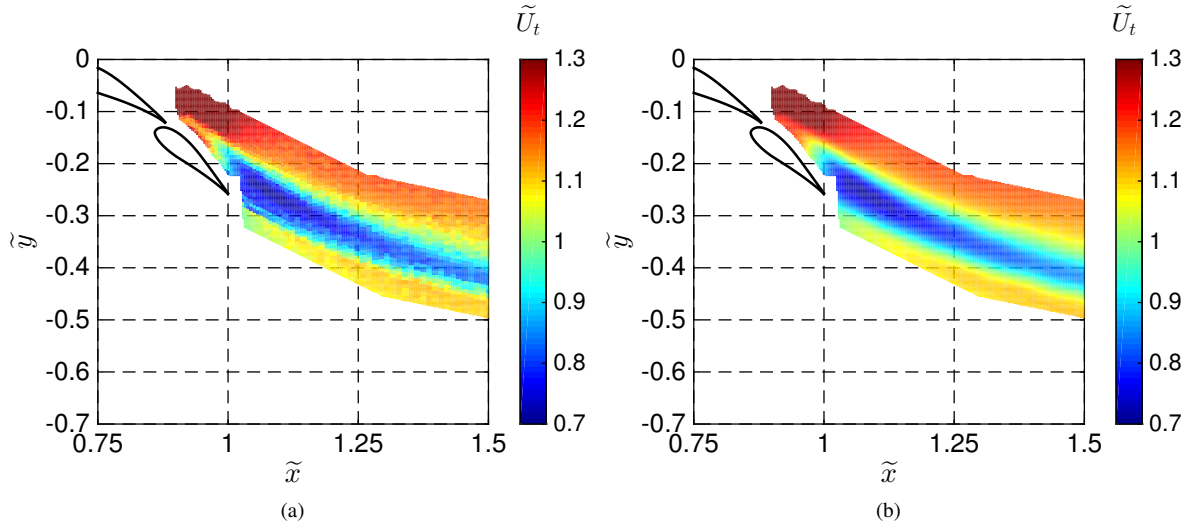

Figure 4.16: Representative results for $\widetilde{U}_t$ data in a) experimental domain set and b) interpolated across full extent of sample domain.

4.3.1 Bilinear Interpolation

Data were interpolated from the experimentally-sampled grid onto a finer grid by using a bilinear interpolation scheme [132, 133]. Consider the case presented in Fig. 4.17(a) in which data are known at four points, and the function is to be evaluated at some other point *P*. As shown in the figure, an arbitrarily-shaped quadrilateral formed by connecting the four data points can also be described by an *x*-*y* or in a computational-index-fixed ξ-η coordinate system. The *x*-*y* coordinate system can be mapped to a unit-square ξ-η coordinate system shown in Fig. 4.17(b) in which the unit-square is discretized into *M* and *N* evenly-spaced stations in the η and ξ direction, respectively. A

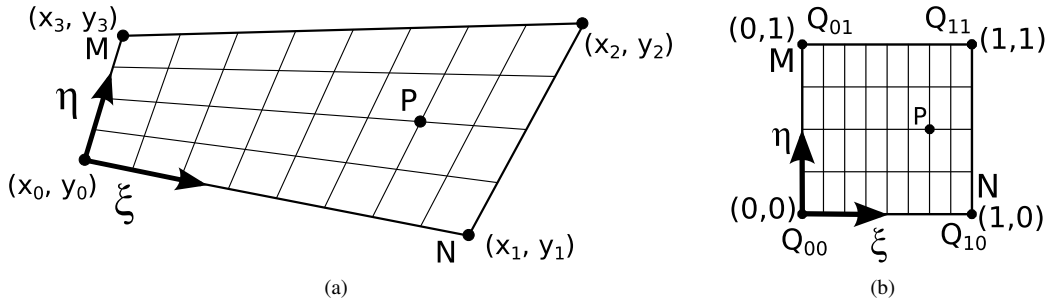

Figure 4.17: Coordinate transformation for bilinear interpolation from a) arbitrary quadrilateral to b) unit square.

linear interpolation scheme can be applied in the x direction between points 0 and 1 and points 3 and 2 to yield

$$x(\xi,0) = \frac{N-\xi}{N-1}x_0 + \frac{\xi-1}{N-1}x_1 \tag{4.61a}$$

$$x(\xi,M) = \frac{N-\xi}{N-1}x_3 + \frac{\xi-1}{N-1}x_2 \tag{4.61b}$$

which can then be interpolated again for some arbitrary value η and is shown to be

$$x(\xi,\eta) = \frac{M-\eta}{M-1}\left(\frac{N-\xi}{N-1}x_0 + \frac{\xi-1}{N-1}x_1\right) + \frac{\eta-1}{M-1}\left(\frac{N-\xi}{N-1}x_3 + \frac{\xi-1}{N-1}x_2\right). \tag{4.62}$$

Similar methods can be applied in the y direction to yield $y(\xi,\eta)$ such that

$$y(\xi,\eta) = \frac{M-\eta}{M-1}\left(\frac{N-\xi}{N-1}y_0 + \frac{\xi-1}{N-1}y_1\right) + \frac{\eta-1}{M-1}\left(\frac{N-\xi}{N-1}y_3 + \frac{\xi-1}{N-1}y_2\right) \tag{4.63}$$

Thus, a coordinate mapping as defined by Eqs. 4.62–4.63 relates the two domains in Fig. 4.17.

An interpolation algorithm can be implemented on the ξ-η unit-square grid in Fig. 4.17(b) where Q_{ij} is the value of some known function f of which the value at point P is desired. Bilinear interpolation consists of two independent interpolations in the ξ and η directions. First, a linear interpolation in the ξ direction at $\eta = 0$ and $\eta = 1$ yields

$$f(\xi,\eta_0) \approx \frac{\xi_1-\xi}{\xi_1-\xi_0}f(Q_{00}) + \frac{\xi-\xi_0}{\xi_1-\xi_0}f(Q_{10}) \tag{4.64a}$$

$$f(\xi,\eta_1) \approx \frac{\xi_1-\xi}{\xi_1-\xi_0}f(Q_{01}) + \frac{\xi-\xi_0}{\xi_1-\xi_0}f(Q_{11}). \tag{4.64b}$$

An interpolation in the η direction results in

$$f(\xi,\eta) \approx \frac{\eta_1-\eta}{\eta_1-\eta_0}f(\xi,\eta_1) + \frac{\eta-\eta_0}{\eta_1-\eta_0}f(\xi,\eta_1), \tag{4.65}$$

and substitution of Eq. 4.64 into Eq. 4.65 yields an estimate for $f(\xi,\eta)$ as

$$\begin{aligned} f(\xi,\eta) \approx \frac{1}{(\xi_1-\xi_0)(\eta_1-\eta_0)}\big[&f(Q_{00})(\xi_1-\xi)(\eta_1-\eta) + f(Q_{10})(\xi-\xi_0)(\eta_1-\eta) + \\ &+ f(Q_{01})(\xi_1-\xi)(\eta-\eta_0) + f(Q_{11})(\xi-\xi_0)(\eta-\eta_0)\big]. \end{aligned} \tag{4.66}$$

The aforementioned bilinear interpolation methodology was applied to a representative data set, and the results, including both raw, uninterpolated data and bilinear-interpolated data, are presented in Fig. 4.18. While the interpolation yields a more-spatially-dense flowfield representation, it is observed that the resulting interpolant is not sufficiently smooth. In this discussion, smoothness is evaluated by the magnitude of the second derivative, also known as the

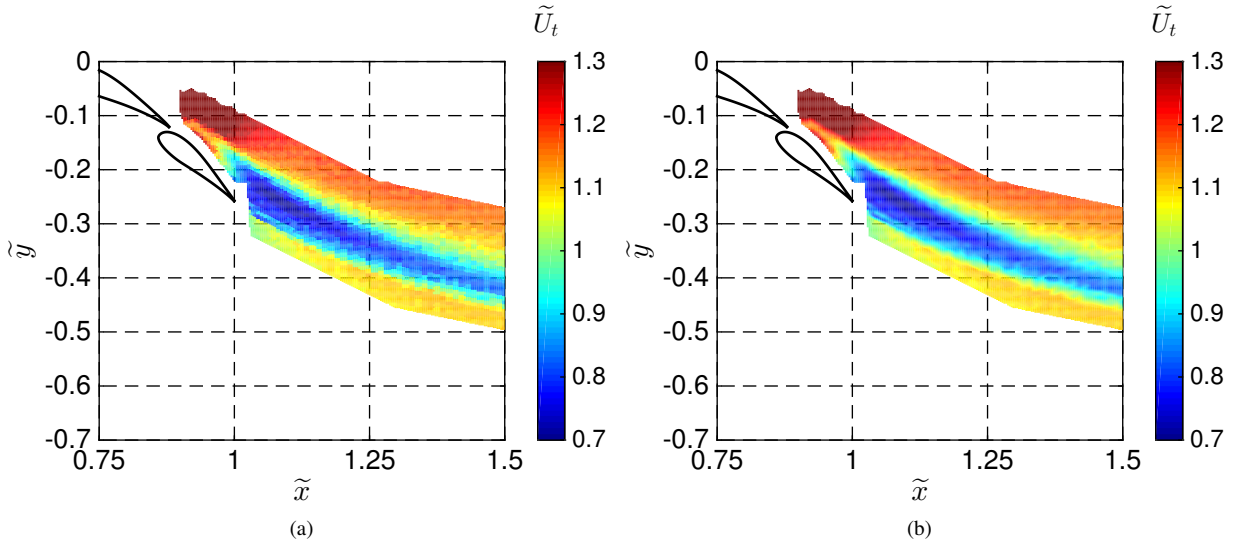

Figure 4.18: Representative experimental results plotted with a) no interpolation and b) bilinear interpolation.

curl of a function. That is to say, a straight line is said to be perfectly smooth. The non-smooth nature of the results is observed by the presence of small "pockets" observed in Fig. 4.18(b). These small pockets occur due to the high spatial density of the raw data and uncertainty, or noise, in these measurements. Implementation of various other interpolation methods all yielded the same pockets in the flowfield. It is surmised that this behavior is an artifact of the interpolation techniques, the densely-located data in the flowfield, and small amounts of uncertainty of the measurements. Previous research indicates that these observations have been observed if interpolation techniques were applied to densely-sampled spatial domain with slight amounts of noise in the raw data [134, 135]. A technique known as regularization can be implemented to accurately interpolate data onto a finer grid while obtaining the desired smoothness in the resulting interpolant.

4.3.2 Regularization

In an effort to generate a smooth surface, a three-dimensional regularization method was employed. In general, regularization is a process which adds additional constraints or information to a problem to avoid overfitting by restricting the smoothness of the resulting function, and a variation of ridge-regression was used in the current study [134–137]. However, instead of seeking to minimize the magnitude of the output data (which is the standard ridge-regression technique), methods implemented in this research minimized the magnitude of the second derivative at discrete points on the interpolated (output) surface through minimum least-squares methods. These calculations were performed with the MATLAB-based RegularizeData3D software package developed by Kintaar and D'Errico [138] and supplemented

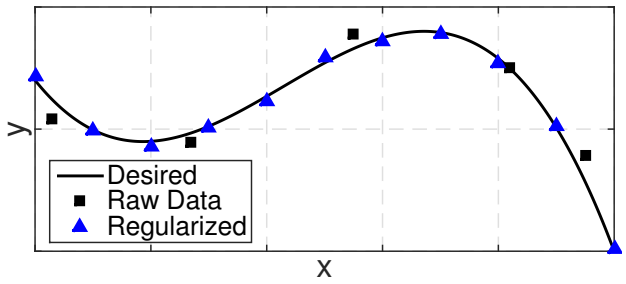

Figure 4.19: Effect of a two-dimensional regularization process.

by some additional modifications by the author. A two-dimensional regularization example will first be presented, and then the theory will be briefly extended into three dimensions.

Consider the data set presented in Fig. 4.19 in which the measured data deviates from a known true solution. The measured experimental data include m different data points defined as (x_{raw}, r) where $\mathbf{r}$ is a vector of length m containing the raw dependent variable values. In addition to increasing the resolution in x, it is desired to decrease the noise ("smoothing the data") in y. A one-dimensional linear interpolation scheme could be used to increase resolution, but the noise would not be removed from the results. For this example, the desired regularized data set is desired at n different points. A system of linear equations will be assembled that incorporate the fidelity (accuracy) and smoothness (magnitude of curl) of the final interpolant. A linear interpolation of the data can be expressed in matrix form by

$$\begin{bmatrix} W_{1,1} & W_{1,2} & \cdots & W_{1,n} \\ W_{2,1} & W_{2,2} & \cdots & W_{2,n} \\ \vdots & & \ddots & \vdots \\ W_{m,1} & W_{m,2} & \cdots & W_{m,n} \end{bmatrix} \begin{bmatrix} r_1 \\ r_2 \\ \vdots \\ r_n \end{bmatrix} = \begin{bmatrix} e_1 \\ e_2 \\ \vdots \\ e_n \end{bmatrix} \tag{4.67}$$

or in compact form as

$$\mathbf{W_f r} = \mathbf{e} \tag{4.68}$$

where $\mathbf{W_f}$ is an m by n matrix that contains the weight values for the linear interpolant, $\mathbf{r}$ is the unknown dependent variables as predicted by the fidelity equation, and $\mathbf{e}$ is the raw dependent-variable data. Weighting values in $\mathbf{W_f}$ are of the form presented in Eqs. 4.64–4.65, and are the quantity by which the value of f at a point is multiplied.

A second set of linear equations can be developed to calculate the second derivative at the x values in the regularized data set. The second derivative at point P_1, shown in Fig. 4.20(a) can be calculated by the difference of the first derivatives D_0 and D_1 by

$$\left.\frac{d^2y}{dx^2}\right|_{P_1} = \frac{D_1 - D_0}{\frac{x_2 - x_0}{2}} \tag{4.69}$$

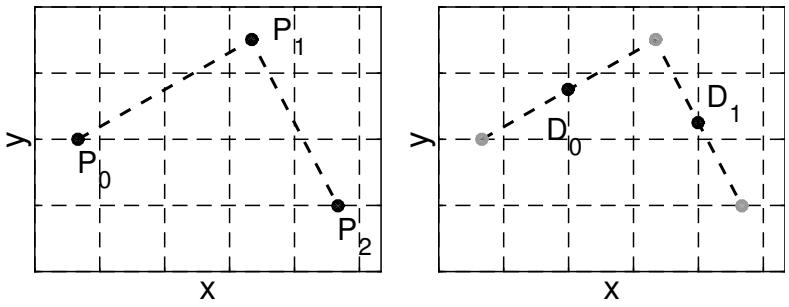

(a) (b)

Figure 4.20: Calculation of second derivative using a) $f(x)$ and b) $f'(x)$.

where, as shown in Fig. 4.20(b),

$$D_0 = \left.\frac{dy}{dx}\right|_{\frac{x_0+x_1}{2}} = \frac{y_1 - y_0}{x_1 - x_0} \tag{4.70a}$$

$$D_1 = \left.\frac{dy}{dx}\right|_{\frac{x_1+x_2}{2}} = \frac{y_2 - y_1}{x_2 - x_1}. \tag{4.70b}$$

As Δx is constant in the given example, the solution is second order. Equation 4.70 can be substituted into Eqn. 4.69 to result in

$$\left.\frac{d^2y}{dx^2}\right|_{P_1} = \begin{bmatrix} \frac{2}{(x_1-x_0)(x_2-x_0)} & \frac{-2}{(x_2-x_1)(x_1-x_0)} & \frac{2}{(x_2-x_1)(x_2-x_0)} \end{bmatrix} \begin{bmatrix} y_0 \\ y_1 \\ y_2 \end{bmatrix} \tag{4.71}$$

which is the second-derivative computation at point P_1. If n different points are contained in the regularized data output, then $n-2$ second derivatives can be calculated. As previously discussed, the second derivative of a perfectly-smooth function is 0. Therefore, as a smooth interpolant is desired, the second derivative at the regularized x values is desired to be 0. Equation 4.71 can be expressed in matrix form at point P_i as

$$\left.\frac{d^2y}{dx^2}\right|_{P_i} = \mathbf{V}_i \mathbf{y}_i \tag{4.72}$$

in which the values of $\mathbf{V}_i$ and $\mathbf{y}_i$ correspond to the three-element matrices presented above in Eq. 4.71. A system equations can be assembled at all n points from Eq. 4.72 to be

$$\begin{bmatrix} V_{1,1} & V_{1,2} & \cdots & V_{1,n} \\ V_{2,1} & V_{2,2} & \cdots & V_{2,n} \\ \vdots & & \ddots & \vdots \\ V_{n-2,1} & V_{n-2,2} & \cdots & V_{n-2,n} \end{bmatrix} \begin{bmatrix} r_1 \\ r_2 \\ \vdots \\ r_{n-2} \end{bmatrix} = \begin{bmatrix} 0 \\ 0 \\ \vdots \\ 0 \end{bmatrix} \tag{4.73}$$

or alternatively written as

$$\mathbf{V}\mathbf{r} = \mathbf{0}. \tag{4.74}$$

As previously mentioned, $\mathbf{V}$ is a tridiagonal matrix used to weight the values that yield the smoothness of the desired function. It is noted that, by definition of the Euler-Lagrange equation, only a straight line will satisfy $d^2y/dx^2 = 0$. Consequently, as it is not desired to have the resulting interpolant be a straight line, the smoothness equations in Eq. 4.74 are used to penalize large variations of the output interpolant and not to generate a closed-form solution.

Different data sets or applications of this method may require different degrees of smoothness in the output interpolant. Thus, a constant k_{smooth} is introduced to scale $\mathbf{V}$ by a factor S according to

$$S = \sqrt{\frac{\text{\# fidelity equations}}{\text{\# derivative equations}}} = k_{smooth}\sqrt{\frac{m}{n-2}} \tag{4.75}$$

This scaling factor relates the stiffness ("importance") of the smoothness to the fidelity of the output. Thus, the user can dictate the degree to which the interpolant is smoothed. The fidelity and smoothness equations are equally weighted if $k_{smooth} = 1$. A very large value of k_{smooth}, such as $+\infty$, will yield a perfectly-smooth interpolant which is a line-of-best-fit through all the data. A small value of k_{smooth}, such as 0.0000001, weights the accuracy of the fidelity equations much more than the smoothness of the output.

The interpolant, which is defined by Eqs. 4.68, 4.74, and 4.75 can be combined into one system of equations where

$$\left[\begin{array}{cccc} W_{1,1} & W_{1,2} & \cdots & W_{1,n} \\ W_{2,1} & W_{2,2} & \cdots & W_{2,n} \\ \vdots & & \ddots & \vdots \\ W_{m,1} & W_{m,2} & \cdots & W_{m,n} \\ \hline SV_{1,1} & SV_{1,2} & \cdots & SV_{1,n} \\ SV_{2,1} & SV_{2,2} & \cdots & SV_{2,n} \\ \vdots & & \ddots & \vdots \\ SV_{n-2,1} & SV_{n-2,2} & \cdots & SV_{n-2,n} \end{array}\right] \left[\begin{array}{c} r_1 \\ r_2 \\ \vdots \\ r_n \end{array}\right] = \left[\begin{array}{c} e_1 \\ e_2 \\ \vdots \\ e_n \\ \hline 0 \\ 0 \\ \vdots \\ 0 \end{array}\right] \tag{4.76}$$

or also

$$\left[\begin{array}{c} \mathbf{W} \\ S\mathbf{V} \end{array}\right] \mathbf{r} = \left[\begin{array}{c} \mathbf{e} \\ \mathbf{0} \end{array}\right]. \tag{4.77}$$

The system defined in Eq. 4.77 is defined by $m+n-2$ equations, but only contains n unknown values (represented as $\mathbf{r}$). Thus, the system is overdetermined, and no values of $\mathbf{r}$ can be calculated to simultaneously satisfy all equations in

the system. Equation 4.77 can be rewritten as

$$\begin{bmatrix} \mathbf{W} \\ S\mathbf{V} \end{bmatrix} \mathbf{r} - \begin{bmatrix} \mathbf{e} \\ \mathbf{0} \end{bmatrix} = \mathbf{0}. \tag{4.78}$$

However, because the system is overdetermined, Eq. 4.78 cannot be satisfied, and values of $\mathbf{r}$ will result in non-zero values on the right-hand side of the equation. These values are the residual of the fit. Thus, the system can be expressed as

$$\begin{bmatrix} \mathbf{W} \\ S\mathbf{V} \end{bmatrix} \mathbf{r} - \begin{bmatrix} \mathbf{e} \\ \mathbf{0} \end{bmatrix} = \varepsilon \tag{4.79}$$

where ε is a column vector of the residuals for each equation in the system. A linear least-squares method was implemented to minimize the value of ε^2 by the standard method in which the equations are defined by [139, 140]

$$\begin{bmatrix} \mathbf{W} \\ S\mathbf{V} \end{bmatrix}^T \begin{bmatrix} \mathbf{W} \\ S\mathbf{V} \end{bmatrix} \mathbf{r} = \begin{bmatrix} \mathbf{W} \\ S\mathbf{V} \end{bmatrix}^T \begin{bmatrix} \mathbf{e} \\ \mathbf{0} \end{bmatrix}. \tag{4.80}$$

The equations in Eq. 4.80 are expressed as a symmetric pentadiagonal matrix which is computationally inexpensive to solve using Gaussian elimination to yield the final values of $\mathbf{r}$.

The two-dimensional regularization method which has been discussed can be readily adapted for three-dimensional regularization with a few small modifications. Consider the three-dimensional regularization case in which a parameter was collected on a Cartesian grid in x and y; these three parameters all make up a three-dimensional regularization problem. Instead of seeking values $\mathbf{r}$ as a function of x only, $\mathbf{r}$ is determined as a function of both x and y. The fidelity equations in Eq. 4.68, when implemented in two dimensions, can be represented by a bilinear interpolation, as previously discussed and defined in Eqs. 4.62–4.63 and 4.66. Calculation of the second derivative must include two partial differentiations, being $\partial/\partial x$ and $\partial/\partial y$. Consequently, Eq. 4.74 can be expressed by

$$\begin{bmatrix} \mathbf{V}_x \\ \mathbf{V}_y \end{bmatrix} \mathbf{r} = \mathbf{0} \tag{4.81}$$

where $\mathbf{V}_x$ and $\mathbf{V}_y$ are the weighting coefficients as defined in Eqs. 4.62–4.63. As the three-dimensional regularized smoothness matrix (Eq. 4.81) contains more equations than the two-dimensional regularized smoothness matrix (Eq. 4.74), the scaling function S is defined to be

$$S = \sqrt{\frac{\text{\# fidelity equations}}{\text{\# derivative equations}}} = k_{smooth}\sqrt{\frac{m}{m(n-2)+n(m-2)}} \tag{4.82}$$

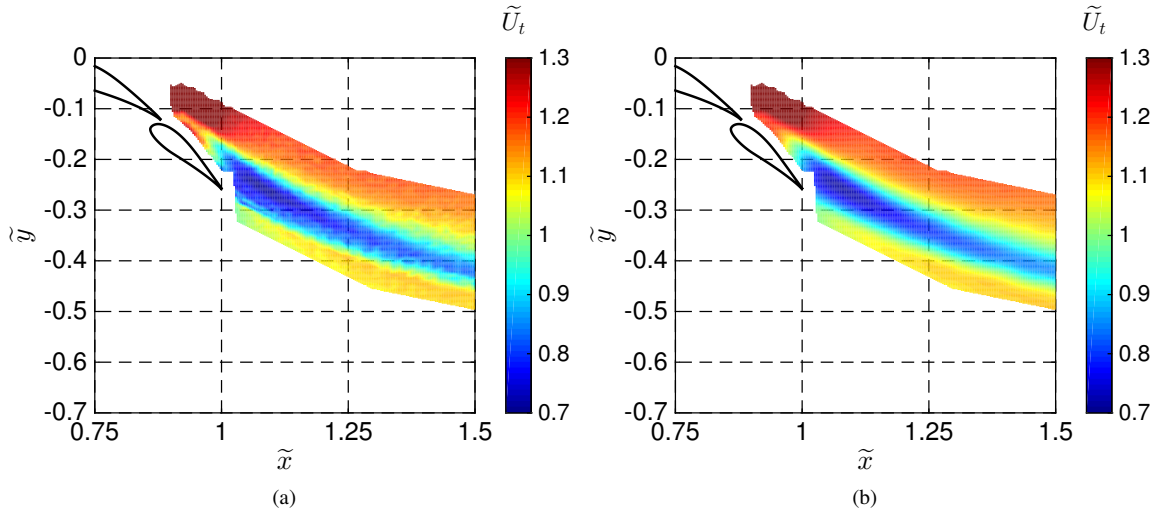

Figure 4.21: Representative data interpolated using a) bilinear interpolation and b) 3-dimensional regularization.

The definition of the normal equations in Eq. 4.80 remain unchanged, and the same linear least-squares methods can be employed to minimize ε^2.

A comparison of the two methods, bilinear interpolation and three-dimensional regularization, to a representative data set is presented in Fig. 4.21. In this result, values of k_{smooth} were taken to be 0.00003 in which the fidelity of the system was weighted $33,333.\overline{3}$ times more heavily than the smoothness of the interpolant, and thus the output values of the interpolated system is very close to the non-regularized data. The regularized data are observed to be superior to the bilinear-interpolated data as the curious "pockets" are not observed in the regularized output, as the regularized data are smoother than the bilinear-interpolated data. Results presented in the remainder of this document were all determined using three-dimensional regularization techniques.

Chapter 5

Baseline Airfoil Aerodynamics and Fluid Dynamics

A baseline configuration of the three-element MFFS(ns)-026 airfoil, referred to as Configuration 10, was examined in great detail utilizing both experimental and computational methods*. The three-element airfoil, plotted in Fig. 5.1, consisted of a main element and two flaps. The location of the flaps can be expressed in both a relative coordinate system (Fig. 3.3) and an absolute coordinate system (Fig. 3.2). Coordinate values are tabulated for the relative and absolute coordinate system in Tables 5.1 and 5.2, respectively.

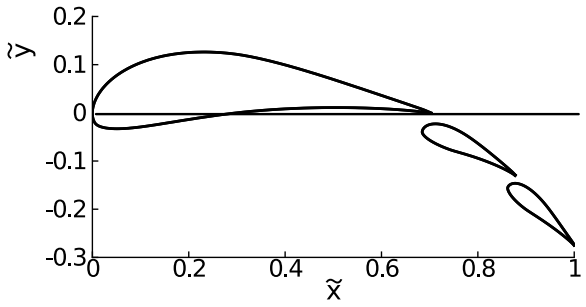

Figure 5.1: Baseline (Configuration 10) multielement airfoil geometry.

Table 5.1: Location of Configuration 10-Airfoil Elements in Relative Coordinates

	Main Element to Flap 1	Flap 1 to Flap 2
gap/c_{sys}	0.0100	0.0100
$overhang/c_{sys}$	0.0150	0.0150
δ_{rel}	26.4 deg	15.9 deg

Table 5.2: Location of Configuration 10-Airfoil Elements in Absolute Coordinates

	Main Element	Flap 1	Flap 2
$(x,y)_{le}$	$(0,0)$	$(0.6907,-0.0178)$	$(0.8619,-0.1352)$
δ	–	26.4 deg	42.3 deg

*Portions of this chapter are based on work also contained in Ref. 141, which was performed in collaboration with then-graduate-students Phil Ansell and Jeff Diebold, who are both co-authors on the submission. All written text and figures in this document were created by the author of this dissertation.

A significant amount of data were collected using various experimental and computational techniques. Experimental time-averaged data included a drag polar, wake profiles, surface flow visualization, off-surface static pressure, off-surface total pressure, total velocity, local flowfield angle of attack, and local sideslip angle (yielding u, v, and w). Unsteady results consisted of total velocity U_t, velocity components in u and v, local flowfield angle of attack, Reynolds stress, turbulent kinetic energy, and turbulent kinetic energy production. Computational results were all time averaged and included total velocity, local flowfield angle of attack, local sideslip angle (and thus velocity in three components in u, v, and w), static pressure, total pressure, density, static temperature, total temperature, and entropy. Many of these results are discussed in this section.

This chapter is organized in the following manner. First, aerodynamic performance of the baseline configuration shown in Fig. 5.1 is presented. Second, time-averaged velocity vectors and pressure data obtained from experimental results are presented, and comparisons are made between the two different types of probes in this section. Next, unsteady fluid dynamics determined from an experimental test is discussed. Finally, an in-depth discussion of the computational results is presented with some comparisons to the experimental data.

5.1 Nondimensionalization

Over the course of this research project, methods were implemented to nondimensionalize data by characteristic values to allow for easy comparisons to be made between different data sets. Throughout this document, nondimensional values are generally denoted by the tilde character ($\tilde{}$) which is placed over the corresponding letter or symbol with the exception of nondimensional coefficients. These coefficients, represented in the notation C_* where $*$ represents an alphanumeric character, are nondimensional in this document unless otherwise stated. The static pressure coefficient C_p was defined by the standard equation

$$C_p = \frac{p - p_\infty}{q_\infty}, \tag{5.1}$$

and a similar coefficient, deemed the coefficient of total pressure, was defined by

$$C_{p,t} = \frac{p_t - p_{t,\infty}}{q_\infty} = \frac{\Delta p_t}{q_\infty} \qquad (\leq 0). \tag{5.2}$$

Thus, the nondimensional head loss at a given point relative to the freestream can be evaluated by Eq. 5.2. Cartesian coordinates, and any other length scale, were normalized by the airfoil length such that

$$[\tilde{x}, \tilde{y}]^T = [x, y]^T / c. \tag{5.3}$$

Velocity values, including U_t, which is defined as

$$U_t = \sqrt{u^2 + v^2 + w^2}, \tag{5.4}$$

as well as (u, v, w) were normalized by the freestream velocity, viz

$$[\widetilde{U}_t, \widetilde{u}, \widetilde{v}, \widetilde{w}]^T = [U_t, u, v, w]^T / U_\infty. \tag{5.5}$$

The velocity components (u, v, w) are aligned with the x, y, and z axes, respectively; the x axis is not necessarily aligned with V_∞. Variables expressed not as a coefficient in the form of C_* and without the tilde symbol ($\tilde{}$) are defined to be dimensional values unless otherwise stated.

5.2 Aerodynamic Performance

An investigation was performed to identify an airfoil geometry, and a set of operating conditions, for which the flow was attached to all three elements but in which wake bursting was observed. The resulting baseline geometry is referred to as Configuration 10, and is plotted in Fig. 5.1. Steady-state aerodynamic performance data, including surface-oil flow visualization as well as lift and drag data, were collected for Configuration 10. Flow visualization, as discussed in Sec. 3.2.12, was performed to ensure that the flow was attached to all three elements of the airfoil, thus confirming that any separation observed in the wake surveys was due to wake bursting and not due to separation from the airfoil surface.

Surface oil flow visualization results on the upper surface of the three-element airfoil at $\alpha = 0.0$ deg and $Re = 1 \times 10^6$ are presented in Fig. 5.2 where flow is from left-to-right in the photograph. The locations of leading edge and trailing edge of the airfoil system are both labeled in the figure; the trailing edges of each flap are also labeled. As seen in the image, a laminar separation bubble is visible on the main element between $\widetilde{x} \approx 0.25$ and 0.29. The trailing edge of the main element is seen as an oil accumulation line at $\widetilde{x} \approx 0.67$. A laminar separation bubble is present on the first flap between $\widetilde{x} \approx 0.71$ and 0.73, and an oil accumulation at $\widetilde{x} \approx 0.86$ indicates the trailing edge of the first flap. A laminar separation bubble on the second flap is present between $\widetilde{x} \approx 0.89$ and 0.91. Thus, overall, there is no trailing-edge stall or massive separation. Hence, the flow is "well-behaved" from a surface perspective and, in the context of this research, is said to be attached.

Lift and drag data shown in Fig. 5.3 were collected over an angle of attack range from approximately -8 to 5 deg in 1 deg increments using an external floor-mounted force balance to measure lift and pitching moment while a wake-integration method was implemented to determine drag. These methods are discussed in detail in Sec. 3.2. As seen

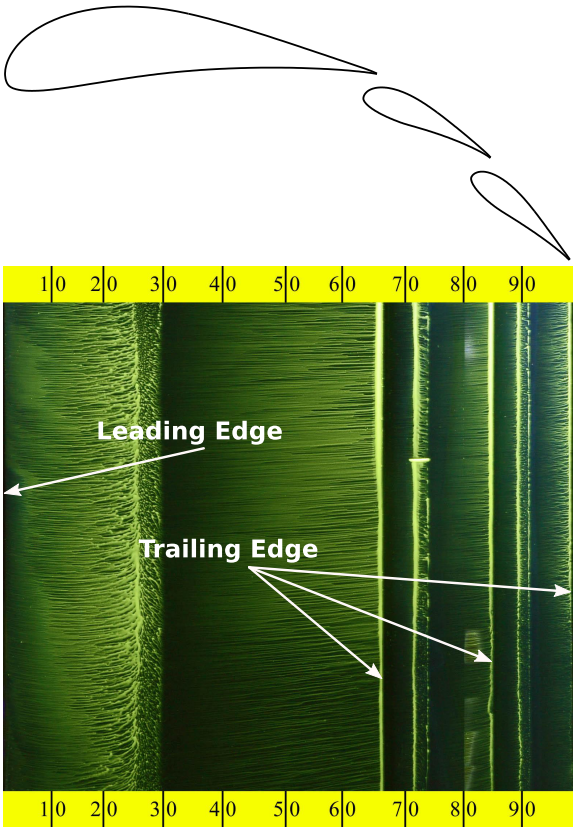

Figure 5.2: Surface oil flow visualization of Configuration 10 showing attached flow at $\alpha = 0$ deg and $Re = 1 \times 10^6$.

in the figure, lift increases in a linear fashion, and stall is observed to occur at $\alpha = 4$ deg. Data could not be taken higher than 5 deg as the unsteady dynamic loads incurred by buffeting would have overloaded the damage resulting in significant damage to the equipment. It is noted that the lift curve slope, $C_{l\alpha}$, was calculated to be 0.065 /deg, which is significantly less than the theoretical value of 0.110 /deg predicted by thin airfoil theory. Viscous effects, including both wake bursting and junction vortex effects, can be attributed to the decreased lift curve. These two topics are investigated later in this document. As discussed later in this document, the thickness of the wake increases with angle of attack and effectively and progressively decambers the airfoil. This wake behavior yields less lift than predicted by thin airfoil theory, which is based on inviscid potential flow. Both the flow visualization and the lift and drag data indicate that the flow is attached, and the system is not stalled between $\alpha = -8$ and 4 deg. Wake profiles were taken 1.88 chords (32.4 in, 0.823 m) downstream of the trailing edge of the model, and the wake profile at $\alpha = 0$ deg and $Re = 1 \times 10^6$ is shown in Fig. 5.3(c). The difference in total pressure $\Delta P_0 = P_{0,w} - P_{0,\infty}$ is plotted against the chord-normal location in the wind tunnel (y). It is noted that the individual wakes from each element are not visible because the wakes merged and interacted to form one large wake at this downstream position. The spreading and merging of these wakes will be discussed in great detail in the remainder of this section.

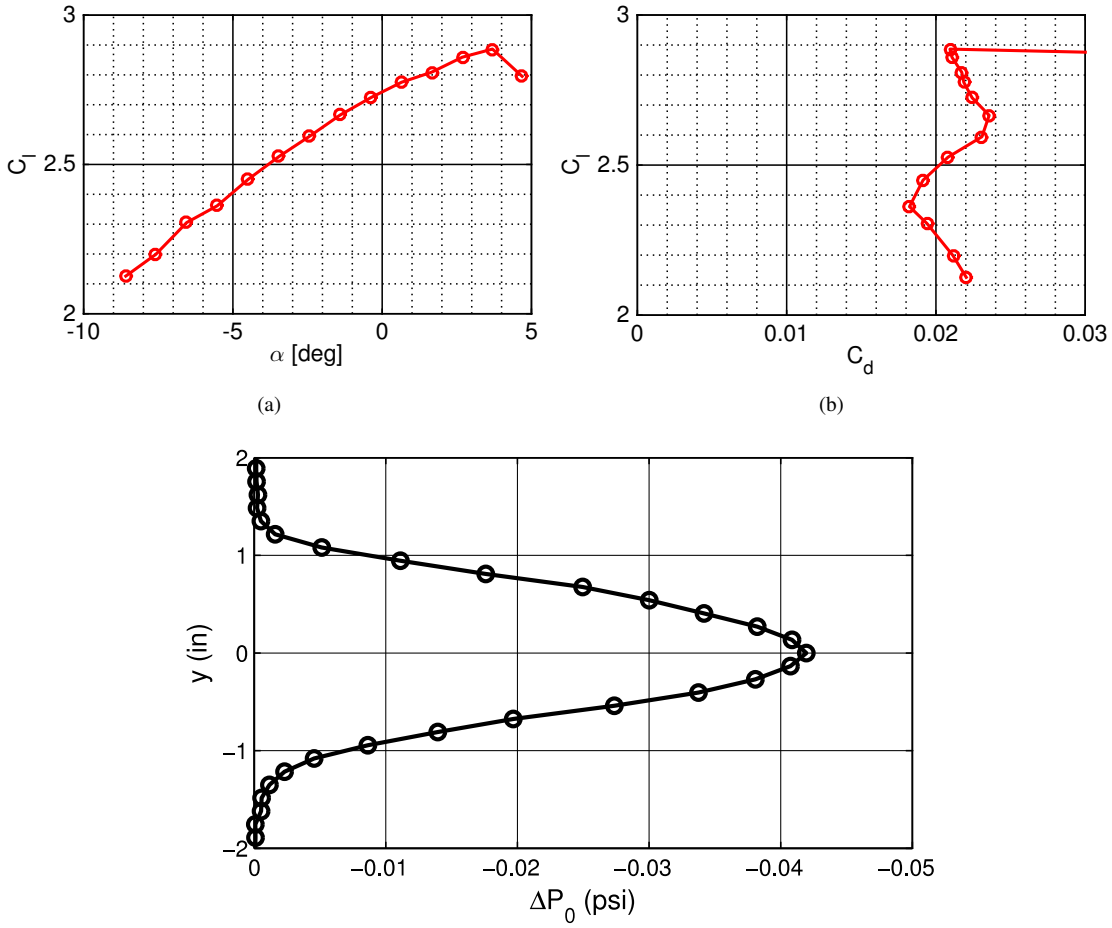

Figure 5.3: Aerodynamic performance metrics for Configuration 10 at $Re = 1 \times 10^6$ depicting a) lift, b) drag, and c) wake profile 1.88 chords downstream of trailing edge at $\alpha = 0.0$ deg.

5.3 Experimental Time-Averaged Results

Off-body time-averaged data were collected in the flowfield using the split-film probe and 7-hole probe discussed extensively in Chap. 4 utilizing the experimental setup detailed in Sec. 3.2.9. These data include both time-averaged and time-dependent data. In this subsection, time-dependent data collected by the split-film probe were time-averaged to allow comparison of data between the 7-hole and split-film probes. A variety of variables, parameters, and metrics are discussed in this section, and some comparisons are made between data collected by the two different probes.

5.3.1 Wake Survey Domains

Data were collected at a constant span station and a wide range of x and y locations using both the split-film probe and 7-hole probe; the sampled domains are presented for both probes in Fig. 5.6. During the split-film probe test, measurements were taken at a spatial resolution of 0.1 in (2.54 mm) in both the x and y directions from a distance 2.87 in (7.29 cm or $0.175c$) upstream of the trailing edge to a distance 1.51 in (3.85 cm or $0.092c$) downstream of the trailing edge for a total travel distance of 4.38 in (11.11 cm or $0.446c$). Data were taken with a surface offset of 0.1 in (0.25 cm or 0.0061c) across a y range between 0.768 in (1.95 cm or $0.0469c$) and 4.64 in (11.8 cm or $0.284c$) in the direction away from the system chord line. Data plotted in Fig. 5.4(a) consist of 1,099 spatial locations at which data were collected.

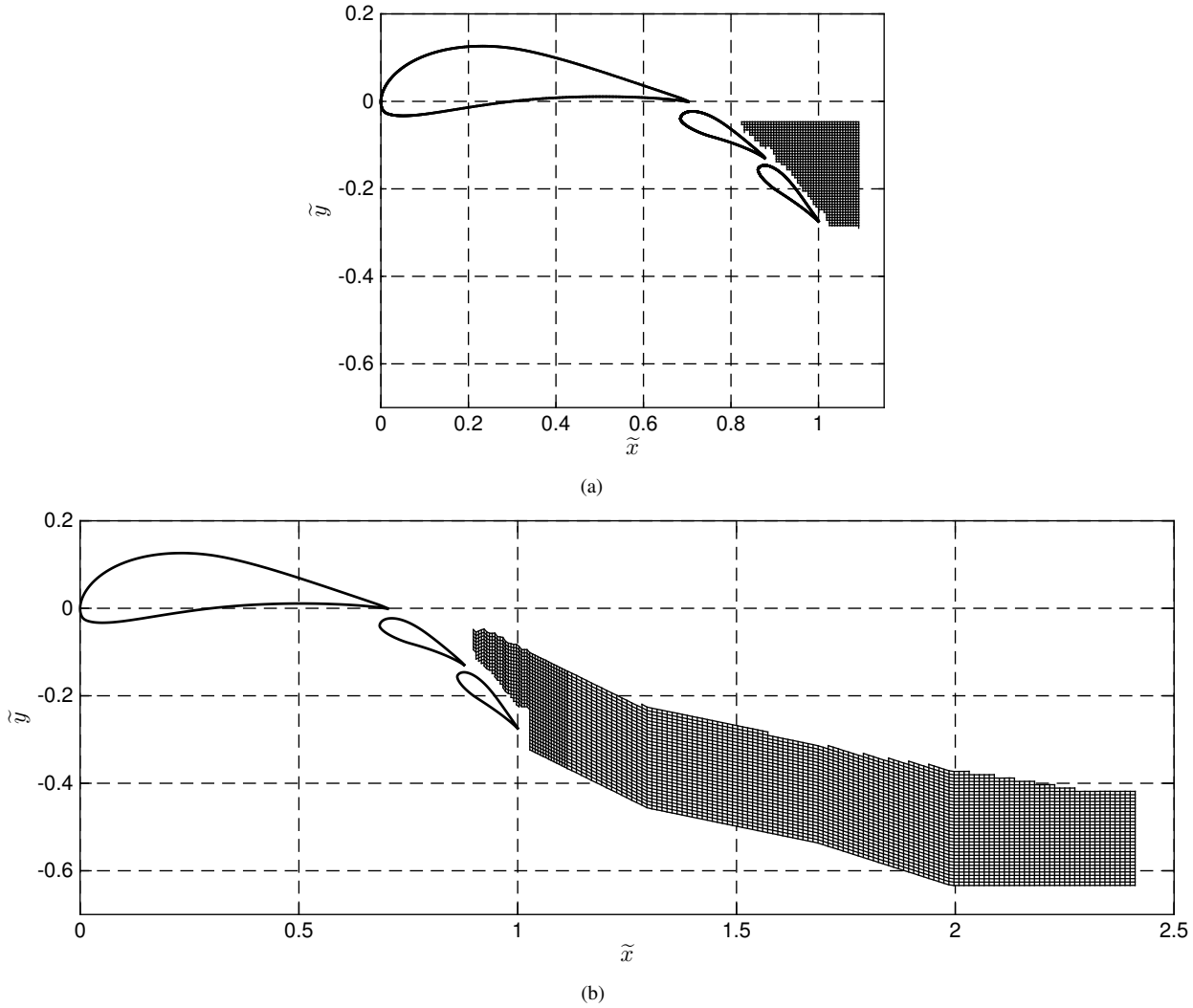

Figure 5.4: Sample domain and experimental survey points for a) split-film probe test and b) 7-hole probe test.

A significant number of modifications were made to the sidewall traverse setup prior to collecting data using the 7-hole probe. For a thorough discussion of the modifications, the reader is referred to Sec. 3.2.9. Data with the 7-hole probe were taken no closer than 0.35 in (8.9 mm or 2.8 probe diameters) to the surface of the airfoil to reduce probe-airfoil interactions and avoid the possibility of collisions between the probe and the airfoil surface. As the wake surveys took in excess of 7 hr to complete with the expanded survey domain, methods were employed to decrease the run time and capture the most-relevant data. The domain, as presented in Fig. 5.4(b), was sampled with a step size in the streamwise direction (Δx) of 0.10 in (2.5 mm) close to the airfoil model and at a step size of 0.188 in (4.76 mm) at further downstream locations while the step size in y (Δy) was 0.125 in (3.18 mm) at all locations in the surveyed region. In addition, the boundaries of the sampled region were specified to capture the burst wake without measuring significant amounts of extraneous data. A total of 4,322 data points were captured in the run presented in Fig. 5.4(b).

As a large number of data points were sampled, the wake surveys presented in this dissertation required many hours of testing. More specifically, the data sets presented in Fig. 5.6 took 3.5 and 7.5 hr to complete, respectively. The longest wake survey tests in this research project took approximately 14 hr of continuous wind tunnel operation to complete.

5.3.2 Total Velocity ($\widetilde{U}_t$)

Results for $\widetilde{U}_t$, acquired via the split-film and 7-hole probes, at $\alpha = 0$ deg and $Re = 1 \times 10^6$ are shown in Fig. 5.5. In the figure, the trailing portion of the first flap is visible, and the entirety of the second flap is shown; the main element is not shown. While results from the two probes may appear to be significantly different upon first examination, they are actually quite similar; similarities in the flowfield will be first discussed prior to an examination of differences.

Results captured by the split-film probe, presented in Fig 5.6(a), are first discussed as these data were collected by a smaller probe that yields less spatial smoothing than that of the 7-hole probe. Data in the figure indicate that the wake of the main element as well as the wake of flap 1 are both burst and were captured as two separate, distinct wakes with little or no merging between the two wakes. The wake from the main element (visible in the upper left corner of the plot) bursts at $\widetilde{x} \approx 0.96$ and $\widetilde{y} \approx -0.12$. At this point, the wake begins to rapidly expand, and the velocity in the wake core also decreases to a minimum time-averaged velocity of $\widetilde{U}_{t,min} = 0.75$. As compared with a non-burst wake, the main element burst wake is much wider and characterized by a greater velocity deficit. Similarly, the wake from the first flap originates near $\widetilde{x} \approx 0.88$ and $\widetilde{y} \approx -0.13$, and bursting occurs at $\widetilde{x} \approx 0.95$ and $\widetilde{y} \approx -0.15$. Both wakes burst at approximately the same $\widetilde{x}$ location; that is, the wakes appear to begin growing at a rapid rate at the same value of $\widetilde{x}$. The wakes continue to spread further downstream from the burst locations and then they begin to interact at $\widetilde{x} \approx 0.97$ and become one thick merged wake upstream of the wake rake. The growth of the wakes is not symmetric about their

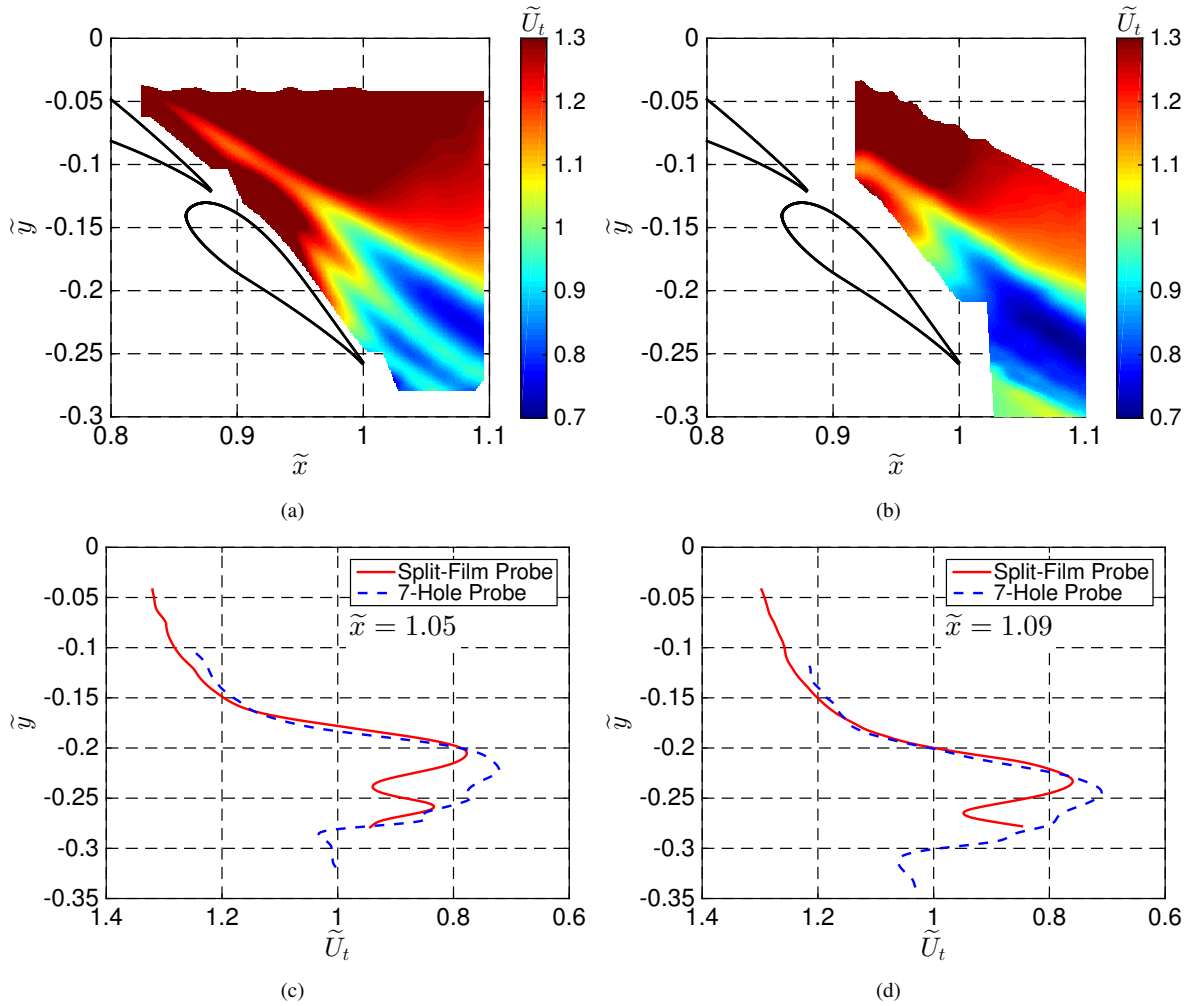

Figure 5.5: Results of time-averaged $\widetilde{U}_t$ from a) split-film probe and b) 7-hole probe, c) line plot for both probes at $\widetilde{x} = 1.05$, and d) line plot for both probes at $\widetilde{x} = 1.09$.

respective centerlines, and the growth rate is diminished after the wakes first merge; this topic is further developed in Sec. 5.3.7.

Detailed Comparison of Experimental Data

Data captured by the 7-hole probe and presented in Fig. 5.6(b)(a,b) indicate the wake of the main element is burst, as visible in the upper-left portion of the figure. A very small portion of the flap 1 wake is visible in the two contour plots. The main-element wake, first visible at $(\widetilde{x}, \widetilde{y})$ of $(0.90, -0.11)$ in the plot, is observed to thicken with increasing downstream distance. Rapid thickening is observed at $\widetilde{x} \approx 0.97$, after which point the thickness of the wake increases by almost an order of magnitude. The minimum velocity in the wake is $\widetilde{U}_{t,min} = 0.71$. As a large surface standoff between the airfoil surface and probe center was required, data were not collected close enough to the flap 2 surface to

be able to fully resolve the flap 1 wake. However, a very small portion of the wake is visible between $0.95 \leq \widetilde{x} \leq 1.01$ in which a $\widetilde{y}$ distance of 0.01 or 0.02 of the wake is resolved. The wake from flap 2 is captured, and the wake is observed to rapidly merge/interact with the wakes of both the main element and flap 1.

Two line plots of $\widetilde{U}_t$ at a constant $\widetilde{x}$ position for the two probes are presented in Fig. 5.5(c,d); these line plots were taken at $\widetilde{x}$ values of 1.05 and 1.09. Line plots are presented with varying values of $\widetilde{y}$ on the vertical axis while the velocity values are on the horizontal axis; note the direction of the horizontal axis is reversed with larger values of $\widetilde{U}_t$ on the left portion of the axis and smaller values of $\widetilde{U}_t$ on the right side of the axis. At both $\widetilde{x}$ locations, good agreement is found between both probes at larger values of $\widetilde{y}$ greater than the location of $\widetilde{U}_{t,min}$ as measured by the split-film probe. It is clear that the measurements from the two probes differ in the wake region. First of all, the minimum value of $\widetilde{U}_t$ is suggested to be different between the two probes as the 7-hole probe yields a lower value of $\widetilde{U}_t$ than that of the split-film probe.In addition, as previously mentioned, the split-film probe measured a larger boundary between the two different wakes than that of the 7-hole probe. Careful inspection of the 7-hole probe data, though, indicates that a very slight increase in $\widetilde{U}_t$ at the same location of the greatest velocity of $\widetilde{U}_t$ as measured by the split-film probe.

Upon first inspection, data presented in Fig. 5.5 appear to be significantly different between the two probes. While differences do exist, the same major flowfield features are observed to some degree in each data set, and these similarities include: bursting of main-element wake, rapid thickening and deceleration of main-element and flap 1 wakes, and significant interaction between main-element and flap 1 wakes. Some of the observable differences include: amount of interaction between main-element and flap 1 wake and minimum velocity in flowfield. These differences may be an artifact of one or a combination of different aspects of the experiment, and these differences are investigated in the remaining portions of this subsection.

Sampling Density and Probe Size

Data points for both the split-film and seven-hole probes were collected in different portions of the flowfield and at slightly-different grid densities. Grid density of both probes was chosen to be larger than that of the probe head to eliminate the effect of spatial aliasing. As mentioned in Chap. 4, the probe width of the split-film probe was taken to be 0.035 in (0.90 mm) while the 7-hole probe diameter measured 0.125 in (3.18 mm). As the split-film probe was smaller in size than the 7-hole probe, a denser experimental grid was able to be taken with the split-film probe than with the 7-hole probe, and the points at which experimental data were captured for each probe are plotted in Fig. 5.6. While data for the 7-hole probe were taken at $\widetilde{x} > 1.10$, data plots in this subsection are only presented at $\widetilde{x}$ that correspond to the same domain as that of the split-film probe data set.

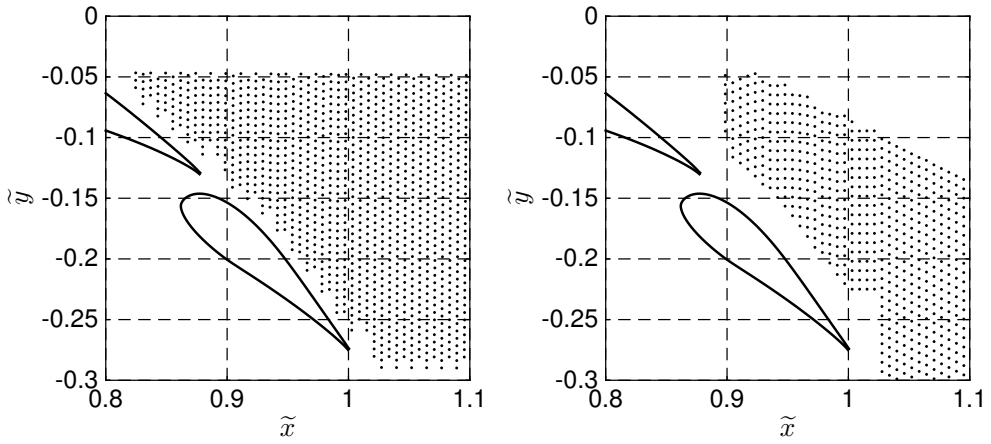

Figure 5.6: Points at which experimental data were captured for a) split-film test and b) 7-hole probe test.

In addition to the fact that the split-film probe data were collected on a finer grid, the probe width of the split-film probe is more than 3.5 times smaller than that of the 7-hole probe. Thus, the combination of denser experimental data and a smaller probe head yielded less spatial smoothing for the split-film probe data set than for the 7-hole probe data set. In an attempt to resolve differences in the two plots presented in Fig. 5.5, the split-film probe data were projected onto the coarser 7-hole probe grid, and the velocity across the wire width was spatially-averaged such that the apparent probe width of a virtual split-film probe was the same as the 7-hole probe [142]. Results plotted in Fig. 5.7 show the down-sampled and spatially-averaged split-film probe data. As observed in the figure, the flap 1 wake is not as clearly defined with less momentum loss in the wake when compared with the originally-collected split-film probe data.

Velocity Gradient Corrections

Previous research efforts have studied the behavior of multi-hole probes in velocity gradients, and a variety of methods have been developed to correct these data [142–144]. It has been shown that the pressure at each port i of a conical probe, such as the one used in this study, can be corrected in a Cartesian coordinate system with an origin metric to the center hole by

$$C_{p_i,cor} = C_{p_i}\left[1 - 2\frac{\chi_p}{d}\left(\frac{y_i}{U_t}\frac{\partial U_t}{\partial y}\right)\right] \tag{5.6a}$$

$$C_{p_i,cor} = C_{p_i}\left[1 - 2\frac{\chi_p}{d}\left(\frac{z_i}{U_t}\frac{\partial U_t}{\partial z}\right)\right] \tag{5.6b}$$

in which C_{p_i} is the pressure coefficient at port i, y_i and z_i are the coordinates of port i relative to the center hole, and χ_p/d is a correction coefficient that has been taken to be 1.4 for a conical probe, which is in accordance with the

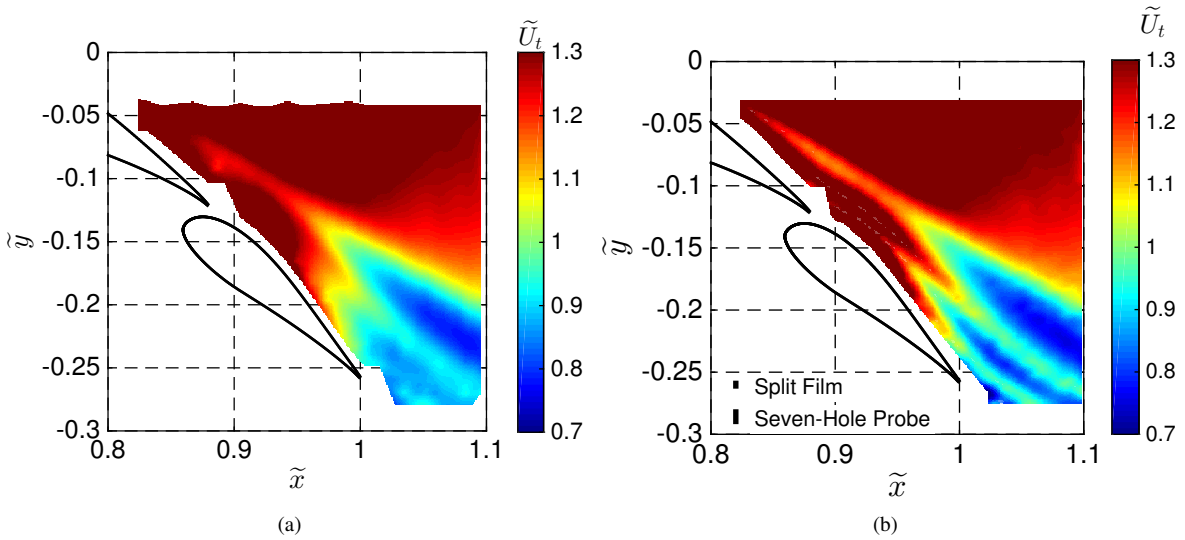

(a) (b)

Figure 5.7: Wake survey depicting $\widetilde{U}_t$ as a) down-sampled and spatially-smoothed split-film data and b) baseline split-film data coplotted with physical split-film and 7-hole probe size.

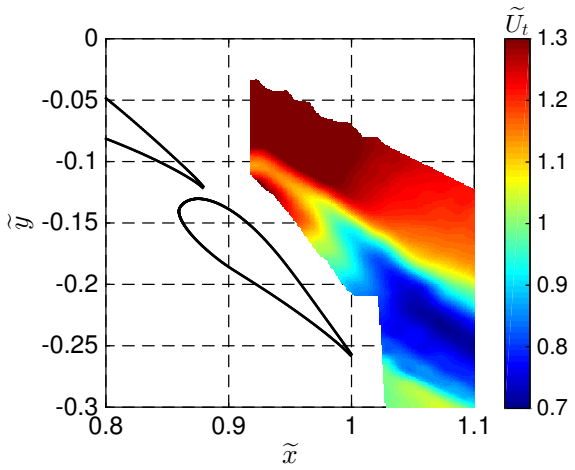

Figure 5.8: Velocity-gradient-corrected 7-hole probe data.

literature [144]. These corrections were applied to the 7-hole probe data presented in Fig. 5.6(b), and the results are plotted in Fig. 5.8. While some minute differences are observed to exist, especially at the boundaries of the wake, the data set remains largely unchanged relative to the uncorrected data.

Effect of Turbulence

In addition, it has been shown that time-averaged pressure probes respond differently to turbulent flow than what is physically present, and these probes may require the implementation of another correction. While the effect of turbulence on multi-hole probes has been documented by a few researchers, little work has been done to develop a

correction method for multi-hole probes in turbulent flowfields, but efforts are underway to develop such a method as of the writing of this document [145–148]. In lieu of a comprehensive correction for multi-hole probes, a correction method originally developed for pitot tubes will be discussed and implemented [145]; it would be interesting to apply the correction methods currently in development to these data at a later date [148]. It is known that a Pitot tube captures artificially-elevated total pressure values in turbulent flows as governed by

$$p_{t,meas} = p + \frac{1}{2}\rho\overline{U_t^2} \tag{5.7}$$

where

$$\overline{U_t^2} = u^2 + v^2 + w^2 + \overline{u'^2} + \overline{v'^2} + \overline{w'^2} \tag{5.8}$$

in which $[u, v, w]$ are the time-averaged mean velocity components in the x, y, and z directions while u', v', and w' are the instantaneous velocity fluctuations in these directions. Combination of Eqs. 5.7 and 5.8 yields

$$p_{t,measured} = p + \frac{1}{2}\rho\overline{U_t^2} + \frac{1}{2}\rho\overline{U_t'^2} \tag{5.9}$$

wherein

$$\overline{U_t'^2} = \frac{\overline{u'^2} + \overline{v'^2} + \overline{w'^2}}{3} \tag{5.10}$$

thus leading to

$$p_{t,measured} = p_{t,true} + \frac{1}{2}\rho\overline{U_t'^2} \tag{5.11}$$

which suggests the over-estimation of total pressure is proportional to the square of the velocity fluctuations ($\overline{U_t'^2}$). As the split-film and 7-hole probe data were collected in different tests, it can prove difficult to use information from one test for another, but an attempt at this method is executed herein. Unsteady total-velocity fluctuations measured by the two-component split-film probe were used to correct the 7-hole probe data set as presented in Eq. 5.11, and those results are presented below in Fig. 5.9. As seen in the figure, the minimum velocity decrement is decreased (yielding an increased value of $U_{t,min}$ when compared to the uncorrected data) and less overall momentum loss in the flow. In addition, a small distinction between the main-element and flap 1 wake is visible at $\widetilde{x} > 1.05$.

Wall Effects

Finite-size multi-hole probes are known to distort and/or displace streamlines in the presence of an aerodynamic body. If the probe is too close to the surface of an airfoil, for example, errors are introduced to the measurement due to

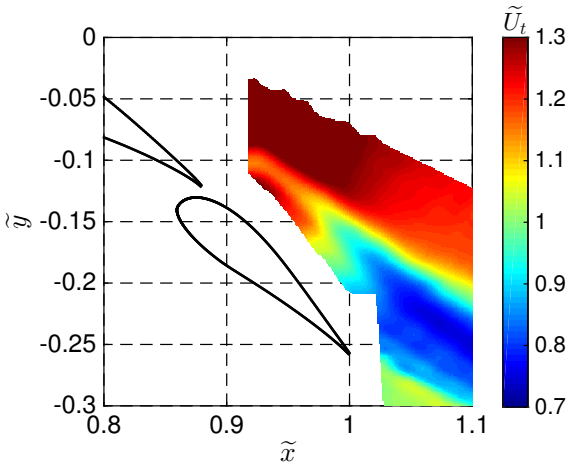

Figure 5.9: Turbulence-corrected 7-hole probe data.

interactions between the probe and surface. For this reason, the probe was moved no closer than two probe outer diameters to the airfoil at any time [145, 149].

Summary of All Effects

A series of wake profiles are presented in Fig. 5.10 for which data were taken at $\widetilde{x} = 1.05$. These wake profiles show the baseline results from both probes in addition to the corrected data using the aforementioned methods. As seen in the figure, minimal effects are observed for the 7-hole probe velocity shear correction, but larger effects are noticed with the turbulence correction. The data corrected for unsteady aerodynamics in Fig. 5.9 indicates an increase in $\widetilde{U}_t$ for a given value of $\widetilde{y}$ when compared to the baseline 7-hole probe data. Despite these increases, significant differences remain when compared to the split-film probe. The effect of sample density and spatial smoothing due to probe head geometry is shown in the figure as a light purple line. As seen in the figure, the magnitude of momentum loss for both the main-element and flap 1 wake is decreased relative to the baseline split-film data. In addition, decreased momentum is observed between these two wakes. Once again, while the correction is observed to yield better agreement with the 7-hole probe data, significant deviations still exist. As mentioned earlier in this section, significant on-going efforts at the University of Illinois are being undertaken by Diebold to quantify the effect of turbulence upon multi-hole pressure probes [148]. Preliminary results from Diebold indicate that the time-averaged multi-hole pressure probes are greatly affected by the local turbulence intensity. While the first-order corrections presented above capture some effects, it would be interesting to determine the effect of turbulence on the 7-hole probe presented in this research.

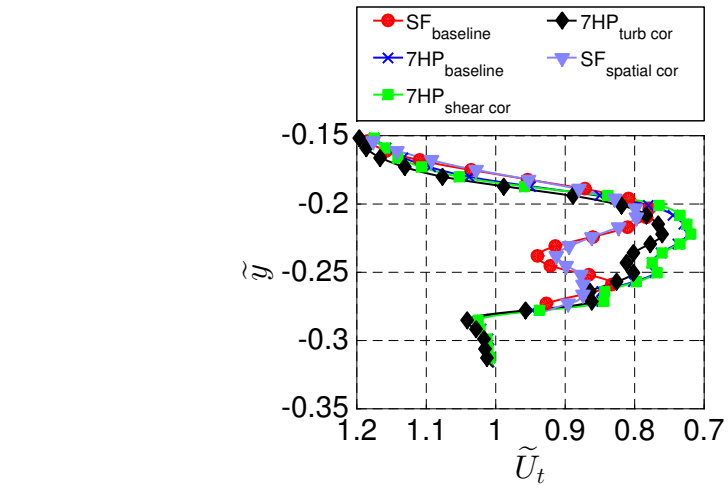

(a)

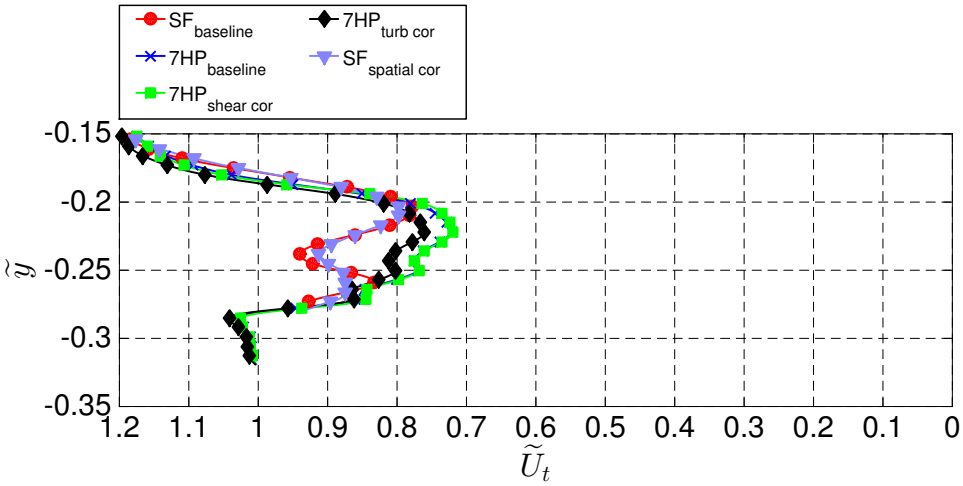

(b)

Figure 5.10: Summary of effects in probe geometry and response to local flowfield shown in a) narrow scale and b) wide scale.

Expanded Domain Results

As presented in Sec. 5.3.1, data with the 7-hole probe were acquired over a very-large sample domain, and results for $\widetilde{U}_t$ are plotted in Fig. 5.11. It is particularly interesting to notice the development of the wake over the large spatial region. A large velocity-deficit region is observed immediately downstream of the trailing edge of flap 2, and the magnitude of the velocity decrement decreases with increasing downstream distance. The expansion and thickening of the wake over this domain is also visible in the figure. While a tighter, more-aggressive shear layer is observed for the upper wake edge close to the airfoil, the gradient $\partial\widetilde{U}_t/\partial\widetilde{y}$ is observed to be be smaller for the upper wake edge at far downstream locations. Very few plots in this dissertation will be presented in which the full domain is presented,

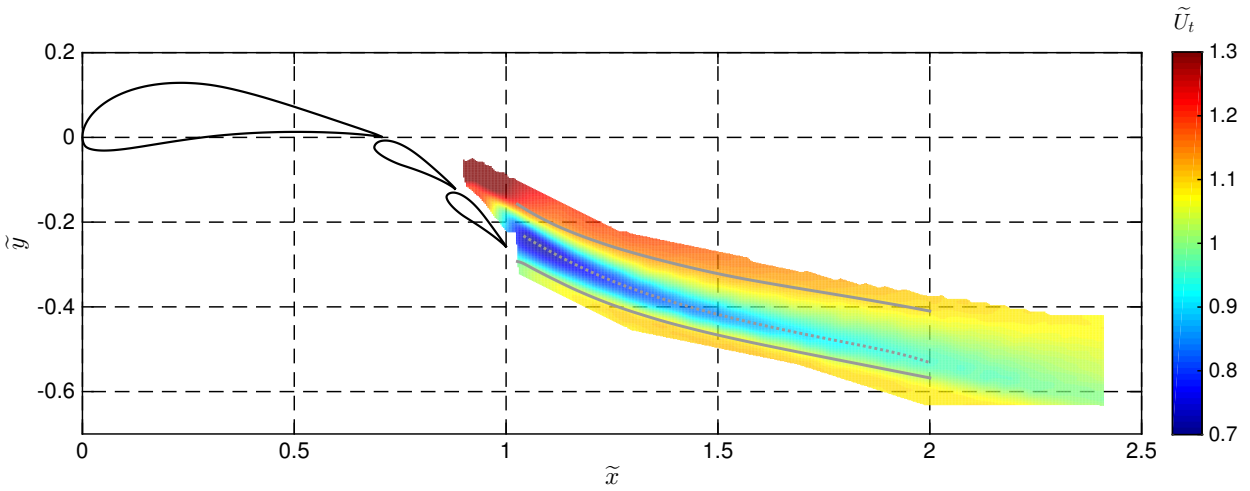

Figure 5.11: Resulting $\widetilde{U}_t$ across full domain captured with 7-hole probe.

but rather information is presented as either a subset of the domain in a region close to the flaps or data are extracted using one of a variety of advanced postprocessing metrics. These advanced metrics will be presented later in this chapter and are used extensively throughout the remainder of this chapter and in Chap. 6.

5.3.3 Wake Cores

Consider the data set, collected by a split-film probe, presented below in Fig. 5.12(c) which are similar to the $\widetilde{U}_t$ contour presented in the previous section which drew comparisons between the split-film and 7-hole probe data. Results plotted in Fig. 5.12(c) indicate the presence of a distinct wake for both the main element and flap 1. While the two wakes interact with each other, it is not suggested that they merge and become one wake but rather behave as two separate wakes within the domain surveyed. Both of these wakes are observed to contain a distinct center region of each wake, and new criterion have been developed to extract the central portion of the wake (referred to as the "wake core"). Representative wake profiles extracted at a constant $\widetilde{x}$ location are presented in Fig. 5.12(a) for an $\widetilde{x}$ location upstream of where they mix, while wake profiles that have merged are shown in Fig. 5.12(b). A methodology was developed to numerically extract the core of each wake based upon maximum and minimum values of the chord-normal velocity gradient ($\partial\widetilde{U}_t/\partial\widetilde{y}$) shown in Fig. 5.12(d). At a constant value of $\widetilde{x}$, the chord-normal velocity gradient was calculated, and the local maximum and minimum values defined the upper and lower edges of the wake core respectively. A contour map of $\partial\widetilde{U}_t/\partial\widetilde{y}$ is shown in Fig. 5.12(d) in which the determined wake core edges are co-plotted as solid gray lines. The wake core edges follow the low momentum region in the flowfield, and this observation suggests that the parameters chosen to define the wake core based upon $\partial\widetilde{U}_t/\partial\widetilde{y}$ also define the edge of the wake core adequately with respect to $\widetilde{U}_t$. Additional parameters which are closely related to the wake cores will be highlighted in Sec. 5.4.

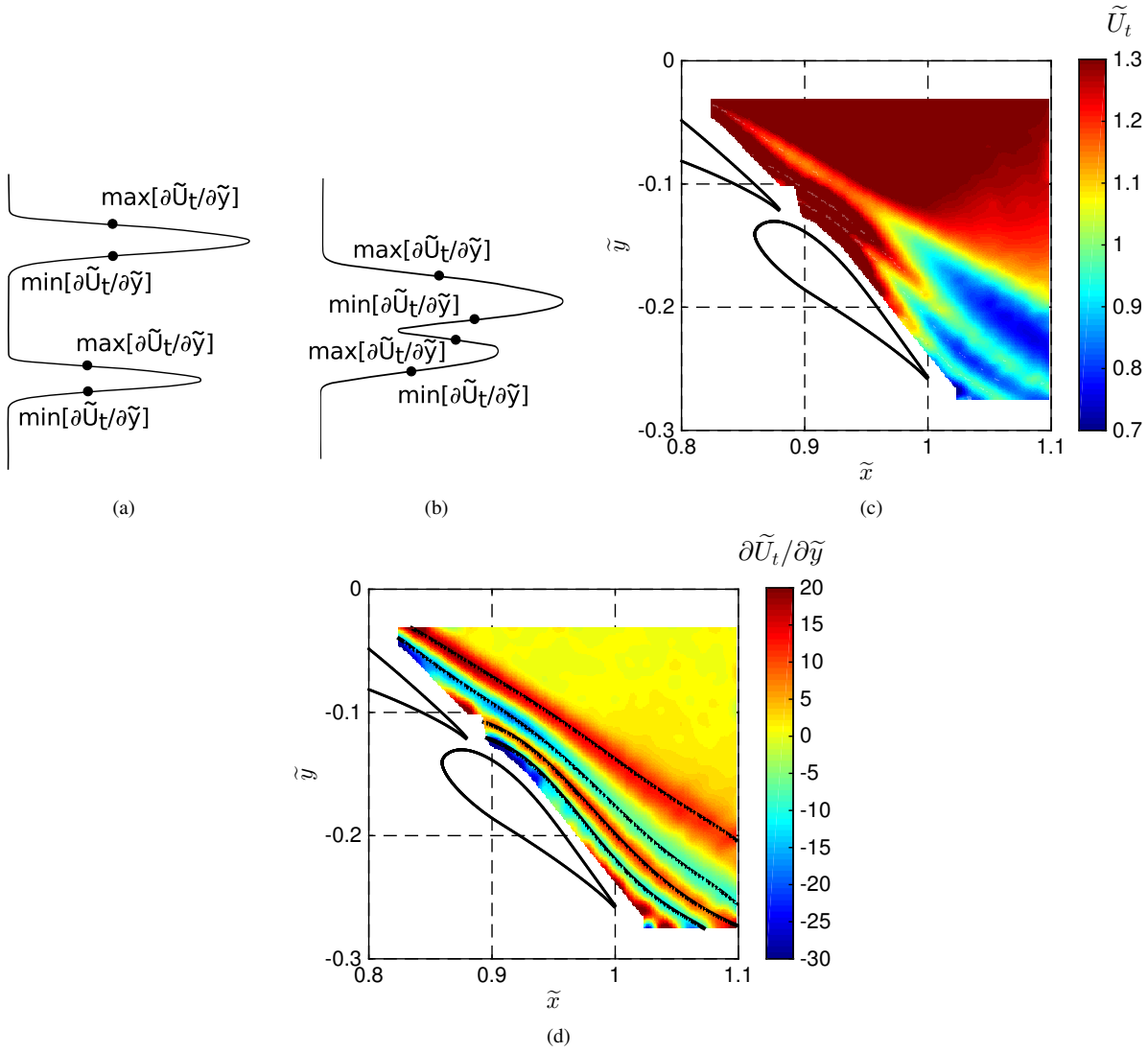

Figure 5.12: Parameters used for determination of wake core edges including a) non-confluent velocity profile sketch, b) confluent velocity profile sketch, c) $\widetilde{U}_t$, and d) time-averaged chord-normal velocity gradient ($\partial\widetilde{U}_t/\partial\widetilde{y}$).

5.3.4 Streamlines

The effect of wake bursting on the direction of the flow was studied, and the resulting streamlines based on u and v are co-plotted with $\widetilde{U}_t$ in Fig. 5.13. As is commonly known, streamlines are a family of curves that are tangent to the time-averaged velocity vector, and the mass flow rate between two streamlines is constant. Thus, an increase in distance between two streamlines corresponds to a slower flow velocity thus maintinaing a constant mass flow rate. Alternatively, closer streamlines indicate the flow is moving faster in this specific location. As shown in Fig. 5.13, the distance between the streamlines in the wake core increases at downstream locations as evidenced by the expanding streamlines. This observation indicates a local flow deceleration in the wake core region. Most significantly, though, is

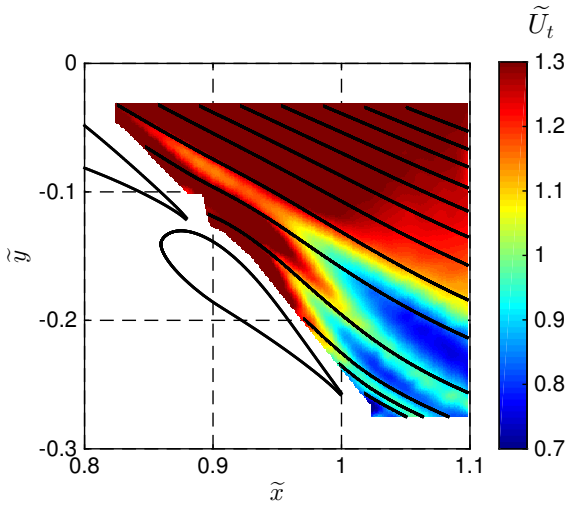

Figure 5.13: Streamlines coplotted with $\widetilde{U}_t$.

that the figure indicates that the streamlines do not follow the edge of the two wake cores, and this observation indicates that the burst wake region cannot be accurately predicted based upon the location of streamlines as is commonly done with coupled inviscid/viscous aerodynamic solvers.

5.3.5 Static and Total Pressure

Data collected through use of the 7-hole probe will be of considerable interest for the remainder of this section, and split-film probe data will not be further discussed until Sec. 5.4 on page 124. In addition to yielding velocity components, data collected from the 7-hole probe include static and total pressure coefficients, as defined in Eqs. 5.1–5.2. Wake surveys at $\alpha = 0$ deg and $Re = 1 \times 10^6$ for these two parameters are presented in Fig. 5.14. Consider the static pressure results shown in Fig. 5.14(a) in which a strong streamwise pressure gradient $\partial C_p/\partial \widetilde{x}$ is observed. It is this pressure gradient which causes the wake to burst; this behavior is analogous to boundary layer separation from a surface. The chord-normal pressure gradient $\partial C_p/\partial \widetilde{y}$ is also visible in Fig. 5.14(a) which causes curvature in the flowfield as the flowfield returns to the freestream condition ($u = U_\infty$, $v = w = 0$) far downstream. It is also known that this chord-normal pressure gradient results in asymmetric wake development. In addition, data suggest that $\partial C_p/\partial \widetilde{y} \neq 0$ in the burst wake region, which indicates that the boundary-layer equations cannot necessarily be applied to predict the behavior of the burst wakes. If the wakes were thinner and not burst, it is possible that this assumption ($\partial C_p/\partial \widetilde{y} = 0$) may be able to be applied with reasonable accuracy for a wake, but this assumption is certainly not valid for large, thick, burst wakes. If a streamline-fixed coordinate system is considered, the pressure gradient $\partial C_p/\partial \widetilde{y}$, in which $\widetilde{y}$ is in the "streamwise" direction, is less than the gradient observed in the Cartesian coordinate system, but the gradient is still nonzero across the burst wake.

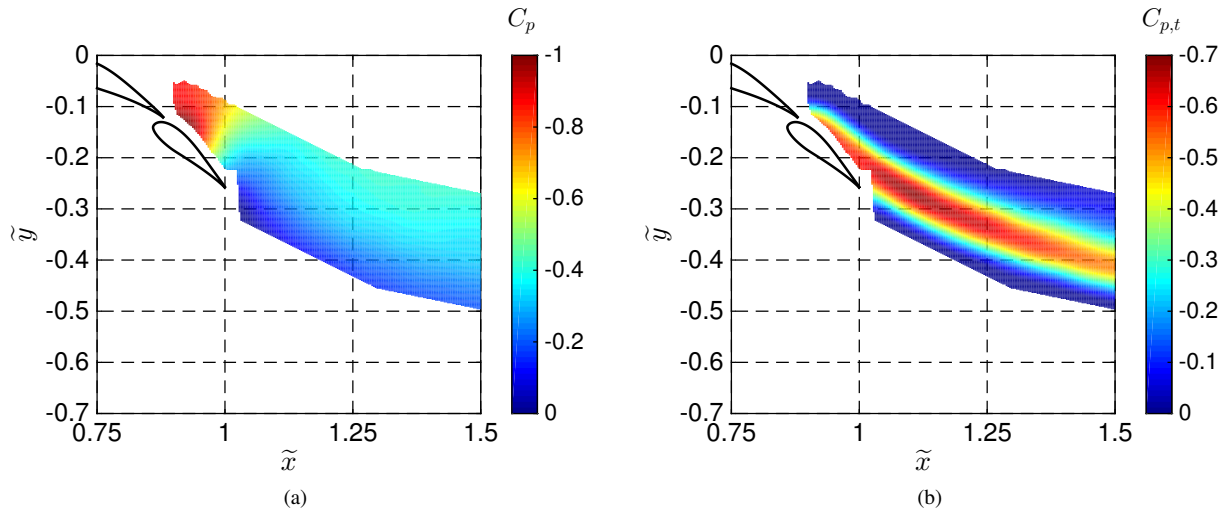

Figure 5.14: Pressure results for Configuration 10 at $\alpha = 0$ deg and $Re = 1 \times 10^6$ including a) C_p and b) $C_{p,t}$.

5.3.6 Wake Thickness and Growth Rate

In many cases, boundary layer and wake development is characterized by one of numerous metrics which quantify the thickness of the boundary layer or wake. Typically, the edge of a boundary layer is declared to be the point at which $U = 0.99U_e$, where U_e is the external velocity, and is taken to be U_∞ for a flat plate boundary-layer flow. Sometimes, in flowfields involving airfoils or wings, U_e is defined as the velocity at a given point for the inviscid solution. However, it is difficult, if not impossible, to quantify the value of U_e for the highly-curved off-body flowfield in discussion. Thus, it is proposed to use the $C_{p,t}$ parameter to define the edge of the wake. As defined in Eq. 5.2, $C_{p,t}$ is a nondimensional measure of the difference between the local total pressure and the freestream total pressure in which values of $C_{p,t} < 0$ indicate the local flowfield has less total head than that of the freestream condition. Points in the wake were numerically determined in which the local $C_{p,t}$ was less than a threshold value, selected to be -0.10 in this research. Thus, at a constant $\widetilde{x}$ location, a range of $\widetilde{y}$ values exist for which

$$C_{p,t} \leq -0.10. \tag{5.12}$$

A range of $\widetilde{y}$ for a given $\widetilde{x}$ satisfy Eq. 5.12, and the maximum value of this range is denoted as $\widetilde{y}_u$ (for the upper wake edge) while the minimum value is defined as $\widetilde{y}_l$ (for the lower wake edge). The definition of these two $\widetilde{y}$ points leads to a new figure of merit h_w is defined as the distance between the minimum and maximum values in $\widetilde{y}$ at a given $\widetilde{x}$ for which Eq. 5.12 is satisfied, or

$$h_w = \widetilde{y}_u - \widetilde{y}_l. \tag{5.13}$$

Calculations of the figure of merit h_w can be performed with any threshold value of $C_{p,t}$, but -0.10 was selected for results in this research project. Ideally, the wake edges could be defined by the outer-most points for which $C_{p,t} < 0$. However, as seen in Fig. 5.14(b), not all of these points were captured in the wake survey, especially at large values of $\widetilde{x}$; experimental uncertainty and noise also makes it difficult to define the point at which $C_{p,t} = 0$. Thus, to provide a clear comparison between different geometric configurations, the figure of merit in Eqs. 5.12–5.13 was selected. Baseline results for h_w at $\alpha = 0$ deg and $Re = 1 \times 10^6$ are plotted in Fig. 5.15(a), and the computed edges for which $C_{p,t} < -0.10$ are coplotted with $C_{p,t}$ and $\widetilde{U}_t$ in Fig. 5.15(b,c). As seen in Fig. 5.15(a), h_w generally increases with downstream distance, which is the expected trend. The wake is observed to thicken with increasing $\widetilde{x}$ due to both the streamwise adverse pressure gradient and the increase in downstream distance. Results indicate that h_w increases by nearly 30% from $\widetilde{x} \approx 1.0$ to $\widetilde{x} \approx 2.0$. It is noted that a small decrease in h_w is observed immediately downstream of the trailing edge of flap 2 at $\widetilde{x} \leq 1.1$. In this region, large pressure gradients, both in the x and y directions, are observed, as shown in Fig. 5.14(a). It must be stated that the calculated wake edges are not the same as streamlines for the flowfield. If the wake edges were streamlines, a reduction in the distance between two streamlines would indicate an accelerating flowfield. However, this is not the case with the wake edges as they are not defined by streamlines (as shown earlier in Fig. 5.13).

5.3.7 Wake Development and Asymmetry

As briefly discussed earlier in this section, the burst wakes were observed to be asymmetric, and therefore data were further postprocessed in an effort to further quantify the asymmetric wake development. Consider again the $C_{p,t}$ plot, depicting data collected using the 7-hole probe, presented in Fig. 5.15(b). As evidenced in the picture, a momentum deficit exists between the two wake edges, and there is a specific value of $\widetilde{y}$ for a given $\widetilde{x}$ at which $\widetilde{U}_t$ is minimized; this point is defined as $\widetilde{y}_{peak}$. Numerical methods were used to extract the values of $\widetilde{y}_{peak}$ across a wide range of $\widetilde{x}$, and the set of these $(\widetilde{x}, \widetilde{y}_{peak})$ points are referred to collectively as the wake centerline. Figure 5.16(a) presents a plot in which the wake edges and wake centerline are coplotted in a standard Cartesian $\widetilde{x}$-$\widetilde{y}$ figure. As shown in the legend, the wake edges are plotted as solid black lines and the wake centerline is plotted as a teal line. Results in this figure indicate that the wake centerline is closer to $\widetilde{y}_l$ than $\widetilde{y}_u$, and that the centerline moves closer to $\widetilde{y}_l$ with increasing downstream distance.

Results in Fig. 5.16(b) present the wake centerline as a normalized value of the wake thickness. Values are normalized by the parameter $\frac{\widetilde{y}_{peak} - \widetilde{y}_l}{h_w}$ in which a value of 0 corresponds to $\widetilde{y}_l$ and a value of 1 is associated with $\widetilde{y}_u$. As plotted in the figure, the wake centerline is closer to the midpoint of the wake at small values of $\widetilde{x}$, but the centerline moves closer to $\widetilde{y}_l$ further downstream. As previously mentioned, the asymmetry in the flowfield is caused by the curvature of the flowfield. As lift is a result of the flowfield curvature, it is surmised that different flowfield conditions

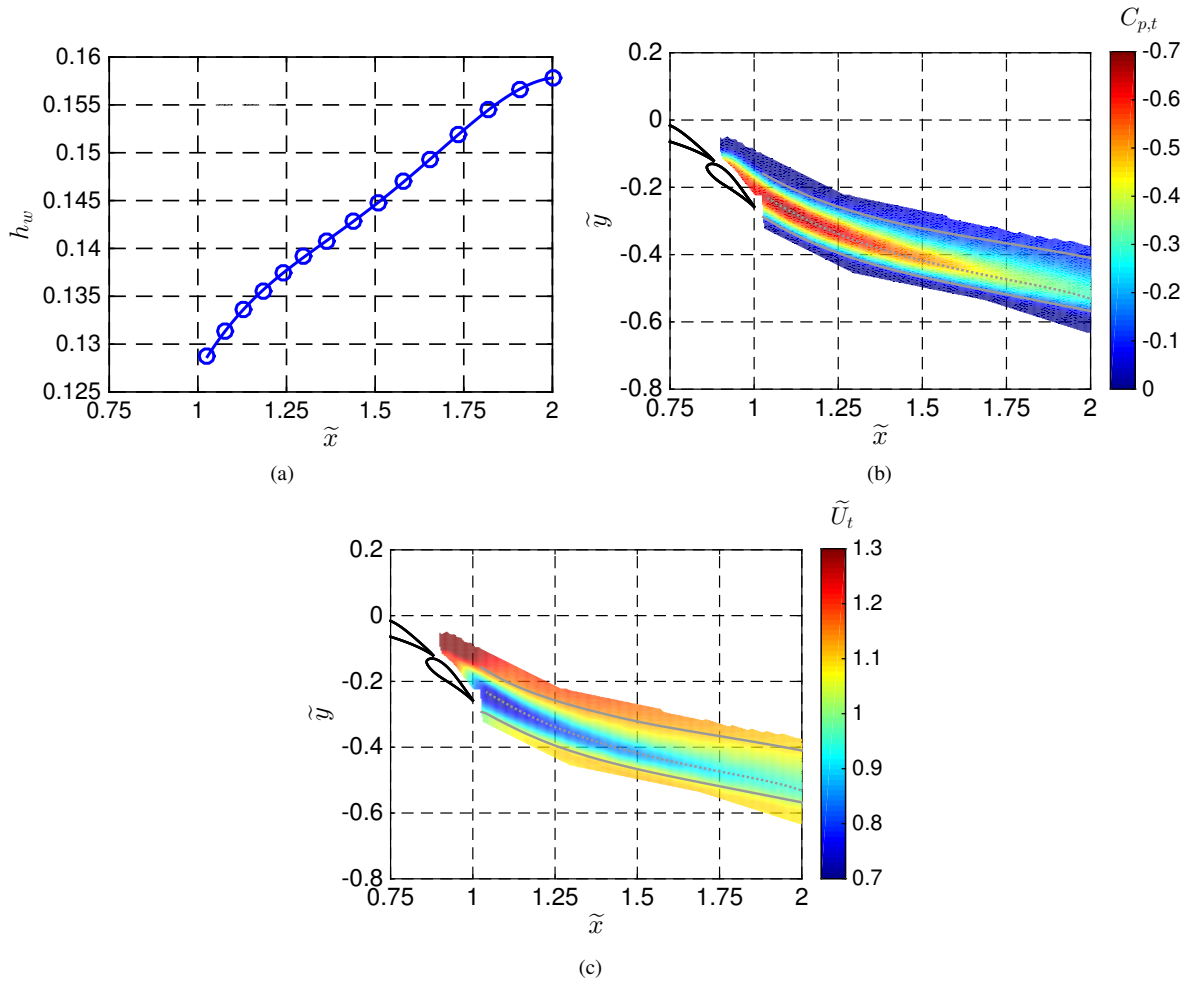

Figure 5.15: Wake edge results for Configuration 10 at $\alpha = 0$ deg and $Re = 1 \times 10^6$ including a) wake thickness (h_w), b) $C_{p,t}$ coplotted with wake edges and c) $\widetilde{U}_t$ coplotted with wake edges.

(yielding different values of C_l) would affect the asymmetry in differing manners. In addition, differing streamwise pressure gradients would also affect the asymmetric wake development. These topics will be further explored in Sec. 5.3.8.

5.3.8 Effect of Angle of Attack

Because flowfields at a higher α experience stronger adverse pressure gradients in the pressure-recovery region, it was expected that the burst wakes at two different α values would exhibit different behavior. For the configuration in discussion in this chapter, data were acquired at α ranging from -4 through $+1$ deg at a freestream Reynolds number of 1×10^6 utilizing the 7-hole probe. Wake surveys were collected in the x-y plane for these conditions, and h_w was calculated for each of these cases using the methods presented above. Wake thickness as a function of α is presented

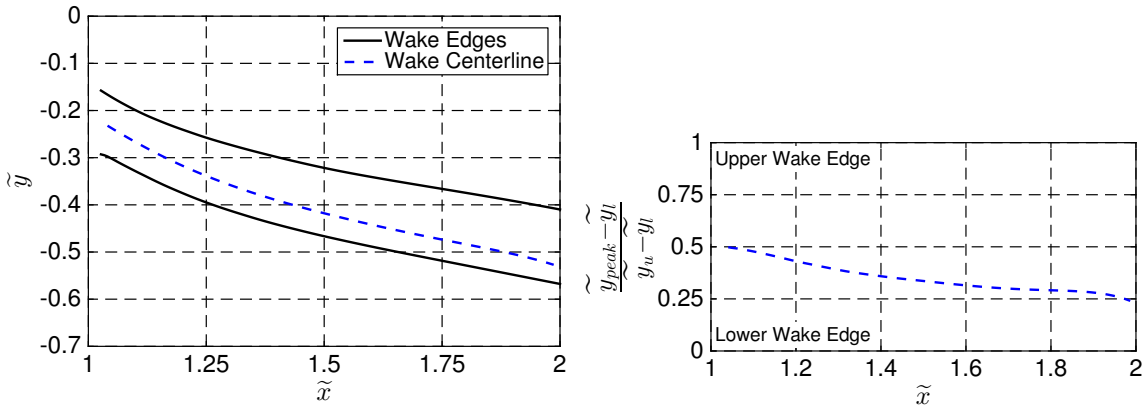

Figure 5.16: Wake centerline positions as evidenced by a) wake edges with centerline in dimensional coordinates and b) normalized wake centerline location.

in Fig. 5.17 in which h_w is presented for a range of α. Unfortunately, the wake survey for $\alpha = +1$ deg was not performed in the proper location at values of $\widetilde{x} > 1.40$ and the upper wake edge was located outside of the sampled domain, but this observation was not known until after the completion of the wind tunnel entry. Consequently, h_w is only tabulated at positions upstream of $\widetilde{x} = 1.40$. The wake thickness for the various α appear quite different in some cases. For cases of $\alpha > -1$ deg, the wake thickness, as defined in Eqs. 5.12–5.13, increases with downstream distance. The rate of increase in h_w is observed to increase with increasing α as well, as is expected. Due to the definition of h_w, an increasing value of h_w indicates there is a larger spatial region for which $C_{p,t} < -0.10$, which is expected with increased values of α. Cases for decreased α indicate that h_w is decreasing with downstream distance, which is to say the central region of the wake in which $C_{p,t} < -0.10$ is decreasing. The reader is reminded that although h_w is decreasing, this does not suggest that the wake thickness as a whole is decreasing. This observation

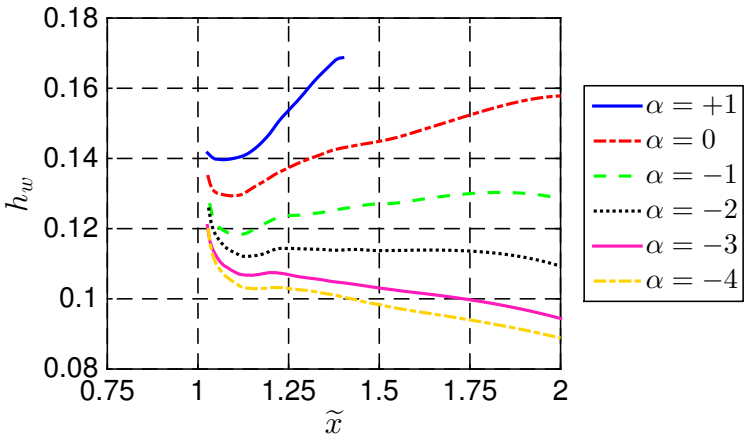

Figure 5.17: Effect of α on h_w at $Re = 1 \times 10^6$.

simply indicates that the momentum deficit in the central portion of the wake is smaller than at larger α, thus yielding smaller and progressively decreasing values of h_w with increasing downstream distance. The characteristic decrease in h_w immediately downstream of the system trailing edge is present in all cases.

The relationship between the wake edges and the flowfield as a whole is presented in Fig. 5.18 in which $\widetilde{U}_t$ is coplotted with the wake edges for a range of α. All of the data sets in the figure are plotted on the same scale, so easy comparisons between the different runs can be readily made. The plots clearly convey the large, thick wakes of the larger α runs when compared to the smaller, thinner wakes of decreased α; this trend is especially noticeable when the wake edges are compared between different cases. Curiously, the momentum deficit region in which $1.05 \leq \widetilde{x} \leq 1.25$ has similar values of $\widetilde{U}_{t,min}$ for the different cases, yet the area for which the decreased momentum is present is larger for cases at larger α; this is visualized by noticing the increased size of the blue contour region in the six plots in Fig. 5.18. Wake centerlines, depicted as dotted gray lines, are coplotted in the figure to present the asymmetric nature of the burst wakes. Numerous similarities are observed between the different cases as the wake centerline is observed to be closer to the lower wake edge for all of the cases, especially at further downstream locations. As previously mentioned, results in Fig. 5.17 indicate a decrease in h_w immediately downstream of the system trailing edge ($\widetilde{x} < 1.1$). Upon careful examination of the wake edges in Fig. 5.18, this region of the flowfield is visible. In this region, the curvature of the upper surface of the airfoil system has caused the upper wake edge to be oriented more in the $-\widetilde{y}$ direction than that of the lower wake edge. A short distance downstream from the trailing edge, though, the two wake edges diverge and the wake is observed to thicken.

Nondimensional static and total pressure coefficient data are plotted for an α of -4, -2, and 0 deg in Fig. 5.19 in which the wake edges are not presented. As evidenced in the figure, the static pressure gradient for the increased α cases is larger in the wake region ($\widetilde{x} > 1.25$) than for the cases of decreased α. Because larger α yields increased flow curvature and higher values of C_l, larger magnitudes of C_p are required to return the flowfield vector to the freestream conditions at α of 0 deg than at α of -4 deg. Differences in C_p values between the α of -4 deg and 0 deg range between 0 and 0.2 at different portions of the flowfield. As previously mentioned, it is this pressure gradient which contributes to the asymmetric wake development. Total head losses, plotted as $C_{p,t}$ are also shown in Fig. 5.19 for the same α conditions, and the results indicate that larger total-pressure losses are experienced at higher α than at decreased α, as expected. The increase in magnitude of $C_{p,t}$ with respect to α also yields an increase in C_d due to increased momentum deficit. In addition to an increase in magnitude of $C_{p,t}$ at higher α than at lower α, the main region of momentum deficit extends further downstream. This large region of decreased flow velocity causes a decambering of the airfoil system, thus yielding less lift than if wake bursting was not present. Decreased values of $C_{p,t}$ at lower freestream α yield smaller, thinner wakes as quantified by h_w and presented in Fig. 5.17.

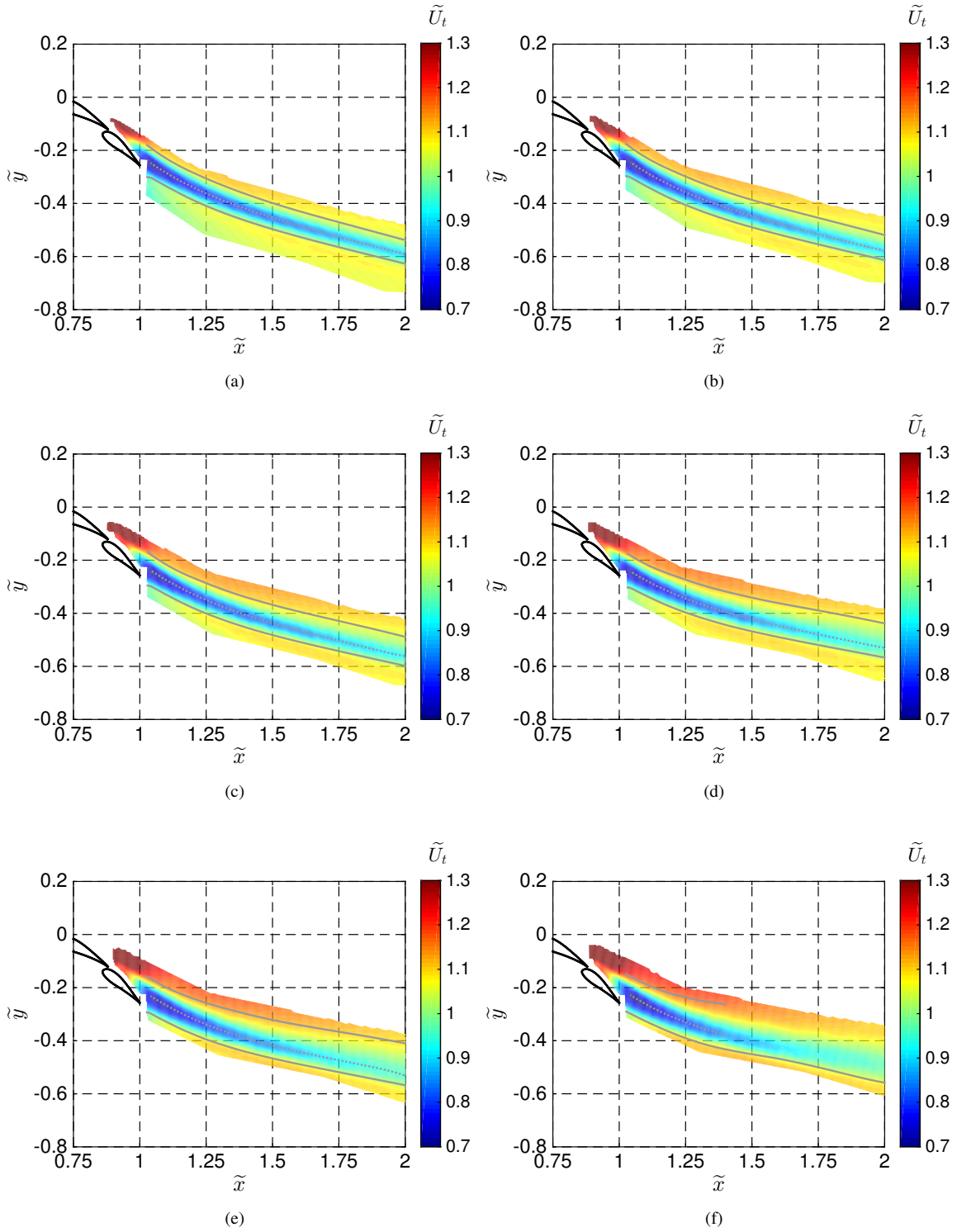

Figure 5.18: Contour plots of $\widetilde{U}_t$ for range of α including a) -4 deg, b) -3 deg, c) -2 deg, d) -1 deg, e) 0 deg, and f) 1 deg.

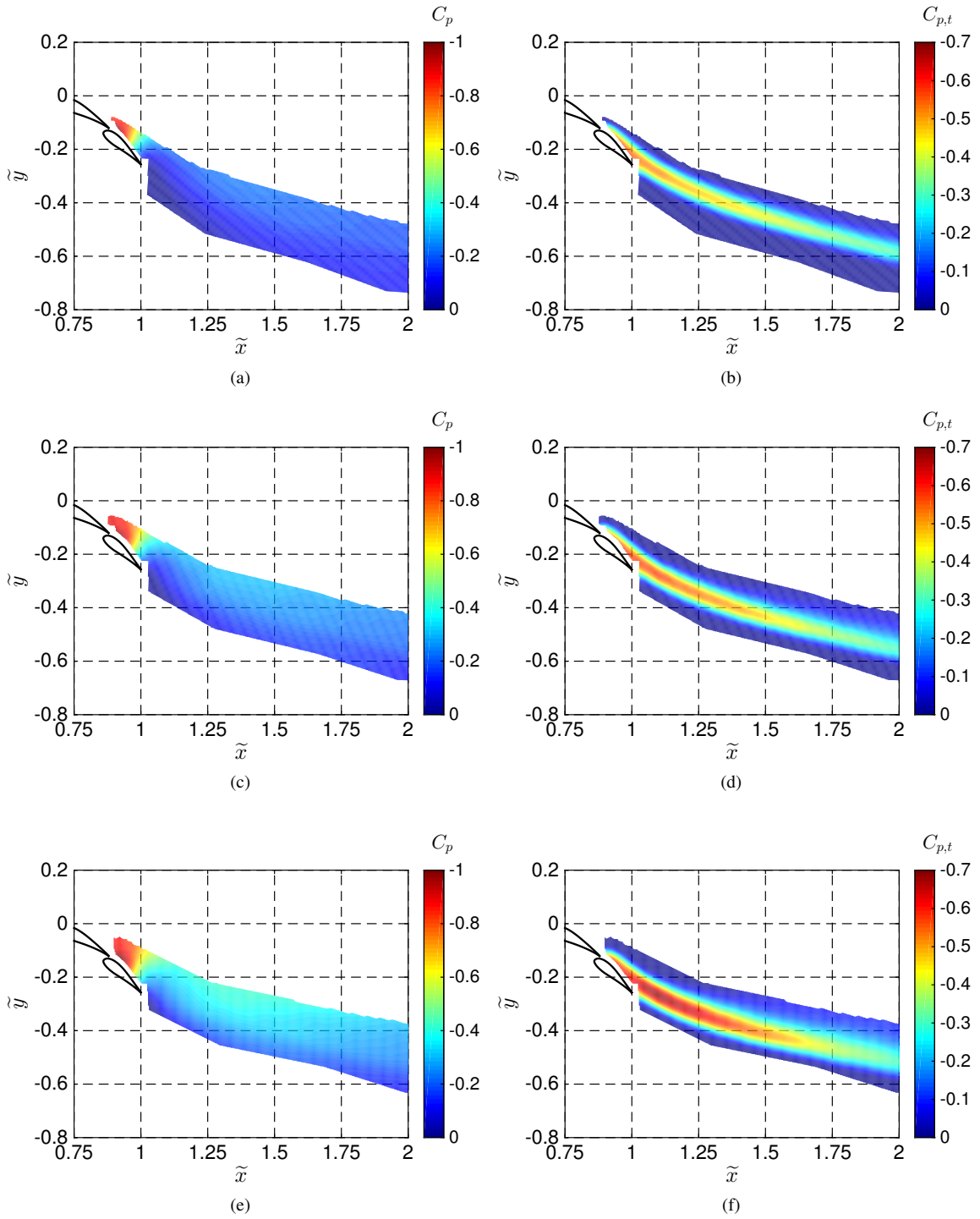

Figure 5.19: Effect of α on C_p and $C_{p,t}$ for range of α including a) -4 deg C_p, b) -4 deg $C_{p,t}$, c) -2 deg C_p, d) -2 deg $C_{p,t}$, e) 0 deg C_p, and f) 0 deg $C_{p,t}$.

5.3.9 Effect of Freestream Reynolds Number

As wake development is an inherently viscous phenomenon, there will be a Reynolds number effect upon the flowfield. Experimental data were collected with the 7-hole probe at freestream Reynolds numbers of 0.6×10^6, 0.8×10^6, and 1×10^6, and results including both the h_w relationship and wake surveys are plotted in Fig. 5.20. As depicted in Fig. 5.20, h_w is observed to increase with downstream distance for freestream Reynolds numbers of 800×10^3 and 1×10^6. The growth rate of h_w at 800×10^3, as depicted by the red dashed line, is less than that of the baseline 1×10^6 case. In addition to a reduced growth rate, cases at a lower *Re* are observed to have a decreased value of $h_{w,max}$, as seen in the figure. It is curious to carefully examine the results associated with $Re = 600 \times 10^3$. As plotted in the figure, the wake thickness, as quantified by h_w, is not observed to increase at $\widetilde{x} > 1.20$, but rather h_w is observed to be nearly constant in these locations. As discussed in Sec. 5.3.8, it is observed that decreased values of $C_{p,t}$ in the wake will yield lower values of h_w as the total area of the momentum deficit region will be decreased. It is because of this relationship that h_w is nearly-constant for larger values of $\widetilde{x}$.

Contour plots of $\widetilde{U}_t$ presented in Fig. 5.20(b-d) provide further insight into the flowfield at each of the three freestream conditions. When comparing the normalized velocity $\widetilde{U}_t$, it is observed that the momentum deficit region at $Re = 600 \times 10^3$ extends downstream for the furthest distance of the three cases, and that the $Re = 1 \times 10^6$ case has less total velocity decrement at further downstream locations. This observation is visible by noting the extent of the dark blue region in the central portion of the wake. Consequently, even though h_w is suggested to be the largest for the highest freestream Reynolds numbers, the momentum deficit as evidenced by $\widetilde{U}_t$ suggests increased wake bursting at lower Reynolds numbers. Thus it is observed that one must consider numerous figures of merit when evaluating the presence of burst wakes and cannot solely rely on one metric. Asymmetric wake development is observed to be similar for all three cases with the wake centerline located closer to the lower wake edge than the upper wake edge.

5.4 Experimental Unsteady Results

The nature of unsteady velocity components is of great interest with regard to wake bursting, and these fluctuations will be extensively discussed in this section. All data presented in this section were experimentally collected using the split-film probe, and information in this section will be dedicated to the presentation and discussion of these experimental results. A thorough discussion regarding the theory and operation of the split-film probe is presented in Sec. 4.1 on page 71. While turbulence can be characterized by numerous different parameters, the current study investigates the burst wake flowfield using Reynolds stresses, turbulence kinetic energy, and production of turbulence kinetic energy.

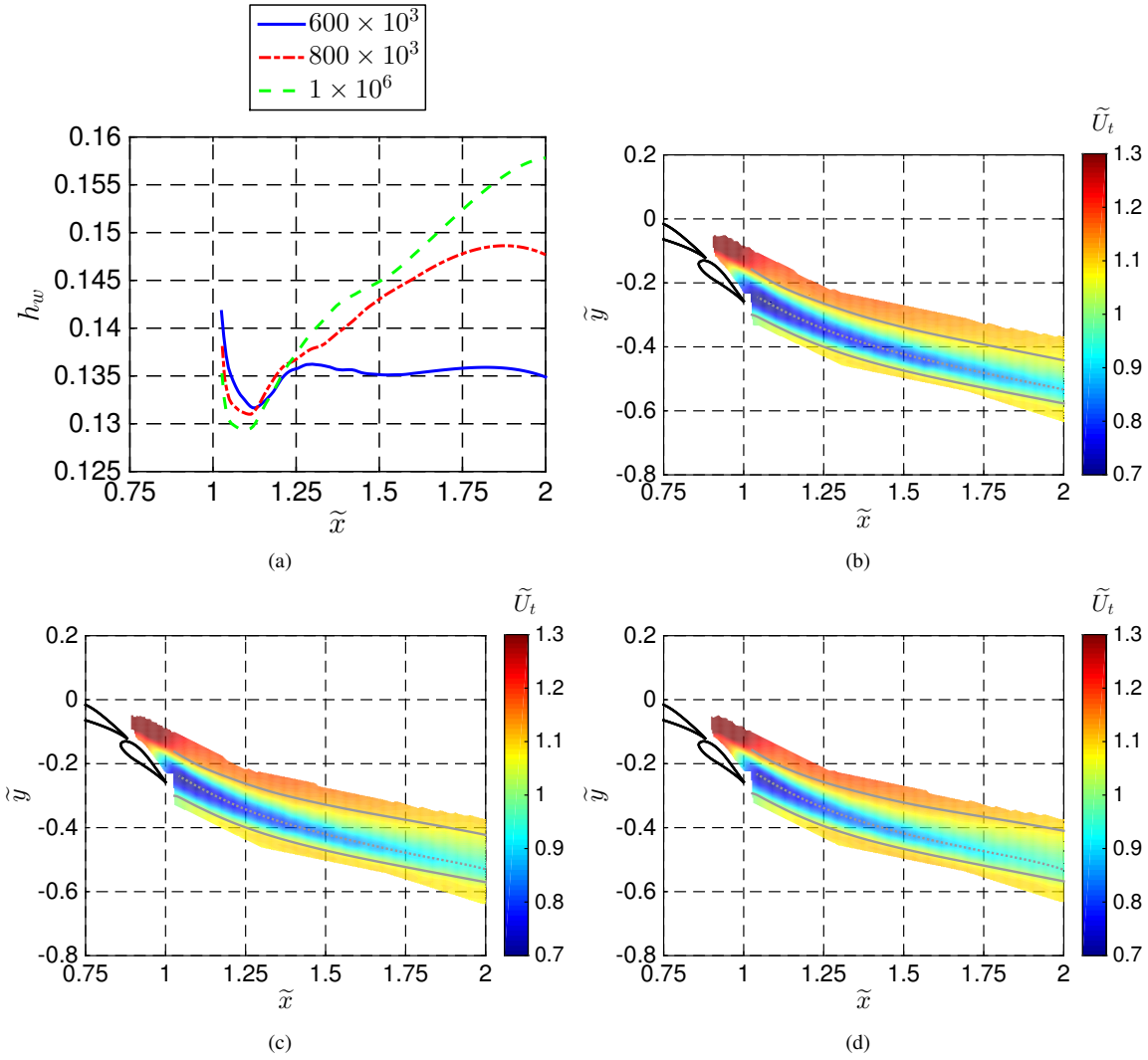

Figure 5.20: Effect of freestream *Re* on burst wakes quantified by a) h_w, and contours of $\widetilde{U}_t$ at b) 600×10^3, c) 800×10^3, and d) 1×10^6.

5.4.1 Governing Equations

Examination of a turbulent flow, such as the flowfield in discussion throughout this dissertation, indicates that the velocity and the pressure at a specific point in space are not constant with respect to time. In these unsteady flows, it is known that small fluid particles referred to as eddies, transport fluctuations in both the streamwise and transverse directions. The true flow is composed of a mean flowfield which is superimposed with a flowfield containing these unsteady eddies. Eddies are generated at specific locations in the flowfield, and the physical size of these eddies is dependent upon numerous factors in the flowfield. As discussed later, these eddies can be characterized by the

frequency content of the unsteady fluctuations in which large eddies pertain to low frequencies and small eddies correspond to high frequencies.

It is common to represent a given flowfield in terms of a steady and fluctuating component using a technique known as Reynolds averaging. The significance of the unsteady components of a flow, in particular the velocity components, is apparent through application of Reynolds averaging to the governing equations. When a flow is Reynolds-averaged, each dependent variable in the governing equations is decomposed into a time-averaged component and a fluctuation [64, 150, 151]. It is important to state that the mean component of the flowfield can be a steady turbulent flow; in this case, the word "steady" refers to the constant nature of the global flowfield and aerodynamic body with respect to time and not necessarily of the individual fluid particles. A derivation of the unsteady equations of motion for a two-dimensional flow are presented in this subsection. Throughout these derivations, the actual flowfield using the notation u, the time-averaged component as $\overline{u}$, and the unsteady fluctuation as u', are defined by

$$u = \overline{u} + u' \tag{5.14a}$$

$$v = \overline{v} + v' \tag{5.14b}$$

$$p = \overline{p} + p' \tag{5.14c}$$

in which

$$\overline{u'} = 0 \tag{5.15a}$$

$$\overline{v'} = 0 \tag{5.15b}$$

$$\overline{p'} = 0. \tag{5.15c}$$

Assuming incompressible flow, it is therefore known that

$$\rho' = 0 \tag{5.16a}$$

$$T' = 0. \tag{5.16b}$$

While Reynolds averaging considers both the mean and unsteady components of the flowfield in the equation derivation, the true flowfield cannot truly be decomposed in this manner. That is to say that the mean flow components affect the unsteady fluctuations, and the unsteady fluctuations affect the mean fluid motion. The relationship between the mean and unsteady flowfields is demonstrated with the following example. Consider the term uv which is composed of two velocity components which both have steady and fluctuating components. Using the rules of time

averaging, it is shown that

$$\begin{aligned} uv &= (\overline{u}+u')(\overline{v}+v') \\ &= \overline{uv}+\overline{u}v'+u'\overline{v}+u'v' \\ &= \overline{uv}+\overline{u'v'} \end{aligned} \tag{5.17}$$

which clearly indicates that both the mean and fluctuating portions of the flowfield influence each other.

Consider the continuity equation presented in Einstein summation convention as

$$\frac{\partial u_i}{\partial x_i} = 0 \tag{5.18}$$

which can then be decomposed into a set of mean and fluctuating values. By the definition of time-averaging, it is known that

$$\overline{\partial u_i'/\partial x_i'} \tag{5.19}$$

ultimately yields

$$\frac{\partial \overline{u_i}}{\partial x_i} = 0 \tag{5.20a}$$

$$\frac{\partial u_i'}{\partial x_i} = 0. \tag{5.20b}$$

The momentum equations for an incompressible Newtonian fluid with no external body force are

$$\frac{\partial u_i}{\partial t} + u_j\frac{\partial u_i}{\partial x_j} = -\frac{1}{\rho}\frac{\partial p}{\partial x_i} + \nu\frac{\partial^2 u_i}{\partial x_j \partial x_j} \tag{5.21}$$

where the velocity tensor is denoted by u, x represents the spatial tensor, and the kinematic viscosity of the fluid is denoted by ν. Each term in the momentum equation can be split into a mean flow value and a fluctuating component. The resulting equation can then be time-averaged and is shown to be

$$\frac{\partial \overline{u_i}}{\partial t} + \overline{u_j}\frac{\partial \overline{u_i}}{\partial x_j} + \overline{u_j'\frac{\partial u_i'}{\partial x_j}} = -\frac{1}{\rho}\frac{\partial \overline{p}}{\partial x_i} + \nu\frac{\partial^2 \overline{u_i}}{\partial x_j \partial x_j}. \tag{5.22}$$

Equation 5.22 can be combined with Eq. 5.20 to yield

$$\frac{\partial \overline{u_i}}{\partial t} + \overline{u_j}\frac{\partial \overline{u_i}}{\partial x_j} = -\frac{1}{\rho}\frac{\partial \overline{p}}{\partial x_i} + \nu\frac{\partial^2 \overline{u_i}}{\partial x_j \partial x_j} - \frac{\partial \overline{u_i' u_j'}}{\partial x_j} \tag{5.23}$$

which is then rearranged to be expressed in the more-common form

$$\rho\frac{\partial \overline{u_i}}{\partial t} + \rho\overline{u_j}\frac{\partial \overline{u_i}}{\partial x_j} = \frac{\partial}{\partial x_j}\left[-\overline{p}\delta_{ij} + \mu\left(\frac{\partial \overline{u_i}}{\partial x_j} + \frac{\partial \overline{u_j}}{\partial x_i}\right) - \rho\overline{u_i' u_j'}\right] \tag{5.24}$$

in which μ is the dynamic viscosity and ρ is the fluid density. Finally, as time-averaging removes all time dependence of the resulting terms, the temporal component is eliminated, thus giving

$$\rho\overline{u_j}\frac{\partial \overline{u_i}}{\partial x_j} = \frac{\partial}{\partial x_j}\left[-\overline{p}\delta_{ij} + \mu\left(\frac{\partial \overline{u_i}}{\partial x_j} + \frac{\partial \overline{u_j}}{\partial x_i}\right) - \rho\overline{u_i' u_j'}\right]. \tag{5.25}$$

The introduction of the $\overline{u_i' u_j'}$ term is a result of the time averaging the incompressible turbulent mean flow, and these terms are known as the turbulent apparent stresses. Contributions of the turbulent inertia tensor to Eq. 5.25 are not negligible in a turbulent flow and thus cannot be ignored. The magnitudes and components of the turbulent stresses are influenced by fluid properties, local flowfield velocity, geometry, surface roughness, and upstream history of the flowfield; no comprehensive physical laws have yet been developed to analytically resolve the turbulent stresses. The apparent turbulent stress terms are independent variables in the Navier-Stokes equations, and thus the values must either be directly computed or modeled. These stresses are not present in the time-averaged Navier-Stokes equations, and thus are supplementary to the usual viscous stresses of a flow (that is, a flow without turbulent fluctuations). In viscous-dominated regions, the magnitude of the viscous stresses is significantly greater than the turbulent stresses, while the turbulent stresses dominate the viscous stresses in regions with minimal viscous effects.

5.4.2 Reynolds Stresses

Time-dependent measurements were taken with a split-film probe, and the velocity fluctuations in the chordwise direction u' and the chord-normal direction v' were used to determine various turbulence quantities. As discussed in Sec. 5.4.1 and shown in Eq. 5.25, the Reynolds stress quantities in the turbulent conservation of momentum equation are of considerable interest in turbulent flows. A contour map of the $\overline{-u'v'}$ component of the Reynolds stress tensor is presented in Fig. 5.21(a). In addition to the Reynolds stresses, the wake cores have also been presented (see Sec. 5.3.5 on page 116 for further details). As data were collected with a two-component hot wire, only one component of the Reynolds stress tensor was collected. Before the results in the figure are discussed, it is important to state that the anisotropic Reynolds shear stress tensor presented in Fig. 5.21(a) were calculated in a time-averaged streamline-fixed

coordinate system which is aligned with the time-averaged local flow such that $\widetilde{u_r}$ was in the time-averaged direction of local flow (tangent to the streamline) and $\widetilde{v_r}$ was defined orthogonal to the direction of local flow. As discussed in Sec. 4.1, the instantaneous local flowfield angle λ was defined to be

$$\lambda = \arctan\frac{v}{u}, \tag{5.26}$$

and thus the time-averaged local flowfield angle is denoted as $\overline{\lambda}$. A rotation angle $\overline{\lambda}$ was defined to be equal to the time-averaged local flow angle at each spatial location (where λ was defined to be positive in the clockwise direction as defined by a right-handed coordinate system). Figure 5.21(b) presents a contour map of $\overline{\lambda}$ throughout the flowfield in which larger counter-clockwise rotation angles were applied closer to the airfoil surface and decreased rotation angles were present further from the surface. Rotations such as these have been shown to be critical to the validity of Reynolds stresses in highly-curved fields [152]. Application of a simple rotation matrix yielded the Reynolds shear stress in the rotated reference frame by

$$\overline{\widetilde{u_r}'\widetilde{v_r}'} = \overline{(\tilde{u}'\cos\overline{\lambda} - \tilde{v}'\sin\overline{\lambda})(\tilde{u}'\sin\overline{\lambda} + \tilde{v}'\cos\overline{\lambda})}. \tag{5.27}$$

Data in Fig. 5.21(a) suggest elevated levels of turbulence at points in which the magnitude of $-\overline{\widetilde{u'}_r\widetilde{v'}_r}$ represent higher levels of turbulence. A positive value of $-\overline{\widetilde{u'}_r\widetilde{v'}_r}$ indicates fluctuations of $\overline{\widetilde{u'}_r}$ are out of phase with $\overline{\widetilde{v'}_r}$ while a negative value indicates that variations in $\overline{\widetilde{u'}_r}$ are in phase with $\overline{\widetilde{v'}_r}$. Elevated turbulence levels are observed in the shear layers

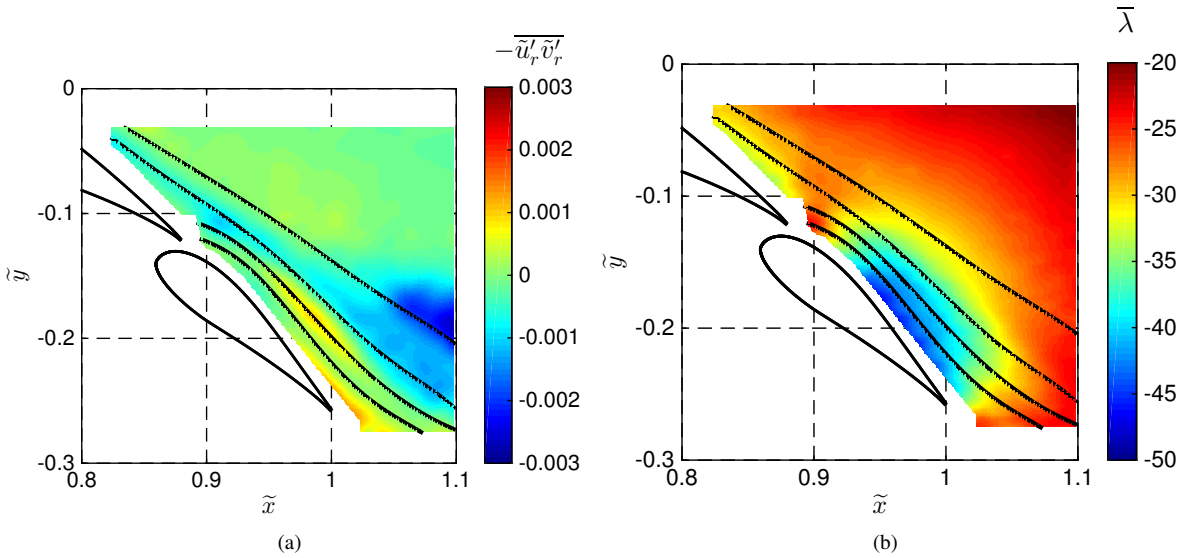

Figure 5.21: Reynolds stress parameters as captured by split-film probe showing a) rotated Reynolds stress tensor and b) value of local rotation angle.

present in the flow including the upper shear layer between the main-element wake and the "outer" flow as well as the shear layer between the main-element and flap 1 wakes. Turbulence levels in the flap 1 wake, before the burst point, are greater than those in the main-element wake before the main-element wake bursts. In general, turbulence spreads into the main-element wake core downstream of the burst point, and turbulence levels increase to as much as four times greater in the burst wake core than those in the non-burst core. Increasing downstream distance is observed to yield higher levels of turbulence, which is the expected result. Reynolds stress values are highest in the main-element upper wake core edge, and elevated Reynolds stress values are observed along the wake core edges of both wakes.

5.4.3 Turbulence Kinetic Energy

An additional metric to quantify turbulence is the turbulence kinetic energy (TKE), which is a measure of the mean kinetic energy per unit mass of the aforementioned eddies in a turbulent flow. TKE (κ), quantified as the RMS of the velocity fluctuations, is calculated in a two-dimensional flow by

$$\kappa = \frac{1}{2}\left(\overline{\widetilde{u}'^2} + \overline{\widetilde{v}'^2}\right). \tag{5.28}$$

As TKE is an isotropic scalar quantity, it is rotationally invariant and thus the value of $\overline{\lambda}$ does not affect the value of κ in the flowfield. Results for κ are presented in Fig. 5.22 in which values of κ are always positive and thus increased turbulence levels are associated with larger values of κ in a flowfield. The intensity of κ, as shown in the figure, increases more in the main-element wake core than in the flap 1 wake core, and less TKE diffusion is observed in the flap 1 wake. Similar to the Reynolds stress trends, increased values of κ are observed at larger downstream distances, and the largest values are present in the upper edge of the main-element wake. However, results indicate that high values of TKE are not confined to only the wake core edges, which is in contrast to the Reynolds stresses which were almost exclusively constrained to the wake core edges. In particular, increased values of κ are observed to occur between the wake core edges of the main element and flap 1 wake. Large values of κ spread away from the upper edge of the main-element wake core at $\widetilde{x} \geq 1.05$.

5.4.4 Production of Turbulence Kinetic Energy

In an effort to determine the origin of the turbulence in the flow, the turbulence kinetic energy production term $\wp$ was calculated, as shown in Fig. 5.23. This production term is calculated by [150]

$$\wp = -2\overline{\widetilde{u}'^2}\frac{\partial \widetilde{u}}{\partial \widetilde{x}} - 2\overline{\widetilde{v}'^2}\frac{\partial \widetilde{v}}{\partial \widetilde{y}} - \overline{\widetilde{u}'\widetilde{v}'}\left(\frac{\partial \widetilde{u}}{\partial \widetilde{y}} + \frac{\partial \widetilde{v}}{\partial \widetilde{x}}\right) \tag{5.29}$$

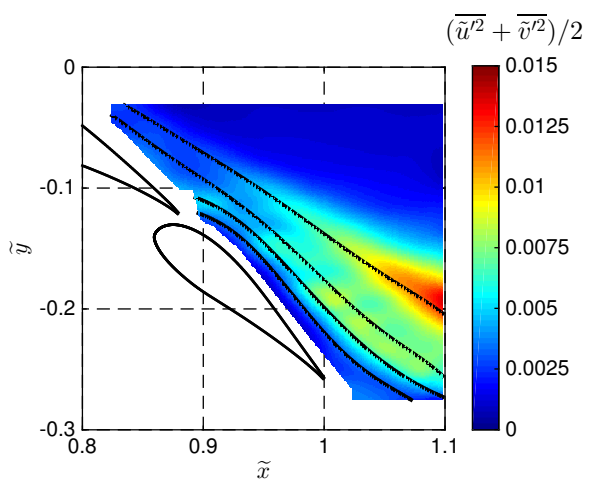

Figure 5.22: Values of turbulence kinetic energy κ in flowfield.

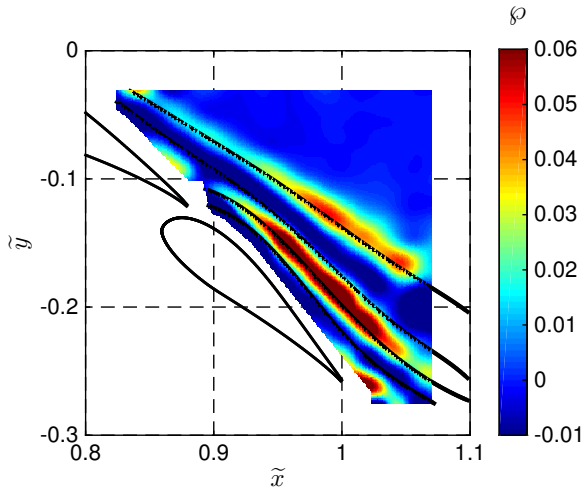

Figure 5.23: Turbulence energy production $\wp$ coplotted with wake edges.

and is one of the components in the governing equations for turbulence kinetic energy (TKE). Regions of high turbulence production, $\wp$, are observed in the shear layers between the main-element wake and the freestream as well as the shear layer between the wake of the main element and flap 1. This increase in turbulence production is a result of increased values of $\widetilde{u}'_r$ and $\widetilde{v}'_r$ as well as elevated values of normal and tangential velocity derivatives. As it is known that shear layers are one of the situations in which turbulence kinetic energy is produced, it is not surprising that elevated values of $\wp$ are observed in the shear layers. The highest levels of turbulence production are observed to be in the shear layer between the wake cores of flap 1 and flap 2. Minimal or no turbulence production is observed in the wake cores, which indicates the majority of turbulence is generated along the wake core edges, but the turbulence is then convected into the wake cores. A few regions of slightly-negative turbulence production $\wp$ are observed in Fig. 5.23. Negative values of $\wp$ indicate kinetic energy is being transferred from turbulence to the mean flow, and are not typically observed in most flowfields [150]. However, as discussed by Beguier [153], negative values of turbulence production can be present in flows with asymmetric velocity profiles, such as the flowfield in discussion.

5.4.5 Frequency Content

Methods were implemented to determine the frequency content of the unsteady flowfield through the calculation and analysis of flowfield spectra. The discussion in this section is concerned with the calculation of spectral content and analysis of the resulting spectra using a variety of techniques.

Data Reduction Techniques

Unsteady data were converted from the time domain to the frequency domain through standard fast Fourier transform (FFT) methods. An FFT algorithm was implemented to calculate the discrete Fourier transform (DFT) of a signal to determine spectral density functions of the original signal [149, 154, 155]. Using the Cooley-Tukey FFT algorithm, the DFT of a signal was calculated by

$$X_k = \sum_{n=0}^{N-1} x_n e^{-\frac{2\pi i}{N} nk} \qquad x = 0, 1, \ldots, N-1 \tag{5.30}$$

in which X_k is the resulting transformed signal in the frequency domain, k is an integer ranging from 0 to $N-1$, x_n are complex numbers, and N is the number of data points in the DFT. Frequency values in the resulting DFT are defined by f_k such that

$$f_k = \frac{k}{N\Delta t} \tag{5.31}$$

wherein Δt is the temporal spacing of data points. In this research, data were collected at a constant temporal spacing. The resulting Fourier transform can be expressed as a one-sided power spectral density function (G_{xx}) by

$$G_{xx}(f) = 2 \lim_{T\to\infty} \frac{1}{T} E\left(|X_k(f,T)|^2\right) \tag{5.32}$$

in which E is the expected value of the bracketed term. Using this method, the power distribution was calculated and observed across the frequency spectrum ranging from 0 Hz to the Nyquist frequency (taken as half of the sampling frequency). Finally, the resulting power spectral density (PSD) was analyzed in which the amplitude was expressed in decibel format (units of dB). A simple conversion from power to decibel was calculated using

$$L_{dB} = 10 \log_{10}\left(\frac{P_1}{P_0}\right) \tag{5.33}$$

where P_0 is a reference level of unity and P_1 is the measured power of the signal.

Power spectral density plots were ensemble averaged, which is a common technique to reduce the effect of random occurrences in the data sets. As 10 sec of data were collected for each spatial point, the resulting signal was divided into five different signals that were exactly 2 sec in length (or 6,000 data points). A PSD was then calculated from each of the five signals, and these five resulting PSDs were ensemble-averaged using a least-squares calculation in which

$$L_{avg} = \sqrt{\frac{1}{n}\sum_{i=1}^{5} L_i^2}. \tag{5.34}$$

This ensemble-averaging technique was applied at each discrete frequency in the resulting PSD.

Power Spectral Density

The unsteady behavior of the burst wake region was further investigated by analyzing the power spectral density (PSD) function of $\widetilde{U}_t$ using data collected by the split-film probe. Spectral content was analyzed at a number of different locations in the flowfield. Two sets of points were selected in relation to the previously-discussed wake core edges; one set was selected along a wake core edge, and one set was chosen in the chord normal direction. The specific locations at which the PSDs were studied are shown in Fig. 5.24. The locations along the wake core edge are depicted by circles while the locations where the PSDs were studied across the wake and wake core, are depicted as squares.

As previously discussed, both the Reynolds stresses and turbulence kinetic energy suggest that most of the energy exists in the wake shear layers. Consequently, a comparison was made of the spectral content of $\widetilde{U}_t$ at various streamwise locations within the main-element upper wake core edge, and results are presented in Fig. 5.25. The spectral content of $\widetilde{U}_t$ is primarily dominated by a frequency band of high-energy density from 1 to 50 Hz at all six locations. This narrow, high-energy frequency band remains nearly-constant in width with increasing downstream direction in the shear layer. However, the energy density within this frequency band is observed to increase with streamwise distance in the shear layer. This observation can be made by comparing Fig. 5.25(a) and (f) across the frequency band from 1 to 50 Hz in which an increase in spectral density from -51 to -37 dB/Hz is present.

The spectral content of $\widetilde{U}_t$ was also compared at numerous chord-normal locations for a given value of $\widetilde{x} = 1.05$, and the reader is referred to Fig. 5.24 to see the locations (depicted as squares). Spectral content is plotted for these six locations in Fig. 5.26. Similar to the content along the shear layer, a region of increased energy is observed from 1 to 50 Hz for most of the locations. Large increases in spectral content are presented in Fig. 5.26(b) and (e) which correspond to points that were located in two different shear layers. It is observed that the energy density from 1 to

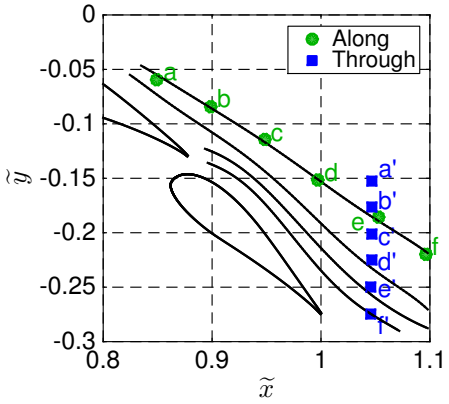

Figure 5.24: Location of points with selected power spectral densities.

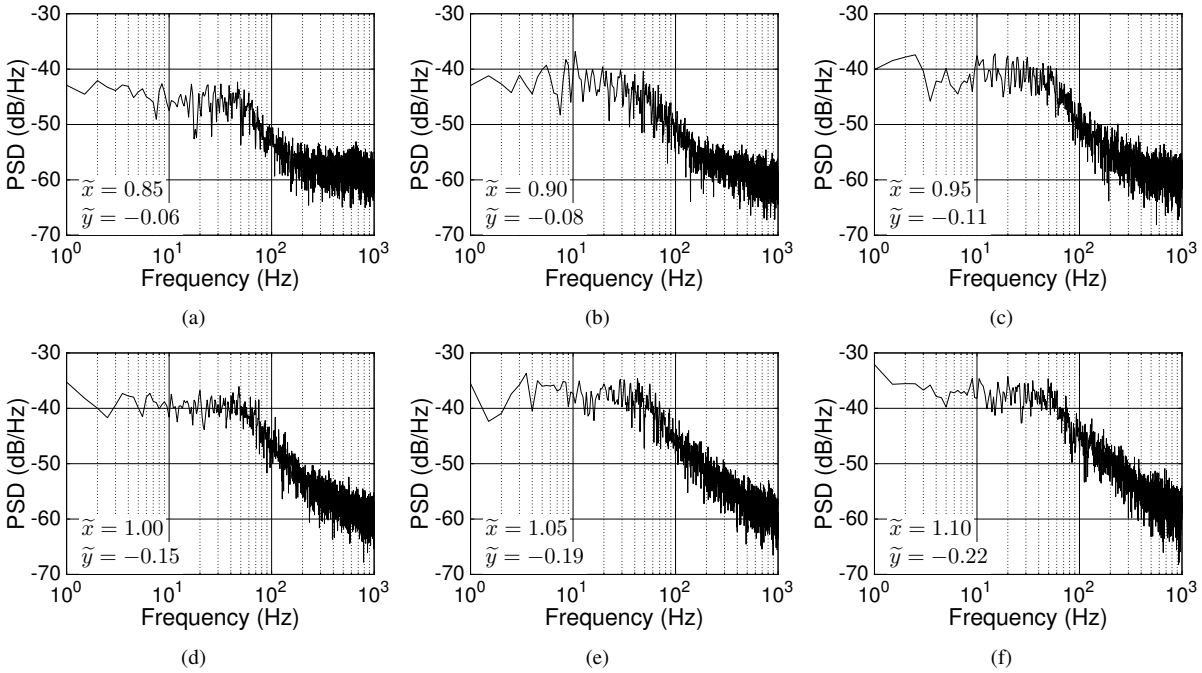

Figure 5.25: Power spectral density plots along main-element upper wake core at a) $\widetilde{x} = 0.85$, b) $\widetilde{x} = 0.90$, c) $\widetilde{x} = 0.95$, d) $\widetilde{x} = 1.00$, e) $\widetilde{x} = 1.05$, and f) $\widetilde{x} = 1.10$.

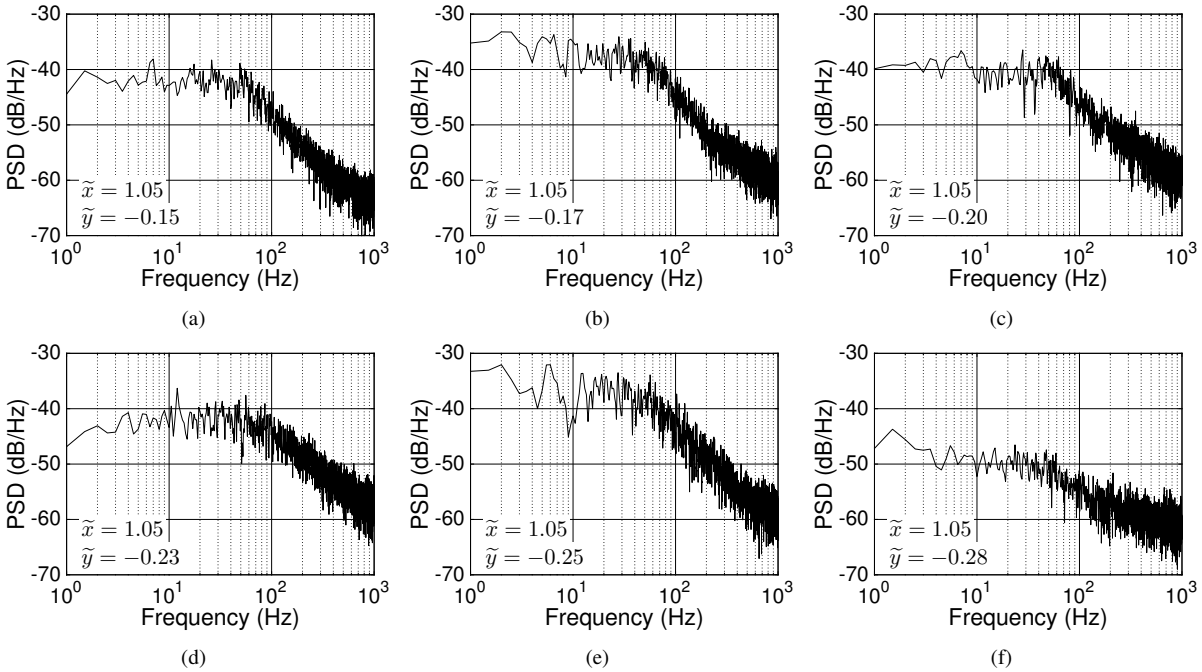

Figure 5.26: Power spectral density plots through shear layer at $\widetilde{x} = 1.05$ and a) $\widetilde{y} = -0.15$, b) $\widetilde{y} = -0.175$, c) $\widetilde{y} = -0.20$, d) $\widetilde{y} = -0.225$, e) $\widetilde{y} = -0.25$, and f) $\widetilde{y} = -0.275$.

50 Hz decreases with increased distance from the main-element shear layer, as evidenced in Fig. 5.26(a), (c–d), and (f). Spectral content in the shear layers of the main element was different than the energy in the shear layer of flap 1. The energy from 1 to 50 Hz in the shear layers of the main element, shown in Fig. 5.26(b,e), is larger than the energy in the flow from 1 to 50 Hz in the shear layer of flap 1 in Fig. 5.26(f).

Broadband Frequency Content

As mentioned above, spectral content was observed to be elevated at frequencies below 150 Hz at many locations throughout the shear layer. Due to this observation, the energy within the flowfield was further characterized by integrating the PSD of $\widetilde{U}_t$ across the frequency band from 1 to 150 Hz by

$$I_{1-150} = \int_1^{150} L_{avg} df \tag{5.35}$$

where I is the resulting integrated energy and L_{avg} is the ensemble-averaged PSD content. A contour plot of I_{1-150} is plotted in Fig. 5.27. Results in the figure suggest that the regions corresponding to the greatest concentrations of integrated energy are the shear layers from the wake of the main element, which is also the region of greatest turbulence, as previously discussed. In general, striking similarities are observed between Fig. 5.27 and Figs. 5.21–5.22. Therefore, it is suggested that the turbulent characteristics of the wake shear layer are the primary contributors to the spectral content within the burst wake region, and that the turbulent eddies are of a relatively large scale.

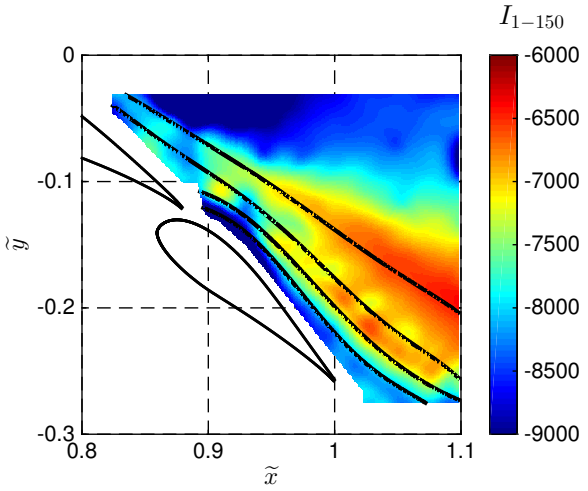

Figure 5.27: Integrated PSD energy from 1 to 150 Hz coplotted with wake edges

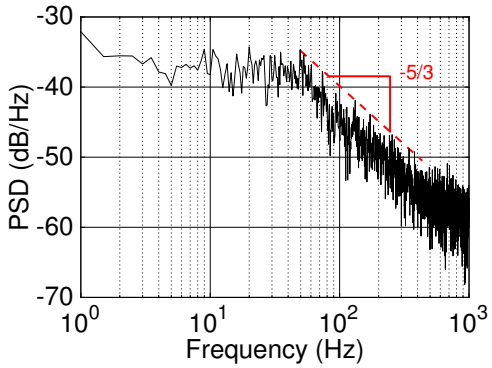

Figure 5.28: Power spectral density plot showing energy cascade consistent with Kolmogorov $-5/3$ rule.

Kolmogorov Scaling

It is well known that the large-scale eddies are the energy containing eddies (small frequency) and that viscous dissipation occurs for the small eddies (large frequency). The cascade of energy in the intermediary scales is known as the inertial subrange, and the Kolmogorov $-5/3$ law indicates that the slope of the PSD in the inertial subrange is $-5/3$ if the flow is dominated by turbulent diffusion [150]. A PSD spectra of $\widetilde{U}_t$ at $\widetilde{x} = 1.10$ and $\widetilde{y} = -0.22$ presented in Fig. 5.28 displays turbulent energy transfer behavior that is consistent with the Kolmogorov $-5/3$ law in the shear layer. Consequently, the data set is said to be dominated by turbulent diffusion at frequencies greater than 150 Hz. As data were only postprocessed up to 1,000 Hz, the upper limit of the inertial subrange cannot be determined.

5.5 Computational Predictions

Computational simulations were performed using both MSES, a coupled inviscid/viscous panel-method solver, and USM3D, an unstructured RANS code. Details regarding the capabilities and theory of these solvers are discussed extensively in Sec. 3.3 on page 59 and Sec. 3.4 on page 62 for MSES and USM3D, respectively. Information in this section quantifies the performance of these two computational codes in terms of numerous different parameters including: domain size, grid density, and turbulence model (for USM3D only). In addition, computational predictions for the baseline airfoil are presented later in this section, but a detailed comparison between the computational predictions and the previously-discussed experimental results is presented in the next section.

5.5.1 Characterization of MSES Flow Solver

Solutions in MSES are computed on an intrinsic grid such that the grid lines are in directions either parallel or orthogonal to the streamlines, as shown in Fig. 5.29. While grid spacing is adaptively determined by the code with the

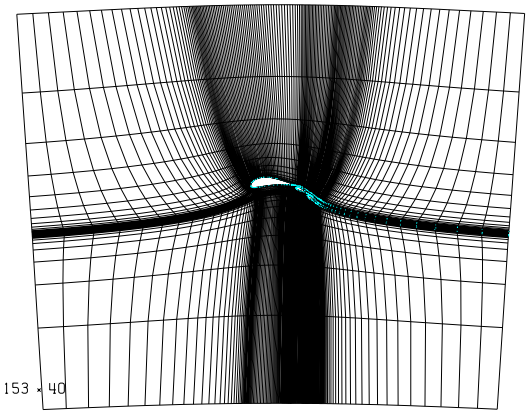

Figure 5.29: Computational intrinsic grid upon convergence in MSES solver.

previously-discussed methods in Sec. 3.3, the user is provided with some control over the resolution of the grid and the specification of the computational domain size. The effects of these two parameters will now be discussed.

Domain Sizing

The size of the outer domain is declared by the user through the input files to MSES. Over the course of this research, the computational domain was declared to extend a certain distance upstream of the leading edge, downstream of the trailing edge, above the airfoil, and below the airfoil; these four distances were specified to be the same value. As the outer walls of the domain are aligned with the streamlines, the size of the computational domain has less effect upon the flowfield than if the outer domain boundaries were aligned with a Cartesian grid [77, 156]. A range of domain sizes, from $1c_{sys}$ upstream and downstream of the airfoil system (corresponding to a total domain width of $3c_{sys}$) to $7c_{sys}$ upstream and downstream of the airfoil (yielding a domain $15c_{sys}$ wide) were studied, and various aerodynamic performance data are presented in Fig. 5.30. As shown in the figure, there is little variation in C_l, C_d, or C_m for domains larger than $5c_{sys}$ in width, but larger deviations are observed for smaller computational domains.

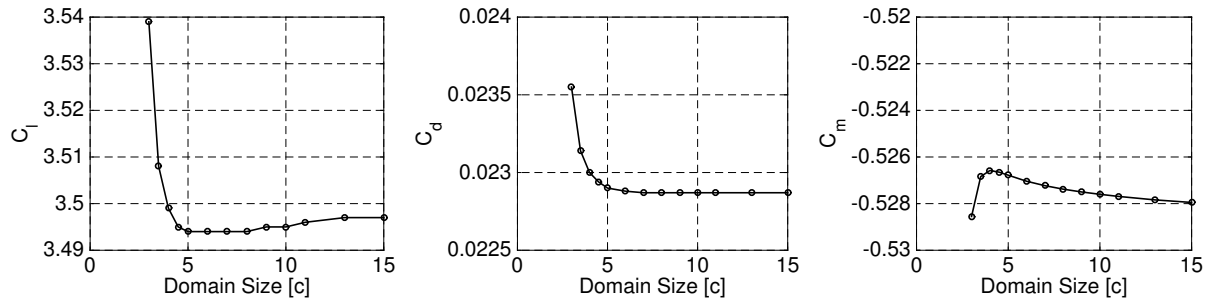

Figure 5.30: Effect of computational domain sizing in MSES quantified by a) C_l, b) C_d, and c) C_m.

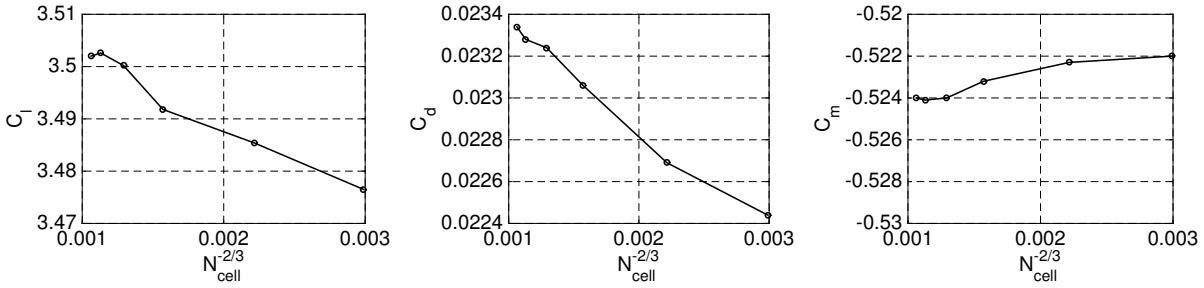

Figure 5.31: Effect of computational grid density and size in MSES quantified by a) C_l, b) C_d, and c) C_m.

Consequently, a computational domain of width $5c_{sys}$ was utilized for the all remaining computational simulations in MSES presented in this document.

Grid Size

A study was also performed to determine the appropriate grid density in MSES. A total of six different grid sizes, which were all uniformly scaled in the x and y directions from the coarsest grid, were implemented using the grid refinement option in the MSES program. No modifications to the grid were made in MSET. The relationship between these six grids and various aerodynamic performance metrics are presented in Fig. 5.31, in which grid size is presented using the standard $N^{-2/3}$ metric where N is the total number of cells. Results indicate inconsequential changes in C_m over the grid sizes studied and small, yet not-insignificant, variations in C_l and C_d. Larger variations in C_l are present for the coarser grids, but little variation in C_l is observed for cases at which $N^{-2/3} \leq 0.0013$ (or a total cell count of 21,000 cells). As a result of these trends, all computations in this document performed with MSES were computed on a grid of approximately 21,000 cells.

5.5.2 Characterization of USM3D Flow Solver

A number of RANS simulations were performed using USM3D, an unstructured RANS solver developed and supported by NASA Langley. The quasi-two-dimensional simulations were executed inside a rectangular prism control volume in which the computational domain extended $10c_{sys}$ in all directions from the geometry. Reflection planes were used on the side walls of the volume, and characteristic inlet/outlet conditions were prescribed on the other four faces. Grids were generated using VGrid using the advancing front/advancing layer techniques. A higher concentration of cells was prescribed at the leading and trailing edges of the airfoils, and some refinement was also performed in the wake region of interest. Investigations were performed to justify the selection of computational domain size, computational span of the airfoil, grid size, and turbulence model. Each of these is independently discussed herein.

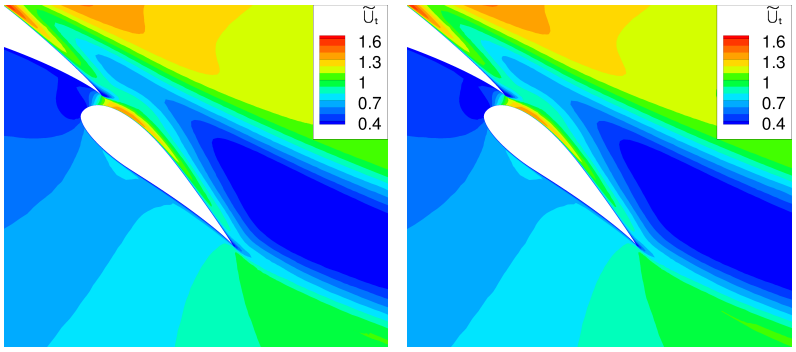

(a) (b)

Figure 5.32: Flowfields predicted with a) inflow/outflow box boundary condition and b) no-flux inviscid wall boundary condition.

Domain Sizing

As mentioned in the introduction, the top and bottom of the computational domain were both specified to be a characteristic inflow/outflow boundary condition. To justify the selection of control volume sizing, a second simulation was performed with inviscid, no-flux boundary conditions for the top and bottom walls of the computational domain. This study was performed to defend the selection of the computational domain sizing and prove that the presence of the outer boundaries of the computational domain did not adversely affect the computed aerodynamic quantities of interest. The results from these two simulations are presented in Fig. 5.32. As seen in the figure, no significant differences in the flowfield are observed between the two different cases. In addition, the computed values of C_l were differed by less than 0.01 between both cases. As the external no-flux boundary condition may impose a pressure gradient on the far field streamlines, it is known that the value of C_l can be affected by the presence of the control volume boundaries. Because of the minimal differences in C_l and indiscernible differences in the flowfields, the size of the control volume was deemed to be sufficiently large.

Effect of Computational Span

A parametric study was completed in USM3D to determine the effect of the size of the control volume, in particular the span, on the computational results. In general, it is desired to obtain an accurate solution with as few cells as possible. Thus, as simulations were quasi-two-dimensional, the number of cells can be significantly reduced by decreasing the span of the quasi-two-dimensional geometry. Five different geometries were simulated including a span of $0.02c$, $0.04c$, $0.06c$, $0.08c$, and $0.10c$. These simulations were performed using the one-equation Spalart-Allmaras (SA) turbulence model, which has been shown to perform reasonably well for high-lift multielement airfoil flowfields [29]. Aerodynamic results, including both a lift curve and a drag polar, at $Re = 1 \times 10^6$ are plotted in Fig. 5.33. As seen

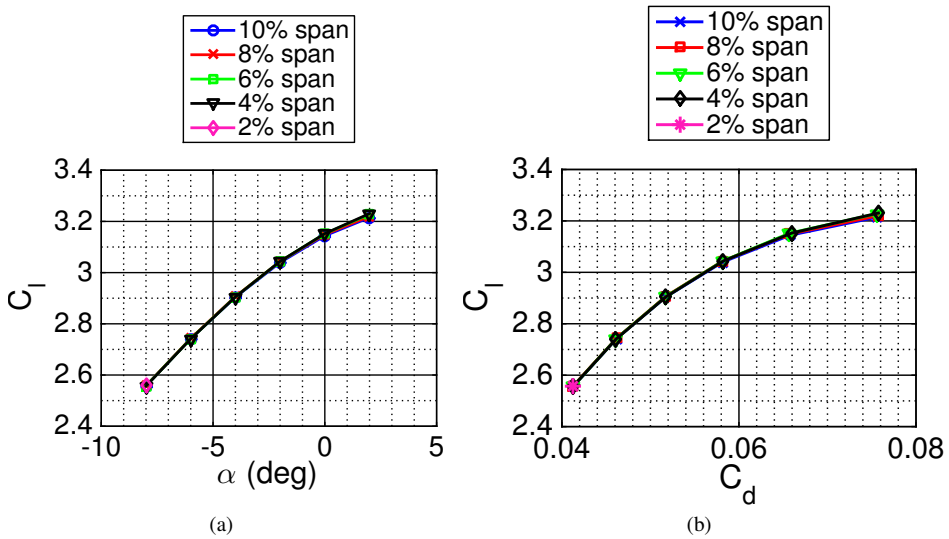

Figure 5.33: Effect of airfoil span on computational results including a) lift curve and b) drag polar.

in the figure, imperceptible variations are observed in C_l and C_d over the range of span lengths studied. It is noted, however, that solutions rarely converged with the $0.02c$ span solution; convergence was only achieved at $\alpha = -8$ deg. Because of the minimal variations in C_l and C_d and convergence issues at $0.02c$, it was concluded that the control volume could be a minimum of $0.04c$ in span, which was the value used for the remainder of all simulations in this document unless otherwise noted.

Grid Convergence

A grid-convergence study was carried out to determine and justify the selection of grid resolution for the baseline airfoil at an α of 0 deg and a freestream Reynolds number of 1×10^6. This study was executed with the k-ε as convergence was readily achieved across a wide range of mesh densities. Four grids ranging in size from 1.1 million cells to 2.3 million cells were used for this study, and these grids were all derivatives of a baseline mesh. Refinement and coarsening of the grids was performed by altering the inviscid and viscous scaling factors prior to grid generation in VGrid. Plots of the four grids are presented in Fig. 5.34 for both a wide view (top row) and a close-up detailed view centered around the flaps (bottom row). As seen in the figure, the finer meshes have both smaller cells in the outer boundaries of the domain as well as smaller cells near the airfoil body when compared to the coarser meshes.

To quantify the effect of grid discretization, a Richardson extrapolation exercise was performed to determine the values of both C_l and C_d for an infinitely-fine grid. In such a study, a solution was sought of the form

$$y_{raw} = y_{true} + C\delta^p \tag{5.36}$$

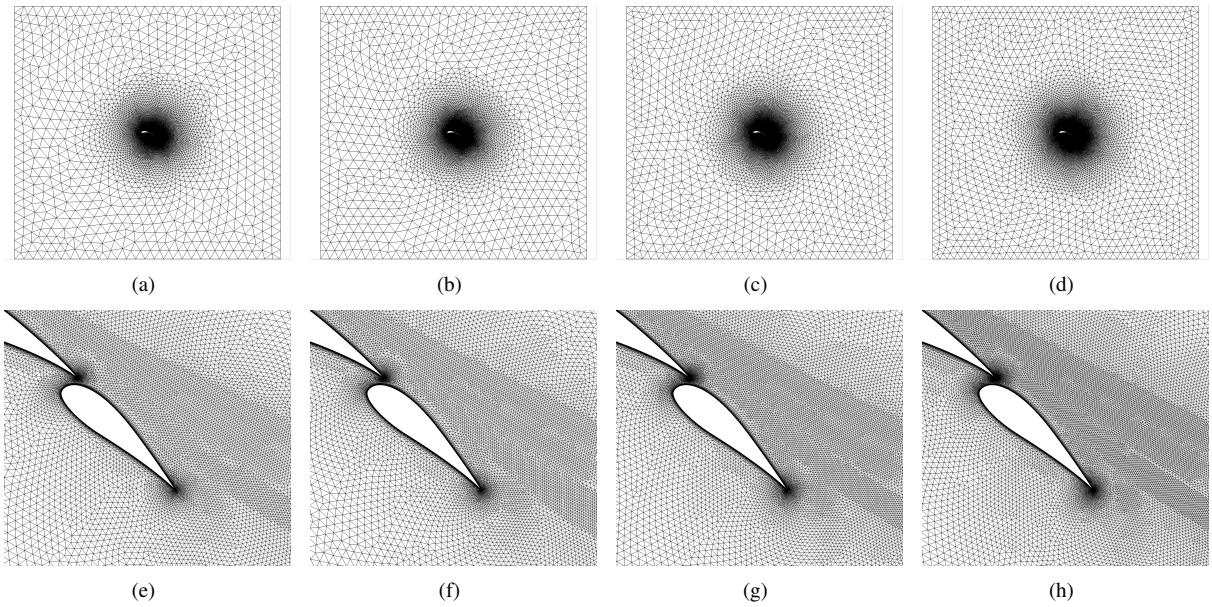

Figure 5.34: Four computational grids for grid-convergence study with k-ε turbulence model showing a) coarse grid wide view, b) medium grid wide view, c) fine grid wide view, d) ultra-fine grid wide view, e) coarse grid detailed view, f) medium grid detailed view, g) fine grid detailed view, and h) ultra-fine grid detailed view.

in which y_{raw} is the value of a parameter (C_l or C_d) from the computational runs, y_{true} is the predicted result for an infinitely-fine grid, C is a constant, δ is a measure of grid size (taken to be average cell volume), and p is the order of accuracy for the solution [157]. These fits were determined for both C_l and C_d and the results are presented in Fig. 5.35 in which the computed values and the infinitely-fine grid solutions are presented against $N^{-2/3}$ where N is the total number of cells; thus a small value of $N^{-2/3}$ corresponds to a fine grid while a large value of $N^{-2/3}$ is

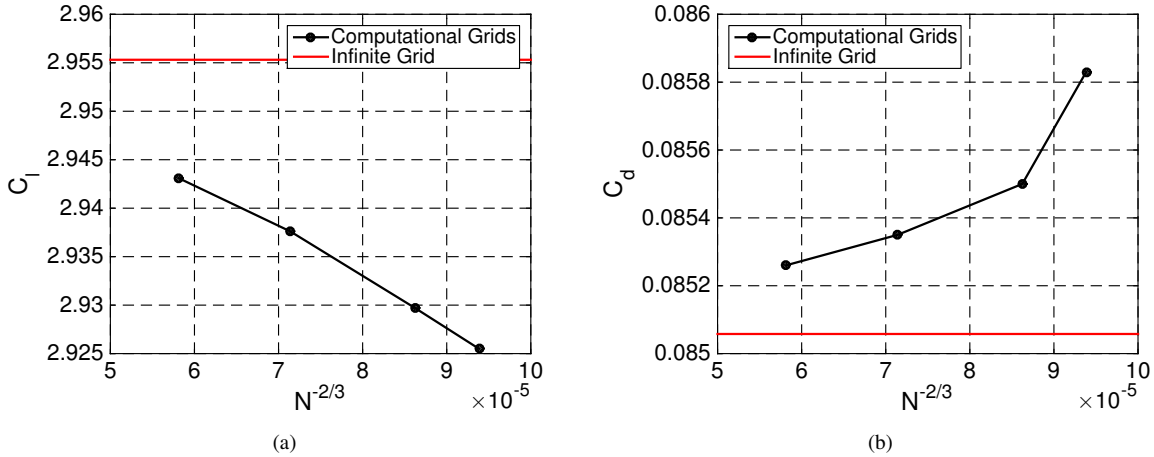

Figure 5.35: Richardson extrapolation study for USM3D grids for a) C_l and b) C_d.

associated with a coarse grid. The largest deviations from the exact solution are observed for the coarse grid while the smallest deviations exist with the finest grid, which is the expected trend. In addition, the rate of change of deviation decreases with increasing grid density. That is to say that large changes in C_l and C_d are present when comparing the coarse and medium grids, but a smaller change exists between the fine and ultra-fine grids. As seen in the figure, larger deviations from the infinitely-fine grid solution are observed in C_d for both the medium and coarse grid while smaller deviations are noted for the fine and ultra-fine solutions. As a result of this study, the fine grid was selected for the remainder of the solutions presented in this document as it yielded an adequate balance between solution accuracy and computational cost.

Turbulence Model Selection

A variety of one- and two-equation turbulence models can be used in USM3D, and an investigation was performed to select the most-appropriate turbulence model for the flowfield in discussion. Simulations were performed with SA, SST (shear stress transport), k-ε, and k-ω. For the two-equation models, values of freestream turbulence intensity and freestream turbulent-to-laminar eddy viscosity (μ_t/μ_l) were prescribed. Values for these parameters have been determined through a variety of turbulence model calibration studies by NASA Langley, and recommended values for each turbulence model were provided in documentation for USM3D. The selected values for each of these turbulence models are included in Table 5.3.

Simulations were performed using the four turbulence models for the flowfield in discussion, and results are presented in Fig. 5.36. The region shown in the figure is similar to the region shown for the experimental data previously presented in Fig. 5.5; the trailing portion of flap 1 is visible and the entirety of flap 2 is visible. All solutions in Fig. 5.36 were calculated on the same mesh to offer a fair comparison. It is clear that all turbulence models significantly over-predict the amount of separation in the wake region when compared to the experimentally-captured data in Fig. 5.5. This topic will be directly addressed in great detail later in this document in Sec. 5.6 on page 150. It is noted that the color scale shown in Fig. 5.36 is slightly expanded when compared to the experimental results to allow for more detailed comparisons between the computational runs. The reader is assured that the same contour scale is used in Sec. 5.6 in which detailed comparisons are made between the experimental and computational data sets.

Table 5.3: Turbulence Model Parameter Values

Turbulence Model	Input Flag (ivisc)	Freestream Turbulence	Freestream μ_t/μ_l
SA	2	—	—
SST	8	1.2247×10^{-5}	0.009
k-ε	6	0.001	1.0
k-ω	5	1.2247×10^{-5}	0.009

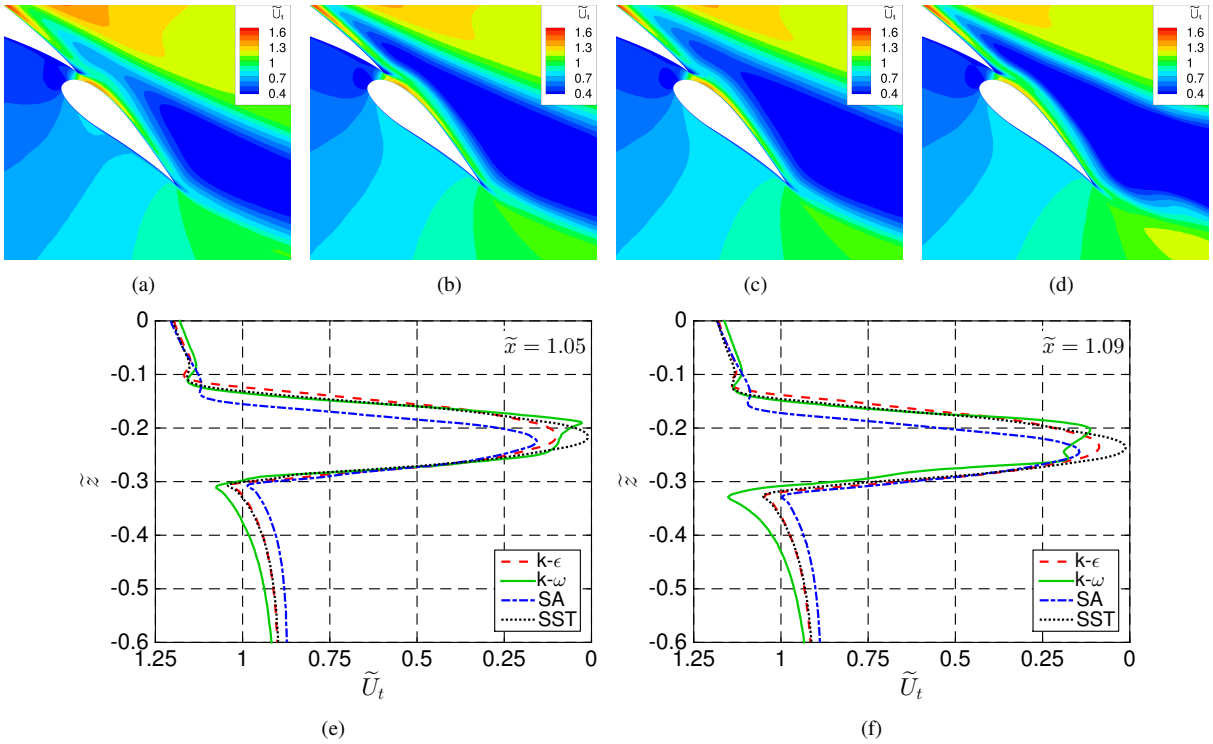

Figure 5.36: Results capturing effect of turbulence model selection for a) SA, b) SST, c) k-ε, d) k-ω, e) line plot of results at $\widetilde{x} = 1.05$, and f) line plot of results at $\widetilde{x} = 1.09$.

Despite the discrepancies between the experimental and computational data, it is interesting to note the differences in the predictions for each of the turbulence models. None of the turbulence models suggest separation from the surface of either of the flaps, and all suggest wake bursting of the main element wake. In addition, results using all four turbulence models suggest significant merging between the wake of the main element and flap 1. The flowfield on the lower shear layer just downstream of the system trailing edge as predicted by the k-ω turbulence model, seen in Fig. 5.36(d), exhibits some unique behavior despite the fact that the solution was adequately converged. Due to this fact, the k-ω turbulence model was not used in any other simulations presented in this chapter.

Data were extracted at constant $\widetilde{x}$ values of 1.05 and 1.09 from the computational simulations, and these results are presented in Fig. 5.36(e,f). Despite the observation that all turbulence models overpredict the amount of wake bursting, it is interesting to compare the differences between the four turbulence models using the same grid. As shown in the figure, the SA and k-ε turbulence models indicate the minimum velocity at $\widetilde{x}$ of 1.05 with minimum $\widetilde{U}_t$ values of 0.16 and 0.10, respectively. The results from the SA turbulence model also yielded the thinnest wake at both spatial locations. It is observed that the minimum $\widetilde{U}_t$ at both spatial locations is 0 indicating no fluid movement at these locations.

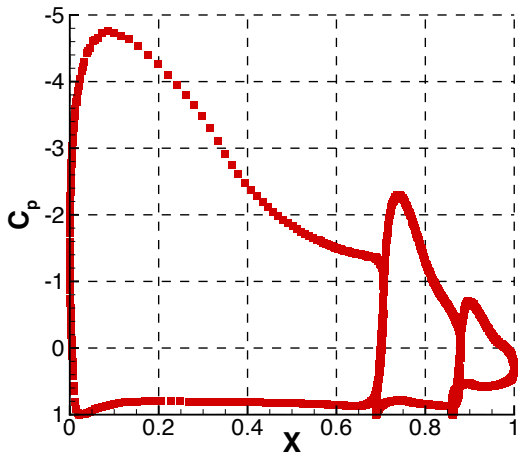

Figure 5.37: Coefficient of pressure for Configuration 10 at $\alpha = 0$ as predicted by SA turbulence model.

Airfoil performance and flowfield behavior is dependent upon the pressure distribution around the multielement airfoil system, and a plot of C_p on the surface of all three elements is shown in Fig. 5.37 at an $\alpha = 0$ deg and $Re = 1 \times 10^6$ using the SA turbulence model. As the simulation assumed fully-turbulent flow for all viscous regions, transition is not observed over any of the surfaces. Most significantly, the pressure peaks for each element are observed to decrease with increasing downstream distance, which is known to yield improved aerodynamic performance than the opposite case. Low values of C_p are observed on the lower surface of the main element and flap 1 which helps increase C_l. While these regions of slow-moving air can be prone to surface separation, results do not indicate any separation from the lower surface of the airfoil. A small portion of the C_p curve near the leading edge of flap 2 is observed to have larger magnitudes of C_p for the lower surface than the upper surface, which decreases the value of C_l for the system.

Effect of Turbulence Model Inputs

Two-equation turbulence models, such as those used in this research project, require the user to specify the value of two different parameters, and methods implemented in USM3D require the user to declare the value of freestream turbulence intensity and the turbulent viscosity ratio. The default values for these parameters have been determined by the developers of USM3D through a series of turbulence-model validation studies, and these values are presented above in Table 5.3 on page 142. While the default values were used for each of the turbulence models, it was desired to quantify the effect of changing the values of the parameters. Two different sets of computations were performed with the k-ε turbulence model to capture the effect of freestream turbulence intensity and turbulent viscosity ratio. Computations were performed with three different freestream turbulence intensity values, and results, including both contour plots and a line plot of data extracted at $\widetilde{x} = 1.05$, are presented in Fig. 5.38. As seen in the figure, minimal

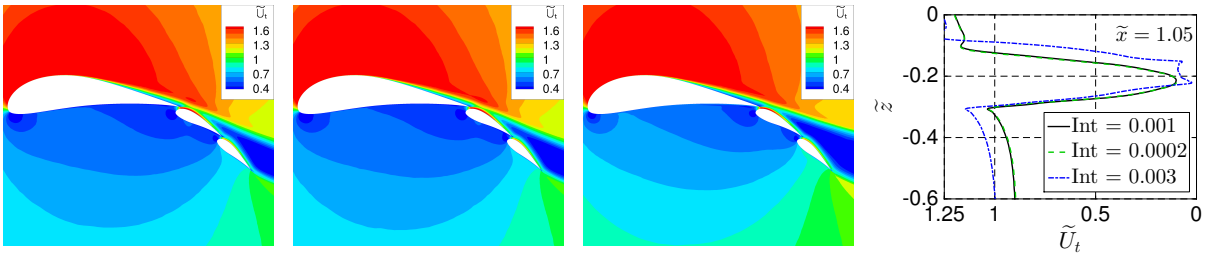

(a) (b) (c) (d)

Figure 5.38: Effect of freestream turbulence intensity on computational results including freestream turbulence intensities of a) 0.001 (baseline), b) 0.0002, c) 0.003, and d) line plots showing data at $\widetilde{x} = 1.05$.

differences exist between the baseline case (freestream turbulence intensity of 0.001) and the decreased freestream turbulence intensity case of 0.0002. This assertion is confirmed by observing minimal differences exist between the forces and moments between the two cases. However, some differences are observed between the baseline case and that of increased freestream turbulence intensity. The case in which the freestream turbulence intensity was 0.003, seen in Fig. 5.38(c) depicts a larger wake than that of the baseline case, and this observation is also seen in the line plot in Fig. 5.38(d). While the effect of the freestream turbulence is thus documented herein, the default values for freestream turbulence intensity (Table 5.3), against which the turbulence models have been validated, were used for all other computations in this research.

A second set of simulations was executed to evaluate the effect the turbulent viscosity ratio (μ_t/μ_l). The three simulations were performed with a turbulent viscosity ratio of 0.5, 1.0, and 1.5; the default value for k-ε is 1.0. As shown in Fig. 5.39, no discernible differences are noticed with varying values of the turbulent viscosity ratio. Nearly-uniform flowfields were predicted, as evidenced by the contour plots and by the line plot at $\widetilde{x} = 1.05$, and excellent agreement was also found in C_l, C_d, and C_m between all three cases. Consequently, it is concluded that the value of the turbulent viscosity ratio, bounded by 0.5 and 1.5, has little effect upon the simulation. Since no discernible differences

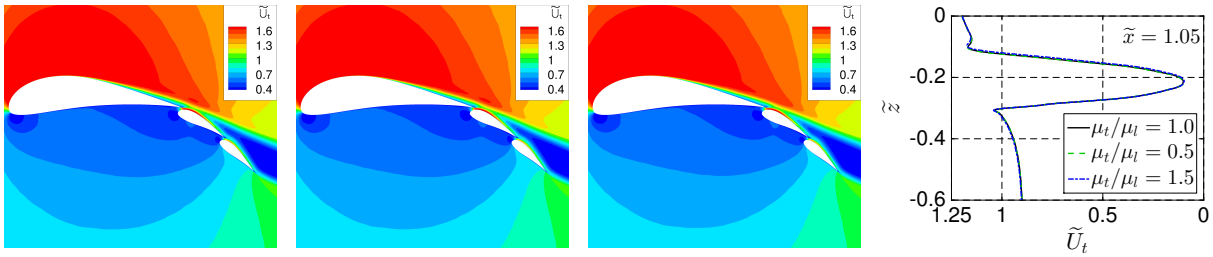

(a) (b) (c) (d)

Figure 5.39: Effect of μ_t/μ_l on computational results including μ_t/μ_l values of a) 1.0 (baseline), b) 0.5, c) 1.5, and d) line plots showing dta at $\widetilde{x} = 1.05$.

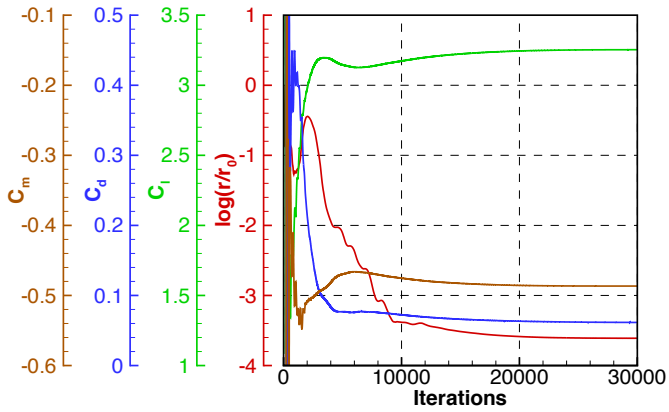

Figure 5.40: Convergence history as represented by residual and aerodynamic forces and moments.

are observed between the three cases, the recommended input values for the two-equation turbulence models were used for the remainder of this project.

Iterative Convergence

Computational convergence is necessary to yield an accurate solution of the flowfield. A variety of parameters were used to evaluate the convergence of a solution including: residual of solution [$\log(r/r_0)$], C_l, C_d, and C_m. Figure 5.40 presents these four variables as a function of the number of iterations. The four values are co-plotted on the same figure with different ranges for the y axis in which each line plot is color-coded and corresponds to the color of the y axis on the left side of the figure. As seen in the figure, the rate of change of all four parameters with respect to the number of iterations approaches 0 at large iteration values. The nature of these lines, approaching a horizontal line, indicates that the solution is adequately converged. Iterative-convergence data presented in Fig. 5.40 are representative of the converged simulations presented in this document.

5.5.3 Flowfield Dependence on α

An additional parametric investigation was performed with each of the turbulence models in which α was varied from -12 to 2 deg in 2 deg increments. The effect of varying α on the burst wake is significant in terms of both the size and presence of the burst wake. While simulations were performed with each of the turbulence models, only results using the SA turbulence model are presented in Fig. 5.41. The presence of two different and distinct wakes are present at cases in which $\alpha \leq -6$ deg, and results indicate a significant amount of mixing between these two wakes. Wakes at larger values of α appear as one large, thick wake, and no separation between the main-element and flap-1 wakes is present. A large momentum deficit region is present in the flow at increased values of α, and the size of this region is observed to increase with α even though the flow is seen to remain attached to the surface of the airfoils at these

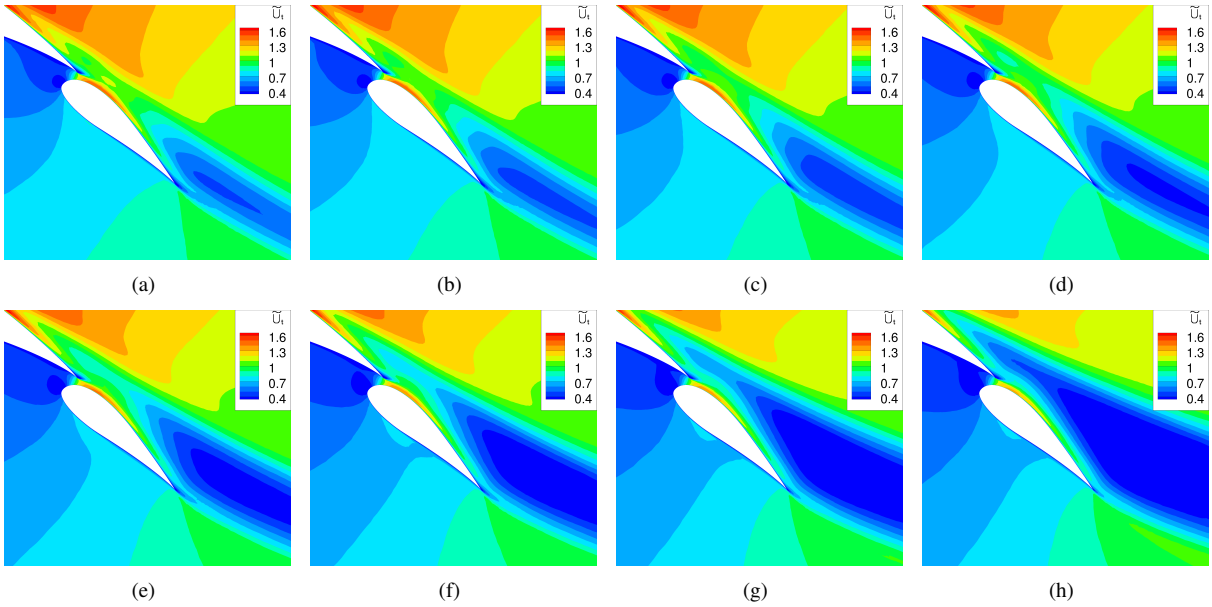

Figure 5.41: Computational results capturing effect of α with SA predictions of U_t at a) -12 deg, b) -10 deg, c) -8 deg, d) -6 deg, e) -4 deg, f) -2 deg, g) 0 deg, and h) 2 deg.

higher values of α. No separation is observed on the surface of the flaps, as shown in Fig. 5.41, at any of the α analyzed. Curiously, despite the increase in α, the flow acceleration between the gap is very similar between all cases. In addition, flow acceleration over the upper surface of flap 2 is observed to decrease at larger α relative to the cases with decreased values of α, which is contrary to the expected trend. This observation is attributed to viscous effects including a larger boundary layer as well as a larger, thicker wake at higher α than at lower α.

Aerodynamic performance of the Configuration 10 airfoil, as predicted by the SA turbulence model corresponding to the flowfields presented in Fig. 5.41, is presented in Fig. 5.42. It is interesting to note that the lift curve indicates a gradual decrease in $C_{l,\alpha}$ with increasing α, and that a linear region is not clearly observed. As evidenced in Fig. 5.41, the increasing thickness of the wake with increasing α effectively and progressively decambers the airfoil thus yielding the non-linear lift curve. Stall is not observed in the range of α simulated. Large values of C_d for the airfoil, as plotted in Fig. 5.42(b), are a result of the thick burst wakes discussed as previously in this section. As expected, lower values of C_d are associated with decreased values of C_l and α due to the decrease in wake bursting at lower angles of attack. The large increase in C_d at increased α yields lower values of l/d at larger α, as seen in Fig. 5.42(c), in which the largest l/d values are observed at the lowest values of α.

Figure 5.43 presents a variety of parameters in the same plot. This hybrid plot includes contour intervals at a constant C_p which are colored by $\widetilde{U}_t$ and the unstructured mesh, shown in gray, in the background. Results in the figure were computed at $\alpha = 0$ deg and $Re = 1 \times 10^6$ using the SA turbulence model. Figures such as these provide a

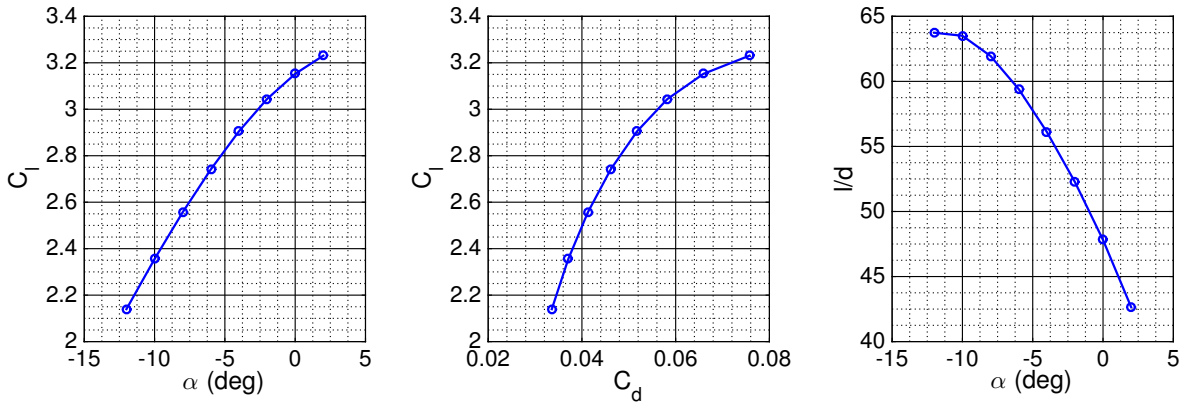

(a) (b) (c)

Figure 5.42: Aerodynamic performance of Configuration 10 including a) lift curve, b) drag polar, and c) l/d.

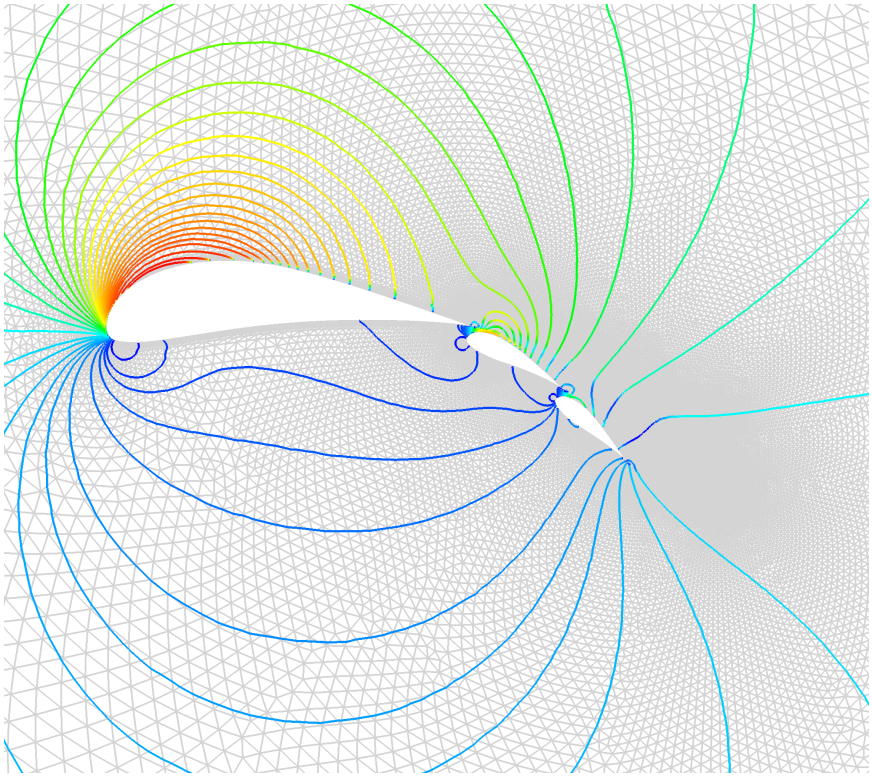

Figure 5.43: Hybrid plot showing isolines of constant C_p colored by $\widetilde{U}_t$.

useful way to simultaneously compare two or three different parameters which provides insight into the relationship between these different parameters. It is prudent to present the unstructured mesh in the figure so that the relationship between the cell density and C_p contour intervals throughout the solution domain. In addition, the C_p contour lines are colored by $\widetilde{U}_t$ and provides insight into the relationship between C_p and $\widetilde{U}_t$ over a wide spatial region.

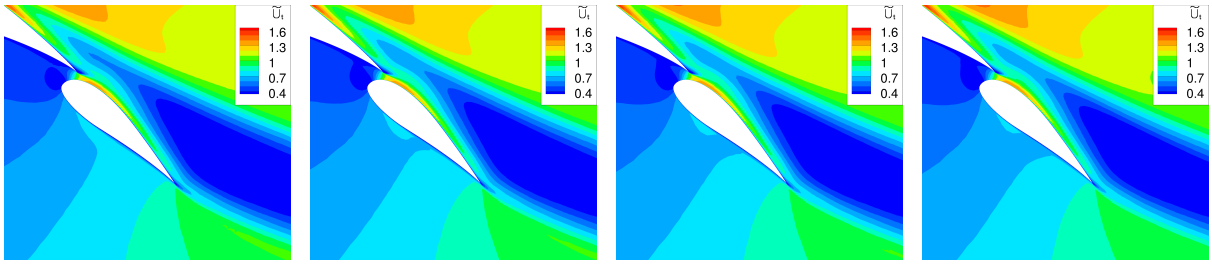

(a) (b) (c) (d)

Figure 5.44: Effect of Reynolds number on burst-wake flowfield according to fully-turbulent USM3D simulations at a) $Re = 0.6 \times 10^6$, b) 0.8×10^6, c) 1.0×10^6, and d) 1.2×10^6.

5.5.4 Reynolds Number Effect

Four fully-turbulent RANS simulations were performed in USM3D to determine the effect of freestream Reynolds number on burst wakes. Results were calculated with the SA turbulence model at freestream Reynolds numbers ranging from 0.6×10^6 to 1.2×10^6, and results are plotted in Fig. 5.44. As seen in the figure, very few changes are observed to exist between the four different flowfields. This is a surprising result as the burst wakes are a viscous flowfield feature and it was thought that the behavior and strength of these wakes would have been affected by the freestream Reynolds number. It is stated, however, that these four simulations were performed with fully-turbulent USM3D calculations, which was the only publicly-released version of the code at the time of these simulations, and thus the effect of the transition point was not captured in these specific simulations. Some computations using a developmental version of USM3D with fixed transition are presented in Sec. on page 159 later in this document. As it is known that the freestream Reynolds number affects the laminar-to-turbulent transition point, it is hypothesized that burst wakes are at least somewhat affected by the transition point on an airfoil, even though the fully-turbulent RANS simulations did not capture this effect.

5.5.5 Dimensionality of Flowfield

It is known that airfoils, which are two-dimensional geometries, generally yield two-dimensional flowfields. However, it was desired to determine if the flowfield associated with wake bursting was two-dimensional or three-dimensional in nature. Due to the three-dimensional flowfield resulting from the juncture flow in the wind tunnel, it was not practical to interrogate the experimental 7-hole probe results to determine the flow dimensionality, and thus computational results were further examined. The results presented in Fig. 5.45 in which $\widetilde{u}$, $\widetilde{v}$, and $\widetilde{w}$ at two span stations were calculated with the SA turbulence model on a $0.10c$ airfoil system. Contour plots shown on the left side of the figure are taken at the center-span location of the airfoil while the results on the right side of the figure correspond data on

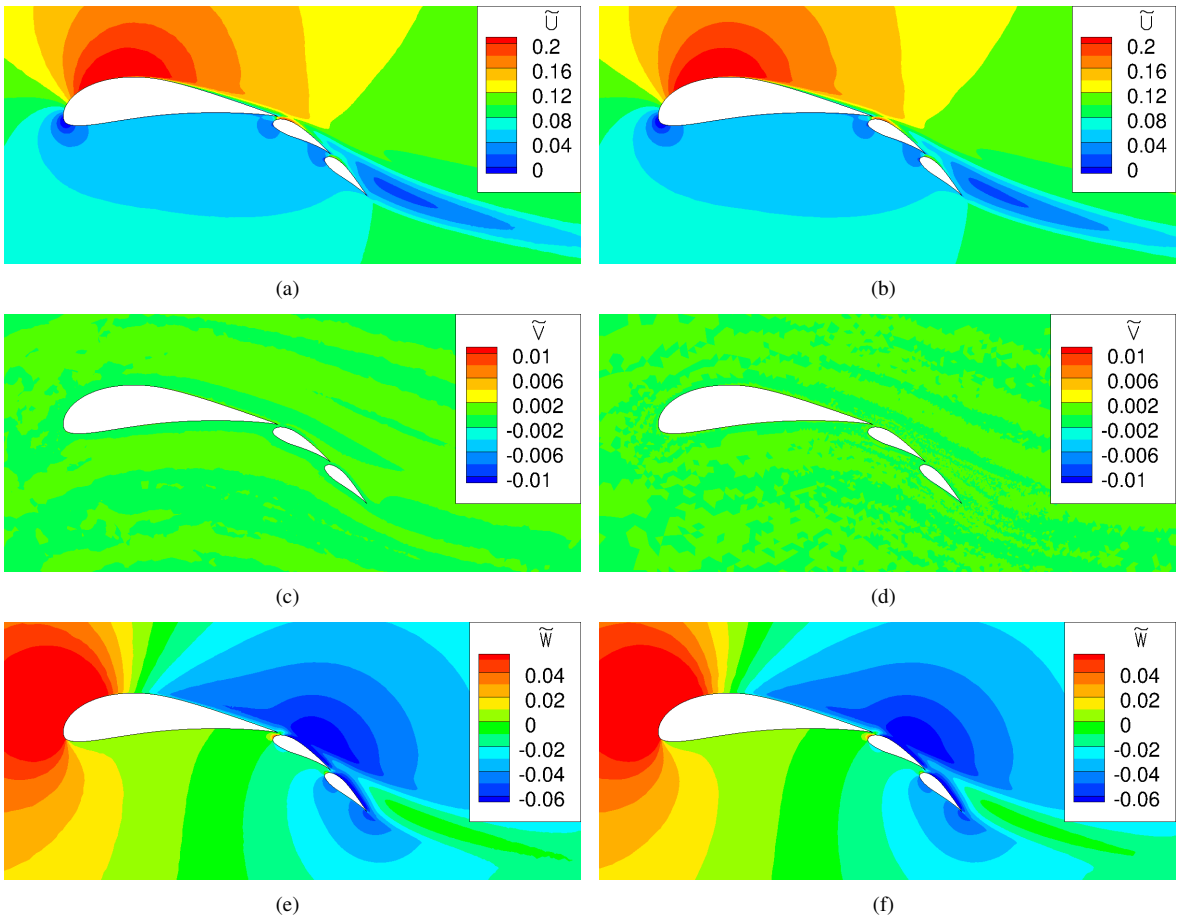

Figure 5.45: Computational flowfield plotting three components of velocity tensor including a) $\widetilde{u}$ at $\widetilde{x} = 0.00$, b) $\widetilde{u}$ at $\widetilde{x} = 0.05$, c) $\widetilde{v}$ at $\widetilde{x} = 0.00$, d) $\widetilde{v}$ at $\widetilde{x} = 0.05$, e) $\widetilde{w}$ at $\widetilde{x} = 0.00$, and f) $\widetilde{w}$ at $\widetilde{x} = 0.05$.

the reflection plane. As is seen in the subfigures, no discernible differences exist between the center-span slice and the reflection-plane slice. In addition, the contour plot of $\widetilde{v}$ indicates the spanwise velocity is zero at all locations in the flowfield. These two observations suggest that multielement airfoils with wake bursting can be accurately computed or tested in a two-dimensional manner.

5.6 Comparison between Computations and Experiments

As previously mentioned, differences were observed between the experimentally-captured burst-wake flowfield and the results as predicted by computational methods, and a detailed discussion of both the differences and the causes of these differences follows. In this section, results from experimental and computational tools are presented side-by-side with the same contour limits throughout this section to allow easy comparison between the data sets.

5.6.1 Baseline Comparison

An experimental and computational investigation of the Configuration 10 airfoil was presented earlier in this chapter through Secs. 5.3–5.5, and a detailed comparison of all the different tools is presented throughout this section. Computations were executed in both USM3D and MSES, and the grids for the simulations are presented in Fig. 5.46. As previously discussed, the wake region was refined for USM3D while the intrinsic streamline-fixed grid as computed in MSES does not allow significant grid control by the user. Results from the 7-hole probe, USM3D, and MSES are plotted together over approximately the same spatial location for comparison in Fig. 5.47, and significant differences between the three results are apparent. As discussed in Sec. 3.3, the viscous region of the MSES solution is not computed with the Navier-Stokes equations as only the Euler equations are solved throughout the domain. The outer Euler solution is coupled with the viscous region through the displacement thickness. As a result, data are not directly computed in the boundary-layer or wake regions of the flow, because similarity solutions are applied for the boundary layer profiles. Therefore, these regions are blanked out in the figure so as not to mislead the reader. As seen in the Fig. 5.47(c), the structured intrinsic grid is coplotted with the solution to make the wake region more clearly visible. When comparing the results, it is clear that the size and location of the main-element burst wake is different between the three data sets. A large, thick separated region is present for the USM3D simulation, which was computed using the SA turbulence model; a moderately-large wake was captured with the 7-hole probe; and a smaller, thinner wake was predicted using MSES. In addition to the size of the wake, the wakes begin to thicken significantly at different streamwise locations. Predictions from USM3D suggest that the wake begins to thicken at a point upstream of the flap 1 trailing edge while data from the 7-hole probe and MSES predict thickening near the mid-chord location of flap 2. It is known through prior experience that the boundary-layer equations, upon which the theory of MSES is based, poorly predict large, separated flows such as the flowfield presented in this document. Consequently, the discrepancies between the 7-hole probe and USM3D calculations are of more interest than comparisons to the MSES results. While RANS simulations have some difficulty predicting separated flows, it was expected that the experimen-

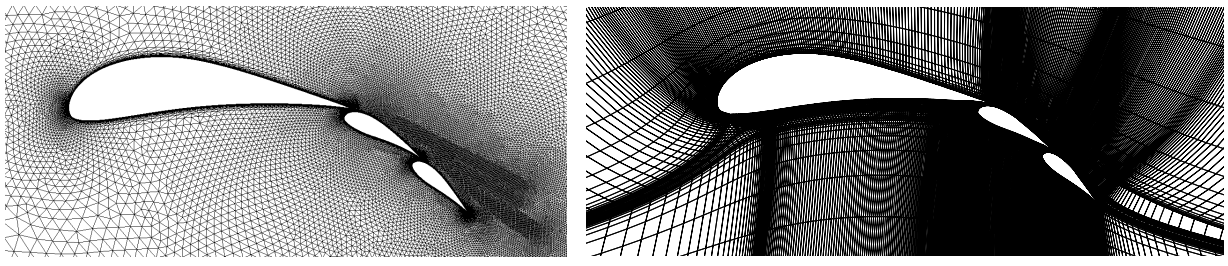

(a) (b)

Figure 5.46: Detailed view of computational grid used including a) unstructured tetrahedral grid (USM3D) and b) structured intrinsic grid (MSES).

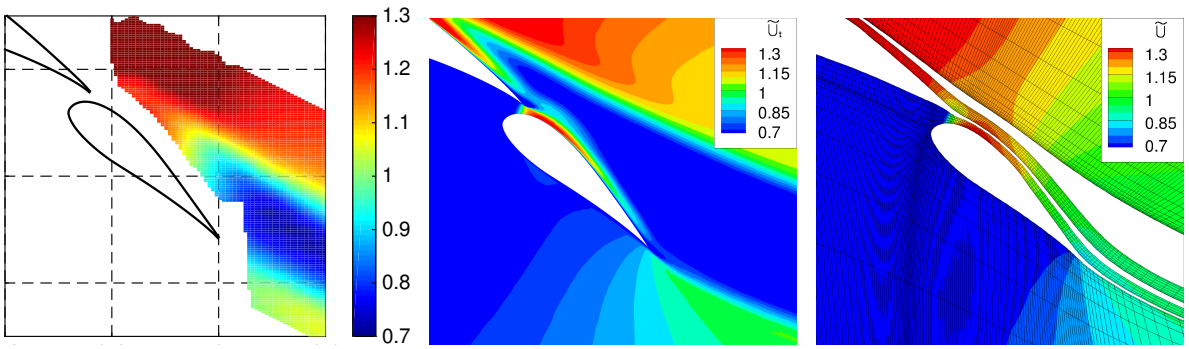

(a) (b) (c)

Figure 5.47: Burst-wake flowfield captured by a) 7-hole probe, b) RANS solver (USM3D), and c) inviscid/viscous coupled method (MSES).

tal and RANS results would agree more-closely than the results suggest. The effects of laminar-to-turbulent transition was not captured in these simulations; it is common to execute computations with fully-turbulent boundary layers. The reader is referred to Sec. 5.6.4 on page 159 for a discussion relating to fixed-transition computational simulations.

5.6.2 Test Section Wall Behavior

An investigation was performed to evaluate the behavior of the air on the surfaces of the test section to determine if any adverse aerodynamic effects were being caused by the walls. A layer of black adhesive contact paper was applied to the surface of the wind tunnel. The application of this contact paper proved to be extremely difficult due to the formation of bubbles under the contact paper, challenges maintaining alignment of the contact paper, and applying the paper in a secure manner such that the paper was not ripped off by the fast-moving air. In particular, it was also very difficult to apply the contact paper around the curved surfaces of the airfoil such that the paper remained attached to the wooden wind-tunnel floor. This paper was applied to ensure the cleanliness of the test section and to provide a dark background against which fluorescent dye could be easily visualized and photographed. Glass-cleaning solution was used to thoroughly clean the surface of the wind tunnel to which the paper was applied before installing the contact paper. After the paper was applied, a rag was used to apply motor oil and a compressed-nitrogen airbrush was used to apply the fluorescent leak-detector dye/mineral oil mixture. Efforts were taken to apply the mixture as uniformly as possible, but this was difficult to do over such a large spatial region. For further details on the techniques, the reader is directed to Sec. 3.2.12 on page 57.

Photographs at an α of 0 deg and freestream Reynolds number of 1×10^6 over the wind tunnel floor and sidewall are presented in Fig. 5.48. Despite numerous attempts by the researcher, a test was not successfully completed in

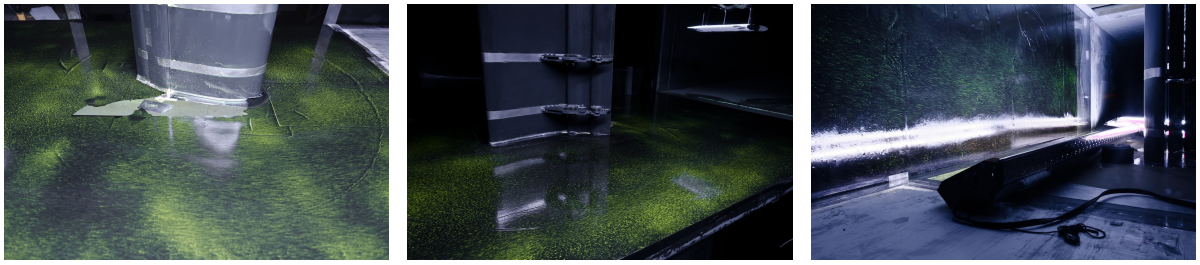

(a) (b) (c)

Figure 5.48: Surface oil flow visualization on wind tunnel a) floor over upper surface, b) floor around lower surface, and c) sidewall.

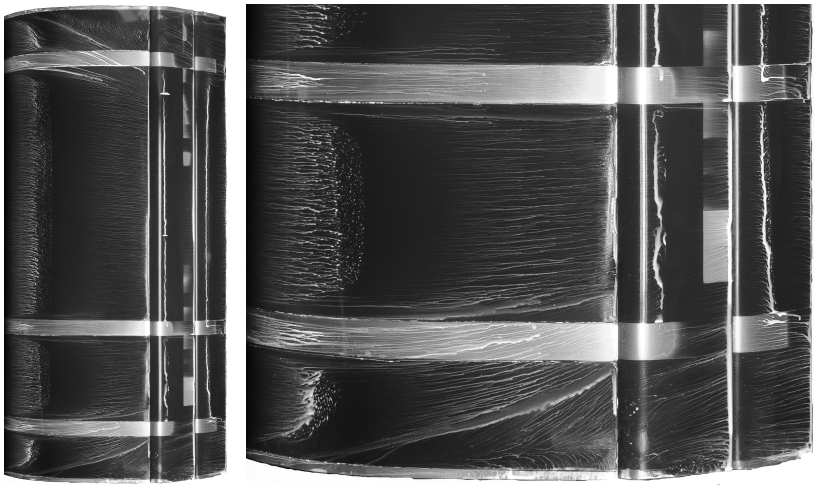

(a) (b)

Figure 5.49: Flow visualization showing juncture vortices on upper surface including a) wide view and b) detailed view.

which the contact paper remained attached at the junction between the airfoil upper surface and wind tunnel floor. This ripped contact paper is observed in Fig. 5.48(a). All three photographs indicate the flow is attached to the wind tunnel walls and floor.

The flow visualization of the upper surface warrants further investigation. A photograph capturing the full-span flow visualization is shown in Fig. 5.49 in which three-dimensional flowfield features are observed. Large vortices over the airfoil are observed at the junctions between the airfoil and both the ceiling and floors. Detailed examination of the floor-airfoil boundary photograph in Fig. 5.49(b) indicates that a large primary vortex exists in addition to a smaller necklace vortex. These two counter-rotating vortices introduce a spanwise component of velocity which invalidates the assumption that the flowfield was purely two-dimensional. The effect of these vortices is examined in detail later in this section.

5.6.3 Simulation of 2D Wind Tunnel Environment

It is widely known that the presence of wind tunnel walls affects the flowfield around a test article, and the effect is accentuated with high values of flow curvature and lift. The wind tunnel walls act as a no-flux plane and thus increase the chord-normal pressure gradient as the flow must return to the straight freestream conditions in less distance than if the walls were not present. To quantify the effects of the testing environment, a computational simulation was executed with the wind tunnel walls acting as the outer domain boundaries, as shown in Fig. 5.50. The quasi-two-dimensional simulation did not simulate the entire span of the airfoil due to computational cost and computing limitations. Instead, a slice of the airfoil was simulated with the wind tunnel walls. No-flux reflection-plane boundary conditions were specified for the top and bottom wind tunnel walls in addition to the reflection plane walls on the ends of the airfoil. The inlet plane was prescribed to be a characteristic inflow/outflow plane while the outlet plane was defined to be a full-extrapolation surface; this boundary condition was necessary to obtain computational convergence. A visualization of the computational domain and grid, with the wind tunnel walls defined by the outer edges of the domain, is presented in Fig. 5.50(a). The resulting flowfield, shown in Fig. 5.50(b), exhibits many of the same characteristics as the free-air computational simulations discussed earlier in this chapter. Results indicate a large, thick burst wake with a minimum velocity in the wake of approximately 0.2, which is significantly less than the experimentally-collected value of $\widetilde{U}_t = 0.71$. These results indicate that the differences between the experimental and computational results are not due to the pressure gradient caused by the presence of the wind tunnel walls as good agreement is seen between Fig. 5.50(b) and the previously-presented Fig. 5.47(b).

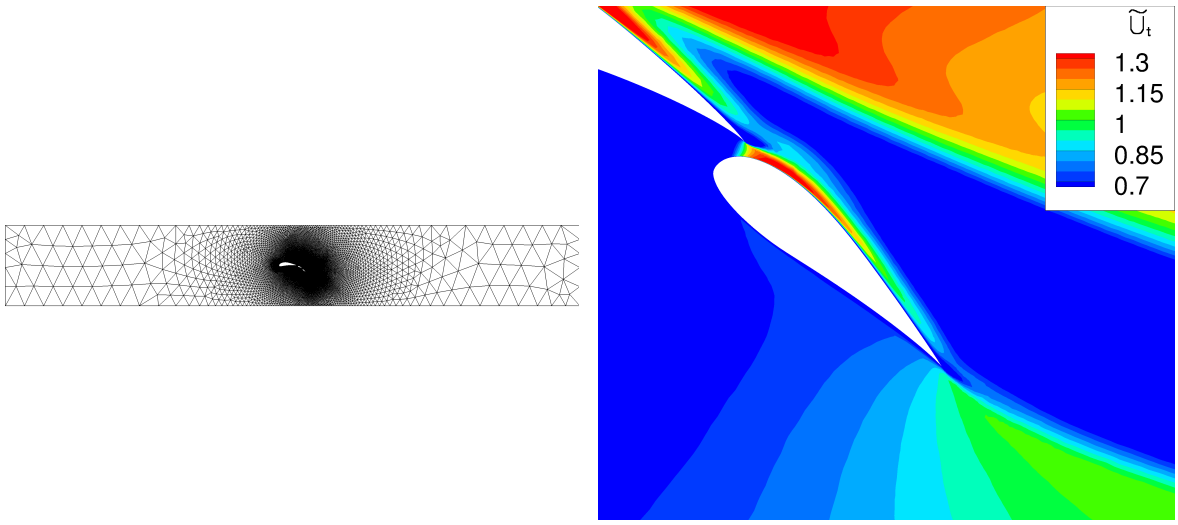

(a) (b)

Figure 5.50: Simulation of wind-tunnel test facility in USM3D solver including a) computational mesh and b) $\widetilde{U}_t$ contour plot.

5.6.4 Spanwise Wake Survey

Flow visualization results (Fig 5.49) indicate that the flowfield over the airfoil was not purely two-dimensional due to the presence of a necklace vortex and juncture flow interactions. Consequently, methods were implemented to determine the actual lift distribution over the airfoil to yield the sectional C_l at the spanwise position at which wake-survey data were collected. The governing wake-survey equations are developed and presented in Sec. 3.2.8, and in summary, the derivation yielded the spanwise circulation per unit length γ by

$$\gamma(z) = -\int_W \xi(y,z)dy, \tag{3.61}$$

and the spanwise sectional lift distribution as

$$C_l(z) = \frac{2}{U_\infty c(z)}. \tag{3.63}$$

These equations are implemented in the following portions of this section.

Experimental Results

A series of wake surveys were performed in the y-z plane at a constant x, or streamwise, location. The details of the testing methods are presented in the experimental methods chapter in Sec. 3.2.9 on page 45, and information in this section is dedicated to the discussion of experimental results. Results shown in Fig. 5.51 include both nondimensional total velocity $\widetilde{U}_t$ and nondimensional streamwise vorticity $\widetilde{\xi}$ coplotted with the wind tunnel walls (shown as solid black lines) and three-dimensional velocity vectors. Data are presented as if the reader were looking down the wind tunnel; the floor of the wind tunnel is on the bottom of the plot, the upper surface of the airfoil model (facing away from the control room) is on the left side of the figure, and the freestream velocity is going away from the reader and into the page. The directional arrows in the figure are all the same length in a three-dimensional volume with 45 deg arrowheads. However, when projected onto a two-dimensional plane, such as the plane in the figure, the skewness and perceived length of the arrows change based upon the velocity into the plane. Points with larger components of u yield arrows that are seen as shorter in length with increased arrowhead skewness. A flatter arrowhead indicates a larger component of u while an arrowhead with 45 deg head angle indicates no velocity in the x direction. The length of each of the vectors is also an indication of the magnitude of the total velocity, or speed, of the flow at each individual point. Efforts were taken to isolate the location of the important flowfield features, and experimental data were only taken in the regions of interest at a step size of 0.40 in ($0.0245c_{sys}$ or 1.02 cm) in $\widetilde{y}$ and 0.25 in ($0.0153c_{sys}$ or 0.635 cm) in $\widetilde{z}$; wake surveys took approximately 11 hours to complete and included $6,540$ data points. Data were taken as close to

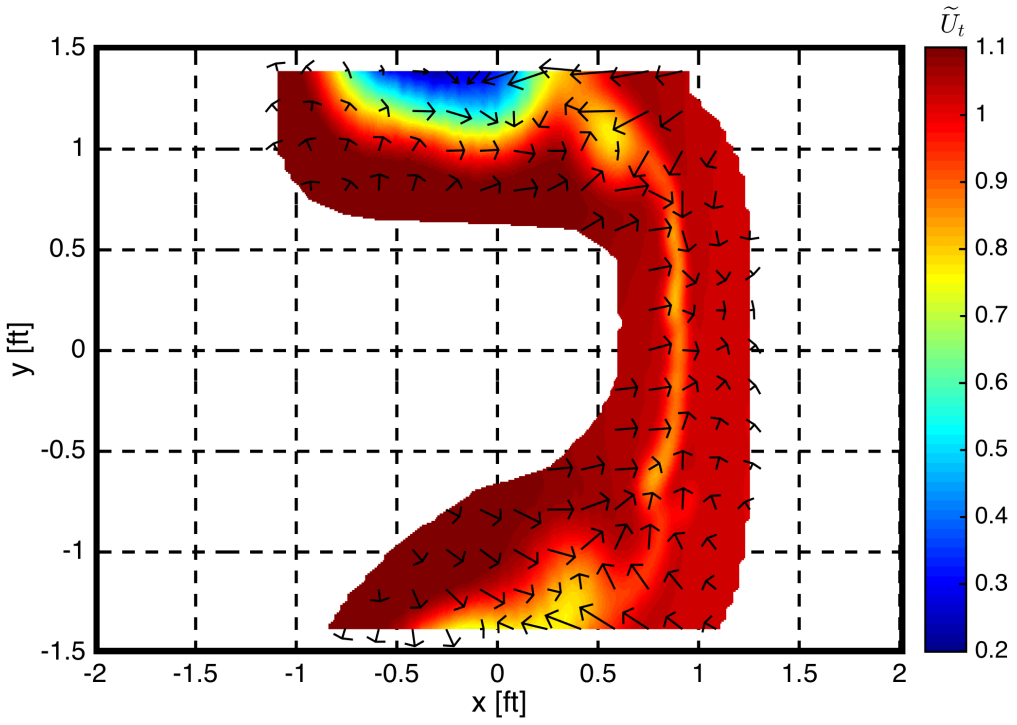

(a)

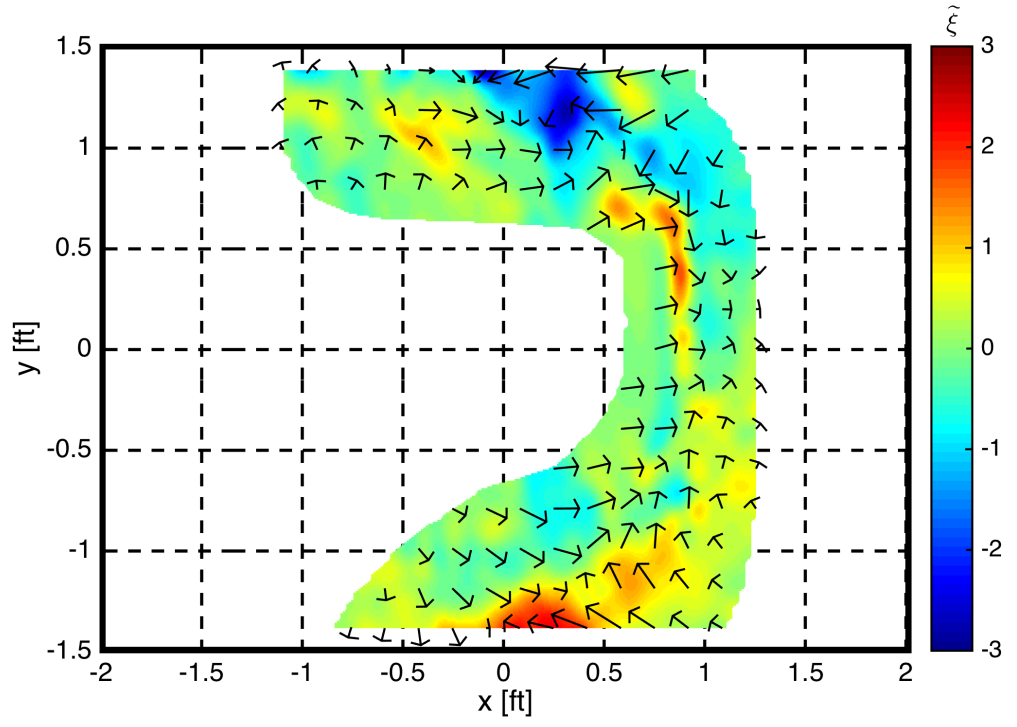

(b)

Figure 5.51: Wake survey in *y*-*z* showing wind tunnel walls, three-dimensional velocity vectors, and a) total velocity and b) streamwise vorticity ξ.

the wind tunnel floor and ceiling as was possible given experimental constraints from the size and orientation of the probe mount.

Consider first the $\widetilde{U}_t$ data plotted in Fig. 5.51(a) in which numerous key features of the flowfield are observed. A low-momentum wake region is observed at a wide range of $\widetilde{z}$ values at $\widetilde{y}$ of approximately 2.25 over the majority, but not entirety, of the airfoil span. In addition, a large vortex is observed both at the top of the test section and at the bottom of the test section as indicated by increased vorticity in the x direction. Finally, a region of low momentum is also observed near $(\widetilde{y}, \widetilde{z})$ of approximately (2.05, 1.60). The significance of these features are all worthy of discussion. As stated earlier, the airfoil wake is observed, and it is this wake that was used to determine the C_d of the airfoil when the airfoil polars were collected. It is curious to note that the wake does not extend over the entire span of the airfoil in the wind tunnel but seems to be mostly-two-dimensional in which $0.6 < \widetilde{y} < 1.5$. It is noted that the x-z wake survey data were collected at a $\widetilde{z}$ value of 1.171, and the wake is suggested to be two-dimensional in this location. The small low-momentum region observed at $(\widetilde{y}, \widetilde{z})$ of (2.05, 1.60) is due to the clamps supporting the flap closest to the ceiling. The flowfield is clearly not two-dimensional, as evidenced by the large vortices at the top and bottom of the test section and the three-dimensionality of the wake, despite the mostly two-dimensional airfoil geometry that was tested. (Slight three-dimensional effects are attributed to the flap clamps.) The presence of these vortices introduces significant three-dimensionality into the flowfield which alters the aerodynamic performance of the airfoil system including aerodynamic performance values and wake survey data. Results indicate that the vortex on the top of the test section may be associated with a larger momentum-deficit region than the vortex on the test section floor. When analyzing experimental results throughout this entire document, the reader is encouraged to recall the presence of these vortices.

A contour plot of nondimensional streamwise vorticity throughout the sampled domain is shown in Fig. 5.51(b). As data were only collected at one location in $\widetilde{x}$, vorticity values could only be calculated in the streamwise direction as spatial derivatives in the x direction could not be calculated. As was shown in Fig. 5.51(a), the wind tunnel walls are presented as solid black lines, and three-dimensional velocity vectors are also shown at select points throughout the region. A vortex sheet associated with the wake from the airfoil system is visible in the results at $\widetilde{y} \approx 2.20$, as are the two counter-rotating vortices at the top and bottom of the sampled domain. It is easy to observe the presence of these vortices as evidenced by $\widetilde{\xi}$. It is established in the literature that high-lift airfoils, such as the one tested in this research report, are sometimes adversely affected by the junction between the airfoil geometry and the test-section walls [158–160]. These juncture flows yield rotating vortices such as those observed in this dissertation. It is possible that the implementation of a strong boundary-layer control device may remove these vortices by removing the test-section boundary layer through the test section, although this hypothesis has not been tested.

Mathematical operations presented in Eqs. 3.61–3.63 ultimately yield the spanwise lift distribution over the airfoil, and results are presented in Fig. 5.52 in terms of both $\widetilde{z}$ and η where η is defined by

$$\eta = \frac{z}{b}. \tag{5.37}$$

The case in which $\eta = 0$ is constrained to the lower location at which data were collected, and $\eta = 1$ is associated with the upper edge of the sample domain. As data were only collected in the domain as shown, the lift distribution could only be determined in the region in which data were collected. Consequently, it was necessary to assume that the airfoil exists between the regions in which data were collected. While this assumption is not entirely valid due to aerodynamic effects outside the sample domain and close to the wind tunnel walls, it is taken to be a reasonable assumption for the current discussion. The ultimate spanwise lift distribution for the multielement airfoil is presented in Fig. 5.52, and the location of the previously-discussed *x*-*y* wake curves is marked with a dashed red line. As seen in the figure, the spanwise load distribution is not constant, which was the expected result given the conclusions derived from Fig. 5.51. Surprisingly-large decreases in C_l are observed near both ends of the airfoil, and some deviations are present between these edges. The sectional lift distribution is larger at locations closer to the tunnel floor (smaller values of η) than those observed closer to the ceiling. Most significantly, the values of C_l at the spanwise location at which the *x*-*y* surveys were executed is suggested to be 2.78, slightly more than the entire-span value presented in Fig. 5.3, but less than the computational simulations at α of 0 deg.

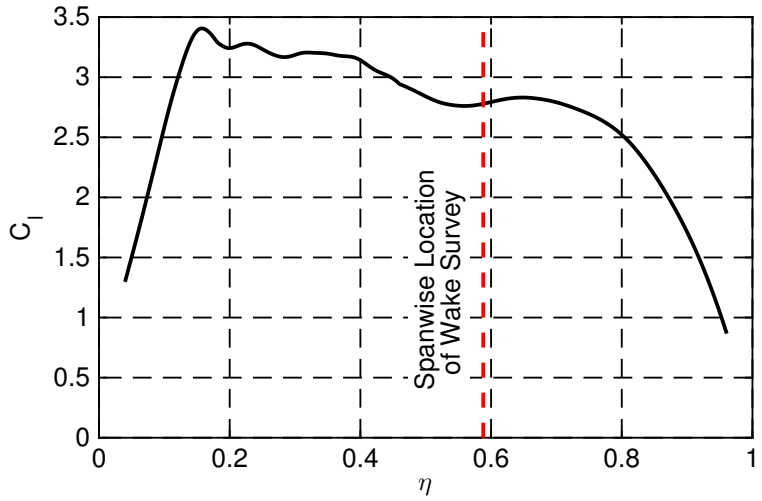

Figure 5.52: Spanwise lift distribution of airfoil with wake-survey sample location marked by dashed red line.

Computational Simulations at Desired Sectional C_l with Fixed Transition

To further compare the computational and experimental data sets, a RANS simulation with the SA turbulence model was performed in which the desired C_l was prescribed to be 2.78 (the sectional C_l at the span station at which the x-y wake survey data were collected). Upon convergence, the α for the computational flowfield was determined to be -5.52 deg. The experimentally-collected 7-hole probe data and the USM3D-calculated flowfield are both presented in Fig. 5.53. While the agreement between the two flowfields is better for the case in which C_l was matched instead of α, discrepancies between the two data sets still exist as the burst wake region is predicted to be larger in the computational simulation than the experimental results. In addition to the larger, thicker wake, the RANS simulation predicted a minimum total-velocity value ($\widetilde{U}_{t,min}$) to be 0.36 while the experimental data suggest a minimum total velocity of 0.71. Thus the computational simulation yields a thicker wake with less momentum than the experimental data suggest. It is again stated that these computational simulations were performed with fully-turbulent boundary layers over all three elements (as is the standard case for most computational predictions).

It is known that low Reynolds number flowfields, such as those examined in this project, are affected by the laminar-to-turbulent transition point on the airfoil. Consequently, some fixed-transition computations were executed with a developmental version of USM3D. The transition points for the airfoil were determined with MSES, and these transition points were specified to the NEWTL module of the USM3D program. The methods employed in USM3D force laminar boundary-layer development for a user-specified range of airfoil coordinates. As previously stated, MSES was utilized to determine the transition point on the upper and lower surfaces for all three elements,

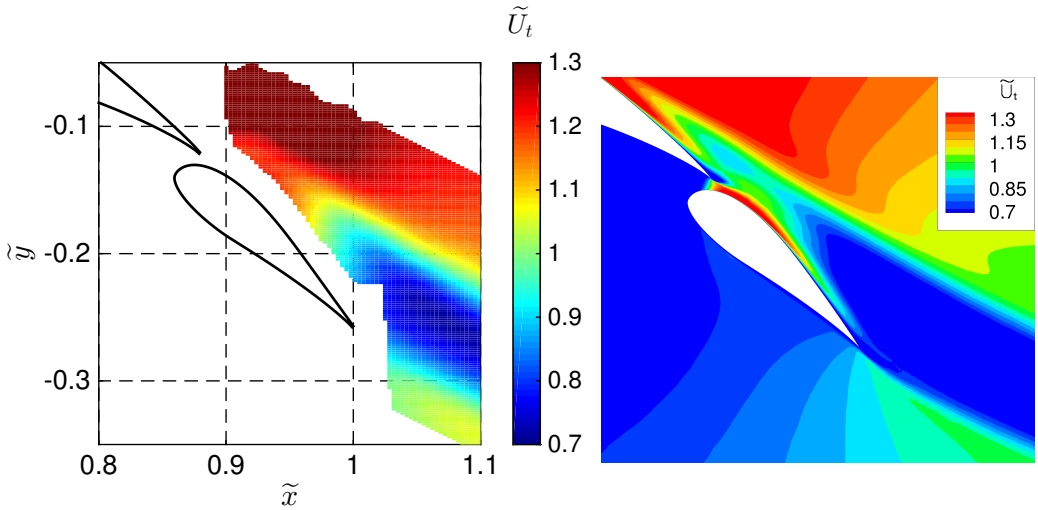

Figure 5.53: Comparison between experimental data and computational data at $C_l = 2.78$ including a) 7-hole probe data and b) USM3D results.

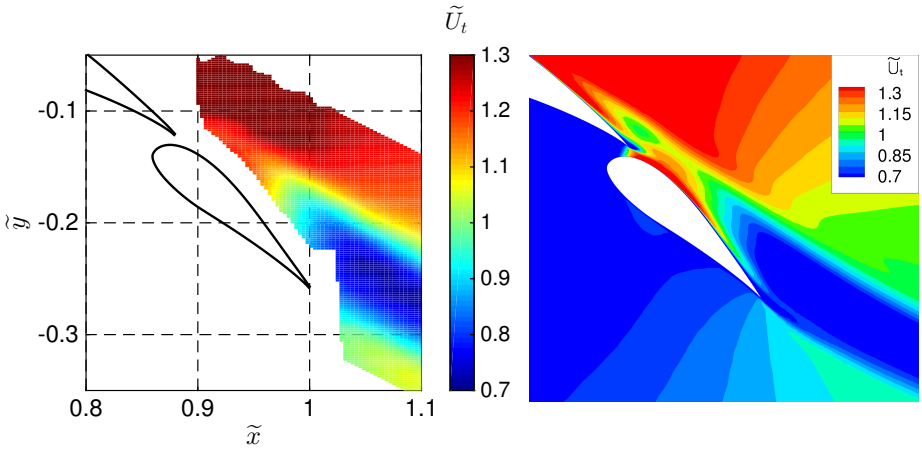

Figure 5.54: Burst-wake flowfield captured by a) 7-hole probe and b) fixed-transition RANS solver (USM3D).

and these transition points were declared to NEWTL through an input file. Figure 5.54 presents experimental and computational results at $C_l = 2.78$ with fixed transition for all three elements. As seen in the figure, better agreement between the experimental and computational results is observed than for the baseline comparison shown above in Fig. 5.47. Computations are still observed to over-predict the extent of wake bursting, but the difference between the two results are markedly less than those discussed earlier in this document. By including the effect of laminar-to-turbulent transition and specifying the desired C_l, reasonable agreement is observed between the experimental and computational results. Consequently, it is stated that wake bursting is indeed affected by the transition point over each airfoil element, and computations must be performed with fixed transition to accurately predict the flowfield.

5.7 Summary of Baseline Airfoil Aerodynamics

Burst wakes for a three-element airfoil were explored and studied using a variety of experimental and computational techniques. A set of operating conditions were determined for which the flow was attached to the surface of all three airfoil elements but in which wake bursting was observed in the flowfield. Attached flow was verified through surface oil flow visualization. Aerodynamic performance data were collected, and results indicate the large burst wakes effectively decamber the airfoil system at a given angle of attack. That is to say that the wakes cause less curvature in the flow when compared with an inviscid flowfield in which burst wakes are not present. The decambering of the airfoil system results in a decreased lift-curve slope relative to typical two-dimensional airfoil values.

Two different probes, including a split-film probe and a 7-hole probe, were used to capture the off-surface flowfield in a low-speed, low-turbulence wind tunnel in a variety of spatially-continuous wake surveys. Agreement between the two probes was acceptable but not perfect when different experimental effects were considered and evaluated.

Numerous metrics were developed to define wake thickness and other important features of the flowfield. Data were collected over a wide spatial region so that the development and formation of the burst wakes could be examined, and results suggest a thickening of the asymmetric burst wakes downstream of the main-element trailing edge. The unsteady data from the split-film probe yielded a variety of turbulence quantities and frequency content throughout the flowfield. These results indicate that increased turbulence levels exist in the burst wakes, and that the majority of the turbulence was produced in the shear layers surrounding the burst wakes.

Computational simulations were executed with a coupled viscous/inviscid panel solver and a fully-viscous Reynolds-averaged Navier Stokes (RANS) program. A quasi-two-dimensional domain was implemented for the RANS solver, and results indicate that the time-averaged burst-wake flowfield is two-dimensional with no significant spanwise variation in the results. The importance of increased grid resolution in the wake region was confirmed, and a grid-convergence study indicated the mesh resolution was sufficiently fine. An analysis of the results indicates that the four turbulence models utilized in the flowfield all significantly over-predict the size and momentum deficit of the burst wakes at all angles of attack.

A detailed comparison of the experimental and computational flowfields suggested surprisingly-poor agreement between the two sets of tools. Experimental data indicated less wake bursting at a given α relative to the fully-turbulent computational simulations. A thorough investigation to determine artifacts of the wind-tunnel testing environment was performed, and some of these effects were successfully quantified. The flow-visualization and wake-survey data indicate significant juncture-flow interference effects between the airfoil and the wind tunnel walls that resulted in two large vortices. These vortices in turn created a three-dimensional flowfield in the wind tunnel. Additional wake survey data were collected to determine the spanwise lift distribution, and the sectional C_l at which the wake survey data were taken was determined. Computational simulations at this determined value of C_l yielded better agreement between the computational and experimental results, but some differences remained. Finally, some computational simulations were performed at the desired C_l that incorporated the transition point, and reasonably-good agreement was found between the computational and experimental results. Thus, the importance of the laminar-to-turbulent transition point cannot be understated when simulating low-Reynolds-number wake bursting.

Chapter 6

Additional Configuration Results

A variety of multielement airfoil geometry configurations were studied to understand the effects of various parameters on the presence, strength, and behavior of the burst wakes. These efforts were taken to yield insight into the behavior of the burst wakes due to geometric variations such that the aerodynamic performance can be maximized by minimizing the strength of the burst wake. Previous research indicates that the aerodynamic flowfield is dependent upon the position of the flaps, the freestream α, and the freestream Re [35, 161]. Numerous different airfoil geometries were analyzed with computational tools, but only a few select cases were experimentally studied in the wind tunnel. Tests in the wind tunnel frequently took in excess of 6 hr with the longest survey taking 12 hr. On the other hand, computational simulations with a low-order viscous/inviscid-coupled method could be readily computed in a matter of seconds. Five different configurations of the baseline MFFS(ns)-026 airfoil were selected for extensive computational and experimental analysis. Each of these configurations isolated a change in a parameter of the relative coordinate system (gap, overhang, and deflection angle) relative to the baseline configuration, Configuration 10. Information in this chapter is solely dedicated to a discussion of these parametric changes; the reader is referred to Chap. 5 for an extensive discussion of Configuration 10.

This chapter is organized in the following manner. A discussion of various metrics to quantify wake bursting are presented first in the chapter. Next, a set of parametric sweeps are presented in which low-order computational methods were employed to analyze a wide variety of MFFS(ns)-026 configurations at different freestream conditions. Then, a thorough investigation of wind tunnel results is presented corresponding to geometric changes in gap size, overhang distance, and relative deflection angle. At the end of the chapter, a summary of the key results and findings regarding the location of the flaps is presented.

6.1 Additional Wake Metrics

A variety of metrics were developed to quantify the extent to which a wake was burst, and the previously-discussed h_w metric discussed in Sec. 5.3.6 is one such metric that was used for the experimental results. As will soon be apparent to the reader, some types of data were more conducive to be quantified by a given metric than another type of data. For

instance, the h_w metric previously discussed with the experimental results cannot be applied to solutions calculated by MSES because computations in MSES do not yield the values of total pressure in the wake region as this portion of the flowfield is not explicitly computed. Instead, Falkner-Skan boundary-layer profiles are applied between the upper- and lower-surface dividing streamlines. It is noted that metrics presented in this section do not replace the metrics presented in Chap. 5, but rather these new metrics supplement the previously-discussed metrics.

Results calculated by MSES are considered suitable to be analyzed from from a boundary-layer perspective as the boundary-layer thickness δ can be readily calculated from parameters which are calculated by MSES. The kinematic shape parameter H_k was calculated by [90]

$$H_k = \frac{\overline{H} - 0.290M_e^2}{1 + 0.113M_e^2} \tag{6.1}$$

from which the boundary-layer thickness δ could be found by

$$\delta = \theta \left(3.15 + \frac{1.72}{H_k - 1} \right) + \delta^*. \tag{6.2}$$

The dividing streamlines defining the upper and lower edges of the inviscid flowfield around an airfoil element are offset from the surface by a distance δ^* normal to the airfoil surface. In addition to defining the outer edge of a boundary layer around an airfoil, these dividing streamlines also specify the edges of a viscous wake behind an airfoil. Therefore, it is possible to calculate the distance between the two dividing streamlines at any value of x or ξ in the wake region. (The reader is reminded that ξ is the streamwise coordinate in a coordinate system fixed to the streamline and streamline-normal directions as previously discussed in Sec. 3.3.2.) Wake thickness based upon this definition is defined as δ_w and $\delta_{w_{\xi-\eta}}$ Cartesian and intrinsic-grid coordinate systems, respectively. A schematic defining these two metrics for both coordinate systems is plotted in Fig. 6.1 in which the wake from one airfoil is plotted with the wake-thickness definitions. In addition to the dividing streamline positions, MSES also determines the wake centerline location, as defined by the point of minimum velocity for a given value of ξ, and this point is plotted as a red square in the figure.

While the maximum wake thickness $\delta_{w_{\xi-\eta}}$ can be easily calculated in the streamline-fixed coordinate system, it is desired to determine δ_w and other wake parameters in the more-standard x-y coordinate system. To calculate these metrics in the Cartesian coordinate system, it is first necessary to determine the value of x for which δ_w is maximized. By definition, the location of maximum thickness is the point at which the rate of change of δ_w in the x direction is 0, or rather

$$\frac{\partial \delta_w}{\partial x} = 0. \tag{6.3}$$

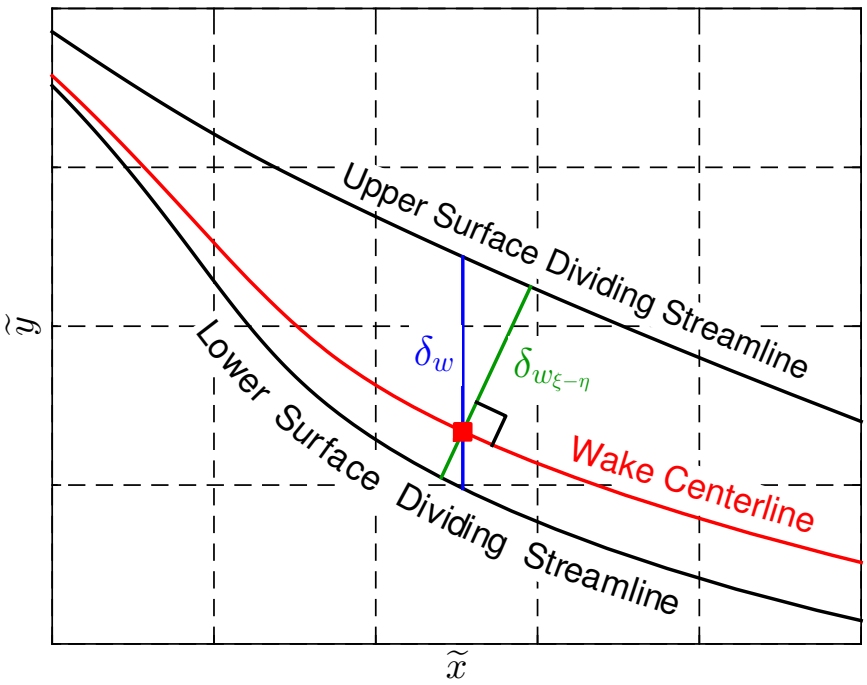

Figure 6.1: Definition of wake thickness in Cartesian and intrinsic-grid coordinate systems.

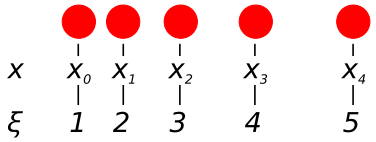

Figure 6.2: Coordinate transformation from streamwise coordinate x to computational coordinate ξ.

It is possible to compute the value of $\partial\delta_w/\partial x$ by implementing a central-difference five-point-stencil scheme according to the standard equation

$$f'(x) \approx \frac{-f(x+2h)+8f(x+h)-8f(x-h)+f(x-2h)}{h} \tag{6.4}$$

where h is the grid spacing between points and is a constant value. However, as the computational grid spacing is non-uniform in the x direction, it was necessary to map the Cartesian coordinate x to a computational coordinate ξ, as shown in Fig. 6.2. As depicted in the figure, the computational coordinate ξ is equal to the grid point index number for a specific coordinate. After this mapping was performed, it is clear that $\Delta\xi = 1$ in the computational domain. The chain rule can be applied to Eq. 6.3 to calculate the wake thickness by

$$\frac{\partial\delta_w}{\partial x} = \frac{\partial\delta_{w_{\xi-\eta}}}{\partial\xi}\frac{\partial\xi}{\partial x} = \frac{\left(\frac{\partial\delta_{w_{\xi-\eta}}}{\partial\xi}\right)}{\left(\frac{\partial x}{\partial\xi}\right)}. \tag{6.5}$$

The general finite-difference formula presented in Eq. 6.4 can be combined with Eq. 6.5 to yield [157, 162]

$$\frac{\partial \delta_{w_{\xi-\eta}}}{\partial \xi} = \frac{-\delta_{w_{\xi-\eta},i+2} + 8\delta_{w_{\xi-\eta},i+1} - 8\delta_{w_{\xi-\eta},i-1} + \delta_{w_{\xi-\eta},i-2}}{12\Delta} \tag{6.6a}$$

$$\frac{\partial x}{\partial \xi} = \frac{-x_{i+2} + 8x_{i+1} - 8x_{i-1} + x_{i-2}}{12\Delta} \tag{6.6b}$$

in which i corresponds to the i^{th} wake-centerline point and $\Delta = 1$ as the index difference between any two coordinates in ξ is 1. Substitution of Eq. 6.6 in to Eq. 6.5 yields

$$\frac{\partial \delta_w}{\partial x}_i \approx \frac{-\delta_{w_{\xi-\eta},i+2} + 8\delta_{w_{\xi-\eta},i+1} - 8\delta_{w_{\xi-\eta},i-1} + \delta_{w_{\xi-\eta},i-2}}{-x_{i+2} + 8x_{i+1} - 8x_{i-1} + x_{i-2}}. \tag{6.7}$$

Consider the case presented in Fig. 6.3 in which the upper and lower surface dividing streamlines are coplotted with the wake centerline. As shown in Fig 6.3(a), the value of $\partial \delta_w / \partial x$ is not necessarily zero at a specific ξ coordinate, but rather the point, depicted as a solid red square, occurs between computational coordinate i and $i+1$. While the exact point of maximum thickness in Cartesian coordinates cannot be precisely known, a good estimate can be made. If it is assumed that

$$\frac{\partial^2 \delta_w}{\partial x^2} = 0 \tag{6.8}$$

and thus

$$\frac{\partial \delta_w}{\partial x} = C \tag{6.9}$$

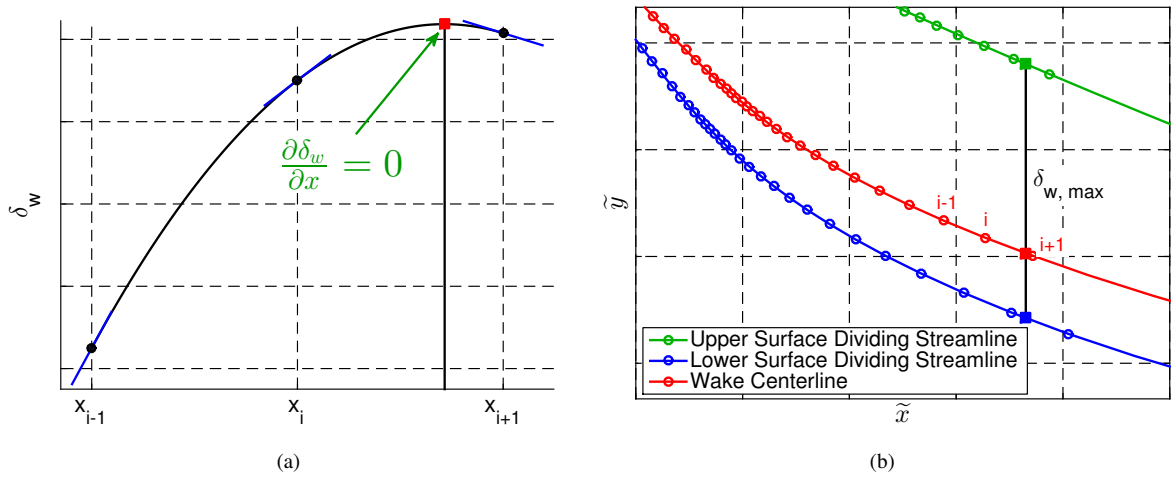

Figure 6.3: Calculation of maximum wake thickness and point of maximum thickness including a) wake thickness and growth rate and b) dividing streamlines coplotted with wake centerline and $\delta_{w,\,max}$.

in which C is a constant, estimates for $(x,y)_{\delta,max}$ and δ_{max} can be found by

$$x_{\delta,max} = x_i + \left| \frac{\left.\frac{\partial \delta_w}{\partial x}\right|_i}{\left.\frac{\partial \delta_w}{\partial x}\right|_{i+1} - \left.\frac{\partial \delta_w}{\partial x}\right|_i} \right| (x_{i+1} - x_i) \tag{6.10a}$$

$$y_{\delta,max} = y_i + \left| \frac{\left.\frac{\partial \delta_w}{\partial x}\right|_i}{\left.\frac{\partial \delta_w}{\partial x}\right|_{i+1} - \left.\frac{\partial \delta_w}{\partial x}\right|_i} \right| (y_{i+1} - y_i) \tag{6.10b}$$

$$\delta_{max} = \delta_i + \left| \frac{\left.\frac{\partial \delta_w}{\partial x}\right|_i}{\left.\frac{\partial \delta_w}{\partial x}\right|_{i+1} - \left.\frac{\partial \delta_w}{\partial x}\right|_i} \right| (\delta_{i+1} - \delta_i) \tag{6.10c}$$

which can be thought of as a linear weighted average of the values at i and $i+1$. These estimated values of $(x,y)_{\delta,max}$ are plotted as a solid red square in Fig. 6.3(b). The corresponding locations on the dividing streamline at $x_{\delta,max}$ are presented as solid green and blue squares in the figure. The discussion presented in this section regarding the determination of δ_{max} can be extended to estimate x, y, or δ_w given a desired value of one of the parameters.

A new parameter, denoted as the wake-thickness parameter WTP, was developed and utilized to quantify the overall thickness of a wake, and thus the degree to which the wake exhibited bursting characteristics. This parameter is visualized in Fig. 6.4, and it is defined as the integrated area between the upper- and lower-surface dividing streamlines between an upstream point x_u and a downstream point x_d as in

$$WTP = 1000 \int_{x_u}^{x_d} \left(y_{\text{upper dividing}} - y_{\text{lower dividing}} \right) dx. \tag{6.11}$$

The value of x_d was selected to be the estimated value of $x_{\delta,max}$ as calculated in Eq. 6.10(a), and the limits of integration were thus defined to be

$$x_d = x_{\delta,max} \tag{6.12a}$$

$$x_u = \max \left(\begin{bmatrix} x_d - 0.15 \\ x_{te} \end{bmatrix} \right) \tag{6.12b}$$

in which x_{te} is the trailing-edge x coordinate.

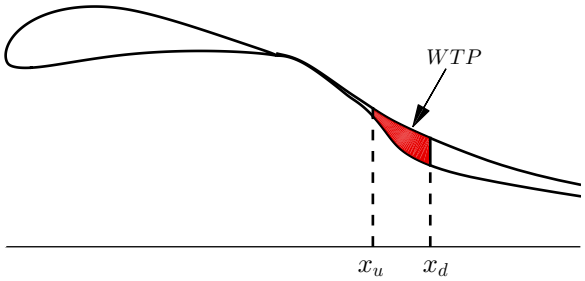

Figure 6.4: Visual representation of wake-thickness parameter WTP.

6.2 Computational Parametric Sweeps

Previous research indicates that the position of flap elements in a multielement airfoil affects the aerodynamic performance and wake development of the airfoil. Consequently, a wide variety of airfoil systems with the MFFS(ns)-026 airfoil were computationally examined to determine the relationship between flap position and wake bursting. Four different parametric sweeps were performed with MSES totaling 6,088 different computational simulations requiring nearly 51 hours of computational time, and these sweeps are presented in this section. The first three parametric sweeps examine the effect of flap 1 and flap 2 position in which the gap size and overhang distance are equal for both flaps with a variety of freestream conditions. A comprehensive sweep examining both the position of flap 1 and flap 2 at different gap size and overhang distances is presented last in this section.

6.2.1 Effect of Flap 1 and Flap 2 Location at Equal Relative Coordinates

A parametric sweep was performed at an α of 0 deg and a freestream Reynolds number of 1×10^6, which are the same freestream conditions for Configuration 10, which was previously discussed in Chap. 5. For this study, the flaps were located in the same relative coordinate position such that $gap_1 = gap_2$ and $overhang_1 = overhang_2$ but $\delta_1 \neq \delta_2$. More specifically, it δ_1 and δ_2 were defined to be 26.1 and 16.2 deg, respectivitely. Relative coordinates included gap sizes ranging between 0.005 and 0.05 while overhang distances were between -0.03 and 0.06. The reader is reminded that the gap size and overhang distance are nondimensionalized by the multielement-airfoil system chord length. A variety of aerodynamic performance parameters, such as C_l, C_d, and l/d, and wake metrics, as presented in Sec. 6.1, were determined for each case. Aerodynamic performance parameters are presented in Fig. 6.5 in which the contour plots are only presented in regions which were geometrically possible (i.e. configurations for which both gap size and overhang distance are small) and for which MSES converged. In general, convergence for numerous configurations was obtained at gap sizes greater than 0.01. The x and y axes in the figure are arranged in a manner that is visually representative of an airfoil in which the freestream velocity is from the left side of the figure to the right side of the figure. In this manner, configurations with larger overhang distances (that is to say the flap is tucked under the previous

element more than than that of smaller overhang distances), are presented on the left side of the figure. In addition, configurations with a larger gap size are shown on the lower portion of the figure, as if the flap were moving further away from the upstream element. All plots are presented over the same domain.

As seen in Fig. 6.5(a), the location of the two flaps affects the value of C_l by as much as 19% in the region computed. Variations in the overhang distance are observed to have a larger effect upon C_l than the gap size. This result is expected due to the circulation effect for multielement airfoils in which a flap increases the circulation, and thus lift, of the previous element by increasing the velocity, or decreasing C_p, at the trailing edge of the upstream element [4]. Data show that the effect of gap size is markedly less than that of the overhang distance; the largest changes in gap size for a given $overhang_{1,2}$ are less than 5% while different overhang distances cause variations in excess of 15%. Large values of C_l are observed for overhang distances between 0.01 and 0.04 and gap sizes between 0.01 and 0.03 with a maximum value of nearly 3.5.

Drag data shown in Fig. 6.5(b) present the relationship between C_d and the relative position of flap 1 and flap 2. It is observed that the C_d can vary as much as 38% in the range of flap positions. In general, drag is minimized at smaller, and even negative, overhang distances and small gap sizes. Similar to the previously-discussed C_l relationship, the overhang distance affects C_d more than the gap size. As seen in the figure, C_d varies as much as 20% for a range of

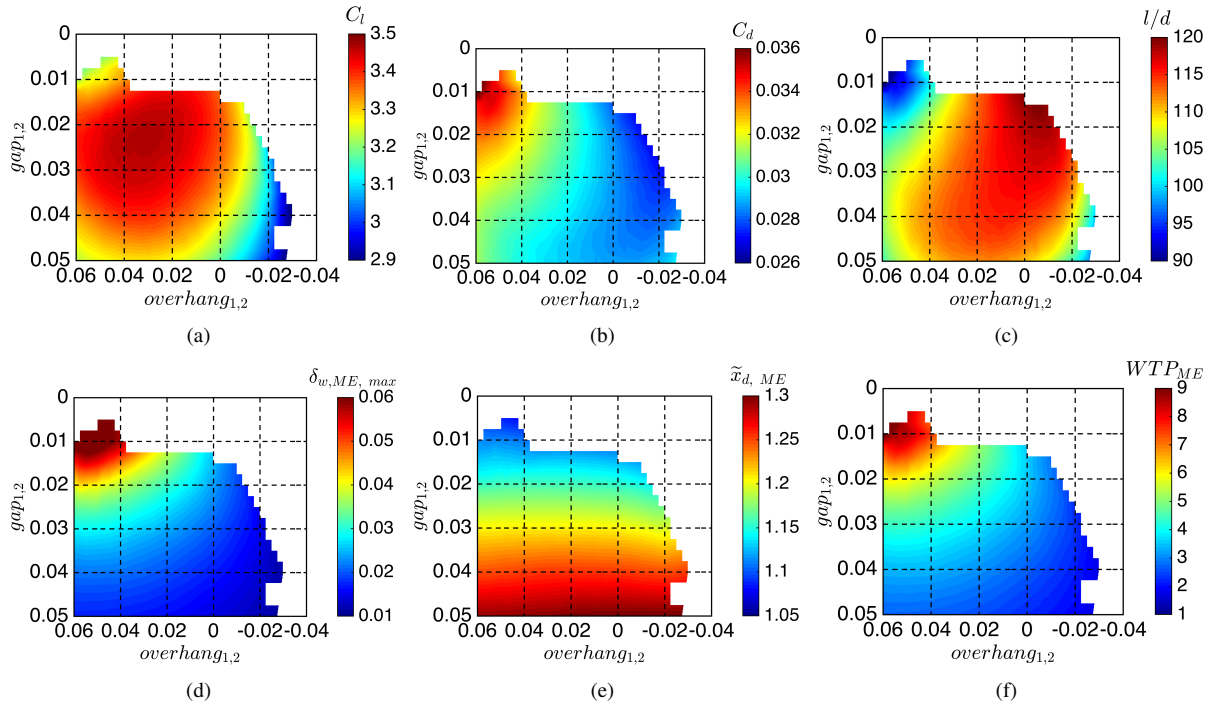

Figure 6.5: Effect of flap location in which gap_1=gap_2 and $overhang_1$=$overhang_2$ and δ_1=26.1 deg and δ_2=16.2 deg for freestream α=0 deg and Re=1×10^6 including a) C_l, b) C_d, c) l/d, d) $\delta_{w\ ME,\ max}$, e) $\widetilde{x}_{d,\ ME}$, and f) WTP_{ME}.

overhang distances at a constant gap size while maximum variations in C_d for variable $gap_{1,2}$ at a given $overhang_{1,2}$ are as high as 15%. The differences between these two maximum values are less than the differences observed with respect to C_l.

Aerodynamic efficiency, defined as l/d, as a function of flap position, is plotted in Fig. 6.5(c). Similar to the previous observations with C_l and C_d, l/d is more affected by changes in overhang distance than gap size in the region presented. Increased values of l/d are observed for small gap size and small overhang distances with decreased performance at larger overhang distances. This observation indicates that the variations in C_d have a larger effect than the variations in C_l for configurations with a small gap size and small overhang distance in which values of l/d are observed in excess of 120. High-lift systems are many times constrained by a desired value of C_l; thus it is desired to maximize l/d for positions near maximum C_l for a given α. As previously mentioned, elevated values of C_l are observed for $0.01 \leq overhang \leq 0.04$ and $0.01 \leq gap_{1,2} \leq 0.03$, and l/d is slightly decreased relative to the maximum value of l/d in the results. Thus, a configuration for which C_l is maximized may only decrease l/d by approximately 8% is more desirable than one for which l/d is maximized but a drop in C_l may be as much as 10%. While the tradeoff between maximizing l/d or C_l are of similar values, design engineers of high-lift systems typically aim to maximize C_l instead of l/d as aircraft performance in takeoff or approach performance, including approach speed and rotation speed, is closely related to C_l.

As discussed in Sec. 6.1, a variety of wake metrics can be used to quantify the extent to which a wake is burst. Computational and experimental results indicate the main-element wake bursts more than the wake from either flap 1 or flap 2, and therefore wake metrics were only calculated for the main-element wake. One of these metrics, δ_w, is the thickness of the wake in an x-y coordinate system at a range of $\widetilde{y}$ values. The maximum wake thickness for the main-element wake, denoted as $\delta_{w,ME,\,max}$, is presented in Fig. 6.5(d). For clarification, it is pointed out that $\delta_w,\ ME,\ max$ is the maximum value of δ_w for the main element ("ME"). Interestingly, the maximum thickness is approximately the same for the half of the domain extending from the lower left corner of the plot (large gap size and large overhang distances) to the upper right corner (small gap size and small overhang distance) across all overhang distances. Values of $\delta_{w,ME,\,max}$ are observed to be less than 0.02 in this region. The maximum wake thickness increases rapidly at increased overhang distances and decreased gap sizes to as much as 6 times thicker than other configurations. As previously mentioned, the smallest wake thicknesses are observed at small (even negative) overhang distances and large gap sizes. This trend is expected because C_l decreases in this portion of the plot due to decreased circulation effect and decreased velocity (or increased C_p) for which the main element trailing edge dumps the flow. Regions with the largest C_l correspond to moderately-thick wakes while configurations for which l/d is maximized contain small-to-medium sized wakes.

A second wake metric, the location at which the maximum thickness occurs, is denoted as $\widetilde{x}_{d,\,ME}$ and results are plotted in Fig. 6.5(e). This value is the x coordinate at which the $\delta_{w,ME,\,max}$ occurs, as defined in Fig. 6.3. Curiously, this value is observed to be mostly independent of $overhang_{1,2}$ and is essentially solely dependent upon $gap_{1,2}$. Only slight variations in $\widetilde{x}_{d,\,ME}$ are observed for smaller overhang distances in which $\widetilde{x}_{d,\,ME}$ decreases for a given gap size. As seen in the figure, decreased values of $\widetilde{x}_{d,\,ME}$ occur at smaller gap sizes while increased $\widetilde{x}_{d,\,ME}$ are observed at increased gap sizes. Thus, the wake continues to thicken at a larger range of $\widetilde{x}$ for large gap sizes, but the wake for small gap sizes thickens over a decreased range of $\widetilde{x}$.

Finally, the integrated main-element wake area WTP_{ME}, as defined in Fig. 6.4, is shown in Fig. 6.5(f). Trends in WTP_{ME} closely mimic the trends in $\delta_{w,ME,\,max}$ with decreased values of WTP_{ME} observed at large gap sizes and small overhangs, and increased WTP_{ME} is present for configurations with small gap size and large overhang distance. Results indicate that the WTP_{ME} increases by as much as a factor of 9 over the domain sampled. Consequently, it is observed that size of the wake, or the extent to which a wake is burst, is largely dependent upon the location of the two flaps. In general, increases in WTP_{ME} are affected more by increases in $\delta_{w,ME,\,max}$, or the thickness of the wake, than by increases in $\widetilde{x}_{d,\,ME}$, or the x value for maximum wake thickness. Results suggest that there is a strong relationship between WTP_{ME}, $\delta_{w,ME,\,max}$, and l/d. Configurations with elevated values of WTP_{ME} correspond to configurations with large $\delta_{w,ME,\,max}$ which, in general, result in decreased values of l/d. This trend holds true for all configurations with large gap sizes and small, or possibly negative, overhang distances. While decreased values of WTP_{ME} are observed in this region, the improper placement of the two flaps results in C_l values that are significantly lower than the C_l values at other points in the sample domain.

6.2.2 Effect of α at Equal Relative Coordinates

In addition to the results presented above in Fig. 6.5, simulations in MSES were also performed at an α of -2 and 2 deg for a freestream Reynolds number of 1×10^6. Data presented in this section include both aerodynamic performance and wake thickness metrics, and a discussion of all these topics is presented in this subsection.

Aerodynamic Performance

A variety of aerodynamic performance metrics, including C_l, C_d, and l/d, are shown in Fig. 6.6, and contour plots in the figure are presented on the same scale to allow easy comparison of the magnitude of values in addition to examining the trends for each parameter.

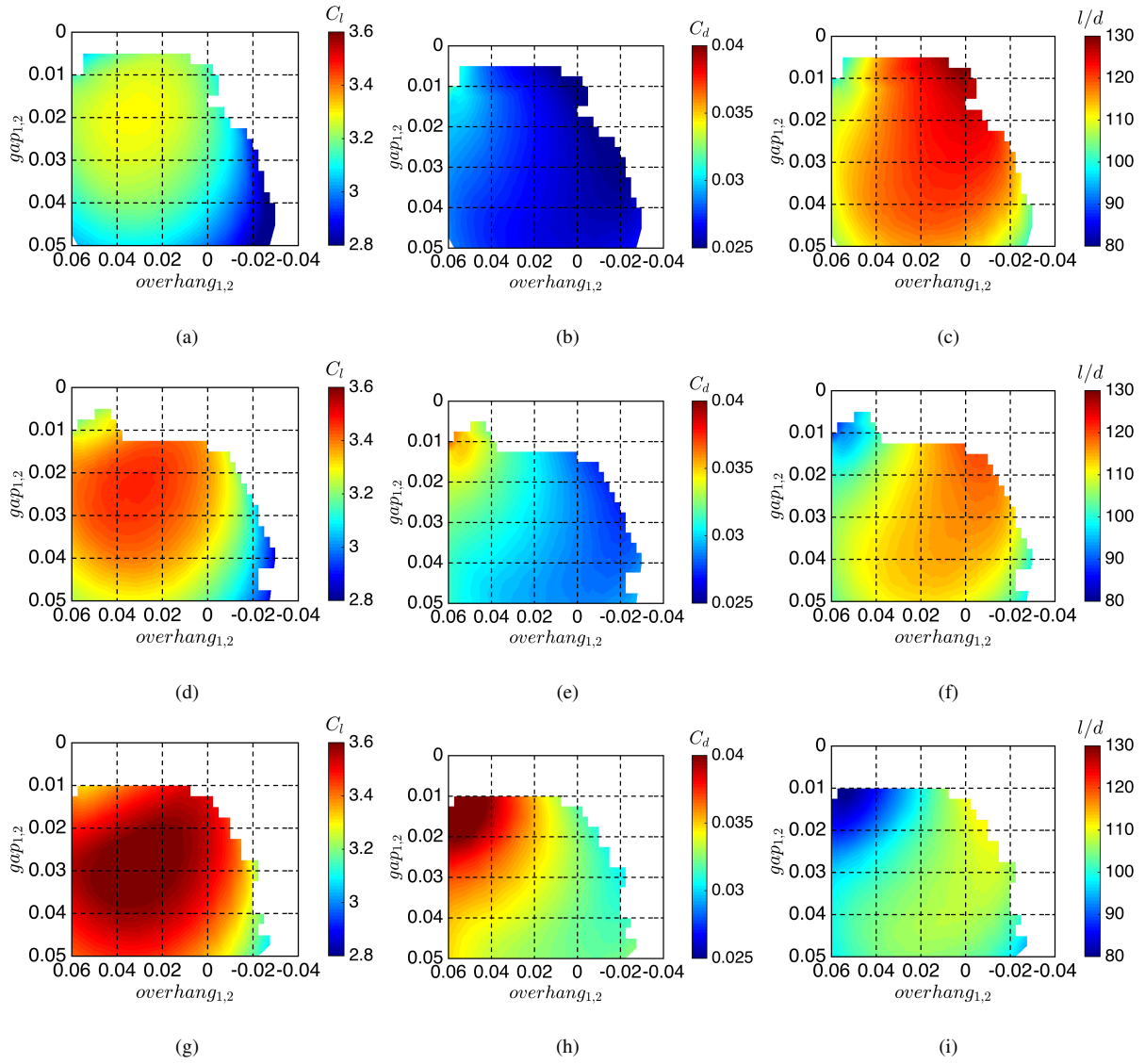

Figure 6.6: Effect of α on aerodynamic performance for a range of airfoil configurations including a) C_l, b) C_d, and c) l/d at α=-2 deg; d) C_l , e) C_d, and f) l/d at α=0 deg; and g) C_l, h) C_d, and i) l/d at α=2 deg.

Trends in C_l are presented in Fig. 6.6(a,d,g) for α of -2, 0, and 2 deg, respectively. As expected, elevated values of C_l are observed for increased α as stall was not observed for these α values. In addition to the values of C_l, it is interesting to note the differences in trends in C_l with respect to α. Similar to the previously-discussed results, all configurations suggest a rapid decrease in C_l at small overhang values, such as $overhang_{1,2} < 0$, across a range of gap sizes. Results also indicate the configurations for maximum C_l at a given α are not the same for each α. The trends in Fig. 6.6(a) suggest the configuration for maximum C_l at decreased α is located near $overhang_{1,2} = 0.03$ and $gap_{1,2} = 0.018$, but data for in increased α in Fig. 6.6(g) suggest configurations for the highest values of C_l are approximately $overhang_{1,2} = 0.03$ and $gap_{1,2} = 0.028$. Thus, it is observed that $overhang_{1,2}$ has a minimal effect on

the configuration with maximum C_l while an increase in α requires an increase in $gap_{1,2}$ to for a configuration in which C_l is maximized.

In addition to aerodynamic performance, the differing behavior between a variety of configurations can be investigated with pressure distributions, and two sets of C_p curves are plotted in Fig. 6.7. Data shown in Fig. 6.7(a) are the C_p distributions for the configuration at which C_l was maximized at each α, and data in Fig. 6.7(b) are plotted for the configuration in which C_l is maximized at α of 0 deg. Consider first the pressure curves shown in Fig. 6.7(a). As previously mentioned, configurations for maximum C_l are independent of overhang, but a larger α yields an increase in $gap_{1,2}$ for which C_l is maximized. It is noted that significant differences in C_p over the main element are observed for different α values, but very few differences in C_p are observed over the flaps for these three α. The pressure at the main-element trailing edge, also known as the trailing-edge dump pressure, remains unchanged between the three pressure plots. Few variations exist in the main-element pressure distribution when the results in Fig. 6.7(a) and Fig. 6.7(b) are compared. Pressure distributions over the flap for each of the configurations and each α are essentially the same. Consequently, despite an increase in circulation around the multielement system, it appears that the thicker wakes at increased α suppress the pressure distribution around the two flaps.

Returning to Fig. 6.6, drag data for a range of α are plotted in Fig. 6.6(b,e,h). As was observed with C_l, an increase in α yields higher values of C_d, which is the expected trend, and the highest values of C_d are observed for configurations with a small gap size and a large overhang distance. Differences in the trends of C_d with different configurations are different for the three α computed. Figure 6.6(b), at $\alpha = -2$ deg, yields less drag than the cases for higher α. This observation is due to increases in both the skin friction and pressure drag on the airfoil surfaces in addition to larger, stronger burst wakes at higher α. Larger values of α yield stronger pressure gradients in the flowfield, thus

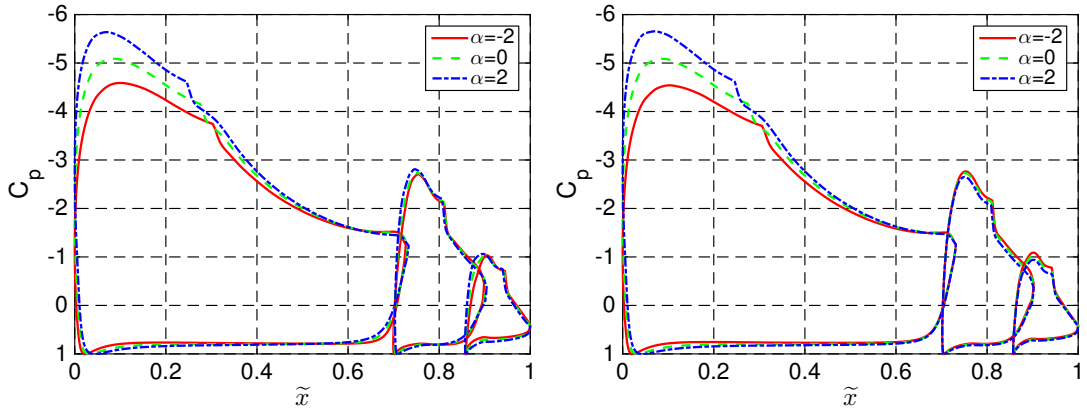

Figure 6.7: Pressure distributions at various α (in deg) including a) configuration for which C_l is maximized for each α and b) configuration for which C_l is maximized at α of 0 deg.

increasing the size and strength of the burst wakes than those observed at lower α. Data in Fig. 6.6(b,e,h) indicate a weak decrease in C_d as a function of gap and overhang when compared to the configurations with maximum C_d, and decreases are observed to be approximately 0.006 between maximum and minimum C_d for the domain presented. On the contrary, steeper decreases in C_d are observed for $\alpha = 2$ deg, as plotted in Fig. 6.6(h). In this condition, the difference between maximum and minimum C_d for the different configurations is approximately 0.01, which is markedly larger than the difference of 0.006 for $\alpha = -2$ deg. Thus, for the airfoil geometry studied in this research project, cases for increased α are less forgiving to changes in C_d than trends at lower α.

Aerodynamic efficiency, quantified by l/d, is shown in Fig. 6.6(c,f,i) for the same α as previously identified. As α increases, a reduction of l/d is observed. As previously identified, an increase in α yields more lift and more drag, and this drag increase is due to skin-friction and pressure drag as well as the increased C_d from larger, thicker wakes. When the lift-to-drag ratio is considered, it is obvious that the increased C_d at larger α affects the l/d ratio more than elevated values of C_l. Configurations with the lowest l/d are those with small gap size and large overhang distances, which is the same trend observed with regard to C_d. The largest values of l/d for a given α are suggested to occur with geometries in which $gap_{1,2} = 0.015$ and $overhang_{1,2} = -0.01$, and this configuration for maximum l/d remains largely unchanged with respect to α.

Similar to the previous discussion relating to C_l, it is valuable to examine the airfoil pressure distributions for configurations in which l/d is maximized, and results are plotted in Fig. 6.8. The three pressure distributions in Fig. 6.8(a) are the configurations for which l/d is maximized at each α. The main element C_p curves are obviously larger and stronger for increased α, and the x position for which the magnitude of C_p is maximized moves upstream with increasing α. In addition, the transition point moves forward. These trends are what is expected with increasing

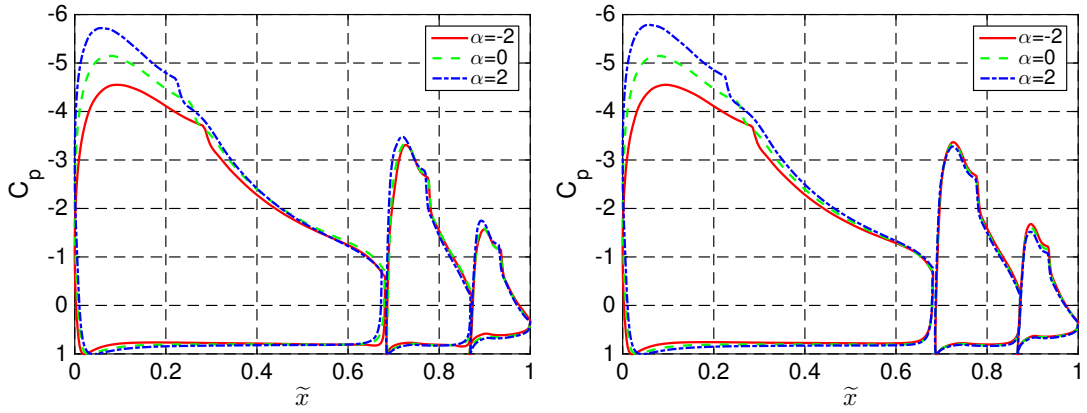

Figure 6.8: Pressure distributions at various α (deg) including a) configuration for which l/d is maximized for each α and b) configuration for which l/d is maximized at α of 0 deg.

α. While large differences in the main-element C_p curve are observed, minimal differences in C_p exist over the two flaps. A slight increase in maximum magnitude of C_p is present over both flaps for increased α, but the difference between the three pressure distributions over the flaps is markedly less than differences observed in the main-element C_p distributions. In fact, almost indiscernible differences in both flap C_p distributions are observed at α of -2 and 0 deg. A careful examination of Fig. 6.8(a) and Fig. 6.7(a), presented above, suggest differences in the pressure distributions for maximum l/d when compared to maximum C_l at each α. The pressure distributions over the main element in Fig. 6.8(a) have decreased values of the maximum magnitude of C_p, and the distributions near the minimum C_p appear to be "flatter" for $\widetilde{x} < 0.2$. Significant differences are observed over the flaps between Fig. 6.7(a) and Fig. 6.8(a), as increased flap loading is observed for maximum l/d when compared to maximum C_l.

Figure 6.8(b) shows the C_p distributions at three α for the configuration in which l/d is maximized at $\alpha = 0$ deg. The dashed green line in Fig 6.8(b) is the same as that in Fig. 6.8(a), but the pressure distributions at both -2 and 2 deg are different between the two subplots. Similar trends as those previously discussed with regard to Fig. 6.8(a) are observed for the C_p distribution over the main element at all three α. However, even less differences are observed in the C_p distributions over the the flaps. Data suggest a slight increase in the maximum magnitude of C_p at decreased α over both flaps, which is the opposite trend as that in Fig. 6.8(a).

Analysis of Burst Wakes

The effect of α upon a variety of wake metrics is shown in Fig. 6.9. These metrics, including $\delta_{w,ME,\,max}$, $\widetilde{x}_{d,\,ME}$, and WTP_{ME} as defined in Eq. 6.10, are useful to quantify the extent to which a wake is burst and the location of maximum wake thickness. Similar to before, the wake metrics shown in the figure are presented on the same color scale to allow easy comparisons of the various plots across different α. A discussion of each of these parameters now follows.

Figure 6.9(a,d,g) presents the effect of α on the maximum main-element wake thickness, $\delta_{w,ME,\,max}$, as defined above in Fig. 6.3. In general, $\delta_{w,ME,\,max}$ increases with larger α, which is the expected trend. This trend is expected as the larger adverse pressure gradients in the off-surface pressure-recovery region are stronger for flows with increased circulation, which occurs at larger α; this pressure gradient causes the wake bursting to occur. Configurations with small gap sizes and large overhang distances yield large, thick wakes, and this trend causes C_d to rise for these configurations. Results also indicate that cases with larger gap sizes and smaller overhang distances result in decreased wake thickness. In addition, the cases with large gap size and small overhang distance are less sensitive to flap position than if the same perturbations were applied to configurations with small gap size and large overhang distances. When comparing Fig. 6.9(a,d,g) to Fig. 6.6(a,d,g), it is apparent that the configuration for maximum lift does not correspond with minimum or maximum values of $\delta_{w,ME,\,max}$, but rather that maximum C_l is observed for cases with moderately-thick wakes.

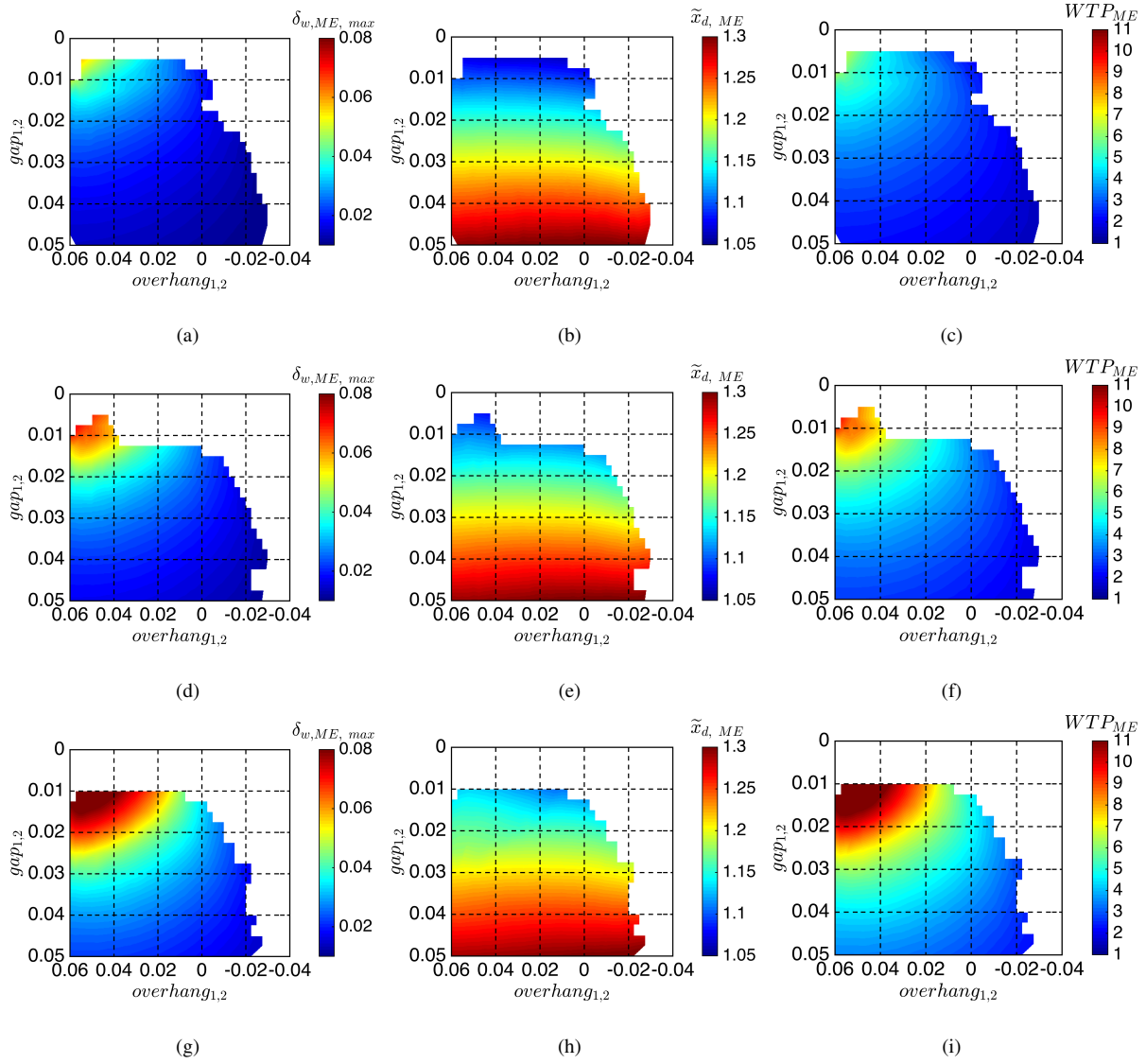

Figure 6.9: Effect of α on wake development for range of airfoil configurations including a) $\delta_{w,ME,\ max}$, b) $\widetilde{x}_{d,\ ME}$, and c) WTP_{ME} at α=-2 deg; d) $\delta_{w,ME,\ max}$, e) $\widetilde{x}_{d,\ ME}$, and f) WTP_{ME} at α=0 deg; and g) $\delta_{w,ME,\ max}$, h) $\widetilde{x}_{d,\ ME}$, and i) WTP_{ME} at α=2 deg.

A second wake metric worthy of discussion is the x coordinate at which the maximum wake thickness occurs, and this value is denoted as $\widetilde{x}_{d,\ ME}$. As seen in Fig. 6.9(b,e,h), $\widetilde{x}_{d,\ ME}$ is largely independent of *overhang* at all three α, but significant dependence on both *gap* and α is noted. Slight decreases in $\widetilde{x}_{d,\ ME}$ with respect to overhang distance at a given gap size are observed, but these changes are only approximately 0.02, at maximum. Large gap sizes at a given *overhang* yield maximum wake thickness further downstream, and smaller gap sizes produce wakes that are thickest just downstream of the main element; this trend is observed at all three α. Maximum values of $\widetilde{x}_{d,\ ME}$, observed at $gap_{1,2} = 0.05$, are approximately 1.30, and this value is observed to be independent of α. On the contrary, the

minimum value of $\widetilde{x}_{d,\,ME}$ changes with α. As solutions at all α did not necessarily converge for $gap_{1,2} < 0.01$, it is prudent to compare $\widetilde{x}_{d,\,ME}$ at $gap_{1,2} = 0.01$. At this gap size, minimum values of $\widetilde{x}_{d,\,ME}$ are 1.08 and 1.14 at α of -2 and 2 deg, respectively.

The main-element wake-thickness parameter, WTP_{ME}, is plotted in Fig. 6.9(c,f,i). As previously stated, this parameter quantifies the extent to which a wake is burst. As expected, WTP_{ME} increases with α as a higher α yields larger, thicker wakes than those wakes at lower α. Maximum values of WTP_{ME} at α of -2 deg are approximately 5.1, but the maximum WTP_{ME} is in excess of 11 for α of 2 deg. In general, WTP_{ME} exhibits the same trends as $\delta_{w,ME,\,max}$ as minimal variations in $\widetilde{x}_{d,\,ME}$ with respect to overhang are present, as previously discussed. Larger gap sizes produce thinner wakes than the wakes at decreased gap sizes for a given overhang distance. Similarly, smaller, thinner wakes are present for smaller overhang distances than those at larger overhang distances for a given gap size.

Comparisons of pressure distributions over the airfoil are another useful way to compare the aerodynamics of multiple configurations simultaneously, and pressure distributions for a variety of configurations are plotted in Fig. 6.10. Consider first the data presented in Fig. 6.10(a) which present pressure distributions at an α of 0 deg in which $overhang_{1,2} = 0.01$ for both configurations and $gap_{1,2}$ is 0.015 and 0.050 for the two configurations. In this figure, the effect of gap size at a given overhang distance can be discerned. Configurations with a larger gap size yield a decrease in loading on the main element and increased lift on both of the flaps. These differences in the pressure distributions are a result of multielement-airfoil aerodynamics, the most significant of which is the circulation effect. As documented by Smith [4], a flap, or even a lumped vortex, which is located slightly behind and under the previous element causes increased velocity (or decreased C_p) at the trailing edge of the previous element than if the upstream element were analyzed as a single-element airfoil. For the multielement airfoil, if the Kutta condition is enforced, an increased trailing-edge velocity creates increased circulation on the upstream element than the circulation of an isolated single-element airfoil. Elevated circulation of the upstream element causes increased suction peaks on the upper surface of the upstream element than for the isolated airfoil. The pressure distribution for the main element in a multielement airfoil system does not satisfy the Kutta condition by itself. However, the Kutta condition is satisfied by the combination of the main-element and downstream element(s). Returning to a comparison of the two configurations shown in Fig. 6.10(a), the configuration in which $gap_{1,2} = 0.050$ corresponds to a flap element that is located in an inefficient position. As the flap is further away from the trailing edge of the upstream element, the circulation on the downstream element does not increase the trailing-edge dump velocity, which in turn yields less loading on the upstream element than that of a smaller-gap configuration. It is impossible to isolate the various effects of multielement airfoil aerodynamics and all effects must be considered simultaneously. The other multielement airfoil effect that is relevant to the current discussion is the off-the-surface pressure recovery, which is closely related to the circulation effect. An increase in the trailing-edge velocity of an airfoil reduces the pressure that must be recovered over the

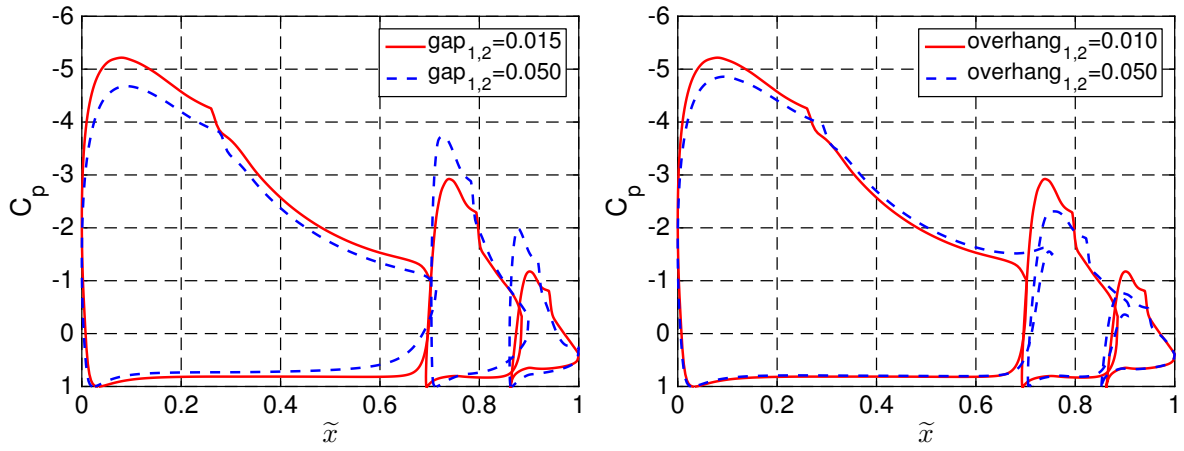

Figure 6.10: Pressure distributions at α of 0 deg exhibiting effect of a) gap size at $overhang_{1,2}$=0.01 and b) overhang distance at $gap_{1,2}$=0.015.

surface of the airfoil element. As a decreased adverse pressure gradient is applied to the boundary layer, the boundary layer at the trailing edge is thinner than if all the pressure were to be recovered over the single-element airfoil. Consequently, the pressure is recovered in a more-efficient manner than if pressure was recovered over the surface of the airfoil. In addition to the differences in C_p over the main element, significant differences are observed over both flaps. The deflection angle of the two flaps is the same in the two configurations presented. If the configuration with a small gap size is considered, it is apparent that the relative angle of attack of the flap is less than if the flap were analyzed in isolation at the given deflection angle. This decrease in local angle of attack is due to the turning of the flow from the upstream element. As the flaps are located further away from the main element, the flaps are not affected by the flow turned by the main element as much as if the flaps were located in close proximity to the upstream element. The reduction in flow curvature results in an increase in local angle of attack for the flaps, thus increasing the loading on the two flaps.

Two configurations for which $gap_{1,2}$=0.015 at various overhang distances are plotted in Fig. 6.10(b). First, the reader is reminded that the relative chord lengths of each element are unchanged between the two configurations, but an increase in overhang distance yields a decreased system chord than that for a smaller overhang distance. If the system chord is defined to be unity, the size of all airfoils as projected on the x axis must be increased. Thus, the increase in chord length projected on the x axis does not indicate a change in the relative chord lengths for the airfoil. As overhang distance is increased from a baseline of 0.010, the loading on all three elements is decreased, and this observation is explained by primarily considering the circulation effect. An airfoil with a larger overhang distance is tucked under the upstream element more than that for a configuration with decreased overhang distance. By considering the lift of the downstream element as a lumped vortex at the center of lift, it is apparent that a vortex

located far enough upstream can in fact decrease the trailing edge velocity (or increse C_p) at the trailing edge of the upstream element. A reduction in the velocity at the trailing edge of the upstream element results in decreased circulation for the upstream element to satisfy the Kutta condition, and thus the loading on the upstream element is reduced relative to that of a flap located further downstream.

6.2.3 Effect of Re at Equal Relative Coordinates

As wake bursting is an inherently viscous phenomenon, it was desired to determine the effect of a range of *Re* on the flowfield. Five parametric sweeps in *gap* and *overhang* were performed at $\alpha = 0$ deg and at freestream Reynolds numbers of 0.6×10^6, 0.8×10^6, 1×10^6, 2×10^6, and 3×10^6. Similar to the discussion in Sec. 6.2.1 and Sec. 6.2.2, data in this subsection will include a discussion of aerodynamic performance parameters followed by an analysis of burst wake metrics. Parametric sweeps were executed over the same gap size and overhang distance domain, and results are only presented for adequately-converged solutions.

Aerodynamic Performance

It is known that different Reynolds numbers can significantly affect aerodynamic performance parameters, and these differences in the flowfield are observed through different laminar-separation bubbles (in terms of size and location) as well as differing stall characteristics. In addition to these two parameters which exist over all airfoils, the flowfield for the airfoil presented in this document is also affected by the behavior of the viscous burst-wake region. Standard aerodynamic performance metrics are presented for C_l, C_d, and l/d at five different Reynolds numbers for α=0 deg, and results are shown in Fig. 6.11. The figure presents a variety of performance metrics in each column with different Reynolds numbers in each row. Data are only presented for configurations in which adequate convergence in MSES was achieved. Fewer configurations converged at lower Reynolds numbers than at higher Reynolds numbers, which is a trend observed to be true in MSES as low Reynolds-number flowfields can be difficult to predict and resolve.

A wide variety of trends for C_l at all five Reynolds numbers are presented in Fig. 6.11(a,d,g,j,m), the leftmost column, with increasing Reynolds numbers going down the column. As expected, larger values of C_l exist for increased Reynolds numbers, and this trend is typical for both single-element and multielement airfoils. The trend of increasing C_l with increasing *Re* is observed as both the boundary layer and wake thickness decreases for higher Reynolds number flows. As viscous flowfield features, such as boundary layers and wakes, scale with Reynolds number, the large wake will effectively decamber the multielement system yielding less curvature around the multielement airfoil and a decrease in lift. The configuration for maximum C_l is different at each Reynolds number, and an increase in Reynolds number suggests the configuration at which C_l is maximized corresponds to a configuration with decreased gap size and increased overhang distance.

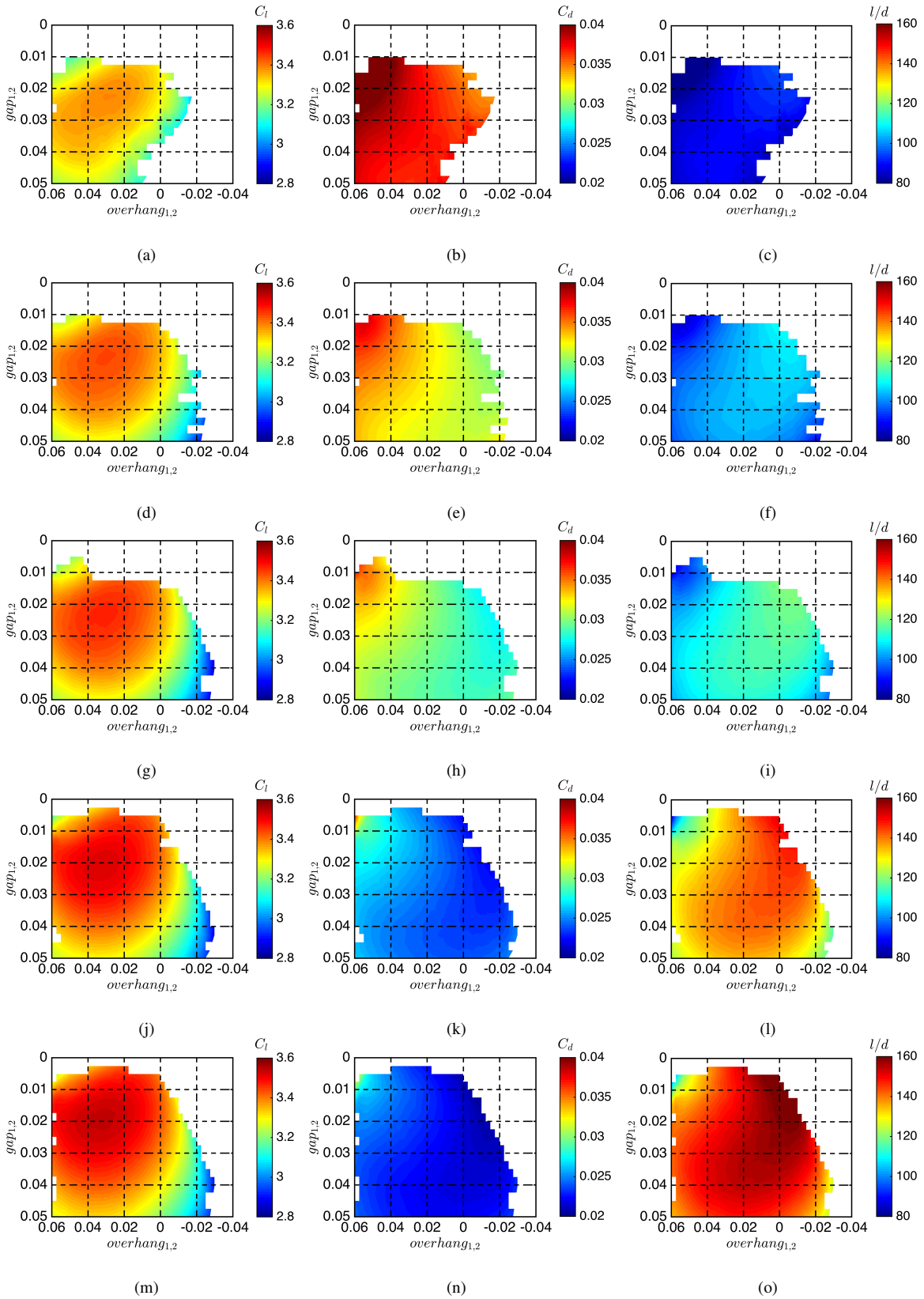

Figure 6.11: Effect of *Re* on aerodynamic performance for range of airfoil configurations including C_l (a,d,g,j,m), C_d (b,e,h,k,n), and l/d (c,f,i,l,o) for *Re* of 0.6×10^6, 0.8×10^6, 1×10^6, 2×10^6, and 3×10^6, respectively.

Drag data at a range of Reynolds numbers are presented in Fig. 6.11(b,e,h,k,n), the center column, and values of C_d are observed to decrease with increasing Reynolds numbers. The increase in drag at lower Reynolds numbers is due to the larger, thicker boundary layers and wakes that result from increased viscous domination and decreased inertial effects. The variation in C_d over the Reynolds numbers simulated is greater than a factor of two between the lowest C_d at Re=3×10^6 and the highest C_d at Re=0.6×10^6. The difference in C_d at a constant overhang distance and variable gap size is smaller than the trends for constant gap size and variable overhang distance. Elevated values of C_d exist for small gap sizes and large overhang distances at all Reynolds numbers; decreased C_d is present for smaller overhang distance.

A marked effect of Reynolds number upon l/d is plotted in Fig. 6.11(c,f,i,l,o) in which larger values of l/d occur at larger Reynolds numbers. As large variations in C_d and smaller differences in C_l are observed for different Reynolds numbers, trends in l/d closely mimic the trends of C_d. These trends are observable with low l/d at small Reynolds numbers, and larger l/d at larger Reynolds numbers. Increased values of l/d are predicted for small overhang distances, and the smallest l/d occurs for configurations with a small gap size and a large overhang distance; this trend is observed at all Reynolds numbers. In general, the highest l/d exists for a small gap size and a small (and even negative) overhang distance.

Analysis of Burst Wakes

As previously developed in Sec. 6.1, a variety of metrics can be used to quantify the burst wake region. Results for each of three important metrics ($\delta_{w,ME,\,max}$, $\widetilde{x}_{d,\,ME}$, and WTP_{ME}) are shown in Fig. 6.12 for five different freestream Reynolds numbers ranging from 0.6×10^6 to 3×10^6. Each column in the figure presents three different wake metrics, and each row of the figure presents data at a given Reynolds number. While simulations were performed over a wide domain of $gap_{1,2}$ and $overhang_{1,2}$, convergence in MSES was only achieved for some configurations. As is typical throughout this document, results are only presented for converged solutions. Discussion in this section is limited to the main-element wake.

Consider first the results for $\delta_{w,ME,\,max}$ shown in Fig. 6.12(a,d,g,j,m), or the leftmost column. As defined in Fig. 6.3, the $\delta_{w,ME,\,max}$ parameter is the maximum thickness of the main-element wake. Large, thick wakes occur in which configurations have a small gap size and a large overhang distance, and thinner wakes exist for large-gap and small-overhang configurations. As seen in the figure, the difference in wake thickness between these two regions can be as high as a factor of six. A decrease in wake size with an increase of Reynolds number is observed over the simulated configuration domain, with minimum values of $\delta_{w,ME,\,max}$ of 0.01 at Re=3×10^6 and a value of 0.025 for the same configuration at Re=0.6×10^6.

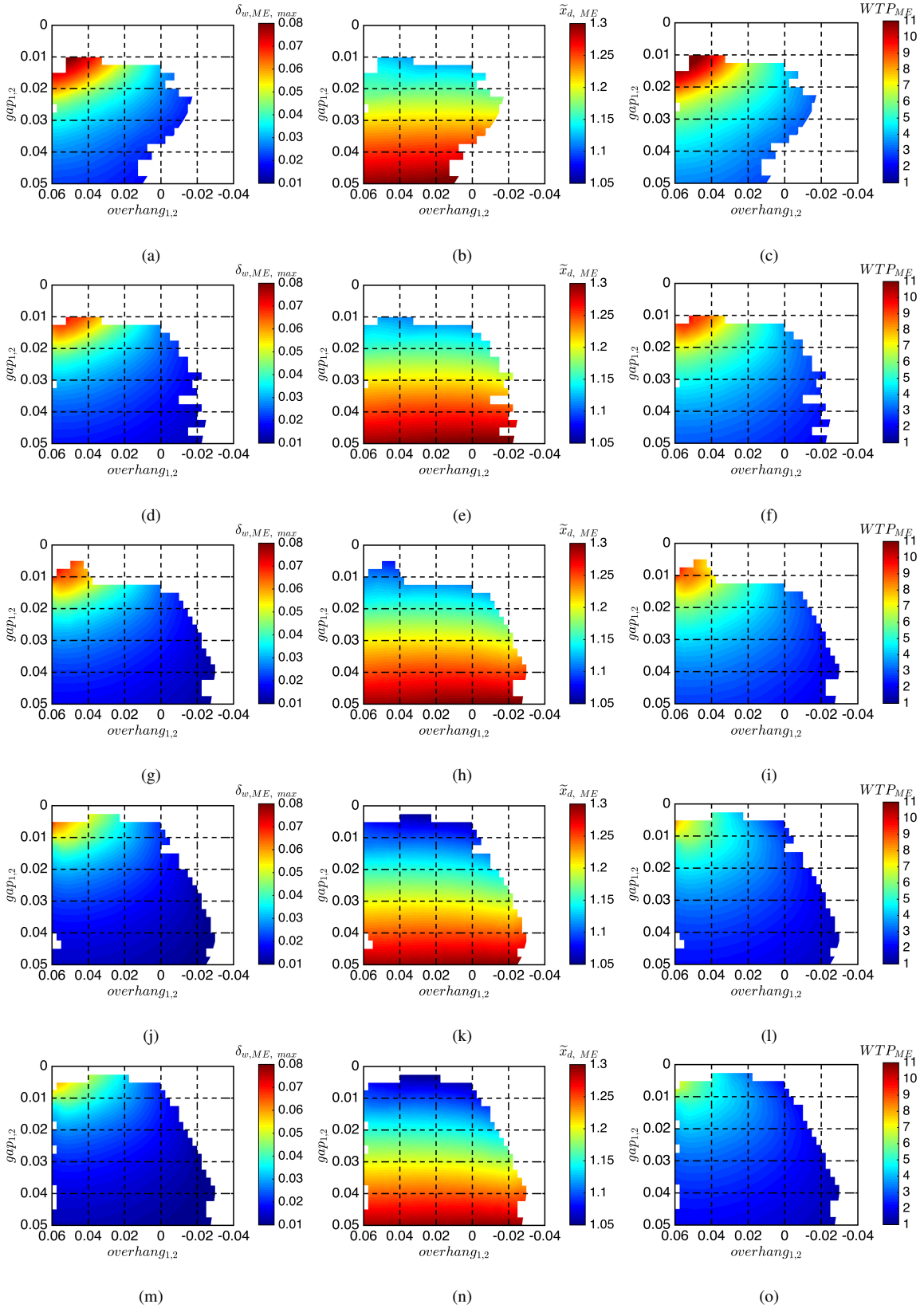

Figure 6.12: Effect of *Re* on aerodynamic performance for range of airfoil configurations including $\delta_{w,\,ME,\,max}$ (a,d,g,j,m), $\widetilde{x}_{d,\,ME}$ (b,e,h,k,n), and WTP_{ME} (c,f,i,l,o) for *Re* of 0.6×10^6, 0.8×10^6, 1×10^6, 2×10^6, and 3×10^6.

Table 6.1: Configurations Analyzed for Coupled Flap 1 and Flap 2 positions

Relative Coordinate	Lower Bound	Upper Bound	Increment
gap_1	0.01	0.03	0.01
gap_2	0.005	0.05	0.005
$overhang_1$	-0.01	0.06	0.01
$overhang_2$	0	0.06	0.01

The x location for which the wake thickness is maximized, or $\widetilde{x}_{d,\,ME}$, is plotted in Fig. 6.12(b,e,h,k,n), the center column. As previously observed, the overhang distance has minimal effect upon $\widetilde{x}_{d,\,ME}$ for a given gap size, but gap size affects $\widetilde{x}_{d,\,ME}$. A large gap size yields a wake that bursts further downstream than that of a configuration with a small gap size. Data suggest that increasing freestream Reynolds number decreases $\widetilde{x}_{d,\,ME}$ for small-gap-size configurations; a configuration with a gap size of 0.015 at all overhangs yields $\widetilde{x}_{d,\,ME}\approx 1.15$ at $Re=0.6\times10^6$ while while $\widetilde{x}_{d,\,ME}\approx 1.11$ at $Re=3\times10^6$. Little variation in $\widetilde{x}_{d,\,ME}$ is observed as a function of Reynolds number for configurations with large gap sizes.

Figure 6.12(c,f,i,l,o), the rightmost column, presents WTP_{ME} as a function of Reynolds number. The WTP metric, as proposed in Sec. 6.1, quantifies the extent to which a wake is burst. Data indicate that WTP_{ME}, the wake-thickness parameter for the main-element wake, is a function of both gap size and overhang distance. The largest values of WTP_{ME} occur at small gap size and large overhang distances while decreased WTP_{ME} occur at large gap size and small overhang distances. It is not surprising that trends in WTP_{ME} closely follow those of C_d shown above in Fig. 6.11(b,e,h,k,n). Increasing freestream Reynolds numbers yield decreased WTP_{ME} for a given configuration, and this reduction in WTP_{ME} is observed to be as large as $\Delta WTP_{ME}\approx 2.0$.

6.2.4 Coupled Effect of Flap 1 and Flap 2 Positions

Configurations presented in Sec. 6.2.2 and Sec. 6.2.3 were defined by $gap_1 = gap_2$ and $overhang_1 = overhang_2$ in which both relative coordinates were normalized by the system chord length. While this analysis was useful, it is not necessarily the best manner in which the relative coordinates should be defined. As the main-element chord length is significantly larger than the flap 1 chord length, the proper gap size and overhang distance is not necessarily the same. In this section, a study was performed in which the gap and overhang distances were systematically changed for both flap 1 and flap 2, and the configurations selected are shown in Table 6.1. Data were analyzed in a square test matrix such that every combination of gap_1, gap_2, $overhang_1$, and $overhang_2$ was considered, which resulted in a total of 2,882 different configurations that were physically possible and were simulated in MSES.

A variety of aerodynamic-performance and wake metrics were calculated for each of the configurations, and results are shown in Fig. 6.13. Each plot presents a parameter at a range of $overhang_1$, $overhang_2$, and gap_2 configurations,

as outlined in Table 6.1. A subset of the data are presented in the figure by down-selecting the values of $overhang_1$ in an effort to make the trends and values more easily discerned than if the full sample of $overhang_1$ values were plotted. Each column in the figure represents a given parameter, and the three rows of subfigures present data at gap_1 of 0.010, 0.020, and 0.030 for the top, middle, and bottom rows, respectively. The same domain of $overhang_1$, $overhang_2$, and gap_2 is presented in all plots, even though some combinations of relative coordinates are not physically possible. These data are plotted in this domain and on the same color scale such that easy comparisons can be made between each of the figures.

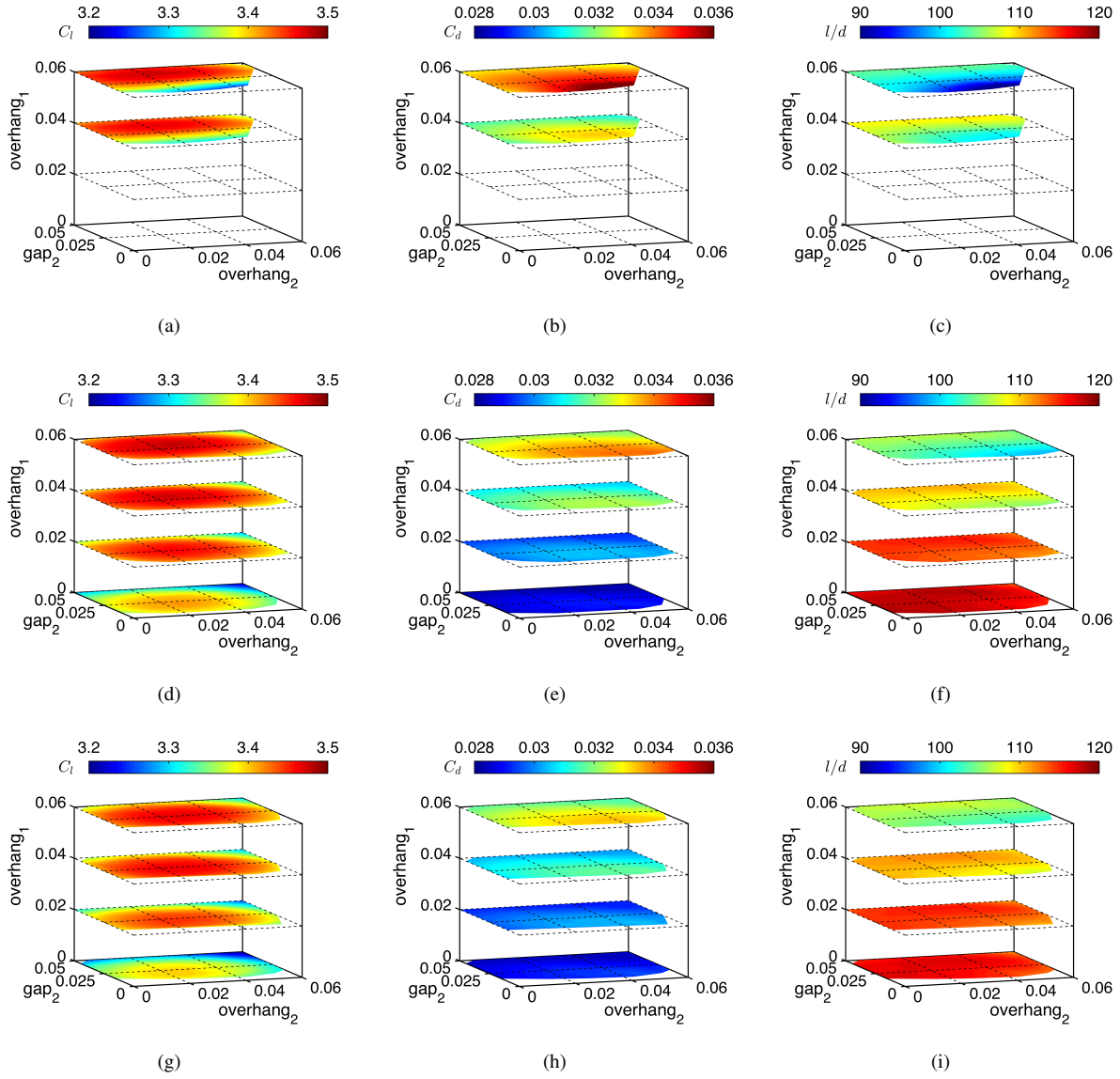

Figure 6.13: Coupled effect of gap_1, gap_2, $overhang_1$, and $overhang_2$ upon aerodynamic performance for range of airfoil configurations including a) C_l, b) C_d, and c) l/d at gap_1=0.010; d) C_l, e) C_d, and f) l/d at gap_1=0.020; and g) C_l, h) C_d, and i) l/d at gap_1=0.030

Lift data for the range of configurations are shown in Fig. 6.13(a,d,h), or the leftmost column. Data in the three subplots indicate that larger values of C_l are observed for large values of $0.025 \leq gap_2 \leq 0.045$ and $0.01 \leq overhang_2 \leq 0.03$ for a given gap_1 and $overhang_1$. While this region is largely independent of gap_1, some dependence upon $overhang_1$ is observed in which an increase in $overhang_1$ moves the region of high C_l to configurations with larger gap_2. It is curious to note that $overhang_1$ and gap_2 are related in such a manner, as it would typically be expected that trends would be isolated to only changes in flap 1 or only changes in flap 2. This observation indicates that it is very difficult, if not impossible, to choose a "best" configuration for a multielement airfoil as all four relative coordinates examined in this study are coupled to the other parameters. Maximum values of C_l are observed to monotonically increase with larger $overhang_1$, but that a region of $overhang_2$ yields more lift than other configurations. Data suggest that variations in C_l over the domain examined range from minimum values of 3.20 to maximum values of 3.51, or an increase of approximately 10%. While the maximum values of C_l are largely unaffected by gap_1, the configurations for which C_l is maximized decreases in gap_2 and increases in $overhang_2$ for larger gap_1. Sharp decreases in C_l are observed for small $overhang_1$ and large values of gap_2 and $overhang_2$ at a given gap_1. It is noted, of course, that these trends are not comprehensive for any multielement airfoil, but rather are observed for the multielement airfoil in discussion.

Variations in C_d are presented in the middle column, or Fig. 6.13(b,e,h), in the same domain as the C_l data. Contrary to trends in C_l, significant variation in C_d is observed at different gap_1. For a given $overhang_1$ such that $overhang_1 geq 0.04$ (the region in which convergence in MSES was achieved) the C_d decreases by as much as 11% from gap_1=0.01 to gap_1=0.03. Additionally, C_d is observed to increase with increasing $overhang_1$, which is the same trend observed with C_l. As seen in the figure, configurations with increased drag occur at small gap sizes and large overhang distances; minimum drag is observed for small $overhang_1$, small $overhang_2$, large gap_1 and large gap_2. That is to say that decreased drag occurs with large gap sizes and small overhang distances for both flaps.

The rightmost column of Fig. 6.13 plots l/d as a function of all parameters; data are specifically shown in Fig. 6.13(c,f,j) for gap_1 of 0.01, 0.02, and 0.03, respectively. Data indicate that l/d is strongly dependent upon all four relative coordinate values. For a given gap_1 and $overhang_1$ (thus only considering the movement of flap 2), increased l/d results from configurations with larger slightly smaller $overhang_2$ and larger gap_2. While both $overhang_2$ and gap_2 affect l/d, more variation is observed with respect to gap_2 than to $overhang_2$. Trends for a specified gap_1, gap_2, and $overhang_2$ indicate that l/d decreases with larger $overhang_1$ values. While both C_l and C_d increase with respect to $overhang_1$, the increase in C_d is larger than that of C_l, thus resulting in larger l/d for configurations with low C_d. These configurations are observed for smaller $overhang_1$ and smaller gap_1.

Similar to data presented earlier in this section, wake metrics are presented in Fig. 6.14. These three parameters, $\delta_{w,ME,\,max}$, $\widetilde{x}_{d,\,ME}$, and WTP_{ME} are the same metrics as previously defined and discussed. The three-dimensional contour plots are shown over the same domain as the previously-discussed aerodynamic performance data. The effect

of various configurations upon $\delta_{w,ME,\,max}$ is plotted in the leftmost column, or Fig. 6.14(a,d,g). As seen in the figure, increased gap_2 (bottom row of the figure) yields smaller and thinner wakes than configurations with small gap_1 for all combinations of gap_2 and $overhang_2$. For a given gap_1, the thickest wakes correspond to configurations with small gap_2 and large $overhang_1$. These results are in agreement with the gap_1=gap_2 and $overhang_1$-$overhang_2$ results discussed in Secs. 6.2.1–6.2.3. Thus, the smallest wakes for the MFFS(ns)-026 airfoil are observed at small gap_1 and gap_2 as well as small $overhang_1$ and $overhang_2$. It is also observed that the smaller and thinner wakes result in better aerodynamic performance including both reduced C_d and increased l/d as previously shown in Fig. 6.13.

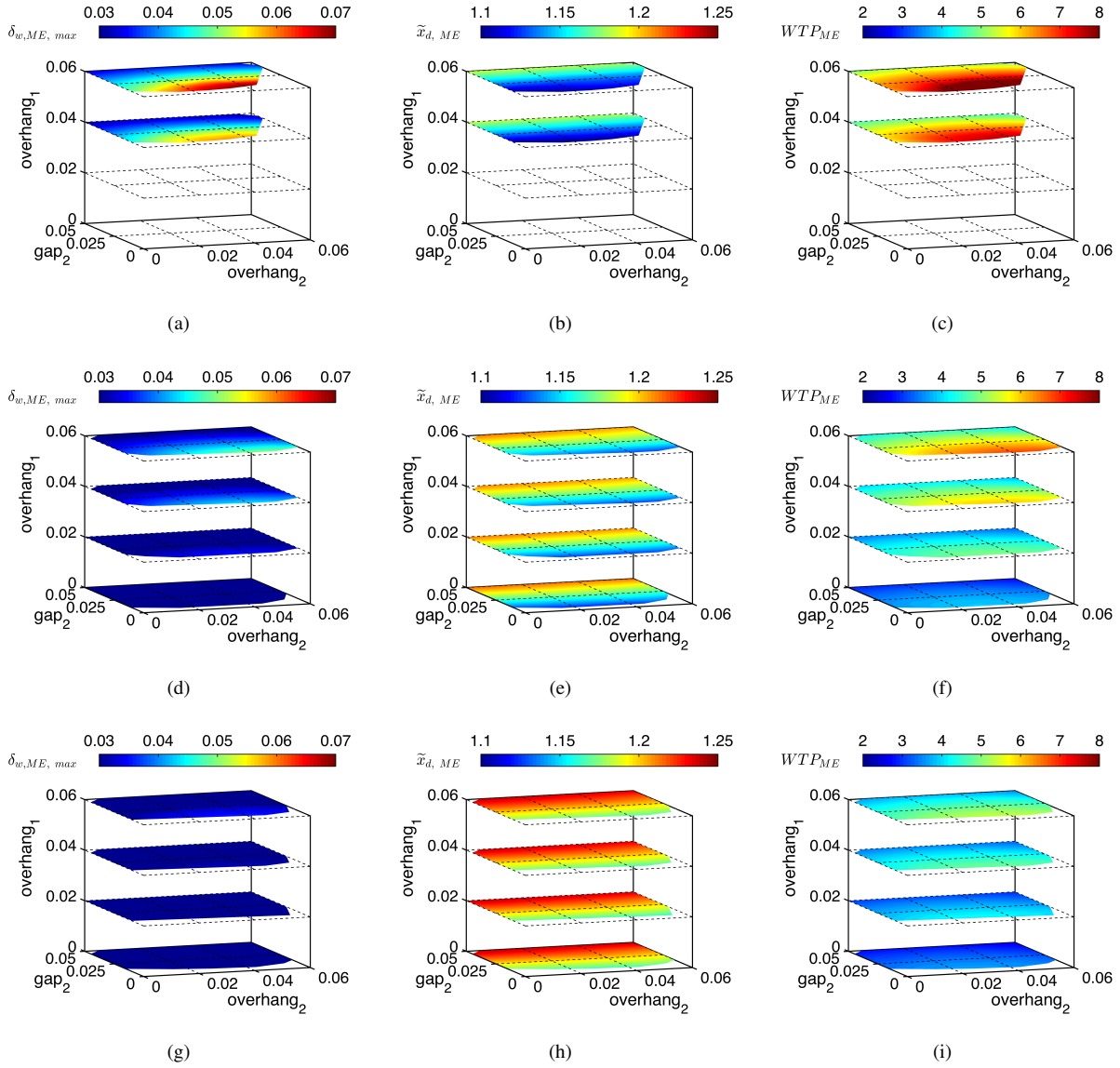

Figure 6.14: Coupled effect of gap_1, gap_2, $overhang_1$, and $overhang_2$ upon burst wake metrics for range of airfoil configurations including a) $\delta_{w,ME,\,max}$, b) $\widetilde{x}_{d,\,ME}$, and c) WTP_{ME} at gap_1=0.010; d) $\delta_{w,ME,\,max}$, e) $\widetilde{x}_{d,\,ME}$, and f) WTP_{ME} at gap_1=0.020; and g) $\delta_{w,ME,\,max}$, h) $\widetilde{x}_{d,\,ME}$, and i) WTP_{ME} at gap_1=0.030.

Consider the $\widetilde{x}_{d,\,ME}$ trends shown in Fig. 6.14(b,e,h). For a given gap_1 and $overhang_1$, the data in the figure closely mimic the aforementioned data in Figs. 6.9 and 6.12; $\widetilde{x}_{d,\,ME}$ is mostly dependent upon gap and is essentially unaffected by the value of either $overhang_1$ or $overhang_2$. In addition, an increase in $\widetilde{x}_{d,\,ME}$ is observed with increasing gap_2 for a prescribed gap_1 and $overhang_1$; this increase is as large as 6% when comparing large gap_2 configurations to small gap_2 airfoils. When examining all figures in the column, $\widetilde{x}_{d,\,ME}$ is suggested to increase with increasing gap_1. Curiously, the effect upon $\widetilde{x}_{d,\,ME}$ of increasing gap_1 is nearly the same as the effects of larger gap_2; increases from small gap_1 airfoils to large gap_1 configurations are approximately 7%. This trend was not expected as flap 1 is larger than flap 2, and the element upstream of flap 1 is significantly larger than the element upstream of flap 2. Nevertheless, the effect of both gap sizes is nearly the same.

Finally, WTP_{ME} is plotted in Fig. 6.14(c,f,i), or the rightmost column of the figure. As seen in the plots, all four relative coordinates affect the main-element wake-thickness parameters; large effects are caused by gap_1 and gap_2 while moderate effects are caused by changes in $overhang_1$ and $overhang_2$. The trends in WTP_{ME} in Fig. 6.14(c,f,i) closely mimic the trends in Fig. 6.14(a,d,g) in which increased $\delta_{w,ME,\,max}$ correspond to increased WTP_{ME} and smaller $\delta_{w,ME,\,max}$ are related to decreased WTP_{ME}. In general, decreased WTP_{ME}, indicating smaller and thinner wakes, is observed for larger gap sizes for both flap 1 and flap 2. While both gap sizes affect WTP_{ME}, it is noted that larger variations are caused by gap_1 than by gap_2 with increases in WTP_{ME} due to gap_1 in excess of 300% while gap_2 yields increases of approximately 100%. Large variations in WTP_{ME} are also observed for changes in $overhang_1$ and $overhang_2$. Similar to trends with respect to gap size, a change in $overhang_1$ causes a larger increase in WTP_{ME} than the increase caused by $overhang_2$. It must be noted that a close resemblance between WTP_{ME} and l/d exists in the figure in which an increase of WTP_{ME} yields decreased values of l/d. While this conclusion is not surprising, it indicates that the rapid rise in C_d is in large part due to the larger, thicker wakes for increased overhang distances. Minor increases in C_l are offset by large increases in C_d thus yielding decreased l/d.

6.2.5 Summary of Computational Parametric Sweeps

The data and discussion presented in this section investigated the effect of flap placement and the resulting flowfield. Extensive parametric sweeps were performed at a range of α and Re for over 6,000 different airfoil configurations. One set of parametric sweeps was performed in which $gap_1 = gap_2$ and $overhang_1 = overhang_2$ for given values of δ_1 and δ_2. A second set of sweeps was performed to capture the coupled effect of independently changing gap_1, gap_2, $overhang_1$, and $overhang_2$; once again, δ_1 and δ_2 remained unchanged for these sweeps. The aerodynamic performance of these airfoils was discussed. Numerous new metrics were developed and presented earlier in this chapter, and these metrics were used to quantify the magnitude of wake bursting in the flowfield.

The first set of parametric sweeps was performed with $\delta_1 = 26.1$ deg and $\delta_2 = 16.2$ deg for configurations in which $gap_1 = gap_2$ and $overhang_1 = overhang_2$ at $\alpha = 0$ deg and $Re = 1 \times 10^6$. The configuration with maximum C_l at α of 0 deg was defined by $gap_{1,2} \approx 0.025$ and $overhang_{1,2} \approx 0.030$. It was observed that l/d for the range of configurations analyzed did not necessarily trend with C_l or C_d, but rather was affected by both lift and drag instead of being largely affected by only one variable. In general, l/d was maximized for small, or even slightly negative, values of $overhang_{1,2}$ and $gap_{1,2}$ of approximately 0.015. Trends in maximum wake thickness, $\delta_{ME,max}$, and wake thickness parameter, WTP_{ME}, exhibited the same trends as those observed with respect to C_d in which configurations with larger $gap_{1,2}$ and $overhang_{1,2}$ performed better than the contrary. No discernible trend was observed between either $\delta_{ME,max}$ or WTP_{ME} and the aforementioned C_l trends. The point at which the maximum wake thickness was observed, $\widetilde{x}_{d,ME}$, was primarily affected by gap size and inconsequentially affected by overhang distance. Configurations for decreased $gap_{1,2}$ yielded a decrease in $\widetilde{x}_{d,ME}$. That is to say that decreased gap size caused the point of maximum wake thickness to be closer to the airfoil trailing edge than that of increased gap size. Despite the upstream movement of $\widetilde{x}_{d,ME}$ with decreased $gap_{1,2}$, WTP_{ME} was affected by $\delta_{ME,max}$ more than by $\widetilde{x}_{d,ME}$. Wake thickness was minimized for large gap and small overhang conditions. Despite this observation, these configurations with thin wakes did not correspond with maximum l/d as a sharp decrease in C_l was noted for these airfoils. Trends for aerodynamic performance and wake metrics remained largely unchanged with varying α or Re, but some variations were observed. In particular, an increased value of α resulted in a configuration for maximum C_l with increased $gap_{1,2}$ and $overhang_{1,2}$. However, the configuration for maximum l/d was largely unchanged at different α. An increase in freestream Reynolds number resulted in a configuration with maximum C_l with larger gap sizes and overhang distances. Despite this observation, the l/d trends remained largely unchanged. No significant variations were observed in any of the wake metrics for changing α or Re.

A second parametric sweep was performed such that δ_1 and δ_2 were held constant while systematically varying gap_1, gap_2, $overhang_1$, and $overhang_2$ for $\alpha = 0$ deg and $Re = 1 \times 10^6$. Results indicate that an increase in $overhang_1$ is shown to increase C_l for all configurations. However, this increase in C_l is accompanied by a sharp increase in C_d which ultimately leads to maximum l/d for very small values of $overhang_1$. In general, trends at a given $overhang_1$ and gap_1, that is to say only flap 2 is being moved, indicate the same trends as the coupled results discussed in the previous paragraph. Curiously, gap_2 has very little effect upon l/d while gap_1 significantly affects l/d. Smaller values of gap_1 yield increased l/d. As was seen in the previously-discussed analyses, the thickest wakes are observed for configurations with large values of $overhang$ and small gap. An increase in gap_1 and/or gap_2 shifts $\widetilde{x}_{d,ME}$ in a downstream direction, and the contrary is true for decreased gap sizes. Finally, large values of WTP_{ME} were observed for cases with a small gap_1 and small gap_2. These thick wakes decrease l/d in this region.

Table 6.2: Location of Experimentally-Studied Airfoil Defined in Relative Coordinates

Airfoil	Main Element to Flap 1			Flap 1 to Flap 2			
Configuration	gap_1	$overhang_1$	$\delta_{r,1}$	gap_2	$overhang_2$	$\delta_{r,2}$	Purpose
10	0.0100	0.0150	26.4 deg	0.0100	0.0150	15.9 deg	Baseline
11	0.0100	0.0150	22.0 deg	0.0100	0.0150	10.0 deg	Decreased δ
13	0.0100	0.0000	26.4 deg	0.0100	0.0000	15.9 deg	Decreased *overhang*
15	0.0200	0.0150	26.4 deg	0.0200	0.0150	15.9 deg	Increased *gap*
16	0.0050	0.0150	26.4 deg	0.0050	0.0150	15.9 deg	Decreased *gap*

Data discussed above can be synthesized into a variety of recommendations regarding multielement airfoil design. First, it must be stated that the "best" *gap*, *overhang*, and δ combination for one airfoil is not necessarily the same as for a different airfoil, and thus the flap rigging must be included in the design process. In general, it is desired to have small gap sizes for the flaps to increase the lift over the multielement airfoil without causing confluent boundary layers or surface separation. While the overhang distance is not as significant as the gap size, it is recommended to have very small (in magnitude), or even zero, overhang distance. As the gap size and the overhang distance are typically normalized by the system chord length, it may be desired to have a slightly smaller gap size for downstream elements than for the larger upstream elements. Again, these statements are merely guidelines for future airfoil designers, and not specific recommendations.

6.3 Experimental Tests

While an exhaustive series of configurations were examined computationally in the previous section, it is not possible to perform such an exhaustive study using experimental methods due to limitations in testing time. Consequently, a small subset of airfoil configurations were selected for detailed experimental investigation. Each of these five configurations isolated a parametric change in a relative coordinate for both flap 1 and flap 2, and thus the five experimentally-studied configurations were defined by flaps that were located at different spatial positions. The relative coordinates that defined each configuration are presented in Table 6.2, and a succinct description, or "purpose," of each configuration is also included in the table. These configurations were selected in an attempt to determine the effect of gap, overhang, and δ on the presence and behavior of the burst wakes. Coordinates as defined by the absolute coordinate system are presented in Table 6.3, though the purpose of each configuration is not as readily observed from this table. Experimental configurations can be studied using a variety of different experimental methods, and data in this section are presented using four different techniques. These four methods include two-dimensional wake surveys collected in the *x-y* plane with a 7-hole probe, determination of various wake metrics, surface oil flow visualization, and measurement of aerodynamic performance.

Table 6.3: Location of Experimentally-Studied Airfoil Defined in Absolute Coordinates

Airfoil Configuration	Flap 1 $(x,y)_{le}$	Flap 1 $\delta_{abs,1}$	Flap 2 $(x,y)_{le}$	Flap 2 $\delta_{abs,2}$	Purpose
10	$(0.6907, -0.0178)$	26.4 deg	$(0.8619, -0.1352)$	42.3 deg	Baseline
11	$(0.6724, -0.0195)$	22.0 deg	$(0.8478, -0.1150)$	32.0 deg	Decreased δ
13	$(0.6889, -0.0117)$	26.4 deg	$(0.8653, -0.1261)$	42.3 deg	Decreased *overhang*
15	$(0.6943, -0.0283)$	26.4 deg	$(0.8612, -0.1559)$	42.3 deg	Increased *gap*
16	$(0.6889, -0.0126)$	26.4 deg	$(0.8623, -0.1248)$	42.3 deg	Decreased *gap*

6.3.1 Effect of Relative Deflection Angle

An investigation was performed to determine the effect of the relative deflection angle, δ, for each flap. As presented in Table 6.2, Configuration 11 was defined by decreased δ_1 and δ_2 relative to Configuration 10, the baseline configuration. This section presents the effect of decreased δ on the burst-wake flowfield and aerodynamic performance.

Baseline Comparison

Aerodynamic Performance

It is known that viscous flowfield features, such as wakes, can influence the aerodynamic performance of an airfoil. A variety of aerodynamic metrics are shown in Fig. 6.15 for both the baseline and low-δ configurations. A comparison of the lift data, plotted in Fig. 6.15(a), indicate significant differences between the baseline and low-δ configuration. Most significantly, the lift curve for the low-δ case is shifted down in the $-C_l$ direction, and this shift is due to the decreased camber of the multielement airfoil system. Data suggest the reduction in C_l at a given α is as large as 0.8. As the difference in C_l at a given α between the two configurations is constant across all α in which $\alpha < \alpha_{stall,\ positive}$, the slope of the lift curves, C_{l_α}, is the same. Stall is observed to occur at 4 deg for the baseline airfoil but at only 2.5 deg for the low-δ configuration. A sharper, more-aggressive, drop in C_l at $\alpha > \alpha_{stall,\ positive}$ is observed for the baseline configuration, but a more-forgiving reduction in C_l is noted for the low-δ configuration.

Figure 6.15(b) presents a drag polar for each configuration across a range of α at $Re = 1 \times 10^6$. Decreased values of C_d for the low-δ configuration compared to the baseline configuration are observed across all values of C_l, and this trend is visible with the small-δ polar that is shifted in the $-C_d$ direction. The shape of the two polars is somewhat similar, but some differences are noticed. Both configurations indicate a large increase in C_d between $C_{l,max} - 0.6 \leq C_l \leq C_{l,max} - 0.4$ and $C_{l,max} - 0.2 \leq C_l \leq C_{l,max} - 0.1$. However, C_d is observed to increase more rapidly for the low-δ configuration than the baseline configuration in the middle portion of the drag polar for which $C_{l,max} - 0.4 \leq C_l \leq C_{l,max} - 0.2$.

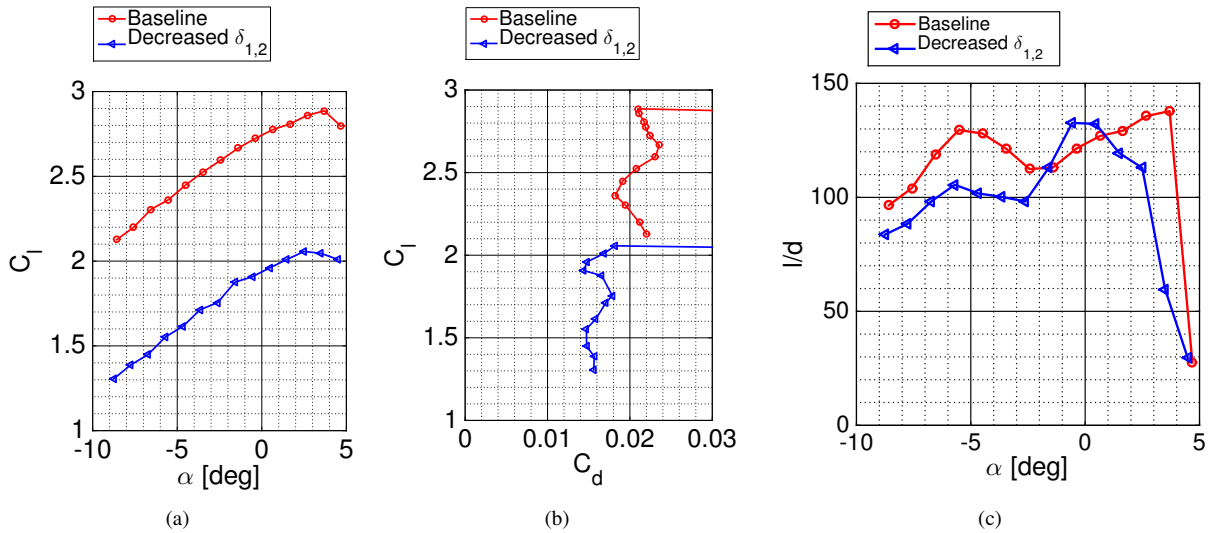

Figure 6.15: Effect of decreased flap deflection angle (Configuration 11) upon aerodynamic performance including a) C_l, b) C_d, and c) l/d.

Finally, l/d for the two configurations is shown in Fig. 6.15(c). The baseline configuration yields increased l/d for $\alpha \leq -1$ deg and $\alpha \geq 1$ deg; conversely, the low-δ case corresponds with higher l/d for -2 deg $\leq \alpha \leq 1$ deg. Drag data for both configurations occur in which -6 deg $\leq \alpha \leq -3$ deg yield a region of decreased l/d. A marked decrease in l/d is observed at high α, which results in the rapid rise in C_d near stall that was previously mentioned. The soft, gradual stall of the low-δ results in more gradual changes in C_l, C_d, and l/d for the low-δ airfoil than the baseline case. A sharp stall of the baseline airfoil, which results in a decrease in C_l and a large increase in C_d, corresponds to a rapid decrease in l/d at $\alpha = 4$ deg.

Wake Survey

A series of wake surveys were experimentally executed to determine the nature of wake bursting, and results are plotted in Fig. 6.16. Contour plots of $\widetilde{U}_t$, $C_{p,t}$, and C_p are shown for both the baseline configuration, as shown in the left column, and the decreased δ configuration, shown in the right column at a freestream Reynolds number of 1×10^6 and α of 0 deg. Contour plots are presented for $\widetilde{U}_t$, $C_{p,t}$, and C_p in the leftmost, center, and rightmost columns, respectively. As was observed in Chap. 5, trends in $\widetilde{U}_t$ closely mimic the trends in $C_{p,t}$, which is the expected trend as a reduction in total head is associated with a reduction in velocity for subsonic, incompressible flows. This trend is visible by comparing Fig. 6.16(a,c) with Fig. 6.16(b,d) for the baseline and small-δ configurations, respectively. In general, the wake for the low-δ configuration is smaller and thinner than that of the baseline configuration. This is the expected trend as the streamwise pressure gradient, seen in Fig. 6.16(f) is substantially weaker than that in Fig. 6.16(e). Returning to the $\widetilde{U}_t$ plots, the maximum momentum deficit, or smallest value of $\widetilde{U}_t$, at small values of $\widetilde{x}$ are large for

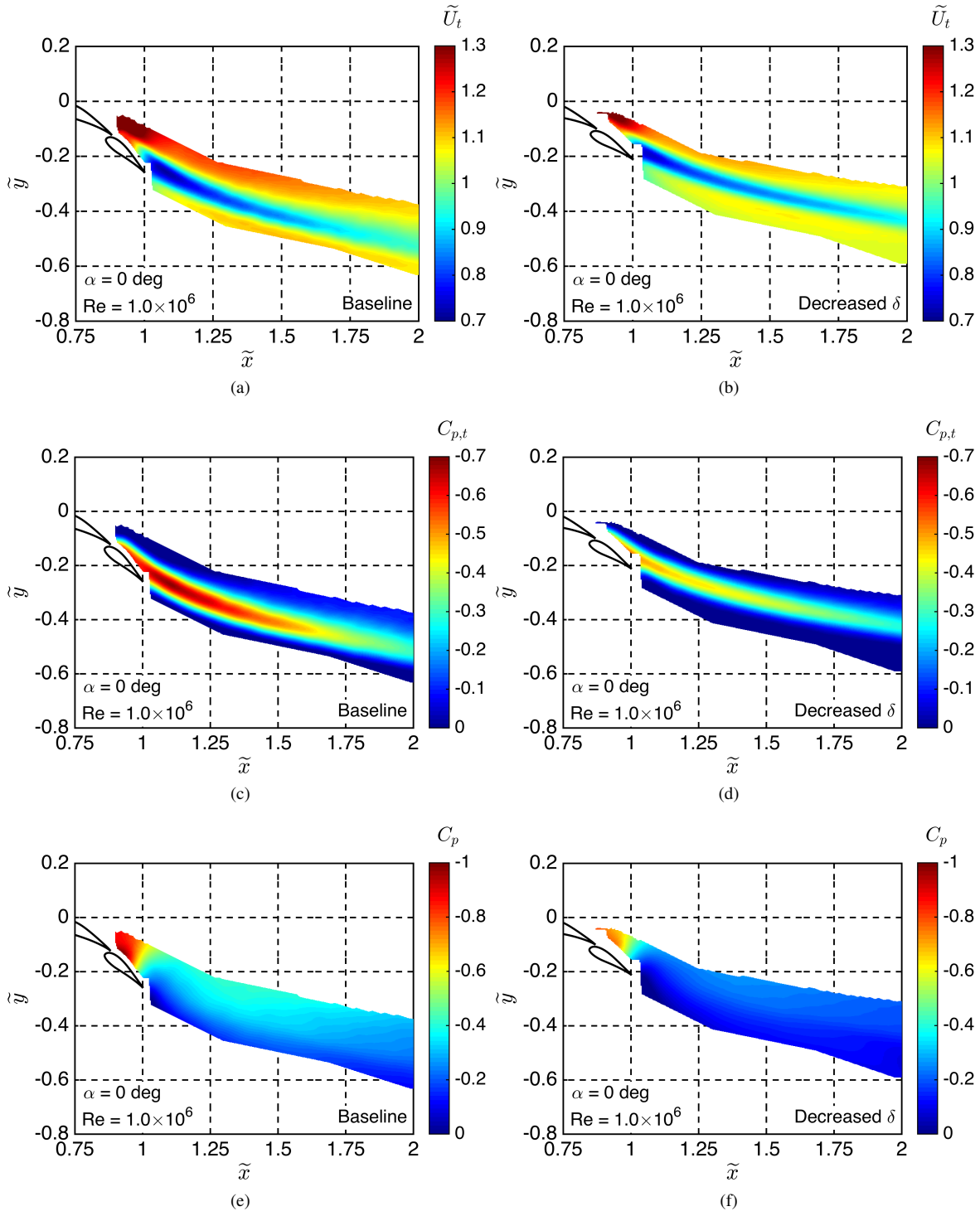

Figure 6.16: Two-dimensional wake surveys capturing effect of decreased flap deflection angle for a) $\widetilde{U}_t$ c) $C_{p,t}$ and e) C_p for the baseline configuration; and b) $\widetilde{U}_t$, d) $C_{p,t}$, and f) C_p for the decreased flap deflection angle configuration.

the baseline configuration than the reduction in $\widetilde{U}_t$ for the small-δ configuration. Thus, the wake of the baseline configuration is said to be wider, thicker, and "deeper" than the low-δ case with a narrower, thinner, and "shallower" wake. The so-called depth of the wake refers to the minimum value of $\widetilde{U}_t$ in which a deep wake indicates a low value of $\widetilde{U}_{t,\,min}$ while a shallower wake refers to a wake with increased $\widetilde{U}_{t,\,min}$. While the baseline wake is deeper than that of the low-δ for $\widetilde{x} \leq 1.6$, the baseline-configuration wake is slightly, and almost insignificantly, shallower than that of the low-δ wake at larger values of $\widetilde{x}$. As previously mentioned, the trends in $C_{p,t}$ closely mimic the trends for $\widetilde{U}_t$ in which the baseline-configuration yields decreased $C_{p,t,\,min}$ at low $\widetilde{x}$, and larger values of $C_{p,t,\,min}$ at larger $\widetilde{x}$. In addition, the reduction in $C_{p,t}$ indicates a wider, thicker wake for the baseline configuration than the decreased-δ airfoil; this observation is true for both low $\widetilde{x}$ and larger $\widetilde{x}$. The coefficient of static pressure, C_p is shown in Fig. 6.16(e,f) for the baseline and low-δ configurations, respectively. Increased pressure gradients in both the streamwise and chord-normal directions are observed for the baseline configuration than the pressure gradients of the low-δ airfoil. Similar to the behavior of viscous boundary layers, the thickness and presence of a burst wake is affected by the streamwise pressure gradient. Thus, as the static pressure gradient is larger for the baseline configuration, the wake of the baseline case is larger and deeper than that of the low-δ configuration.

In addition to the contour plots presented in Fig 6.16, the wakes can also be visualized and studied through the use of wake profiles. In this research project, one-dimensional wake profiles were extracted at a specified value of $\widetilde{x}$ for the range of $\widetilde{y}$ across the wake. Data were extracted at $\widetilde{x}$ of 1.05, 1.25, 1.50, and 2.00 for both the baseline [Fig. 6.16(a)] and low-δ configuration [Fig. 6.16(b)], and results are shown in Fig. 6.17 wherein the baseline configuration and low-δ configuration are coplotted in the figure. The streamwise position at which each profile was extracted are labeled in the caption and on each of the figures. All wake profiles contain data in which $\widetilde{U}_t \geq 1$, and this result is necessary to maintain continuity across the wind-tunnel test section. As the streamlines in the middle of the wake expand, streamlines in the flow outside the wake region will contract, thus yielding values of $\widetilde{U}_t$ that are slightly higher than the freestream value. This local increase in momentum decreases in magnitude with increasing distance from the wake region, and the wake profile will approach 1 near the wind tunnel walls. As seen in the figure at all $\widetilde{x}$, the wakes for the small-δ configuration are shifted in the $+\widetilde{y}$ direction. As the flap deflection angles are decreased, there is less camber for the airfoil system, thus leading to decreased flow curvature which in turn causes a movement of the wakes in the $+\widetilde{y}$ direction. As visualized in the wake-deficit contour plots previously discussed, the small-δ configuration yields smaller and thinner wakes than the wake created from the baseline configuration. Spanwise positions in which $\widetilde{x} \leq 1.6$ indicate $\widetilde{U}_{t,\,min}$ is smaller for the baseline configuration than for the small-δ airfoil. That is to say the baseline configuration has increased momentum deficit than the small-δ configuration in this range of $\widetilde{x}$. On the contrary, the small-δ configurations suggest increased momentum deficit, or decreased $\widetilde{U}_{t,\,min}$ than the baseline configuration at $\widetilde{x} \geq 1.6$.

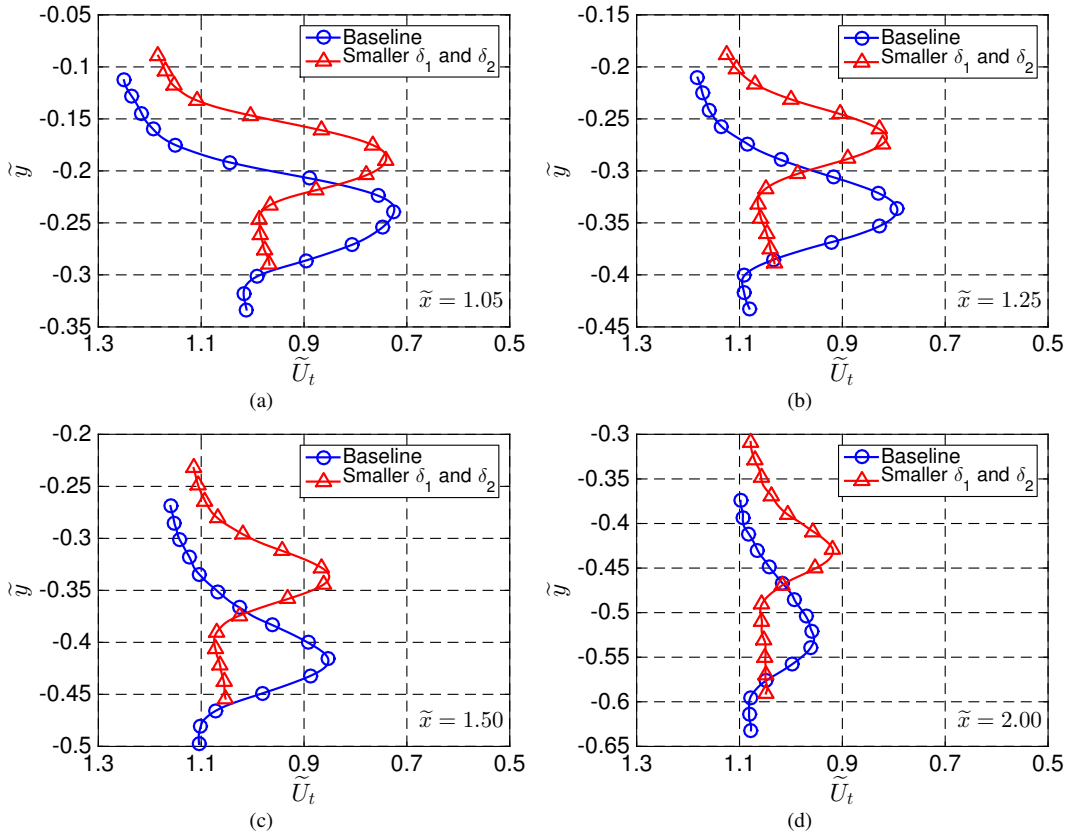

Figure 6.17: Effect of decreased flap deflection angle as evidenced by wake profiles at a) $\widetilde{x} = 1.05$, b) $\widetilde{x} = 1.25$, c) $\widetilde{x} = 1.50$, and d) $\widetilde{x} = 2.00$.

Wake Metrics

A variety of wake metrics, including wake edges and wake thickness, can be calculated for each of the airfoil configurations, and these results are plotted in Fig. 6.18. The wake edges and wake centerline for the baseline configuration and the low-δ airfoil are plotted in Fig. 6.18(a) in which solid lines represent the wake edges and dotted lines define the wake centerline location. As visualized above in the wake profiles plots shown in Fig. 6.17, the wakes for the decreased-δ airfoil are shifted in the $+\tilde{y}$ direction relative to the baseline configuration. The wake edges for the baseline configuration are observed to spread apart with increasing downstream distance, and this observation is confirmed by Fig. 6.18 in which the wake of the baseline configuration increases with downstream distance, but the wake thickness for the decreased-δ configuration is largely unchanged with increasing $\widetilde{x}$. The reader is reminded that the wake thickness h_w is defined by the distance between a contour of constant $C_{p,t}$, and the constant h_w is partially attributed to the weaker pressure gradients and decreased total-head losses in the low-δ configuration than in the baseline airfoil.

Figure 6.18(c) presents the normalized wake centerline location which is defined as

$$\frac{\widetilde{y}_{peak} - \widetilde{y}}{\widetilde{y}_u - \widetilde{y}_l}. \tag{6.13}$$

A value of 0 indicates a point on the lower wake edge while a value of 1 corresponds to the upper wake edge, and text labels for the upper and lower wake edges are shown in the figure. As seen in the Fig. 6.18(c), the centerline of each wake is approximately equidistant from the upper and lower wake edge in $1 \leq \widetilde{x} \leq 1.15$, or locations that are immediately downstream of the trailing edge. In general, the wake centerline approaches the lower wake edge with increasing downstream distance, which suggests increased asymmetry with larger $\widetilde{x}$. The baseline case is more asymmetric than the low-δ case, and this observation is attributed to the stronger chord-normal pressure gradient applied to the baseline configuration wake.

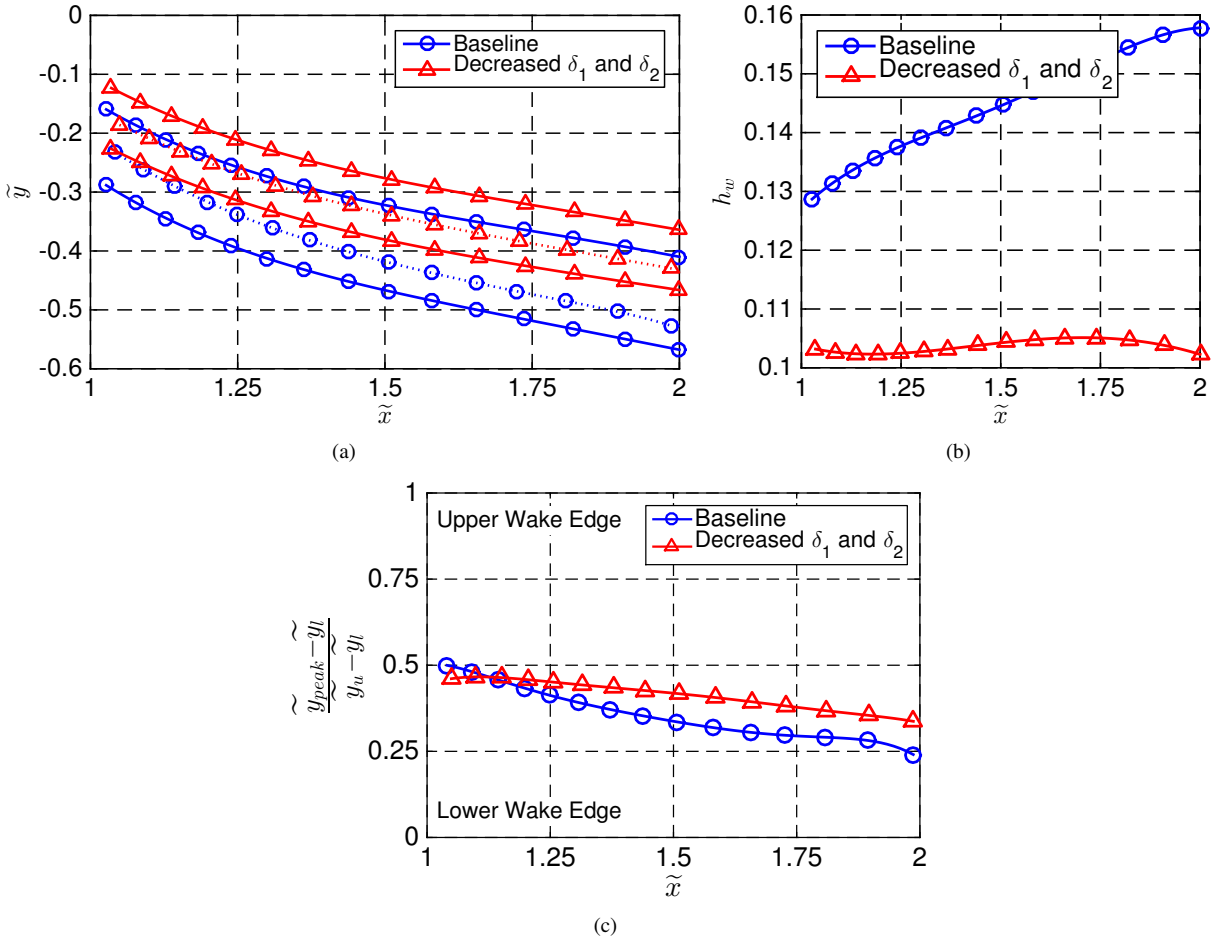

Figure 6.18: Wake thickness for the baseline and decreased δ configuration including a) wake edges and wake centerline, b) wake thickness as defined by h_w, and c) normalized wake centerline location.

Effect of α

Additional wind-tunnel experiments were performed to determine the effect of both decreased δ and freestream α. Contour plots for both the baseline and small-δ configurations are plotted in Fig. 6.19 with the baseline configuration in the left column and the reduced-δ airfoil on the right column. Each row corresponds to a given α (-2, -1, and 0 from top to bottom). A discussion of the baseline results, shown in Fig. 6.19(a,c,e) is presented above in Sec. 5.3.8, and the discussion in this section is focused upon the differences between the two configurations. Contour plots of $\widetilde{U}_t$ for both configurations over $-2 \leq \alpha \leq 0$ deg are shown in the figure, but any significant difference in trends with increasing α are hard to visualize in these contour plots. Each configuration suggests that an increase in α does not correspond with a decrease in $\widetilde{U}_{t,\,min}$ over the domain, but rather that the value of $\widetilde{U}_{t,\,min}$ remains nearly constant for all α tested. Curiously, the value of $\widetilde{U}_{t,\,min}$ at a given $\widetilde{x}$ is observed to increase with increasing α. This result was not necessarily expected as the stronger adverse pressure gradients applied to the airfoil at larger α were thought to increase the wake depth, or value of $\widetilde{U}_{t,\,min}$. However, this result indicates that the multielement airfoil performs better at an α of 0 deg than at an α of -2 deg, thus indicating a good design for the design point of $\alpha = 0$ deg. As the wake development was carefully considered during the design process, it is evident that the airfoil designer successfully achieved good control of the wake development for the design point. A comparison of the baseline and small-δ configuration results at a given α indicate that the wakes of the small-δ are thinner than those of the baseline configuration. As only minor differences are visible in Fig. 6.19 for both of the configurations, a series of wake profiles were extracted from the data set and are plotted in Fig. 6.20 for a series of $\widetilde{x}$ locations. Even when data sets at different α are visualized by wake profiles, only minor differences are observed, as shown in Fig. 6.20. As previously stated, wakes at decreased α include slightly-decreased $\widetilde{U}_{t,\,min}$ than the cases at higher α. Results at low $\widetilde{x}$, immediately downstream of the trailing edge, are closely aligned with each other, but some differences in wake location are observed for larger $\widetilde{x}$. More specifically, the wake for α of 0 deg is observed to move slightly in the $+\widetilde{y}$ direction, but neither the width nor wake shape are significantly different with changes in α.

Effect of Freestream Reynolds Number

A variety of experimental tests were performed in an effort to determine the relationship between freestream Reynolds number and burst wakes at different flap deflection angles. Wind tunnel tests were performed at $Re = 0.6 \times 10^6$, 0.8×10^6, and 1×10^6, and the standard contour plots of $\widetilde{U}_t$ are shown in Fig. 6.21. As previously discussed, the baseline configuration results [Fig. 6.21(a,c,e)] suggest that the wake thickness and minimum $\widetilde{U}_t$ both decrease with decreasing Reynolds number. Both of these trends are expected as the viscous wakes are affected by the freestream Reynolds number in a manner very similar to that of boundary layers in which decreased *Re* yields larger, thicker boundary layers than higher *Re* flows. Similar to the result with respect to α, the wakes from the decreased-δ case are

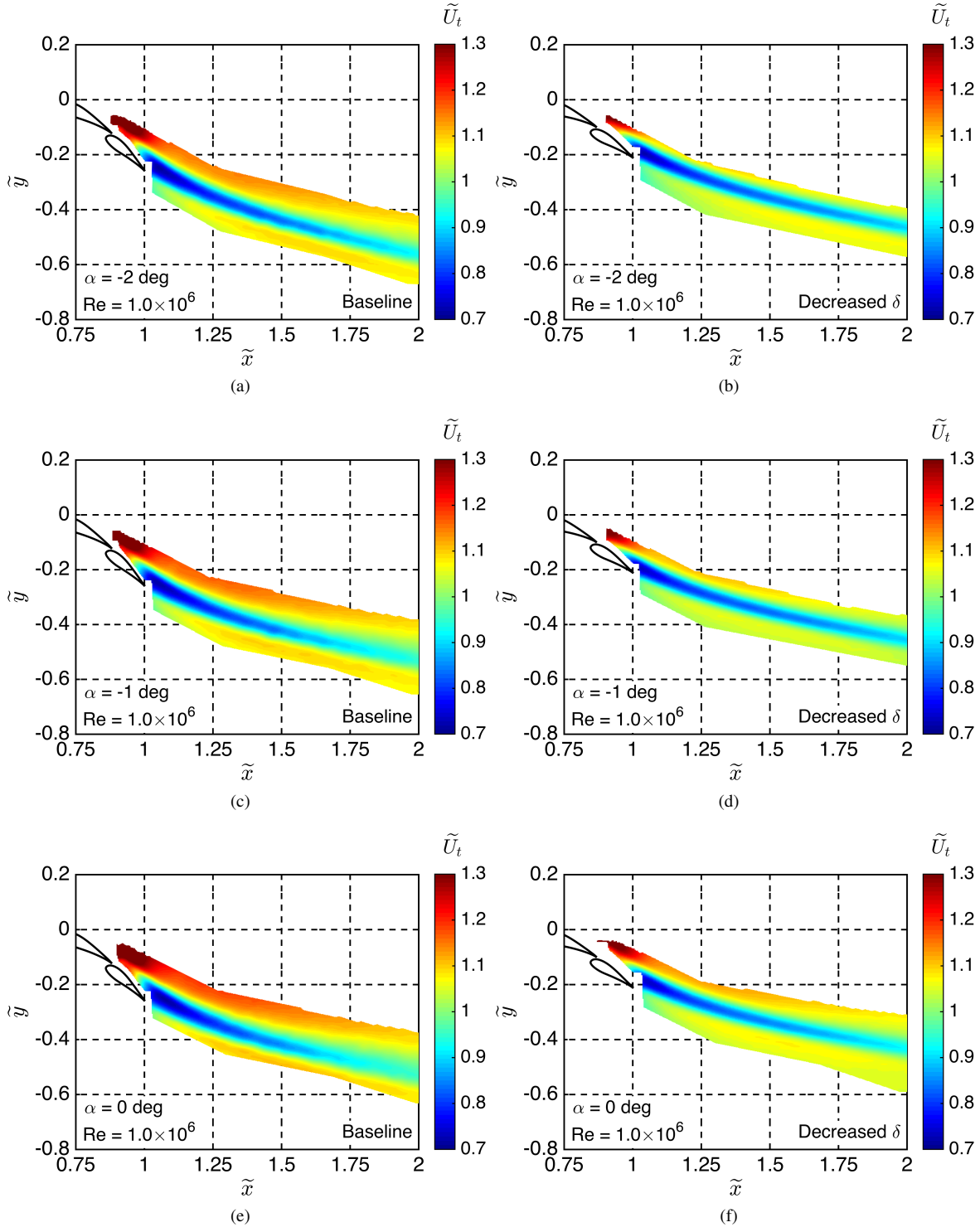

Figure 6.19: Two-dimensional wake surveys capturing effect of decreased flap deflection angle and freestream α for a) α=−2 deg, c) α=−1 deg, and e) α=0 deg for the baseline configuration; and b) α=−2 deg, d) α=−1 deg, and f) α=0 deg for the decreased-δ case.

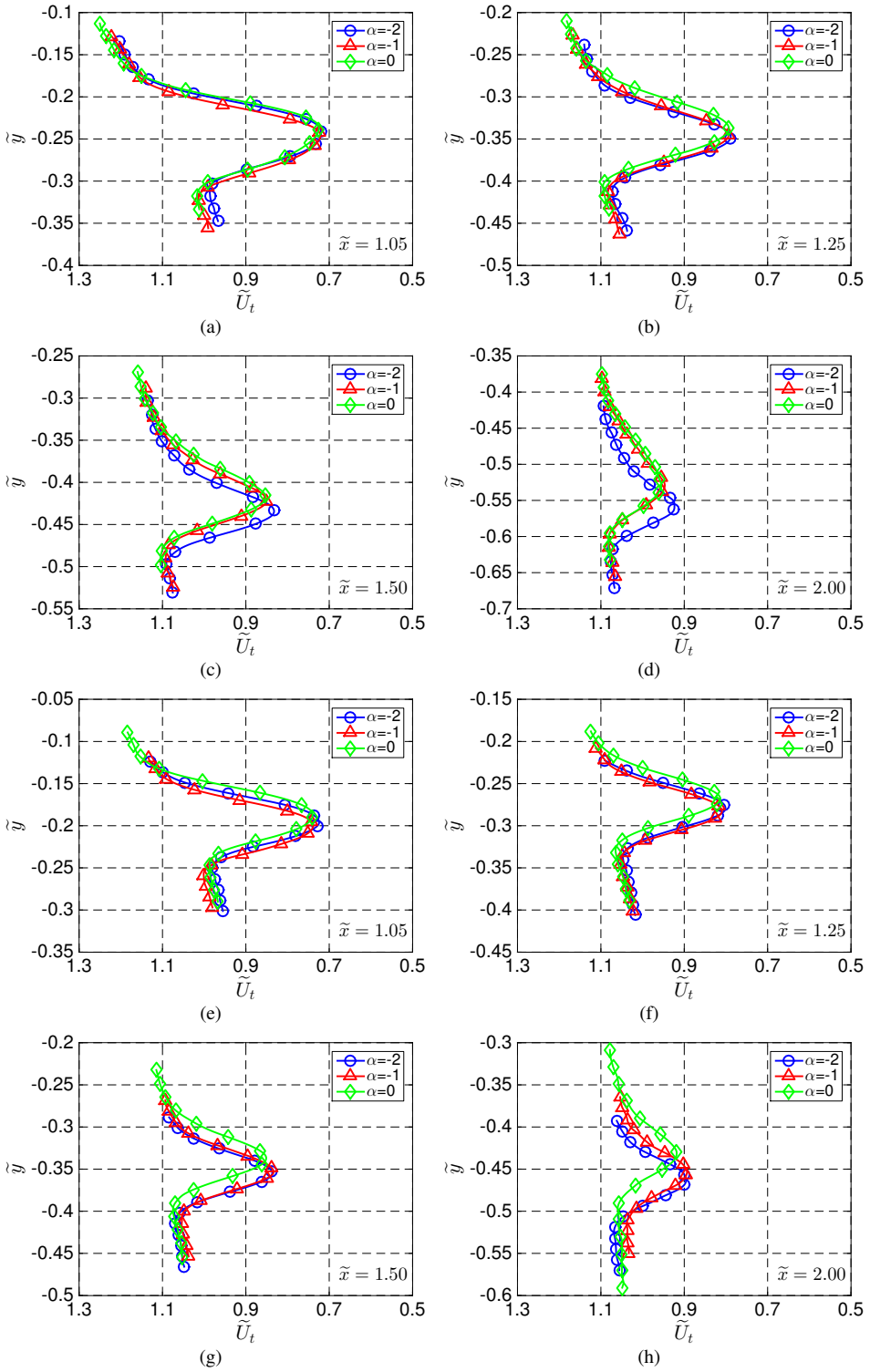

Figure 6.20: Effect of decreased deflection angle and freestream α evidenced by wake profiles at a) $\widetilde{x} = 1.05$, b) $\widetilde{x} = 1.25$, c) $\widetilde{x} = 1.50$, and d) $\widetilde{x} = 2.00$ for the baseline configuration; and e) $\widetilde{x} = 1.05$, f) $\widetilde{x} = 1.25$, g) $\widetilde{x} = 1.50$, and h) $\widetilde{x} = 2.00$ for the small-δ configuration.

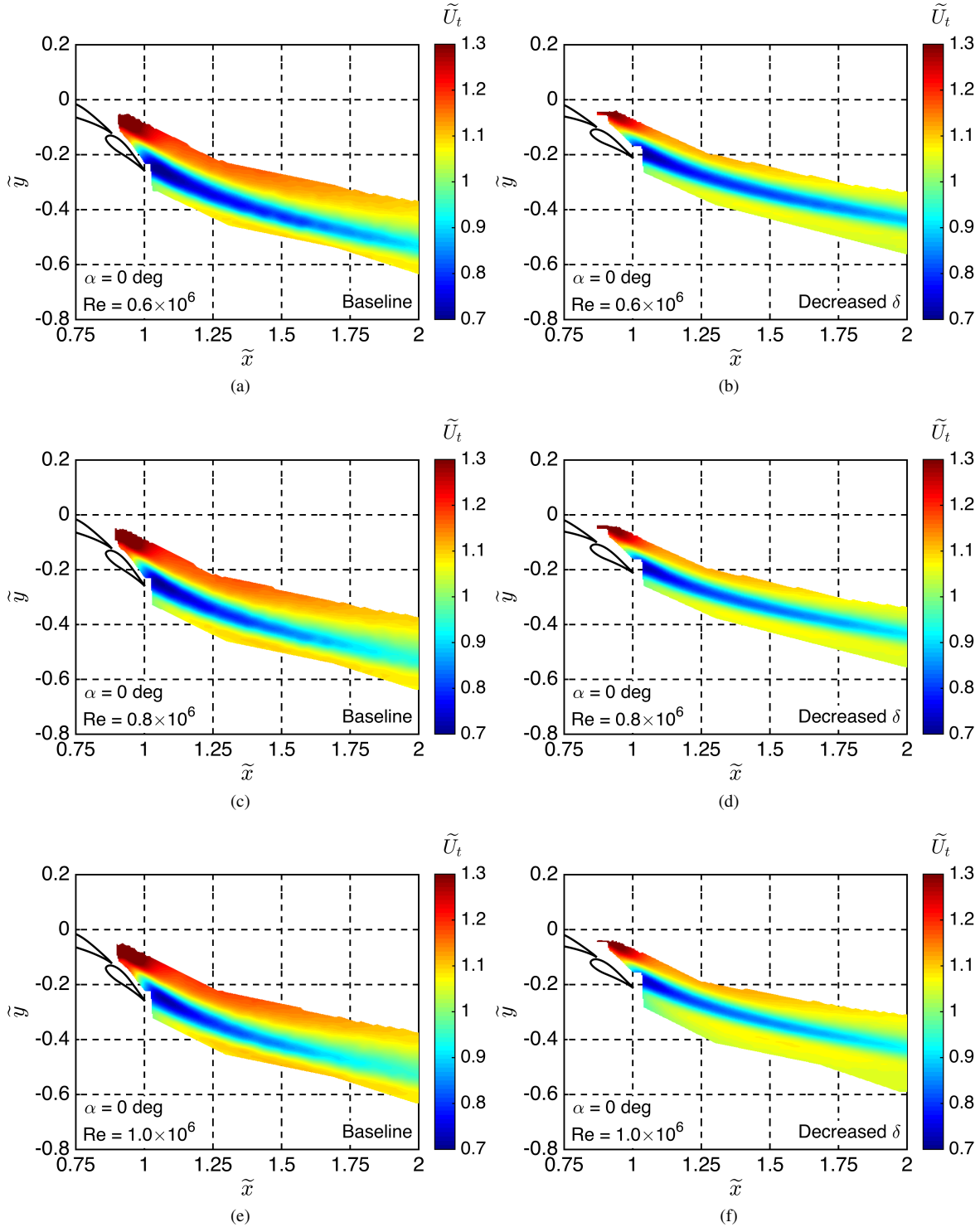

Figure 6.21: Two-dimensional wake surveys with effect of δ and freestream *Re* for a) *Re*=0.6×10^6, c) *Re*=0.8×10^6, and e) *Re*=1×10^6 for baseline airfoil; and b) *Re*=0.6×10^6, d) *Re*=0.8×10^6, and f) *Re*=1×10^6 for the decreased-δ configuration.

thinner than those of the baseline airfoil. Considering the results in Fig. 6.21, it is clear that the larger, thicker wakes at lower *Re* also yield decreased $\widetilde{U}_{t,\ min}$ for both small and large values of $\widetilde{x}$.

6.3.2 Effect of Gap Size

As defined above in Table 6.2, Configurations 15 and 16 isolate an increase and decrease in gap size relative to the baseline Configuration 10. Three different experimental tests at freestream Reynolds numbers ranging from 0.6×10^6 to 1×10^6 were performed for the three configurations in discussion.

Effect of Increased Gap Size

The first discussion of results will compare the aerodynamics of the baseline Configuration 10 with a configuration with a larger gap size, which is Configuration 15. These two configurations will be extensively discussed in this section.

Aerodynamic Performance

Aerodynamic performance data, including a lift curve, drag polar, and l/d plot, for the two configurations in discussion are presented in Fig. 6.22. The lift curve presented in Fig. 6.22(a) indicates the baseline configuration has increased C_l at a given α than that of the large-gap configuration. This is the expected trend as the multielement aerodynamic topic known as the circulation effect is less effective for multielement airfoils with larger gaps. As the downstream elements move further away from the upstream element, less circulation at the control point is applied in the chord-normal direction and the circulation vector contains both a horizontal and vertical component. The reduction in circulation pointed in the chord-normal direction moves the inviscid trailing-edge stagnation point in the streamwise direction, thus requiring less circulation on the element to satisfy the Kutta condition. Because of the decreased curvature around the multielement airfoil, weaker pressure gradients are applied to the wake, thus yielding less wake bursting for the large-gap airfoil than the baseline configuration. The lift curve slope, C_{l_α}, of the baseline configuration is larger than the C_{l_α} for the large-gap configuration, and both slopes are less than the theoretical 2π. It is known that separation in a flowfield can affect C_{l_α}, and thus the reduction in C_{l_α} for both cases is attributed to the wake bursting, as discussed later in this section. Similarly, the decreased lift-curve slope for the baseline configuration is attributed to increased wake bursting relative to the increased-gap configuration. Stall is observed for the baseline configuration at α of 4 deg, and stall was not observed for the larger gap configuration over the range of α tested. This range of α was selected such that the loads, both lift and drag, did not exceed the maximum loads on the force balance.

A drag polar for each airfoil is presented in Fig. 6.22(b). First, it is observed that the baseline configuration has increased C_l at a given C_d, visualized by the drag polar that is moved in the upward direction. When the magnitude of

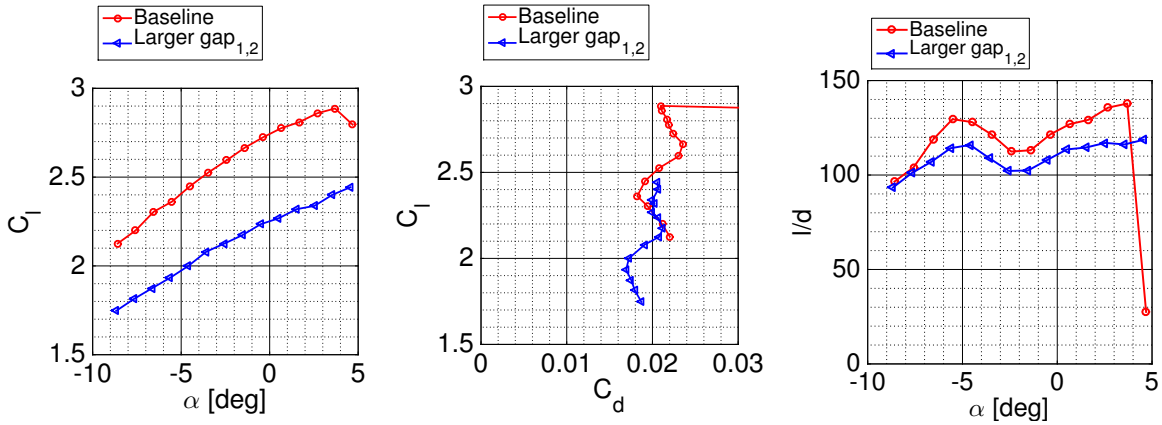

Figure 6.22: Effect of increased gap size upon aerodynamic performance including a) C_l, b) C_d, and c) l/d.

C_l is not considered, both airfoils exhibit similarly-shaped drag polars, thus indicating C_d is not considerably affected by C_l, which is an interesting and unexpected trend. It was thought that C_d would be dependent upon C_l as increased circulation yields increased wake bursting, but this is not the case. Both drag polars indicate a decrease in C_d for lower values of C_l followed by a slight increase in C_d with respect to C_l and then a final decrease in C_d as C_l increases toward $C_{l,\,max}$.

The coupled effect of both C_l and C_d is captured in Fig. 6.22(c) in which l/d is plotted as a function of α. Increased l/d is observed for the baseline configuration at almost all α than that of the configuration with the larger gap size, and thus it is observed that the increase in C_l at a given α dominates the increase in C_d for the same α. The aforementioned "bump" in the middle of the drag polar is observed with a decrease in l/d in the range of $-5 \leq \alpha \leq 0$ deg. Increased values of l/d are observed outside of this range, and $(l/d)_{max}$ occurs at the highest values of α for which data were collected and before stall.

Wake Survey

Wake surveys with the baseline configuration and an increased gap size configuration are shown in Fig. 6.23 for $\widetilde{U}_t$, $C_{p,t}$, and C_p. As previously observed earlier in this section and in Chap. 5, trends in $\widetilde{U}_t$ and $C_{p,t}$ closely mimic each other, as seen when comparing Fig. 6.23(a,c) with Fig. 6.23(b,d). The momentum-deficit region for the larger gap size configuration is significantly smaller than that of the baseline configuration, and less bursting of the main-element wake is observed. This observation is evidenced by the larger, thicker wake for the increased gap size as well as a smaller region in which $\widetilde{U}_t \leq 0.7$ (the dark blue region of the plot). Careful examination of Fig. 6.23(e) near the trailing edge of flap 2 indicates that the main-element and flap 1 wakes are not merged, and that a small momentum deficit region for flap 2 exists for which $\widetilde{x} \leq 1.10$. All three wakes merge at $\widetilde{x} \approx 1.10$, which is further downstream

than the merging for the baseline configuration in which the wakes merge at $\widetilde{x} < 1.0$. Curvature of the flowfield, evidenced by the $\widetilde{y}$ location of the wake for a given $\widetilde{x}$, is essentially unchanged between the two configurations. Data in Fig. 6.23(e,f) present the difference in the chord-normal pressure gradient between both configurations. A noticeably weaker $\partial C_p/\partial \widetilde{y}$ pressure gradient exists for the large gap size configuration when compared with the baseline pressure gradient, and this weaker pressure gradient yields a more well-behaved wake. In addition to a decreased pressure gradient in $\widetilde{y}$, the large-gap configuration yields decreased $\partial C_p/\partial \widetilde{x}$ relative to the baseline configuration, and it is this streamwise pressure gradient that causes both wakes and boundary layers to separate. Thus, the smaller pressure gradient for the large-gap case yields less separation in the wake, which is manifested with decreased momentum deficit, as previously discussed. A number of wake profiles depicting $\widetilde{U}_t$ at a constant $\widetilde{x}$ for a range of $\widetilde{y}$ are presented in Fig. 6.24. The x axis is oriented such that decreased $\widetilde{U}_t$ is on the right portion of the axis and larger values of $\widetilde{U}_t$ are on the leftmost end of the axis, which is the standard method for wake-deficit plots. Similar to the previously-discussed low-δ configuration, a series of wake profiles were extracted from the data shown in Fig. 6.23 at a number of different $\widetilde{x}$ locations. Slices were taken at $\widetilde{x}$ values of 1.05, 1.25, 1.50, and 2.00 for both the baseline configuration [Fig. 6.23(a)] and the large-gap configuration [Fig. 6.23(b)]; the locations of the slices are marked in each subfigure and in the caption for the figure. All wake profiles presented in the figure contain values of $\widetilde{U}_t$ at the edge of the wake that are in excess of the freestream value of 1.0. This local increase in momentum at the edge of the wakes is due to the conservation of mass across the airfoil test section. That is to say, as less mass flux exists in the low-momentum portion of the wake, another part of the flowfield must be greater than the freestream $\widetilde{U}_t$ of 1.0 to maintain continuity. As the walls of the test section are approached, the value of $\widetilde{U}_t$ will approach 1.0. This observation of local velocity greater than the freestream velocity is present in all wake profiles examined in this research, and the phenomona will not be discussed with any remaining wake profiles to avoid redundancy. The wake profile at $\widetilde{x} = 1.05$, just downstream of the airfoil trailing edge, presented in Fig. 6.24(a) clearly shows that the main-element and flap-1 wakes have fully merged in the baseline configuration, but that separate wakes exist for the main element, flap 1, and flap 2 for the large-gap airfoil. Increased momentum deficit is observed for the baseline configuration in which $\widetilde{U}_{t,min} = 0.71$ while $\widetilde{U}_{t,min} = 0.82$ for the large-gap airfoil. Figure 6.24(b) presents wake profiles at $\widetilde{x}$ of 1.25. At this location, it is clear that the three wakes for the large-gap configuration have fully merged as only one wake is observed for this configuration, which was not the case for the large-gap airfoil at $\widetilde{x} = 1.05$. Asymmetry is observed for both wakes, and the "upper" half of the wake profile is wider than the "lower" portion of the wake profile for both configurations. Wake profiles at $\widetilde{x}$ of 1.50, shown in Fig. 6.24(c), indicate the minimum momentum deficit is slightly less for the large-gap configuration than the baseline configuration, but the wake for the large-gap airfoil is slightly wider than the baseline airfoil. As was observed at $\widetilde{x} = 1.25$, both wakes are asymmetric about the $\widetilde{y}$ value for which $\widetilde{U}_{t,min}$ occurs. Finally, wake profiles captured further downstream, plotted in Fig. 6.24(d) suggest the wakes of the large-gap configuration are slightly

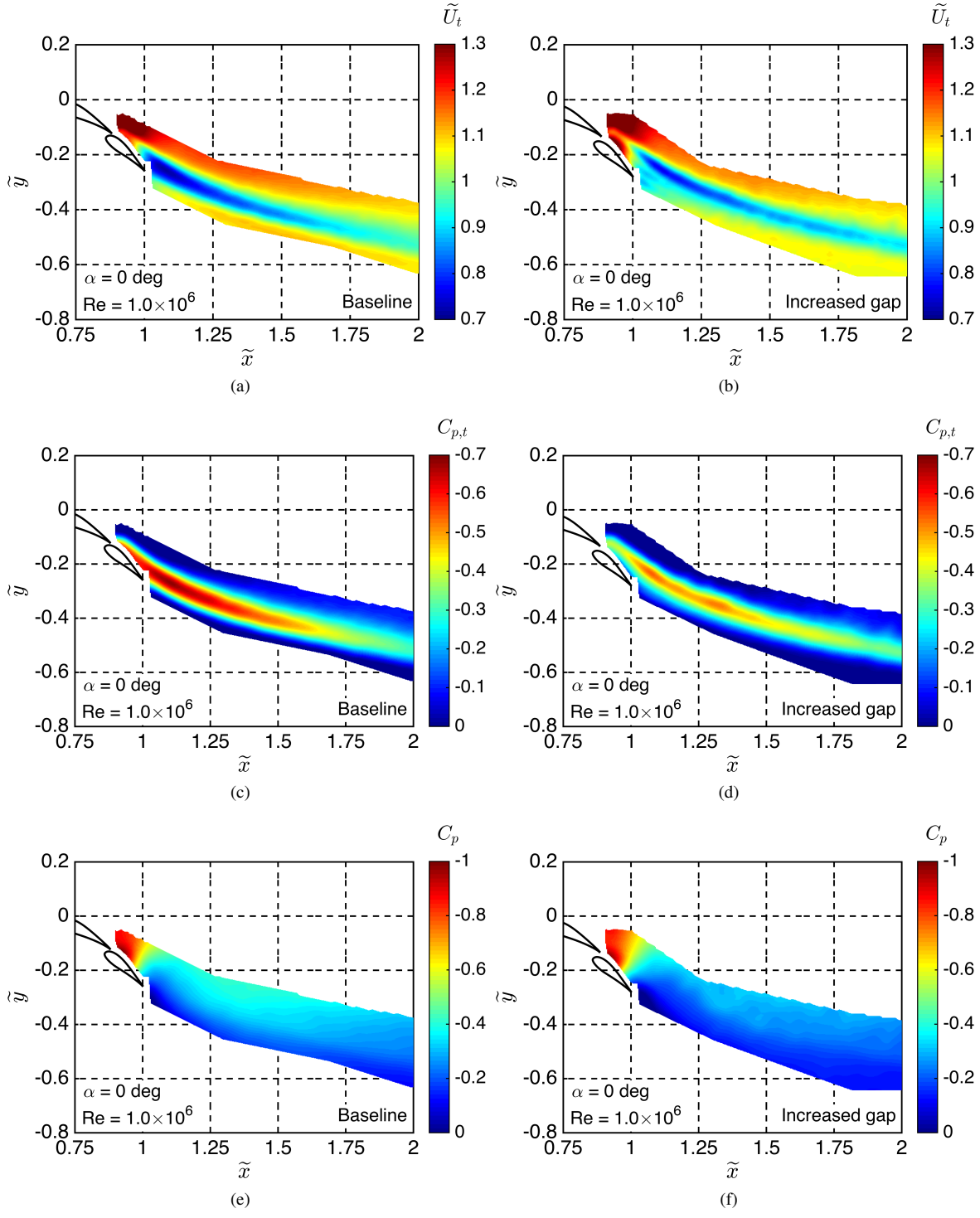

Figure 6.23: Two-dimensional wake surveys capturing effect of increased gap size for a) $\widetilde{U}_t$, c) $C_{p,t}$, and e) C_p for the baseline configuration; and b) $\widetilde{U}_t$, d) $C_{p,t}$, and f) C_p for the increased gap size configuration.

wider and have decreased $\widetilde{U}_{t,min}$ than those of the baseline configuration. That is to say that the wake of the large-gap configuration has less momentum than that of the baseline configuration.

Wake Metrics

Figure 6.25 shows the wake thickness of both the baseline configuration and the large-gap configuration. The wake edges and wake centerlines for both configurations are plotted in Fig. 6.25(a) in which the wake edges are plotted as solid lines and the wake centerlines are shown with dotted lines; the color and marker style in the plot indicates the appropriate configuration. Examination of the wake edges and wake centerlines in Fig. 6.25(a) indicates the large-gap configuration exhibits a slightly larger wake thickness close to the trailing edge of the system, but a significantly smaller wake thickness further downstream. Even though the wake profiles for the large-gap configuration are slightly wider at $\widetilde{x}$ of 1.50, shown in Fig. 6.24(b), the decreased momentum deficit for the large-gap wake yields decreased values of h_w for smaller values of $\widetilde{x}$. Although the momentum deficit at $\widetilde{x} \geq 1.50$ is slightly larger for the large-gap

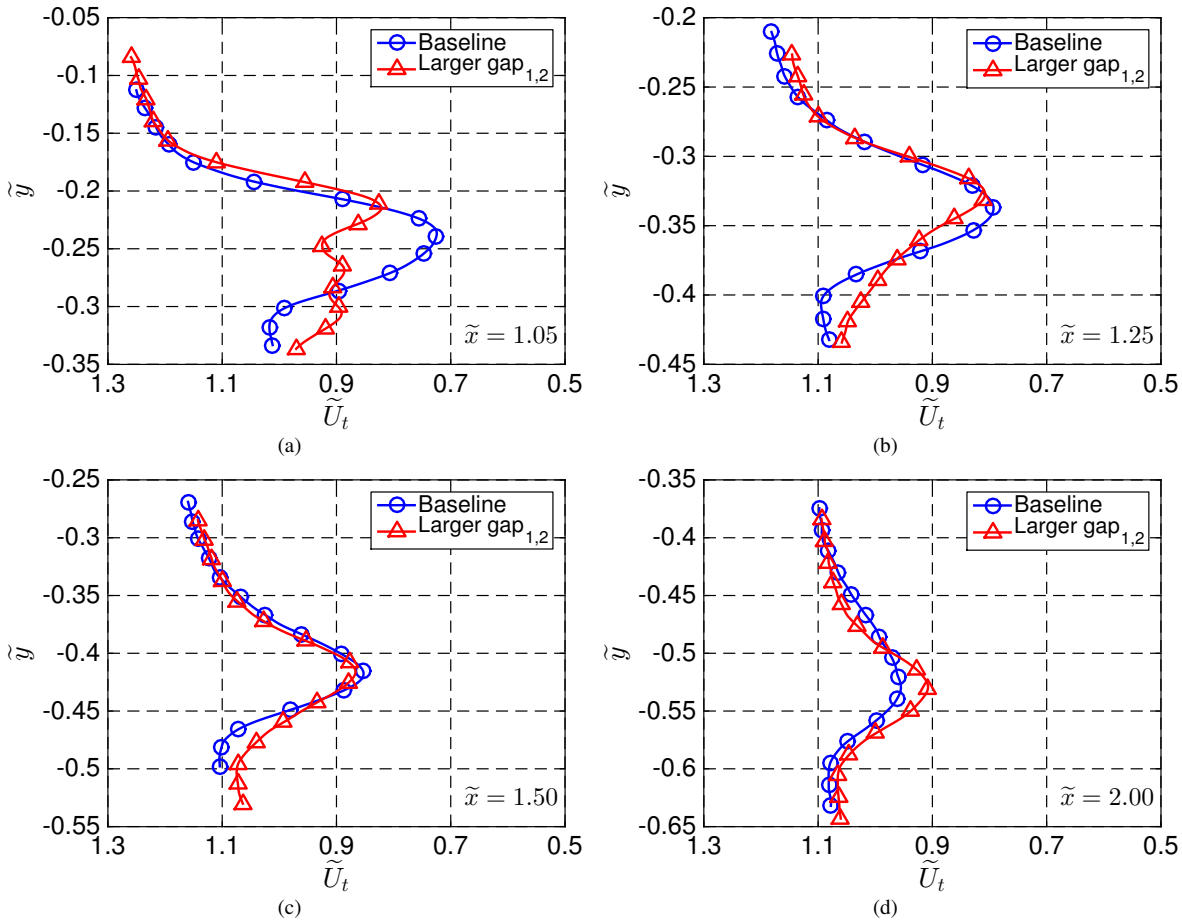

Figure 6.24: Effect of larger gap size evidenced by wake profiles at a) $\widetilde{x} = 1.05$, b) $\widetilde{x} = 1.25$, c) $\widetilde{x} = 1.50$, and d) $\widetilde{x} = 2.00$.

configuration than the baseline configuration, this momentum deficit is associated with $C_{p,t}$ values that are less than the 0.10 cutoff to quantify the wake edges. Thus, the wake thickness of both configurations may exhibit different trends depending upon if the wake thickness is quantified by a value of $C_{p,t}$ or based upon some relationship of $\widetilde{U}_t$. It is therefore critically important that the wakes are examined based upon wake profiles in addition to h_w so all the trends are observed. Returning to Fig. 6.25(b), the slight increase in wake thickness near the trailing edge is a result of the main-element, flap-1, and flap-2 wakes exist as separate wakes and are not merged. Thus, the thickness of the wake across both the flap-2 and main-element wake is slightly larger than that of the baseline configuration. Increased wake asymmetry exists for the large-gap case than for the baseline airfoil in which the wake centerline is closer to the upper wake edge for $\widetilde{x} < 1.25$ for the large-gap airfoil than the baseline airfoil. It is interesting to note that the wake centerlines for both configurations at $\widetilde{x} > 1.4$ are at the same $\widetilde{y}$ values for a given $\widetilde{x}$ despite the fact that the wake thicknesses are different.

Effect of Freestream Reynolds Number

As previously mentioned, wake surveys at a range of Reynolds numbers were performed for each of the airfoil configurations and the results are plotted in Fig. 6.26. The baseline configuration is shown in the left column while the increased gap size configuration is shown in the right column; each row portrays data at freestream Reynolds numbers between 0.6×10^6 and 1×10^6. As the burst wake is a viscous region, it was expected that the wake would scale with Reynolds number, and differences in the flowfields are indeed observed with changing Reynolds numbers. The largest, thickest wakes are observed at $Re = 0.6 \times 10^6$ as evidenced by the width of the wake and the region of low momentum. Results in Fig. 6.26(a) indicate the region for which $\widetilde{U}_t < 0.90$, evidenced by the light blue color, extends as far downstream as $\widetilde{x} = 1.96$, but the wake in Fig. 6.26(e), which is the baseline configuration at $Re = 1 \times 10^6$, indicates

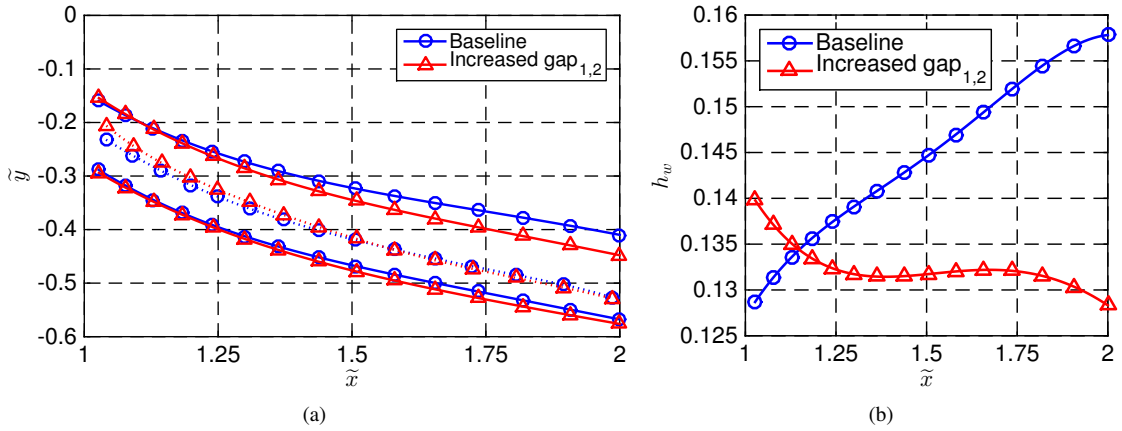

Figure 6.25: Wake thickness for the baseline and large-gap configuration including a) wake edges and wake centerline and b) wake thickness as defined by h_w.

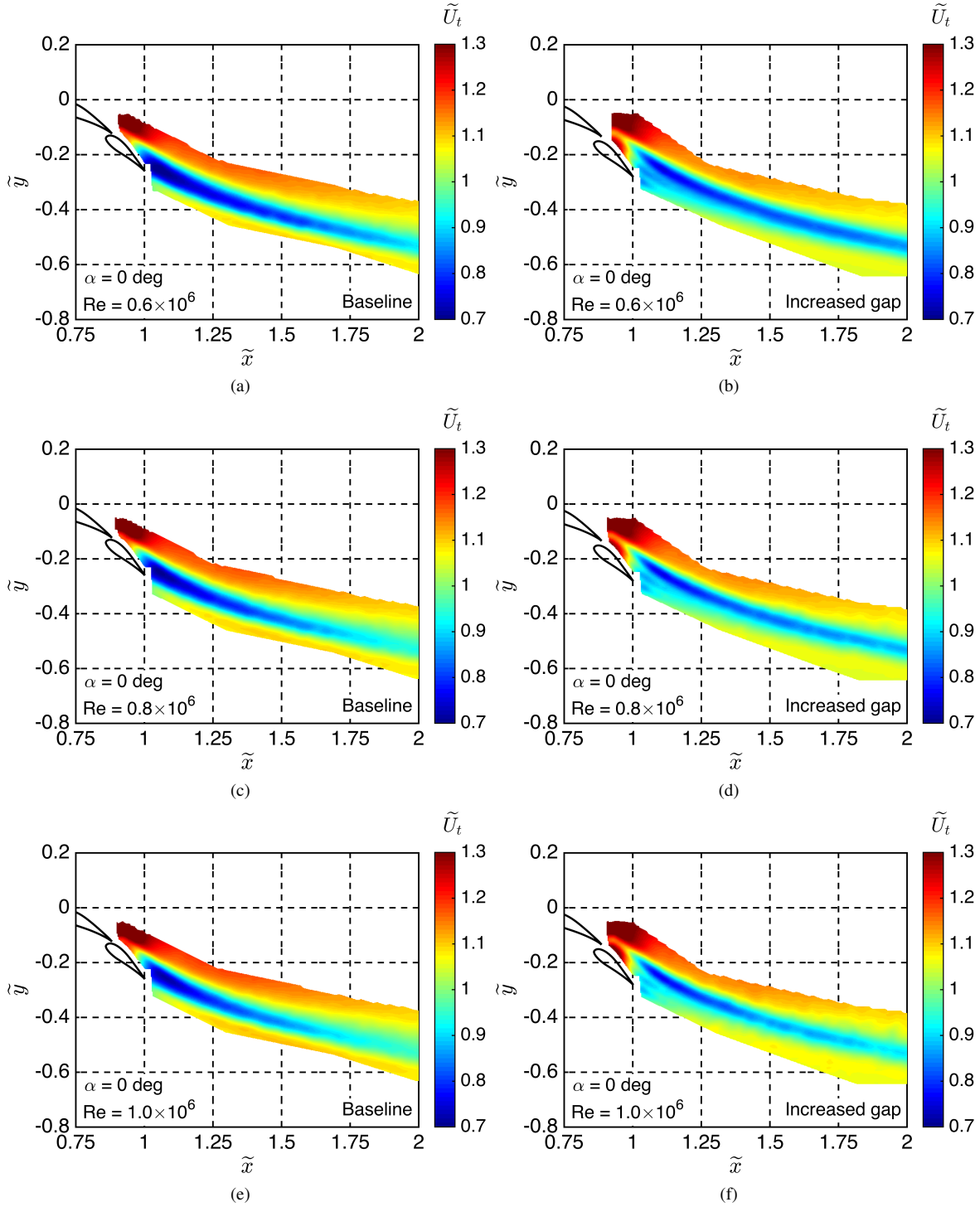

Figure 6.26: Effect of larger gap size and Reynolds number on $\widetilde{U}_t$ for a) Re=0.6×10^6, c) Re=0.8×10^6, and e) Re=1×10^6 for the baseline configuration; and b) Re=0.6×10^6, d) Re=0.8×10^6, and f) Re=1×10^6 for the increased gap size configuration.

the maximum $\widetilde{x}$ for which $\widetilde{U}_t < 0.90$ is $\widetilde{x} = 1.65$. Both the baseline configuration and the wide-gap configuration yield thicker wakes at lower Reynolds numbers than at larger Reynolds numbers. The total deflection of the wake, caused by the curvature of the flowfield, is essentially unchanged with respect to Reynolds number for both configurations.

Numerous wake profiles were extracted from the data presented in Fig. 6.26 at different different values of $\widetilde{x}$, and the results are plotted in Fig. 6.27. Plots in the left column correspond to the baseline configuration, and the right column of plots present data from the large-gap configuration; the four rows correspond to the four different values of $\widetilde{x}$ at which data were extracted. Each subplot presents wake profiles at freestream Reynolds numbers of 0.6×10^6, 0.8×10^6, and 1×10^6, as labeled in the legend. Data in Fig. 6.27(a,c,e,g) include wake profiles at four values of $\widetilde{x}$ for the baseline configuration. As seen in the plots, the wake expands in thickness with increasing downstream distance, which is the expected growth pattern for a viscous wake. In addition, the value of $\widetilde{U}_{t,min}$ decreases with increasing $\widetilde{x}$. These two observations are typical for wake development to satisfy the conservation of momentum across the airfoil wake. The thickness of the wakes is relatively unaffected by the freestream Reynolds number, but the minimum value of $\widetilde{U}_t$ increases with larger Reynolds numbers. This observation correlates with the previous conclusion in the discussion of Fig. 6.26. A series of four wake profiles are presented in Fig. 6.27(b,d,e,h), and data suggest that the wake widens and the minimum $\widetilde{U}_t$ increases with increasing downstream distance. This trend was also observed with the baseline configuration. Three separate distinct wakes, corresponding to the three different airfoil elements, exist at $\widetilde{x} = 1.05$ for all three tested Reynolds numbers. A simple comparison between the two different configurations at a given $\widetilde{x}$ provides additional insight into the differences in wake development for the two configurations. Trends to not necessarily exist for which the wake has less momentum for the two configurations at a range of $\widetilde{x}$. At some streamwise locations, the baseline configuration has less momentum than the large-gap configuration, but the opposite is true at most other positions.

Effect of Decreased Gap Size

While the effect of increasing the gap size was previously examined in this document, it is also useful to determine the effect of decreasing the gap size upon the burst-wake flowfield and aerodynamic performance. As defined in Table 6.2, Configuration 16 corresponds to a decrease in gap size relative to Configuration 10, and these two configurations will be extensively discussed in this section.

Aerodynamic Performance

Aerodynamic performance metrics, such as lift curves and drag polars, are plotted in Fig. 6.28. Similar to what is seen in Fig. 6.22(a) for the large-gap configuration, data in Fig. 6.28 indicate significant differences in C_l exist when the baseline and small-gap configurations are compared in which, for a given α, the value of C_l for the small-

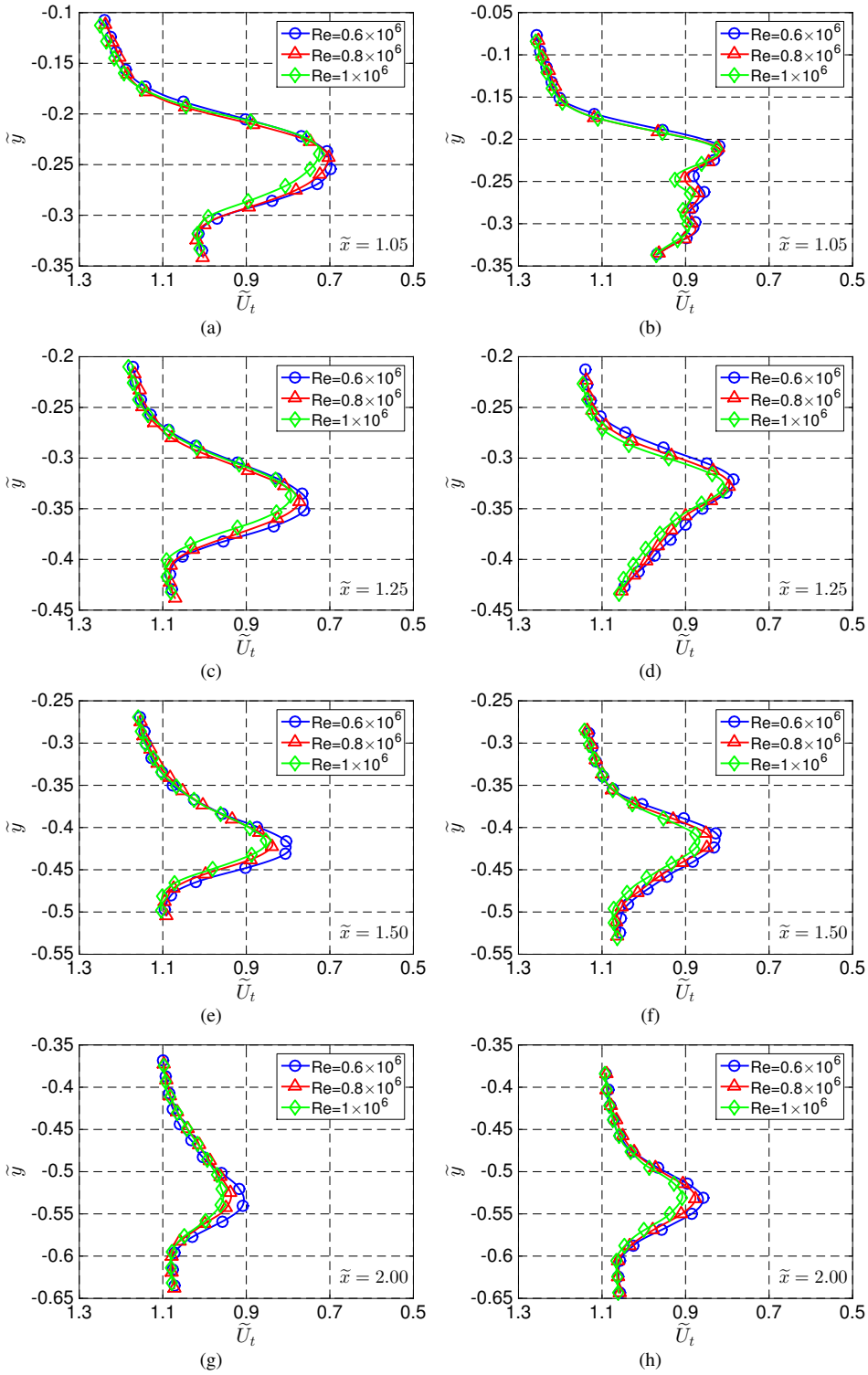

Figure 6.27: Wake profiles depicting effect of larger gap size and Reynolds number for a) $\widetilde{x} = 1.05$, c) $\widetilde{x} = 1.25$, e) $\widetilde{x} = 1.50$, and g) $\widetilde{x} = 2.00$ for the baseline configuration; and b) $\widetilde{x} = 1.05$, d) $\widetilde{x} = 1.25$, f) $\widetilde{x} = 1.50$, and h) $\widetilde{x} = 2.00$ for the large-gap configuration.

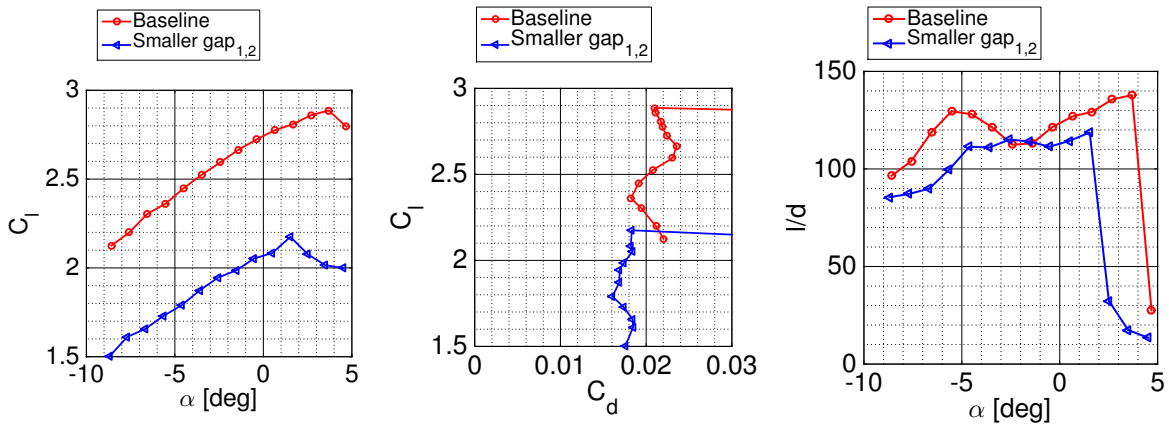

(a) (b) (c)

Figure 6.28: Effect of decreased gap size upon aerodynamic performance including a) C_l, b) C_d, and c) l/d.

gap configuration is decreased by approximately 0.7 when compared to the baseline case. This marked decrease in C_l indicates that gap sizes that are too small can significantly and adversely affect the lift of a multielement airfoil system. Despite the marked decrease in C_l for a given α, the lift curve slopes, C_{l_α}, are nearly the same for the two configurations. While C_{l_α} is slightly decreased for the small-gap airfoil, the differences in the lift curve slope are no more than 4%, which is contrary to the large-gap airfoil in results in Fig. 6.22(a) in which a significant reduction in C_{l_α} was observed for the large-gap airfoil relative to the baseline airfoil. Returning to Fig. 6.28. the stall angle of the baseline and small-gap configuration are different as the small-gap airfoil stalls at an α approximately 2.5 deg before stall occurs for the baseline airfoil. Stall characteristics for the small-gap airfoil indicate only slight decreases in C_l at $\alpha > \alpha_{stall}$.

Drag polar data for the two configurations are presented in Fig. 6.28(b) for both configurations. While the significant decrease in C_l for the small-gap airfoil is observed, a leftward shift of the small-gap polar compared to the baseline configuration polar is observed, and this shift obviously indicates a decrease in C_d. Despite the fact that each configuration is composed of the same elemental airfoil shapes, significant differences are observed in the shape of the drag polars. Drag increases at small α for the small-gap airfoil while C_d decreases for the baseline airfoil at small α. A relatively-narrow low-drag bucket is observed at $C_{l,max} - 0.15 \leq C_l \leq C_{l,max}$ for each configuration, but the small-gap airfoil data indicate a wider and more-forgiving low-drag bucket than that of the baseline airfoil.

Figure 6.28(c) presents the l/d ratio for both configurations, and significant differences in l/d are observed between the two airfoils. Examination of the small-gap airfoil indicates a region in which l/d is nearly constant in which $-5 \leq \alpha \leq 3$ deg. In this region, values of l/d deviate no more than 8% from l/d_{max} of 119, observed at $\alpha = 1.8$ deg, and thus the airfoil is observed to perform well across a wider range of α when compared to the baseline airfoil. A sharp drop in l/d is observed in which the airfoil is stalled. The baseline airfoil yields widely-varying l/d

across $-6 \leq \alpha \leq 4$ deg in which elevated values of l/d occur in which $-6 \leq \alpha \leq -3$ deg and also $1 \leq \alpha \leq 4$ deg. The airfoil yields decreased l/d between these two regions, and variations in l/d are as large as 21% over the range $-3 \leq \alpha \leq 1$ deg.

Surface Oil Flow Visualization

Surface oil flow visualization is a useful method to determine the behavior of the flow on the surface of an airfoil. Useful information that can be extracted from surface oil flow includes whether the flow is attached or separated, presence/location of laminar separation bubbles, and qualitative shear distributions. Using methods described in Sec. 3.2.12 on page 57, the flow visualization image presented in Fig. 6.29 was captured for the small-gap airfoil configuration. In the image, flow proceeds from the left to the right, and the upper surface of the main element and both flaps are visible. The silver horizontal lines in the figure are pieces of stainless steel that were part of the airfoil construction. The flow is well behaved over the main element and flap 1, as evidenced by the attached streaklines. However, a small portion of flow close to the flap 2 trailing edge indicates some surface flow separation, as labeled with the arrow in the figure. This trailing-edge separation certainly affects the wake of the airfoil system, as discussed throughout the remainder of this section.

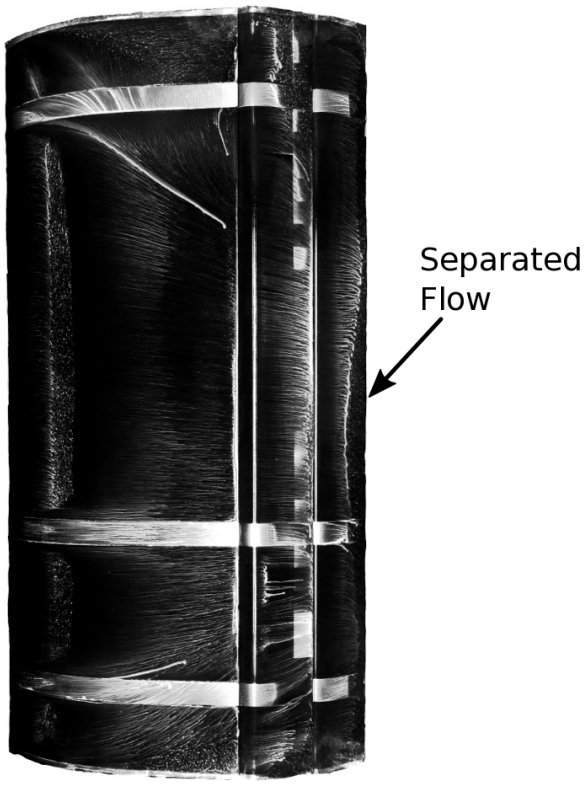

Figure 6.29: Surface oil flow visualization of small-gap airfoil exhibiting trailing-edge separation over flap 2.

Wake Survey

Two-dimensional wake surveys for the baseline and small-gap configuration at $\alpha = 0$ deg and $Re = 1 \times 10^6$ are shown in Fig. 6.30. The left column of plots in the figure corresponds to the baseline configuration, and the plots in the right column are results for the small-gap airfoil. Each column of plots presents a given wake survey parameter (including $\widetilde{U}_t$, $C_{p,t}$, and C_p). Wakes for the small-gap configuration have slightly less momentum and decreased values of $C_{p,t}$ relative to the baseline configuration. The decreased values of $C_{p,t}$ for the small-gap configuration suggest more head losses when compared to the baseline airfoil. It is important to observe that a small amount of separation is observed over the downstream portion of flap 2 as evidenced by the wake survey. This separation is also visible in the surface oil flow visualization which was discussed earlier in this section. As shown in Fig. 6.30(e,f), stronger streamwise pressure gradients are present for the small-gap configuration than the baseline configuration for both small and large values of $\widetilde{x}$. In particular, the streamwise pressure gradient $\partial C_p/\partial \widetilde{x}$ over flap 2 is stronger for the small-gap configuration than the baseline airfoil. Similar to an explanation earlier in this document, a smaller gap size creates more circulation in the chord-normal direction for the control point at $3c/4$. To satisfy the Kutta condition, the circulation on the upstream element must also increase. Thus, the stronger pressure gradient over the airfoil system is too aggressive, thus leading to separation on the upper surface of flap 2. While a larger, thicker wake with increased momentum deficit is observed near the trailing edge of the small-gap airfoil when compared to the baseline airfoil, the increased momentum deficit is not observed at downstream locations ($\widetilde{x} > 1.3$), and this observation indicates significant differences in the wake development at smaller $\widetilde{x}$ while the wakes exhibit very similar behavior at larger $\widetilde{x}$. Static pressure values and gradients, presented in Fig. 6.30(e,f), warrant a brief discussion. In this figure, the streamwise pressure gradient $\partial C_p/\partial \widetilde{x}$ in the wake region is larger for the small-gap configuration than for the baseline airfoil, and the stronger streamwise pressure gradient promotes increased wake thickening (or separation/bursting) than for a weaker streamwise pressure gradient. In addition to the streamwise pressure gradient, slightly larger $\partial C_p/\partial \widetilde{y}$ is observed for the small-gap airfoil relative to the baseline configuration. As previously discussed, this pressure gradient causes increased wake asymmetry.

Wake profiles for both configurations were extracted from data shown in Fig. 6.30 at four different $\widetilde{x}$ locations, as shown in Fig. 6.31. These data were extracted at streamwise coordinates $\widetilde{x}$ of 1.05, 1.25, 1.50, and 2.00. As previously mentioned, significant differences between the two configurations exist close to the trailing edge, as plotted in Fig. 6.31(a), in which the small-gap configuration yields significantly lower values of $\widetilde{U}_{t,min}$ than the minimum values for the baseline configuration. Despite this observation, the width of the wake profile is approximately the same for both configurations. Data shown in Fig. 6.31(b) indicate differences exist between the baseline configuration and small-gap configuration, but the difference in $\widetilde{U}_{t,min}$ between the two airfoils is markedly decreased compared to the profiles at $\widetilde{x} = 1.05$. At $\widetilde{x}$ of 1.25, the small-gap configuration yields slightly smaller values of $\widetilde{U}_{t,min}$ than the baseline airfoil, which a similar trend observed at upstream locations. While significant differences are observed

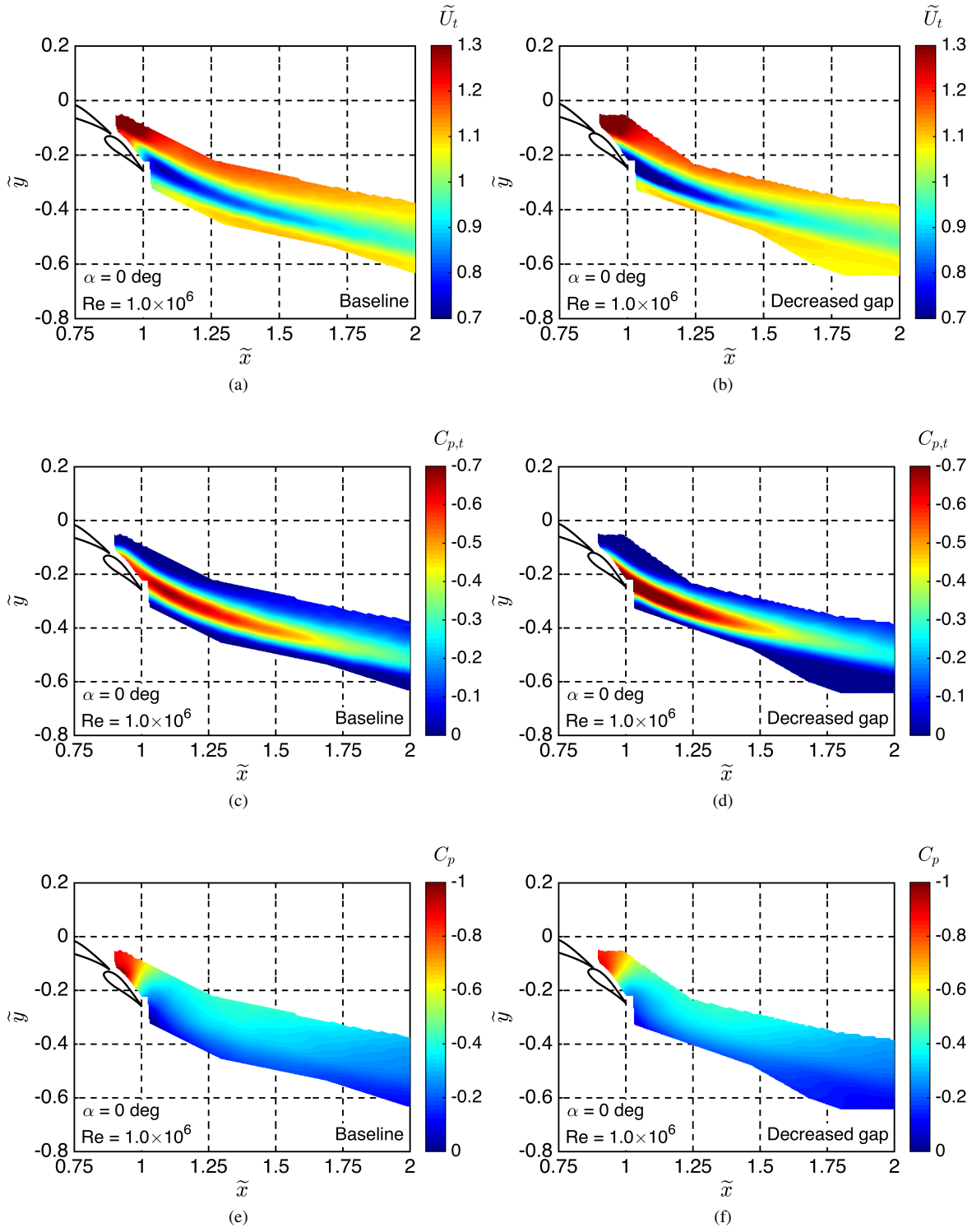

Figure 6.30: Two-dimensional wake surveys capturing effect of decreased gap size for a) $\widetilde{U}_t$, c) $C_{p,t}$, and e) C_p for the baseline configuration; and b) $\widetilde{U}_t$, d) $C_{p,t}$, and f) C_p for the decreased-gap configuration.

close to the trailing edge, wake profiles for the two configurations in which $\widetilde{x} \geq 1.5$ are remarkable similar [seen in Fig. 6.31(c,d)]. These similarities are evidenced by similar values of $\widetilde{U}_{t,min}$, nearly-equal wake profile width, and similar behavior near the edges of the wake profiles. While data suggest the baseline airfoil yields slightly decreased $\widetilde{U}_{t,min}$ compared to the low-gap case, which is contrary to the observations at upstream locations, the differences in magnitude of these values is small.

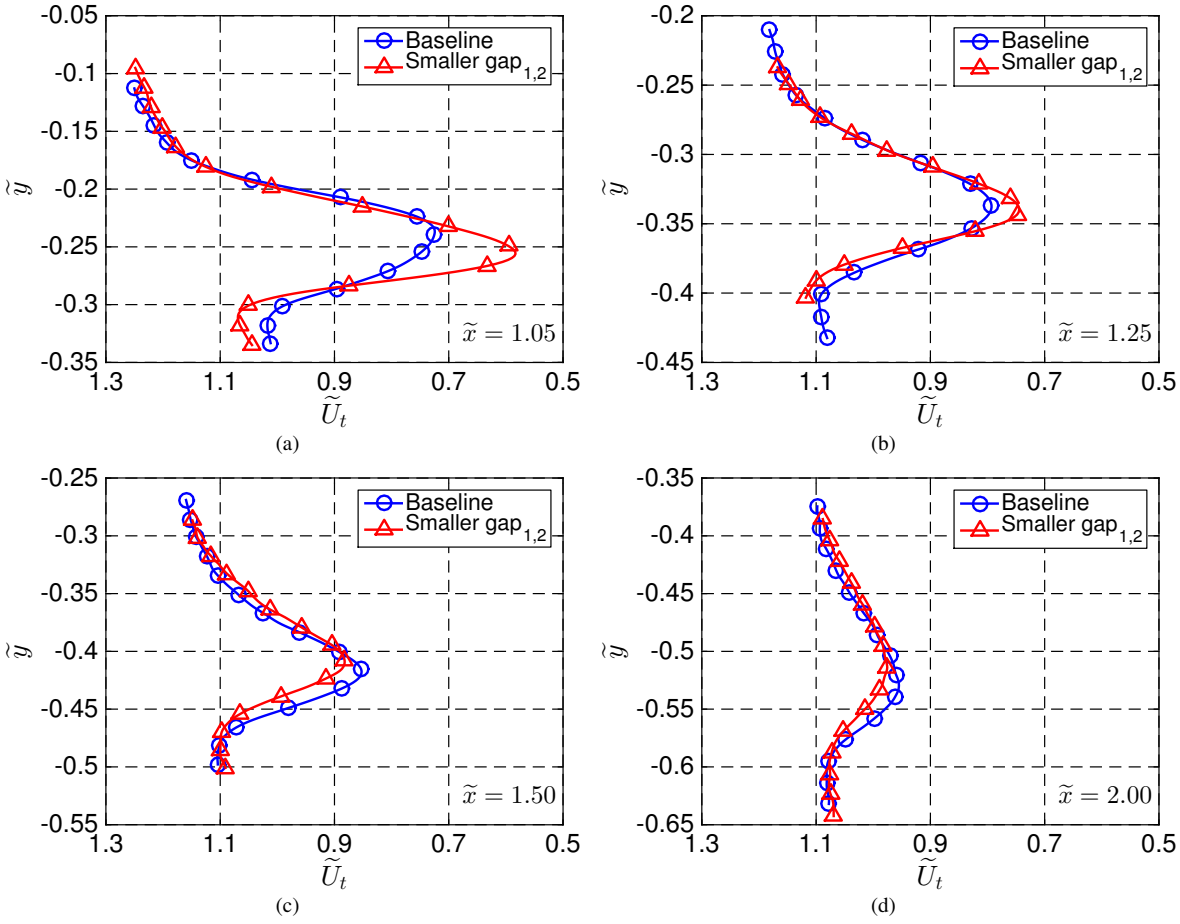

Figure 6.31: Effect of smaller gap size evidenced by wake profiles at a) $\widetilde{x} = 1.05$, b) $\widetilde{x} = 1.25$, c) $\widetilde{x} = 1.50$, and d) $\widetilde{x} = 2.00$.

Wake Metrics

Comparisons between the baseline airfoil and the small-gap configuration can be made with numerous different wake metrics. The metrics of greatest interest in this discussion include the wake edges, wake centerline, and wake thickness as quantified by h_w, as plotted in Fig. 6.32. As seen in the figure, the wake edges for the small-gap configuration are slightly displaced in the $+y$ direction, which indicates less curvature in the flowfield as a whole. Despite the fact that the small-gap configuration wake edges are displaced in the y direction, the magnitude of this displacement is

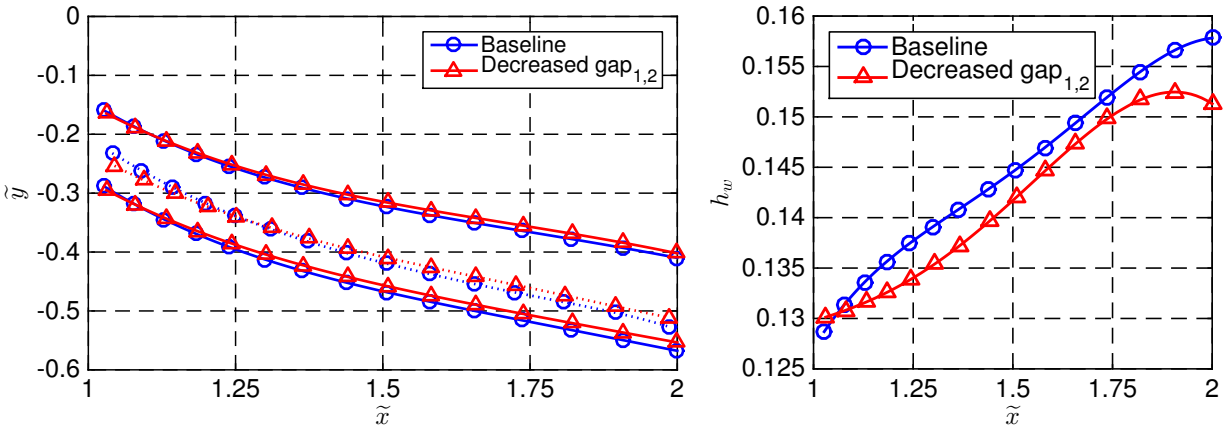

Figure 6.32: Wake thickness for the baseline and small-gap configuration including a) wake edges and wake centerline and b) wake thickness as defined by h_w.

nearly equal for the upper and lower wake edges, thus yielding similar values of h_w for the two airfoil configurations. A decrease in h_w for the small-gap configuration is observed for which $\widetilde{x} \geq 1.80$ which indicates the area for which $C_{p,t} \leq 0.10$ is decreased in these downstream locations. Some differences in the wake centerline exist between the two configurations, as seen in Fig. 6.32(a), and larger differences are observed for $\widetilde{x} \leq 1.20$ than at larger values of $\widetilde{x}$. At small $\widetilde{x}$, the centerline of the baseline configuration wake is closer to the upper wake edge than for the small-gap airfoil. Closer agreement of centerline position for the two configurations is noted at larger values of $\widetilde{x}$.

Effect of Freestream Reynolds Number

Figure 6.33 presents wake surveys and $\widetilde{U}_t$ for the baseline and small-gap configurations as a function of freestream Reynolds number. As is the case earlier in this section, results for the baseline airfoil are shown in the left column, and plots for the small-gap configuration are presented in the right column; each row of plots contains results at a given freestream Reynolds number. Trends observed for increasing *Re* with both configurations are similar in which larger, thicker wakes with decreased $U_{t,min}$ are observed for lower *Re* than the high-*Re* cases. Separation from the upper surface of flap 2 is observed at all *Re*, and the separation point moves slightly upstream for the low-*Re* case. This is the expected trend as airfoils separate more rapidly at lower *Re* than at higher *Re*. In general, the wakes for the low-gap size configuration yield smaller $\widetilde{U}_{t,\,min}$ at small values of $\widetilde{x}$ when compared to the baseline case. Nevertheless, the wakes for the small-gap airfoil yield decreased values of $U_{t,\,min}$ at larger values of $\widetilde{x}$.

A series of wake profiles, extracted from data in Fig. 6.33, are presented in Fig. 6.34 for both the baseline and small-gap airfoil. In general, the wakes of the small-gap airfoil are slightly smaller than the wakes of the baseline airfoil, which corresponds with decreased C_d at a given α in the drag polar plotted in Fig. 6.28(b). Increased momentum deficit

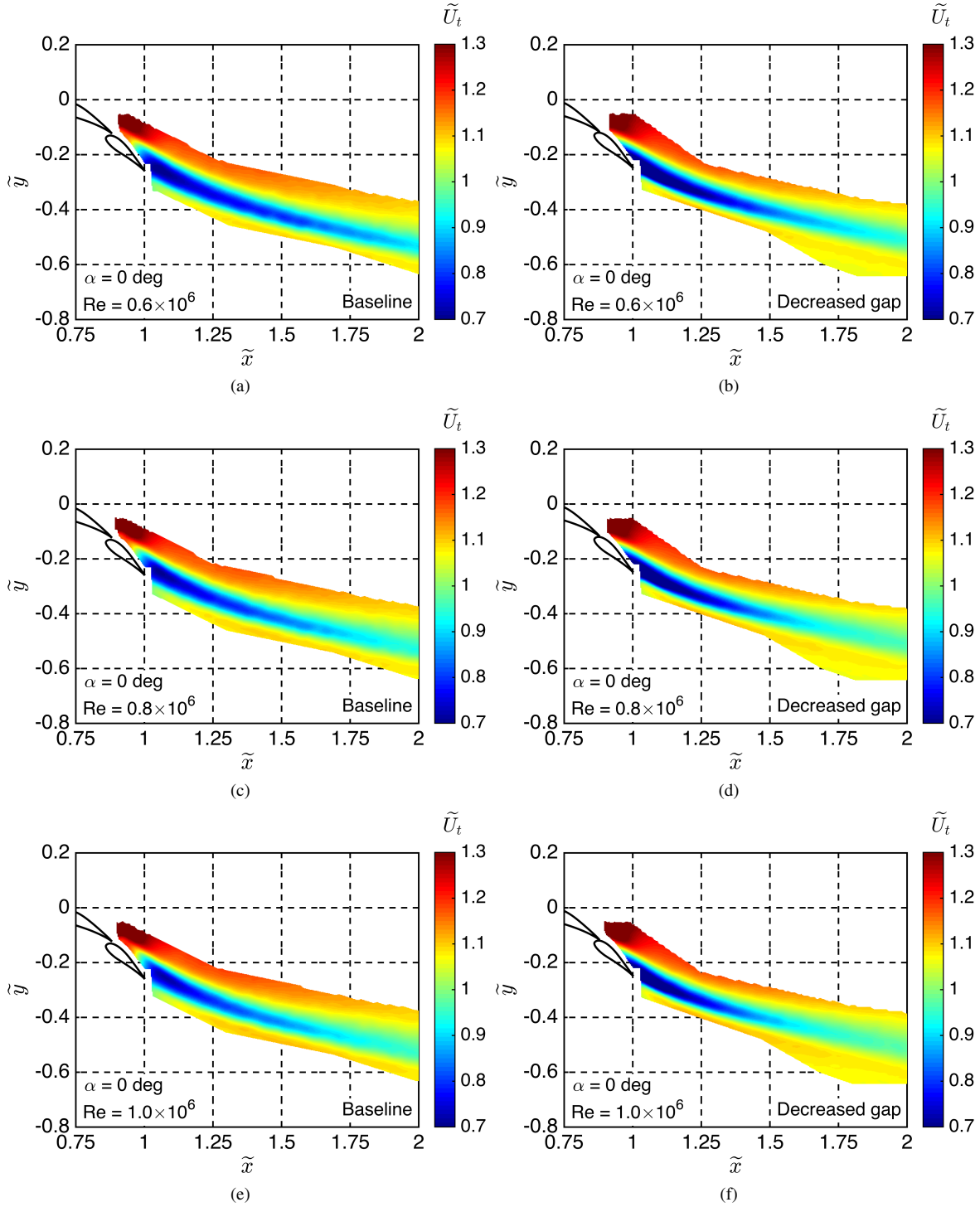

Figure 6.33: Effect of smaller gap size and Reynolds number on $\widetilde{U}_t$ for a) Re=0.6×10^6, c) Re=0.8×10^6, and e) Re=1×10^6 for the baseline configuration; and b) Re=0.6×10^6, d) Re=0.8×10^6, and f) Re=1×10^6 for the decreased gap size configuration.

at decreased *Re* is observed for the small-gap airfoil, and minimum values of $\widetilde{U}_{t,\,min}$ are observed to be approximately 5% for the case at which $Re = 0.6 \times 10^6$ than the case at $Re = 1 \times 10^6$. Regions in which $\widetilde{U}_t \geq 1$ are observed in the wake profiles, and these regions occur partly due to maintaining continuity across the wind tunnel test section. The minimum values of $\widetilde{U}_t$ at $\widetilde{x}$ are only slightly less than 1 as the wake continues to spread out with decreasing $\widetilde{U}_{t,\,min}$ with increasing downstream distance. Comparisons between the baseline configuration and the small-gap configuration suggest there is a decreased effect of *Re* for the small-gap case than for the baseline configuration. The decreased effect of *Re* for the small-gap configuration is attributed to the separated flow from the surface of flap 2, which is observed at all *Re* tested.

6.3.3 Effect of Overhang Distance

The final relative coordinate that was parametrically studied in the wind tunnel is overhang distance. A comparison of Configuration 10, the baseline configuration, to Configuration 13 yields the effect of decreased overhang distance. Results in this section include wake surveys, wake metrics, aerodynamic performance, and the effect of freestream *Re* upon configurations with differing *overhang*.

Baseline Comparison

Aerodynamic Performance

Aerodynamic performance metrics for the two configurations are plotted in Fig. 6.35. Significant differences in C_l between the two configurations exist, as presented in Fig. 6.35(a). A reduction in C_l is observed with decreasing downstream distance across all α in which differences in C_l at a given α are as large as 0.52. The decreased lift indicates decreased flow curvature for the low-overhang configuration when compared with the baseline configuration, and it is observed that this decrease in flow curvature does not significantly affect the wake development (as discussed later in this section). This observation suggests that the presence of wake bursting is not solely dependent upon lift, but that it can also be affected by other parameters such as flap location. Decreased C_{l_α} for the small-overhang case relative to the baseline configuration is seen in the plot. Stall characteristics of the small-overhang airfoil are slightly more forgiving, and less drastic, than the stall of the baseline airfoil. Similar to the reduction in C_l, it is observed that the decreased lift-curve slope is not solely affected by the wake bursting. Despite a marked decrease in C_l, the small-overhang configuration yields decreased C_d, as shown in Fig. 6.35(b) in which C_d at a given $(C_{l,\,stall,\,positive} - C_l)$ is decreased by approximately 0.002 at all $(C_{l,\,stall,\,positive} - C_l)$. That is to say that the drag polar for the small-overhang configuration is shifted down (reduced C_l) and to the left (decreased C_d), but the shape of the drag polar is very similar between the two airfoils. Both configurations suggest a large drag rise in the central part of the drag polar in which $0.1 \leq C_{l,\,stall,\,positive} - C_l \leq 0.4$. It is clear that the relative reduction in C_l and C_d of the small-overhang airfoil

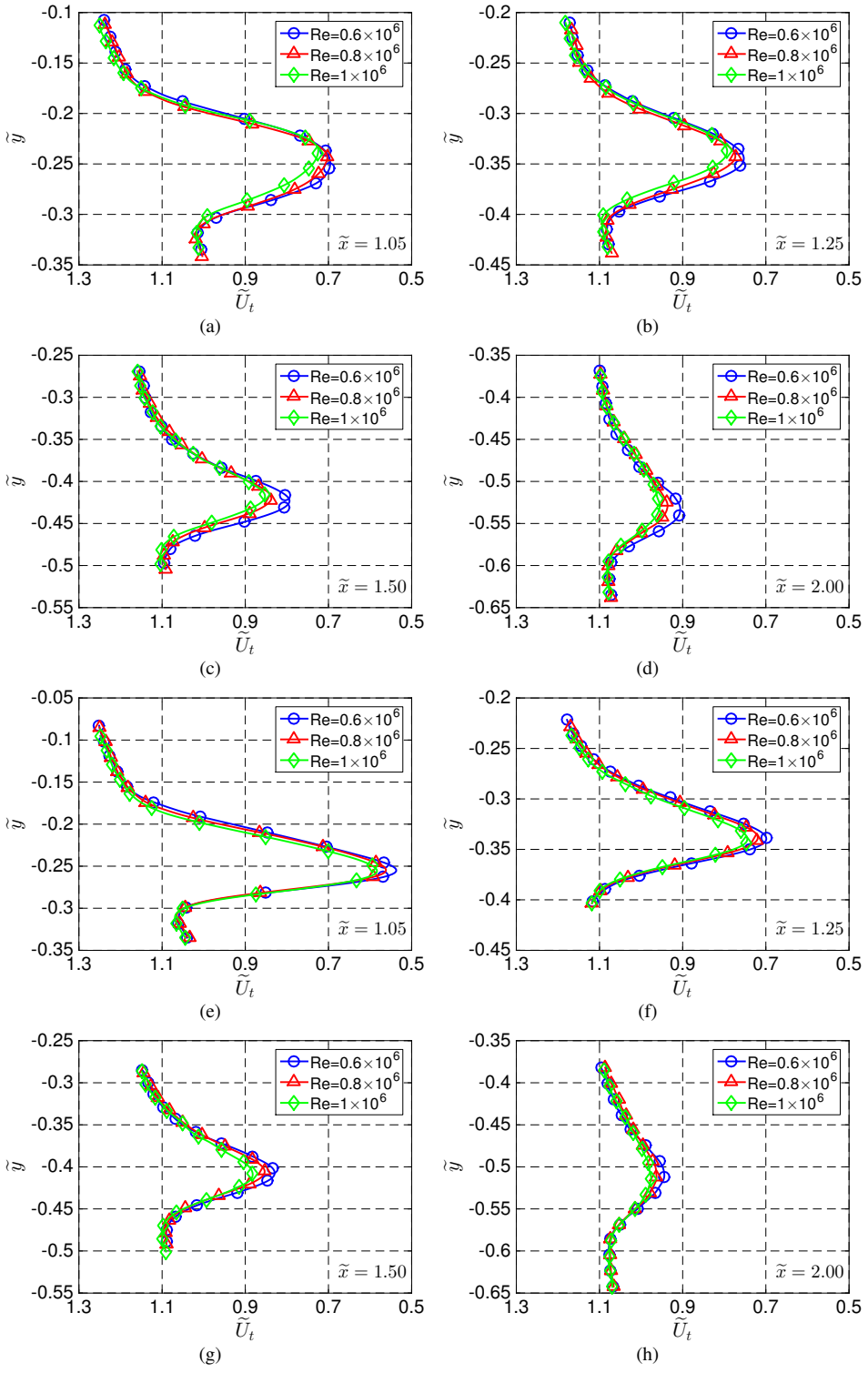

Figure 6.34: Wake profiles depicting effect of smaller gap size and Reynolds number for a) $\widetilde{x} = 1.05$, b) $\widetilde{x} = 1.25$, c) $\widetilde{x} = 1.50$, and d) $\widetilde{x} = 2.00$ for the baseline configuration; and e) $\widetilde{x} = 1.05$, f) $\widetilde{x} = 1.25$, g) $\widetilde{x} = 1.50$, and h) $\widetilde{x} = 2.00$ for the small-gap configuration.

compared to the baseline airfoil results in very similar l/d trends, as shown in Fig. 6.35(c). Curiously, the data suggest increased l/d for both moderately-small and moderately-larg eC_l with decreased l/d for decreased moderate C_l. The maximum values of l/d are slightly less than 140 for both airfoils.

Wake Survey

A two-dimensional wake survey was performed at $\alpha = 0$ deg and $Re = 1 \times 10^6$, as plotted in Fig. 6.36. As is customary in the rest of this section, the baseline configuration is plotted in the left column while the decreased-overhang airfoil data are shown in the right column. Each row in the figure presents a given aerodynamic parameter including $\widetilde{U}_t$, $C_{p,t}$, and C_p for the two configurations. Previously-identified similarities between $\widetilde{U}_t$ and $C_{p,t}$ are seen in the figure. Results indicate that the wakes from each of the different elements have merged at a point immediately behind the trailing edge as separate wakes are not visible. Momentum in the flow, quantified in part by $\widetilde{U}_t$, is minimized immediately behind the trailing edge in which $\widetilde{U}_{t,\,min} = 0.69$. In general, striking similarities are observed between the flowfield of the baseline configuration and the flowfield resulting from the low-overhang case. By comparing Fig. 6.36(a,b), it is observed that the wake for the low-overhang configuration is deflected the same amount as the baseline configuration, which suggests that the downwash of the two configurations is approximately equal. Data indicate that the value of $\widetilde{U}_{t,\,min}$ at a given $\widetilde{x}$ for the two configurations is essentially the same value at all $\widetilde{x}$. In addition, the static pressure for the two cases, shown in Fig. 6.36, indicates similar trends between between the baseline and low-overhang configurations. The flowfield indicates similar values of C_p at a given $\widetilde{x}$ position as well as similar pressure gradients in both the x and y directions. As previously mentioned, increased magnitude of $\partial C_p/\partial \widetilde{x}$ creates large, thicker wakes and promotes wake bursting while the chord-normal pressure gradient, $\partial C_p/\partial \widetilde{y}$, yields asymmetric wake development.

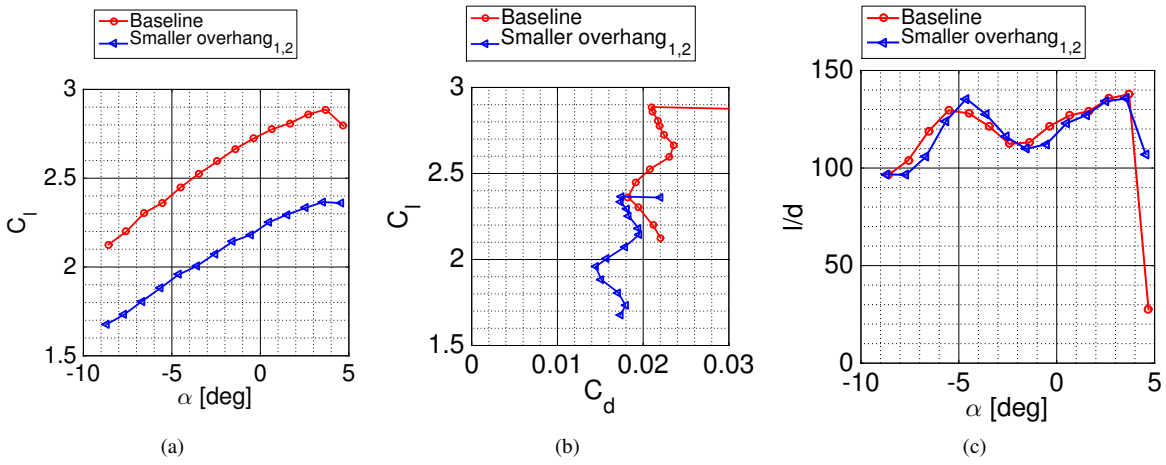

Figure 6.35: Effect of decreased overhang distance upon aerodynamic performance including a) C_l, b) C_d, and c) l/d.

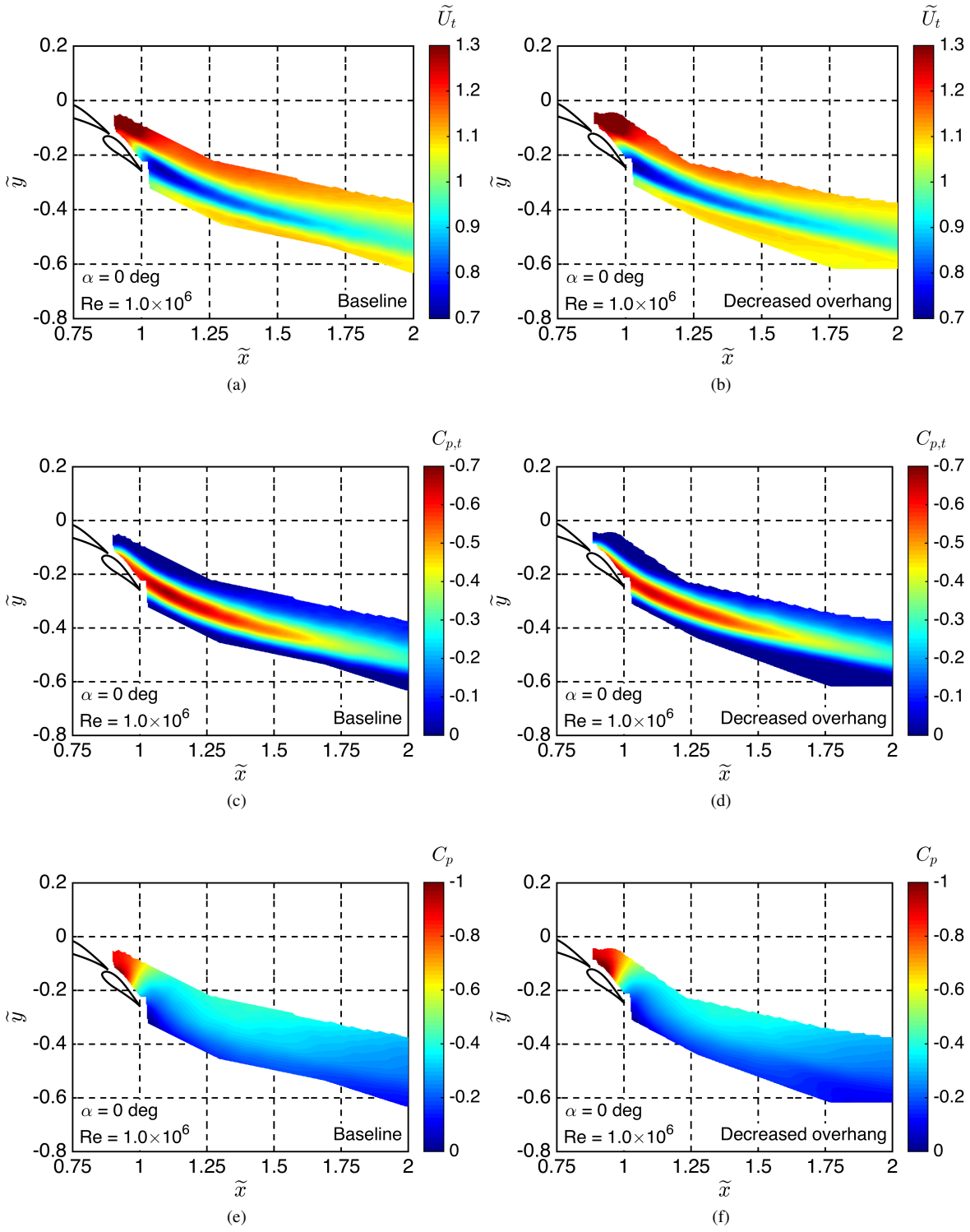

Figure 6.36: Two-dimensional wake surveys capturing effect of decreased overhang distance for a) $\widetilde{U}_t$, c) $C_{p,t}$, and e) C_p for the baseline configuration; and b) $\widetilde{U}_t$, d) $C_{p,t}$, and f) C_p for the decreased overhang distance configuration.

In addition to the contour plots in Fig. 6.36, a number of wake profiles are presented in Fig. 6.37 for the baseline and low-overhang configurations. The four profiles were extracted at $\widetilde{x}$ of 1.05, 1.25, 1.50, and 2.00, as labeled on the figure and in the caption. The upper portion of the wake profile for the baseline and small-overhang airfoils are nearly identical across a wide range of $\widetilde{x}$. While some small differences in the lower portion of the wake profiles are observed, these differences are significantly smaller than the differences in wake profiles presented earlier in this section. The wake for the small-overhang configuration is slightly narrower than the baseline configuration, and these thinner wakes are known to reduce drag over the multielement airfoil. Finally, it is noted that the wake centerline locations, or the $\widetilde{y}$ coordinate for which $\widetilde{U}_t$ is minimized at a given $\widetilde{x}$, is nearly the same for the two configurations at all $\widetilde{x}$.

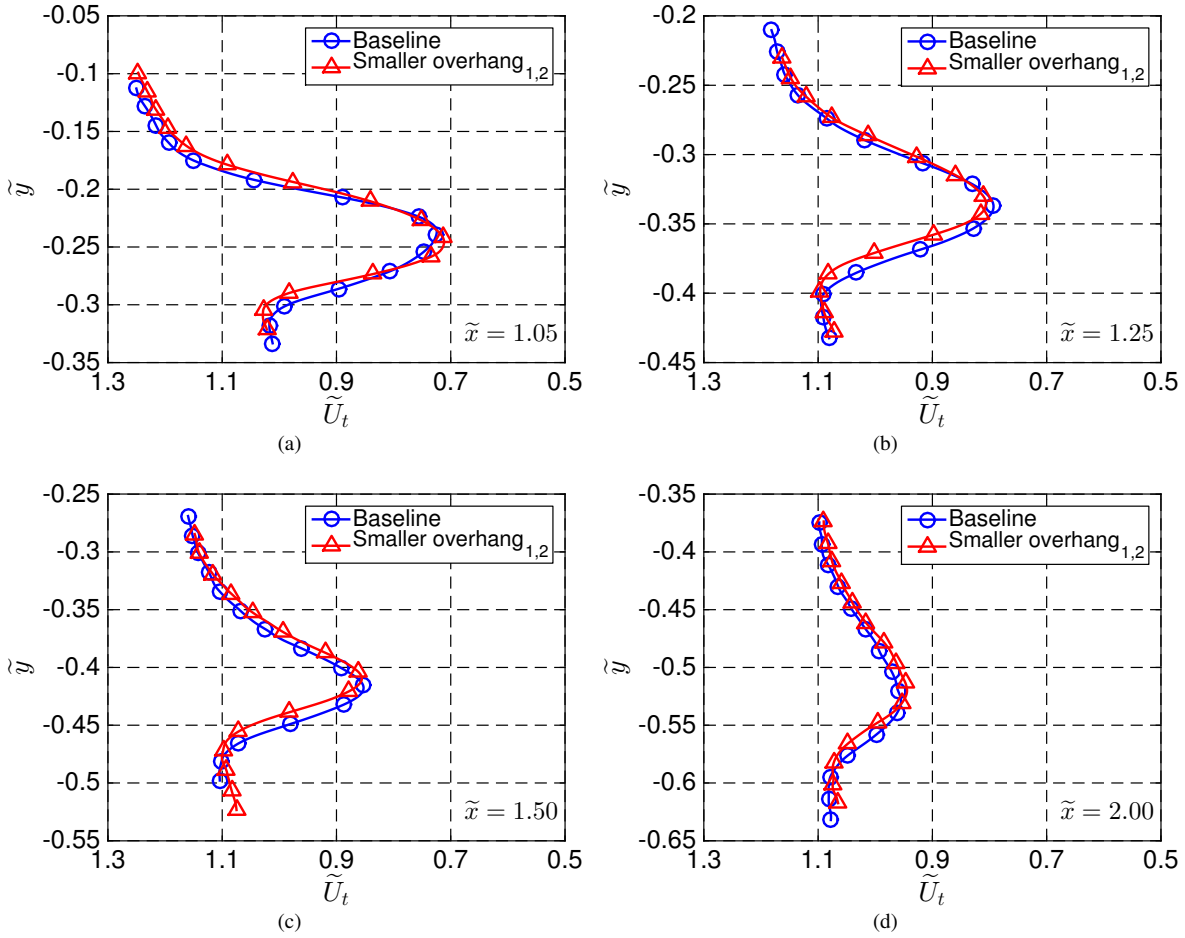

Figure 6.37: Effect of decreased overhang distance as evidenced by wake profiles at a) $\widetilde{x} = 1.05$, b) $\widetilde{x} = 1.25$, c) $\widetilde{x} = 1.50$, and d) $\widetilde{x} = 2.00$.

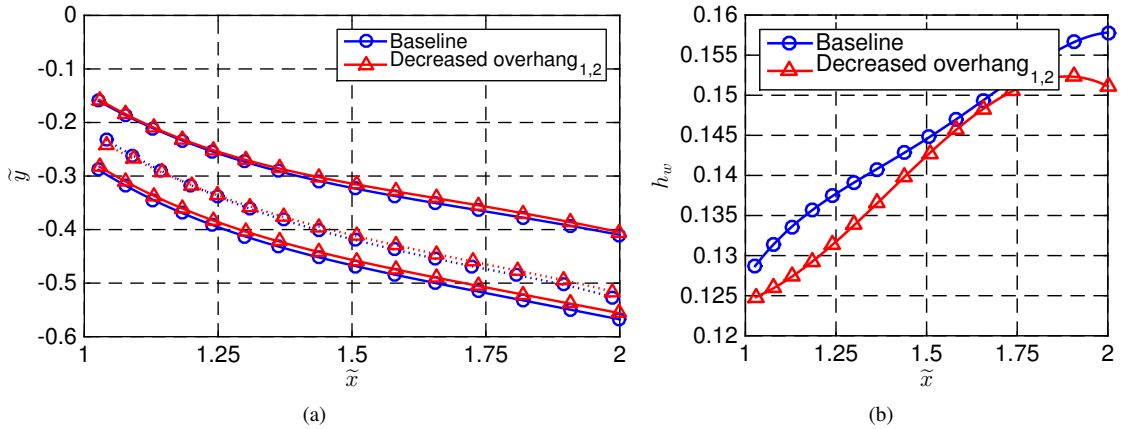

Figure 6.38: Wake thickness for the baseline and decreased-overhang configuration including a) wake edges and wake centerline and b) wake thickness as defined by h_w.

Wake Metrics

Wake development for the decreased-overhang configuration and baseline airfoil can be quantified by previously-discussed wake metrics, and results are plotted in Fig. 6.38. Upper and lower wake edges as well as the wake centerline for both configurations are plotted in Fig. 6.38(a). Similar to the previously-discussed wake profiles, striking similarities are observed between the baseline and low-overhang configurations. The upper wake edge and wake centerline are at nearly the same spatial locations, but some minor differences are observed for the lower wake edge. The small-overhang airfoil yields lower wake edges that are slightly increased in $\widetilde{y}$ when compared to the baseline configuration, and this observation yields decreased h_w as shown in Fig. 6.37(b). Results for both configurations indicate wake growth with increasing $\widetilde{x}$ wherein the small-overhang configuration creates slightly narrower wakes at all $\widetilde{x}$ than the baseline airfoil. Wake thickness, quantified by h_w, for the small-overhang configuration decreases for $\widetilde{x} \geq 1.85$, but the baseline wake increases for $\widetilde{x} \leq 2$, or over the entire sampled domain.

Effect of Freestream Reynolds Number

Figure 6.39 presents the coupled effect of decreased *overhang* and *Re* upon the flowfield in which contour plots of $\widetilde{U}_t$ are presented. Each row represents results from a given configuration, and the three columns include data at freestream *Re* of 0.6×10^6, 0.8×10^6, and 1×10^6. Trends with regards to *Re* are similar for the baseline and small-overhang configuration in which increased wake thickness and depth increase with decreasing *Re*. Many similarities are present for the wakes of the baseline and low-overhang configurations at a given Reynolds number. Similarities are observed in wake location (indicating the effect of downwash) and wake width. Overall, it is curious to observe the striking similarities between the baseline configuration and the low-overhang airfoil.

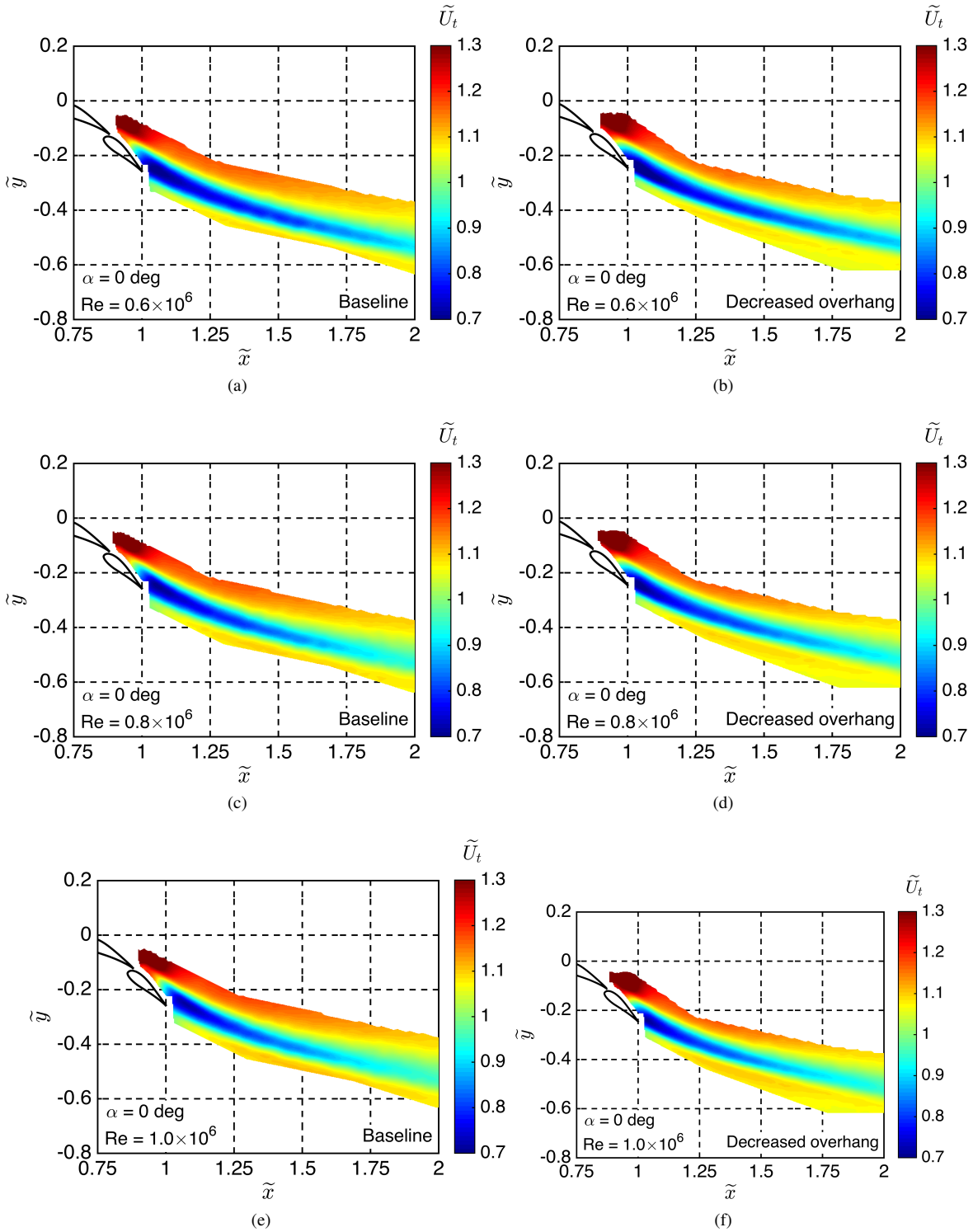

Figure 6.39: Two-dimensional wake surveys with effect of *overhang* and freestream *Re* for a) Re=0.6×10^6, c) Re=0.8×10^6, and e) Re=1×10^6 for baseline airfoil; and b) Re=0.6×10^6, d) Re=0.8×10^6, and f) Re=1×10^6 for the small-overhang airfoil.

A more-detailed examination of the contour plots presented in Fig. 6.39(b,d,f) is shown in Fig. 6.40 in which wake profiles were extracted at four different $\widetilde{x}$ locations, and results are presented at three different *Re*. Decreased *Re* is observed to result in decreased $\widetilde{U}_{t,\,min}$ and slightly-thicker wakes. Wakes are observed to exist at approximately the same $\widetilde{y}$ for all *Re* which indicates the wake position is not significantly affected by viscous effects, but is rather affected by inviscid phenomena.

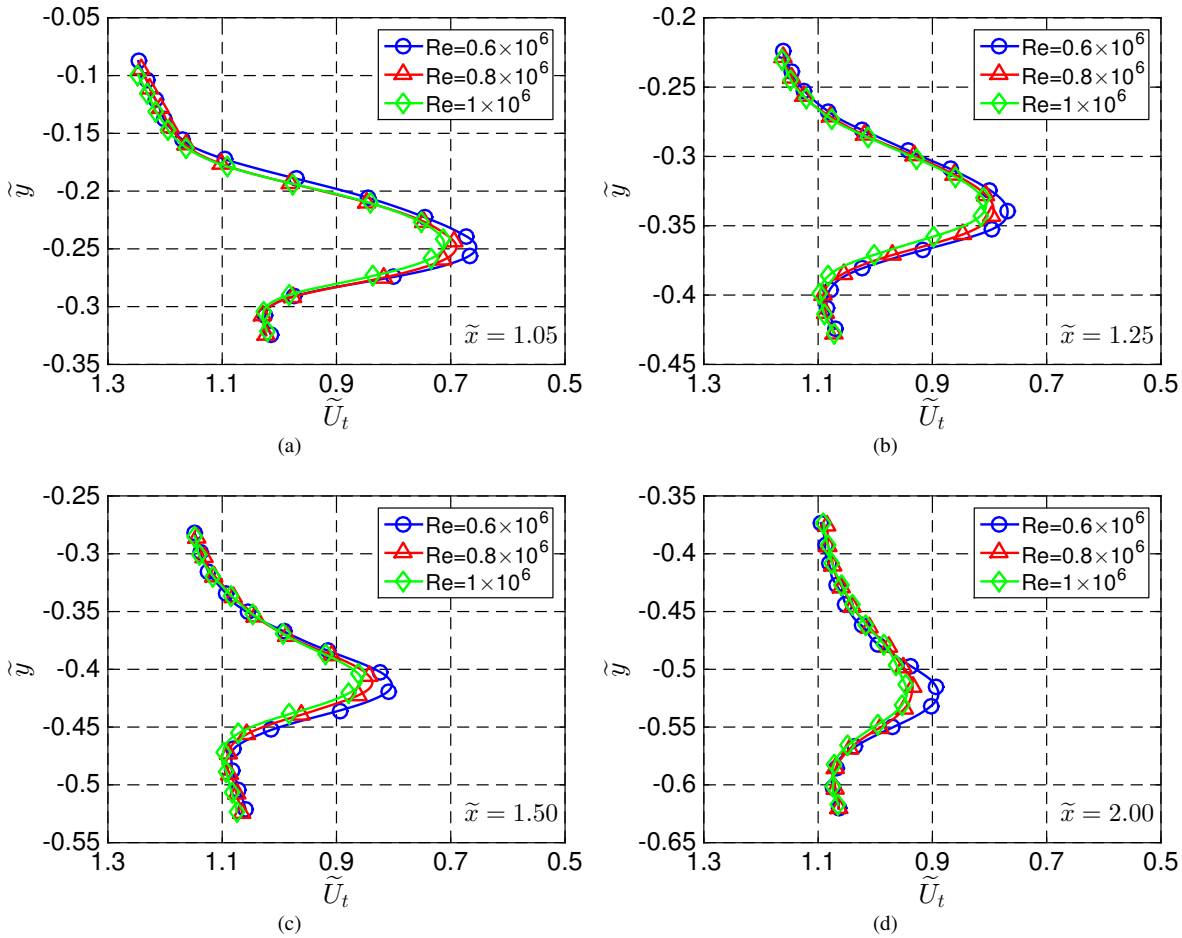

Figure 6.40: Effect of *Re* and decreasing *overhang* as evidenced by wake profiles at a) $\widetilde{x} = 1.05$, b) $\widetilde{x} = 1.25$, c) $\widetilde{x} = 1.50$, and d) $\widetilde{x} = 2.00$.

6.3.4 Summary of Experimental Parametric Sweeps

This section discussed the effect of the airfoil configuration (flap rigging) upon the aerodynamic performance and resulting flowfield of a three-element airfoil as evidenced by a variety of experimental methods. Five airfoil configurations were selected for detailed investigation to parametrically isolate the effect of gap size, overhang distance, and flap deflection angle upon the aerodynamic flowfield. Two-dimensional wake surveys with a 7-hole probe captured

the development of the burst wake flowfield across a large spatial region in both the x and y directions for a variety of α and Re. As expected, increased wake bursting resulted from increased α and decreased Re. Static pressure coefficients in the flowfield show large variations in C_p across the burst wake, thus indicating the boundary-layer equations cannot be accurately applied to the burst-wake flowfield as the assumption of constant C_p across the wake is invalid. Experimental data indicate that C_l and the amount of wake separation exhibit trends in the same direction. Nevertheless, some conditions were observed with minimal variation in lift but increased separation in the wake. Large, thick wakes resulted from configurations with a small gap size, large overhang distance, and increased flap deflection angle. Configurations with very small flap gap sizes resulted in boundary-layer separation from the upper surface of the airfoil. Despite the decreased bursting for the large-gap airfoil, a large decrease in C_l was observed with only a moderate decrease in C_d resulting in decreased l/d relative to the baseline airfoil. In general, wake bursting was affected more by gap size and deflection angle than that of overhang distance. Similar to the aforementioned MSES results, it is recommended to rig the flaps with a moderate gap size (≈ 0.020) such that large values of C_l are obtained without a large degree of either wake or boundary-layer separation.

6.4 Quantitative Burst Wake Thresholds

Results presented in this chapter yield insight into the behavior of a burst-wake flowfield as quantified by a variety of different wake metrics (discussed above in Sec. 6.1 on page 162). While these metrics quantify various features in the wake, no parameters were presented to classify the global wake features as compared to other wakes. In this section, three thresholds are presented for the flowfield by answering the following questions:

- Is the wake burst?
- At what spatial point can the wake said to be burst?
- Is the wake slightly, moderately, or severely burst?

Each of these three thresholds will be discussed in turn. Results shown throughout this section are presented such that each of the thresholds can be calculated for a given flowfield. Thus, the specific airfoil and set of operating conditions for each of these flowfields is not significant to the discussion of these thresholds. Therefore, the airfoil and freestream conditions are not identified for any of the cases in this section. The thresholds proposed in this section are applied to multielement flowfield in discussion, and the values are deemed to be appropriate for the current analyses. It is possible, however, that the specific values of the thresholds proposed in this section are not appropriate for a different flowfield.

6.4.1 Defining Existence of Burst Wake

A flowfield, whether predicted computationally or captured experimentally, can exhibit well-behaved and attached flow, surface-separated flow, or off-the-surface separation. The former two of these classifications are simple to determine by inspecting the flowfield along the surface of each airfoil element. The final type of flowfield exhibits off-the-surface wake separation. No methods currently exist to define whether or not a wake is burst, and thus a novel definition to declare whether or not a wake is burst is presented herein.

Consider the computationally-predicted flowfield shown in Fig. 6.41(a,b) in which contour plots are shown for both $\widetilde{U}_t$ and $C_{p,t}$. The domain shows the downstream portion of flap 1, the entirety of flap 2, and the flowfield above and downstream of the flaps. It is noted that the results for which $\widetilde{x} < 1.00$ and below the pressure surface of each element has been blanked in the plots to draw attention to the wake region. Results in Fig. 6.41 were computed on the A1 airfoil for $\alpha = 0$ deg and $Re = 1 \times 10^6$. As shown in the figure, the main-element wake is observed to rapidly thicken in the highly-curved flowfield above flap 2. While some thickening is observed, some wakes presented earlier in this chapter exhibited much thicker wakes than those in Fig. 6.41. Thus, it is proposed that the flowfield in Fig. 6.41 is burst, but to a lesser degree than some previously-discussed results.

It is desired to develop a quantitative threshold to define whether or not a wake is burst. Thus, if a given flowfield is found to exceed this threshold, the wake is said to be burst. The previously-discussed flowfield shown in Fig. 6.41 is of greater interest because the flowfield appears to be only slightly burst. A detailed contour plot of $C_{p,t}$ is presented in Fig. 6.41(c) for contour levels of -1.0, -0.75, -0.50, -0.25, and 0. As was the case with the previously-discussed results in this chapter, a low-momentum region is associated with the main-element wake, as expected. An isoline for which $C_{p,t} = -0.50$ is accentuated as a thicker pale green contour level. The area enclosed within this contour level is also plotted in pale green in Fig. 6.41(d). While a contour level for the flowfield can be extracted for any value of $C_{p,t}$, a value of -0.50 was deemed appropriate for the current multielement airfoil and flowfield conditions. The eccentricity of a shape, e, is a metric used to quantify the amount that a given shape deviates from being a circular shape in which $e = 0$ represents a circle and $0 < e < 1$ defines an ellipse. A slender shape corresponds to increased e while a rounder shape is defined by decreased e. The length of the semi-major axis (a) and the semi-minor axis (b) for the wake region are defined as shown in Fig. 6.42 from which the eccentricity can be calculated by

$$e = \sqrt{1 - \frac{b^2}{a^2}}. \tag{6.14}$$

For the given flowfield, the eccentricity was calculated to be $e = 0.9993244$. As elevated values of e are associated with longer, thinner shapes, the wake region in discussion is quite long and skinny.

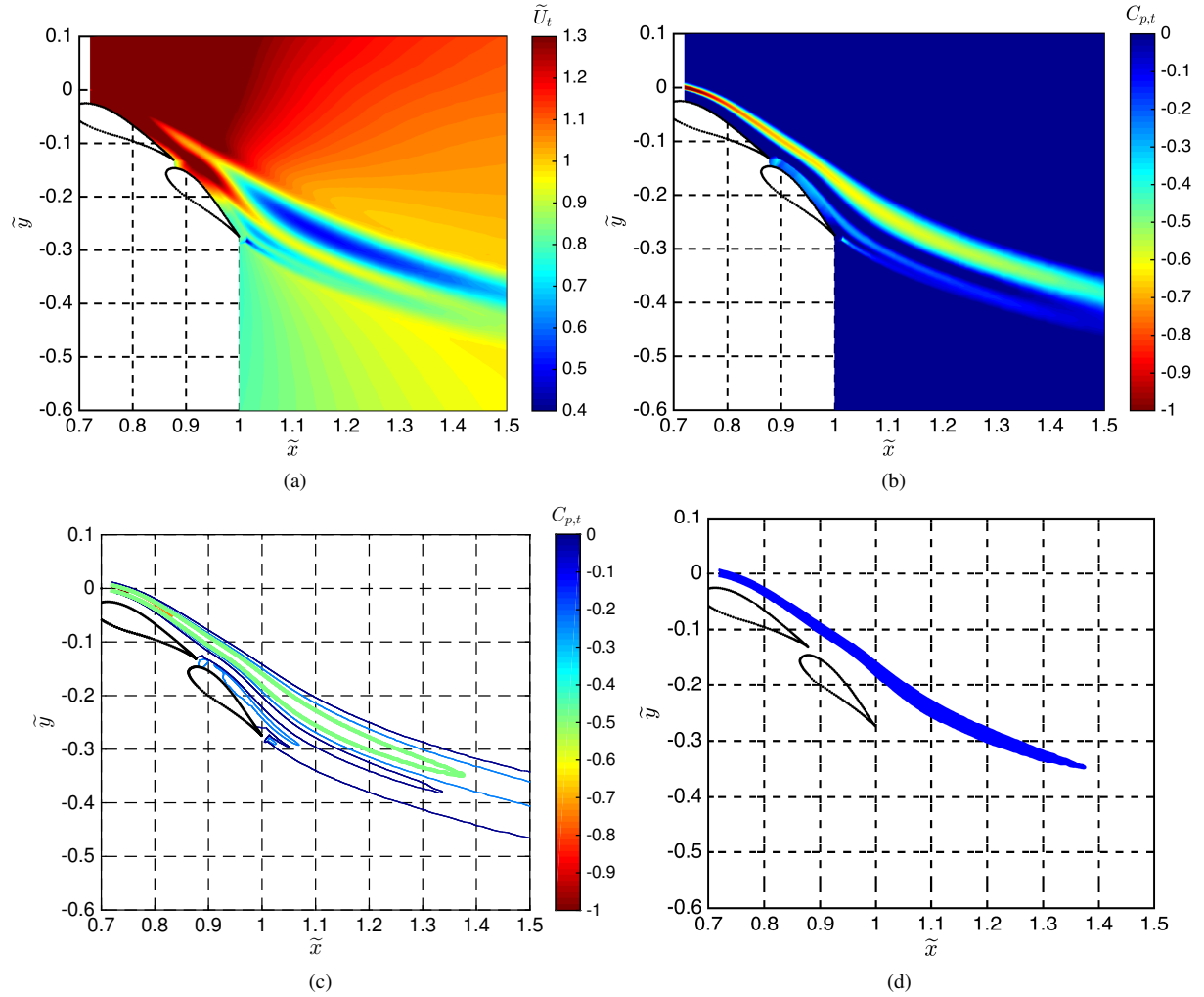

Figure 6.41: Wake region of computationally-predicted flowfield exhibiting minimal wake bursting as shown by a) $\widetilde{U}_t$ and b) $C_{p,t}$, c) contour levels of $C_{p,t}$ and d) region bounded by $C_{p,t} = -0.50$.

To establish the threshold of e to quantify the existence of a burst wake, flowfields were calculated for airfoil A1 at a range of α and Re. Figure 6.43 shows contour plots of $C_{p,t}$ for a range of α and Re. The lefthand column shows results at $Re = 1 \times 10^6$ for α of -4, 0, and 4 deg while the righthand column presents results at $\alpha = 0$ deg for $Re = 0.6 \times 10^6$, $Re = 1 \times 10^6$, and 3×10^6. Larger wakes, indicating more severe wake bursting, are observed for increasing α and decreasing Re, as expected. An increase in α results in a stronger adverse pressure gradient thus leading to increased wake thickening. Viscous effects, captured by changes in Re, are known to affect the behavior of both boundary layers and wakes, as seen in Fig. 6.43(b,d,f). The cases for increased wake bursting result in thicker wakes and increased values of $\widetilde{x}$ for which $C_{p,t} = -0.50$. As previously identified in Fig. 6.42, increased wake thickness yields decreased e and increased range of $\widetilde{x}$ results in increased e. A summary of e for the range of α and Re is presented in Table 6.4. While the dimensional variation in e is in the third or fourth significant digit, a clear trend exists for which more-burst

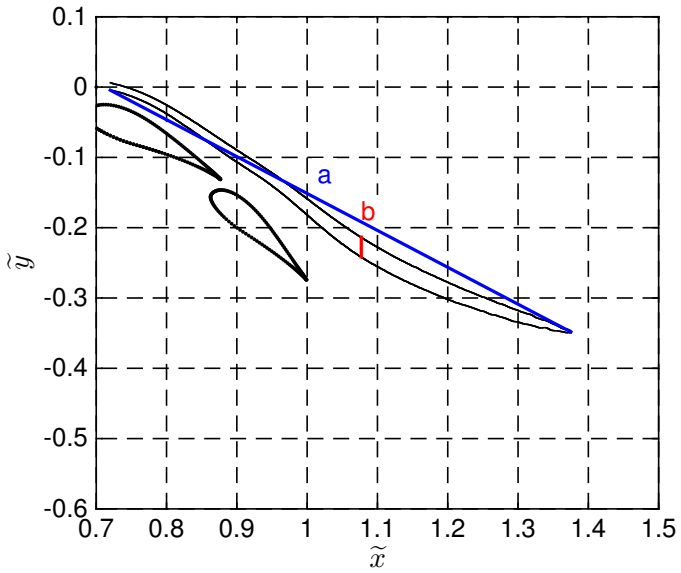

Figure 6.42: Definition of parameters used to quantify the existence of a burst wake.

wakes yield decreased e relative to less-burst wakes. Values of e are elevated for all flowfields in discussion as the wakes are longer and slender when compared to a circle for which $e = 0$.

Table 6.4: Eccentricity for Flowfields at a Range of α and Re

α	Re	e
-4 deg	1×10^6	0.9996319
0 deg	1×10^6	0.9993244
4 deg	1×10^6	0.9982974
0 deg	0.6×10^6	0.9988128
0 deg	1×10^6	0.9993244
0 deg	3×10^6	0.9994622

It is prudent to compare the baseline results at $\alpha = 0$ deg and $Re = 1 \times 10^6$ with results at a range of α and Re shown in Fig. 6.43 and presented in Table 6.4. As previously observed, the baseline case plotted in Fig. 6.41 was observed to exhibit only slightly-burst wakes. While the amount that a wake thickens is a continuous spectrum from zero pressure gradient to highly-curve multielement airfoil flowfields, a threshold based upon e is presented to definitively quantify the existence of a burst wake. Based upon the data, it is proposed that a wake is burst for flowfields in which $e < 0.994$, as also shown in Table 6.5.

6.4.2 Spatial Point of Wake Bursting

If the existence of a burst wake has been confirmed, it is possible to determine the spatial point at which the wake begins to burst. This point, $\widetilde{x}_b$, is determined based upon the behavior of the previously-identified $C_{p,t} = -0.50$ contour

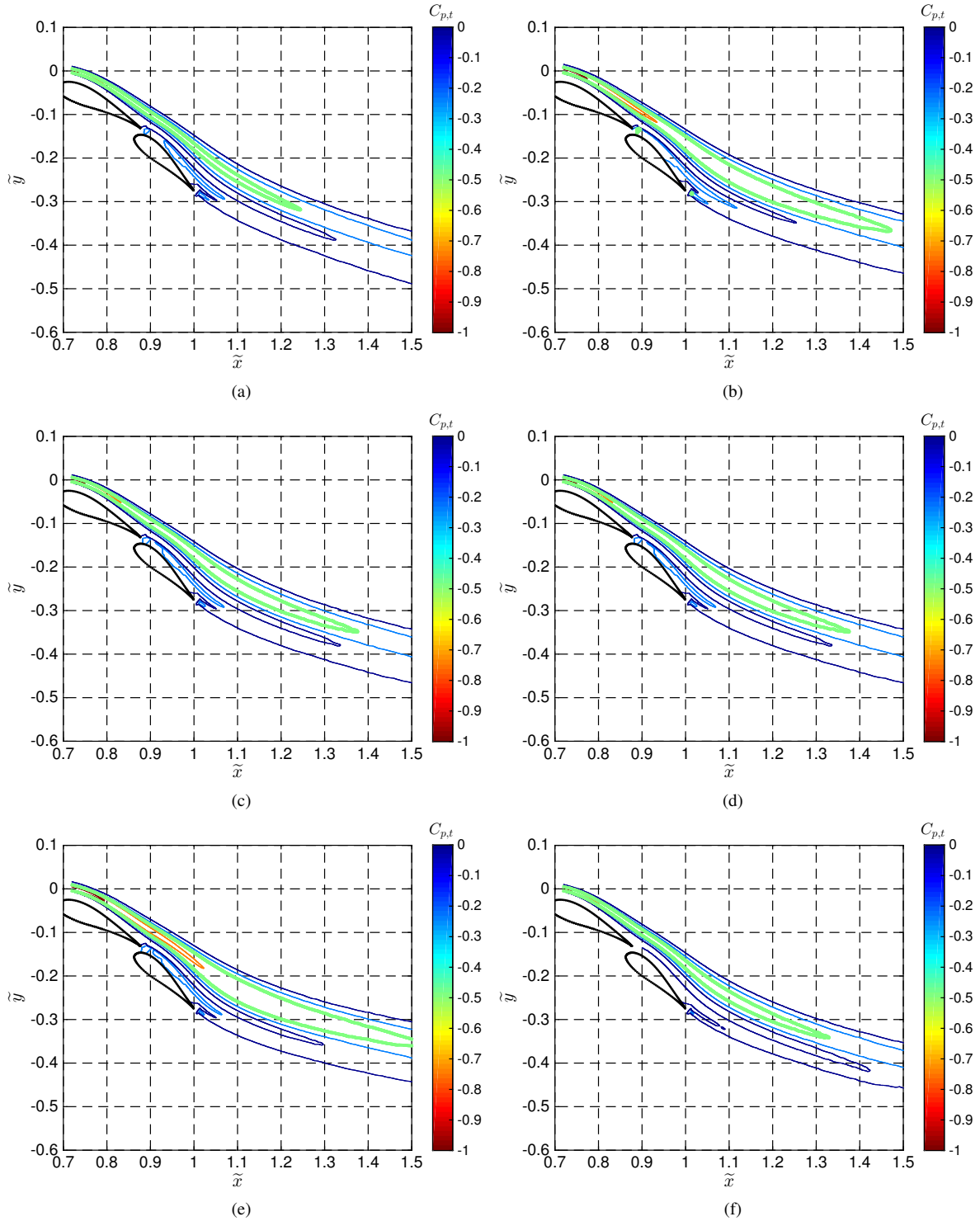

Figure 6.43: Contours of $C_{p,t}$ with accentuated contour line of $C_{p,t} = -0.50$ for airfoil A1 at $Re = 1 \times 10^6$ for a) $\alpha = -4$ deg, c) $\alpha = 0$ deg, and e) $\alpha = 4$ deg; and $\alpha = 0$ deg for b) $Re = 0.6 \times 10^6$, d) $Re = 1 \times 10^6$, and f) $Re = 3 \times 10^6$.

Table 6.5: Threshold of e Quantifying Existence of Burst Wakes

$e < 0.994$	the wake is burst
$e \geq 0.994$	the wake is not burst

interval. At a given value of $\widetilde{x}$, the distance in $\widetilde{y}$ between the contour level of $C_{p,t} = -0.50$ can be determined, as shown in Fig. 6.44(a,b) and denoted as τ. Values of τ can be extracted for a range of $\widetilde{x}$ for each of the simulations shown in Fig. 6.43, and the results for various α and *Re* are shown in Fig. 6.45. As previously shown, larger and thicker wakes are observed for increased α and decreased *Re*, and this trend is further evidenced by τ. While a slight difference in the $\widetilde{x}$ for which τ is maximized differs slightly between the different cases, the wakes are observed to increase in thickness until $\widetilde{x} \approx 1.1$. In addition to τ, the rate at which the wake thickens, $\partial\tau/\partial\widetilde{x}$, is plotted in Fig. 6.44(c,d). While the maximum value of τ is observed at $\widetilde{x} \approx 1.1$, the maximum value of $\partial\tau/\partial\widetilde{x}$ occurs at $\widetilde{x}$ of approximately 1.0. Similar to τ, the point at which the wakes grow the fastest seems to be independent of both α and *Re*. Finally, the second derivative of τ with respect to $\widetilde{x}$ is shown in Fig. 6.44(e,f) for the different cases. Larger values of $\partial^2\tau/\partial\widetilde{x}^2$ suggest a more rapid change in the wake behavior than cases with smaller $\partial^2\tau/\partial\widetilde{x}^2$. In the figure, a maximum value of $\partial^2\tau/\partial\widetilde{x}^2$ is observed at $\widetilde{x} \approx 0.95$ for the various simulations. This is the spatial point at which the wake begins to grow at a very rapid rate when compared to the upstream wake behavior and is declared to be the burst point, denoted by $\widetilde{x}_b$. Given that $\partial\tau/\partial\widetilde{x} > 0$, the burst point is stated to be the point at which $\partial^2\tau/\partial\widetilde{x}^2$ is maximized.

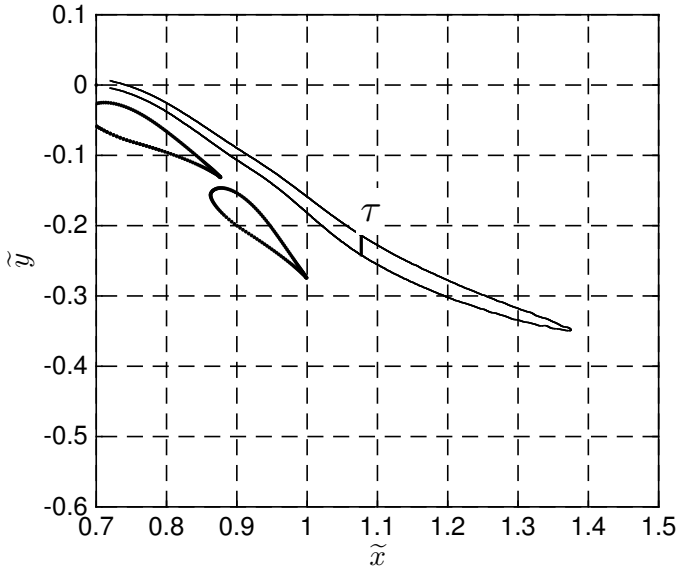

Figure 6.44: Definition of wake parameter τ, the distance between isolines of $C_{p,t} = -0.50$.

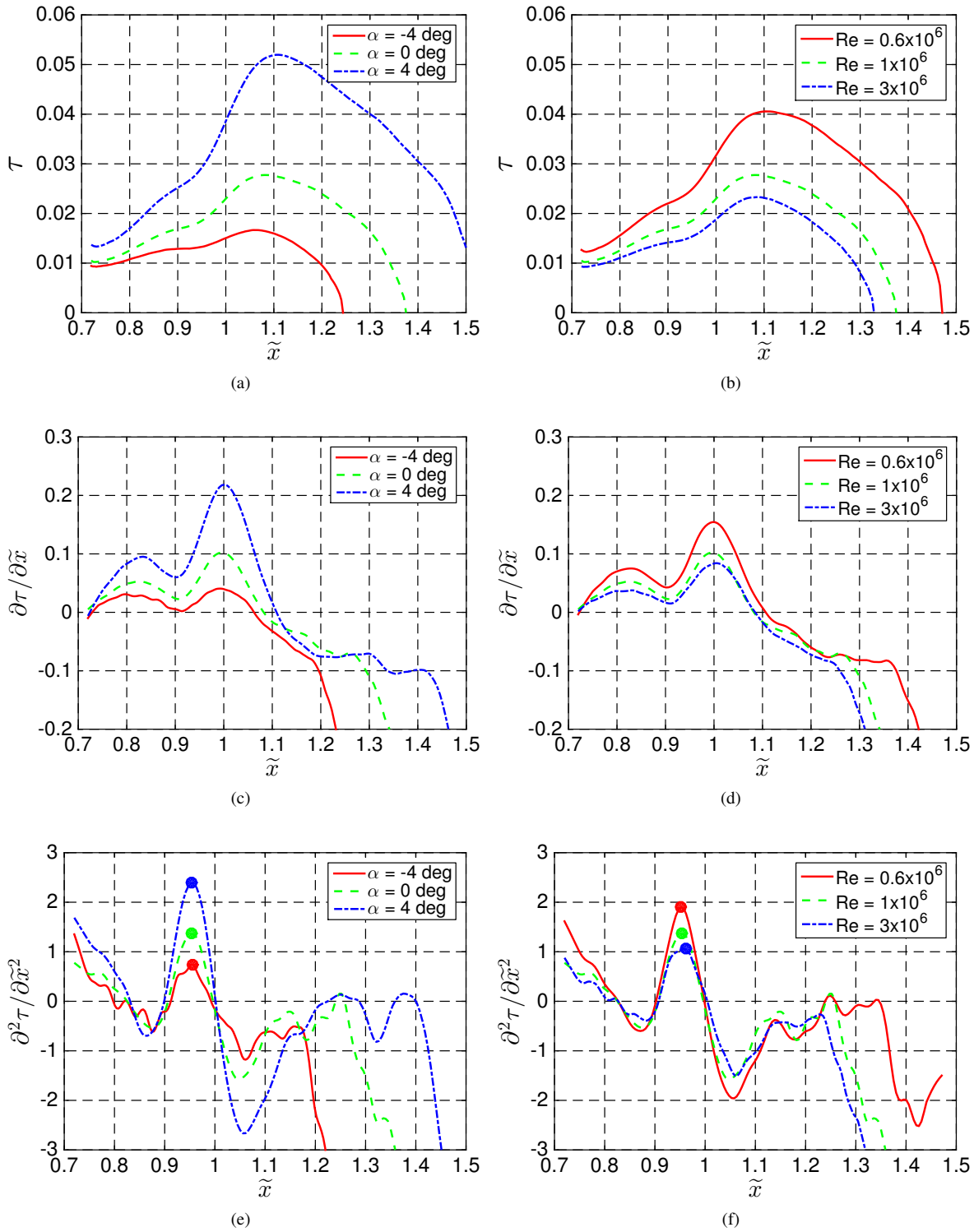

Figure 6.45: Various wake metrics including a) τ for a range of α, b) τ for a range of *Re*, c) $\partial\tau/\partial\widetilde{x}$ for a range of α, d) $\partial\tau/\partial\widetilde{x}$ for a range of *Re*, e) $\partial^2\tau/\partial\widetilde{x}^2$ for a range of α, and f) $\partial^2\tau/\partial\widetilde{x}^2$ for a range of *Re*.

6.4.3 Extent of Wake Bursting

In addition to the aforementioned thresholds quantifying the existence of wake bursting and the point at which bursting begins, it is valuable to quantify the extent to which a wake is burst. A metric such as this would allow easy comparisons between different flowfields and the size of the wakes. Consider once again the total-velocity and total-pressure contour plot shown in Fig. 6.41 for the flowfield in which the wake is barely burst. As previously discussed, the contour line for which $C_{p,t} = -0.50$ was extracted for further analyses. The region bounded by $C_{p,t} = -0.50$ is shown in Fig. 6.46 in which the raw computational points are shown in Fig. 6.46(a) and the enclosed, bounded region is shown as a solid blue shape in Fig. 6.46(b).

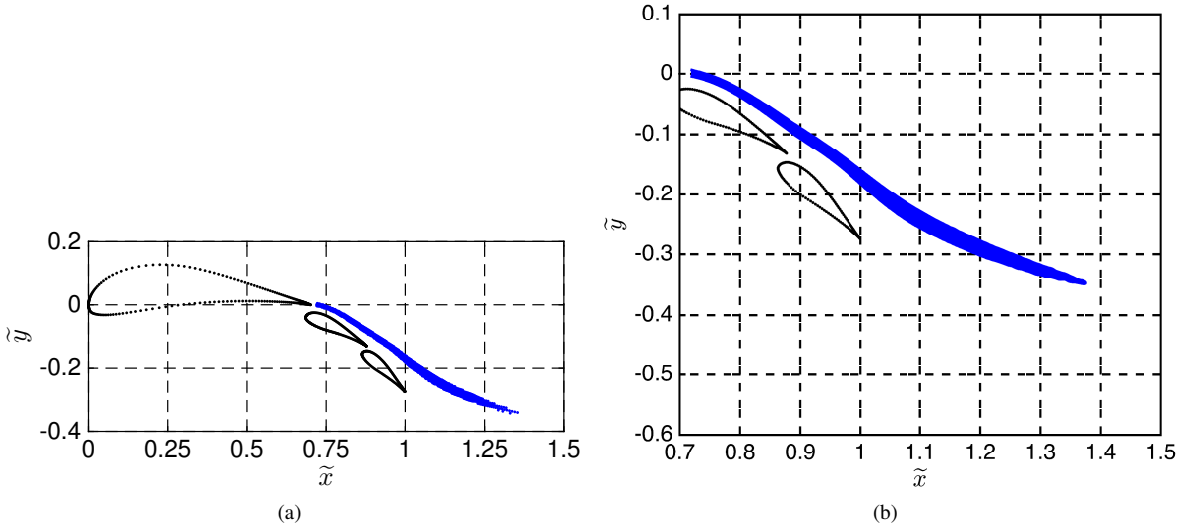

Figure 6.46: Enclosed spatial region for which $C_{p,t} \leq -0.50$ for a) wide system view and b) zoomed view.

As seen in Fig. 6.43, the size of the region for which $C_{p,t} \leq -0.50$ can be used to visualize the size of the burst wake. This region encloses the "deepest" portion of the wake in which the smallest velocities and greatest total-head losses are present. A spatial integration in the $\widetilde{x}$ direction of the area, s, between the two edges of the contour line is calculated by

$$s = \int (\widetilde{y}_{\text{upper edge}} - \widetilde{y}_{\text{lower edge}}) d\widetilde{x}. \tag{6.15}$$

This variable s, defined to be the integrated area of losses, can be used to classify the overall extent of bursting as compared to other flowfields. Equation 6.15 can be used to calculate the area s for each of the flowfields shown in Fig. 6.43, and results are shown in Table 6.6. Upon analyzing the data in the table and the results shown in Fig. 6.43, three thresholds are proposed to quantify whether the wakes are slightly, moderately, or severely burst. These thresholds with respect to s can be applied to a flowfield in which wake bursting exists as defined in Table 6.5.

Table 6.6: Integrated Area s Enclosing $C_{p,t} \leq -0.50$ for a Range of α and Re

α	Re	s
-4 deg	1×10^6	0.0065961
0 deg	1×10^6	0.0124028
4 deg	1×10^6	0.0267268
0 deg	0.6×10^6	0.0203407
0 deg	1×10^6	0.0124028
0 deg	3×10^6	0.0095397

Table 6.7: Threshold of e Quantifying Existence of Burst Wakes

Threshold	Strength of Wake Bursting
$s \leq 0.010$	slight
$0.010 < s < 0.020$	moderate
$s \geq 0.020$	severe

The wake is considered slightly burst if $s \leq 0.010$, moderately burst in which $0.010 < s < 0.020$, and severely burst if $s \geq 0.020$, as also presented in Table 6.7.

6.5 Summary of Cross-Configuration Aerodynamics

An investigation regarding the effect of different relative coordinate values upon wake bursting and aerodynamic performance is presented in this chapter. The study was executed such that the parametric effect of gap size, overhang distance, and flap deflection angle could be determined. Computational results investigated the coupled effect of these parameters while experimental methods established the independent effect of each parameter. Data were computationally collected using low-fidelity computational programs and experimentally measured with a 7-hole probe. A variety of wake metrics to quantify wake bursting were developed and presented in the first portion of this chapter. These parameters included the maximum wake thickness, the location at which thickness is maximized, and a new wake-thickness parameter which included the effect of wake thickness and downstream position. The value of quantifying the burst wakes by these metrics was established later in the chapter.

Computational simulations were performed using MSES, which is a low-fidelity inviscid/viscous panel method code. An exhaustive set of configurations were analyzed to determine the independent and coupled effect of each of the three relative coordinates. The first study established the effects in which the gap and/or overhang distances were equal for both flap 1 and flap 2. The largest C_l were observed at small gap sizes and moderate overhang distances while l/d was maximized for small-gap, large-overhang configurations. Large, thick wakes were generated by configurations with smaller gap sizes and larger overhang distances, and adverse aerodynamic performance was observed in this

region. A second exhaustive set of computations were performed to determine the coupled effect of these relative coordinates in which the values were not equal for flap 1 and flap 2. In this case, it was observed that the aerodynamics for the configurations were significantly affected by the gap size of each configuration and affected, but to a lesser extent, by the overhang distances.

Five configurations were selected for detailed examination using experimental methods, and these configurations isolated the independent effects of gap size, overhang distance, and flap deflection angle. No configurations were selected in which two relative coordinates were changed. The gap size and overhang distance for the two flaps was the same for both flaps. In this study, the results indicate that the gap size significantly affects the wake development and the aerodynamic performance of the multielement airfoil. The flap deflection angle suggested that decreased δ resulted in weaker pressure gradients thus leading to decreased lift and decreased wake bursting. Finally, it was established that overhang distance significantly affected C_l, but had almost no effect upon l/d when compared to the baseline configuration. Despite these differences in C_l, very few differences in wake development were observed for changes in overhang distance.

A variety of criterion are presented in this document to quantitatively classify the burst wake flowfield for easy comparison to other wakes. Thresholds are proposed to define if the wake is burst, at what spatial point the wake is burst, and the severity of wake bursting. A bounding contour line of constant $C_{p,t}$ was extracted from the flowfield, and analyses were performed on the shape, size, and location of this contour interval. The slenderness of the wake, as quantified by eccentricity of the contour interval, was used to define the existence of wake bursting with long, thin wakes being classified as not burst and thicker wakes suggesting a burst wake. A threshold based upon curvature of thew wake thickness was developed to define the spatial point at which the wake is said to be burst. Finally, the size of the momentum-deficit region in the flowfield is proposed to determine whether the wake is slightly, moderately, or severely burst.

Chapter 7

Design of Airfoils to Minimize Burst Wakes

The extensive discussion in Chaps. 5–6 is presented to understand the nature of burst wakes due to a variety of different parameters that affect the structure and behavior of these wakes. While insight has been gained into the flowfield, and the adverse aerodynamic effects of burst wakes has been documented throughout this dissertation, it is not sufficient to only understand the burst-wake flowfields. It is desired to determine and implement methods to reduce the effect of wake bursting on a multielement airfoil flowfield. Consequently, three different airfoil design exercises were performed, and are presented herein. These three designs are presented with increasing complexity ranging from altering the shape of the main element while maintaining flap location through altering the shape of all elements and the location of the flaps. A variety of design and analysis tools were developed to facilitate the design of multielement airfoils, and these enhancements and modifications are presented in this chapter in addition to the airfoil designs. It is noted that parametric sweeps of the relative coordinates defining the flap position are presented in Sec. 6.2 on page 167.

As previously mentioned, three airfoil designs were completed relative to the baseline MFFS(ns)-026 airfoil, and these designs are summarized in the following manner:

- Design A: modified main element for given flap geometry and position at a design point of Re=1×10^6 for both a given C_l and a given α
- Design B: modified main element for given flap geometry and position at a design point of Re=3×10^6 for both a given C_l and a given α
- Design C: altered main element, flap geometry, and flap position for fixed chord lengths at a design point of Re=1×10^6 for both a given C_l and a given α

As listed above, the three designs are referred to as A, B, and C. Iterations within each design are referred to by the airfoil design and iteration number (i.e. A2, A3, ..., B2, ... C2, ...). The two main-element airfoil designs were designed to a given C_l and α to consider the situation in which the wing incidence angle on an aircraft is unable to be changed, yet a desired takeoff or approach C_l is required. Freestream Reynolds numbers of 1×10^6 and 3×10^6 were selected for these exercises. The final design is presented in which lessons learned from the previous parametric sweeps and

design exercises were considered to yield additional insight into the airfoil design process to mitigate or reduce burst wakes. The discussion of these three airfoil designs not only led to the final airfoil design, but the discussion is also dedicated to the design process that the author implemented to achieve the final design. In this manner, it is hoped that future airfoil designers could utilize similar logic and steps to mitigate wake bursting at freestream conditions similar to those discussed in this document.

This chapter is structured in the following manner. First, the workflow and design process to achieve the final airfoil design is presented. A variety of tools that were developed to facilitate rapid design and analysis of multielement airfoils affected by burst wakes are discussed. The information in these early sections include both enhancements to airfoil design software including the implementation of numerous wake metrics to quantify the effect of wake bursting. The latter portions of the chapter are dedicated to a discussion of each of the airfoil designs and the processes implemented to achieve these airfoil designs; designs are presented in increasing complexity throughout this chapter.

7.1 Workflow

A wide variety of computational tools were used to design and analyze the multielement airfoils presented in this chapter. Airfoils were designed in MFOIL/PROFOIL using an inverse conformal-mapping technique, and each of the airfoils in the multielement airfoil system was designed in isolation. Numerous different parameters in the PROFOIL input file were used to specify various aspects of the elemental airfoil. After all three elements were designed in isolation, the elemental airfoils were assembled into a multielement system for inviscid analysis using MCARF. A more thorough discussion of the MFOIL/PROFOIL program is presented in Sec. 3.5. Viscous analyses were then performed using a variety of tools added by the author over the course of this research project. The computational program MSES was tightly integrated into the MFOIL/PROFOIL design tool such that viscous analyses computed by MSES could be analyzed inside MFOIL/PROFOIL to yield rapid feedback for airfoil performance at a desired α and Re.

7.2 Enhancements to MFOIL

Throughout the course of this research, numerous modifications and additions were made to the MFOIL code. MFOIL is a MATLAB-based program which is integrated with PROFOIL for the purpose of multipoint inverse airfoil multielement airfoil design [113, 114]. Twenty-five different `*.m` files comprise the program, and a dependency tree for version 2.8 of the program, which includes modifications made during the course of this research, is depicted in Fig. 7.1. The tree is a convenient way to visualize function and subfunction relationships in MFOIL with the function names printed inside the various bubbles. The different-colored arrows represent subfunctions which are called from

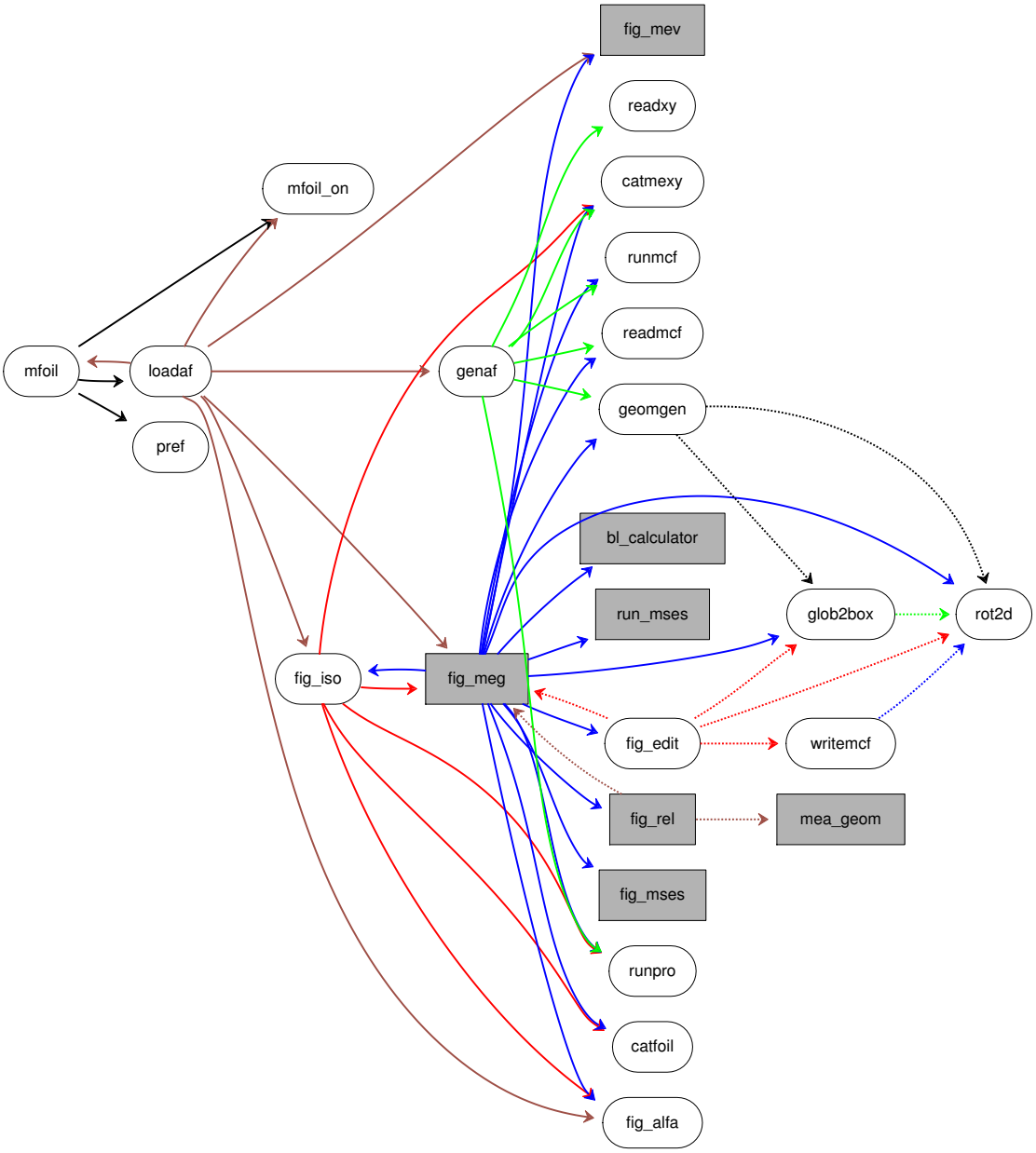

Figure 7.1: Dependency tree for MFOIL v. 2.8 with new or heavily-modified scripts depicted as gray boxes.

the originating function. For example, the arrow pointing from `mfoil` to `pref` indicates that the subfunction `pref` is called by `mfoil` during the operation of `mfoil`. Few or no modifications were made to the scripts depicted as white rounded bubbles, while the dark gray boxes represent codes which were either heavily modified or are new to the MFOIL program, which are discussed in this section. For a more thorough explanation of MFOIL/PROFOIL, please refer to Sec. 3.5 on page 68.

Significant functionality was added to MFOIL by the author to allow the user to specify the location of a multiele-ment airfoil in relative coordinates instead of only absolute coordinates. The absolute coordinate system, as defined

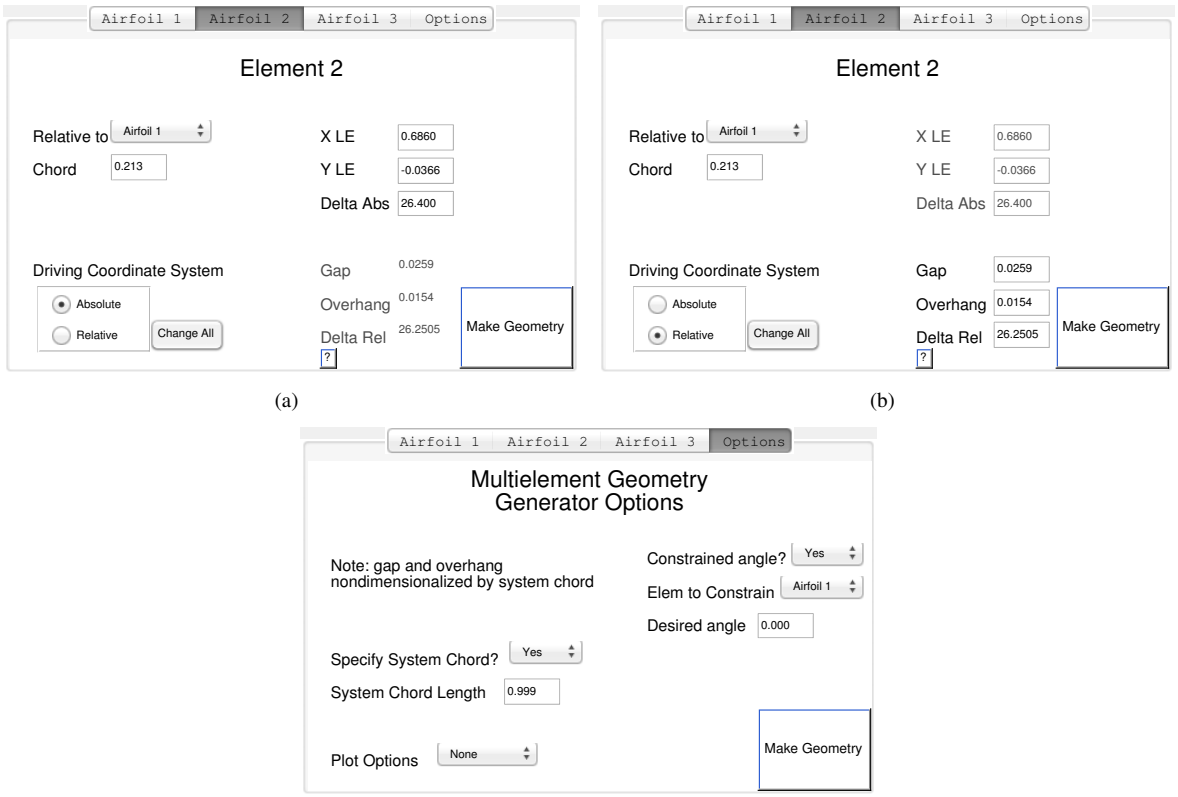

Figure 7.2: Multielement Airfoil Geometry Window functionality added to MFOIL allowing user to specify location of an airfoil in a) absolute coordinates, b) relative coordinates, or to c) specify various geometry generation parameters.

in Fig. 3.2, prescribes the location of the elements in terms of leading edge location and absolute deflection angle. A relative coordinate system, in which the elements are defined based upon parameters that govern the flow, is presented in Fig. 3.3. Upon execution of MFOIL with a multielement airfoil, the new Multielement Geometry Window, shown in Fig. 7.2, was presented to the user. Tab controls were located at the top of the window; a tab for each airfoil element existed in which the user was able to control the coordinates of each airfoil element, and an options tab added control regarding the multielement airfoil geometry generation. When first displayed to the user, as shown in Fig. 7.2(a), the absolute coordinates for each element as read in from the input file were displayed to the user in the upper right portion of the tab. Upon convergence of the the PROFOIL program which yielded the multielement airfoil geometry, the relative coordinates, which are displayed in the lower right portion of the figure next to the "Make Geometry" button, were calculated. By default, the user was given control of the absolute coordinate system unless chosen otherwise with the radio button in the lower left portion of the window. When selected, the absolute coordinate values were deactivated, and the user was given control of the relative coordinates, as shown in Fig. 7.2(b). Values could be entered in these three text boxes and appropriate transformations were applied to create the multielement geometry upon selection of

the "Make Geometry" push button. These transformations are described in detail in Sec. 3.1. Selection of this button called the `mea_geom` function in MATLAB using the syntax

```
afout = mea_geom(coordinates, chords, relative to, delta, overhang, gap, options)
```

where the resulting geometry was returned in `afout` and in which the input values were mandated to be prescribed included:

- `coordinates...` a cell array of length *N* containing two columns and numerous rows for the airfoil coordinates in `coordinates{j}` where *N* is the number of airfoil elements; coordinates wrap counter-clockwise around the airfoil, per standard convention
- `chords...` a one-dimensional floating-point vector containing *N* numeric entries prescribing the relative chord lengths; discussed in greater detail later in this section
- `relative to...` *N* integers in a one-dimensional vector defining the element to which the current element is defined
- `delta...` relative deflection angle in degrees as one-dimensional floating-point vector; value in index 1 is irrelevant if main element is constrained to *x* axis
- `overhang...` overhang distance for each element nondimensionalized by system chord length as one-dimensional floating-point vector; value in index 1 is irrelevant if main element is constrained to the origin
- `gap...` *N*-valued vector containing gap size for each element normalized by system chord length; value in index 1 is irrelevant if main element is constrained to the origin

A variety of choices can be specified in the variable `options`, and graphical control of these values is possible through the Options tab, as shown in Fig. 7.2(c). While these values can be declared by the user, it is not necessary to specify any of the following flags:

- `'SYSCHORD', [numeric]...` desired system chord length, as specified by `numeric`, for converged multi-element airfoil geometry; note that if this is specified, the chord lengths specified in `CHORDS` above will all be scaled by an appropriate value to yield the desired system chord length
- `'E_DELTA', [numeric1 numeric2]...` absolute deflection angle of element `numeric1` is desired to be `numeric2`, where `numeric2` is in degrees and `numeric1` is an integer
- `'U_PLOT', ['lines' or 'filled']` a plot of the resulting geometry, presented as a line plot or as filled elements

Finally, for the sake of clarity, an example call to the code may be something such as

```
afout = mea_geom([coords{1} coords{2} coords{3}, [0.8 0.2 0.1], [1 1 2], [0 26 16], [0.7
   0.01 0.01], [0 0.02 0.02], 'SYSCHORD', 1.000, 'E_DELTA', [0.0 1], 'U_PLOT', 'lines');
```

This multielement geometry generator was integrated into MFOIL for automated geometry creation and coordinate handling.

7.2.1 MSES Integration

As discussed in Sec. 3.5, MFOIL leverages MCARF, an inviscid aerodynamic analysis program, to predict aerodynamic performance of the airfoil system. While inviscid analysis is advantageous due to the low computational cost, viscous effects may dominate the aerodynamic flowfield, and thus the airfoil may never yield the performance predicted by the inviscid analysis. These adverse effects may be encountered through stall or through poor wake behavior, such as burst wakes. Therefore, the viscous analysis capabilities of MSES were added into MFOIL to yield viscous predictions for a single-element or multielement airfoil. This section discusses the details of that integration; further details of MSES can be found in Sec. 3.3.

MSES calculations were automatically performed in the `work/MSES` subdirectory through execution of the `run_mses` and `bl_calculator` MATLAB scripts. The `run_mses` code was first called through

```
[mses_solution hvec] = run_mses(coordinates, alpha, Reynolds number, Mach number,
   viscous mode, airfoil name, plot options);
```

in which the MSES solution is returned in `mses_solution` and a handle to a plot, if desired, is stored in `hvec`. Inputs to the program include

- `coordinates...` an N-dimensional structure array in which coordinates are stored in `coords(i).x` and `coords(i).y`; same format as is returned by `mea_geom` code
- `alpha...` scalar number of α for analysis
- `Reynolds number...` scalar integer for Reynolds number, if in viscous mode, for analysis
- `Mach number...` freestream Mach number
- `viscous mode...` either `'v'` for viscous analysis or `'i'` for inviscid operation; if inviscid analysis is desired, the input for freestream Reynolds number is ignored
- `airfoil name...` airfoil name as string (maximum of 32 characters, as limited by MSES)
- `plot options...` string as defined by either `'line'` to plot final C_p plots or `'none'` to not plot anything; handle of this resulting plot returned in `hvec`

and all of the above inputs are mandatory from which run scripts were automatically generated to execute MSET, MSES, and MPLOT. Grids were generated in MSET with the surface curvature exponent b in Eq. 3.64 declared as 0.05, and were then elliptically smoothed in MSET prior to being written out in an unformatted binary file for reading in by MSES. MSES was run to a maximum of 50 iterations, and convergence was monitored graphically and with text output to the MATLAB command window. Finally, the boundary-layer dump file and streamline grid file were exported through MPLOT. Results from MSES stored in the structure array `mses_solution(i).*` are all returned in the boundary-layer dump file, as discussed by Drela [90], and include:

- `streamline...` dividing streamline for upper and lower surface of elements (from streamline grid file)
- `x...` x airfoil coordinate wrapping counter-clockwise from upper surface of trailing edge to lower surface of trailing edge (from user inputs)
- `y...` y airfoil coordinate following same convention as x
- `s...` arc length coordinate vector
- `cp...` surface C_p
- `ueao...` boundary-layer edge velocity U_e/a_0
- `delta_star...` displacement thickness δ^*
- `theta...` momentum thickness θ
- `hbar...` shape parameter δ^*/θ
- `cf...` surface skin friction coeffient
- `rtheta...` kinetic energy thickness
- `mach...` boundary-layer edge Mach number
- `wake...` coordinates for wake centerline
- `hk...` kinematic shape parameter H_k (calculated as discussed below)
- `delta...` boundary-layer thickness (calculated as discussed below)

Unless otherwise noted, information in the above list was imported from the boundary-layer dump file bl.*. The bl.* file contains information on the upper and lower surfaces of each element as well as data along the wake centerline. As discussed in Chap. 5, the wake centerline is defined as the location in y for a given x at which the magnitude of the

total momentum vector, or velocity vector at incompressible freestream conditions, was minimized. In the data file, an 11-column output is returned for the upper surface of a given element starting at the stagnation point followed by two line breaks and then an 11-column output for the lower surface which also begins at the stagnation point. After these outputs, a 10-column section includes data for the wake centerline. The appropriate values for the upper surface, lower surface, and wake centerline were extracted from the file and appropriately stored in `mses_solution(i).*`. While many values in `mses_solution(i).*` were read in from the boundary-layer dump file, some values were read from the streamline dump file, and others were calculated from provided quantities. Automated scripts extracted the index numbers for the dividing streamline for each element from the MPLOT.out file, and then the streamlines were read from the grid dump file. All streamlines were imported from the grid.* file, and the appropriate dividing streamlines were subsequently extracted from this data set. The elemental forces and moments as well as the system forces and moments, in particular C_l, C_d, and C_m, were also extracted from the MPLOT.out file and stored in the `mses_results` structure array. All of the file management, data reading, and necessary calculations were automatically performed by the `run_mses` code. An optional code, named `bl_calculator` could be run after `run_mses` to calculate the surface normals of the airfoil and provides a graphical depiction of the boundary-layer thickness δ around each element. This step was not required, however. A number of wake metrics, as presented and derived in Sec. 6.1, were calculated for each solution.

The data generated by MSES were plotted in MFOIL in the two windows shown in Fig. 7.3. Viscous pressure distributions were plotted in Fig. 7.3(a) while text outputs of the system lift, drag (in drag counts), and l/d were presented in the lower right portion of the window (shown in blue). The elemental forces and moments as well as the dividing-streamline grid were presented in as seen in Fig. 7.3(b). In addition to the standard airfoil performance values, three wake metrics, namely $x_{thickest}$, δ_{max}, and WTP were shown as text outputs in the window. A discussion of these metrics is presented above in Sec. 6.1 on page 162.

7.3 Airfoil Design Exercise A: Main Element Alterations for Re $= 1 \times 10^6$

As previously discussed in this dissertation, the baseline MFFS(ns)-026 airfoil yielded poor aerodynamic performance which was attributed, in large part, to the burst wakes. Consequently, it was desired to design an aerodynamically superior multielement airfoil relative to this baseline airfoil a design point for which $Re = 1 \times 10^6$ and $C_l = 3.40$. It was desired to design the airfoil to a given value of C_l to achieve a reduction in C_d for a given C_l and not the trivial reduction in C_d due to lower C_l. The multielement airfoil systems presented in this section were tuned with δ_1 and δ_2 to yield the desired C_l for $\alpha = 0$ deg. As the main element was of significant interest in this design exercise, it was desired to obtain nearly-identical flow angularity over the main element such that the pressure distribution and

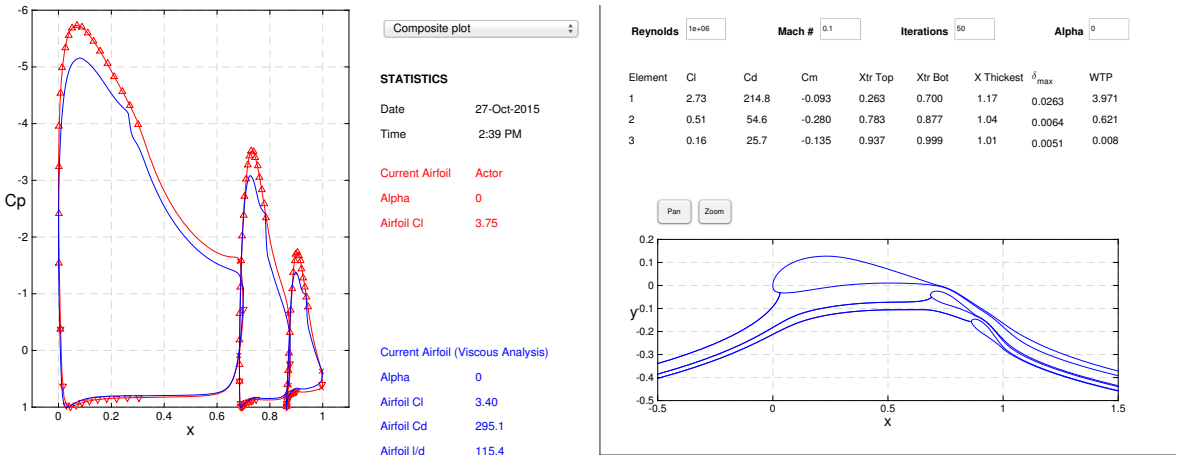

(a) (b)

Figure 7.3: Windows added to MFOIL to convey results from MSES including a) pressure distributions and b) flow-field and elemental results.

transition point could be easily controlled for a given α. If α were varied to achieve a given C_l instead of δ, the flow over the main element would be significantly different, and the desired control of C_p and the transition point would be lost. Returning to the design constraints, airfoils are sometimes designed such that the maximum t/c is a certain value to account for structural requirements. Consequently, the multielement airfoils presented in this section were designed such that the main-element t/c was 0.20, in which c is the elemental chord length. By considering the elemental chord lengths and elemental t/c, it is apparent that $(t/c_{sys})_{max}$ is 0.14 for the main element. The relative positions for each flap and the chord lengths for the three elements remain unchanged for all airfoils presented in this section, and these coordinates are identified in Table 7.1. The absolute coordinates $(\widetilde{x},\widetilde{y})_{le}$ are also presented in the table. As the chord lengths for all elements were not altered, the $(t/c)_{max}$ for the main element was defined to be 0.20 for all airfoil iterations in this section. Each of these three airfoils were designed in isolation in which numerous parameters, either physical or aerodynamic, were prescribed for each airfoil. These parameters included the following: α^*-ϕ curve, K_s (a manner to control trailing edge thickness and shape), *REC* (a way to control the pressure-recovery region), C_{m_0}, and $(t/c)_{max}$. While many other inverse-design parameters can be defined in PROFOIL, only those parameters previously

Table 7.1: Relative and Absolute Coordinates for all Airfoils in Design Exercise A

	Main Element	Flap 1	Flap 2
c/c_{sys}	0.700	0.213	0.182
gap	–	0.025	0.015
overhang	–	0.015	0.000
x_{le}	0.00	0.686	0.865
y_{le}	0.00	-0.037	-0.151

listed were used to design airfoils in this chapter. A good discussion of each of these parameters can be found in Ref. 109.

A systematic set of steps was executed to achieve the final airfoil design presented later in this section. The baseline MFFS(ns)-026 airfoil is presented at the beginning of this section, and then each successive iteration is discussed. Each iteration in the design process is presented and is always compared to the previous iteration. Throughout this section, each airfoil is plotted with a unique color to allow easy comparisons between iterations. The iteration being actively discussed in this document is plotted with solid lines while the previous iteration is plotted as dashed lines.

7.3.1 MFFS(ns)-026 ("Baseline") Airfoil

The three-element MFFS(ns)-026 airfoil, originally designed by Ragheb [55], is comprised of a main element and two flaps and serves as the baseline airfoil against which the designed airfoils are compared. Figure 7.4 shows the α^*-ϕ curves for the baseline airfoil in addition to the viscous C_p distribution and resulting airfoil shape. The ϕ values bounding each segment of the airfoil are presented as small circles. In this manner, the relationship between the α^*-ϕ curves, pressure distribution, and airfoil shape can be readily understood. In addition to the α^*-ϕ curve, the inverse-design parameters used to design the baseline airfoil are listed in Table 7.2. As described above in Sec. 3.5, the *REC* parameter controls the shape of the pressure-recovery behavior, K_s is a manner to specify the airfoil thickness and pressure distribution near the trailing edge, C_{m_0} is the zero-lift pitching moment, and $(t/c)_{max}$ is the maximum thickness-to-chord ratio.

In addition to the aerodynamic performance and airfoil shape, the α^*-ϕ curves for the upper and lower surfaces for all three elements are plotted in Fig. 7.4. More points are specified on the upper surfaces than the lower surfaces as more control of the upper surface was desired than the lower surface. A noticeable kink exists in some of the α^*-ϕ curves shown in the figure. When considering the upper surface, larger values of α^* at larger values of ϕ relax the adverse pressure gradient. While the α^*-ϕ curve can be used to control the upstream portion of the pressure-recovery region, the *REC* parameter controls the downstream adverse pressure gradient. The laminar-to-turbulent transition point significantly affects the aerodynamic performance of low-Reynolds-number airfoils, and this transition behavior

Table 7.2: Inverse-Design Parameters for Main Element of MFFS(ns)-026 ("Baseline") Airfoil

	Main Element	Flap 1	Flap 2
REC_u	0.05	0.20	0.20
REC_l	0.20	0.20	0.20
K_s	0.30	0.15	0.15
C_{m_0}	-0.20	-0.16	-0.10
$(t/c)_{max}$	0.200	0.205	0.205

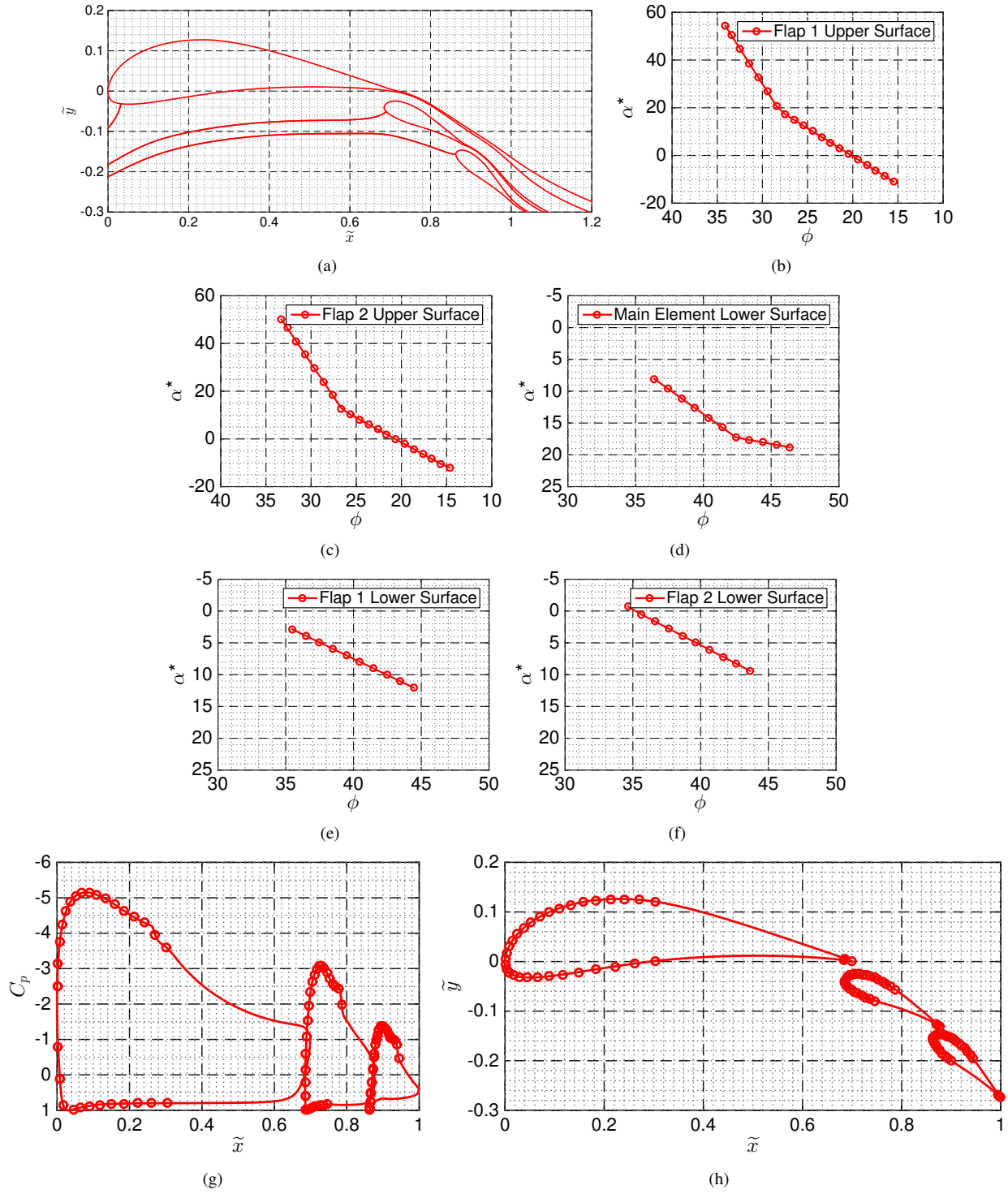

Figure 7.4: Baseline airfoil design parameters including a) α^*-ϕ for main-element upper surface, b) α^*-ϕ for flap 1 upper surface, c) α^*-ϕ for flap 2 upper surface, d) α^*-ϕ for main element lower surface, e) α^*-ϕ for flap 1 lower surface, f) α^*-ϕ for flap 2 lower surface, g) viscous C_p distribution coplotted with ϕ points, and h) airfoil coordinates coplotted with ϕ points.

can be controlled with the α^*-ϕ curve. For the design point $Re = 1 \times 10^6$ and $\alpha = 0$ deg, the transition point for the main element occurs upstream of the final ϕ value. If laminar flow is desired over a larger range of $\widetilde{x}$ values, the α^*-ϕ curve can be tuned appropriately. As the flowfield is significantly affected by the main-element aerodynamic performance, the importance of the main-element transition point cannot be understated. Increased $\widetilde{x}$ for which laminar flow exists, also known as an increased laminar run, yields a smaller boundary layer at the trailing edge of the main element when compared to a decreased laminar run for a given pressure gradient. However, classic boundary-layer theory indicates that a boundary layer in an adverse pressure gradient are larger and thicker than boundary layers in favorable pressure gradients. Thus, the boundary layer thickness over the airfoil can be controlled by both the transition point and the magnitude of the pressure recovery gradient. Viscous simulations in MSES indicate that l/d for the baseline airfoil at the design point is 115. Wake metrics, as defined above in Sec. 6.1 on page 162, were calculated for the baseline airfoil at the design point for which $WTP = 3.97$, $\delta_{max} = 0.0263$, and $\widetilde{x}_d = 1.17$.

7.3.2 Airfoil A2

In an effort to increase l/d and decrease wake thickness, a second airfoil was designed for the design point of $Re = 1 \times 10^6$ and $\alpha = 0$ deg. The five Inverse-Design Parameters for Main Element of the main element of both the baseline airfoil and A2 airfoil are presented in Table 7.3; none of these inverse-design parameters were changed for this iteration. The reader is reminded that only the main element was altered in this design; the flap geometry and location were unchanged relative to the baseline airfoil. Even though the parameters in Table 7.3 were not changed, the α^*-ϕ curve for the main element was altered, as shown in Fig. 7.5(a,b). The resulting C_p distribution and geometry are also shown in the figure. Most notable is the weaker adverse pressure gradient over the upper surface for $0.00 \leq \widetilde{x} \leq 0.38$ and the downstream movement of the transition point.

It was desired to relax the adverse pressure gradient and magnitude of the pressure peak over the upstream portion of the main-element upper surface, and this was achieved by decreasing α^* for airfoil A2 relative to the baseline case. The modified α^*-ϕ curve is seen in Fig. 7.5(c) in which the baseline airfoil is plotted in dashed red lines with triangles, and airfoil A2 is shown as a solid blue line with circles. As previously mentioned, the triangles and circles

Table 7.3: Inverse-Design Parameters for Main Element of Baseline Airfoil and Airfoil A2

	Baseline Airfoil	Airfoil A2
REC_u	0.05	0.05
REC_l	0.20	0.20
K_s	0.30	0.30
C_{m_0}	-0.20	-0.20
$(t/c)_{max}$	0.200	0.200

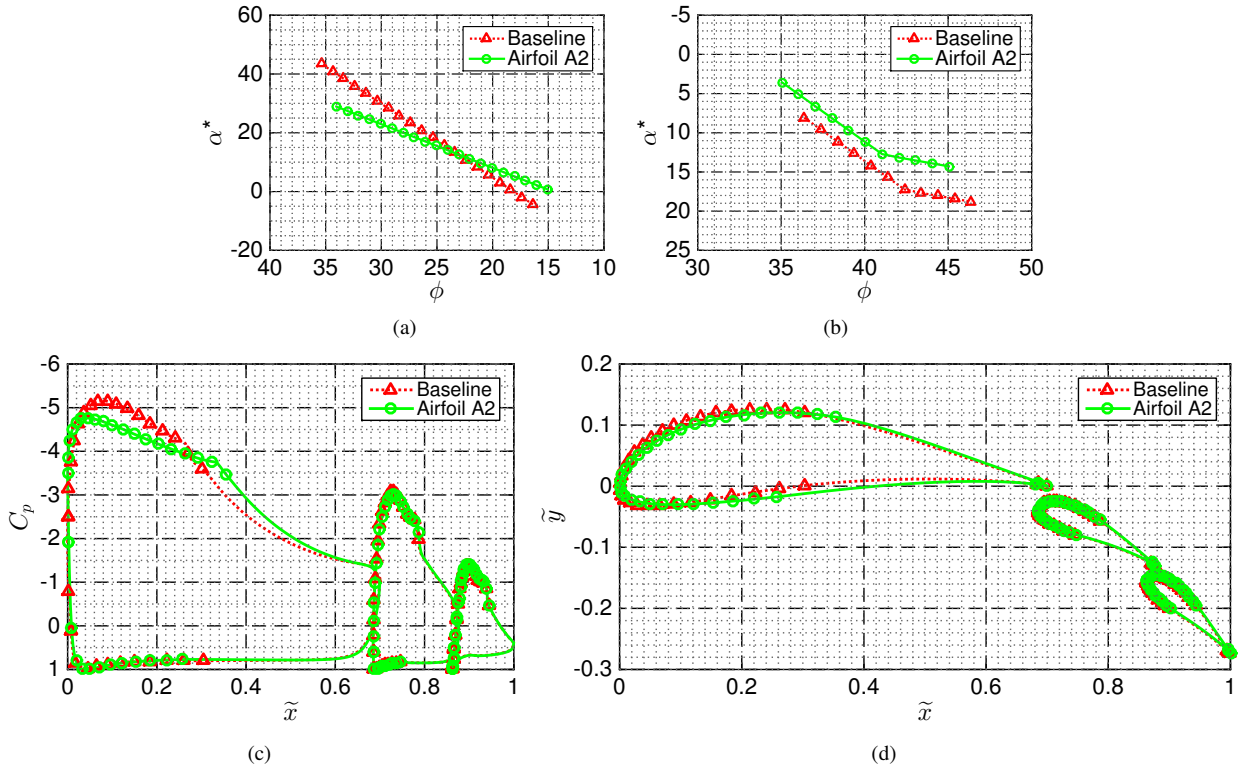

Figure 7.5: Baseline airfoil and airfoil A2 design parameters including a) α^*-ϕ for main-element upper surface, b) α^*-ϕ for main-element lower surface, c) viscous C_p distribution coplotted with ϕ points, and d) airfoil coordinates coplotted with ϕ points.

correspond to the ϕ values for the conformally-mapped airfoil. While the same number of α^*-ϕ pairs were used to define both airfoils, the minimum values of ϕ for the main-element upper surface of airfoil A2 are decreased relative to the baseline case. This translates into increased control of the upper surface C_p distribution at increased $\widetilde{x}$, as seen in both the pressure distribution and the geometry. The pressure peak for airfoil A2 is reduced to -4.9 from -5.2 for the baseline airfoil. Transition over the main element is observed to occur at one ϕ value larger (decreased $\widetilde{x}$) than ϕ_{min}, and this result was used to push the transition point in the downstream direction. The baseline airfoil included two ϕ values downstream of the transition point. A more aggressive pressure gradient exists in the pressure-recovery region over the main element for airfoil A2. Despite the significant changes to the main element that yielded changes in the aerodynamic flowfield, the pressure distributions over both flaps remain essentially unchanged.

Airfoil A2 yielded marked improvement in aerodynamic performance relative to the baseline airfoil, because the smaller, thinner wake of airfoil A2 yielded an increase in l/d. As presented in Table 7.4, the lift-to-drag ratio of airfoil A2 was increased by 13.0% with nearly a 20% reduction in wake thickness. In addition to smaller $\delta_{w,\,ME,\,max}$, the $\widetilde{x}$ for the maximum wake thickness moves slightly upstream for airfoil A2. The thinner wake and the decreased $\widetilde{x}_{d,\,ME}$ yielded a 21.2% decrease in WTP for the newly-designed airfoil.

Table 7.4: Aerodynamic Performance of Airfoil A2 Compared to Baseline Airfoil

	Baseline Airfoil	Airfoil A2	Percent Improvement Relative to Baseline
l/d	115	130	13.0%
$\delta_{w\ ME,\ max}$	0.026	0.021	19.2%
$\widetilde{x}_{d,\ ME}$	1.17	1.16	0.85%
WTP_{ME}	3.97	3.13	21.2%

7.3.3 Airfoil A3

Modifications were made to the inverse-design parameters that defined airfoil A2 to yield the airfoil for the third iteration, A3. As seen in Table 7.5, no modifications were made to the five specific design parameters, but alterations were made to the α^*-ϕ curve. Plots for the α^*-ϕ curves, C_p distributions, and airfoil coordinates are shown in Fig. 7.6. As seen in the figure, the α^* values on the upper surface for larger ϕ (towards the leading edge) were further decreased, and the α^* values for low ϕ (in the downstream direction) were increased. In other words, the α^*-ϕ curve for the upper surface of airfoil A3 is "flatter" than that of airfoil A2. A reduction in α^* for the lower surface of A3 relative to airfoil A2 yielded an improved pressure distribution on the pressure side of the airfoil. In addition, the α^*-ϕ curve is shifted in the $-\phi$ direction yielding slightly less control in the downstream portion of the lower surface, which seen in the airfoil coordinate plot. Upon examination of Fig. 7.6(c), the pressure peak is seen to have moved upstream and the transition point is located slightly downstream for airfoil A3 when compared to airfoil A2. The pressure peak for both airfoils is approximately the same value of -4.9, but the pressure gradient in both the laminar and turbulent regions of the airfoil is slightly different. Airfoil A3 yields a slightly stronger adverse pressure gradient for $\widetilde{x} \leq 0.20$ and a slightly weaker pressure gradient in which $1.20 \leq \widetilde{x} \leq 0.36$. A marked change in the pressure gradient occurs at increased $\widetilde{x}$ for airfoil A3, thus yielding a stronger pressure gradient in the downstream portion of the pressure-recovery region. As observed at the trailing edge of the main-element airfoil, the air is dumped from the main element at approximately the same C_p for both airfoil A2 and A3. Similar to the observations with regard to airfoil A2, little changes in the C_p distribution over the two flaps is present.

Table 7.5: Inverse-Design Parameters for Main Element of Airfoil A2 and Airfoil A3

	Airfoil A2	Airfoil A3
REC_u	0.05	0.05
REC_l	0.20	0.20
K_s	0.30	0.30
C_{m_0}	-0.20	-0.20
$(t/c)_{max}$	0.200	0.200

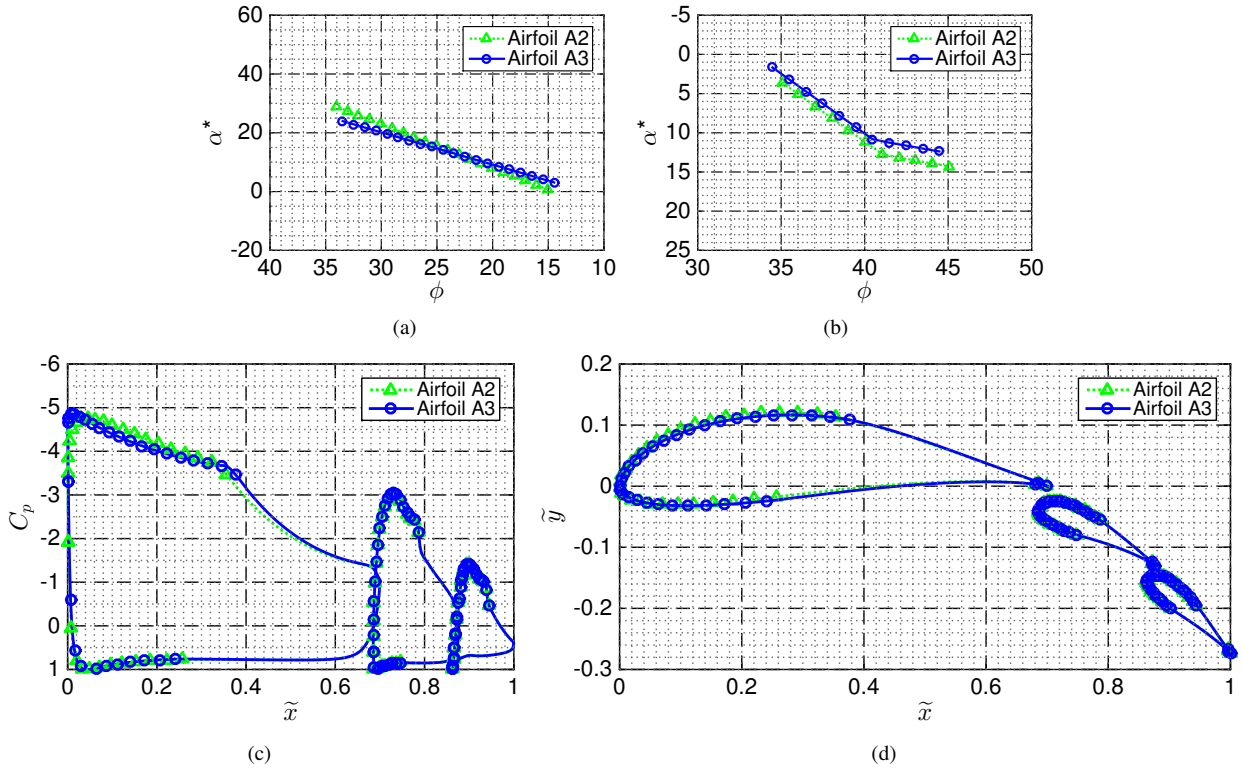

Figure 7.6: Airfoil A2 and A3 design parameters including a) α^*-ϕ for main-element upper surface, b) α^*-ϕ for main-element lower surface, c) viscous C_p distribution coplotted with ϕ points, and d) airfoil coordinates coplotted with ϕ points.

Table 7.6: Aerodynamic Performance of Airfoil A3 Compared to Airfoil A2 and Baseline Airfoil

	Airfoil A2	Airfoil A3	Percent Improvement Relative to A2	Percent Improvement Relative to Baseline
l/d	130	134	2.99%	16.5%
$\delta_{w\ ME,\ max}$	0.021	0.020	4.76%	23.1%
$\widetilde{x}_{d,\ ME}$	1.16	1.16	0.00%	0.85%
WTP_{ME}	3.13	2.94	6.07%	25.9%

Aerodynamic performance of airfoil A3 is presented in Table 7.6 in which easy comparisons can be made to airfoil A2. Improvements in the four parameters are presented for airfoil A3 relative to both airfoil A2 and the baseline airfoil. A 5% decrease in maximum wake thickness yields decreased WTP_{ME} and increased l/d. No improvements in $\widetilde{x}_{d,\ ME}$ are observed for airfoil A3 compared to airfoil A2, but nevertheless the decreased wake thickness translates into decreased WTP_{ME}. As presented in the table, airfoil A3 yields a 23.1% increase in l/d relative to the original baseline airfoil. Results for airfoil A2 and airfoil A3 both suggest that l/d can be significantly improved with decreased wake bursting resulting from more well-behaved boundary layers over the main element.

7.3.4 Airfoil A4

The fourth iteration, denoted as A4, includes minor changes in REC_u, K_s, and C_{m_0}, as presented below in Table 7.7. Parameters for which values differ in airfoil A4 when compared to airfoil A3 are shown in bold text with a light blue background, while unchanged parameters are shown with white background without bold text. A decrease in REC_u for airfoil A4 yields a slight decrease in $\partial C_p/\partial \widetilde{x}$ at the beginning of the pressure-recovery region over the main-element upper surface, as seen in Fig. 7.7. This reduced pressure gradient is visible at $\widetilde{x} \approx 0.02$, which is the location of the pressure peak. The somewhat-large change in K_s changes the pressure distribution near the trailing edge such that $\partial C_p/\partial \widetilde{x}$ is decreased immediately upstream of the trailing edge for both the upper and lower surfaces. Despite these changes, the pressure is dumped at the same C_p for airfoils A3 and A4. An additional ϕ point was added to the downstream portion of the main-element upper surface ($\phi \approx 13.2$) and resulted in a "flatter" pressure distribution up to $\widetilde{x} = 0.40$, which is an increase of 0.02 relative to airfoil A3. The reduction in C_{m_0} results in decreased main-element camber thus resulting in less elemental lift from the main element. When carefully examined, the reduction in aft loading is manifested in the airfoil coordinates as a downward shift of the lower surface near the trailing edge of the main element. A reduction in C_l from the main element stipulates that the flap loading must be increased through increased flap deflection angle such that the system C_l remained at the desired value of 3.40. This increase in C_l for flap 1 is evidenced by a stronger pressure peak for airfoil A4 when compared to airfoil A3. Despite this increase in the pressure peak, the C_p distribution in the pressure-recovery region is nearly identical for the two airfoils. Thus, a very large $\partial C_p/\partial \widetilde{x}$ is observed at the transition point ($\widetilde{x} \approx 0.78$).

Aerodynamic performance and wake metrics metrics are presented in Table 7.8 for airfoils A3 and A4 and improvements in metrics for airfoil A4 relative to both A3 and the baseline case. As seen in the table, the maximum wake thickness was decreased by 20.0% relative to airfoil A3, but l/d increased by only 5.22%. This result indicates that viscous wake bursting-effects affect C_d less than the effects of the burst wake upon C_d for the baseline airfoil. While the burst wake increases C_d relative to a non-burst wake, most of the contributions to C_d are caused by viscous effects other than the main-element burst wake.

Table 7.7: Inverse-Design Parameters for Main Element of Airfoil A3 and Airfoil A4

	Airfoil A3	Airfoil A4
REC_u	0.05	**0.02**
REC_l	0.20	0.20
K_s	0.30	**0.50**
C_{m_0}	−0.20	**–0.15**
$(t/c)_{max}$	0.200	0.200

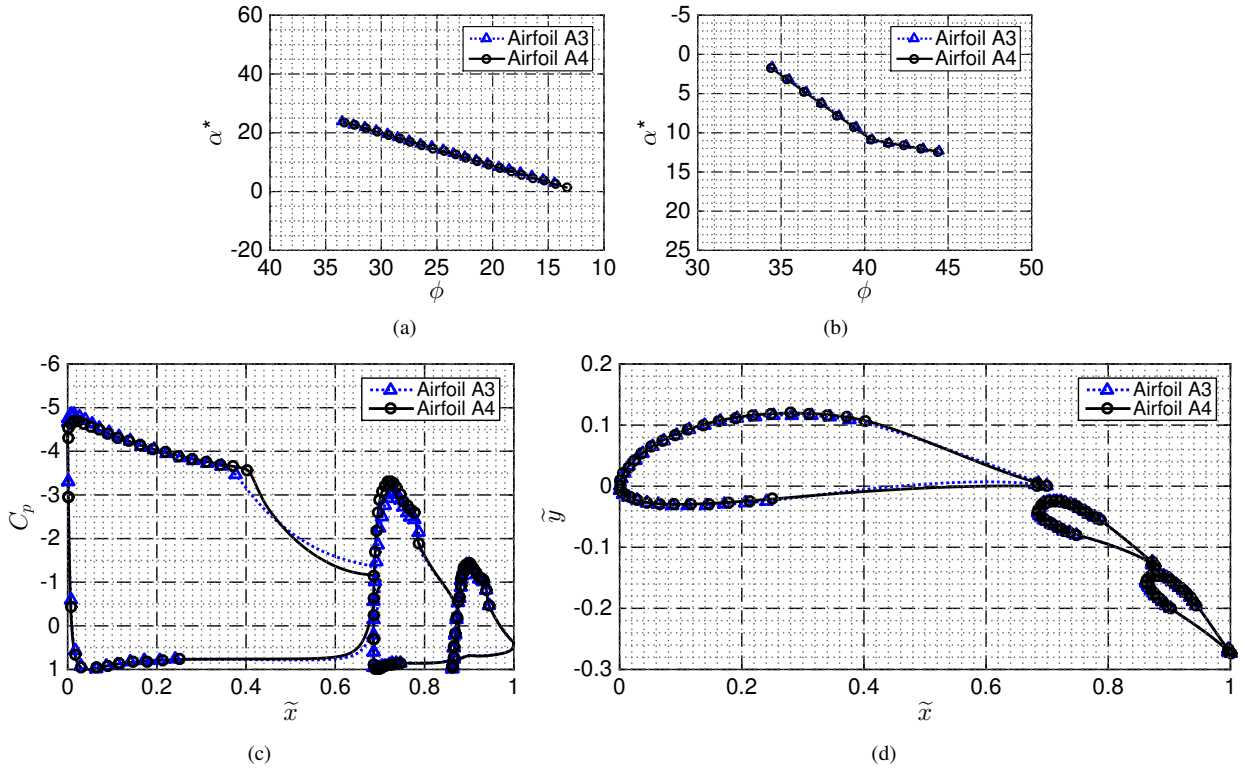

Figure 7.7: Airfoil A3 and A4 design parameters including a) α^*-ϕ for main-element upper surface, b) α^*-ϕ for main-element lower surface, c) viscous C_p distribution coplotted with ϕ points, and d) airfoil coordinates coplotted with ϕ points.

Table 7.8: Aerodynamic Performance of Airfoil A4 Compared to Airfoil A3 and Baseline Airfoil

	Airfoil A3	Airfoil A4	Percent Improvement Relative to A3	Percent Improvement Relative to Baseline
l/d	134	141	5.22%	38.5%
$\delta_{w\ ME,\ max}$	0.020	0.016	20.0%	38.5%
$\widetilde{x}_{d,\ ME}$	1.16	1.17	−0.86%	0.00%
WTP_{ME}	2.94	2.47	6.07%	37.8%

It is prudent to compare the original baseline airfoil with the final design iteration, airfoil A4. The C_p distribution and airfoil coordinates are shown in Fig. 7.8 in which a red line represents the baseline airfoil, and a black line corresponds to airfoil A4. As previously discussed throughout this section, aerodynamic performance is improved if the transition point is moved downstream and if $\partial C_p/\partial\widetilde{x}$ is decreased in the upstream portion of the pressure-recovery region. The combination of a weaker adverse pressure gradient and increased laminar run results in a thinner boundary layer at the main-element trailing edge. Consequently, this smaller, thinner wake is not affected by the strong off-surface pressure gradient than the effects observed with a larger, thicker wake. Through the combination of numerous inverse-design parameters, the transition point was moved from $\widetilde{x}$ of 0.31 to 0.40, thus increasing the laminar run over

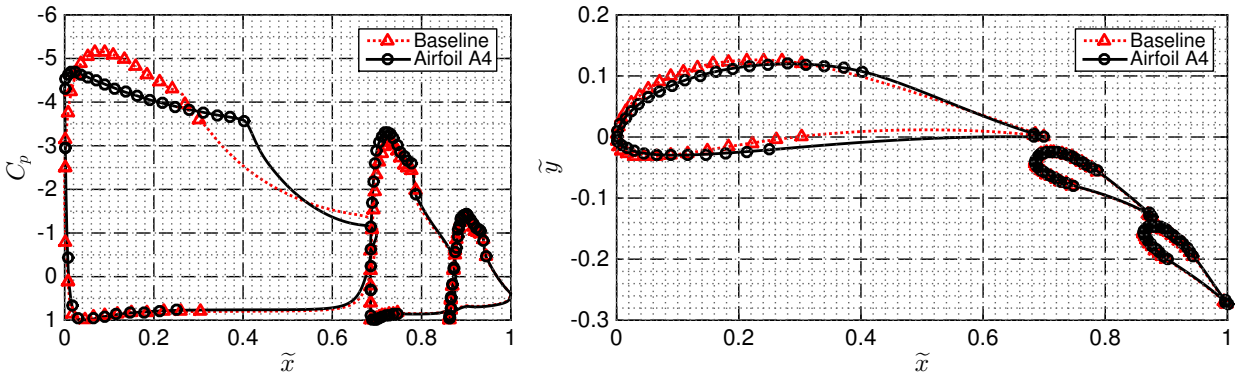

(a) (b)

Figure 7.8: Baseline airfoil and airfoil A4 data including a) C_p distribution and b) airfoil coordinates.

the main-element upper surface and yielding a l/d increase in excess of 38% for airfoil A4 when compared to the baseline airfoil. Significant lessons learned in this section include the importance of a flatter, weaker adverse pressure gradient over the main-element upper surface which results in less boundary-growth in this region than the growth due to a stronger pressure gradient. While the pressure gradient is increased in the downstream portion of the pressure-recovery region, it is apparent that the trade for reduced pressure gradient, and thus less boundary-layer growth, in the upstream portion of the airfoil outweighs the stronger pressure gradient, yielding increased boundary-layer growth, in the downstream portion of the airfoil.

Navier-Stokes fixed-transition computations were performed with USM3D for the baseline A1 airfoil and the designed A4 airfoil for freestream $Re = 1 \times 10^6$ and $C_l = 3.40$ (the design point for the airfoil). Transition points for the upper and lower surfaces of all three elements were calculated by MSES and then declared for the USM3D simulation. The resulting flowfields for the two airfoils are presented below in Fig. 7.9. Upon first inspection, the two flowfields present similar features, especially in the wake formation, but careful comparison indicates there are differences in the flowfields. The main-element wake for airfoil A4 is only slightly thinner than that of airfoil A1, but the values of $U_{t,\,min}$ are different for the two cases. For a given $\widetilde{x}$, airfoil A4 has slightly larger values of $U_{t,\,min}$ than that of airfoil A1. However, the slightly-thinner and weaker main-element wake of airfoil A4 is accompanied by a slightly thicker and larger flap 1 wake when compared to airfoil A1. This is manifested by decreased $U_{t,\,min}$ at a given $\widetilde{x}$ than that of the baseline airfoil. The resulting l/d for the baseline configuration and airfoil A4 were calculated to be 70.8 and 75.9, respectively, which is an increase in l/d of 5.10, or a relative increase of 7.20%. It is observed that the l/d ratios for both airfoils as calculated by USM3D are significantly less than the values predicted with MSES. The reader is reminded that all turbulence models have been shown to over-predict the presence of wake bursting. However, an increase in l/d for airfoil A4 is observed relative to A1 for both the MSES and USM3D simulations. Higher-fidelity computational simulations or wind tunnel tests would be needed to definitively determine the l/d

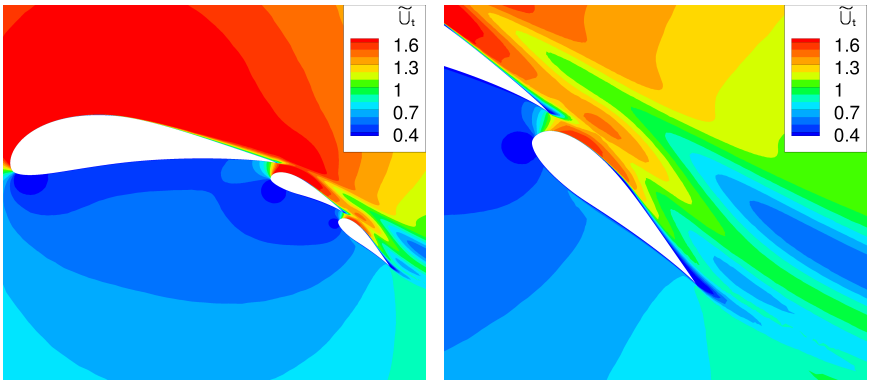

(a)

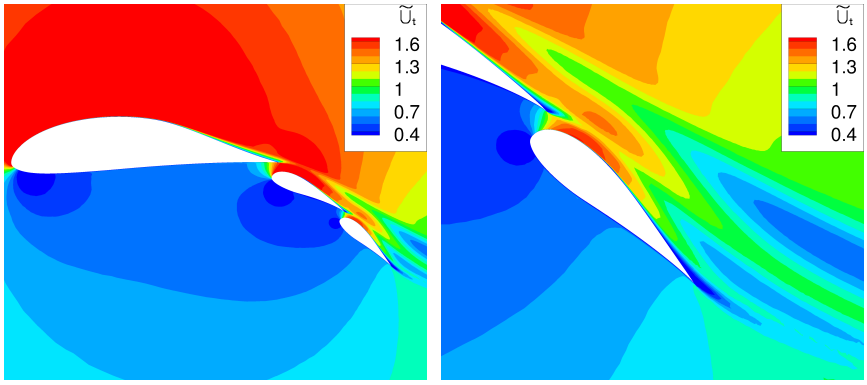

(a)

Figure 7.9: Computational predictions for airfoils showing $\widetilde{U}_t$ at wide and zoomed views including a) airfoil A1 and b) airfoil A4.

for both airfoils. Finally, it is concluded that the combination of a less-burst main-element wake and a more-burst flap 1-wake is desirable as the l/d is increased for airfoil A4 relative to the baseline airfoil. The accuracy of these computational simulations can be improved with advances in turbulence modeling, especially in the wake, and by considering unsteady turbulent flowfield characteristics.

7.4 Airfoil Design Exercise 2: Main Element Alterations for Re $= 3 \times 10^6$

As the baseline MFFS(ns)-026 multielement airfoil was designed to a target Reynolds number of 1×10^6, the airfoil did not perform at higher Reynolds numbers such as 3×10^6. Consequently, efforts were undertaken to design a multielement airfoil with better performance than the baseline airfoil for a design point of $Re = 3 \times 10^6$, $C_l = 3.45$, and $\alpha = 0$ deg. As previously mentioned, it was necessary to design the airfoils to a constant C_l to yield reduced wake bursting for a given set of operating conditions and not to reduce wake bursting through the trivial condition in which C_l (or α) is decreased. In this section, the designer was primarily concerned with the aerodynamic flowfield

surrounding the main element, and therefore the pressure distribution and transition were carefully controlled for the design angle of attack. Consequently, C_l for the multielement airfoil was controlled with flap deflection angle and not with freestream α. The airfoils designed herein were constrained by a $(t/c)_{max}$ of 0.20 for the main element which corresponds to $(t/c_{sys})_{max}$ of 0.14 when considering the relative chord lengths shown above in Table 7.1 in Sec. 7.3. Neither the position nor the shape of the two flap elements were changed in these design efforts; all efforts were placed upon improving the design of the main element. Each airfoil was designed in isolation according to the α^*-ϕ curve, *REC* parameter to control the pressure recovery, the K_s trailing edge parameter, C_{m_0}, $(t/c)_{max}$, and sometimes maximum camber.

As was the case for the previously-discussed airfoil design, information in this section presents the design iterations that led to the final airfoil design. Each airfoil is plotted with a unique line color, and the airfoil in discussion is shown with a solid line and circle points while the previous airfoil to which the current airfoil is being compared is plotted as a dashed line with triangle markers.

7.4.1 MFFS(ns)-026 ("Baseline") Airfoil

The baseline airfoil is the MFFS(ns)-026 baseline airfoil, and the design of this airfoil is presenteded in the previous section. It is not necessary to discuss the design parameters for the airfoil as an overview is presented above in Sec. 7.3.1 on page 242. However, it is prudent to present the aerodynamic performance of the airfoil at the design point of $Re = 3 \times 10^6$, and the airfoil coordinates and viscous pressure distribution shown in Fig. 7.10. Examination of the pressure distribution indicates the flow over the main-element upper surface transitions at $\widetilde{x} \approx 0.21$ which is upstream of the transition for $Re = 1 \times 10^6$ that occurred at $\widetilde{x} = 0.25$. This result is expected as flows are known to transition sooner with higher Reynolds number flows than lower Reynolds number flows. As seen in the figure, transition occurs

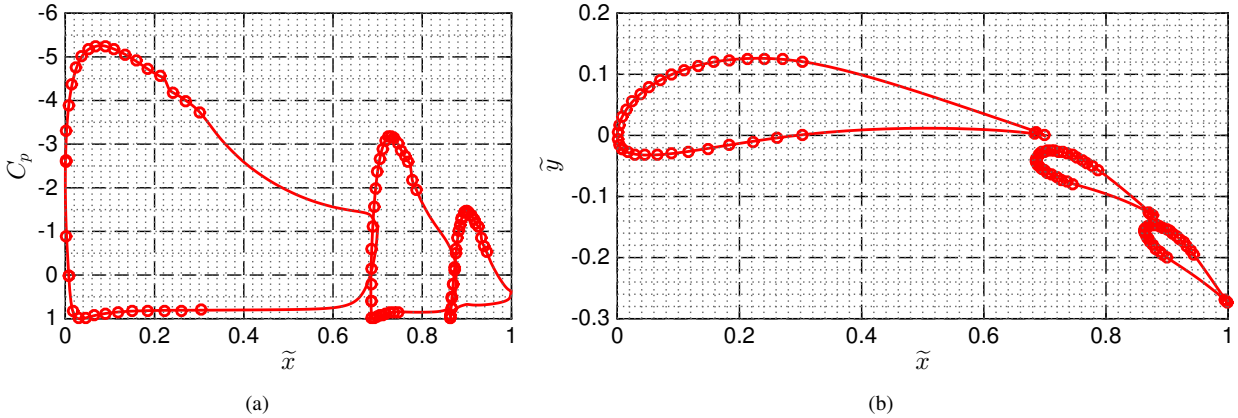

(a) (b)

Figure 7.10: Baseline airfoil aerodynamic performance at Re=3×10^6 including a) C_p distribution shown with ϕ values and b) airfoil coordinates coplotted with ϕ values.

three ϕ values upstream of the furthest-downstream ϕ for the main-element upper surface. This characteristic is not necessarily desired as the α^*-ϕ curve could be implemented to yield increased control of the transition point. The main-element suction peak, minimized at $C_p \approx -5.25$, is slightly stronger than the case for $Re = 1 \times 10^6$. A viscous analysis was performed in MSES which yielded l/d of 156, $\delta_{w,\,ME,\,max}$ of 0.020, $\widetilde{x}_d$ of 1.15, and WTP of 2.98. These results indicate increased l/d and decreased wake thickness relative to the lower-Reynolds-number performance. The trends observed agree well with data discussed in Chap. 6 as well as standard boundary-layer theory which suggests increased wake thickness for lower Reynolds numbers.

7.4.2 Airfoil B2

The second design iteration for the design point at $Re = 3 \times 10^6$, referred to as airfoil B2, was designed with a variety of parameters identified in Table 7.9. While most values are the same as the baseline airfoil, an additional maximum camber constraint was added to airfoil B2 to yield increased control of the airfoil pressure distribution. Use of this camber parameter allowed the designer to carefully design the upper-surface pressure distribution in the upstream portion of airfoil B2. In addition to the physical parameters in Table 7.9, two α^*-ϕ curves were used to define the upper- and lower-surface pressure distributions as plotted in Fig. 7.11. As shown in the figure, a slight increase in α^* over the airfoil upper surface corresponds with an increase in upper-surface curvature. Similarly, a marked increase in α^* over the lower surface increases the lower-surface camber. Pressure distributions for both airfoils are plotted in Fig. 7.11(c), and noticeable differences are observed. Similar to the previous design efforts, it was quickly concluded that a flatter C_p distribution in the upstream portion of the pressure recovery region moves the transition point downstream, thus reducing the wake thickness. A slight increase in pressure is observed for airfoil B2 in $\widetilde{x} \leq 0.12$, but a decrease in pressure is observed for airfoil B2 between $\widetilde{x}$ of 0.12 and 0.30. The stronger adverse pressure gradient in the aft portion of the B2 airfoil dumps the flow at the main-element trailing edge at a slightly larger C_p than the baseline geometry. Examination of the airfoil coordinates indicates that the $\widetilde{x}$ coordinate for $(t/c)_{max}$ moves slightly upstream for airfoil B2 compared to the baseline airfoil. Pressure distributions over the two flaps are essentially unchanged between the two airfoils.

Table 7.9: Inverse-Design Parameters for Main Element of Baseline Airfoil and Airfoil B2

	Baseline Airfoil	Airfoil B2
REC_u	0.05	0.05
REC_l	0.20	0.20
K_s	0.30	0.30
C_{m_0}	-0.20	-0.20
$(t/c)_{max}$	0.20	0.20
$camber_{max}$	–	**0.11**

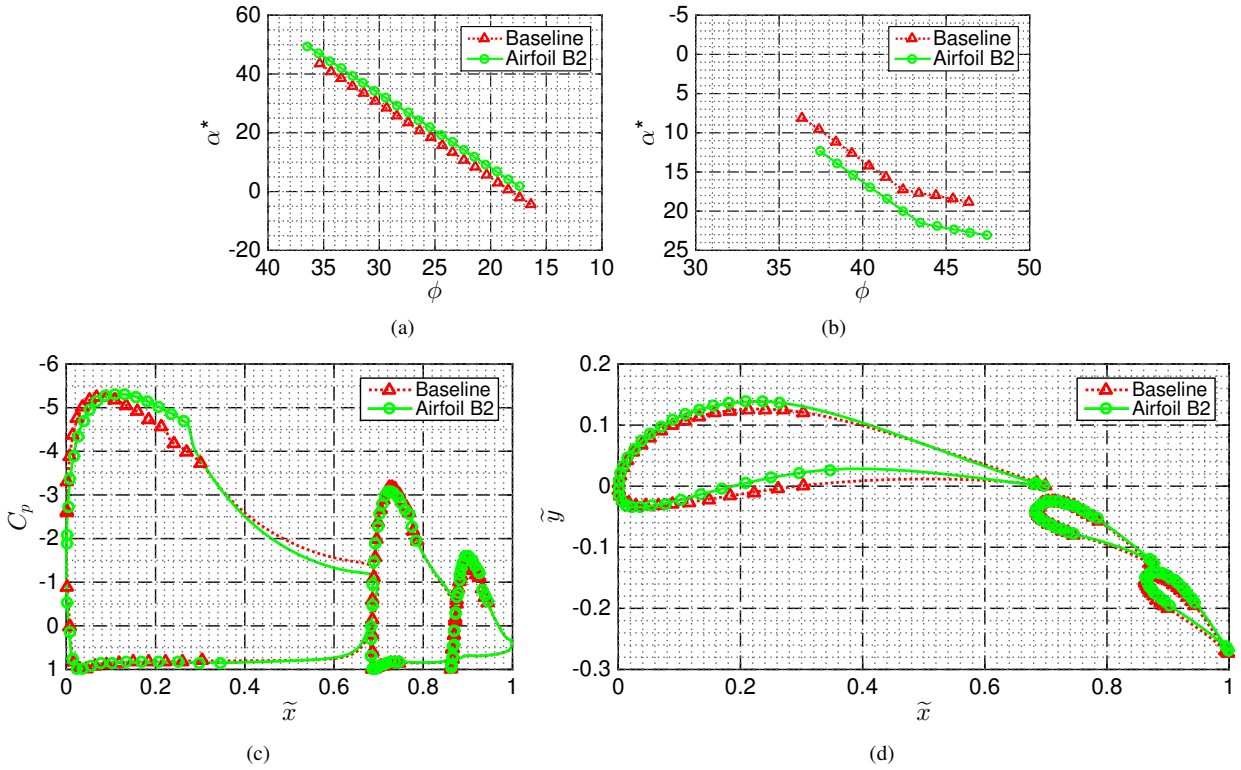

Figure 7.11: Baseline airfoil and airfoil B2 design parameters including a) α^*-ϕ for main-element upper surface, b) α^*-ϕ for main-element lower surface, c) viscous C_p distribution coplotted with ϕ points, and d) airfoil coordinates coplotted with ϕ points.

Similar to the previous airfoil designs, a variety of wake metrics were calculated for airfoil B2 in addition to the standard aerodynamic efficiency l/d. All of these parameters are presented in Table 7.10 for the baseline and B2 airfoils in addition to the performance increase of B2 relative to the baseline. Results indicate a significantly thinner wake for airfoil B2 yields a significant increase in l/d. A 25.0% decrease in $\delta_{w,\,ME,\,max}$ yields a 22.5% of WTP_{ME}. While $\widetilde{x}_{d,\,ME}$ for airfoil B2 is slightly further downstream, it is observed that this change does not significantly affect the value of WTP_{ME}. Similar to the $Re = 1 \times 10^6$ airfoil design, it is apparent that a longer laminar run and flatter upper-surface C_p distribution thin the wake and lead to increased aerodynamic efficiency.

Table 7.10: Aerodynamic Performance of Airfoil B2 Compared to Baseline Airfoil

	Baseline Airfoil	Airfoil B2	Percent Improvement Relative to Baseline
l/d	156	175	12.2%
$\delta_{w\,ME,\,max}$	0.020	0.015	25.0%
$\widetilde{x}_{d,\,ME}$	1.15	1.16	-0.87 %
WTP_{ME}	2.98	2.31	22.5%

7.4.3 Airfoil B3

A variety of modifications to airfoil B2 resulted in the next design iteration, airfoil B3. While most inverse-design parameters were unchanged from airfoil B2 to airfoil B3, a slight decrease in K_s was implemented to yield a better C_p distribution near the main-element trailing edge. Values of these parameters are presented in Table 7.11 for airfoils B2 and B3. Figure 7.12 depicts the α^*-ϕ curves for the upper and lower surfaces in addition to the C_p distribution and airfoil coordinates. In general, the α^*-ϕ curve for the upper surface is flatter for airfoil B3 than for airfoil B2. While it may look curious or like a mistake, the rapid decrease in α^* at $\phi = 16$ is critically important to control the pressure distribution immediately upstream of the transition point. If this point were in line with the rest of the α^*-ϕ curve, transition would occur upstream of the point for which it occurs in airfoil B3. A comparison of the adverse pressure gradient indicates that the magnitude of $\partial C_p/\partial \widetilde{x}$ for $\widetilde{x} \leq 0.35$ is significantly less for airfoil B3. This weaker pressure gradient causes the transition point to move downstream, thus increasing the laminar run and thinning the boundary layer. Despite the weaker, flatter C_p distribution for which $\widetilde{x} \leq 0.35$, no discernible differences exist for the upper-surface coordinates of the two airfoils. This observation further verifies the necessity to utilize inverse-design methods to yield an airfoil geometry as opposed to specifying the coordinates and then obtaining the aerodynamic performance. Significantly fewer ϕ values were used to control the lower-surface pressure distribution to further rely upon K_s to dictate the pressure distribution near the trailing edge and thus also over the lower surface. Pressure distributions over the two flaps are slightly different for the two airfoils in which decreased suction peaks are observed for airfoil B3 relative to airfoil B2. If the airfoil coordinates are carefully observed, it is clear that airfoil B3 is comprised of increased thickness in the downstream portion of the airfoil than that of airfoil B2. In addition, decreased curvature of the lower surface is noted.

A variety of performance and wake metrics are presented in Table 7.12 as absolute numbers in addition to percentage increases relative to both airfoil B2 and the baseline geometry. Design modifications resulting in airfoil B3 yield a reduction in maximum wake thickness of 18.8% relative to airfoil B2, or a 35.0% decrease relative to the baseline case. As previously observed, the decrease in wake thickness translates into a marked decrease in WTP_{ME},

Table 7.11: Inverse-Design Parameters for Main Element of Airfoils B2 and B3

	Airfoil B2	Airfoil B3
REC_u	0.05	0.05
REC_l	0.20	0.20
K_s	0.30	**0.20**
C_{m_0}	-0.20	-0.20
$(t/c)_{max}$	0.20	0.20
$camber_{max}$	0.11	0.11

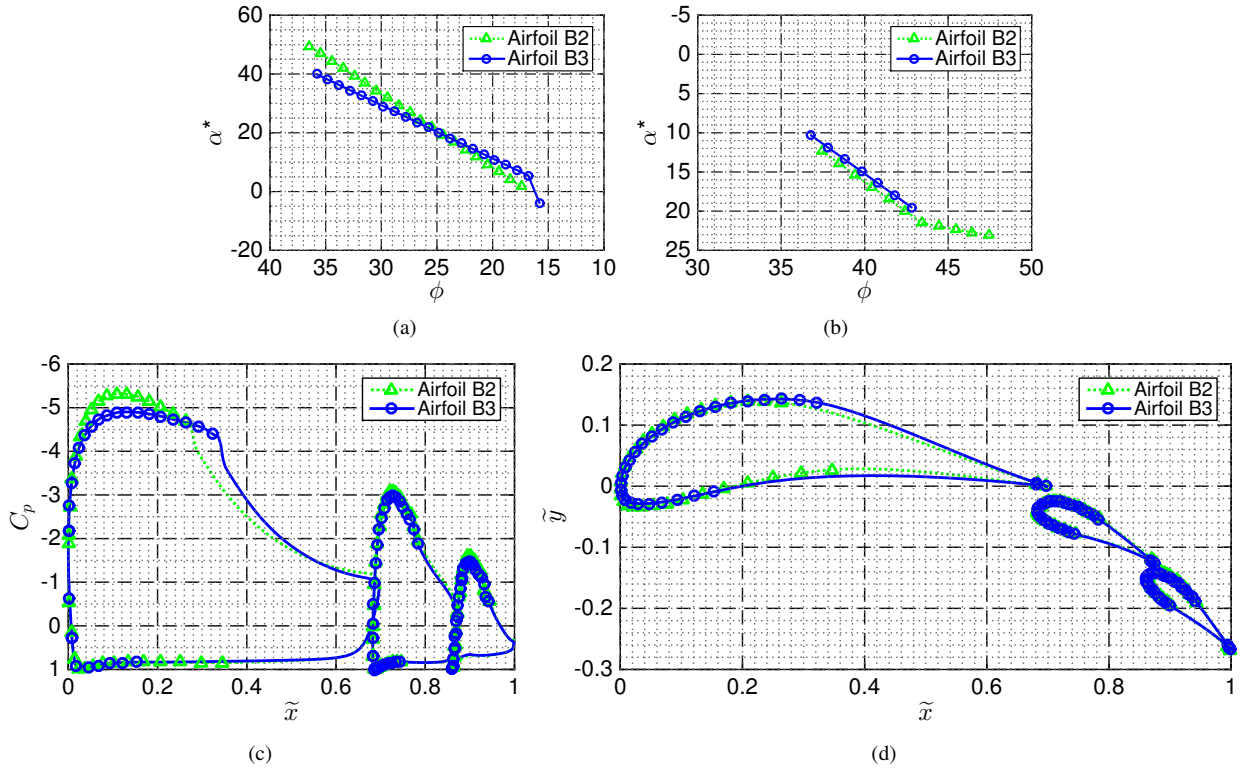

Figure 7.12: Airfoil B2 and airfoil B3 design parameters including a) α^*-ϕ for main-element upper surface, b) α^*-ϕ for main-element lower surface, c) viscous C_p distribution coplotted with ϕ points, and d) airfoil coordinates coplotted with ϕ points.

Table 7.12: Aerodynamic Performance of Airfoil B3 Compared to Airfoil B2 and Baseline Airfoil

	Airfoil B2	Airfoil B3	Percent Improvement Relative to B2	Percent Improvement Relative to Baseline
l/d	175	196	12.0%	25.6%
$\delta_{w\ ME,\ max}$	0.016	0.013	18.8%	35.0%
$\widetilde{x}_{d,\ ME}$	1.16	1.15	0.86%	0.00%
WTP_{ME}	2.31	1.95	15.6%	34.6%

thus indicating less wake bursting in the main-element wake. This reduction in wake bursting yields a 12.0% increase in l/d between airfoils B3 and B2.

7.4.4 Airfoil B4

The standard Inverse-Design Parameters for Main Element of airfoil B4 are the same as those for airfoil B3, as presented in Table 7.13. No modifications were made to theses six parameters as the values for these parameters were considered appropriate for the resultant pressure distribution. Even though no modifications were made in these numbers, significant changes were made to the main-element α^*-ϕ curves, shown in Fig. 7.13. Further flattening of

the upper-surface α^*-ϕ curve was declared for airfoil B4 relative to airfoil B3, which was already flatter than airfoil B2. In addition to the flatter α^*-ϕ curve, the value of ϕ_{min} for the upper surface is less for airfoil B4 than for B3. This reduction in ϕ_{min} yields control of the pressure distribution and airfoil geometry at larger $\widetilde{x}$. No modifications were made to the slope of α^*-ϕ over the lower surface, but an upward and leftward shift in the curve is observed. That is to say that ϕ_{max} is larger for airfoil B4 than for B3 over the lower surface, and that α^* for a given ϕ is reduced for airfoil B4. Pressure distributions shown in Fig. 7.13(c) for the two airfoils exhibit significant differences between the two airfoils. A region for which $\partial C_p/\partial\widetilde{x} \approx 0$ exists over airfoil B4 for which $0.14 \leq \widetilde{x} \leq 0.36$. In addition, the pressure peak for airfoil B4 is not present, and the value of $C_{p,\,min}$ for airfoil B4 is approximately 0.35 less than that of B3. As the α^*-ϕ curve controls the pressure distribution at larger $\widetilde{x}$, the transition point was moved downstream to $\widetilde{x} \approx 0.41$; the strong portion of the pressure-recovery region also begins at this point. As the flat pressure gradient extended to larger $\widetilde{x}$, the adverse pressure gradient in the downstream portion of the main element is stronger for airfoil B4 than B3. Even though increased pressure is observed near the trailing edge of B4 when compared to B3, both airfoils dump the flow at the same C_p. However, it is noted that the C_p dumped at the main element trailing edge is increased relative to the baseline airfoil. As the pressure at the trailing edge for airfoil B4 is decreased, and is therefore closer to the freestream pressure to which the pressure must be recovered, a weaker streamwise pressure gradient is applied to the wake which in turn decreases the size of the burst wake. Even though a slight shift in the α^*-ϕ curve was implemented for the lower surface, the pressure distributions over the lower surface are essentially the same for airfoils B4 and B3. Despite this fact, minor differences in the airfoil coordinates are observed for $\widetilde{x} \geq 0.25$. Finally, it is observed that the pressure distributions over both flaps are the same for both multielement airfoils.

An improvement in all performance metrics were observed for airfoil B4 when compared to airfoil B3, and these values are presented in Table 7.14. The thinner wake of airfoil B4 results in decreased WTP_{ME} although the point of maximum thickness remains unchanged. A 18.8% reduction in $\delta_{w,\,ME,\,max}$ for airfoil B4 corresponds to a 15.6% reduction in WTP_{ME} at the design point under consideration. When compared to the baseline, the wake for airfoil B4 is 40% thinner than that of the baseline geometry. In addition, a marked decrease in WTP_{ME} is observed, thus translating into a 34.6% improvement in l/d between airfoil B4 and the original airfoil.

Table 7.13: Inverse-Design Parameters for Main Element of Airfoils B3 and B4

	Airfoil B3	Airfoil B4
REC_u	0.05	0.05
REC_l	0.20	0.20
K_s	0.20	0.20
C_{m_0}	-0.20	-0.20
$(t/c)_{max}$	0.20	0.20
$camber_{max}$	0.11	0.11

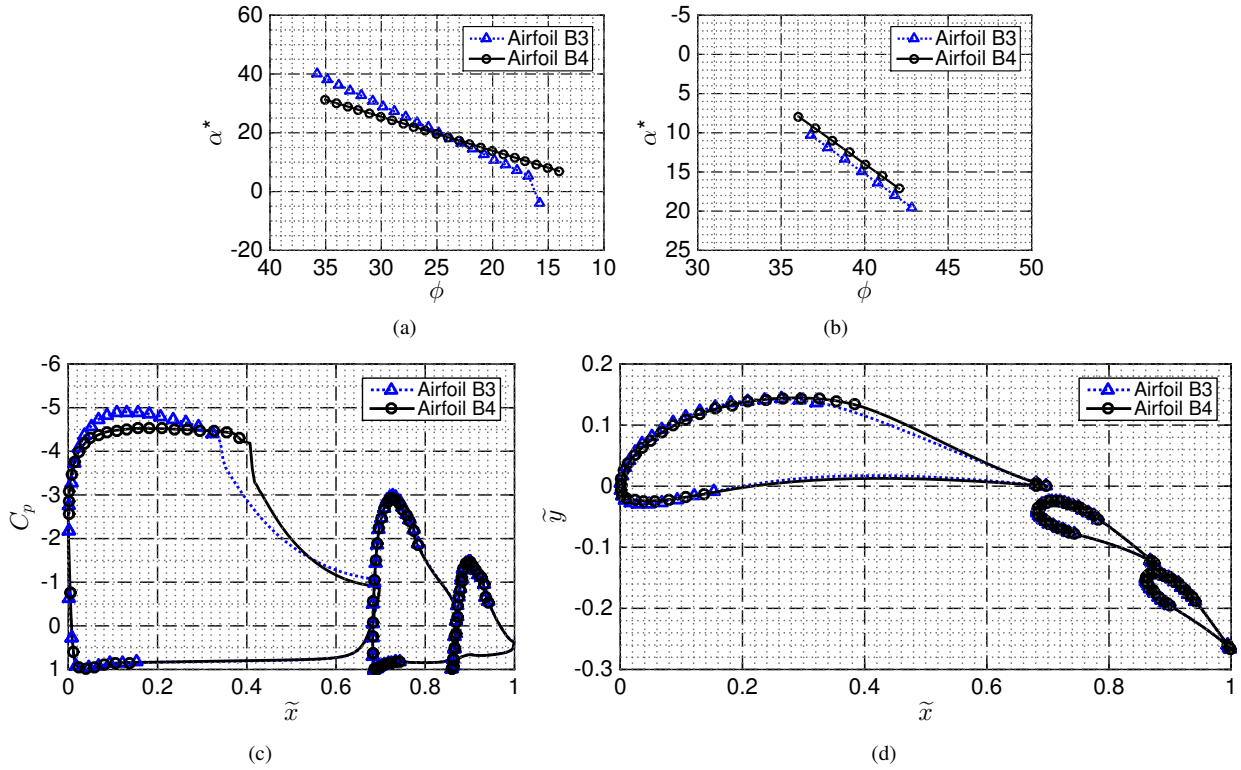

Figure 7.13: Airfoil B3 and airfoil B4 design parameters including a) α^*-ϕ for main-element upper surface, b) α^*-ϕ for main-element lower surface, c) viscous C_p distribution coplotted with ϕ points, and d) airfoil coordinates coplotted with ϕ points.

Table 7.14: Aerodynamic Performance of Airfoil B4 Compared to Airfoil B3 and Baseline Airfoil

	Airfoil B3	Airfoil B4	Percent Improvement Relative to B3	Percent Improvement Relative to Baseline
l/d	196	210	7.14%	34.6%
$\delta_{w\ ME,\ max}$	0.013	0.012	7.69%	40.0%
$\widetilde{x}_{d,\ ME}$	1.15	1.15	0.00%	0.00%
WTP_{ME}	1.95	1.74	10.8%	41.6%

7.4.5 Airfoil B5

An additional design iteration, airfoil B5, was designed with further modifications to the inverse-design values for the aforementioned airfoil B4. As shown in Table 7.15, increased aft loading of the main element was achieved by slightly increasing the magnitude of C_{m_0}, the zero-lift pitching moment. Despite the increase in aft loading, the maximum camber of the airfoil remained unchanged. Changes were not made to the five other parameters shown in the table. As shown in Fig. 7.14, no changes were made to the α^*-ϕ curve on either the upper or lower surface for which ϕ values existed for airfoil B4, but the value of ϕ_{min} was decreased by 1 deg for airfoil B5 relative to B4. As

Table 7.15: Inverse-Design Parameters for Main Element of Airfoils B4 and B5

	Airfoil B4	Airfoil B5
REC_u	0.05	0.05
REC_l	0.20	0.20
K_s	0.20	0.20
C_{m_0}	−0.20	**–0.21**
$(t/c)_{max}$	0.20	0.20
$camber_{max}$	0.11	0.11

Table 7.16: Aerodynamic Performance of Airfoil B5 Compared to Airfoil B4 and Baseline Airfoil

	Airfoil B4	Airfoil B5	Percent Improvement Relative to B4	Percent Improvement Relative to Baseline
l/d	210	224	6.67%	43.6%
$\delta_{w\ ME,\ max}$	0.012	0.010	16.7%	50.0%
$\widetilde{x}_{d,\ ME}$	1.15	1.15	0.00%	0.00%
WTP_{ME}	1.74	1.55	10.9%	48.0%

previously mentioned, this additional point is able to control the pressure distribution at larger $\widetilde{x}$ than for airfoil B4, and thus transition can also be pushed downstream. The pressure distributions for both airfoils are shown in the figure, and it is apparent that the flat C_p curve is extended to larger $\widetilde{x}$ for airfoil B5. In addition, the transition point is moved downstream by $\widetilde{x} = 0.02$. A slight decrease in C_p over the upper surface is observed for $\widetilde{x} \leq 0.40$, and the magnitude of $\partial C_p/\partial \widetilde{x}$ is larger for airfoil B5 than that of B4. An increase in the magnitude of C_{m_0} results in decreased pressure over $\widetilde{x} \geq 0.40$, and thus a stronger adverse pressure gradient is present for airfoil B5 when compared to airfoil B4. A slight reduction in C_p at the main-element trailing edge is noted, thus requiring a weaker pressure gradient in the wake to recover pressure to the freestream conditions and resulted in decreased wake bursting.

Table 7.16 presents the standard metrics used to quantify the airfoil performance at the design point, and all metrics for airfoil B5 are improved relative to airfoil B4. A 16% reduction in wake thickness results in a 10.9% reduction in WTP. Previous design iterations indicated a closer relationship between these two parameters than airfoils B4 and B5. Even though the maximum wake thickness is less for airfoil B5, the wake thickness of airfoil B5 increases more rapidly at decreased $\widetilde{x}$. As the wake is relatively thicker at lower $\widetilde{x}$, the tradeoff between minimizing $\delta_{w,\ ME,\ max}$ and increased wake thickness near the airfoil system trailing edge yields a decrease in WTP_{ME} of nearly 11%. Marked improvements of airfoil B5 relative to the baseline airfoil are observed, with a 43.6% increase in l/d and a 50% reduction in maximum wake thickness.

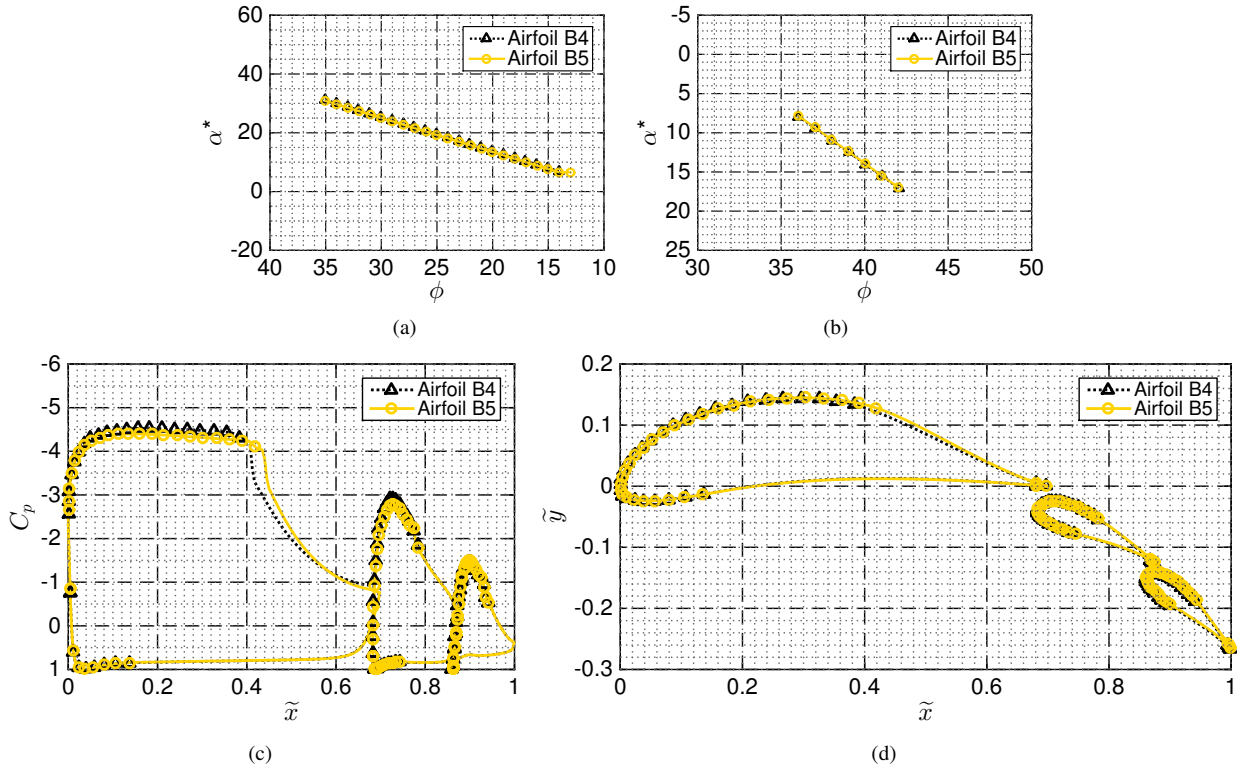

Figure 7.14: Airfoil B4 and airfoil B5 design parameters including a) α^*-ϕ for main-element upper surface, b) α^*-ϕ for main-element lower surface, c) viscous C_p distribution coplotted with ϕ points, and d) airfoil coordinates coplotted with ϕ points.

7.4.6 Airfoil B6

The sixth design iteration (B6) for a freestream Re of 3×10^6 was designed according to parameters shown in Table 7.17 and Fig. 7.15. Efforts were taken to improve the pressure distribution near the main-element trailing edge, and these efforts are reflected in increased REC_u and K_s. In addition, the α^*-ϕ curve over the main-element upper surface, shown in Fig. 7.15(a), is slightly steeper for airfoil B6 than the slope for airfoil B5. As seen in the pressure distribution, a steeper α^*-ϕ curve translates into increased magnitude of $\partial C_p/\partial \widetilde{x}$ for $0.10 \leq \widetilde{x} \leq 0.41$. Improvements

Table 7.17: Inverse-Design Parameters for Main Element of Airfoils B5 and B6

	Airfoil B5	Airfoil B6
REC_u	0.05	**0.20**
REC_l	0.20	0.20
K_s	0.20	**0.50**
C_{m_0}	-0.21	-0.21
$(t/c)_{max}$	0.20	0.20
$camber_{max}$	0.11	0.11

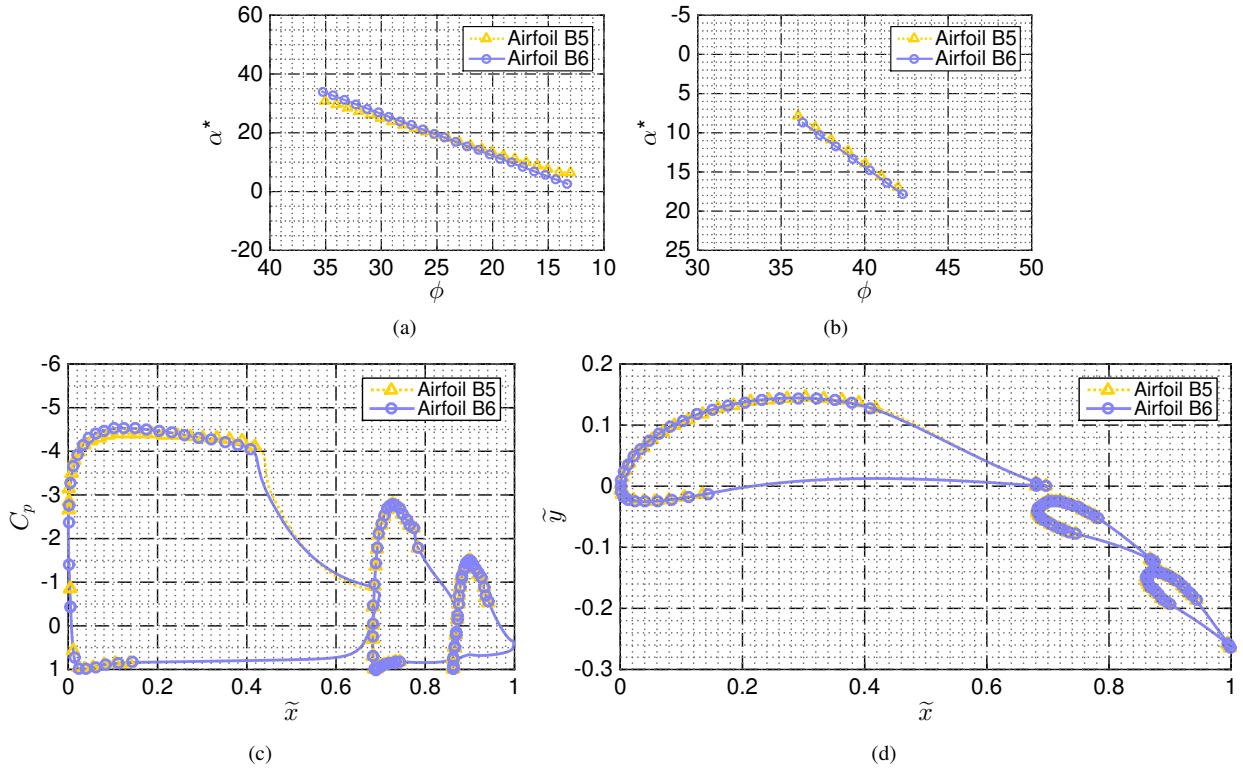

Figure 7.15: Airfoil B5 and airfoil B6 design parameters including a) α^*-ϕ for main-element upper surface, b) α^*-ϕ for main-element lower surface, c) viscous C_p distribution coplotted with ϕ points, and d) airfoil coordinates coplotted with ϕ points.

in the upper-surface pressure distribution near the main-element trailing edge are indicated by slightly decreased pressure for airfoil B6 than airfoil B5 in this region. Despite the same values of ϕ_{min} for the upper surface of both airfoils, the $\widetilde{x}$ at which ϕ_{min} occurs is further upstream for airfoil B6 than for airfoil B5, and thus transition over the main element moves slightly forward relative to airfoil B5. This forward movement thus relaxes the adverse pressure gradient over the aft portion of the airfoil, and this results in decreased boundary layer growth due to the lower pressure gradient. It is therefore observed that both the transition location and the magnitude of the adverse pressure gradient must be considered when attempting to mitigate the presence of burst wakes. As seen in Fig. 7.15(c), no significant differences exist over the lower surface of each airfoil, and C_p is dumped from the main element at the same value for both airfoils.

Four different metrics to evaluate the effectiveness of airfoil B6 are shown in Table 7.18 as absolute values and as improvements relative to airfoil B5 and the baseline case. It is interesting to note that the tradeoff between a weaker adverse pressure gradient compared to a forward transition point yields a decrease in WTP_{ME} and an increase in l/d. Differences in maximum wake thickness are smaller than $0.001c_{sys}$, the smallest significant digit for δ_w. Despite the equal value of $\delta_{w,\,ME,\,max}$, a reduction in WTP_{ME} is observed. A 1.3% increase in l/d results from the very minor

Table 7.18: Aerodynamic Performance of Airfoil B6 Compared to Airfoil B5 and Baseline Airfoil

	Airfoil B5	Airfoil B6	Percent Improvement Relative to B5	Percent Improvement Relative to Baseline
l/d	224	227	1.34%	45.5%
$\delta_{w\ ME,\ max}$	0.010	0.010	0.00%	50.0%
$\widetilde{x}_{d,\ ME}$	1.15	1.15	0.00%	0.00%
WTP_{ME}	1.55	1.52	1.93%	49.0%

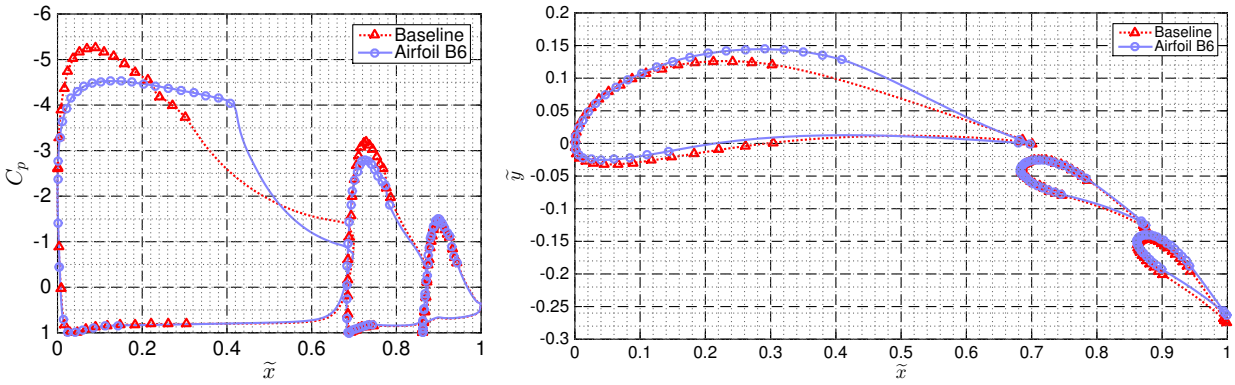

Figure 7.16: Baseline airfoil and airfoil B6 data including a) C_p distribution and b) airfoil coordinates.

changes in the pressure distribution of both airfoils. When considering all the design changes of airfoil B6 relative to the baseline airfoil, a 45.5% improvement in l/d and a 49.0% reduction of WTP_{ME} are observed.

A final comparison between the baseline airfoil and airfoil B6 is shown in Fig. 7.16 in which both C_p and the airfoil coordinates are plotted. The baseline airfoil is plotted as a dashed red line and airfoil B6 is shown as a solid lavender line. When comparing the pressure distributions of both airfoils, numerous key observations are made. First, the pressure distribution for airfoil B6 is very flat over the main-element upper surface when compared to that of the baseline airfoil. In addition, the transition point for airfoil B6 is moved downstream from the baseline case. This longer laminar run thins the boundary layer relative to a case with a shorter laminar run. The large region for which the magnitude of $\partial C_p/\partial\widetilde{x}$ is very small extends over a larger range of $\widetilde{x}$, the adverse pressure gradient downstream of the transition point for airfoil B7 is significantly stronger than the baseline case. Finally, the C_p at which the pressure is dumped from the main element is decreased for airfoil B6. As more pressure is recovered over the surface than in the wake region, the streamwise pressure gradient acting upon the wake is decreased, which decreases the effect of the burst wake.

Similar to the previously-discussed airfoil design, fixed-transition RANS computations were performed on the B1 and B6 airfoils at $Re = 3\times10^6$ and $C_l = 3.40$. MSES was utilized to determine the upper- and lower-surface transition points for all three elements, and these values were subsequently declared to the NEWTL module of USM3D. A wide

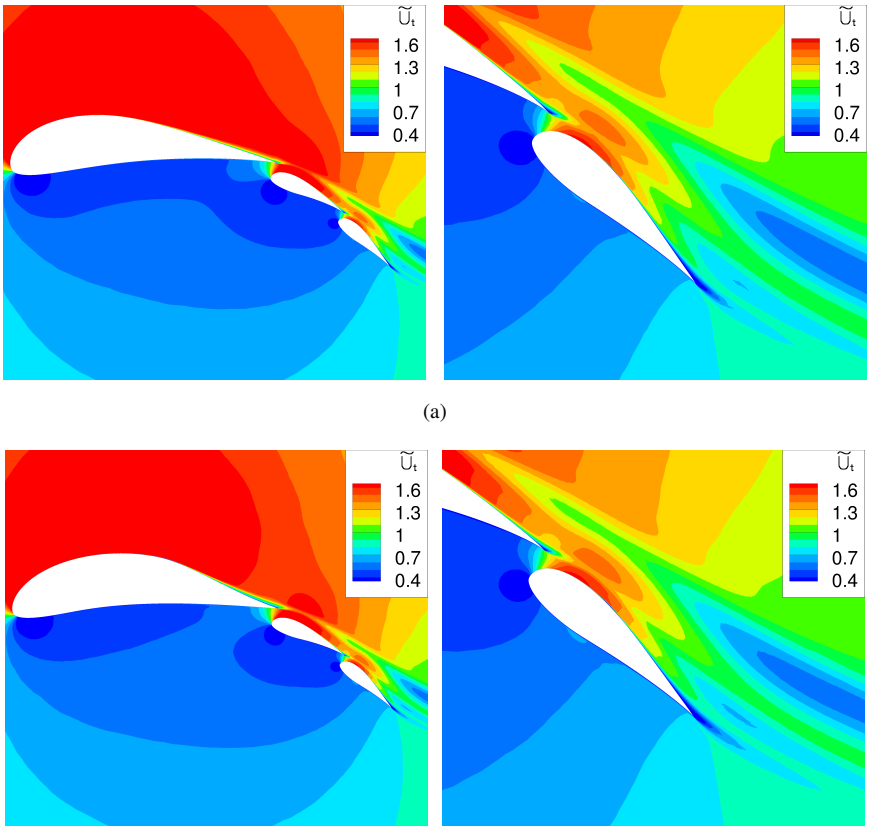

Figure 7.17: Computational predictions for airfoil B1 and airfoil B6 with wide and zoomed views including a) airfoil B1 $\widetilde{U}_t$ and b) airfoil B6 $\widetilde{U}_t$.

and detailed view of the calculated flowfields for both airfoils are shown in Fig. 7.17 such that the two flowfields can be readily compared. It is seen in the figure that the burst wake for both the main element and flap 1 of airfoil B6 (the bottom row) is smaller than that of the baseline airfoil. Consequently, the decreased size of this momentum-deficit region decreases the drag and thus dramatically increases the performance of the multielement airfoil system. The increased laminar run and the decreased wake size both contribute to the decrease in C_d. The B6 airfoil yields an 18.2% decrease in C_d or a 22.5% increase in l/d.

7.5 Airfoil Design Exercise 3: Redesign All Elements for Re $= 1 \times 10^6$

The third and final multielement airfoil design included airfoil design for all three elements to a design point of $Re = 1 \times 10^6$, $C_l = 3.40$, and $\alpha = 0$ deg. To account for structural constraints, the main element was constrained such that $(t/c)_{max} = 0.20$ or $(t/c_{sys})_{max} = 0.14$ based upon the elemental chord lengths. Thickness constraints were not applied to the two flaps as the structural support for an airfoil (or wing) is carried in the main-element wing box.

Relative chord lengths for the three elements were not changed from the baseline MFFS(ns)-026 airfoil, but changes were made to *gap*, *overhang*, and δ for the two flaps. Similar to the previous two designs, C_l was tuned to be 3.40 with the flap deflection angles. As the flowfield around the main element was of interest in an effort to decrease wake bursting, it was necessary to maintain a given α for the main element such that the pressure distribution and transition point could be controlled.

Five different iterations are presented in this section, and the logic the designer used to step from iteration to iteration is outlined and discussed. The parameters that were changed between each iteration are outlined, and the logic for these changes is also discussed. Each iteration is depicted as a unique line color, and the iteration of interest is shown as a solid line while the previous iteration is plotted with a dashed line.

7.5.1 MFFS(ns)-026 ("Baseline") Airfoil

Similar to the previous two airfoil designs, the baseline iteration for this design point was taken to be the previously-discussed MFFS(ns)-026 airfoil as defined above in Table 7.1 on page 241. Parameters used to generate the airfoil coordinates were previously identified and discussed in Sec. 7.3.1, and thus no further discussion of these design parameters are presented in this section. Nevertheless, it is useful to once again present the C_p distribution and airfoil coordinates in Fig. 7.18. As seen in the figure, the suction peaks for the main element, flap 1, and flap 2 are approximately -5.2, -3.1, and -1.4, respectively. Transition over the upper surface of the main element occurs at 0.26, for flap 1 at 0.78, and for flap 2 at 0.94. Examination of Fig. 7.18(b) indicates the main-element upper surface has very little camber for $\widetilde{x} \geq 0.40$ and thus the aft camber is provided by the lower surface. All three elements have rounded leading edges.

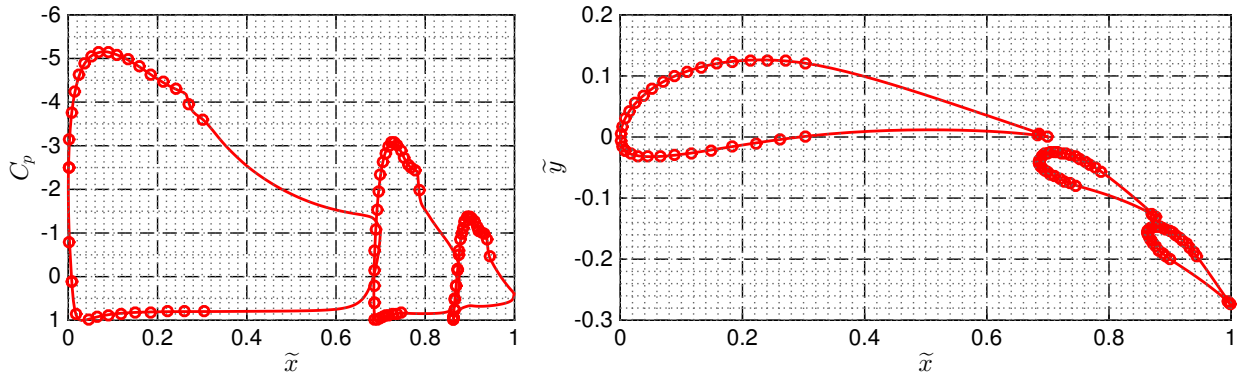

Figure 7.18: Baseline airfoil data shown by a) C_p distribution and b) airfoil coordinates.

7.5.2 Airfoil C2

The second airfoil design iteration, airfoil C2, was designed as a derivative of airfoil A4, the final design for the main-element alterations for $Re = 1 \times 10^6$. Design changes for airfoil C2 were made relative to airfoils C1 and B7, and the inverse design parameters are shown in Table 7.19 for all three elements. The trailing-edge pressure parameter K_s was increased for the main element and flap 1 in an effort to thicken the airfoil and improve the pressure distribution near the trailing edge. In addition, the $(t/c)_{max}$ constraint for flap 1 was removed to allow for more control of the pressure distribution over this flap. Flap deflection angles for airfoil C2 were slightly decreased compared to the baseline airfoil to yield that target C_l of 3.40. Increased loading was generated by flap 1 by increasing C_{m_0}, and thus the camber, for the airfoil. Only minor changes were made in *gap* or *overhang* for both flaps.

In addition to the previously-listed inverse-design parameters, the aerodynamic performance of the airfoil was specified through the α^*-ϕ curves in Fig. 7.19. The α^*-ϕ curves for the main element of airfoil A4 were implemented as the main element for airfoil C2, and these curves are plotted in Fig. 7.19(a,d). Throughout the course of this design process, it was found that few changes to the main element were necessary to maintain superior performance despite the geometry changes over the two flaps. While minor changes to the main element were made in some iterations presented later in this section, most design alterations were associated with the two flaps. As shown in Fig. 7.19(b) the α^*-ϕ curve for the flap 1 upper surface was slightly flattened to reduce the magnitude of $\partial C_p/\partial \widetilde{x}$ in the forward part of flap 1. This design change also moved the transition point downstream due in part to the weaker adverse pressure gradient. As shown in the airfoil coordinates, airfoil C2 has a slightly smaller flap 1 leading-edge radius than that of the baseline airfoil, which is due to the flatter pressure distribution of flap 1.

Four aerodynamic performance and wake metrics are presented in Table 7.20 as absolute metrics for the two airfoils as well as percent improvement relative to the baseline airfoil. Design modifications to the main element as well as both flaps yielded a significantly thinner wake for airfoil C2. The thinner wake of airfoil C2, which is 38.5% thinner than that of the baseline airfoil, yielded a 37.8% decrease in WTP_{ME} with very similar values of $\widetilde{x}_{d,\,ME}$. It is

Table 7.19: Inverse-Design Parameters for Baseline Airfoil and Airfoil C2

	Baseline Airfoil			Airfoil C2		
	Main Element	Flap 1	Flap 2	Main Element	Flap 1	Flap 2
REC_u	0.05	0.20	0.20	**0.02**	0.20	0.20
REC_l	0.20	0.20	0.20	0.20	0.20	0.20
K_s	0.30	0.15	0.15	**0.50**	**0.80**	0.15
C_{m_0}	−0.20	−0.16	−0.10	**–0.15**	**–0.22**	−0.10
$(t/c)_{max}$	0.200	0.205	0.205	0.200	**–**	0.205
gap	–	0.025	0.015	–	0.025	0.016
overhang	–	0.015	0.000	–	0.014	0.002
δ	–	26.4	16.1	–	26.0	15.8

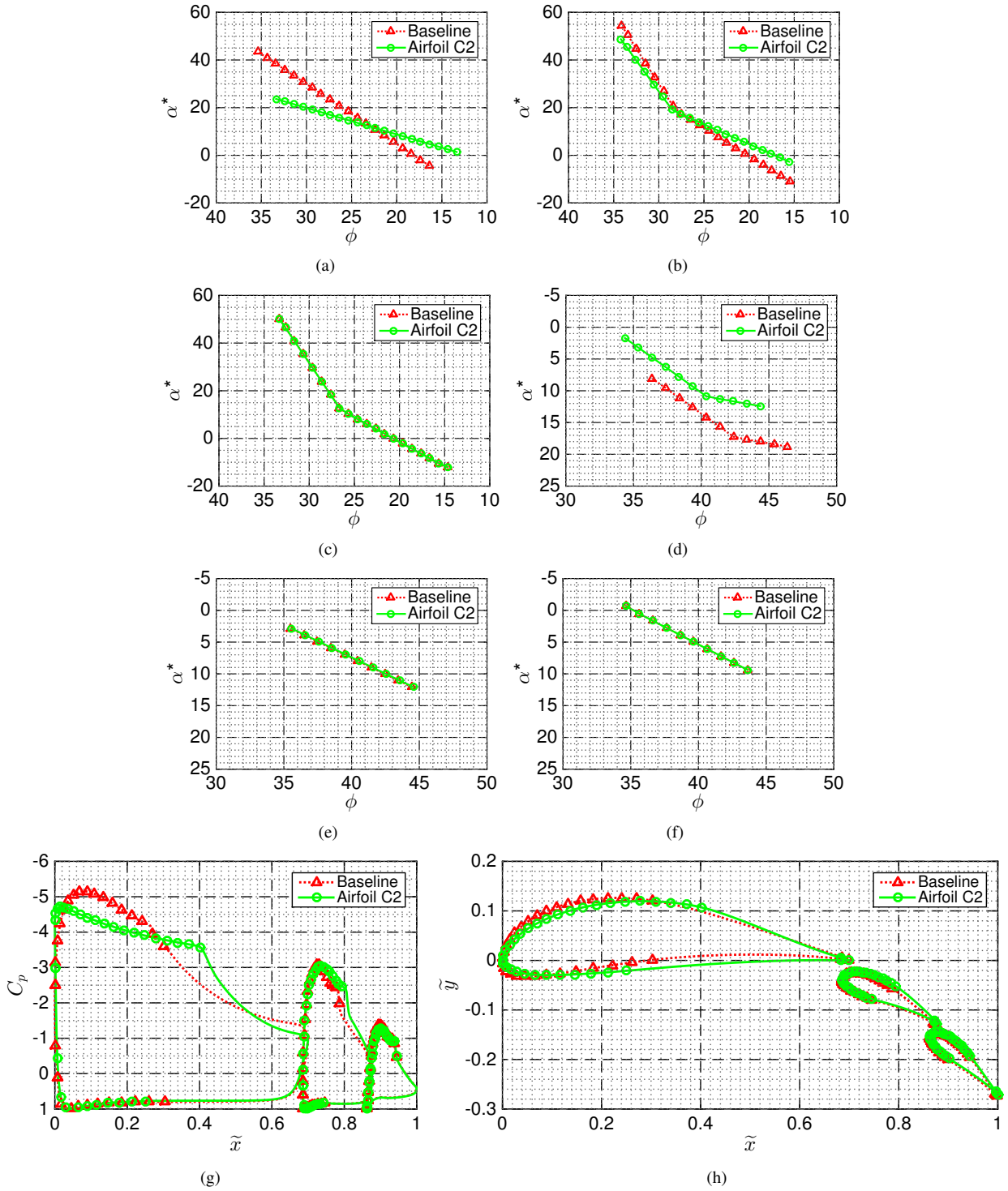

Figure 7.19: Baseline airfoil and airfoil C2 design parameters including α^*-ϕ for a) main-element, b) flap 1, and c) flap 2 upper surfaces; α^*-ϕ for d) main element, e) flap 1, and f) flap 2 lower surfaces, g) viscous C_p distribution coplotted with ϕ points, and h) airfoil coordinates coplotted with ϕ points.

Table 7.20: Aerodynamic Performance of Airfoil C2 Compared to Baseline Airfoil

	Baseline Airfoil	Airfoil A2	Percent Improvement Relative to Baseline
l/d	115	144	25.2%
$\delta_{w\ ME,\ max}$	0.026	0.016	38.5%
$\widetilde{x}_{d,\ ME}$	1.17	1.16	0.85%
WTP_{ME}	3.97	2.47	37.8%

noted that l/d for airfoil A4, the design changes implemented for only the main element at $Re = 1 \times 10^6$, was 134; therefore airfoil C2 results in elevated l/d relative to both the baseline airfoil as well as airfoil A4.

7.5.3 Airfoil C3

Further design changes to airfoil C2 resulted in a third iteration referred to as airfoil C3, and a summary of parameters used to design the airfoil are included in Table 7.21. While an increase in C_{m_0} was applied to all three elements, the pitching moment of flap 2 was increased by 50% relative to airfoil C3. This change was made in an effort to increase loading on flap 2 thus reducing the loading on both the main element and flap 1. It was desired to decrease the loading on these two airfoils such that the streamwise adverse pressure gradient in the main-element wake was weaker. In addition, it was desired to increase the aft loading of each element to reduce the suction peak magnitude, which was a key conclusion of the previous two airfoil designs discussed earlier in this chapter.

Changes for the main-element α^*-ϕ curves shown in Fig. 7.20(a,d) yield indiscernible changes in the main-element pressure distribution despite the increase in C_{m_0}. More significant changes are observed over the flap 1 and flap 2 airfoils. The flap 1 upper-surface α^*-ϕ curve seen in Fig. 7.20(b) resulted in a sharper leading-edge radius and slightly-larger C_p for the forward portion of airfoil C3; this pressure increase corresponds to the desired decreased loading over flap 1. However, this decreased loading at $0.72 \leq \widetilde{x} \leq 0.80$ was obtained at the expense of a sharper and stronger leading-edge suction peak for airfoil C3. Careful examination of the C_p distribution over flap 2 indicates

Table 7.21: Inverse-Design Parameters for Airfoils C2 and C3

	Airfoil C2			Airfoil C3		
	Main Element	Flap 1	Flap 2	Main Element	Flap 1	Flap 2
REC_u	0.02	0.20	0.20	0.02	0.20	0.20
REC_l	0.20	0.20	0.20	0.20	0.20	0.20
K_s	0.50	0.80	0.15	0.50	0.80	**0.40**
C_{m_0}	−0.15	−0.22	−0.10	−0.16	−0.23	−0.15
$(t/c)_{max}$	0.200	–	0.205	0.200	–	**0.18**
gap	–	0.025	0.016	–	0.025	0.018
$overhang$	–	0.014	0.002	–	0.015	0.002
δ	–	26.0	15.8	–	26.2	16.2

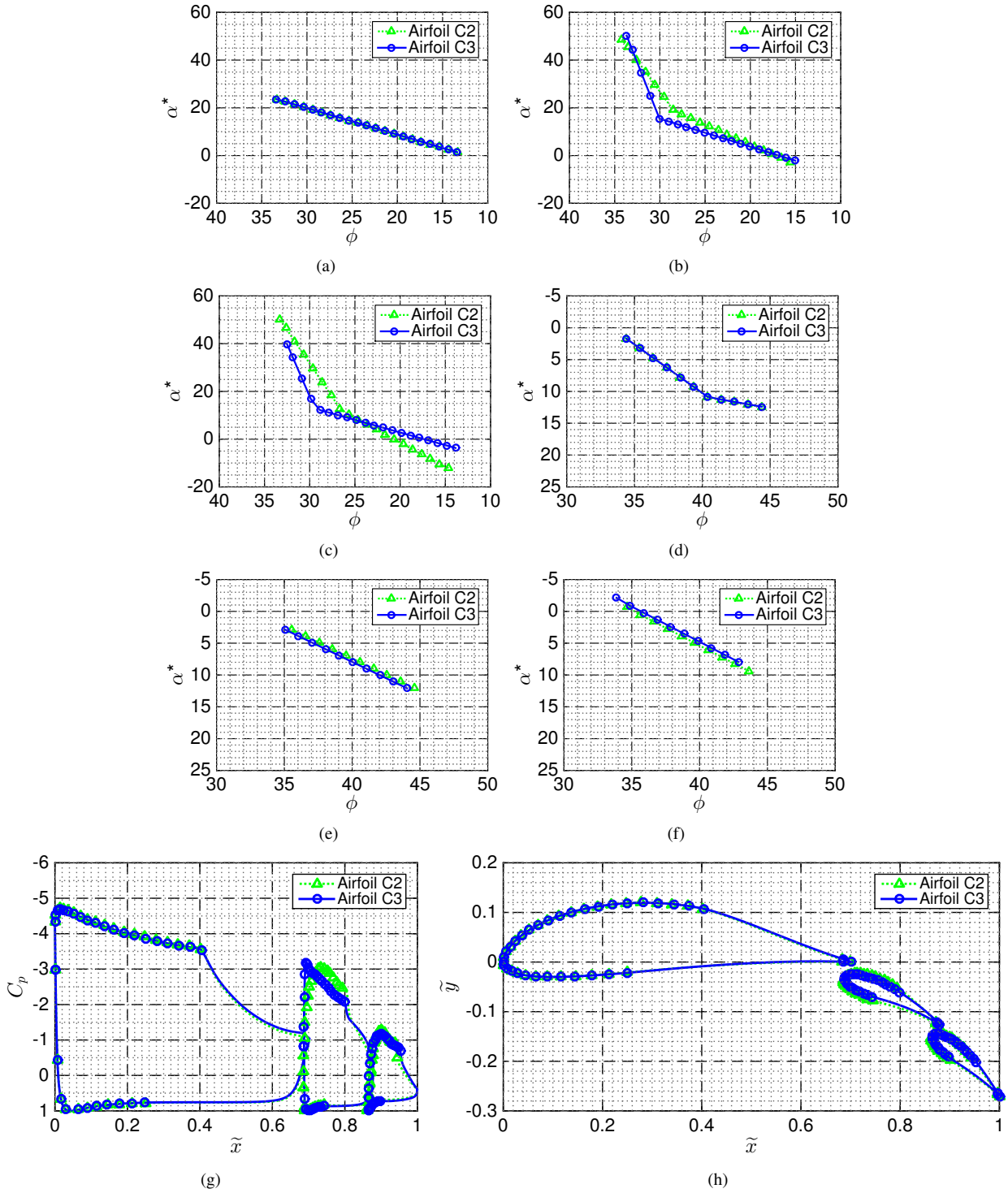

Figure 7.20: Airfoils C2 and C3 design parameters including α^*-ϕ for a) main-element, b) flap 1, and c) flap 2 upper surfaces; α^*-ϕ for d) main element, e) flap 1, and f) flap 2 lower surfaces, g) viscous C_p distribution coplotted with ϕ points, and h) airfoil coordinates coplotted with ϕ points.

Table 7.22: Aerodynamic Performance of Airfoil C3 Compared to Airfoil C2 and Baseline Airfoil

	Airfoil C2	Airfoil C3	Percent Improvement Relative to C2	Percent Improvement Relative to Baseline
l/d	144	149	3.47%	30.0%
$\delta_{w\ ME,\ max}$	0.016	0.016	0.00%	38.5%
$\widetilde{x}_{d,\ ME}$	1.16	1.17	-0.862%	0.00%
WTP_{ME}	2.47	2.45	0.810%	38.3%

increased aft loading and decreased suction peak for airfoil C3, which was the desired result. The transition point for flap 2 was moved slightly downstream, but no significant changes in transition were observed for the main element or flap 1.

Table 7.22 shows the standard four aerodynamic performance metrics to quantify the airfoil performance. Data are presented as absolute numbers as well as improvements relative to both airfoil C2 and the baseline airfoil. Airfoil C3 results in no change in main-element maximum wake thickness, $\delta_{w,\ ME,\ max}$, but a slight movement downstream of $\widetilde{x}_{d,\ ME}$ is observed. Despite these two observations, a small decrease in WTP_{ME} is observed. This 0.810% improvement is attributed to thinner wakes at upstream locations but a more-rapid increase in $\delta_{w,\ ME}$ approaching $\widetilde{x}_{d,\ ME}$. While airfoil C3 yields only a sight improvement in WTP_{ME}, the l/d of the system is improved by nearly 3.5% between airfoil C2 and C3. Because little change is observed in the wakes, this improvement in l/d is attributed to decreased skin-friction drag over the three airfoil elements. This observation further indicates that the viscous wakes and boundary layers affect l/d, and design decisions must consider both of these effects. The performance of airfoil C3 to the baseline case is presented in the right-most column of the table, and a 30% improvement in l/d for airfoil C3 is noted.

7.5.4 Airfoil C4

Table 7.23 compares the inverse-design parameters for airfoils C3 and C4. In general, this design iteration served as an iteration to make minor modifications to the C_p distributions over both flaps of airfoil C3. Building off of observations and conclusions from airfoil C3, the pitching moment for both flaps was slightly decreased in an attempt to decrease the loading on the two flaps and shift more of the loading to the main element. Decreased pressure gradients over the two flaps decreases the adverse pressure gradient applied to the main-element wake. However, decreased pressure over the main element yields less pressure recovery over the main element and thus the air is dumped form the main-element trailing edge at a slightly lower pressure. Therefore, the loads for the three elements must be carefully considered with a tradeoff between decreased streamwise pressure gradient with decreased flap loading and decreased main-element pressure recovery resulting from increased main-element loading. The thickness constraint over flap 2 was removed

Table 7.23: Inverse-Design Parameters for Airfoils C3 and C4

	Airfoil C3			Airfoil C4		
	Main Element	Flap 1	Flap 2	Main Element	Flap 1	Flap 2
REC_u	0.02	0.20	0.20	0.02	0.20	0.20
REC_l	0.20	0.20	0.20	0.20	0.20	0.20
K_s	0.50	0.80	0.40	0.50	0.80	0.40
C_{m_0}	−0.16	−0.23	−0.15	−0.16	**–0.19**	**–0.12**
$(t/c)_{max}$	0.200	–	0.18	0.200	–	**–**
gap	–	0.025	0.018	–	0.025	0.018
$overhang$	–	0.015	0.002	–	0.015	0.007
δ	–	26.2	16.2	–	26.2	16.3

for the fourth design iteration such that the designer obtained increased control over the flap 2 pressure distribution and the resulting airfoil coordinates. Airfoils C3 and C4 are located at essentially the same relative coordinate positions.

The α^*-ϕ curves for airfoils C3 and C4 are plotted in Fig. 7.21. Efforts in this design iteration were focused upon the two flaps and thus no modifications were made to the main-element airfoil. As shown in Fig. 7.21(b), an additional ϕ point was added to the aft portion of flap 1 to reduce the adverse pressure gradient in the forward portion of the airfoil and subsequently move the transition point downstream. In addition, the decreased C_{m_0} decreased the aft loading and increased the forward loading of the airfoil, and this increased loading is associated with a decrease in pressure for the laminar flow region in which $\widetilde{x} \leq 0.81$. A smaller pressure peak and increased $\widetilde{x}$ at which the strong adverse pressure gradient begins both contribute to decreased magnitude of $\partial C_p/\partial \widetilde{x}$ in the forward portion of the airfoil. The pressure distribution plot indicates that the flap 1 upper-surface transition point was successfully moved in the downstream direction and that the suction peak was decreased. In addition to the flap 1 design improvements, design alterations were made to flap 2 as plotted in Fig. 7.21(c,f), which primarily result in the decreased C_{m_0} for flap 2. Despite the large changes in α^*-ϕ for the flap 2 lower surface, only slight modifications in C_p are noted over flap 2 when comparing airfoils C3 and C4.

Table 7.24 presents the standard aerodynamic and wake performance metrics for C4 relative to both C3 and the baseline configuration. A slight increase in l/d is observed when comparing C4 to C3, but there are no quantifiable improvements in the wake metrics. This observation indicates that the aerodynamic performance improvement in C4 is primarily driven by the flow on the surface of each of the three elements. As seen in the table, C4 yields a 31.3% improvement in l/d relative to the baseline airfoil, and this improvement in l/d is primarily driven by an approximately 38% increase in wake metrics.

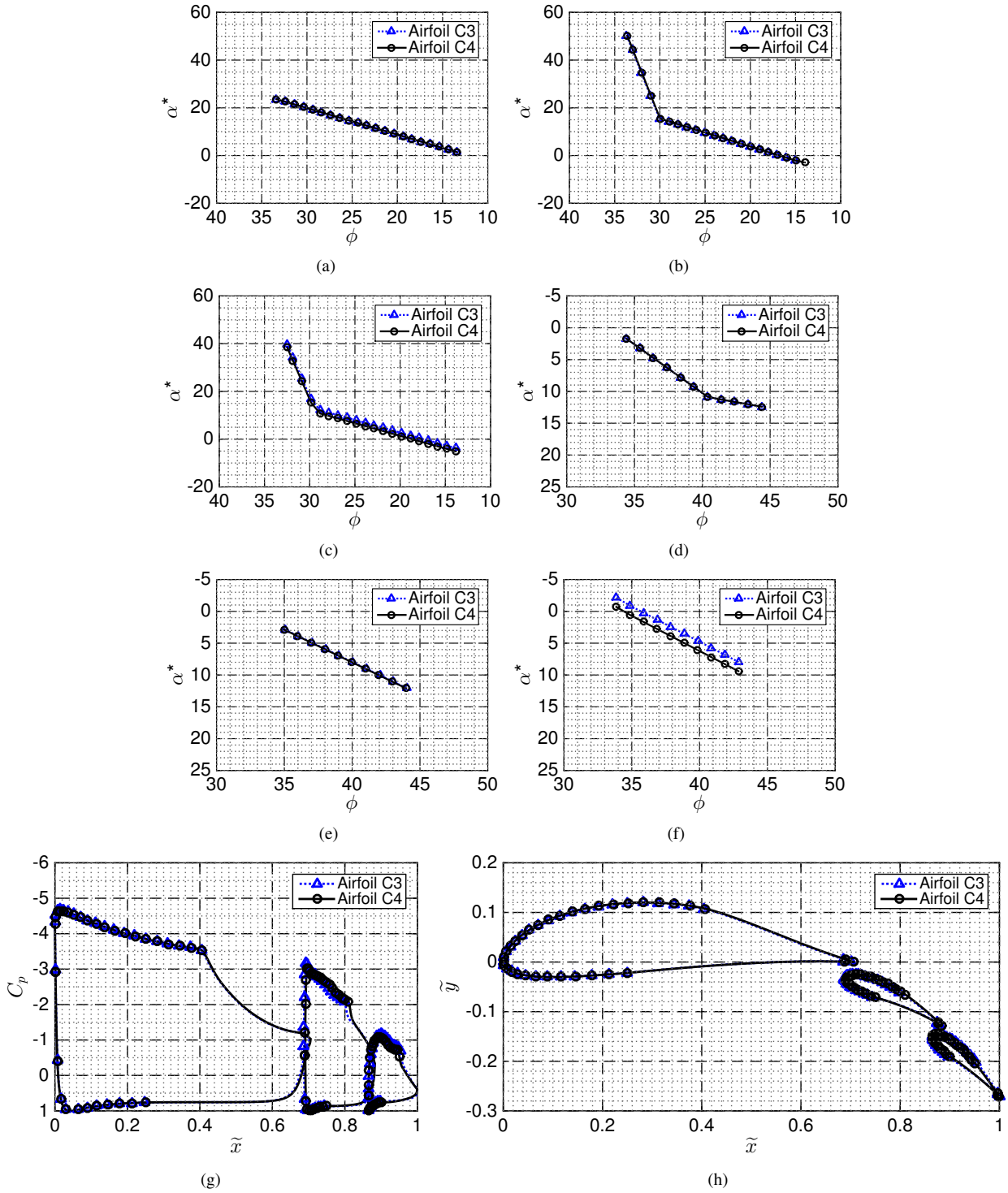

Figure 7.21: Airfoils C3 and C4 design parameters including α^*-ϕ for a) main-element, b) flap 1, and c) flap 2 upper surfaces; α^*-ϕ for d) main element, e) flap 1, and f) flap 2 lower surfaces, g) viscous C_p distribution coplotted with ϕ points, and h) airfoil coordinates coplotted with ϕ points.

Table 7.24: Aerodynamic Performance of Airfoil C4 Compared to Airfoil C3 and Baseline Airfoil

	Airfoil C3	Airfoil C4	Percent Improvement Relative to C3	Percent Improvement Relative to Baseline
l/d	149	151	1.34%	31.3%
$\delta_{w\ ME,\ max}$	0.016	0.016	0.00%	38.5%
$\widetilde{x}_{d,\ ME}$	1.17	1.17	0.00%	0.00%
WTP_{ME}	2.45	2.45	0.00%	38.3%

7.5.5 Airfoil C5

The final design iteration in this airfoil design is referred to as C5, and it is designed according to parameters in Table 7.25 and Fig. 7.22. Decreased *REC* parameters for both the main-element lower surface was selected to increase the pressure recovery over the main element to reduce the pressure recovery in the wake which leads to wake bursting. Similarly, the decreased *REC* values for flap 1 recovered more pressure over the surface of flap 1 than the previous design. While previous knowledge indicates the pressure may be recovered more efficiently in the wake than over the airfoil surface, it is observed that the stronger streamwise pressure gradient in the wake may lead to wake bursting if too much pressure is recovered in the viscous wake. A slight increase in pitching moment was applied to each element to slightly increase the aft loading, albeit possibly at the expense of a larger leading-edge suction peak. The main-element upper surface ϕ_{min} was decreased by 2 deg to increase the $\widetilde{x}$ range for the desired weak $\partial C_p/\partial\widetilde{x}$ that decreases the strength of wake bursting.

Figure 7.22 also presents the α^*-ϕ curves for the upper and lower surfaces of each element. The slope of α^*-ϕ over the main-element upper surface decreased the adverse pressure gradient in $\widetilde{x} \leq 0.48$, thus leading to an increased laminar run and thinner boundary layer at the transition point. The decreased *REC* also resulted in increased C_p at the main-element trailing edge and therefore decreasing the adverse pressure gradient in the wake which leads to larger, thicker wakes. The increased flap 1 pitching moment resulted in decreased forward loading with the exception of the

Table 7.25: Inverse-Design Parameters for Airfoils C4 and C5

	Airfoil C4			Airfoil C5		
	Main Element	Flap 1	Flap 2	Main Element	Flap 1	Flap 2
REC_u	0.02	0.20	0.20	0.02	**0.02**	0.20
REC_l	0.20	0.20	0.20	**0.02**	**0.02**	0.20
K_s	0.50	0.80	0.40	0.50	**0.50**	0.40
C_{m_0}	−0.16	−0.19	−0.12	**–0.175**	**–0.21**	**–0.14**
$(t/c)_{max}$	0.200	–	–	0.200	–	–
gap	–	0.025	0.018	–	0.026	0.018
$overhang$	–	0.015	0.007	–	0.015	0.007
δ	–	26.2	16.3	–	26.1	16.1

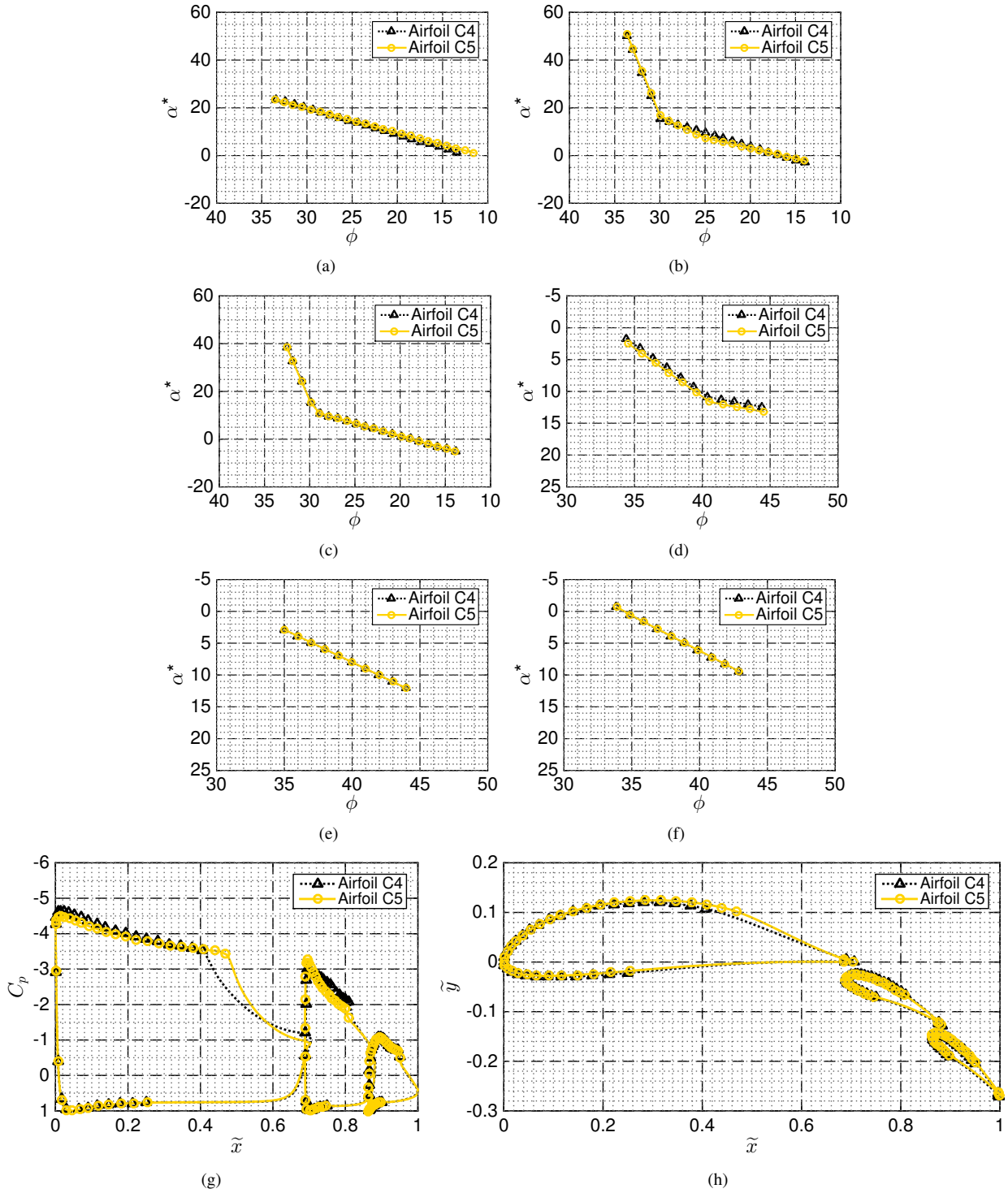

Figure 7.22: Airfoils C4 and C5 design parameters including α^*-ϕ for a) main-element, b) flap 1, and c) flap 2 upper surfaces; α^*-ϕ for d) main element, e) flap 1, and f) flap 2 lower surfaces, g) viscous C_p distribution coplotted with ϕ points, and h) airfoil coordinates coplotted with ϕ points.

stronger suction peak; this trend has been previously observed in this research project. Minimal changes were made to flap 2 and thus little variation in the flap 2 C_p distributions for airfoils C4 and C5 are observed.

Performance metrics for airfoil C5 are presented in Table 7.26 as relative improvements and absolute numbers. The design modifications presented in this section yielded a 12.5% decrease in wake thickness, but an increase in $\widetilde{x}_{d,\,ME}$. Despite the increase in $\widetilde{x}_{d,\,ME}$, the thinner wake yielded an 11% decrease in WTP_{ME} for airfoil C5 relative to C4. An increase in l/d of nearly 6% was achieved by reducing the strength of bursting for the main-element wake. When compared to the baseline performance, airfoil C5 yields a 31% increase in l/d and a 38% thinner wake.

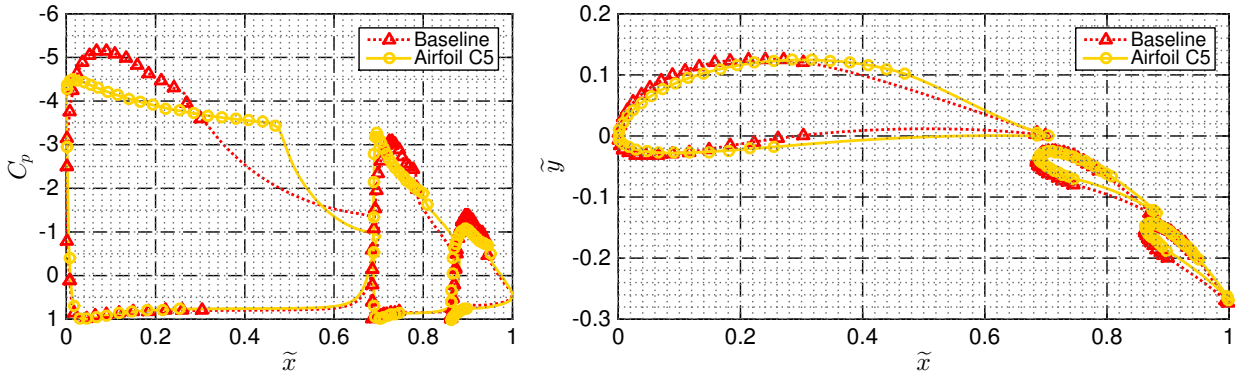

(a) (b)

Figure 7.23: Baseline airfoil and airfoil C5 data including a) C_p distribution and b) airfoil coordinates.

A comparison of the final airfoil, C5, to the baseline MFFS(ns)-026 airfoil is plotted in Fig. 7.23. Most significantly, the airfoil C5 main-element pressure gradient is significantly decreased relative to the baseline C_p distribution. This decreased pressure gradient and increased $\widetilde{x}$ for which the strong pressure gradient is present results in a downstream shift in the transition point. As previously observed, an increased laminar run decreases the boundary-layer height relative to a shorter-laminar-run case, and this thinner boundary layer results in decreased wake thickness and wake bursting. The pressure peak on the main element is significantly weaker, and more of the pressure is recovered over the surface of the airfoil than in the wake. This behavior results in a weaker off-the-surface pressure gradient yielding a thinner wake. The pressure peak for flap 1 is significantly sharper thus allowing for decreased magnitude of

Table 7.26: Aerodynamic Performance of Airfoil C5 Compared to Airfoil C4 and Baseline Airfoil

	Airfoil C4	Airfoil C5	Percent Improvement Relative to C4	Percent Improvement Relative to Baseline
l/d	151	160	5.96%	31.3%
$\delta_{w\,ME,\,max}$	0.016	0.014	12.5%	38.5%
$\widetilde{x}_{d,\,ME}$	1.17	1.18	−0.855%	0.00%
WTP_{ME}	2.45	2.18	11.0%	38.3%

$\partial C_p/\partial \widetilde{x}$ as the pressure-recovery region begins at a decreased $\widetilde{x}$ for airfoil C5 than for the baseline case. Both flap 1 and flap 2 are unloaded for airfoil C5 relative to the baseline airfoil, which results in a weaker off-the-surface pressure gradient and decreases the strength of the burst wake.

Finally, two fixed-transition RANS computations were calculated for airfoils C1 and C5 in which the transition points were determined from MSES calculations for freestream conditions of $Re = 1 \times 10^6$ and $C_l = 3.40$. A wide and detailed view of the flowfields for airfoils C1 and C5 are shown in Fig. 7.24. Both the main-element and flap-1 wakes for airfoil C5 are thinner than that of the baseline case. In addition, the flowfield from airfoil C5 has decreased $\widetilde{U}_t$ at a given $\widetilde{x}$ than that of airfoil C1. Both of these observations indicate that airfoil C5 has superior performance compared to the baseline airfoil. The l/d ratio for airfoil C5 was determined to be 76.4, which is an increase of 5.6 or 8.33% relative to the baseline C1 airfoil. While the RANS-calculated l/d for airfoil C5 is significantly less than that of the MSES-predicted l/d, it is again stated that the turbulence models all over-predict the presence of wake bursting. It is also stated that airfoil C5 has slightly superior performance than that of airfoil A4 in which the l/d for airfoil C5 l/d is 0.7% larger than that of airfoil A4.

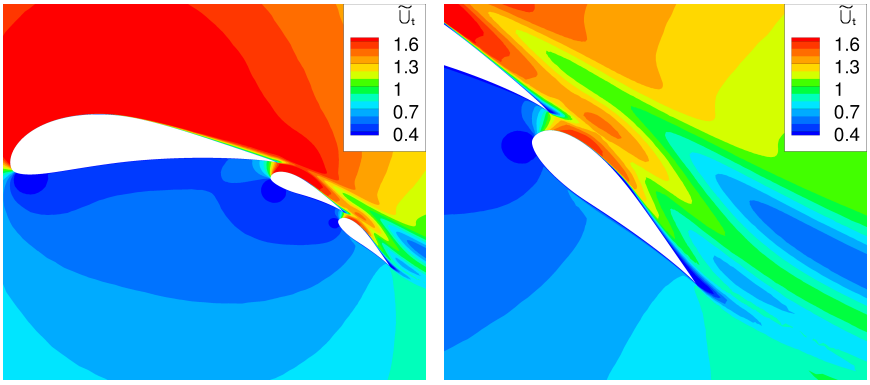

Figure 7.24: Computational predictions for airfoil C1 and airfoil C5 at wide and zoomed views including a) airfoil C1 $\widetilde{U}_t$and b) airfoil C5 $\widetilde{U}_t$.

7.6 Summary of Airfoil Designs to Mitigate Wake Bursting

A series of airfoils were designed in this chapter to provide insight into designs that result in smaller, thinner wakes relative to a baseline configuration. Three different designs were presented for different freestream conditions and constraining the design of various elements. Main-element geometry alterations for a target Re of 1×10^6 was first presented followed by a design point of $Re = 3 \times 10^6$. Building upon conclusions from these first two designs, a third airfoil design was presented for $Re = 1 \times 10^6$ in which the shape of all airfoil elements were changed. Final airfoil designs indicated both decreased wake thickness and increased l/d in excess of 50%. Various iterations for each airfoil design are presented in the chapter, and the logic used to proceed from one airfoil design to the next iteration are discussed; this systematic approach is presented to help future airfoil designers understand the design considerations that affect wake bursting.

Numerous key observations and conclusions were identified throughout this chapter. In general, the size of the wakes was decreased by moving the transition point further downstream. By increasing the laminar run over the airfoils, a thinner boundary layer was shed at the trailing edge of the airfoil resulting in a thinner wake. In addition, it was concluded that wake bursting was reduced by decreasing the magnitude of $\partial C_p/\partial \widetilde{x}$ in the laminar portion of the flowfield. This pressure gradient was achieved by designing a thin, sharp suction peak near the leading edge of each airfoil as well as increasing the $\widetilde{x}$ for which the strong pressure recovery region was encountered. In general, it is desired to decrease the adverse pressure gradient applied to the viscous wake, referred to as off-the-surface pressure recovery. For multielement airfoils, the pressure can be recovered more efficiently off the surface of the airfoil as opposed to recovering all of the pressure over a single-element airfoil. Nevertheless, results indicate that a streamwise pressure gradient can be too strong which may result in increased wake bursting. A variety of parameters, including thickness distribution and pitching moment for each airfoil element, must be carefully considered for the airfoil design, and no clear conclusions can be drawn for either of these parameters.

Implementation of the conclusions presented in this chapter allows airfoil designers to mitigate the strength of burst wakes in a multielement airfoil flowfield. These improvements result in increased aerodynamic efficiency for the aircraft thus resulting in a more efficient aircraft design. It is known that one of the limitations limiting $C_{l,\,max}$ for multielement airfoils is the presence of burst wakes, and thus the observations in this chapter will allow an airfoil (or wing) to operate at increased $C_{l,\,max}$ and α_{max} prior to encountering stall. An increase in these performance metrics can be important to approach and landing conditions.

Chapter 8

Summary, Conclusions, and Recommendations

A thorough investigation of high-lift aerodynamic flowfields using both experimental and computational tools is presented in this dissertation. An introduction to these flowfields is first presented in this document, and this is followed by an exhaustive discussion of the experimental and computational methods utilized. Both steady and unsteady flowfield parameters, including a detailed exploration of turbulence values, are then discussed for a baseline airfoil configuration. Additional results include the effect of flap position upon the flowfield, and finally a set of airfoil designs which improve aerodynamic performance are presented.

8.1 Summary

Research presented in this dissertation investigated high-lift multielement airfoil flowfields using a variety of techniques, and the particular flowfield feature was the wake development behind the multielement airfoil system. High-lift airfoils are used to increase lift (and thus reduce stall speed) for takeoff and landing configurations. In some instances, strong adverse pressure gradients off the surface of a multielement airfoil may negatively affect the aerodynamic performance. If this adverse pressure gradient is too aggressive, one or more of the viscous wakes may separate from itself in a phenomena referred to as wake bursting. The sudden expansion and thickening of the separated wakes has been shown to decrease lift and increase drag. Additionally, if the wakes are sufficiently separated, the maximum achievable angle of attack for an aircraft may be limited due to the wake separation and not due to the more-common surface separation. In general, burst wakes are not desired, and efforts are taken to reduce the effect of these wakes.

The investigation entered around the aerodynamics of the three-element MFFS(ns)-026 multielement airfoil comprised of a main element and two flap elements. This airfoil, designed to operate at a target Reynolds number of 1×10^6, was not designed as part of this dissertation as the airfoil had been previously designed. The MFFS(ns)-026 airfoil defines only the profiles for the three elements and the relative chord lengths, but the location of the flaps is not defined. Consequently, a variety of different flap locations can be used to define various multielement airfoil configurations. A coordinate system which defined the location of each element relative to the upstream element

was implemented in this research; the three degrees of freedom that defined the flap location are gap size, overhang distance, and relative flap deflection angle.

Many pieces of hardware were designed and manufactured such that the three-element airfoil could be experimentally tested in a wind tunnel. A set of tongue-and-groove clamps were implemented to attach the flaps to the main element airfoil so the aerodynamic performance of the entire airfoil system. Because of the high loads generated by multielement airfoils, additional supports connected all three airfoil elements at both the top and bottom of the wind tunnel. Because of the support necessary at each end of the airfoil, extensive adaptations were made to both the floor and ceiling. A complex set of devices, named the Flap Positioning System, were designed such that each flap could be located in a wide range of positions for the wind-tunnel tests. In this manner, the flaps could be moved to an extensive range of gap sizes, overhang distances, and relative deflection angles. While this system was designed in the current research project, the Flap Positioning System can be used for future experimental tests. Additional hardware was designed such that the two-dimensional traverse could be installed on the side of the wind tunnel such that wake surveys were collected in the chord-normal plane.

Experimental data were collected in the University of Illinois 3 ft $\times$ 4 ft low-speed low-turbulence wind tunnel for freestream Reynolds numbers between 0.6×10^6 and 1×10^6 for a range of angle of attack. Numerous types of data were collected for these tests including airfoil performance, surface oil flow visualization, unsteady off-body split-film measurements, 7-hole probe wake surveys. The flow visualization techniques were implemented to ensure the flow was attached to the surface of the airfoil and thus any separated region in the wake was due to wake bursting and not surface separation. Airfoil performance data were collected using a three-component force balance and two-dimensional wake integration in an effort to understand the relationship between the flap positions and the aerodynamic performance. A variety of two-dimensional wake profiles were also extracted far downfield of the airfoil trailing edge. Two-dimensional comprehensive wake surveys were performed with both a split-film probe and a 7-hole pressure probe at a given spanwise location. Unsteady two-component velocity measurements were captured with the split-film probe which yielded both time-averaged velocity measurements which could be used to determine a variety of turbulence parameters and evaluate the frequency content. The 7-hole probe yielded time averaged data such as static pressure, total pressure, and all three components of velocity.

Numerous different wake metrics were developed to quantify the extent to which a wake is burst, deemed the strength of wake bursting, and these methods were implemented for a variety of experimental and computational runs. These metrics were based upon various parameters in the flowfield including total pressure and displacement thickness, and the use of these metrics yielded easy and quantifiable differences between different flowfields. Some of these metrics were applied to experimental data while others were applied to computational simulations; different metrics were utilized depending upon flowfield parameters collected through the experiments or simulations.

Burst wakes were simulated using two computational solvers of varying fidelity. A simple panel code relying on inviscid/viscous coupling through the displacement thickness was utilized. This code, MSES, has been shown to predict low-Reynolds-number flowfields, such as those examined in this document, with reasonable accuracy. Multi-element airfoil flowfields are computed using an intrinsic grid in which the flowfield solution and computational grid are calculated simultaneously. In addition to MSES, a higher-fidelity RANS code was utilized. The code, USM3D, computationally solves the Navier-Stokes equations with a variety of different turbulence models.

A detailed and thorough investigation of the baseline airfoil with a given flap position was performed using both experimental and computational tools. Experimental wake surveys were collected with the aforementioned split-film probe and 7-hole probe. As data were captured over a wide range of spatially-continuous Cartesian points, the development of the wake could be meticulously examined. A thorough investigation of various turbulence quantities were calculated, and the relationship between these unsteady parameters and the time-averaged wake development was studied. The effect of angle of attack and freestream Reynolds number was also examined in these tests. Experimental data collected in the wind tunnel were compared with computational simulations using both MSES and USM3D using both two-dimensional contour plots and wake profiles. Grid-convergence and turbulence-model-selection studies were also performed.

Additional efforts were undertaken to determine the effect of the flap position upon the burst wake flowfield using the both MSES and the 7-hole probe. Numerous parametric sweeps were computationally evaluated to establish the "best" location for the flaps for a desired lift coefficient or lift-to-drag ratio. A select subset of geometries were experimentally examined in the wind tunnel. As the experimental wake surveys took many hours to capture for one flowfield, fewer experimental tests were performed than the number of computational runs.

Finally, a variety of airfoil designs are developed and presented to reduce the strength of wake bursting at a given design point. Airfoils were designed using the MFOIL/PROFOIL airfoil design software, and computations in MSES were used to quantify the extent of wake bursting in the resulting flowfields. Designs were presented to evaluate the effect of both the main element as well as all three elements upon the wakes. Design considerations included both structural and aerodynamic requirements for a multielement airfoil.

8.2 Conclusions

This research examined the nature of burst wakes in a spatially-continuous domain using both experimental and computational methods. Prior this study, no experimental tests were performed in the x-y plane as only wake profiles had been previously captured. A variety of comparisons were made between the experimental and computational data, and the detailed comparisons in this document had not been previously performed. Therefore, numerous insightful

conclusions can be stated and defended based upon research presented in this document. These conclusions include the following:

- Methods were developed to identify different regions of the burst wake, and the center of the wake, deemed the "wake core," was of particular interest. The location of the wake core was specified by the velocity gradient (or shear) in the streamwise direction. Data indicate the flowfield in the wake core, especially the turbulent fluctuations, was significantly different than the region outside of the wake core. Unsteady data indicate the majority of the turbulence is produced in the shear layers bounding the wake core, and almost no turbulence is produced in the wake core. The elevated levels of turbulence are diffused into both the wake core and outer flow with increasing downstream distance. Extremely high levels of turbulence and turbulence production was present in the shear layers between wakes shed from different elements. Unsteady frequency content was captured with the split-film probe, and elevated energy levels were found at low frequencies with decreasing energy at higher cascades, as confirmed with a Kolmogorov energy cascade.

- A variety of metrics have been developed to quantify the extent to which a wake is burst, deemed the "strength of wake bursting." These metrics are defined based upon total pressure and displacement thickness proved to be valuable for comparisons between different flowfields. Metrics applied to different flowfields include various measurements of wake thickness in addition to integrated wake area.

- Experimentally-acquired data using both the split-film and 7-hole probe suggested some differences for the two flowfields, despite the same operating conditions and airfoil geometry for the results. Ultimately, these differences are attributed to a variety of parameters related to probe head geometry and probe response. The larger 7-hole probe yielded increased spatial smoothing than the split-film probe, and this observation yielded less distinction between the wakes from the main-element and flap 1. As the split-film probe was smaller, data were taken on a finer grid than the 7-hole probe, and this resulted in a significant amount of spatial smoothing for the 7-hole probe. Finally, the 7-hole probe, which is used to determine steady-state flowfield variables, is adversely affected by turbulence intensity. The combination of these effects yields data sets that exhibit better, albeit not perfect, agreement.

- Comparisons between experimental and computational data indicated larger differences than typically observed for high-lift flows in which the computational simulations indicate larger, thicker wakes than the experimentally-collected data. Ultimately, the differences in the results can be attributed to numerous sources. First, artifacts of the wind-tunnel testing environment were examined, and a large junction vortex was observed at both ends of the airfoil. These vortices resulted in decreased downwash in the plane at which data were collected, thus resulting in decreased C_l relative to a flowfield without these vortices. A two-dimensional wake survey was performed at

a given streamwise location, and the lift distribution for the airfoil was subsequently determined. As the location of the *x*-*y* wake surveys was known, the local C_l at this plane was determined, and computational simulations were performed at this decreased C_l. Agreement between the computational and experimental simulations was markedly improved. Computational RANS simulations for which transition was prescribed resulted in significantly improvements, and very close agreement, between computational and experimental results. Future simulations should be performed with either free or forced transition; fully-turbulent computations yield poor prediction of burst wakes.

- The effect of different freestream conditions, including both *Re* and α, upon wake bursting was determined using both experimental and computational tools. Larger *Re* resulted in smaller wakes with less merging between the various wakes than those at decreased *Re*, and this result is in agreement with traditional boundary-layer theory. Larger Reynolds numbers yielded decreased minimum velocity in the wake core as well as thinner wakes. In addition, the strength of wake bursting was observed to significantly increase with larger α. The larger wakes at higher α resulted in increased decambering, and thus decreased lift, for the multielement airfoil system than the theoretical increase in C_l for a given increase in α.

- Careful examination of the computational results indicated that the burst wakes are an inherently two-dimensional flowfield structure with no significant spanwise velocity component. Consequently, it is stated that burst-wake flowfields can be sufficiently simulated within a purely two-dimensional computational domain. These results could not be confirmed with the 7-hole probe due to the two large junction vortices which created a spanwise velocity component.

- Different flap settings result in various flowfields, and the effect of relative deflection angle, gap size, and overhang distance was determined in this research. Larger flap deflection angles yield increased flowfield curvature which in turn increases the strength of wake bursting by increasing the streamwise pressure gradient in the wake region. This increased pressure gradient in turn increases the burst-wake separation. Similarly, the effect of gap size upon the burst wake flowfield was determined. In general, larger gap sizes decrease the strength of wake bursting relative to a small-gap configuration. Decreased wake bursting is quantified by increased minimum velocity in the wake and decreased wake thickness. Extremely small gap sizes were shown to cause flow separation from the trailing edge of flap 2. In general, minimal differences in the burst-wake flowfield were observed for small- or large-overhang simulations, and it is therefore concluded that the gap size affects wake bursting more than the overhang distance.

- Aerodynamic performance data were collected for a wide number of airfoil configurations. It was observed that increased flap deflection angles resulted in increased C_l and C_d for a given freestream condition, and overall an

increase in l/d was observed for larger flap deflection angles. For a given double-slotted airfoil in which the flaps were located at the same relative coordinates, increased C_l was observed for small-gap moderate-overhang configurations; the small-gap, large-overhang configurations yielded increased values of l/d. An additional study in which the flaps were not located at the same relative coordinates was performed, and results indicate that the aerodynamic performance was significantly affected by the gap size of each configuration and affected by the overhang distance to a lesser extent.

- Three thresholds were developed to quantitatively classify the nature of a burst wake. A criterion based upon the slenderness of the wake is proposed such that long, thin wakes are defined to be not burst while larger, thicker wakes are burst. A wake is said to be burst at the point for which the wake thickness rapidly increases. A third metric based upon the size of the inner portion of the wake is presented to classify the flowfield as slightly, moderately, or severely burst.

- Numerous airfoil designs which exhibit decreased wake bursting for a given freestream condition are shown in this dissertation. Ultimately, the upper-surface transition point and the pressure gradient upstream of this transition point were observed to significantly affect the strength of wake bursting. Smaller and thinner wakes were generated by airfoils with an aft upper-surface transition point and very weak streamwise pressure gradients upstream of this point. Thus, wake bursting is decreased with "wider" and "flatter" C_p curves over the main element. Designs were presented for two different Reynolds numbers, and these observations were noted for both design points.

- One airfoil design for a given freestream condition was presented in which the coordinates for all three elements were altered. In addition to an aft upper-surface transition point, the presence of wake bursting was minimized by thin flaps and narrow upper-surface pressure peaks. The effect of wake bursting was decreased for increased pressure at the main-element trailing edge. As increased pressure at the trailing edge requires less pressure recovery in the wake region, a weaker streamwise pressure gradient is applied to the wakes, thus decreasing the size of the wakes.

8.3 Recommendations

Throughout the course of the research presented in this document, a thorough investigation of the high-lift wake-bursting investigation was performed. During this research, a variety of possibilities for future studies were formulated. The recommendations for future research include:

- An examination of freestream Reynolds number and angle of attack was performed in this research, but future projects could study the unsteady burst-wake flowfield at different freestream conditions. Such variations in freestream conditions include both α and Reynolds number, as outlined in this study, in addition to freestream turbulence values. It is known that freestream turbulence levels can significantly affect the flowfield, and the relationship between freestream turbulence and wake bursting will improve the understanding of wake bursting as well as improved the fidelity of comparisons between experimentally-collected data and computational results.

- Unsteady fluctuations were only captured in two dimensions, and thus some components of the shear stress tensor were not measured. Additional studies experimentally investigating the three-dimensional turbulent effects would be useful. It would be particularly beneficial if three-dimensional unsteady velocities and pressures could be measured in a burst-wake flowfield. These efforts will provide additional data to which computational solvers can be validated in all three dimensions.

- Unsteady computations using large-eddy simulations or higher-order methods at the freestream Reynolds numbers presented in this research will yield additional insight into the separated wake and allow detailed comparisons between the experimental and computational data. Currently, LES simulations are too expensive to simulate Reynolds numbers in this research at adequate grid density. Computational expense of large-eddy simulations, and other higher-fidelity methods, significantly increases with larger Reynolds numbers due to the increased scale of turbulent eddies that must be accurately resolved. Based upon the current rate of computational advancement, it is expected that this computational study will be sufficiently cheap to perform within the next five years.

- Data collected at higher Reynolds numbers than those examined in this research project will allow wake bursting to be understood across a wide range of scales from small-scale race car wings through large-wing transport aircraft. Wake bursting is an inherently viscous phenomena, and thus Reynolds number significantly affects the burst wake. Experiments at these higher freestream Reynolds numbers would be particularly valuable as very little data exist at or near Reynolds numbers for large-transport aircraft during takeoff or landing conditions.

- Three dimensional wake bursting, such as that over an aircraft wing, would aid in understanding wake bursting over a slotted wing. Three-dimensional aerodynamics over aircraft wings fundamentally change the aerodynamic flowfield when compared to a two-dimensional airfoil, and the burst wake will also change over three-dimensional wings. The relationship between surface separation and wake separation over wings would yield additional insight into the mediation of wake bursting. Additional effects that would be prudent to consider include the hardware used to attach the flaps to a wing. These support brackets yield additional aerodynamic complexity to the flowfield, and these effects could significantly affect wake bursting.

- Further work is needed to understand the effect of turbulence upon steady-state multi-hole pressure probes. First-order corrections for multi-hole probes exist, but significant weaknesses exist in these corrections. Consequently, improved correction formulae would increase the fidelity of the experimentally-measured data.

Appendix A

Airfoil Coordinates

The airfoil coordinates for the MFFS(ns)-026, A4, B6, and C5 multielement airfoils are included in this appendix. Data in these tables are presented for a system chord length of unity, and the flaps coordinates are presented as part of the multielement airfoil.

MFFS(ns)-026 Configuration 10 Main Element	
x	*y*
0.7001000	0.0000000
0.6986007	0.0005837
0.6944980	0.0023672
0.6882252	0.0050161
0.6797152	0.0082157
0.6688911	0.0120139
0.6558953	0.0164728
0.6408838	0.0215708
0.6240263	0.0272776
0.6055008	0.0335404
0.5854949	0.0402958
0.5642003	0.0474633
0.5418121	0.0549527
0.5185244	0.0626606
0.4945301	0.0704763
0.4700172	0.0782804
0.4451687	0.0859494
0.4201602	0.0933544
0.3951606	0.1003648
0.3703302	0.1068452
0.3458216	0.1126556
0.3217827	0.1176424
0.2983097	0.1215248
0.2752705	0.1241906
0.2525823	0.1257629
0.2303728	0.1262841
0.2087530	0.1257753
0.1878151	0.1242697
0.1676374	0.1217918
0.1483058	0.1183605
0.1299091	0.1140175
0.1125171	0.1088212
0.0961885	0.1028242
0.0809904	0.0960788
0.0669879	0.0886602
0.0542253	0.0806558
0.0427389	0.0721471
0.0325726	0.0632186
0.0237627	0.0539765
0.0163247	0.0445338
0.0102698	0.0349993
0.0056147	0.0254913
0.0023641	0.0161491
0.0005047	0.0071191

Continued ... *MFFS(ns)-026 Main Element*	
x	*y*
0.0000243	-0.0014434
0.0009156	-0.0093496
0.0031649	-0.0163555
0.0067635	-0.0220114
0.0124264	-0.0261167
0.0205766	-0.0290511
0.0308602	-0.0310465
0.0432165	-0.0320887
0.0576587	-0.0321625
0.0741878	-0.0312450
0.0927812	-0.0293845
0.1134456	-0.0266869
0.1362042	-0.0232646
0.1609993	-0.0192949
0.1876767	-0.0150087
0.2160467	-0.0105861
0.2459013	-0.0061931
0.2770113	-0.0019976
0.3091213	0.0017699
0.3418162	0.0049259
0.3746416	0.0074441
0.4072553	0.0093511
0.4393344	0.0106775
0.4705800	0.0114680
0.5007166	0.0117739
0.5294899	0.0116525
0.5566661	0.0111616
0.5820292	0.0103603
0.6053800	0.0093067
0.6265337	0.0080590
0.6453187	0.0066770
0.6615748	0.0052232
0.6751524	0.0037693
0.6859233	0.0024013
0.6937468	0.0012075
0.6985060	0.0003438
0.7001000	0.0000000

MFFS(ns)-026 Configuration 10 Flap 1	
x	*y*
0.8766970	-0.1312628
0.8763618	-0.1309411
0.8754361	-0.1299871
0.8740223	-0.1284763
0.8721431	-0.1265263
0.8697507	-0.1242013
0.8668249	-0.1214937
0.8633973	-0.1184043
0.8595035	-0.1149572
0.8551776	-0.1111810
0.8504553	-0.1071076
0.8453738	-0.1027715
0.8399720	-0.0982098
0.8342898	-0.0934618
0.8283682	-0.0885689
0.8222491	-0.0835743
0.8159744	-0.0785232
0.8095862	-0.0734624
0.8031262	-0.0684406
0.7966349	-0.0635089
0.7901509	-0.0587222
0.7836980	-0.0541430
0.7772892	-0.0498221
0.7709379	-0.0457864
0.7646559	-0.0420623
0.7584614	-0.0386772
0.7523774	-0.0356491
0.7464229	-0.0329864
0.7406137	-0.0306983
0.7349720	-0.0287951
0.7295232	-0.0272779
0.7242872	-0.0261404
0.7192820	-0.0253778
0.7145317	-0.0249855
0.7100620	-0.0249502
0.7058927	-0.0252537
0.7020439	-0.0258803
0.6985410	-0.0268175
0.6954075	-0.0280463
0.6926491	-0.0295423
0.6902705	-0.0312784
0.6882911	-0.0332172
0.6867275	-0.0353106
0.6855966	-0.0375099

Continued ... MFFS(ns)-026 Flap 1	
x	*y*
0.6849258	-0.0397608
0.6847631	-0.0419752
0.6853031	-0.0441448
0.6865937	-0.0464118
0.6885071	-0.0488372
0.6910158	-0.0513756
0.6940962	-0.0540017
0.6977323	-0.0566990
0.7019105	-0.0594498
0.7066106	-0.0622334
0.7118060	-0.0650336
0.7174712	-0.0678376
0.7235794	-0.0706278
0.7300978	-0.0733805
0.7369897	-0.0760692
0.7442159	-0.0786404
0.7518937	-0.0810315
0.7601020	-0.0833763
0.7687060	-0.0858498
0.7775632	-0.0884807
0.7865484	-0.0912734
0.7955466	-0.0942146
0.8044524	-0.0972806
0.8131681	-0.1004407
0.8216042	-0.1036594
0.8296779	-0.1068986
0.8373132	-0.1101182
0.8444395	-0.1132775
0.8509924	-0.1163345
0.8569120	-0.1192472
0.8621440	-0.1219718
0.8666381	-0.1244640
0.8703505	-0.1266762
0.8732317	-0.1285653
0.8752184	-0.1300388
0.8763403	-0.1309564
0.8766970	-0.1312628

MFFS(ns)-026 Configuration 10 Flap 2	
x	*y*
1.0000000	-0.2743160
0.9989742	-0.2739972
0.9983192	-0.2730490
0.9973102	-0.2715213
0.9959634	-0.2694842
0.9942593	-0.2669751
0.9922003	-0.2639961
0.9898169	-0.2605618
0.9871388	-0.2567027
0.9841940	-0.2524533
0.9810104	-0.2478523
0.9776158	-0.2429414
0.9740372	-0.2377656
0.9703018	-0.2323720
0.9664353	-0.2268103
0.9624629	-0.2211317
0.9584080	-0.2153894
0.9542926	-0.2096378
0.9501360	-0.2039332
0.9459539	-0.1983352
0.9417401	-0.1929026
0.9374871	-0.1876714
0.9332076	-0.1826623
0.9289116	-0.1779017
0.9246082	-0.1734181
0.9203128	-0.1692365
0.9160415	-0.1653730
0.9118068	-0.1618419
0.9076224	-0.1586595
0.9035078	-0.1558378
0.8994825	-0.1533804
0.8955625	-0.1512900
0.8917660	-0.1495716
0.8881163	-0.1482256
0.8846359	-0.1472464
0.8813426	-0.1466305
0.8782498	-0.1463821
0.8753700	-0.1464902
0.8727142	-0.1469245
0.8702965	-0.1476595
0.8681420	-0.1486704
0.8662790	-0.1499239
0.8647357	-0.1513838
0.8635489	-0.1530136

Continued ... MFFS(ns)-026 Flap 2	
x	*y*
0.8627855	-0.1547571
0.8625865	-0.1566796
0.8629358	-0.1588948
0.8637242	-0.1613891
0.8649490	-0.1641224
0.8666012	-0.1670656
0.8686737	-0.1701977
0.8711622	-0.1734994
0.8740604	-0.1769480
0.8773550	-0.1805216
0.8810306	-0.1842017
0.8850729	-0.1879673
0.8894660	-0.1917915
0.8941907	-0.1956436
0.8992322	-0.1994690
0.9046911	-0.2032641
0.9105870	-0.2071433
0.9167785	-0.2111842
0.9231632	-0.2153753
0.9296523	-0.2196940
0.9361659	-0.2241078
0.9426314	-0.2285801
0.9489821	-0.2330703
0.9551568	-0.2375366
0.9610991	-0.2419362
0.9667567	-0.2462263
0.9720819	-0.2503644
0.9770301	-0.2543091
0.9815611	-0.2580192
0.9856375	-0.2614546
0.9892263	-0.2645755
0.9922975	-0.2673427
0.9948260	-0.2697163
0.9967874	-0.2716578
0.9981588	-0.2731116
0.9989540	-0.2740108
1.0000000	-0.2743160

A4 Main Element	
x	*y*
0.7004000	0.0000000
0.6987302	0.0004266
0.6940731	0.0018805
0.6868980	0.0042330
0.6772494	0.0072955
0.6651495	0.0111658
0.6508273	0.0159491
0.6345408	0.0216446
0.6165605	0.0282140
0.5971599	0.0355710
0.5766093	0.0435955
0.5551667	0.0521315
0.5330742	0.0609989
0.5105518	0.0699937
0.4877976	0.0788983
0.4649847	0.0874790
0.4422633	0.0954883
0.4197673	0.1026488
0.3974870	0.1084342
0.3749787	0.1127279
0.3520177	0.1159046
0.3288279	0.1181104
0.3055676	0.1193976
0.2823804	0.1197928
0.2594003	0.1193214
0.2367581	0.1180057
0.2145838	0.1158664
0.1929976	0.1129343
0.1721108	0.1092411
0.1520324	0.1048170
0.1328697	0.0997046
0.1147173	0.0939564
0.0976596	0.0876254
0.0817789	0.0807655
0.0671539	0.0734448
0.0538474	0.0657415
0.0419117	0.0577339
0.0313987	0.0495032
0.0223545	0.0411477
0.0148076	0.0327773
0.0087798	0.0245041
0.0042969	0.0164532
0.0013825	0.0087825
0.0000539	0.0016819
0.0003546	-0.0045531

Continued ... *A4 Main Element*	
x	*y*
0.0028917	-0.0097248
0.0079305	-0.0142065
0.0150754	-0.0183045
0.0242239	-0.0218843
0.0353447	-0.0248384
0.0483936	-0.0271058
0.0633508	-0.0286816
0.0802238	-0.0295625
0.0989986	-0.0297498
0.1196220	-0.0293367
0.1419900	-0.0284435
0.1659539	-0.0271437
0.1913486	-0.0254980
0.2179944	-0.0235630
0.2456952	-0.0213664
0.2743485	-0.0189213
0.3038390	-0.0163516
0.3339146	-0.0138224
0.3643056	-0.0114102
0.3947456	-0.0091697
0.4249723	-0.0071372
0.4547288	-0.0053380
0.4837651	-0.0037857
0.5118390	-0.0024872
0.5387173	-0.0014407
0.5641763	-0.0006394
0.5880031	-0.0000690
0.6099952	0.0002889
0.6299623	0.0004612
0.6477258	0.0004795
0.6631200	0.0003881
0.6759903	0.0002389
0.6862172	0.0001441
0.6938157	0.0001495
0.6986886	0.0000978
0.7004000	0.0000000

A4 Flap 1	
x	*y*
0.8774462	-0.1307292
0.8771095	-0.1304081
0.8761797	-0.1294554
0.8747594	-0.1279467
0.8728717	-0.1259996
0.8704691	-0.1236784
0.8675311	-0.1209756
0.8640896	-0.1178921
0.8601800	-0.1144518
0.8558369	-0.1106831
0.8510958	-0.1066180
0.8459943	-0.1022909
0.8405713	-0.0977388
0.8348670	-0.0930010
0.8289226	-0.0881189
0.8227800	-0.0831354
0.8164815	-0.0780959
0.8100694	-0.0730470
0.8035854	-0.0680373
0.7970702	-0.0631180
0.7905629	-0.0583438
0.7840874	-0.0537773
0.7776568	-0.0494694
0.7712845	-0.0454469
0.7649826	-0.0417363
0.7587693	-0.0383648
0.7526678	-0.0353506
0.7466970	-0.0327018
0.7408729	-0.0304278
0.7352176	-0.0285386
0.7297566	-0.0270355
0.7245099	-0.0259120
0.7194954	-0.0251631
0.7147373	-0.0247844
0.7102612	-0.0247623
0.7060870	-0.0250787
0.7022346	-0.0257176
0.6987296	-0.0266665
0.6955953	-0.0279063
0.6928375	-0.0294127
0.6904607	-0.0311583
0.6884843	-0.0331056
0.6869247	-0.0352067
0.6857987	-0.0374124
0.6851336	-0.0396684

Continued ... *A4 Flap 1*	
x	*y*
0.6849773	-0.0418864
0.6855245	-0.0440575
0.6868237	-0.0463238
0.6887470	-0.0487470
0.6912668	-0.0512815
0.6943592	-0.0539021
0.6980085	-0.0565924
0.7022007	-0.0593347
0.7069157	-0.0621082
0.7121268	-0.0648969
0.7178082	-0.0676880
0.7239333	-0.0704639
0.7304691	-0.0732011
0.7373786	-0.0758731
0.7446226	-0.0784265
0.7523183	-0.0807982
0.7605451	-0.0831218
0.7691685	-0.0855732
0.7780460	-0.0881816
0.7870520	-0.0909515
0.7960717	-0.0938701
0.8049991	-0.0969139
0.8137364	-0.1000525
0.8221940	-0.1032507
0.8302886	-0.1064704
0.8379441	-0.1096719
0.8450899	-0.1128144
0.8516611	-0.1158563
0.8575976	-0.1187555
0.8628451	-0.1214683
0.8673530	-0.1239507
0.8710771	-0.1261550
0.8739680	-0.1280382
0.8759618	-0.1295079
0.8770880	-0.1304234
0.8774462	-0.1307292

A4 Flap 2	
x	*y*
1.0000000	-0.2738097
0.9997885	-0.2734907
0.9991341	-0.2725421
0.9981261	-0.2710137
0.9967808	-0.2689757
0.9950784	-0.2664653
0.9930215	-0.2634849
0.9906405	-0.2600490
0.9879651	-0.2561880
0.9850233	-0.2519365
0.9818429	-0.2473333
0.9784517	-0.2424201
0.9748768	-0.2372418
0.9711451	-0.2318456
0.9672825	-0.2262812
0.9633140	-0.2205998
0.9592632	-0.2148547
0.9551518	-0.2091002
0.9509991	-0.2033927
0.9468210	-0.1977918
0.9426110	-0.1923562
0.9383616	-0.1871221
0.9340856	-0.1821100
0.9297929	-0.1773463
0.9254927	-0.1728598
0.9212002	-0.1686751
0.9169316	-0.1648087
0.9126993	-0.1612746
0.9085171	-0.1580894
0.9044045	-0.1552648
0.9003810	-0.1528046
0.8964624	-0.1507114
0.8926671	-0.1489904
0.8890184	-0.1476418
0.8855387	-0.1466602
0.8822458	-0.1460420
0.8791532	-0.1457914
0.8762733	-0.1458975
0.8736172	-0.1463300
0.8711990	-0.1470632
0.8690438	-0.1480727
0.8671799	-0.1493249
0.8656356	-0.1507836
0.8644476	-0.1524127
0.8636830	-0.1541556

Continued ... *A4 Flap 2*	
x	*y*
0.8634827	-0.1560780
0.8638304	-0.1582934
0.8646171	-0.1607882
0.8658399	-0.1635225
0.8674901	-0.1664668
0.8695605	-0.1696003
0.8720466	-0.1729037
0.8749424	-0.1763543
0.8782345	-0.1799303
0.8819075	-0.1836129
0.8859472	-0.1873814
0.8903377	-0.1912087
0.8950596	-0.1950640
0.9000985	-0.1988930
0.9055548	-0.2026918
0.9114479	-0.2065752
0.9176366	-0.2106204
0.9240184	-0.2148160
0.9305044	-0.2191391
0.9370150	-0.2235576
0.9434773	-0.2280344
0.9498250	-0.2325290
0.9559965	-0.2369996
0.9619357	-0.2414033
0.9675904	-0.2456973
0.9729126	-0.2498392
0.9778581	-0.2537873
0.9823865	-0.2575006
0.9864605	-0.2609388
0.9900471	-0.2640622
0.9931164	-0.2668316
0.9956432	-0.2692070
0.9976032	-0.2711498
0.9989737	-0.2726046
0.9997682	-0.2735043
1.0000000	-0.2738097

B6 Main Element	
x	*y*
0.6978000	0.0000000
0.6961147	0.0005070
0.6914093	0.0022056
0.6841477	0.0049793
0.6743875	0.0086654
0.6621829	0.0133723
0.6477936	0.0192005
0.6315062	0.0261376
0.6136188	0.0341253
0.5944286	0.0430507
0.5742252	0.0527604
0.5532798	0.0630600
0.5318409	0.0737277
0.5101280	0.0845156
0.4883315	0.0951609
0.4666099	0.1053850
0.4450929	0.1148935
0.4238928	0.1233532
0.4028638	0.1301546
0.3814635	0.1352522
0.3595012	0.1391337
0.3372081	0.1419314
0.3147446	0.1436961
0.2922564	0.1444626
0.2698751	0.1442563
0.2477270	0.1430941
0.2259402	0.1409982
0.2046354	0.1380001
0.1839214	0.1341330
0.1639038	0.1294286
0.1446897	0.1239292
0.1263762	0.1176896
0.1090473	0.1107658
0.0927841	0.1032135
0.0776672	0.0951011
0.0637638	0.0865094
0.0511277	0.0775186
0.0398105	0.0682096
0.0298607	0.0586780
0.0213106	0.0490309
0.0141807	0.0393741
0.0084902	0.0298177
0.0042531	0.0204922
0.0014653	0.0115424
0.0001173	0.0031224

Continued ... *B6 Main Element*	
x	*y*
0.0002021	-0.0045843
0.0017148	-0.0113281
0.0046870	-0.0165696
0.0098742	-0.0202783
0.0176467	-0.0229390
0.0276022	-0.0246291
0.0396841	-0.0253237
0.0539272	-0.0250099
0.0703707	-0.0236619
0.0890076	-0.0213168
0.1098452	-0.0180876
0.1329100	-0.0140830
0.1583460	-0.0093505
0.1862342	-0.0043746
0.2162486	0.0002240
0.2478542	0.0041828
0.2805507	0.0073777
0.3138706	0.0097777
0.3473887	0.0114105
0.3807218	0.0123420
0.4135297	0.0126611
0.4455102	0.0124668
0.4763968	0.0118617
0.5059533	0.0109440
0.5339708	0.0098058
0.5602624	0.0085288
0.5846605	0.0071855
0.6070129	0.0058367
0.6271801	0.0045360
0.6450326	0.0033276
0.6604491	0.0022560
0.6733119	0.0013623
0.6835323	0.0007425
0.6911511	0.0004113
0.6960661	0.0001658
0.6978000	0.0000000

B6 Flap 1	
x	*y*
0.8746214	-0.1247022
0.8742806	-0.1243952
0.8733376	-0.1234823
0.8718955	-0.1220353
0.8699806	-0.1201693
0.8675476	-0.1179491
0.8645763	-0.1153679
0.8610981	-0.1124255
0.8571486	-0.1091446
0.8527626	-0.1055522
0.8479761	-0.1016789
0.8428272	-0.0975575
0.8373549	-0.0932234
0.8316003	-0.0887141
0.8256050	-0.0840693
0.8194116	-0.0793303
0.8130628	-0.0745403
0.8066019	-0.0697442
0.8000712	-0.0649889
0.7935124	-0.0603235
0.7869654	-0.0558009
0.7804555	-0.0514821
0.7739971	-0.0474169
0.7676042	-0.0436313
0.7612894	-0.0401511
0.7550715	-0.0370027
0.7489738	-0.0342031
0.7430151	-0.0317602
0.7372114	-0.0296824
0.7315850	-0.0279791
0.7261609	-0.0266510
0.7209586	-0.0256908
0.7159957	-0.0250934
0.7112958	-0.0248536
0.7068838	-0.0249574
0.7027789	-0.0253862
0.6990002	-0.0261239
0.6955725	-0.0271574
0.6925183	-0.0284672
0.6898427	-0.0300291
0.6875493	-0.0318161
0.6856561	-0.0337907
0.6841779	-0.0359051
0.6831301	-0.0381104
0.6825379	-0.0403525

Continued ... *B6 Flap 1*	
x	*y*
0.6824461	-0.0425428
0.6830462	-0.0446670
0.6843902	-0.0468642
0.6863536	-0.0491983
0.6889080	-0.0516255
0.6920292	-0.0541214
0.6957011	-0.0566705
0.6999096	-0.0592555
0.7046341	-0.0618566
0.7098480	-0.0644589
0.7155255	-0.0670502
0.7216398	-0.0696142
0.7281577	-0.0721285
0.7350423	-0.0745681
0.7422530	-0.0768813
0.7499038	-0.0790029
0.7580768	-0.0810622
0.7666442	-0.0832363
0.7754663	-0.0855579
0.7844198	-0.0880352
0.7933908	-0.0906586
0.8022743	-0.0934080
0.8109733	-0.0962562
0.8193981	-0.0991708
0.8274659	-0.1021170
0.8351005	-0.1050574
0.8422309	-0.1079541
0.8487923	-0.1107677
0.8547243	-0.1134584
0.8599719	-0.1159849
0.8644842	-0.1183049
0.8682162	-0.1203729
0.8711181	-0.1221477
0.8731243	-0.1235402
0.8742599	-0.1244109
0.8746214	-0.1247022

B6 Flap 2	
x	*y*
1.0000000	-0.2636195
0.9989237	-0.2633096
0.9982547	-0.2623868
0.9972228	-0.2608988
0.9958455	-0.2589149
0.9941042	-0.2564721
0.9920015	-0.2535728
0.9895678	-0.2502306
0.9868331	-0.2464749
0.9838261	-0.2423393
0.9805751	-0.2378614
0.9771083	-0.2330819
0.9734538	-0.2280445
0.9696393	-0.2227953
0.9656915	-0.2173828
0.9616362	-0.2118571
0.9574981	-0.2062703
0.9532999	-0.2006757
0.9490619	-0.1951284
0.9448012	-0.1896871
0.9405128	-0.1844100
0.9361902	-0.1793331
0.9318464	-0.1744762
0.9274918	-0.1698655
0.9231361	-0.1655288
0.9187952	-0.1614905
0.9144851	-0.1577663
0.9102187	-0.1543698
0.9060099	-0.1513171
0.9018782	-0.1486194
0.8978430	-0.1462800
0.8939201	-0.1443010
0.8901277	-0.1426871
0.8864888	-0.1414381
0.8830256	-0.1405480
0.8797554	-0.1400129
0.8766918	-0.1398367
0.8738468	-0.1400082
0.8712305	-0.1404972
0.8688565	-0.1412781
0.8667488	-0.1423261
0.8649349	-0.1436073
0.8634417	-0.1450854
0.8623048	-0.1467236
0.8615891	-0.1484646

Continued ... *B6 Flap 2*	
x	*y*
0.8614354	-0.1503700
0.8618305	-0.1525525
0.8626661	-0.1550010
0.8639384	-0.1576762
0.8656381	-0.1605493
0.8677576	-0.1635996
0.8702922	-0.1668084
0.8732353	-0.1701532
0.8765730	-0.1736128
0.8802899	-0.1771691
0.8843713	-0.1808017
0.8888009	-0.1844844
0.8935589	-0.1881872
0.8986296	-0.1918566
0.9041125	-0.1954865
0.9100291	-0.1991898
0.9162417	-0.2030464
0.9226488	-0.2070472
0.9291619	-0.2111717
0.9357014	-0.2153899
0.9421946	-0.2196669
0.9485748	-0.2239641
0.9547804	-0.2282417
0.9607546	-0.2324585
0.9664450	-0.2365735
0.9718031	-0.2405457
0.9767843	-0.2443350
0.9813476	-0.2479017
0.9854554	-0.2512071
0.9890739	-0.2542124
0.9921727	-0.2568796
0.9947260	-0.2591699
0.9967089	-0.2610455
0.9980976	-0.2624522
0.9989040	-0.2633235
1.0000000	-0.2636195

C5 Main Element	
x	*y*
0.7036000	0.0000000
0.7018593	0.0004438
0.6969732	0.0019958
0.6894222	0.0046204
0.6793289	0.0082064
0.6668127	0.0128655
0.6521841	0.0186881
0.6357781	0.0256390
0.6179315	0.0336216
0.5989678	0.0424735
0.5791878	0.0519846
0.5588586	0.0618994
0.5382102	0.0719324
0.5174309	0.0817673
0.4966685	0.0910580
0.4760509	0.0993594
0.4551517	0.1060990
0.4334359	0.1113968
0.4109817	0.1157314
0.3879861	0.1191698
0.3646068	0.1217470
0.3409957	0.1234793
0.3172986	0.1243735
0.2936517	0.1244345
0.2701884	0.1236754
0.2470428	0.1221098
0.2243451	0.1197526
0.2022140	0.1166271
0.1807648	0.1127588
0.1601131	0.1081784
0.1403671	0.1029299
0.1216212	0.0970594
0.1039658	0.0906140
0.0874903	0.0836503
0.0722731	0.0762386
0.0583776	0.0684498
0.0458633	0.0603562
0.0347877	0.0520430
0.0251948	0.0436099
0.0171139	0.0351572
0.0105741	0.0267913
0.0056032	0.0186408
0.0022179	0.0108595
0.0004335	0.0036209
0.0002840	-0.0028225

Continued ... *C5 Main Element*	
x	*y*
0.0022829	-0.0081019
0.0067666	-0.0125688
0.0134738	-0.0166770
0.0222481	-0.0202557
0.0330203	-0.0231948
0.0457470	-0.0254529
0.0604373	-0.0270066
0.0771011	-0.0278280
0.0957026	-0.0279318
0.1162138	-0.0274171
0.1385559	-0.0264060
0.1625777	-0.0249838
0.1881084	-0.0232277
0.2149669	-0.0212030
0.2429604	-0.0189565
0.2719495	-0.0165030
0.3018031	-0.0139558
0.3322846	-0.0114874
0.3631073	-0.0091789
0.3939908	-0.0070835
0.4246604	-0.0052326
0.4548482	-0.0036443
0.4842958	-0.0023238
0.5127542	-0.0012686
0.5399857	-0.0004672
0.5657638	0.0000962
0.5898745	0.0004449
0.6121156	0.0006047
0.6322980	0.0006095
0.6502451	0.0004958
0.6657934	0.0003130
0.6787898	0.0001153
0.6891184	0.0000268
0.6968275	0.0000915
0.7018264	0.0000898
0.7036000	0.0000000

C5 Flap 1	
x	*y*
0.8811232	-0.1265805
0.8808171	-0.1262349
0.8800128	-0.1252241
0.8788410	-0.1236776
0.8772958	-0.1217703
0.8752755	-0.1195786
0.8727312	-0.1170733
0.8696899	-0.1142427
0.8661812	-0.1111077
0.8622317	-0.1076935
0.8578693	-0.1040285
0.8531242	-0.1001429
0.8480277	-0.0960694
0.8426132	-0.0918422
0.8369148	-0.0874972
0.8309678	-0.0830717
0.8248080	-0.0786044
0.8184712	-0.0741356
0.8119931	-0.0697084
0.8053963	-0.0653721
0.7986967	-0.0611554
0.7919239	-0.0570724
0.7851153	-0.0531474
0.7783082	-0.0494048
0.7715383	-0.0458703
0.7648390	-0.0425658
0.7582437	-0.0395102
0.7517861	-0.0367230
0.7455000	-0.0342200
0.7394160	-0.0320127
0.7335628	-0.0301124
0.7279703	-0.0285290
0.7226685	-0.0272682
0.7176837	-0.0263326
0.7130350	-0.0257279
0.7087396	-0.0254563
0.7048155	-0.0255074
0.7012727	-0.0258622
0.6981242	-0.0265037
0.6953925	-0.0274127
0.6931099	-0.0285672
0.6912686	-0.0299561
0.6898533	-0.0315505
0.6888835	-0.0332868
0.6883814	-0.0350871

Continued ... *C5 Flap 1*	
x	*y*
0.6884882	-0.0368611
0.6892966	-0.0387228
0.6907331	-0.0407850
0.6927443	-0.0429846
0.6953197	-0.0452993
0.6984549	-0.0477075
0.7021377	-0.0501860
0.7063502	-0.0527185
0.7110771	-0.0552932
0.7163016	-0.0578936
0.7219976	-0.0605006
0.7281347	-0.0630956
0.7346843	-0.0656578
0.7416143	-0.0681456
0.7489856	-0.0704392
0.7569344	-0.0726411
0.7654157	-0.0749896
0.7742535	-0.0775497
0.7833043	-0.0803371
0.7924382	-0.0833417
0.8015370	-0.0865381
0.8104937	-0.0898898
0.8192118	-0.0933547
0.8276047	-0.0968859
0.8355944	-0.1004357
0.8431110	-0.1039555
0.8500914	-0.1073972
0.8564788	-0.1107137
0.8622219	-0.1138586
0.8672741	-0.1167866
0.8715940	-0.1194507
0.8751415	-0.1218107
0.8778577	-0.1238065
0.8797185	-0.1253234
0.8807830	-0.1262615
0.8811232	-0.1265805

C5 Flap 2	
x	*y*
1.0000000	-0.2679449
0.9997778	-0.2676256
0.9992193	-0.2666880
0.9983864	-0.2652166
0.9972714	-0.2633169
0.9958144	-0.2610310
0.9939961	-0.2583428
0.9918419	-0.2552549
0.9893754	-0.2517919
0.9866184	-0.2479821
0.9835925	-0.2438573
0.9803204	-0.2394519
0.9768248	-0.2348030
0.9731289	-0.2299500
0.9692556	-0.2249340
0.9652278	-0.2197982
0.9610675	-0.2145870
0.9567952	-0.2093470
0.9524296	-0.2041278
0.9479691	-0.1989789
0.9434145	-0.1939243
0.9387907	-0.1889786
0.9341219	-0.1841707
0.9294301	-0.1795305
0.9247383	-0.1750863
0.9200696	-0.1708624
0.9154446	-0.1668814
0.9108839	-0.1631659
0.9064100	-0.1597357
0.9020450	-0.1566055
0.8978082	-0.1537876
0.8937194	-0.1512945
0.8898003	-0.1491350
0.8860718	-0.1473119
0.8825522	-0.1458259
0.8792609	-0.1446785
0.8762201	-0.1438665
0.8734516	-0.1433810
0.8709779	-0.1432145
0.8688160	-0.1433747
0.8669767	-0.1438579
0.8654562	-0.1446274
0.8642636	-0.1456408
0.8634596	-0.1468368
0.8631657	-0.1482673

Continued ... *C5 Flap 2*	
x	*y*
0.8633615	-0.1500194
0.8639593	-0.1520628
0.8649697	-0.1543587
0.8663922	-0.1568791
0.8682266	-0.1596056
0.8704748	-0.1625219
0.8731363	-0.1656078
0.8762022	-0.1688443
0.8796611	-0.1722163
0.8835032	-0.1757061
0.8877158	-0.1792896
0.8922829	-0.1829388
0.8971922	-0.1866011
0.9025568	-0.1902788
0.9083958	-0.1941035
0.9145507	-0.1981615
0.9209080	-0.2024364
0.9273722	-0.2068977
0.9338607	-0.2115042
0.9403006	-0.2162097
0.9466278	-0.2209650
0.9527854	-0.2257206
0.9587226	-0.2304273
0.9643936	-0.2350373
0.9697574	-0.2395049
0.9747765	-0.2437868
0.9794169	-0.2478414
0.9836474	-0.2516300
0.9874396	-0.2551153
0.9907678	-0.2582616
0.9936088	-0.2610342
0.9959428	-0.2633988
0.9977510	-0.2653210
0.9990165	-0.2667543
0.9997514	-0.2676420
1.0000000	-0.2679449

References

[1] Taylor, H. A., *Fairey Aircraft Since 1915*, Putnam Aeronautical Books, 2003.

[2] Fairey, C. R., "Controlling Device for Aeroplanes," *US patent number 1,313,680*, 1919.

[3] Mack, M. D. and McMasters, J. H., "High Reynolds Number Testing in Support of Transport Airplane Development," AIAA Paper 92-3982, AIAA Aerospace Ground Testing Conference, Nashville, TN, 1992.

[4] Smith, A. M. O., "High-Lift Aerodynamics," *Journal of Aircraft*, Vol. 12, No. 6, 1975, pp. 501–530.

[5] Gartshore, I., "Predictions of the Blowing Required to Suppress Separation from High-Lift Aerofoils," AIAA 70-872, CASI/AIAA Meeting on the Prospects for Improvement in Efficiency of Flight, 1970.

[6] Abbott, I. and Miller, R. B., "Tests of a Highly Cambered Low-Drag Airfoil Section with a Lift-Control Flap," NASA TR 74843, 1943.

[7] Jacobs, E. N., Abbott, I., and Davidson, M., "Preliminary Low-Drag-Airfoil and Flap Data from Tests at Large Reynolds Numbers and Low Turbulence," NACA TM 74843, 1943.

[8] Lindblad, I. and deCock, K., "CFD Prediction of Maximum Lift of a 2D High-Lift Configuration," AIAA Paper 99-3180, AIAA Applied Aerodynamics Conference, Norfolk, VA, 1999.

[9] Rudolph, P. K. C., "High-Lift Systems on Commercial Subsonic Airliners," NASA Contractor Report 4746, Ames Research Center, 1996.

[10] Eyi, S., Chand, K. K., Lee, K. D., Rogers, S. E., and Kwak, D., "Multi-Element High-Lift Design Using the Navier-Stokes Equations," AIAA Paper 96-1943, AIAA Fluid Dynamics Conference, New Orleans, LA, 1996.

[11] Kroo, I., "Adventures in Aircraft Design with John McMasters," 2009 AIAA Aerospace Sciences Meeting and Exhibit, Orlando, FL, 2009.

[12] Bier, N., Rudnik, R., Quest, J., and Rechlin, A., "Stall Behavior of the HINVA KH-A320-HA Highlift Model in ETW," .

[13] Antunes, A. P., da Silva, R. G., and Azevedo, J. L. F., "A Study of Transport Aircraft High-Lift Design Approaches," AIAA Paper 2007-38, AIAA Aerospace Sciences Meeting and Exhibit, Reno, NV, 2007.

[14] Howe, G. D., "Optimization of 2-D Flap Geometry Using Matlab and Fun3D," AIAA Paper 2011-823, AIAA Aerospace Sciences Meeting, Orlando, FL, 2011.

[15] Coiro, D. P., Nicolosi, F., and Grasso, F., "Design and Testing of Multi-Element Airfoil for Short-Takeoff-and-Landing Ultralight Aircraft," *Journal of Aircraft*, Vol. 46, No. 5, 2009, pp. 1795–1807.

[16] Cerra, D. F. and Katz, J., "Design of a High-Lift, Thick Airfoil for Unmanned Aerial Vehicle Applications," *Journal of Aircraft*, Vol. 45, No. 5, 2008, pp. 1789–1793.

[17] Eyi, S., Lee, K. D., Rogers, S. E., and Kwak, D., "High-Lift Design Optimization Using the Navier-Stokes Equations," AIAA Paper 95-0477, Aerospace Science Meeting, Reno, NV, 1995.

[18] Biber, K. and Zumwalt, G. W., "Experimental Studies of a Two-Element Airfoil with Large Separation," AIAA Paper 92-0267, AIAA Aerospace Sciences Meeting, Reno, NV, 1992.

[19] Bier, N., Keye, S., Rohlmann, D., and von Deetzen, S., "Design of a Wind Tunnel Model for Maximum Lift Predictions Based on Flight Test Data," AIAA Paper 2013-2930, AIAA Applied Aerodynamics Conference, San Diego, CA¡ 2013.

[20] Rudnik, R. and Schwetzler, D., "High lift INflight VAlidation (HINVA) - Overview about the 1st Flight Test Campaign," AIAA Paper 2014-2843, AIAA Applied Aerodynamics Conference, Atlanta, GA, 2014.

[21] Rudnik, R., Bier, N., Quest, J., and Schulz, M., "Flight Test Tailored ETW Testing of a Commercial Transport High Lift Configuration," AIAA Paper 2015-1559, AIAA Aerospace Sciences Meeting, Kisimmee, FL, 2015.

[22] Fisher, J., Gertsen, W. M., Wise, W., Walter, H., Little, H., and McGuckin, M., "Flight Test Results on the use of High Lift Boundary Layer Control Applied to a Modified Liaison Airplane," Cessna Aircraft Company, TR 1339-7 Model 319A. 1956.

[23] Kirkpatrick, D. and Woodward, D., "Priorities for High-Lift Testing in the 1990s," AIAA Paper 90-1413, AIAA Aerodynamic Ground Testing Conference, Seattle, WA, 1990.

[24] Hardin, J. D., Potter, R. C., van Dam, C. P., and Yip, L. P., "Two-Dimensional Computational Analysis of a Transport High-Lift System and Comparison with Flight-Test Results," AIAA Paper 93-3533, AIAA Applied Aerodynamics Conference, Monterey, CA, 1993.

[25] Cornish, J. J., III, "Practical High Lift Systems Using Distributed Boundary Layer Control," Aerophysics Department, Mississippi State University. Research Report 19, pp. 14–21.

[26] Antoniadlis, A. F., Tsoutsanis, P., and Drikakis, D., "Numerical Accuracy in RANS Computations of a High-Lift Multielement Airfoil and Aircraft Configurations," AIAA Paper 2015-0317, AIAA Aerspace Sciences Meeting, Kisimmee, FL, 2015.

[27] Slotnick, J. P., Hannon, J. A., and Chaffin, M., "Overview of the First AIAA CFD High Lift Prediction Workshop," AIAA Paper 2011-862, AIAA Aerospace Sciences Meeting, Orlando, FL, 2011.

[28] Rumsey, C. L., Slotnick, J. P., Long, M., Stuever, R. A., and Wayman, T. R., "Summary of the First AIAA CFD High-Lift Prediction Workshop," *Journal of Aircraft*, Vol. 48, No. 6, November 2011, pp. 2068–2079.

[29] Rumsey, C. L. and Slotnick, J. P., "Overview and Summary of the Second AIAA High Lift Prediction Workshop," AIAA Paper 2014-0747, AIAA Aerospace Sciences Meeting, National Harbor, MD, 2014.

[30] Kamenetskiy, D. S., Bussoletti, J. E., Hilmes, C. L., Venkatakrishnan, V., Wigton, L. B., and Johnson, F. T., "Numerical Evidence of Multiple Solutions for the Reynolds-Averaged Navier-Stokes Equations for High-Lift Configurations," AIAA Paper 2013-0663, AIAA Aerospace Sciences Meeting, Grapevine, TX, 2013.

[31] Biber, K., "Stall Hysteresis of an Airfoil with Slotted Flap," *Journal of Aircraft*, Vol. 42, No. 6, 2005, pp. 1462–1470.

[32] Spaid, F. W., "High Reynolds Number, Multielement Airfoil Flowfield Measurements," *Journal of Aircraft*, Vol. 37, No. 3, 2000, pp. 499–507.

[33] Ashby, D. L., "Experimental and Computational Investigation of Lift-Enhancing Tabs on a Multi-Element Airfoil," NASA TR 110432, 1996.

[34] Lin, J. C. and Doninik, C. J., "Parametric Investigation of a High-Lift Airfoil at High Reynolds Numbers," *Journal of Aircraft*, Vol. 34, No. 4, 1997, pp. 485–491.

[35] Pomeroy, B. W., Williamson, G. A., and Selig, M. S., "Experimental Study of a Multielement Airfoil for Large Wind Turbines," AIAA Paper 2012-2892, AIAA Applied Aerodynamics Conference, New Orleans, LA, 2012.

[36] Narsipur, S., Pomeroy, B. W., and Selig, M. S., "CFD Analysis of Multielement Airfoils for Wind Turbines," AIAA Paper 2012-2781, AIAA Applied Aerodynamics Conference, New Orleans, LA, 2012.

[37] Petrov, A. V., "Certain Types of Separated Flow over Slotted Wings," *Fluid Mechanics: Soviet Research*, Vol. 7, No. 5, September-October 1978, pp. 80–89.

[38] Nakayama, A., Kreplin, H. P., and Morgan, H. L., "Experimental Investigation of Flowfield About a Multielement Airfoil," *AIAA Journal*, Vol. 28, No. 1, 1988, pp. 14–21.

[39] Chin, V. D., "Flowfield Measurements about a Multi-Element Airfoil at High Reynolds Numbers," AIAA Paper 93-3137, AIAA Fluid Dynamics Conference, Orlando, FL, 1993.

[40] Schneider, S., Campbell, B., Bucci, G., and Sullivan, J. P., "An Experimental Simulation of Flap Flow on Multielement Airfoils at High Reynolds Number," AIAA Paper 94-2613, AIAA Aerospace Ground Testing Conference, Colorado Springs, CO, 1994.

[41] Hoffenberg, R., Sullivan, J. P., and Schneider, S., "Wake Measurements in a Strong Adverse Pressure Gradient," NASA CR 197272, 1995.

[42] Hoffenberg, R. and Sullivan, J. P., "Simulation of High-Lift Wake Behavior," AIAA Paper 97-0718, AIAA Aerospace Sciences Meeting, Reno, NV, 1997.

[43] Hoffenberg, R. and Sullivan, J. P., "Measurement and Simulation of Wake Deceleration," AIAA Paper 98-0522, AIAA Aerospace Sciences Meeting, Reno, NV, 1998.

[44] Hoffenberg, R., *Simulation of High-Lift Wake Behavior*, Ph.D. thesis, Purdue University, 1997.

[45] Driver, D. M. and Mateer, G. G., "Wake Flow in Adverse Pressure Gradient," AIAA Paper 2000-01-5511, AIAA World Aviation Conference, San Diego, CA, 2000.

[46] Roos, F. W., "Experimental Studies of Wake Retardation in a Simulated High-Lift-System Flow Field," AIAA Paper 97-1813, AIAA Aerospace Sciences Meeting, Reno, NV, 1997.

[47] Liu, X., Thomas, F. O., and Nelson, R. C., "An Experimental Investigation of Wake Development in Arbitrary Pressure Gradients," AIAA Paper 99-0677, AIAA Aerospace Sciences Meeting, Reno, NV, 1999.

[48] Starke, A. R., Henkes, R. A. W. M., and Tummers, M. J., "Effects of Curvature and Pressure Gradient on a Turbulent Near Wake," *Experimental Thermal and Fluid Science*, Vol. 19, 1999, pp. 49–56.

[49] Valarezo, W. O., Dominik, C. J., McGhee, R. J., Goodman, W. L., and Paschal, K. B., "Multi-Element Airfoil Optimization for Maximum Lift at High Reynolds Numbers," AIAA Paper 91-3332-CP, 1991.

[50] Adair, D. and Horne, W. C., "Characteristics of Merging Shear Layers and Turbulent Wakes of a Multi-Element Airfoil," NASA TM 100053, 1988.

[51] Meredith, P. T., "Viscous Phenomena Affecting High-Lift Systems and Suggestions for Future CFD Development," *High-Lift System Aerodynamics*, AGARD-CP-515, proceedings from 71st Fluid Dynamics Panel Meeting, Banff, Alberta, Canada, October 1992, pp. 19–1 to 19–8.

[52] Ying, S. X., Spaid, F. W., McGinley, C. B., and Rumsey, C. L., "Investigation of Confluent Boundary Layers in High-Lift Flows," *Journal of Aircraft*, Vol. 36, No. 3, May-June 1999, pp. 550–562.

[53] Khodadoust, A., *An Experimental Study of the Flowfield on a Semispan Rectangular Wing with a Simulated Glaze Ice Accretion*, Ph.D. thesis, Department of Aerospace Engineering, University of Illinois at Urbana-Champaign, Urbana IL, 1993.

[54] Selig, M. S. and McGranahan, B., "Wind Tunnel Aerodynamic Tests of Six Airfoils for Use on Small Wind Turbines," NREL Subcontractor Report, NREL/SR-500-34515, October, 2004.

[55] Ragheb, A. M. and Selig, M. S., "Multi-Element Airfoil Configurations for Wind Turbines," AIAA Paper 2011-3971, AIAA Applied Aerodynamics Conference, Honolulu, HI, 2011.

[56] Pomeroy, B. W., *Experimental Investigation of Multielement Airfoils for Large-Scale Wind Turbines*, Master's thesis, University of Illinois at Urbana-Champaign, 2012.

[57] Sutherland, W., "The Viscosity of Gases and Molecular Force," *Philosophical Magazine*, Vol. 36, 1893, pp. 507–531.

[58] Noe, S. C., *Force Balance Measurements of Wind-Turbine Airfoil Performance with Simulated Leading-Edge Ice Accretions*, Master's thesis, University of Illinois at Urbana-Champaign, 1996.

[59] Barlow, J. B., Rae, W. H., Jr., and Pope, A., *Low-Speed Wind Tunnel Testing*, Wiley-Interscience, New York, NY, 3rd ed., 1999, pp 328-346.

[60] Garner, H. C., Rogers, E. W. E., Acum, W. E. A., and Maskell, E. C., "Subsonic Wind Tunnel Wall Corrections," AGARDograph 109, 1966.

[61] Thom, A., "Blockage Corrections in a High Speed Wind Tunnel," Aeronautical Research Committee R&M 2033, 1943.

[62] Maskell, E. C., "A Theory of the Blockage Effects on Bluff Bodies and Stalled Wings in a Closed Wind Tunnel," Aeronautical Research Committee TN 3400, 1965.

[63] Jones, B. M., "Measurement of Profile Drag by the Pitot-Traverse Method," British Aeronautical Research Council R&M 1688, London, England, 1936.

[64] Schlichting, H., *Boundary-Layer Theory*, McGraw-Hill Book Company, New York, 8th ed., 2000.

[65] Lee, S., *Effects of Supercooled Large Droplet Icing on Airfoil Aerodynamics*, Ph.D. thesis, University of Illinois at Urbana-Champaign, 2001.

[66] Lu, B. and Bragg, M. B., "Airfoil Drag Measurement with Simulated Leading-Edge Ice Using the Wake Survey Method," AIAA Paper 2003-1094, Aerospace Sciences Meeting, Reno, NV, 2003.

[67] Betz, A., "A Method for the Direct Determination of Wing-Section Drag," translated from "Zeitschrift für Flugtechnik und Motorluftschiffahrt"," NACA TM 337, 1925.

[68] Maskell, E. C., "Progress Towards a Method for the Measurement of the Components of the Drag of a Wing of Finite Span," RAE Technical Report 72232, 1972.

[69] Lanzetta, M., Mele, B., and Tognaccini, R., "Advances in Aerodynamic Drag Extraction by Far-Field Methods," *Journal of Aircraft*, Vol. Journal of Aircraft Early Edition, 2015.

[70] Carre, A., Cordero-Gracio, M., Gomez, M., and Ponsin, J., "Wake-Integral Method for Drag Prediction," 11th World Congress on Computational Mechanics, Barcelona, Spain, 2014.

[71] Diebold, J. M., *Aerodynamics of a Swept Wing with Leaving-Edge Ice at Low Reynolds Number*, Master's thesis, University of Illinois at Urbana-Champaign, 2012.

[72] Cummings, R. M., Giles, M. B., and Shrinivas, G. N., "Analysis of the Elements of Drag in a Three-Dimensional Viscous and Inviscid Flowfield," AIAA Paper 96-2482, 14th Applied Aerodynamics Conference, Conference, New Orleans, LA, 1996.

[73] Kusunose, K., "Development of a Universal Wake Survey Data Analysis Code," AIAA Paper 97-2294, AIAA Applied Aerodynamics Conference, Atlanta, GA, 1997.

[74] Zaber Technologies, *A-LST-E High-Load Closed-Loop Motorized Linear Stages User's Manual*, 2-605 West Kent Ave. N., Vancouver, BC, Canada, September 30, 2015.

[75] Zaber Technologies, *Binary Protocol Manual*, 2-605 West Kent Ave. N., Vancouver, BC, Canada, September 30, 2015.

[76] Whalen, E., *Aerodynamics of Runback Ice Accretions*, Ph.D. thesis, University of Illinois at Urbana-Champaign, 2007.

[77] Drela, M., *A User's Guide to MSES 3.05*, MIT Department of Aeronautics and Astronautics, July, 2007.

[78] Drela, M., *Two-Dimensional Transonic Aerodynamic Design and Analysis using the Euler Equations*, Ph.D. thesis, Massachusetts Institute of Technology, M.I.T. Report No. 187, 1986.

[79] Drela, M. and Giles, M. B., "ISES: A Two-Dimensional Viscous Aerodynamic Design and Analysis Code," AIAA Paper 86-0424, AIAA Aerospace Sciences Meeting, Reno, NV, 1986.

[80] Drela, M., Giles, M. B., and Thomkins, W. T., *Newton Solution of Coupled Euler and Boundary-Layer Equations*, Springer-Verlag, Numerical and Physical Aspects fo Aerodynamic Flows III, 1986.

[81] Giles, M. B. and Drela, M., "Two-Dimensional Transonic Aerodynamic Design Method," *AIAA Journal*, Vol. 25, No. 9, 1987, pp. 1199–1206.

[82] Mueller, T. J., editor, *XFOIL: An Analysis and Design System for Low Reynolds Number Airfoils*, Vol. 54, Springer, Low Reynolds Number Aerodynamics, Lecture Notes in Engineering, 1989.

[83] Drela, M., "Newton Solution of Coupled Viscous/Inviscid Multielement Airfoil Flows," AIAA Paper 90-1470, AIAA Fluid Dynamics, Plasma Dynamics, and Lasers Conference, Seattle, WA, 1990.

[84] Drela, M., "Improvements in Low Reynolds Number Airfoil Flow Predictions with ISES and XFOIL," Tech. rep., Massachusetts Institute of Technology, 1990.

[85] Drela, M., "Viscous and Inviscid Inverse Schemes Using Newton's Method," AGARD-FDP-VKI Lecture Series, Brussels, Belgium, 1990.

[86] Drela, M., "Design and Optimization Method for Multi-Element Airfoils," AIAA Paper 93-0969, AIAA Aerospace Design Conference, Irvine, CA, 1993.

[87] Bucci, G. S. and Sullivan, J. P., "An Experimental Simulation of High Lift Wake Flows at High Reynolds Number," AIAA Paper 97-2297, AIAA Applied Aerodynamics Conference, Atlanta, GA, 1997.

[88] Mughal, B. and Drela, M., "A Calculation Method for the Three-Dimensional Boundary-Layer Equations in Integral Form," AIAA Paper 93-0786, AIAA Aerospace Sciences Meeting, Reno, NV, 1993.

[89] Terry, E. L., *Extension of the Aerodynamic Design Program MSES for the Simulation of Boundary Layer Suction*, Master's thesis, Delft University of Technology, 2004.

[90] Drela, M. and Giles, M. B., "Viscous-Inviscid Analysis of Transonic and Low Reynolds Number Airfoils," *AIAA Journal*, Vol. 25, No. 10, 1987, pp. 1347–1355.

[91] Frink, N. T., Pirzadeh, S. Z., Parikh, P. C., Pandya, M. J., and Bhat, M. K., "The NASA Tetrahedral Unstructured Software System (TetrUSS)," *The Aeronautical Journal*, Vol. 104, No. 1040, October 2000, pp. 491–499.

[92] Pandya, M., Frink, N. T., Abdol-Hamid, K., Samareh, J., Parlette, E., and Taft, J., "Enhancements to TetrUSS for NASA Constellation Program," AIAA Paper 2011-1111, AIAA Aerospace Sciences Meeting, Orlando, FL, 2011.

[93] Samareh, J., "GridTool: A Surface Modeling and Grid Generation Tool," Proceedings of the Workshop on Surface Modeling, Grid Generation, and Related Issues in CFD Solutions, NASA CP-3291, May 9-11, 1995.

[94] Frink, N. T., "Salient Features of USM3D Version 6.0," NASA Langley, 2003.

[95] Pirzadeh, S. Z., "Structured Background Grids for Generation of Unstructured Grids by Advancing Gront Method," *AIAA Journal*, Vol. 31, 1993, pp. 257–265.

[96] Samareh, J., "Unstructured Grids on NURBS Surfaces," AIAA Paper 1993-3454, 1993.

[97] Pirzadeh, S. Z., "Unstructured Viscous Grid Generation by Advancing-Layers Method," *AIAA Journal*, Vol. 32, No. 8, August 1994, pp. 1735–1737.

[98] Pirzadeh, S. Z., "Three-Dimensional Unstructured Viscous Grids by the Advancing-Layers Method," *AIAA Journal*, Vol. 34, No. 1, January 1996, pp. 43–49.

[99] Pirzadeh, S. Z., "An Adaptive Unstructured Grid Method by Grid Subdivision, Local Remeshing, and Grid Movement," AIAA 1999-3255, 1999.

[100] Pope, S. and Viken, S., *GridTool Training Manual*, Computer Sciences Corporation, 2003.

[101] Frink, N. T., *Three-Dimensional Upwind Scheme for Solving the Euler Equations on Unstructured Tetrahedral Grids*, Ph.D. thesis, Virginia Polytechnic and State University, 1991.

[102] Wang, Q., Massey, S. J., and Abdol-Hamid, K. S., "Implementation of Advanced Two Equation Turbulence Models in the USM3D Unstructured Flow Solver," NASA CR-2000-210102, April 2000.

[103] Gopalarathnam, A. and Selig, M. S., "A Multipoint Inverse Method for Multi-Element Airfoil Design," AIAA Paper 96-2396, 1996.

[104] Selig, M. S. and Maughmer, M. D., "A Multipoint Inverse Airfoil Design Based on Conformal Mapping," *AIAA Journal*, Vol. 30, No. 5, May 1992, pp. 1162–1170.

[105] Selig, M. S. and Maughmer, M. D., "Generalized Multipoint Inverse Airfoil Design," *AIAA Journal*, Vol. 30, No. 11, November 1992, pp. 2618–2625.

[106] Selig, M. S., "Low Reynolds Number Airfoil Design Lecture Notes," NATO-RTO-VKI Lecture Series, 2003.

[107] Selig, M. S. and Guglielmo, J. J., "High-Lift Low Reynolds Number Airfoil Design," *Journal of Aircraft*, Vol. 34, No. 1, January-February 1997, pp. 72–70.

[108] Selig, M. S., "Multipoint Inverse Design of an Infinite Cascade of Airfoils," *AIAA Journal*, Vol. 32, No. 4, April 1994, pp. 774–782.

[109] Selig, M. S., *PROFOIL: A Multipoint Inverse Airfoil Design Method*, University of Illinois at Urbana-Champaign.

[110] Stevens, W. A., Coradia, S. H., and Braden, J. A., "Mathematical Model for Two-Dimensional Multi-Component Airfoils in Viscous Flows," NASA CR-1843, 1971.

[111] Morgan, H. L., "A Computer Program for the Analysis of Multi-Element Airfoils in Two-Dimensional, Subsonic, Viscous Flow," NASA SP-347, March 1975.

[112] Gopalarathnam, A. and Selig, M. S., "A Multipoint Viscous Design Method for Multi-Element Airfoils," AIAA Paper 98-2404, AIAA Applied Aerodynamics Conference, Albuquerque, NM, 1998.

[113] Gopalarathnam, A., *Hybrid Methods for Inverse Aerodynamic Design*, Ph.D. thesis, University of Illinois at Urbana-Champaign, 1999.

[114] Gopalarathnam, A., "Multipoint Inverse Method for Multielement Airfoil Design," *Journal of Aircraft*, Vol. 35, No. 3, May-June 1998, pp. 398–404.

[115] Saeed, F. and Selig, M. S., "A Multipoint Inverse Airfoil Design Method for Slot-Suction Airfoils," AIAA Paper 95-1857-CP, AIAA Applied Aerodynamics Conference, San Diego, CA, 1995.

[116] Broughton, B. A., *A Hybrid Inverse Design Method for Compled Aerodynamic and Hydrodynamic Geometries*, Ph.D. thesis, University of Illinois at Urbana-Champaign, 2004.

[117] Gopalarathnam, A., Broughton, B. A., McGranahan, B. D., and Selig, M. S., "Design of Low Reynolds Number Airfoils with Trips," *Journal of Aircraft*, Vol. 40, No. 4, July-August 2003, pp. 768–775.

[118] Bruun, H. H., *Hot-Wire Anemometry: Principles and Signal Analysis*, Oxford Science Publications, New York, New York, 1995.

[119] Siddal, R. G. and Davies, T. W., "An Improved Response Equation for Hot-Wire Anemometry," *International Journal of Heat and Mass Transfer*, Vol. 15, No. 2, 1972, pp. 367–368.

[120] Smol'yakov, A. V. and Tkachenko, V. M., *The Measurement of Turbulent Fluctuations: An Introduction to Hot-Wire Anemometry and Related Transducers*, Springer-Verlag, 1983.

[121] Schetz, J. A. and Fuhs, A. E., *Handbook of Fluid Dynamics and Fluid Machinery: Experimental and Computational Fluid Dynamics*, Vol. II, John Wiley & Sons, Inc., 1996.

[122] Olin, J. G. and Kiland, R. B., "Split-Film Anemometer Sensor for Three-Dimensional Velocity-Vector Measurements," Symposium on Aircraft Wake Turbulence, pp 57-79, Seattle, WA, 1970.

[123] Seung-Ho, R., Chang, P. K., and Park, S. O., "A Modified Calibration Technique for the Split Film Sensor," *Journal of Measurement Science and Technology*, Vol. 1, No. 11, 1990, pp. 1076–1084.

[124] Spring, S. A., *An Experimental Mapping of the Flow Field Behind a Glaze Ice Shape on a NACA 0012 Airfoil*, Master's Thesis, Department of Mechanical and Aerospace Engineering, The Ohio State University, Columbus, OH, 1987.

[125] Gallington, R. W., "Measurement of Very Large Flow Angles with Non-Nulling Seven-Hole Probes," Department of Aeronautics, United States Air Force Academy, Colorado Springs, CO, USAFA-TR-80-17, 1980.

[126] Gerner, A. A., Maurer, C. L., and Gallington, R. W., "Non-Nulling Seven-Hole Probes for High-Angle Flow Measurement," *Experiments in Fluids*, Vol. 2, No. 2, 1984, pp. 95–103.

[127] Crawford, J. D., *Design and Calibration of Seven-Hole Probes for Flow Measurement*, Master's thesis, Department of Mechanical and Materials Engineering, Queen's University, Kingston Ontario Canada, 2011.

[128] Zilliac, G. G., "Calibration of Seven-Hole Pressure Probes for Use in Fluid Flows with Large Angularity," NASA TM 102200, 1989.

[129] Zilliac, G. G., "Modelling, Calibration, and Error Analysis of Seven-Hole Pressure Probes," *Experiments in Fluids*, Vol. 14, 1993, pp. 104–120.

[130] Deters, R. W., *Performance and Slipstream Characteristics of Small-Scale Propellers at Low Reynolds Numbers*, Ph.D. thesis, Department of Aerospace Engineering, University of Illinois at Urbana-Champaign, Urbana IL, 2014.

[131] Coleman, H. and Steele, G., *Experimentation, Validation, and Uncertainty Analysis for Engineers*, Wiley-Interscience, 2009.

[132] Turner, P. R., *Guide to Scientific Computing*, Macmillan, New York, NY, pp 74-93, 2001.

[133] Tryggvason, G., "Elementary Grid Generation and Bilinear Interpolation," University of Notre Dame, lecture notes for AME 90936: Computational Fluid Mechanics, 2013.

[134] Wang, Y., Yagola, A., and Yang, C., *Optimization and Regularization for Computational Inverse Problems and Applications*, pp 22-34, 65-105, Springer, New York, NY, 2010.

[135] Gruber, M., *Improving Efficiency by Shrinkage: The James-Stein and Ridge Regression Estimators*, Marcel Dekker, New York, NY, pp 111-166, 1998.

[136] Engl, H., Hanke, M., and Neubauer, A., *Regularization of Inverse Problems*, pp 49-153, Dordrecht, Boston, MA, 1996.

[137] Kintaar, J., "Introduction to Regularizing 3D Data," notes published July 22, 2013.

[138] Kintaar, J., "RegularizeData3D Software Package," Version 1.1, 2014.

[139] Hogg, R. V. and Tanis, E. A., *Probability and Statistical Inference*, Pearson, Upper Saddle River, NJ, 8th ed., pp190-196, 2010.

[140] Devore, J. and Farnum, N., *Applied Statistics for Engineers and Scientists*, Thomson Brooks/Cole, New York, NY, pp 116-140, 2005.

[141] Pomeroy, B. W., Diebold, J. M., Ansell, P. J., and Selig, M. S., "Study of Burst Wakes in a Multielement Airfoil Flowfield," *AIAA Journal*, Vol. 52, No. 4, April 2014, pp. 821–831.

[142] Ligrani, P. M., Singer, B. A., and Baun, L. R., "Spatial Resolution and Downwash Velocity Corrections for Multiple-Hole Pressure Probes in Complex Flows," *Experiments in Fluids*, Vol. 7, 1989, pp. 424–426.

[143] Glahn, A., Hallmann, M., Jeckel, R., and Wittig, S., "Advanced Pneumatic Method for Gradient Flow Analysis," *Experiments in Fluids*, Vol. 15, 1993, pp. 219–226.

[144] Chernoray, V. and Hjärne, J., "Improving the Accuracy of Multihole Probe Measurements in Velocity Gradients," Proceedings of ASME Turbo Expo 2008, GT2008-50492, 2008.

[145] Scribner, C., *The Effect of Turbulence Intensity and Reynolds Number on the Aerodynamic Behaviour of Kiel, Three-Hole, and Seven-Hole Pressure Probes*, Master's thesis, Carleton University, 2011.

[146] Dominy, R. G. and Hodson, H. P., "An Investigation of Factors Influencing teh Calibration of Five-Hole Probes for Three-Dimensional Flow Measurements," *Journal of Turbomachinery*, Vol. 115, 1993, pp. 513–519.

[147] Takahashi, T. T., "Measurement of Air Flow Characteristics Using Seven Hole Cone Probes," AIAA Paper 1997-0600, AIAA Aerospace Sciences Meeting, Reno, NV, 1997.

[148] Diebold, J. M., "Development of a Wake-Survey Technique for Turbulent Flows: With Application to Swept-Wing Icing Aerodynamics," Preliminary Examination Research Proposal, Department of Aerospace Engineering, University of Illinois at Urbana-Champaign, May 2015.

[149] Tavoularis, S., *Measurement in Fluid Mechanics*, Cambridge University Press, London, England, 2005.

[150] Pope, S. B., *Turbulent Flows*, Cambridge University Press, London, England, 2000.

[151] White, F. M., *Viscous Fluid Flow*, McGraw Hill, New York, NY, 2006.

[152] Johnson, D. A., Menter, F. R., and Rumsey, C. L., "The Status of Turbulence Modeling for External Aerodynamics," AIAA Paper 94-2226, AIAA Fluid Dynamics Conference, Colorado Springs, CO, 1994.

[153] Beguier, C., Giralt, F., and Fulachier, L., "Negative Production in Turbulent Shear Flows," *Structure and Mechanisms of Turbulence II*, edited by H. Fiedler, Vol. 76, Lecture Notes in Physics, Universität Berlin, 1977, pp. 22–35.

[154] Figliola, R. S. and Beasley, D. E., *Theory and Design for Mechanical Measurements*, John Wiley & Sons, Inc., 2006.

[155] Bendat, J. S. and Piersol, A. G., *Random Data: Analysis and Measurement Procedures*, John Wiley & Sons, Inc., 2000.

[156] Drela, M., "MSES Domain Size Sensitivity Study," MIT Department of Aeronautics and Astronautics, September, 1996.

[157] Lambert, J. D., *Numerical Methods for Ordinary Differential Systems*, John Wiley & Sons, Inc., 1991.

[158] Paschal, K., Goodman, W., McGhee, R., Walker, B., and Wilcox, P., "Evaluation of Tunnel Sidewall Boundary-Layer Control Systems for High-Lift Airfoil Testing," AIAA Paper 91-3248, AIAA Applied Aerodynamics Conference, Baltimore, MD, 1991.

[159] Simpson, R. L., "Junction Flows," *Annual Review of Fluid Mechanics*, Vol. 33, 2001, pp. 415–443.

[160] Quest, J., Wright, M., Hansen, H., and Mesuro, G., "First Measurements on an Airbus High Lift Configuration at ETW up to Flight Reynolds Number," AIAA Paper 2002-0423, AIAA Aerospace Sciences Meeting, Reno, NV, 2002.

[161] Perry, A. T. and Pomeroy, B. W., "Geometric Effects on the Performance and Wake Development of a Multi-element Airfoil System," AIAA Region III Student Paper Competition, Wright State University, Dayton, OH, 2015.

[162] Chung, T. J., *Computational Fluid Dynamics*, Cambridge University Press, London, England, 2002.